frontiers | Research Topics

Model-informed decision making in the preclinical stages of pharmaceutical research and development

Edited by
Rui Li, Donald E. Mager, Alison Betts, Tristan Scott Maurer, Morgan Craig and David Z. D'Argenio

Published in
Frontiers in Pharmacology
Frontiers in Bioinformatics

ISSN 1664-8714
ISBN 978-2-8325-1476-4
DOI 10.3389/978-2-8325-1476-4

About Frontiers

Frontiers is more than just an open access publisher of scholarly articles: it is a pioneering approach to the world of academia, radically improving the way scholarly research is managed. The grand vision of Frontiers is a world where all people have an equal opportunity to seek, share and generate knowledge. Frontiers provides immediate and permanent online open access to all its publications, but this alone is not enough to realize our grand goals.

Frontiers journal series

The Frontiers journal series is a multi-tier and interdisciplinary set of open-access, online journals, promising a paradigm shift from the current review, selection and dissemination processes in academic publishing. All Frontiers journals are driven by researchers for researchers; therefore, they constitute a service to the scholarly community. At the same time, the *Frontiers journal series* operates on a revolutionary invention, the tiered publishing system, initially addressing specific communities of scholars, and gradually climbing up to broader public understanding, thus serving the interests of the lay society, too.

Dedication to quality

Each Frontiers article is a landmark of the highest quality, thanks to genuinely collaborative interactions between authors and review editors, who include some of the world's best academicians. Research must be certified by peers before entering a stream of knowledge that may eventually reach the public - and shape society; therefore, Frontiers only applies the most rigorous and unbiased reviews. Frontiers revolutionizes research publishing by freely delivering the most outstanding research, evaluated with no bias from both the academic and social point of view. By applying the most advanced information technologies, Frontiers is catapulting scholarly publishing into a new generation.

What are Frontiers Research Topics?

Frontiers Research Topics are very popular trademarks of the *Frontiers journals series*: they are collections of at least ten articles, all centered on a particular subject. With their unique mix of varied contributions from Original Research to Review Articles, Frontiers Research Topics unify the most influential researchers, the latest key findings and historical advances in a hot research area.

Find out more on how to host your own Frontiers Research Topic or contribute to one as an author by contacting the Frontiers editorial office: frontiersin.org/about/contact

Model-informed decision making in the preclinical stages of pharmaceutical research and development

Topic editors

Rui Li — Pfizer, United States
Donald E. Mager — University at Buffalo, United States
Alison Betts — Applied BioMath, United States
Tristan Scott Maurer — Pfizer, United States
Morgan Craig — University of Montreal, Canada
David Z. D'Argenio — University of Southern California, United States

Citation

Li, R., Mager, D. E., Betts, A., Maurer, T. S., Craig, M., D'Argenio, D. Z., eds. (2023). *Model-informed decision making in the preclinical stages of pharmaceutical research and development*. Lausanne: Frontiers Media SA. doi: 10.3389/978-2-8325-1476-4

Table of contents

frontiers | Frontiers in Pharmacology

TYPE Editorial
PUBLISHED 12 April 2023
DOI 10.3389/fphar.2023.1184914

OPEN ACCESS

EDITED AND REVIEWED BY
Luciana Scotti,
Federal University of Paraíba, Brazil

*CORRESPONDENCE
Rui Li,
Rui.Li5@pfizer.com

SPECIALTY SECTION
This article was submitted to Experimental Pharmacology and Drug Discovery, a section of the journal Frontiers in Pharmacology

RECEIVED 12 March 2023
ACCEPTED 27 March 2023
PUBLISHED 12 April 2023

CITATION
Li R, Craig M, D'Argenio DZ, Betts A, Mager DE and Maurer TS (2023), Editorial: Model-informed decision making in the preclinical stages of pharmaceutical research and development. *Front. Pharmacol.* 14:1184914. doi: 10.3389/fphar.2023.1184914

Editorial: Model-informed decision making in the preclinical stages of pharmaceutical research and development

Rui Li[1]*, Morgan Craig[2,3], David Z. D'Argenio[4], Alison Betts[5], Donald E. Mager[6,7] and Tristan S. Maurer[1]

[1]Translational Modeling and Simulation, Medicine Design, Pfizer Inc., Cambridge, MA, United States, [2]Department of Mathematics and Statistics, Université de Montréal, Montréal, QC, Canada, [3]Sainte-Justine University Hospital Research Centre, Montréal, QC, Canada, [4]Department of Biomedical Engineering, University of Southern California, Los Angeles, CA, United States, [5]Applied BioMath, LLC, Concord, MA, United States, [6]Department of Pharmaceutical Sciences, University at Buffalo, State University of New York, Buffalo, NY, United States, [7]Enhanced Pharmacodynamics, LLC, Buffalo, NY, United States

KEYWORDS

drug discovery, modeling and simulation, decision-making, preclinical-to-clinical translation, preclinical stage

Editorial on the Research Topic
Model-informed decision making in the preclinical stages of pharmaceutical research and development

Although late-stage clinical attrition has been long considered as the most significant issue facing the pharmaceutical industry, the probability of technical success in the clinic is largely related to decisions made years earlier in the preclinical stages of Research and Development (R&D); it is at these early stages that decisions are made regarding the molecular target, modality of intervention, drug design and clinical candidate selection. Accordingly, model-informed drug development approaches that have proven useful in the clinic (e.g., quantitative systems pharmacology (QSP) modeling, physiologically based pharmacokinetic (PBPK) modeling, pharmacokinetic-pharmacodynamic (PKPD) modeling) are increasingly leveraged to support decisions in the earlier preclinical stages of R&D. These advances, however, have not been well-represented in the literature. This topic illustrates efforts to apply modeling in target verification, lead compound optimization, clinical candidate selection, and human efficacious dose prediction, with an emphasis on how modeling and simulation is being used to advance hypothesis driven research and support decision making in preclinical research. As a collection, the papers included in this topic will allow researchers to better understand the impact and limitations that such modeling has in real-world drug research, and, in turn, facilitate insight and guidance for future research in quantitative pharmacological modeling and simulation.

Presented as a high-level overview, authors from several pharmaceutical companies shared their collective experiences about how modeling and simulation approaches have been used to inform various decision points from discovery to first-in-human clinical trials (Kondic et al., 2022). Target validation is considered as one of the main areas where QSP can impact drug discovery, however adoption of this approach is slow due to the multiscale nature and complexity of typical QSP models (Chelliah and van der Graaf, 2022). Diving in

further, Bansal et al. (Bansal et al., 2022) discuss the development of a novel QSP model to predict the drug dosing and affinity requirements for potential targets of the complement pathway. They used their model to test the feasibility of developing small- or large-molecule therapies targeting this pathway. Evaluation of the level of target engagement required for efficacy with a QSP model not only validates the feasibility of the targets, but also provides drug design teams with needed goals for identifying efficacious therapies for the feasible targets. Besides confidence in targets, successfully identifying a therapy also relies on forecasting the necessary dosing to achieve clinical efficacy. Three studies in our topic show how preclinical modeling and simulation approaches can be applied to compare and prioritize targets based on required levels of target engagement, and to identify the most promising clinical large-molecule candidates based on optimized human dosing regimens (Kapitanov et al., 2021; Dong et al., 2022; Marcantonio et al., 2022). A similar modeling strategy was also applied to predict the human efficacious dose of small-molecule NaV1.7 inhibitor (Ballard et al., 2021), and to validate a strategy to increase antibody penetration in solid tumors through transient inhibition of antibody-antigen binding (Bordeau et al., 2022).

Beyond prospective predictions, retrospective analysis of existing clinical data through PBPK modeling can provide valuable information about target engagement required for efficacy at the site of action that may not be easily assessed using experimental methods (Ayyar et al., 2022; Bloomingdale et al., 2022). These studies also help to bridge preclinical information with clinical outcome, hence facilitate future discovery and development of similar therapies. Dunlap and Cao (Dunlap and Cao, 2022) additionally discuss why careful consideration of the tissue microenvironment and physiology is critical for accurately predicting *in vivo* drug-target interactions and hence clinical outcomes.

Modeling preclinical data generated by novel tools can further help to better understand the system, facilitate applications of these tools in drug discovery, and provide the foundation for preclinical-to-clinical translation (Parra-Guillen et al., 2021; Lewin et al., 2022). Computational methods, including machine learning, are increasingly used in early drug discovery. A novel computational method to predict the synergistic effects of drug combinations is included in this topic (Nafshi and Lezon, 2021). More recently, Brubaker et al. (Brubaker et al., 2019) developed a method to computationally translate genomic responses to bridge the gaps between lab animals and human. This approach shows good promise for pushing the field of model-informed drug development forward, as translational modeling work is typically based on phenotypic data.

In conclusion, this topic highlights exciting new approaches to advance preclinical drug development and help reduce attrition along the drug development pipeline.

Author contributions

RL and MC drafted the manuscript; the rest of authors reviewed and edited the manuscript.

Acknowledgments

Authors would like to thank all the authors and reviewers for their contributions to this Research Topic.

Conflict of interest

RL and TSM are employed by Pfizer Inc., AB is employed by Applied Biomath, and DM was employed by Enhanced Pharmacodynamics, LLC.

The remaining authors declare that the research was conducted in the absence of any commercial or financial relationships that could be construed as a potential conflict of interest.

Publisher's note

References

Ayyar, V. S., Lee, J. B., Wang, W., Pryor, M., Zhuang, Y., Wilde, T., et al. (2022). Minimal physiologically-based pharmacokinetic (mPBPK) metamodeling of target engagement in skin informs anti-il17a drug development in psoriasis. *Front. Pharmacol.* 13, 862291. doi:10.3389/fphar.2022.862291

Ballard, J. E., Pall, P. S., Vardigan, J., Zhao, F., Holahan, M. A., Zhou, X., et al. (2021). Translational pharmacokinetic-pharmacodynamic modeling of NaV1.7 inhibitor MK-2075 to inform human efficacious dose. *Front. Pharmacol.* 12, 786078. doi:10.3389/fphar.2021.786078

Bansal, L., Nichols, E. M., Howsmon, D. P., Neisen, J., Bessant, C. M., Cunningham, F., et al. (2022). Mathematical modeling of complement pathway dynamics for target validation and selection of drug modalities for complement therapies. *Front. Pharmacol.* 13, 855743. doi:10.3389/fphar.2022.855743

Bloomingdale, P., Bumbaca-Yadav, D., Sugam, J., Grauer, S., Smith, B., Antonenko, S., et al. (2022). PBPK-PD modeling for the preclinical development and clinical translation of tau antibodies for Alzheimer's disease. *Front. Pharmacol.* 13, 867457. doi:10.3389/fphar.2022.867457

Bordeau, B. M., Abuqayyas, L., Nguyen, T. D., Chen, P., and Balthasar, J. P. (2022). Development and evaluation of competitive inhibitors of trastuzumab-HER2 binding to bypass the binding-site barrier. *Front. Pharmacol.* 13, 837744. doi:10.3389/fphar.2022.837744

Brubaker, D. K., Proctor, E. A., Haigis, K. M., and Lauffenburger, D. A. (2019). Computational translation of genomic responses from experimental model systems to humans. *PLoS Comput. Biol.* 15 (1), e1006286. doi:10.1371/journal.pcbi.1006286

Chelliah, V., and van der Graaf, P. H. (2022). Model-informed target identification and validation through combining quantitative systems pharmacology with network-based analysis. *CPT Pharmacometrics Syst. Pharmacol.* 11 (4), 399–402. doi:10.1002/psp4.12766

Dong, S., Nessler, I., Kopp, A., Rubahamya, B., and Thurber, G. M. (2022). Predictive simulations in preclinical oncology to guide the translation of biologics. *Front. Pharmacol.* 13, 836925. doi:10.3389/fphar.2022.836925

Dunlap, T., and Cao, Y. (2022). Physiological considerations for modeling *in vivo* antibody-target interactions. *Front. Pharmacol.* 13, 856961. doi:10.3389/fphar.2022.856961

Kapitanov, G. I., Chabot, J. R., Narula, J., Roy, M., Neubert, H., Palandra, J., et al. (2021). A mechanistic site-of-action model: A tool for informing right target, right compound, and right dose for therapeutic antagonistic antibody programs. *Front. Bioinform* 1, 731340. doi:10.3389/fbinf.2021.731340

Kondic, A., Bottino, D., Harrold, J., Kearns, J. D., Musante, C. J., Odinecs, A., et al. (2022). Navigating between right, wrong, and relevant: The use of mathematical modeling in preclinical decision making. *Front. Pharmacol.* 13, 860881. doi:10.3389/fphar.2022.860881

Lewin, T. D., Avignon, B., Tovaglieri, A., Cabon, L., Gjorevski, N., and Hutchinson, L. G. (2022). An *in silico* model of T cell infiltration dynamics based on an advanced *in vitro* system to enhance preclinical decision making in cancer immunotherapy. *Front. Pharmacol.* 13, 837261. doi:10.3389/fphar.2022.837261

Marcantonio, D. H., Matteson, A., Presler, M., Burke, J. M., Hagen, D. R., Hua, F., et al. (2022). Early feasibility assessment: A method for accurately predicting biotherapeutic dosing to inform early drug discovery decisions. *Front. Pharmacol.* 13, 864768. doi:10.3389/fphar.2022.864768

Nafshi, R., and Lezon, T. R. (2021). Predicting the effects of drug combinations using probabilistic matrix factorization. *Front. Bioinform* 1, 708815. doi:10.3389/fbinf.2021.708815

Parra-Guillen, Z. P., Freshwater, T., Cao, Y., Mayawala, K., Zalba, S., Garrido, M. J., et al. (2021). Mechanistic modeling of a novel oncolytic virus, V937, to describe viral kinetic and dynamic processes following intratumoral and intravenous administration. *Front. Pharmacol.* 12, 705443. doi:10.3389/fphar.2021.705443

frontiers in Pharmacology

ORIGINAL RESEARCH
published: 23 July 2021
doi: 10.3389/fphar.2021.705443

Mechanistic Modeling of a Novel Oncolytic Virus, V937, to Describe Viral Kinetic and Dynamic Processes Following Intratumoral and Intravenous Administration

*Zinnia P. Parra-Guillen[1,2], Tomoko Freshwater[3], Youfang Cao[3], Kapil Mayawala[3], Sara Zalba[1,2], Maria J. Garrido[1,2], Dinesh de Alwis[3] and Iñaki F. Troconiz[1,2]**

[1]Department of Pharmaceutical Technology and Chemistry, School of Pharmacy and Nutrition, University of Navarra, Pamplona, Spain, [2]IdiSNA, Navarra Institute for Health Research, Pamplona, Spain, [3]Merck & Co., Inc., Kenilworth, NJ, United States

V937 is an investigational novel oncolytic non-genetically modified Kuykendall strain of Coxsackievirus A21 which is in clinical development for the treatment of advanced solid tumor malignancies. V937 infects and lyses tumor cells expressing the intercellular adhesion molecule I (ICAM-I) receptor. We integrated *in vitro* and *in vivo* data from six different preclinical studies to build a mechanistic model that allowed a quantitative analysis of the biological processes of V937 viral kinetics and dynamics, viral distribution to tumor, and anti-tumor response elicited by V937 in human xenograft models in immunodeficient mice following intratumoral and intravenous administration. Estimates of viral infection and replication which were calculated from *in vitro* experiments were successfully used to describe the tumor response *in vivo* under various experimental conditions. Despite the predicted high clearance rate of V937 in systemic circulation ($t_{1/2}$ = 4.3 min), high viral replication was observed in immunodeficient mice which resulted in tumor shrinkage with both intratumoral and intravenous administration. The described framework represents a step towards the quantitative characterization of viral distribution, replication, and oncolytic effect of a novel oncolytic virus following intratumoral and intravenous administrations in the absence of an immune response. This model may further be expanded to integrate the role of the immune system on viral and tumor dynamics to support the clinical development of oncolytic viruses.

Keywords: viral dynamics, viral kinetics, mechanistic modeling, oncolytic virus, tumor distribution

OPEN ACCESS

Edited by:
Morgan Craig,
University of Montreal, Canada

Reviewed by:
Adrianne Jenner,
Queensland University of Technology, Australia
Martin Schepelmann,
Medical University of Vienna, Austria

****Correspondence:***
Iñaki F. Troconiz
itroconiz@unav.es

Specialty section:
This article was submitted to Experimental Pharmacology and Drug Discovery, a section of the journal Frontiers in Pharmacology

Received: *05 May 2021*
Accepted: *07 July 2021*
Published: *23 July 2021*

Citation:
Parra-Guillen ZP, Freshwater T, Cao Y, Mayawala K, Zalba S, Garrido MJ, de Alwis D and Troconiz IF (2021) Mechanistic Modeling of a Novel Oncolytic Virus, V937, to Describe Viral Kinetic and Dynamic Processes Following Intratumoral and Intravenous Administration. Front. Pharmacol. 12:705443. doi: 10.3389/fphar.2021.705443

INTRODUCTION

Over the past 4 decades, the oncology treatment landscape has dramatically changed with the development of advanced and targeted immunotherapies, which complement or even replace classical chemotherapy and radiotherapy strategies (Madden, 2018). Oncolytic virus therapy represents one such novel class of immunotherapy. Advantages of this approach rely on the ability of oncolytic viruses to selectively replicate in cancer cells without harming normal tissues. This process leads to a direct lysis of the tumor mass, as well as the generation of a *de novo* anti-tumor immune response or boosting of an existing one (Kaufman et al., 2015).

At present, talimogene laherparepvec (T-Vec or Imlygic®) with intratumoral (i.t) administration is the only FDA-approved oncolytic viral therapy for the treatment of melanoma patients with injectable but non-resectable lesions in the skin and lymph nodes (Pol et al., 2016). Nonetheless, several oncolytic viruses are currently in clinical development to target solid malignancies (Raja et al., 2018). While i. t. administration maximizes the viral load reaching the tumor, it is only feasible for accessible tumors. On the other hand, the intravenous (i.v.) administration would potentially expand oncolytic viral treatment to less accessible tumors as well as obviate the need for interventional radiology, among other benefits. However, systemic administration needs to overcome viral neutralization, liver and spleen sequestration, and vessel extravasation to exceed the a priori unknown "viremic threshold" above which tumor destruction can be achieved (Russell et al., 2012).

To date, there have been only a few published reports describing i. v. administration of oncolytic viruses in clinical trials. In these studies, viral levels as well as biological activities at tumor lesions were observed in some patients (Kaufman and Bommareddy, 2019), however, no evidence for clinical responses have been observed to date (Breitbach et al., 2011; Russell et al., 2014). Furthermore, the currently available data are from early clinical studies with a limited number of patients wherein the endpoints were focused on safety and tolerability rather than therapeutic activity.

In this regard, prior to embarking on large clinical trials, it may be prudent to understand the biology of oncolytic viruses delivery related to tumor response in more detail (Kaufman and Bommareddy, 2019) and mathematical models can provide a quantitative understanding of the biological processes that an oncolytic virus undergoes following different routes of administration.

Various mathematical models to characterize *in vitro* viral dynamics (Bagheri et al., 2011; Titze et al., 2017), *in vivo* behavior limited to tumor size metrics (Bajzer et al., 2008; Eftimie et al., 2011), theoretical frameworks (Wein et al., 2003; Mok et al., 2009; Paiva et al., 2009; Malinzi et al., 2017; Jenner et al., 2018; Cassidy and Humphries, 2019; Al-Tuwairqi et al., 2020) and develop predictive *in-silico* trials (Jenner et al., 2021) have been so far described. To the best of our knowledge, the integration of kinetic parameters including viral distribution to tumor lesions and comparing i. t. and i. v. administrations has not yet been addressed. A greater understanding of these parameters is critical to optimize dosing, schedules, and routes of administration of oncolytic viruses in clinical trial design.

V937 (formerly named CVA21) is a naturally occurring coxsackievirus currently under clinical development. *In vitro* (Shafren et al., 1997a) and *in vivo* (Shafren et al., 2004; Au et al., 2005) oncolytic activity of V937 has been demonstrated in preclinical studies. However, little is known regarding how V937 infection, replication, and tumor distribution *in vivo* relate to the anti-tumor response. The objective of this work was to develop a mechanistic quantitative framework to elucidate the interplay between viral kinetics, dynamics and viral distribution to tumor lesions and then link this information to an anti-tumor response following i. t. and i. v. administration in human xenograft tumor models in immunodeficient mice. The mechanistic model described here will provide the basis to integrate data related to immune response that would allow elucidation of an oncolytic virus driven anti-tumor response under various treatment regimens including combination with immune checkpoint inhibitors.

MATERIALS AND METHODS

Experimental Data

In vitro V937 replication data, *in vivo* V937 levels in sera and tumors, and tumor sizes in control and V937-treated mice in multiple human melanoma xenograft studies were integrated in the analysis to build the mechanistic model (raw data depicted in **Supplementary Figure 1**).

Unpublished in-house data and extracted data from published reports were both processed using R (R Project for Statistical Computing, RRID:SCR_001905) v3.6.1 through RStudio interface (RStudio, RRID:SCR_000432) v1.2.1335. In cases where data were only available from graphs, WebPlotDigitizer (WebPlotDigitizer, RRID:SCR_013996) software was used to extract mean profiles over time. Descriptions of the available data are as follows:

In Vitro Viral Replication

Data of V937 replication in two human melanoma cells lines SK-Mel-28 (NCI-DTP Cat# SK-MEL-28, RRID:CVCL_0526) and ME4405 (RRID:CVCL_C680) and a rhabdomyosarcoma cell line transfected with ICAM-1, RD-ICAM-1, were extracted from Au et al., 2005. In brief, cell monolayers in 6-well plates were treated with approximately 10^6 $TCID_{50}$ (half-maximal tissue culture infectious dose) of V937 over 1 h, however the number of seeded cells is not available. At the various time points (0, 2, 4, 6, 8, 10, 12, 24, and 48 h), the cell monolayers were lysed and the viral yield of the cell lysate was determined in triplicate using an end-point titration assay. Average viral titers were digitalized from reported graphs.

In Vivo Viral Kinetics

Viral RNA measurements of V937 in serum and tumor were obtained from an in-house experiment (**Table 1**).

Ethical review and approval were not required for the animal study as our work presents a modelling exercise on data already published for which the ethical approval was obtained at the time of experiments were performed (by others in other institutions).

Severe combined immunodeficient (SCID) mice were intradermally inoculated with 2×10^6 SK-Mel-28 cells in hind flank on Day −20 for tumor growth. On Day 0, animals were assigned into three groups (n = 16/group) with following treatment regimens: 1) a single i. v. dose of PBS (phosphate-buffered saline), 2) a single retro-orbital dose of 10^4 $TCID_{50}$ V937 (low dose) 3) a single retro-orbital dose of 10^7 $TCID_{50}$ V937 (high dose). Sera and tumors were harvested from two animals per group following euthanasia at various time points.

TABLE 1 | Design of *in vivo* experiments.

References	Mice strain	Mice (n)	$Cells_0$ (n)	TV_0 (mm^3)	Dose	Time points
			Viral kinetic data			
In-house[a]	SCID	16	2.10^6	50–150	1) PBS i.v 2) 10^4 $TCID_{50}$ i.v 3) 10^7 $TCID_{50}$ i.v	3, 6, 24, 48, 72, 168, 336, 408 h post-treatment
			Tumor growth data			
In-house[a]	SCID	4	2.10^6	50–150	1) PBS i.v 2) 10^4 $TCID_{50}$ i.v 3) 10^7 $TCID_{50}$ i.v	0, 14, 17 days post-treatment
Shafren (Shafren et al., 2004)	NOD SCID 4–6 weeks	5	2.10^5	100	1).PBS i.t 2) 10^3 $TCID_{50}$ i.t	0, 8, 14, 21, 30, 35 days post-treatment
	NOD SCID 4–6 weeks	5	2.10^5 per site (2 tumors/ mouse)	200–400	1) PBS i.t[b] 2) 10^3 $TCID_{50}$ i.t[b] 3) PBS i.v 4) 10^3 $TCID_{50}$ i.v	1, 17, 23, 30 days post-treatment
	NOD SCID 4–6 weeks	5	2.10^5	400–600	1) PBS i.t 2) 10 $TCID_{50}$ i.t 3) 10^b $TCID_{50}$ i.t 4) 10^3 $TCID_{50}$ i.t 5) 10^5 $TCID_{50}$ i.t	0, 7, 14, 21, 28, 35days post-treatment
Au (Au et al., 2005)	NOD SCID 4–6 weeks	10	10^6	250–500	1) none	28, 35, 42,49, 56 days post-inoculation

i. v., intravenous (retro-orbital); i. t., intratumoral; n, number of mice or inoculated cells ($cells_0$); NOD: nonobese diabetic; PBS: phosphate-buffered saline; s. c., subcutaneous; SCID, severe combined immunodeficiency; TV_0, tumor volume at the start of the treatment; TCID50: half-maximal tissue culture infectious dose.

[a]*Data from same experiment.*

[b]*Dose administered only to primary tumor site.*

V937 in sera was quantified by both real-time reverse transcriptase polymerase chain reaction (RT-qPCR) (copies/mL) and cell infectivity ($TCID_{50}$/mL), while V937 in tumor samples was quantified by real-time RT-PCR normalized by total RNA (copies/μg RNA). Viral levels were detected in all samples except for two tumor samples harvested at 3 h (low dose V937), and one sample harvested at 17 days (high dose V937).

In this experiment, tumor size was measured using calipers, and the average tumor volumes per group on Day 0 (n = 4), Day 14 (n = 4) and Day 17 (n = 2) were reported.

In Vivo Tumor Growth Inhibition

In addition to the average tumor volumes obtained from the *in vivo* V937 viral kinetic experiment, tumor size data from two publications (Shafren et al., 2004; Au et al., 2005) were compiled for the analysis. Experimental designs are detailed in **Table 1**.

In the studies described by Shafren et al., 2004, data were available from three experimental conditions: 1) single i. t. dose of V937 in mice bearing one tumor lesion, 2) single i. t. dose of V937 in one tumor lesion of mice bearing two tumor lesions, and 3) single i. v. dose of V937 in mice bearing two tumor lesions. In all cases, non-obese diabetic (NOD) SCID female mice were subcutaneously (s.c.) injected with 2×10^5 SK-Mel-28 cells in one or two flanks, and single injection of phosphate buffered saline (PBS) or V937 ($10–10^5$ $TCID_{50}$) was administered when tumors reached a predefined volume. Tumor volume was calculated using the formula for a spheroid. Tumor volumes, were recorded at regular intervals, and average tumor volume were digitalized for analysis.

In vivo growth rate of SK-Mel-28 in NOD-SCID mice following implant of 10^6 cells in one flank from Au et al., 2005 was combined with control groups in SK-Mel-28 study from Shafren et al., 2004 and used for model building.

In addition to SK-Mel-28 cell line, data from control and treated animals inoculated with ME4405 cells were available from Au et al., 2005. This information was used as validation (see Experimental data section of Supplementary Methods and Results for detailed description of experimental design).

Mechanistic-Based Model Building

The mechanistic model was built following a sequential and integrative approach (**Figure 1**). First, *in vitro* data were used to characterize dynamics of viral infectivity and replication. Following, *in vivo* viral kinetics, viral distribution in tumor and tumor growth were described taking into account the viral dynamic model previously developed.

The model, depicted in **Figure 2**, accounted for the following biological processes: 1) viral clearance from sera 2) viral distribution to tumor mass, 3) proliferation of tumor cells 4) uninfected tumor cells (uTC) to be infected by the virus, 5) viral replication in infected tumor cells (iTC), and 6) viral induced death of infected tumor cells.

The following subsections describe, 1) the final model structure and parameter estimates, 2) data analyses as methodology used to build the model, 3) model selection and evaluation.

Model Structure and Parameters

In Vitro *Viral Dynamic Model*

According to the viral mechanism of action and following classical mathematical structures for viral dynamics (Perelson,

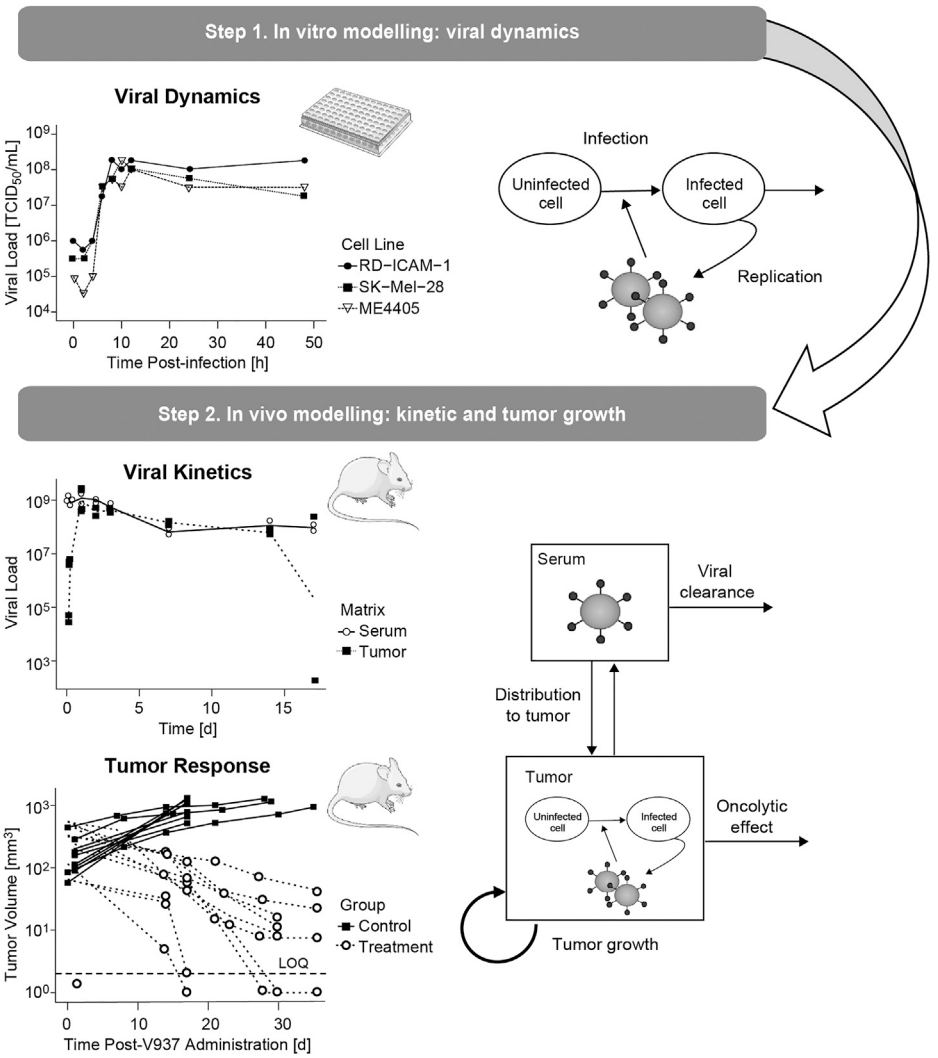

FIGURE 1 | Schematic representation of the modelling and data workflow, highlighting the key processes identified at each step.

2002b), the model described the time course of three main entities: uTC, iTC and viral load in the extracellular medium (VL_{EC}) as shown in **eqs. 1–3**.

uTC can proliferate with a net growth first order rate constant (λ) and be transformed to iTC in the presence of virus in the medium. This infectivity process takes place through a second order rate constant (β) that consumes both, viruses and uninfected tumor cells. Once cells are infected, V937 can replicate within iTC and generate copies of virions (α) per infected cells during its life span. Subsequently, iTC will be killed by viral induced cell death at a rate (δ). Extracellular virions can also be degraded with a first order rate constant (K_{VIR}).

$$\frac{duTC}{dt} = \lambda \times uTC - \beta \times uTC \times VL_{EC} \quad (1)$$

$$\frac{diTC}{dt} = \beta \times uTC \times VL_{EC} - \delta \times iTC \quad (2)$$

$$\frac{dVL_{EC}}{dt} = -\beta \times uTC \times VL_{EC} + \delta \times \alpha \times iTC - K_{VIR} \times VL_{EC} \quad (3)$$

The system was initialized to the administered dose ($TCID_{50}$) in the compartment of VL_{EC}, and number of seeded cells at confluence for uTC (1.2×10^6 cells/well[1]). iTC were considered to be zero at baseline.

Total predicted viral load, which is computed as the sum of viral load in the medium (VL_{EC}) and inside cells ($\alpha \times$ iTS), was fitted to measured viral concentrations from the *in vitro* replication experiment, using the volume of 3 ml per well of a 6-well plate.

Given the short duration of the *in vitro* evaluation, viral degradation and cell proliferation processes were considered

[1]https://www.thermofisher.com/es/es/home/references/gibco-cell-culture-basics/cell-culture-protocols/cell-culture-useful-numbers.html

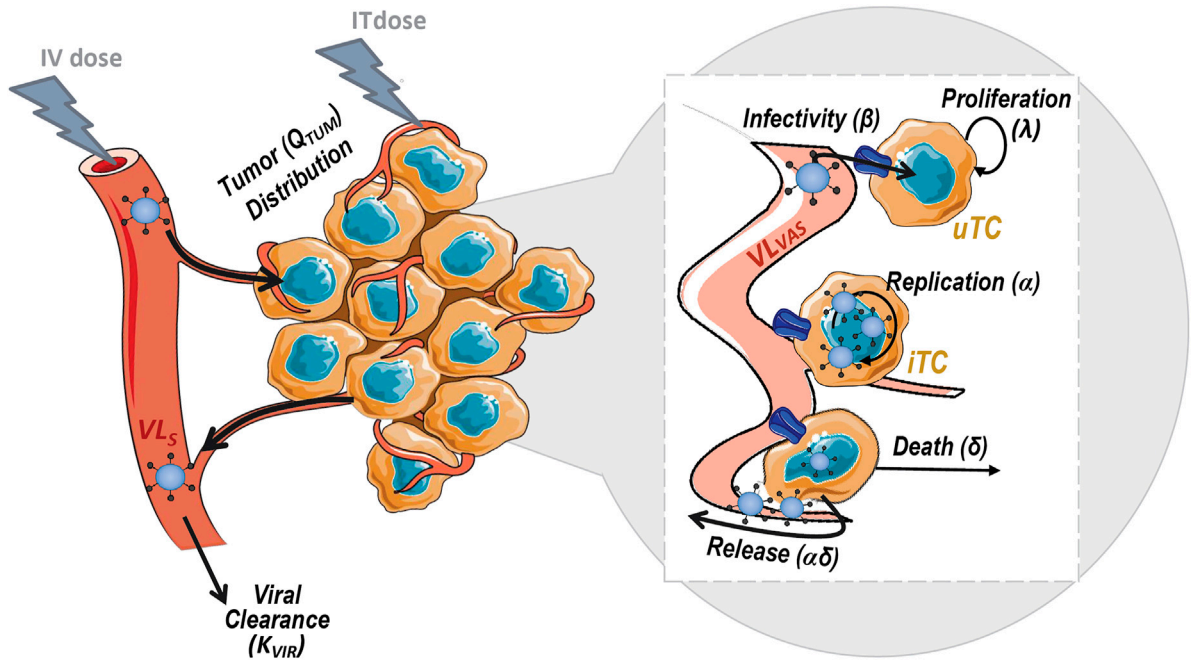

FIGURE 2 | Schematic representation of the mechanistic model for viral kinetics, viral dynamics and tumor growth. uTC, uninfected tumor cells; iTC, infected tumor cells; VL_S, serum viral load and VL_{VAS}, viral load in tumor vasculature.

negligible, and thus their respective parameters, K_{VIR} and λ, were assumed to be zero at this stage.

In Vivo *Viral Kinetic, Viral Dynamics and Tumor Growth Inhibition Model*

To characterize V937 viral kinetics *in vivo*, the time courses of V937 viral load in sera (VL_S) and tumor vasculature (VL_{VAS}) were modeled through a minimum physiological model (**eqs. 4–5**). Mouse-specific tumor blood flow (Q_{TUM};144 ml/d) (Baxter et al., 1995) and real organ volumes were used in the analysis. Tumor vascular volume (V_{VAS}) was assumed to be a 7% of total tumor volume at baseline and serum volume (V_S = 0.974 ml) was fixed at 55% (Baxter et al., 1995) of blood volume in mice [77 ml/kg for a 23 g mouse (Mitruka and Rawnsley, 1981)]. Viral elimination rate (K_{VIR}) and tumor retention factor representing viral affinity for the tumor (RF) were estimated as drug-specific parameters.

$$\frac{dVL_S}{dt} = -Q_{TUM} \times \left(\frac{VL_s}{V_s} - \frac{VL_{VAS}}{RF \times V_{VAS}}\right) - K_{VIR} \times VL_S \quad (4)$$

$$\frac{dVL_{VAS}}{dt} = Q_{TUM} \times \left(\frac{VL_s}{V_s} - \frac{VL_{VAS}}{RF \times V_{VAS}}\right) - \beta \times uTC \times VL_{VAS} + \delta \times \alpha \times iTC \quad (5)$$

The initial values of VL_S and VL_{VAS} at time 0 were set to the administered dose ($TCID_{50}$) and 0, respectively, following i. v. dose. In the case of i. t. administration, VL_S was initialized to 0 and VL_{VAS} to the administered dose at time 0. The kinetic model was linked to the previously developed viral dynamic model at tumor level replacing VL_{EC} by VL_{VAS} in **eqs. 1–2** as follows:

$$\frac{duTC}{dt} = \lambda \times uTC - \beta \times uTC \times VL_{VAS} \quad (6)$$

$$\frac{diTC}{dt} = \beta \times uTC \times VL_{VAS} - \delta \times iTC \quad (7)$$

As for the *in vitro* model, uTC compartment was initialized to the number of initial tumor cells that were derived from measured tumor size at baseline, and iTC was assumed to be zero at baseline.

To identify K_{VIR} and RF drug parameters, predicted viral load concentration in serum (VL_S/V_S in $TCID_{50}$/mL or copies/mL after correction by a factor accounting for the ratio between TCI50 and copies, referred to as RATIO) and in tumor [computed as the sum of vascular, VL_{VAS}, and intracellular levels, $\alpha \times$ iTS, normalized by an estimated factor to account for the amount of RNA (μg) per tumor volume unit, RNAVOL], were fitted to experimental levels of V937 in sera and tumor over time (see *In Vivo Viral Kinetic Experimental Data* section). The parameters α and β were fixed to those obtained *in vitro*, while λ and δ parameters, considered to vary between *in vitro* and *in vivo* experimental scenarios, were estimated by fitting tumor size model predictions (uTC + iTC) to experimental tumor size data (see *Tumor Growth Inhibition Experimental Data* section). Note that tumor size was measured in mm^3 while uTC and iTC are expressed as cell units, therefore a standard conversion factor of 10^6 cells per mm^3 was used (Makkat et al., 2007).

In addition, a proportionality ratio (RATIO) between $TCID_{50}$ and copies was computed to account for the conversion between both metrics as the model describes the dynamics of TCID50/mL and copies/mL, assuming that both variables have same time course but different magnitude.

Data Analysis

For *in vitro* or *in vivo* viral levels, each observation was obtained from a different well or animal; therefore, a naïve pool approach was used (i.e. data were pooled together and analyzed as coming from one single ID). For tumor size data *in vivo*, each mean profile was considered as an independent animal, thus enabling the use of the population approach to characterize inter-subject variability in model parameters as well as residual error.

The software NONMEM 7.4 (NONMEM, RRID: SCR_016986) and the First Order Conditional Estimation method with interaction algorithm were used for the analysis.

Data were logarithmically transformed during the analysis and an additive error model in the logarithmic scale was used to account for the discrepancies between model predictions and observations. A different residual error for each measurement was considered. When the population approach was applied the inter-subject variability was modelled exponentially (Kiang et al., 2012; Mould and Upton, 2012).

Model Selection and Evaluation

Model selection was largely driven by biological plausibility and capability of the model to describe the tendency of the data, taking into account also 1) parameter precision, 2) classical goodness-of-fit plots including observation versus model prediction and conditional weighted residuals over time or over model predictions, and 3) objective function value (OFV, approximately equal to -2xlog- likelihood). When models were nested, a drop of 3.84 or 6.63 in OFV was considered significant at the levels of 5 and 1%, respectively.

Model Exploration

The dynamics of the different entities of the system were explored over the range of evaluated dose levels ($10–10^7$ $TCID_{50}$), comparing outcome after i. v. or i. t. administration including one or two tumor lesions, the latter allowing for exploration of abscopal effects.

In addition, a parameter scan was performed varying one parameter at a time to explore its impact on viral levels and tumor response for selected design scenarios. During the simulation step,, a function (FMOI) was introduced at the infectivity term: $FMOI \times \beta \times uTC \times VL_{VAS}$; this was used to avoid infectivity of cells at very low virus levels just because high number of uninfected tumor cells in a continuous manner, rather than setting viral levels to zero at random value. This function cancels the infection of new cells when the viruses are too low compared to the number of total cells, with FMOI defined as follows:

$$FMOI = \frac{MOI}{MOI + MOI_{50}} \quad (8)$$

Where MOI (multiplicity of infection) is computed as the ratio between viral load levels in the vasculature and total tumor burden (iTS + uTS) and MOI_{50} represents the MOI at which 50% of maximum infectivity is obtained. After a sensitivity analysis, MOI_{50} was fixed to a low value (10^{-6}) that did not affect model characterization of the experimental data.

Simulations were performed in Berkeley-Madonna software (v9.2.1) and plotted in R (v3.6.1) through RStudio interface (v1.2.1335).

Sensitivity Analysis

To evaluate the impact of simultaneously varying all parameters on model output, a global sensitivity analysis was performed following the approximation technique described by Saltelli et al., 2008; Saltelli et al., bib_Saltelli_et_al_2010**2010** of the Sobol's method (Sobol′, 2001) using the SAFE toolbox available as R package (Pianosi et al., 2015), where to have even probabilities of sampling parameters differing in several order of magnitudes the latin hypercubic sampling method from a uniform distribution was used. Tumor size at day 14 was selected as the variable to represent drug response for model output.

Model Applicability

The combined impact of the most influential parameters was explored for two-by-two combinations of different dose levels and dosing routes. To do so, a virtual population (n = 1,000) was simulated varying all other parameters but those of interest (i.e. α and β, α and RF or β vs RF) following the same sampling approach as described for the global sensitivity analysis.

Tumor size profiles of the virtual population were then simulated using combinations of the two parameters of interest over the plausible parameter space. Probability of response under the different scenarios (i.e. combination of parameters, dose levels and dosing routes) was computed as the probability of observing at least 20% tumor shrinkage at day 14.

RESULTS

In Vitro Viral Dynamic Model

The levels of viral load obtained *in vitro* showed an initial decay reflecting infectivity, followed by a rapid increase up to 10^8 $TCID_{50}$/mL, 8–12 h post-infection, indicating viral production (raw data depicted in **Supplementary Figure 1A**).

Due to the availability of only total viral levels, it was not feasible to account for intracellular viral production and subsequent release to the cytoplasm as independent processes. Describing viral replication as a unique process dependent on both cell death and number of copies per cell allowed us to 1) obtain precise estimates of viral infectivity and production and 2) account for intracellular levels without increasing model complexity. As expected from the quick viral plateau reached *in vitro*, a fast death rate constant (δ) was identified, although with low precision due to the lack of cell death time profiles. Accounting for degradation of virus in the medium provided a very low estimate of viral clearance (K_{VIR}), suggesting this process could be neglected without affecting model performance

TABLE 2 | Parameter estimates of final models.

Parameter name	Description	Typical estimate (RSE)	Variability % (RSE)
Viral dynamics			
α ($TCID_{50}$/cell)	Viral particles released per infected cell	208 (27.2%)	
β (1/$TCID_{50}$/h)	Infectivity rate	0.489×10^{-8} (32%)	
$\delta_{invitro}$ (1/h)	Death rate of infected cells *in vitro*	55 (60.7%)	
$\delta_{invitro\_ME4405}$ (1/h)	Death rate of infected cells *in vitro* for ME4405 cell line	332 (58.4%)	
Error (log $TCIDI_{50}$/mL)	Additive residual error of viral load	0.958 (16.2%)	
Viral kinetics			
K_{VIR} (1/d)	Viral degradation rate	232 (14%)	
Q_{TUM} (ml/d)	Blood flow to tumor	144 FIX	
V_S (ml)	Serum volume	0.974 FIX	
F_{VAS} (unitless)	Fraction of tumor vascular volume	0.07 FIX	
RF (unitless)	Retention factor of V937 in the tumor	623 (12.4%)	
RATIO (copies/TCI_{50})	Number of copies per $TCDI_{50}$	170 (4.5%)	
RNAVOL (copies x μg RNA/$TCID_{50}$/mL)	Scaling factor to adjust for RNA levels in tumor	1,580 (50.1%)	
Error (log10 $TCIDI_{50}$/mL)	Additive residual error of serum V937 levels in $TCID_{50}$/mL	0.757 (8.8%)	
Error (log10 copies/mL)	Additive residual error of tumor V937 levels	0.807 (8.4%)	
Error (log10 copies/μg RNA)	Additive residual error of tumor V937 viral load	1.29 (11.2%)	
Tumor growth inhibition			
λ_1 (1/d)	Growth rate of primary lesion	0.0601 (6.8%)	
λ_2 (1/d)	Growth rate of secondary lesion	0.129 (11.1%)	
Tc_0_1 (mm^3)	Baseline tumor size of primary lesion	256 (19.1%)	62.5 (20%)
Tc_0_2 (mm^3)	Baseline tumor size of secondary lesion	148 (22.6%)	
δ_{invivo} (1/d)	Death rate of infected cells *in vivo*	0.17 (16.1%)	54.6 (21.6%)
Error (log10 mm^3)	Additive residual error of tumor size in log scale	0.227 (14.1%)	

($p > 0.05$), probably as a consequence of the short duration of the experiment.

Different α, β or δ parameter estimates for the three available cell lines (RD-ICAM-1, SK-Mel-28 and ME4405) were evaluated. Best results in terms of model performance and parameter precision were obtained using a different δ, estimated to be higher for ME4405 than for RD-ICAM-1 and SK-Mel-28. The use of the different δs provided a significant drop in objective function ($p < 0.05$) and improved parameter precision (from 100% error to less than 60%) (**Table 2**). Nonetheless, α and β estimates did not differ statistically across the three cell lines. Overall, a good description of the *in vitro* data was obtained (**Figure 3A**).

In Vivo Viral Kinetic and Tumor Growth Inhibition Model

I.V. administration of V937 at both 10^4 and 10^7 $TCID_{50}$ resulted in a rapid increase in V937 in sera and tumors, 6–24 h post administration. Despite the 3 log10 difference in dose (10^4 vs 10^7 $TCID_{50}$), similar viral concentrations were observed in plateau suggesting viral capability to replicate *in vivo* (raw data depicted in **Supplementary Figure 1B**).

A semi-physiological pharmacokinetic model that accounts for viral replication in the tumors provided a sufficient description of the available kinetic data in both serum and tumor. Infectivity (β) and replication (α) estimates were fixed to those obtained from the *in vitro* analysis, while physiological parameters (i.e. tumor blood flow, serum volume and fraction of tumor vasculature) were taken from the published literature. The rest of the model parameters were estimated. High V937 elimination ($t_{1/2\_KIV}$ ~4.3 min) and V937 tumor retention (RF), supported by the low initial viral levels and the capability of the virus to efficiently distribute to tumor and quickly replicate, were identified with good precision.

Regarding tumor size data, certain dose response could be identified, but no major differences across routes were experimentally detected, though large variability in tumor size at dosing time was observed (raw data depicted in **Supplementary Figure 1C**). When simultaneously modelling control and treated groups, exponential growth provided a better overall description ($p < 0.001$). Variability across mean tumor profiles was identified on baseline tumor cells and death rate of infected tumor cells. In addition, estimating different baseline and growth rate for secondary tumor lesions produced a significant ($p < 0.01$) decrease in OFV.

Acknowledging that tumor growth/shrinkage could also impact V937 viral distribution to the tumor (i.e. tumor blood flow), different models that assumed changes in Q_{TUM} with tumor mass were explored either assuming a proportional relationship between them (i.e. tumor blood flow and tumor mass) or as a power model that allow to account for the fact that not all tumor mass is perfusable (Ferl et al., 2005). None of the models was supported by the data, neither provided a different description of pharmacokinetic (PK) profiles and therefore this feature in the model was not included.

Overall, the final model was able to satisfactorily describe all sources of *in vivo* data simultaneously (**Figures 3A–C**) enabling precise parameter estimates (**Table 2**). Moreover, the final model structure could adequately describe the limited experimental tumor response data obtained when implanting ME4405 cell line in xenografts (see results section of **supplementary material**).

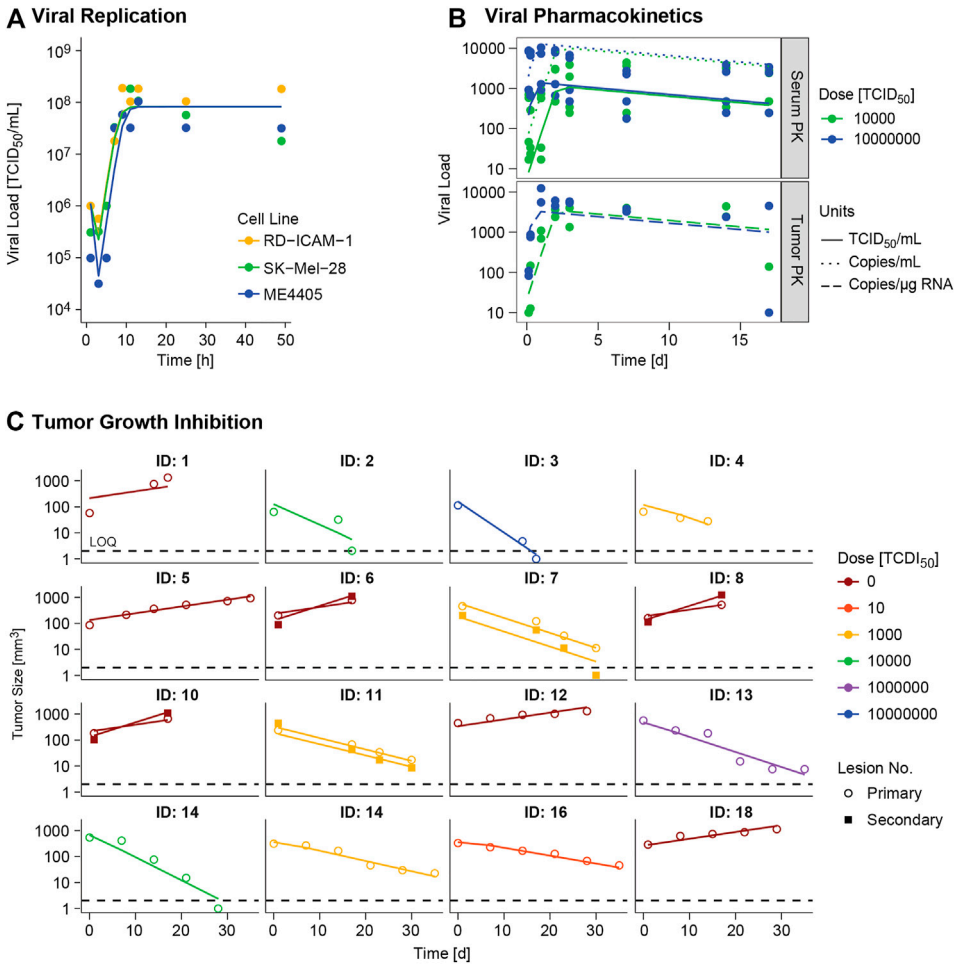

FIGURE 3 | Model evaluation. Model predictions (lines) versus real observations (dots) for **(A)** *in vitro* viral replication model and **(B)** *in vivo* viral kinetic model at typical level, and **(C)** tumor growth inhibition model at individual level for the different experimental scenarios. ID: individual. In panel A viral dynamics of RD-ICAM-1 and SK-Mel-28 are almost equivalent and model predictions appear superimposed.

Model Exploration

The final model was used to explore the behavior of the observed and unobserved elements of the system under different experimental scenarios.

Following i. v. or i. t. administration, V937 reaches a quick equilibrium of distribution between serum (VL_S) and tumor vasculature (VL_{VAS}) as shown in **Figure 4** and at both at the primary and secondary lesion as shown in **Supplementary Figure 2**. Given the estimated high tumor affinity and infectivity, the model predicts that the vast majority of cells get quickly infected (in less than 1 h at a dose of 10^4 $TCID_{50}$) and start to produce new viral copies that return to serum. This aspect, observed at all experimental doses available (**Supplementary Figure 3**), explains the increment in observed circulating levels, despite the fast viral degradation. Time to reach the maximum infectivity of tumor cells, and thus peak viral load levels, depends on both dose and initial tumor burden, with a shortening in time observed as dose level (**Supplementary Figure 3**) or tumor size increases (data not shown). Under these conditions, differences between routes of administration are mainly located at early time points, before maximum infectivity is achieved, but in all cases tumor response is ultimately attained, as also observed experimentally.

Sensitivity Analysis

The impact of varying one model parameter at a time within a plausible parameter space was evaluated as exemplified for α in **Figure 5A** and for the rest of model parameters in **Supplementary Figure 4**. Only changes in viral replication (α), viral infectivity (β) or tumor retention factor (RF) were able to invert the course of tumor response from cure to progression when parameter values were decreased. The rest of parameters showed an impact on the rate of response, like the infected cell death rate (δ), or minor influence on overall profiles, without changing tumor progression.

When performing a global sensitivity analysis to simultaneously explore the impact of model parameter changes on tumor response, similar results were obtained

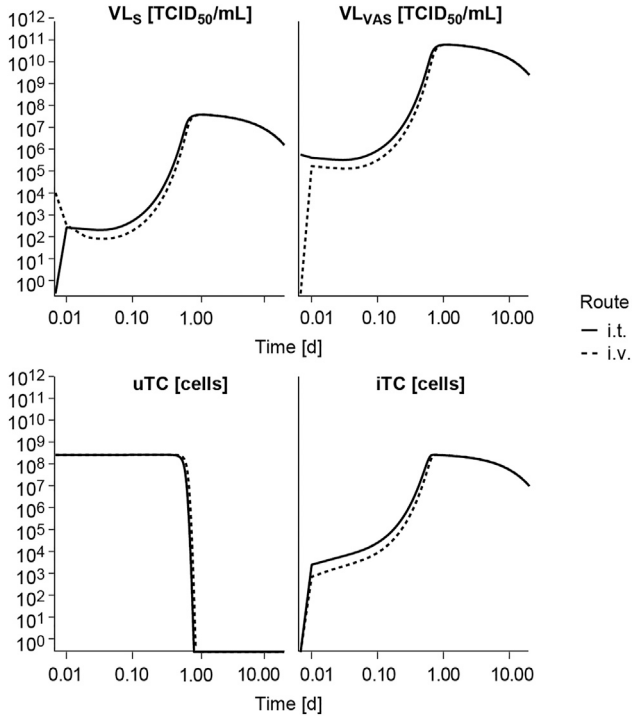

FIGURE 4 | Model exploration. Model predicted time course of the different entities following intravenous (i.v.) or intratumoral (i.t.) single administration of V937 at a dose levels of 10^4 $TCID_{50}$. VL_S, viral load in serum; VL_{VAS}, viral load in tumor vasculature; uTC, uninfected tumor cells; iTC, infected tumor cells. Log-log scale used.

(**Figure 5B**). α, β, RF and δ were the most influential parameters, accounting for around 10–16% of the variability in response as single parameters (first-order index), and 28–40% in total when taking into account the different doses evaluated and routes of administration (**Supplementary Figure 4**). These data highlight the importance of combined effects among parameters to explain model outcome. However, a different scenario is observed for the lowest dose of 10 $TCID_{50}$; this is due to the lack of infectivity and response for most of the simulated parameter vectors, thus leaving the rate of tumor growth and baseline tumor size as the most influential parameters determining tumor size outcome.

Model Applicability

The model was further evaluated to study the probability of observing a response (i.e. tumor shrinkage greater than 20%) for different two-by-two combinations of most influential model parameters with an impact on ultimate response.

This methodology allowed us to identify those areas where the probability of observing a response is almost null or very high, regardless of the combination of all other model parameters. As expected under this system, similar profiles were obtained after i. v. and i. t. administration, with slightly higher probability of response for the latter (data not shown). In all explored scenarios, increasing the dose translated into an increase in the probability of response, covering a wider area of the parameter space (**Figure 6**).

DISCUSSION

Mathematical modelling in immunology and virology has been extensively explored to provide a better understanding of the infection time course and to optimize viral therapies (Perelson, 2002a; Santiago et al., 2017). With the increasing interest in the use of oncolytic viruses in treating cancer, different models that integrate these concepts into a tumor dynamic environment have appeared (Santiago et al., 2017).

In this work, we present a modelling framework using ordinary differential equations that is capable of simultaneously accounting for three key processes of a novel oncolytic virus, V937, currently in clinical development: 1) capability to infect and replicate within tumor cells, 2) pharmacokinetics including distribution of V937 virus to tumor and 3) finally oncolytic V937 effects *in vivo*. To the best of our knowledge, this is the first time that distribution to tumor has been explicitly taken into account to enable characterization of different routes of administration.

To build the framework, an intermediate approach between the classical top-down and bottom-up approaches (i.e. data driven vs biology driven) was followed, thus balancing mechanistic knowledge and available data. Data from different sources, levels of information and even measurement units were integrated, highlighting the importance of quantitative models to combine and exploit experimental data as already shown in other therapeutic scenarios (Campagne et al., 2018; Parra-Guillen et al., 2020).

In this respect, the use of *in vitro* data to identify viral infectivity and replication processes, which are hard to identify only using *in vivo* data, has been of particular relevance. Parameter comparison with other viruses is not straight-forward as different dosing and measurement units (pfu, copies, $TCID_{50}$) are used across experiments. However, in absolute terms, V937 replication capability was within the reported ranges for oncolytic viruses of 50–1,350 virions/cell (Liu et al., 2000), which in most cases come from direct experimental observations and not from modelling exercises. Similarly, estimated *in vitro* death rate was in line with the upper ranges reported by Titze et al., 2017 (1.2–761 1/h) using a similar model structure, as well as the infectivity rate (0.35×10^{-8} to 0.98×10^{-8}). Nonetheless, larger intervals depending on the virus and cell type can be found in the literature for viral infectivity (10^{-7}–10^{-10}) (Bajzer et al., 2008; Mahasa et al., 2017; Cao et al., 2018).

V937 employs the intercellular adhesion molecule I (ICAM-I, CD54) receptor for attachment and viral entry (Shafren et al., 1997a; 1997b); this receptor is overexpressed in numerous malignant cells, including melanoma (Kageshita et al., 1993; Hayes and Seigel, 2009). V937 can also bind to the DAF receptor; however, it appears that DAF may function as a low-affinity attachment receptor either enhancing viral presentation or providing a viral sequestration site for subsequent high-affinity binding to ICAM-1 (Shafren et al., 1997b). Despite different ICAM-I expression in the three *in vitro* cell lines, differences in viral entry across cell lines could not be adequately identified. This could potentially be due to the experimental data and design, e.g. the lack of dose range as well as errors associated with end

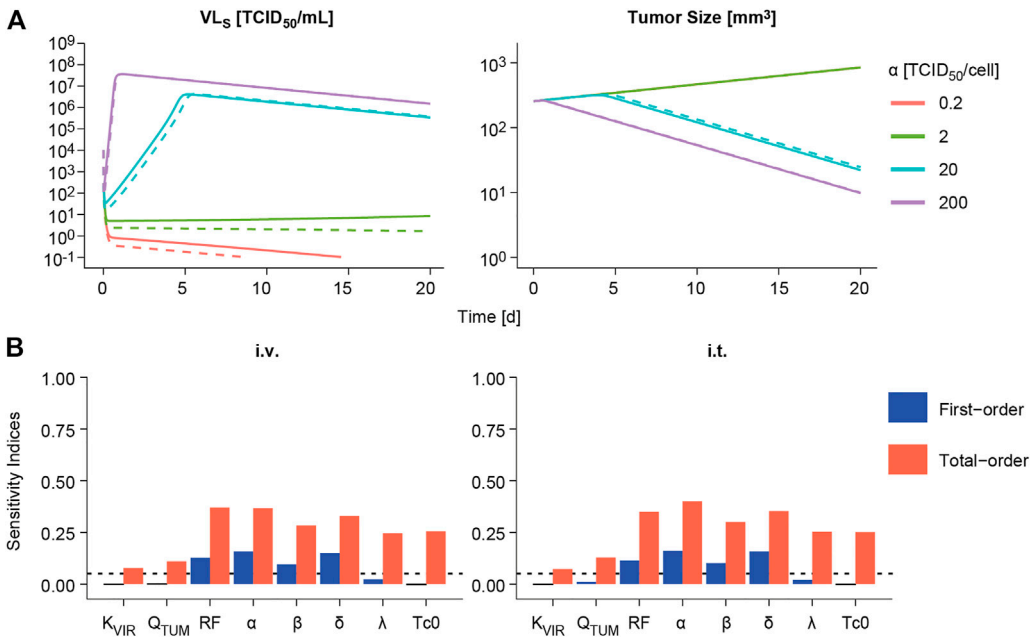

FIGURE 5 | Sensitivity analysis. **(A)** Impact of varying viral replication (α) parameter on the predicted time course of viral concentrations in viral load in serum **(**VL_S, **left panels)** and tumor size volume **(right panel)** following intravenous (dashed line) or intratumoral (solid line) administration of a single V937 dose of 10^4 $TCID_{50}$. **(B)**. First-order and total-order Sobol's sensitivity indices computed using model predicted tumor size at day 14 following intravenous (i.v.) or intratumoral (i.t.) single administration of a V937 dose of 10^4 $TCID_{50}$.

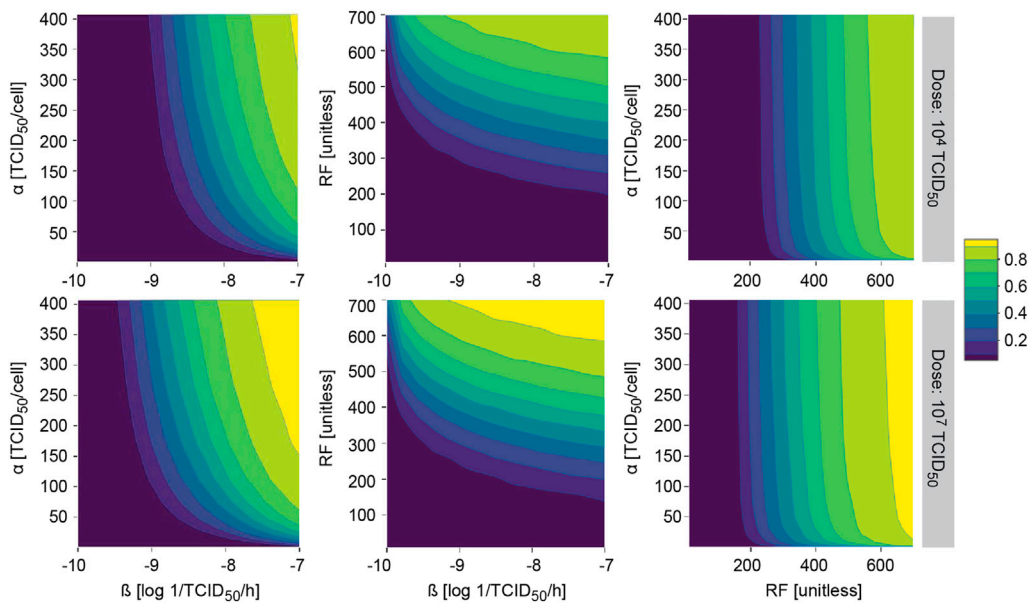

FIGURE 6 | Model applicability. Probability of observing at least 20% of tumor shrinkage at day 14 in a simulated virtual population at different two-by-two parameter combinations after single intratumoral dose. α, viral particles released per infected cell (viral production); β, viral infectivity; RF, retention factor.

point titration for $TCID_{50}$ assessment. However, it could also be due to a sufficiently high ICAM-1 expression levels in all cases (Au et al., 2005) compared to the threshold of 5,000 ICAM-1 molecules per cell required for V937 to exhibit *in vitro* activity (Annels et al., 2018). Nonetheless, and given the mechanistic nature of the model, additional data for example regarding ICAM-I expression could be easily introduced to further refine the model.

In the current model tumor cells infection is predicted to take place quickly and in less than a day due to either the high infectivity rate constant obtained *in vitro* in combination with the high predicted tumor levels after i. t. administration, or the fast tumor distribution and high tumor retention estimated after i. v. distribution. That critical aspect of the model has been explored carefully and is supported by the data. Specifically, viral replication *in vitro* indicated a fast infectivity process, with increasing viral levels reaching a plateau 8–12 h after V937 exposure. Moreover, it has been described that the virus is capable to trigger an extensive lytic destruction of melanoma cells 23 h after infection at a dose level of one TCID50/cell (Shafren et al., 2004), level similar to the one used *in vitro*. Regarding the vivo scenario, a sharp and sustained increase in viral levels at tumor is also observed after i. v. administration, despite the high viral clearance, supporting that infection and replication of the virus takes place fast, given the current model structure.

One novel aspect introduced in this work is the description of viral kinetics and viral distribution to tumor using a semi-physiological pharmacokinetic model that enables simultaneous description of both i. v. and i. t. administration routes. Viral measurements at tumor level are scarce in the literature (Kelly et al., 2008; Workenhe et al., 2014; Garcia-Carbonero et al., 2017; Andtbacka et al., 2019), and even more so over time. However, these types of data have been essential to characterize the tumor compartment in the model. In our modelling framework, the tumor was represented by two sub-compartments: 1) a vascular compartment in fast equilibrium with serum and 2) a cellular compartment which gets infected upon viruses arriving to the vascular compartment. A high retention of the virus at tumor level (RF = 623), which cannot be compared due to lack of literature data, and direct release of newly formed virions to the vascular compartment were required to successfully characterize the data behavior, suggesting no distribution limitations between serum and tumor in our preclinical setting. Moreover, an estimated half-life of 4.3 min, in line with the fast clearance observed for oncolytic viruses in clinical studies (Garcia-Carbonero et al., 2017), was obtained. This result indicates that the sustained levels observed in tumor and plasma are due to V937 capability to infect and replicate in immunodeficient mice, which ultimately leads to a potent oncolytic response as reflected by the infected cell death rate constant (δ) estimate, which is in line with those reported in the literature (Okamoto et al., 2014; Cao et al., 2018).

One of the major hurdles in current drug development in oncolytic viruses, and immune-therapies in general, is the need for predictive animal models (Russell et al., 2012). Certainly, xenograft mouse models that lack an immune system can be limited. However, they present a valuable opportunity to assess the properties of the oncolytic viruses in isolation, without any other limitation, on human tumor cell lines, as illustrated in this work. In this mouse model, viral retention, infectivity and replication at tumor level were identified as the key processes controlling V937 tumor response. These processes are tightly interconnected and difficult to identify simply using tumor response data. Viral infectivity and replication identified *in vitro* experiments could be directly integrated into the *in vivo* model structure to enable an adequate prediction of tumor response, thus providing an *in vitro*/*in vivo* framework for oncolytic viruses that can be used to support the selection between candidates based on their *in vitro* properties.

In this tumor mouse model and despite the rapid systemic clearance, minor differences between i. v. and i. t. routes of administrations were observed due likely to high viral infectivity and replication in the tumor level, as reflected by the corresponding parameter estimates, which in principle can lead to complete tumor eradication. However, this result should be interpreted with caution at the time to translate to other scenarios as the impact of the immune system is not yet considered and its role on the viral infection and proliferation mechanisms cannot be ruled out. In addition, given the small number of animals used in the experiments further data would be needed to validate the current model structure and parameter estimates. In this regard, model development should be seen as an iterative process that needs to be coupled with experimental work in order to reflect biology of the system and maximize model usefulness. As a next step, information from syngeneic mouse models that include not only tumor size measurements, but also kinetic levels in serum (and ideally in tumor as well) and relevant immune response markers, could be integrated into this framework. Such developments could facilitate a mechanistic and quantitative understanding of the dual role that the immune system can play in viral response, potentially limiting viral infectivity as well as triggering a potent anti-tumor immune response.

In summary, a mechanistic framework integrating *in vitro* viral dynamic properties into an *in vivo* system to describe oncolytic effects of V937 on tumor response in immunodeficient mice has been successfully developed. This model allows for a better understanding of the role that the different processes play in the final outcome, and enables selection between oncolytic virus candidates based on *in vitro*/*in vivo* features, such as infectivity. Moreover, the developed model can serve as a backbone to include future additional biological components, such as the immune response, to provide a quantitative understanding of the balance between immune and antiviral response. This would facilitate a better understanding of the limitations of systemic administration in immunocompetent scenarios, guide dosing strategies, and help identify potential combination strategies to ultimately support the development of programs for oncolytic viruses.

DATA AVAILABILITY STATEMENT

The original contributions presented in the study are included in the article/**Supplementary Material**, further inquiries can be directed to the corresponding author.

ETHICS STATEMENT

Ethical review and approval were not required for the animal study as our work presents a modelling exercise on data already

published for which the ethical approval was obtained at the time of experiments were performed (by others in other institutions).

AUTHOR CONTRIBUTIONS

ZP-G, data extraction from literature, model hypothesis, model coding, building, evaluation and interpretation, manuscript writing TF, model hypothesis, model evaluation and interpretation, manuscript writing YC, model hypothesis, model evaluation and interpretation, manuscript writing KM, model hypothesis, model evaluation and interpretation, manuscript writing SO, model hypothesis, manuscript writing MG, model hypothesis, manuscript writing DA, model hypothesis, model evaluation and interpretation, manuscript writing IT, Proyect supervision, model hypothesis, model coding, building, evaluation and interpretation, manuscript writing.

FUNDING

This study received funding from Merck Sharp & Dohme Corp., a subsidiary of Merck & Co., Inc., Kenilworth, NJ, USA. The funder had the following involvement with the study: design and gather, analyze, and interpret the results.

SUPPLEMENTARY MATERIAL

The Supplementary Material for this article can be found online at: https://www.frontiersin.org/articles/10.3389/fphar.2021.705443/full#supplementary-material

REFERENCES

Al-Tuwairqi, S. M., Al-Johani, N. O., and Simbawa, E. A. (2020). Modeling Dynamics of Cancer Virotherapy with Immune Response. *Adv. Differ. Equ* 2020. doi:10.1186/s13662-020-02893-6

Andtbacka, R. H. I., Amatruda, T., Nemunaitis, J., Zager, J. S., Walker, J., Chesney, J. A., et al. (2019). Biodistribution, Shedding, and Transmissibility of the Oncolytic Virus Talimogene Laherparepvec in Patients with Melanoma. *EBioMedicine* 47, 89–97. doi:10.1016/j.ebiom.2019.07.066

Annels, N. E., Arif, M., Simpson, G. R., Denyer, M., Moller-Levet, C., Mansfield, D., et al. (2018). Oncolytic Immunotherapy for Bladder Cancer Using Coxsackie A21 Virus. *Mol. Ther. - Oncolytics* 9, 1–12. doi:10.1016/j.omto.2018.02.001

Au, G., Lindberg, A., Barry, R., and Shafren, D. (2005). Oncolysis of Vascular Malignant Human Melanoma Tumors by Coxsackievirus A21. *Int. J. Oncol.* 26, 1471–1476. doi:10.3892/ijo.26.6.1471

Bagheri, N., Shiina, M., Lauffenburger, D. A., and Korn, W. M. (2011). A Dynamical Systems Model for Combinatorial Cancer Therapy Enhances Oncolytic Adenovirus Efficacy by MEK-Inhibition. *Plos Comput. Biol.* 7, e1001085. doi:10.1371/journal.pcbi.1001085

Bajzer, Ž., Carr, T., Josić, K., Russell, S. J., and Dingli, D. (2008). Modeling of Cancer Virotherapy with Recombinant Measles Viruses. *J. Theor. Biol.* 252, 109–122. doi:10.1016/j.jtbi.2008.01.016

Baxter, L. T., Zhu, H., Mackensen, D. G., Butler, W. F., and Jain, R. K. (1995). Biodistribution of Monoclonal Antibodies: Scale-Up from Mouse to Human Using a Physiologically Based Pharmacokinetic Model. *Cancer Res.* 55, 4611–4622.

Breitbach, C. J., Burke, J., Jonker, D., Stephenson, J., Haas, A. R., Chow, L. Q. M., et al. (2011). Intravenous Delivery of a Multi-Mechanistic Cancer-Targeted Oncolytic Poxvirus in Humans. *Nature* 477, 99–102. doi:10.1038/nature10358

Campagne, O., Delmas, A., Fouliard, S., Chenel, M., Chichili, G. R., Li, H., et al. (2018). Integrated Pharmacokinetic/Pharmacodynamic Model of a Bispecific CD3xCD123 DART Molecule in Nonhuman Primates: Evaluation of Activity and Impact of Immunogenicity. *Clin. Cancer Res.* 24, 2631–2641. doi:10.1158/1078-0432.CCR-17-2265

Cao, Y., Cartwright, E. K., Silvestri, G., and Perelson, A. S. (2018). CD8+ Lymphocyte Control of SIV Infection during Antiretroviral Therapy. *PLOS Pathog.* 14, e1007350. doi:10.1371/journal.ppat.1007350

Cassidy, T., and Humphries, A. R. (2019). A Mathematical Model of Viral Oncology as an Immuno-Oncology Instigator. *Math. Med. Biol. A. J. IMA* 37. 1–35. doi:10.1093/imammb/dqz008

Eftimie, R., Bramson, J. L., and Earn, D. J. D. (2011). Interactions between the Immune System and Cancer: A Brief Review of Non-spatial Mathematical Models. *Bull. Math. Biol.* 73, 2–32. doi:10.1007/s11538-010-9526-3

Ferl, G. Z., Wu, A. M., and DiStefano, J. J. (2005). A Predictive Model of Therapeutic Monoclonal Antibody Dynamics and Regulation by the Neonatal Fc Receptor (FcRn). *Ann. Biomed. Eng.* 33, 1640–1652. doi:10.1007/s10439-005-7410-3

Garcia-Carbonero, R., Salazar, R., Duran, I., Osman-Garcia, I., Paz-Ares, L., Bozada, J. M., et al. (2017). Phase 1 Study of Intravenous Administration of the Chimeric Adenovirus Enadenotucirev in Patients Undergoing Primary Tumor Resection. *J. Immunotherapy Cancer* 5, 71. doi:10.1186/s40425-017-0277-7

Hayes, S. H., and Seigel, G. M. (2009). Immunoreactivity of ICAM-1 in Human Tumors, Metastases and normal Tissues. *Int. J. Clin. Exp. Pathol.* 2, 553–560.

Jenner, A. L., Cassidy, T., Belaid, K., Bourgeois-Daigneault, M.-C., and Craig, M. (2021). In Silico trials Predict that Combination Strategies for Enhancing Vesicular Stomatitis Oncolytic Virus Are Determined by Tumor Aggressivity. *J. Immunother. Cancer* 9 (2), e001387. doi:10.1136/jitc-2020-001387

Jenner, A. L., Coster, A. C. F., Kim, P. S., and Frascoli, F. (2018). Treating Cancerous Cells with Viruses: Insights from a Minimal Model for Oncolytic Virotherapy. *Lett. Biomathematics* 5 (S1), S117–S136. doi:10.1080/23737867.2018.1440977

Kageshita, T., Yoshii, A., Kimura, T., Kuriya, N., Ono, T., Tsujisaki, M., et al. (1993). Clinical Relevance of ICAM-1 Expression in Primary Lesions and Serum of Patients with Malignant Melanoma. *Cancer Res.* 53, 4927–4932. doi:10.1016/0923-1811(93)90825-a

Kaufman, H. L., and Bommareddy, P. K. (2019). Two Roads for Oncolytic Immunotherapy Development. *J. Immunotherapy Cancer* 7, 26. doi:10.1186/s40425-019-0515-2

Kaufman, H. L., Kohlhapp, F. J., and Zloza, A. (2015). Oncolytic Viruses: a New Class of Immunotherapy Drugs. *Nat. Rev. Drug Discov.* 14, 642–662. doi:10.1038/nrd4663

Kelly, K. J., Woo, Y., Brader, P., Yu, Z., Riedl, C., Lin, S.-F., et al. (2008). Novel Oncolytic Agent GLV-1h68 Is Effective against Malignant Pleural Mesothelioma. *Hum. Gene Ther.* 19, 774–782. doi:10.1089/hum.2008.036

Kiang, T. K. L., Sherwin, C. M. T., Spigarelli, M. G., and Ensom, M. H. H. (2012). Fundamentals of Population Pharmacokinetic Modelling. *Clin. Pharmacokinet.* 51, 515–525. doi:10.2165/11634080-000000000-0000010.1007/bf03261928

Liu, Z.-X., Govindarajan, S., Okamoto, S., and Dennert, G. (2000). NK Cells Cause Liver Injury and Facilitate the Induction of T Cell-Mediated Immunity to a Viral Liver Infection. *J. Immunol.* 164. doi:10.4049/jimmunol.164.12.6480

Madden, D. L. (2018). From a Patient Advocate's Perspective: Does Cancer Immunotherapy Represent a Paradigm Shift? *Curr. Oncol. Rep.* 20, 1–7. doi:10.1007/s11912-018-0662-5

Mahasa, K. J., Eladdadi, A., De Pillis, L., and Ouifki, R. (2017). Oncolytic Potency and Reduced Virus Tumor-Specificity in Oncolytic Virotherapy. A Mathematical Modelling Approach. *PLoS One* 12, e0184347. doi:10.1371/journal.pone.0184347

Makkat, S., Luypaert, R., Sourbron, S., Stadnik, T., and De Mey, J. (2007). Quantification of Perfusion and Permeability in Breast Tumors with a Deconvolution-Based Analysis of Second-Bolus T1-DCE Data. *J. Magn. Reson. Imaging* 25, 1159–1167. doi:10.1002/jmri.20937

Malinzi, J., Eladdadi, A., and Sibanda, P. (2017). Modelling the Spatiotemporal Dynamics of Chemovirotherapy Cancer Treatment. *J. Biol. Dyn.* 11, 244–274. doi:10.1080/17513758.2017.1328079

Mitruka, B., and Rawnsley, H. (1981). *Clinical, Biochemical and Hematological Reference Values in normal Experimental Animals and normal Humans*. New York: Masson Publishing.

Mok, W., Stylianopoulos, T., Boucher, Y., and Jain, R. K. (2009). Mathematical Modeling of Herpes Simplex Virus Distribution in Solid Tumors: Implications for Cancer Gene Therapy. *Clin. Cancer Res.* 15, 2352–2360. doi:10.1158/1078-0432.CCR-08-2082

Mould, D., and Upton, R. (2012). Basic Concepts in Population Modeling, Simulation, and Model-Based Drug Development. *CPT: Pharmacometrics Syst. Pharmacol.* 1, 6. doi:10.1038/psp.2012.4

Okamoto, K. W., Amarasekare, P., and Petty, I. T. D. (2014). Modeling Oncolytic Virotherapy: Is Complete Tumor-Tropism Too Much of a Good Thing? *J. Theor. Biol.* 358, 166–178. doi:10.1016/j.jtbi.2014.04.030

Paiva, L. R., Binny, C., Ferreira, S. C., and Martins, M. L. (2009). A Multiscale Mathematical Model for Oncolytic Virotherapy. *Cancer Res.* 69, 1205–1211. doi:10.1158/0008-5472.CAN-08-2173

Parra-Guillen, Z. P., Fontanellas, A., Jiang, L., Jericó, D., Martini, P., Vera-Yunca, D., et al. (2020). Disease Pharmacokinetic-Pharmacodynamic Modelling in Acute Intermittent Porphyria to Support the Development of mRNA-Based Therapies. *Br. J. Pharmacol.* 177, 3168–3182. doi:10.1111/bph.15040

Perelson, A. S. (2002a). Modelling Viral and Immune System Dynamics. *Nat. Rev. Immunol.* 2, 28–36. doi:10.1038/nri700

Perelson, A. S. (2002b). Modelling Viral and Immune System Dynamics. *Nat. Rev. Immunol.* 2, 28–36. doi:10.1038/nri700

Pianosi, F., Sarrazin, F., and Wagener, T. (2015). A Matlab Toolbox for Global Sensitivity Analysis. *Environ. Model. Softw.* 70, 80–85. doi:10.1016/J.ENVSOFT.2015.04.009

Pol, J., Kroemer, G., and Galluzzi, L. (2016). First Oncolytic Virus Approved for Melanoma Immunotherapy. *Oncoimmunology* 5, e1115641. doi:10.1080/2162402x.2015.1115641

Raja, J., Ludwig, J. M., Gettinger, S. N., Schalper, K. A., and Kim, H. S. (2018). Oncolytic Virus Immunotherapy: Future Prospects for Oncology. *J. Immunotherapy Cancer* 6, 140. doi:10.1186/s40425-018-0458-z

Russell, S. J., Federspiel, M. J., Peng, K.-W., Tong, C., Dingli, D., Morice, W. G., et al. (2014). Remission of Disseminated Cancer after Systemic Oncolytic Virotherapy. *Mayo Clinic Proc.* 89, 926–933. doi:10.1016/j.mayocp.2014.04.003

Russell, S. J., Peng, K.-W., and Bell, J. C. (2012). Oncolytic Virotherapy. *Nat. Biotechnol.* 30, 658–670. doi:10.1038/nbt.2287

Saltelli, A., Annoni, P., Azzini, I., Campolongo, F., Ratto, M., and Tarantola, S. (2010). Variance Based Sensitivity Analysis of Model Output. Design and Estimator for the Total Sensitivity index. *Comp. Phys. Commun.* 181, 259–270. doi:10.1016/J.CPC.2009.09.018

Saltelli, A., Ratto, M., Andres, T., Campolongo, F., Cariboni, J., Gatelli, D., et al. (2007). *Global Sensitivity Analysis. The Primer*. John Wiley & Sons. doi:10.1002/9780470725184

Santiago, D., Heidbuechel, J., Kandell, W., Walker, R., Djeu, J., Engeland, C., et al. (2017). Fighting Cancer with Mathematics and Viruses. *Viruses* 9, 239. doi:10.3390/v9090239

Shafren, D. R., Au, G. G., Nguyen, T., Newcombe, N. G., Haley, E. S., Beagley, L., et al. (2004). Systemic Therapy of Malignant Human Melanoma Tumors by a Common Cold-Producing Enterovirus, Coxsackievirus A21. *Clin. Cancer Res.* 10, 53–60. doi:10.1158/1078-0432.CCR-0690-3

Shafren, D. R., Dorahy, D. J., Greive, S. J., Burns, G. F., and Barry, R. D. (1997a). Mouse Cells Expressing Human Intercellular Adhesion Molecule-1 Are Susceptible to Infection by Coxsackievirus A21, *J Virol*, 71, 785–789. doi:10.1128/JVI.71.1.785-789.1997

Shafren, D. R., Dorahy, D. J., Ingham, R. A., Burns, G. F., and Barry, R. D. (1997b). Coxsackievirus A21 Binds to Decay-Accelerating Factor but Requires Intercellular Adhesion Molecule 1 for Cell Entry, *J. Virol.*, 71, 4736–4743. doi:10.1128/JVI.71.6.4736-4743.1997

Sobol, I. (2001). Global Sensitivity Indices for Nonlinear Mathematical Models and Their Monte Carlo Estimates. *Math. Comput. Simul.* 55, 271–280. doi:10.1016/S0378-4754(00)00270-6

Titze, M. I., Frank, J., Ehrhardt, M., Smola, S., Graf, N., and Lehr, T. (2017). A Generic Viral Dynamic Model to Systematically Characterize the Interaction between Oncolytic Virus Kinetics and Tumor Growth. *Eur. J. Pharm. Sci.* 97, 38–46. doi:10.1016/j.ejps.2016.11.003

Wein, L. M., Wu, J. T., and Kirn, D. H. (2003). Validation and Analysis of a Mathematical Model of a Replication-Competent Oncolytic Virus for Cancer Treatment: Implications for Virus Design and Delivery. *Cancer Res.* 63, 1317–1324.

Workenhe, S. T., Simmons, G., Pol, J. G., Lichty, B. D., Halford, W. P., and Mossman, K. L. (2014). Immunogenic HSV-Mediated Oncolysis Shapes the Antitumor Immune Response and Contributes to Therapeutic Efficacy. *Mol. Ther.* 22, 123–131. doi:10.1038/MT.2013.238

Conflict of Interest: Authors TF, YC, KM, and DA were employed by the company Merck & Co, Inc, Kenilworth, United States.

The remaining authors declare that the research was conducted in the absence of any commercial or financial relationships that could be construed as a potential conflict of interest.

Publisher's Note: All claims expressed in this article are solely those of the authors and do not necessarily represent those of their affiliated organizations, or those of the publisher, the editors and the reviewers. Any product that may be evaluated in this article, or claim that may be made by its manufacturer, is not guaranteed or endorsed by the publisher.

frontiers in Bioinformatics

ORIGINAL RESEARCH
published: 13 August 2021
doi: 10.3389/fbinf.2021.708815

Predicting the Effects of Drug Combinations Using Probabilistic Matrix Factorization

*Ron Nafshi and Timothy R. Lezon**

Department of Computational and Systems Biology, University of Pittsburgh, Pittsburgh, PA, United States

Drug development is costly and time-consuming, and developing novel practical strategies for creating more effective treatments is imperative. One possible solution is to prescribe drugs in combination. Synergistic drug combinations could allow lower doses of each constituent drug, reducing adverse reactions and drug resistance. However, it is not feasible to sufficiently test every combination of drugs for a given illness to determine promising synergistic combinations. Since there is a finite amount of time and resources available for finding synergistic combinations, a model that can identify synergistic combinations from a limited subset of all available combinations could accelerate development of therapeutics. By applying recommender algorithms, such as the low-rank matrix completion algorithm Probabilistic Matrix Factorization (PMF), it may be possible to identify synergistic combinations from partial information of the drug interactions. Here, we use PMF to predict the efficacy of two-drug combinations using the NCI ALMANAC, a robust collection of pairwise drug combinations of 104 FDA-approved anticancer drugs against 60 common cancer cell lines. We find that PMF is able predict drug combination efficacy with high accuracy from a limited set of combinations and is robust to changes in the individual training data. Moreover, we propose a new PMF-guided experimental design to detect all synergistic combinations without testing every combination.

Keywords: combination therapies, phenotypic screening, drug discovery, matrix factorization, active learning, experimental design

OPEN ACCESS

Edited by:
Rui Li,
Pfizer, United States

Reviewed by:
JunLin Xu,
Hunan University, China
Rahul Kumar,
Indian Institute of Science, India

****Correspondence:***
Timothy R. Lezon
lezon@pitt.edu

Specialty section:
This article was submitted to Drug Discovery in Bioinformatics, a section of the journal Frontiers in Bioinformatics

Received: *12 May 2021*
Accepted: *30 July 2021*
Published: *13 August 2021*

Citation:
Nafshi R and Lezon TR (2021) Predicting the Effects of Drug Combinations Using Probabilistic Matrix Factorization. Front. Bioinform. 1:708815. doi: 10.3389/fbinf.2021.708815

INTRODUCTION

Complex diseases are increasingly recognized as emerging not from single molecules, but from systemic dysfunction of biological processes. From a systems view, pharmacologically treating complex disease requires engaging multiple components of the dysregulated pathways through polypharmacology or combination therapies. Already combination therapies represent the standard of care for an array of diseases, including cancer (Mokhtari et al., 2017) bacterial infection (Mulani et al., 2019), HIV (Ghosn et al., 2018), neurological and behavior disorders (Ortiz-Orendain et al., 2017). They are also the focus of increasing attention in the search for therapeutics to treat other complex diseases, such as AD (Cummings et al., 2019) and NAFLD (Singh et al., 2017). Unfortunately, discovering effective combination therapies requires either serendipitous discovery in the clinic or laborious searches in pre-clinical models.

Phenotypic approaches have been more successful than target-based approaches in bringing new first-in-class drugs to the clinic (Swinney 2013, 2014), and next-generation *in vitro* disease models

promise to boost the power of phenotypic screens by enhancing their clinical relevance. Screening in patient-derived 3D organoids (Lou and Leung, 2018; Takahashi, 2019) and biomimetic tissue chips that contain multiple interacting cell types in physiological geometries (Mittal et al., 2019; Gough et al., 2021), has proven useful for personalizing therapies for cancer and other complex diseases. Inter-organ side effects have been studied *in vitro* using multiple linked tissue chips (Skardal et al., 2017), paving the way for complete human-on-a-chip disease models. The price of this biological fidelity is a loss of throughput. Although sophisticated disease models more closely resemble their clinical counterparts than do their 2D monoculture predecessors, they are far more expensive to develop and maintain. Large-scale screens and even moderate combination screens are not yet feasible in these systems.

An addressable bottleneck in the phenotypic discovery pipeline is the low hit rate of screens. The overwhelming majority of compounds tested in traditional phenotypic screens are inactive, and the problem is exacerbated in combination screens, where the number of possible combinations scales exponentially with the size of the compound library. Fortunately, the availability of large screening data sets in human cell lines has spurred computational methods for predicting drug efficacies and synergies for complex diseases (Menden et al., 2019; Adam et al., 2020). Deep learning models using Graph Convolutional Networks are a powerful and well explored approach for relating complex relationships between inputs and targets, and many successful models have been developed for predicting values in the drug-interaction network (Sun et al., 2020). Other successful approaches include those that incorporate information on transcriptomic or proteomic profiling (Dawson and Carragher, 2014; Huang et al., 2019; Diaz et al., 2020), compound chemical structures (Sidorov et al., 2019), or drug targets (Yang et al., 2020; Rao et al., 2019; Iwata et al., 2015). Network-based approaches have been applied to create robust methods of identifying therapeutically effective drug combinations (Cheng, Kovács, and Barabási 2019).

Combination screens are amenable to statistical prediction methods that use screening data without supplementing it with details about chemical structures, targets, or OMICS profiles. One particularly powerful approach employs a higher-order factorization machine to predict dose-response surfaces for unique drug combinations using only data from the same screen (Julkunen et al., 2020). The advantages of such methods are that they guard against bias introduced from orthogonal databases, they can be used with unannotated compound libraries, and their predictions are consistent with the data generated in the screen of interest. For methods like this to be effective, the computational and experimental components of the screen must be properly synchronized, so that each informs the other (Stern et al., 2016). A number of studies have addressed the right way to mix computational and experimental work to find effective combination therapies (Calzolari et al., 2008; Gerlee et al., 2013; Kashif et al., 2015; Weiss et al., 2015; Silva et al., 2016; Matlock et al., 2017; Ianevski et al., 2019).

Here we introduce a method for predicting the effects of drug combinations using as input only the effects of other drug combinations. Mathematically, the problem is identical to filling in the missing values of a symmetric matrix containing the effects of drug combinations. Each row and each column of the matrix corresponds to a drug, and the matrix elements are the effects of the drug combinations. If only a subset of the matrix elements are known, the rest can be inferred by decomposing and reconstructing the partial matrix under certain assumptions (Lezon et al., 2006; Lezon and Bahar, 2010). For the current application, we use Probabilistic Matrix Factorization (PMF) (Salakhutdinov and Mnih, 2007), a collaborative filtering algorithm that has proven successful in other problems of the same class (for an introduction to collaborative filtering algorithms, see Aggarwal, 2016).

The PMF algorithm was first developed to recommend movies to Netflix users based on the movies viewed by other users. The core assumption of PMF is that attitudes or preferences that lead to each user's score for a movie are shared by other users with similar taste. PMF recommends that viewers watch movies that similar viewers enjoyed. The method has since been applied to predict values from other large, sparse and imbalanced data sets. Biomedical applications of PMF include predicting diseases associated with transcription patterns (Ha et al., 2020; Mao, Wang, and Zhang 2019), recommending novel indications for drug repurposing (Meng et al., 2021; Yang et al., 2014), and predicting novel targets from drugs (Cobanoglu et al., 2013; Cobanoglu et al., 2015; Li et al., 2020). In the present context, PMF is used to "recommend" drug combinations based on the known effects of similar combinations. We train our model on phenotypic screening data from the NCI ALMANAC (Holbeck et al., 2017), a robust collection of pairwise drug combinations of 104 FDA approved anticancer drugs against 60 common cancer cell lines. We find that knowing the effects of only 50% of drug combinations allows us to classify the effects of the missing combinations as efficacious with 95% accuracy, and we demonstrate how our method can be incorporated into optimal experimental design.

METHODS

NCI ALMANAC

The NCI ALMANAC is a novel, easy-to-use resource created to help researchers identify new combination therapies. The NCI ALMANAC database (Holbeck et al., 2017) is a collection of pairwise combinations of 104 FDA approved anticancer drugs against the NCI-60, a set of 60 common human tumor cancer cell lines collected by the National Cancer Institute. A total of 5,232 drug-drug pairs were evaluated in each of the cell lines; 304,549 experiments were performed to test each drug at either 9 or 15 combination dose points, for a total of 2,809,671 dose combinations. At each dose combination, the percent cell growth after 2 days was measured and recorded, and the efficacy of the combination calculated as the percent of growth inhibition. A combination that has no effect on cell growth compared to control has zero efficacy; a combination that completely halts cell growth has efficacy 100. See the NCI ALMANAC (Holbeck et al., 2017) for details. For each cell line, the combination

efficacies are arranged into a symmetric matrix, $\mathbf{M}_{104x104}$, where each row and column represent a drug, and each element represents the efficacy of a unique drug-drug combination on that cell line. For purposes of PMF (see below), diagonal elements are ignored. The data is then normalized to mean-zero and unit variance for input into the PMF algorithm.

The synergy of each combination is reported by the NCI ALMANAC as a "ComboScore" that measures the difference between the recorded growth rate after testing and the growth rate expected by Bliss Independence (Bliss, 1939). A positive ComboScore indicates a synergistic combination, whereas a negative ComboScore indicates an antagonistic combination. When applying PMF to predict synergies instead of efficacies, we populate the input matrix **M** with ComboScores and normalize as described above.

PMF

Probabilistic Matrix Factorization (PMF) is a collaborative filtering algorithm that factors the low-rank input matrix $\mathbf{M}_{n\times m}$ into the product of two low-rank matrices, $\mathbf{A}_{n\times d}$ and $\mathbf{B}_{m\times d}$ such that $\mathbf{M}_{ij} = \mathbf{A}_i\mathbf{B}_j^T$. Thus, PMF reduces to estimating the two matrices **A** and **B**. The core assumptions of this are that the values of **M** are independent, normally distributed and share a common variance σ^2. Thus, the conditional probability of entries of **M** can be expressed as

$$p\left(\mathbf{M}|\mathbf{A},\mathbf{B},\ \sigma^2\right) = \prod_{i=1}^{n}\prod_{j=1}^{m} N\left(\mathbf{M}_{ij}|\mathbf{A}_i\mathbf{B}_j^T,\ \sigma^2\right)^{I_{ij}}$$

where I_{ij} is the indicator function equal to 1 if $\mathbf{M}_{ij}$ is known and 0 otherwise (Salakhutdinov and Mnih, 2007).

To solve for the matrices **A** and **B**, we place a zero-mean spherical Gaussian prior on each, such that $p(\boldsymbol{A}|\sigma_A) = \prod_{i=1}^{N} N(\boldsymbol{A}_i|0,\sigma_A^2\boldsymbol{I})$ and $p(\boldsymbol{B}|\sigma_B) = \prod_{i=1}^{N} N(\boldsymbol{B}_i|0,\sigma_B^2\boldsymbol{I})$. We can then derive the full posterior distribution of **A** and **B** as $p(\boldsymbol{A},\boldsymbol{B}|\boldsymbol{M},\sigma^2,\sigma_{\boldsymbol{A}}^2,\sigma_{\boldsymbol{B}}^2) \propto p(\mathbf{M}|\mathbf{A},\mathbf{B},\ \sigma^2)p(\boldsymbol{A}|\sigma_{\boldsymbol{A}}^2)p(\boldsymbol{B}|\sigma_{\boldsymbol{B}}^2)$. Maximizing the log-posterior is equivalent to minimizing the sum-of-squared-errors objective function: $L(\boldsymbol{A},\boldsymbol{B}) = \frac{1}{2}\sum_{i=1}^{N}\sum_{i=1}^{M} I_{ij}(\boldsymbol{M}_{ij} - \boldsymbol{A}_i\boldsymbol{B}_j^{\mathrm{T}})^2 + \frac{\lambda}{2}\sum_{i=1}^{N}\|\boldsymbol{A}_i\|_{Fro}^2 + \frac{\lambda}{2}\sum_{j=1}^{M}\|\boldsymbol{B}_j\|_{Fro}^2$, where λ is the regularization rate hyperparameter. We then construct a stochastic gradient descent update scheme by differentiating the loss function in terms of **A** and **B**, such that

$$\frac{\partial}{\partial \boldsymbol{A}_i} L(\boldsymbol{A},\boldsymbol{B}) = \sum_{j=1}^{M} I_{ij}\left(\boldsymbol{M}_{ij} - \boldsymbol{A}_i\boldsymbol{B}_j^T\right)\boldsymbol{B}_j + \lambda\boldsymbol{A}_i$$

$$\frac{\partial}{\partial \boldsymbol{B}_j} L(\boldsymbol{A},\boldsymbol{B}) = \sum_{j=1}^{N} I_{ij}\left(\boldsymbol{M}_{ij} - \boldsymbol{A}_i\boldsymbol{B}_j^T\right)\boldsymbol{A}_i + \lambda\boldsymbol{B}_i$$

Algorithmically, we randomly initialize **A** and **B** from Gaussian distributions and iteratively update them by descending along these gradients until a minimum of $L(\boldsymbol{A},\boldsymbol{B})$ is reached. Applying these rules simultaneously to both **A** and **B** guarantees convergence of the algorithm to a local minimum. However, the stochastic nature of the initial conditions implies that each run of PMF may not necessarily converge to the global minimum, or even the same local minimum. This requires that PMF be run multiple times on different random initializations and then select the most accurate factorization. While this increases the overall computational cost, this is offset by PMF's computational cost scaling linearly with input size and using lightweight low-rank approximations.

Stochastic gradient descent methods are a critical component of machine learning, and methods incorporating momentum and acceleration play an important role when used in conjunction with stochastic gradients (Assran and Rabbat, 2020). Momentum methods help accelerate stochastic gradient descent in the relevant direction and dampen oscillations as a minimum is approached by incorporating the momentum constant γ. The update step with respect to the parameters θ can be expressed as $v_t = \gamma v_{t-1} + \eta\nabla_\theta J(\theta),\ \theta = \theta - v_t$. However, simple momentum methods can be insufficient for complex surfaces. The Nesterov Accelerated Gradient (NAG) (Assran and Rabbat, 2020) improves on this method by "looking ahead" to where the parameters will be to calculate the gradient and is formalized as follows: $v_t = \gamma v_{t-1} + \eta\nabla_\theta J(\theta - \gamma v_{t-1}),\ \theta = \theta - v_t$. Rather than computing the gradient at parameters θ, NAG looks ahead at a rough approximation of where the parameters will be, computing the gradient at $\theta - \gamma v_{t-1}$. This anticipatory update greatly increases optimization and performance of PMF as it approaches a minimum.

RESULTS

PMF Accurately Recovers Drug Synergies From Partial Data

We first investigated the ability of PMF to recover hidden elements in the drug combination efficacy matrix. For each cell line, we randomly hid a fraction of the combination efficacy matrix, creating non-overlapping "training" and "validation" sets. Then, we used PMF to predict the hidden values and complete the matrix. To guarantee a solution, we included only cases where all drugs were present in a single connected component; that is, where a path could be made from any drug to any other drug using common combination partners. PMF recovered training data to arbitrary precision (**Figure 1A**) and recovered test data well, provided a sufficiently large training set (i.e., small fraction of data hidden). Using empirically determined hyperparameters for the regularization rate (λ), learning rate (η), and momentum constant (γ), we found that knowing only 30–50% of the drug-drug interactions was sufficient to recover the remaining values in the matrix to within 10% (**Figures 1B,C**). When selecting combinations with efficacies above a given threshold, PMF performance did not vary strongly with the threshold value (**Figure 2**); that is, the method can predict whether a combination has an effect over 0.9 nearly as well as it can predict whether a combination has an effect over 0.2.

PMF Performance Is Largely Independent of Individual Drug Efficacies

Assuming compounds act independently (i.e., Bliss independence), the most efficacious compound combinations will be combinations of the independently most efficacious compounds. Reasoning that efficacious drugs are more likely

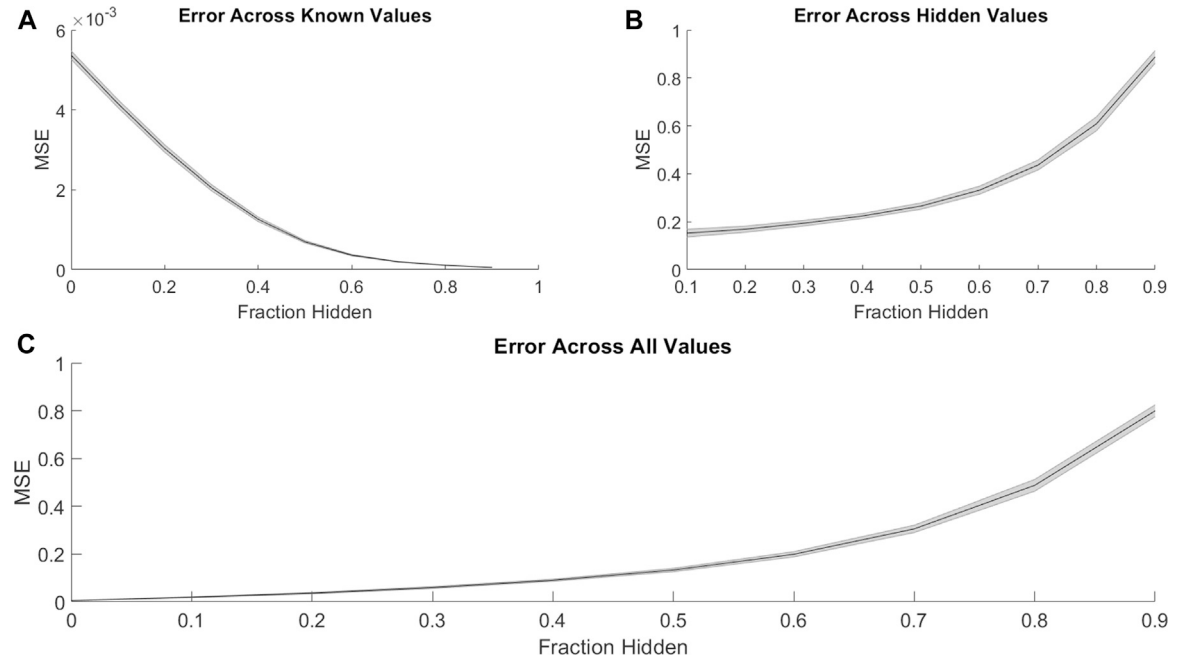

FIGURE 1 | PMF recovers the values of hidden elements of the drug efficacy matrix from only a fraction of interactions. The mean-squared error of PMF in recovering values of **(A)** known, **(B)** hidden, and **(C)** all elements is plotted against the fraction of hidden data. In all panels, the shaded area represents the standard deviation of the mean-squared error over 25 trials across all cell lines.

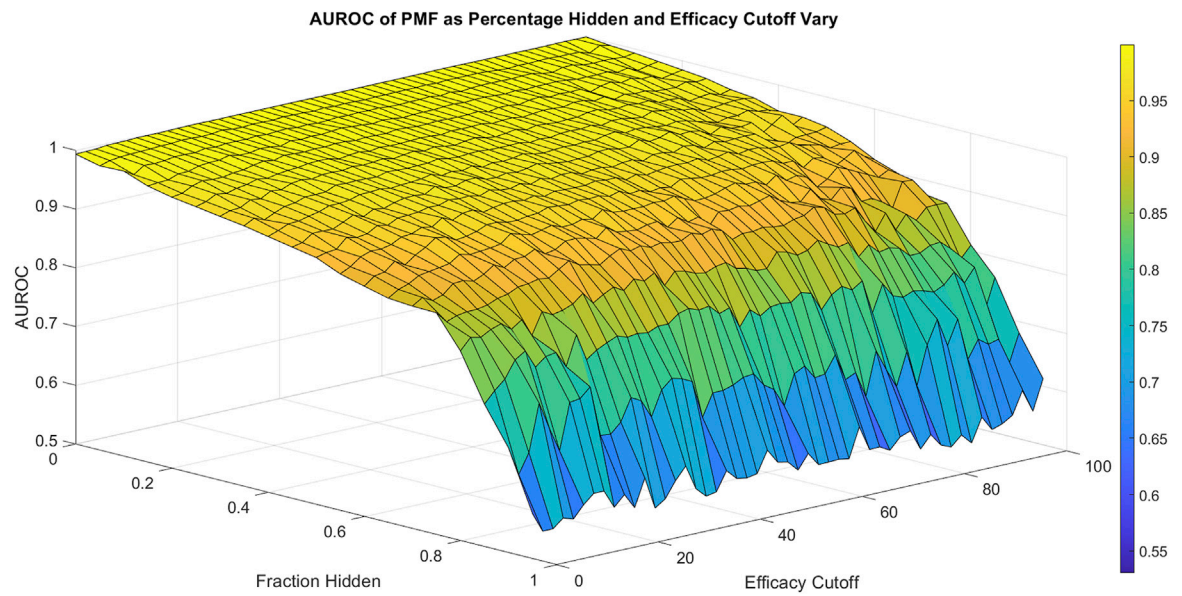

FIGURE 2 | The area under the ROC curve (AUROC) of PMF is shown as the fraction hidden and efficacy cutoff vary on the 786-0 cell line, which is representative of all cell lines. The efficacy cutoff describes the efficacy at which a drug-drug combination is considered active, with combination efficacy defined as 100 minus the percent growth as described in the standard NCI-60 testing protocol (Holbeck et al., 2017). As the fraction hidden decreases, the performance of the model remains high until it drops sharply at 70% hidden and performs with similar accuracy regardless of the efficacy cutoff, decaying to random guesses when the full matrix is hidden. The smooth surface indicates PMF reproduces all elements with equal accuracy and is not heavily affected by outliers.

to influence pathologically relevant mechanisms, we next investigated whether PMF performed better when trained on combinations involving highly efficacious drugs. For each cell line, we rank-ordered the compounds by efficacy and then divided the drug efficacy matrix into halves and quarters to assess if PMF is more accurate when only provided singularly efficacious drugs.

On aggregate we find the differences in accuracy were small, and PMF performance was largely independent of the individual efficacies of the starting set outside of this edge case (**Supplementary Figures 1A,B**). More generally, we found that the most efficacious compounds neither led to the most efficacious combinations, nor were they the best at predicting the values of missing efficacies (**Supplementary Figure 1C**). In fact, individual drug identities did not greatly affect the accuracy of the prediction. We generated an occupancy matrix by randomly selecting 10% of the elements in the combination efficacy matrix. We then randomly shuffled the identities of the drugs while keeping the occupancy matrix static. Repeating this 1,000 times for 1,000 different occupancy matrices, we found PMF predicted the missing values of each matrix with a mean squared error of 0.938 ± 0.0145, and thus performed equally well regardless of the individual drug identities for a given occupancy matrix.

Graph Topology's Influence on PMF Performance

Viewing the problem though a graph lens, the combination efficacy matrix describes an undirected graph in which the N drugs are nodes and known two-drug combinations represent weighted edges (for a primer on network science, see Barabási, 2016). The challenge of PMF is to reconstruct a fully connected graph from a seed network. By using different algorithms for selecting drug combinations for the training set, we investigated how seed network topology influences prediction accuracy. The method described above, where seed drug combinations are selected randomly and independently, is known as an Erdős-Réyni graph (Rényi and Erdős, 1959) that has a Poisson degree distribution (Barabási and Pósfai 2016).

An extension of the Erdős-Réyni graph is the Watts-Strogatz model (Watts and Strogatz, 1998). This method is motivated by the observation that often in real networks, almost any node can be reached by a short number of steps, known as the Small-World Property (Milgram, 1967). The Watts-Strogatz graph is generated by attaching each node to its nearest k neighbors, resulting in a regular lattice structure. Each edge is then randomly reassigned with probability β. When β is 0, no changes are accepted, and the method preserves the original lattice. As β increases, more links will be randomly assigned, and as β approaches 1, all links will be randomly reassigned, resulting in a completely random Erdős-Réyni network. Intermediate values of β result in small-world networks of low diameter (Barabási and Pósfai 2016).

When training data was arranged in a Watts-Strogatz model topology, the performance of PMF increased with β (**Figure 3A**). We attribute the poor performance near β = 0 to the difficulty of predicting combination effects of drugs that are separated by large distances on the seed network. The adjacency matrix for a regular lattice is banded, with the unknown values comprising a contiguous block. Performance improves for values of β near ½, where the small-world property emerges, and peaks at β = 1, the Erdős-Réyni network. Whereas the small-world Watts-Strogatz graph provides a short path between any pair of nodes, the Erdős-Réyni graph contains multiple paths, each carrying evidence for the value of the inferred combination efficacy.

Many real-world networks do not follow a binomial or Poisson degree distribution, and instead follow a power law or scale-free distribution. In a scale-free network, the probability that a node has k edges is proportional to $k^{-\gamma}$, where γ is a scaling exponent between 2 and 3. We explored whether a scale-free distribution in the input data influences the accuracy of the prediction. Using the hidden parameter model (Caldarelli et al., 2002; Söderberg, 2002; Boguñá and Pastor-Satorras, 2003), we generated scale-free seed networks for training PMF. The method performed equally well for scale-free distributions for all values of γ, and predicted unknown values with accuracy comparable to the Watts-Strogatz method (**Figure 3B**).

Designing a combination screen using the above-described graph topologies may not be experimentally convenient; instead, screeners are more likely to select a few well-known compounds and test them in combination with other compounds in a large library. The adjacency matrix of the seed graph in this approach has several rows/columns in which every value is known, while the large majority of have few or no known values (**Figure 3C**). The corresponding graph has several fully connected hubs, with the remaining nodes having very few connections.

We explored the accuracy of PMF by using a hub method construction defined as follows: First, we ensured that every node had exactly one connection. Then, we selected nodes at random to be hubs, and ensured that each hub was fully connected. Finally, the remaining edges were randomly assigned in an Erdős-Réyni random fashion. We found the PMF performed stronger on hub method topologies than random Erdős-Réyni topologies when more than 80% of the network was hidden and the graph was sparse. Moreover, when training data was arranged in a hub model topology, the performance of PMF increased as the number of hubs increased (**Figure 3C**).

Thus, we found that the specific seed topology of the training data did not greatly affect the accuracy of the prediction in identifying synergistic drugs if the topology was a random Erdős-Réyni graph or had a binomial degree distribution, such as the Watts-Strogatz for large β. However, PMF did perform worse when edges were evenly distributed following the Watts-Strogatz model for small values of β or when edges were distributed following a scale-free distribution. Moreover, we found that PMF was more accurate under hub topologies mirroring real drug combination assays when more than 80% of the network was hidden, which is exactly the region of interest if we want to test as few combinations as possible.

PMF Predicts Efficacy, But Not Synergy

The desired output of most phenotypic combination screens is an efficacious and non-toxic combination; however, *de novo*

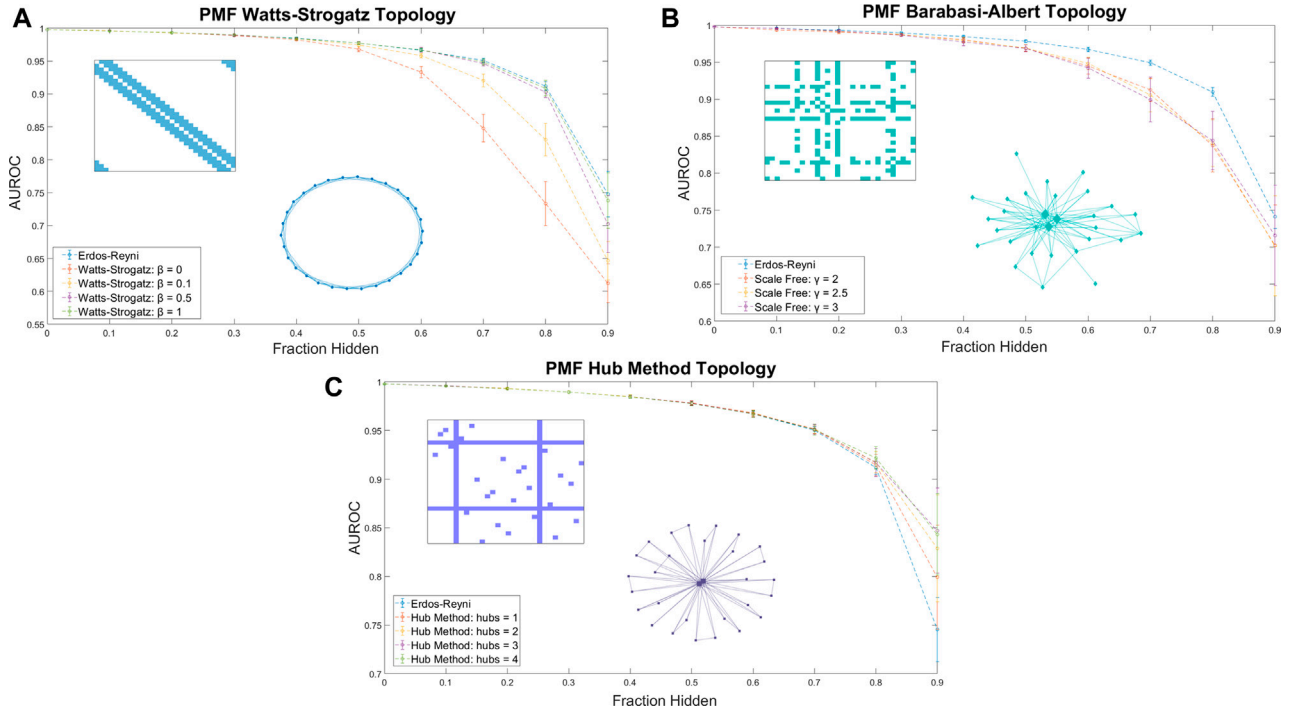

FIGURE 3 | The AUROC of PMF in identifying efficacious combinations as the fraction of the data hidden increases is measured for **(A)** Watts-Strogatz graphs, **(B)** Barabási-Albert scale-free graphs, and **(C)** graphs generated by the Hub Method. Included in each plot is a sample of the adjacency matrix and topology of each network. Error bars represent standard deviation over 25 repeated trials at the same value of β. **(A)** Watts-Strogatz graphs with varying β. When β is near zero, each drug has *k* connections with its nearest neighbors in a lattice structure, and the model performs worse than reproducing from an Erdős-Réyni distribution of equivalent size. As β approaches 1 and the degree distribution of the graph converges to a similar Poisson Distribution of an Erdős-Réyni graph, the accuracy of the predictions begins to approach the level of accuracy seen with purely random topologies. **(B)** Scale-free seed networks perform similarly, regardless of scaling exponent. On aggregate, scale-free graphs perform similarly for all values of γ, and slightly underperform compared to Erdős-Réyni topologies. **(C)** Graphs generated using the hub method with random hubs produce more accurate predictions than other graph types. When most data are hidden, error and standard deviation of the prediction decrease as the number of hubs increases.

development of combination therapeutics will benefit from identifying synergistic drug combinations, whether or not they are efficacious. For example, two drugs that individually have no efficacy may have a moderate effect in combination. Although such a combination may not be clinically useful, it carries structure and pathway information that may serve as the starting point for rational development of combination therapeutics.

PMF was able to recover missing values much less accurately when predicting synergy rather than efficacy. Just as with efficacies (**Figure 1**), PMF recovered training data to arbitrary precision (**Figure 4A**), but it did not recover test data well, unless it had a sufficiently large training set (i.e., small fraction of data hidden) (**Figures 4B,C**). While the accuracy of PMF on predicting synergy was much weaker than PMF predicting efficacy, we still found that the model is robust and performed well in cases where 50–70% of the total matrix was known.

This stark decrease in accuracy and predictive power may result from the lopsided definition of synergy. The ComboScore of each drug combination represents the difference between the observed effect of the combination and the expected effect assuming each drug acts independently. Because the upper bound on efficacy is the same for individual drugs and combinations, a combination of highly efficacious drugs cannot have a high ComboScore, even if it has optimal efficacy. Similarly, combinations with identical efficacies may have different ComboScores, depending on the efficacies of the individual drugs used in the combinations. Thus, a low ComboScore reveals nothing about the efficacy of the combination, but a high ComboScore indicates the combination's component drugs individually have low efficacy (**Supplementary Figure 2**). As ComboScores are calculated from individual and combination efficacies, one can still use PMF to predict combination efficacies, and use these to calculate ComboScores.

PMF as a Tool to Guide Combination Screening

In vitro phenotypic-based screens have several benefits for drug discovery, such as not needing to know the molecular target of a disease and being less restricted by hypotheses (Zheng et al., 2013). However, throughput can be low in such assays, and

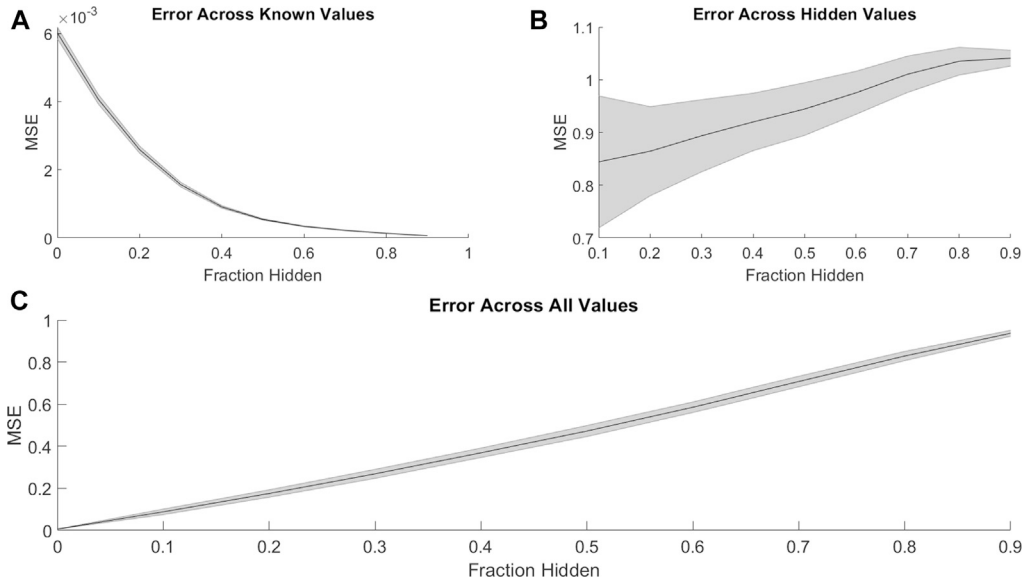

FIGURE 4 | Similar to **Figure 1**, the mean-squared error of PMF in recovering combination synergy of **(A)** known, **(B)** hidden, and **(C)** all elements are plotted against the fraction of hidden data. In all panels, the shaded area represents the standard deviation of the mean-squared error over 25 trials across all cell lines. Once again, PMF recovers all known data to arbitrary precision. PMF performs with much less accuracy when predicting ComboScores rather than efficacies (**Figure 1**). Error is much greater and more uncertain overall in hidden indices and thus across all indices.

increasing the number of compounds to be screened causes experimental effort and cost to rise exponentially. PMF may help combat this issue by guiding combination screens through iterative prediction and testing in an active learning scheme.

We simulated PMF being used in an active learning experimental design as follows. First, we created a random Erdős-Réyni graph topology with 10% of the total combinations known. Then, we used PMF to reproduce the entire combination efficacy matrix and identified the top 5% greatest efficacies as predicted by PMF. We then "tested" these identified efficacious combinations by adding the actual values of the efficacies to the list of known combinations, and then repeated the procedure to discover the next 5%, until the entire matrix is recovered.

PMF-guided screens identified efficacious combinations much more efficiently than naïve random tests (**Figure 5**). In our simulated experiment, PMF identified efficacious combinations at three times the rate of random choice and identified as much as 95% of all highly efficacious combinations while only testing 50% of all available combinations. This finding was consistent across cell lines and was not sensitive to the details of the starting point. Our results suggest that screeners may be able to test a small number of relevant combinations of direct interest and obtain the remaining synergistic combinations following a PMF-guided design. Future studies could fruitfully explore this issue further by optimizing PMF-guided screens as well as investigating its accuracy applied in a physical assay experiment.

Throughout the simulated experiment, we monitored the performance of PMF as measured by AUROC (**Figure 5**). The dip in AUROC observed around the fourth step of the simulated experiment may be due to bias introduced by the active learning. Efficacious combinations are not uniformly distributed across all drugs, and indeed a small subset of drugs is likely to contribute to many of the efficacious combinations. As the experiment progresses, PMF preferentially selects combinations from an efficacious minority of the nodes, mirroring the construction of a scale-free graph. PMF performs worse on scale-free graphs compared to Erdős-Réyni graphs (**Figure 3**), causing the accuracy to decrease as nodes are preferentially tested, and then increase as these nodes are saturated and the rest of the matrix is tested. Future studies might investigate ways to counteract this drop in error by using a more complex method than simply testing the top 5% most efficacious combinations as predicted by PMF.

The Method's Performance Is Not Unique to Cancer

To test the performance of our method in diseases other than cancer, we applied it to data from a small combination screen for Huntington's disease (HD), an autosomal dominant neurodegenerative disease caused by an abnormally long polyglutamine stretch in the huntingin protein (Zuccato et al., 2010). The clinical progression of HD starts with general loss of motor control around the third decade of life. This is followed by mood and personality changes, and eventual dementia and death. To date, there are no drug-like molecules that can prevent or slow

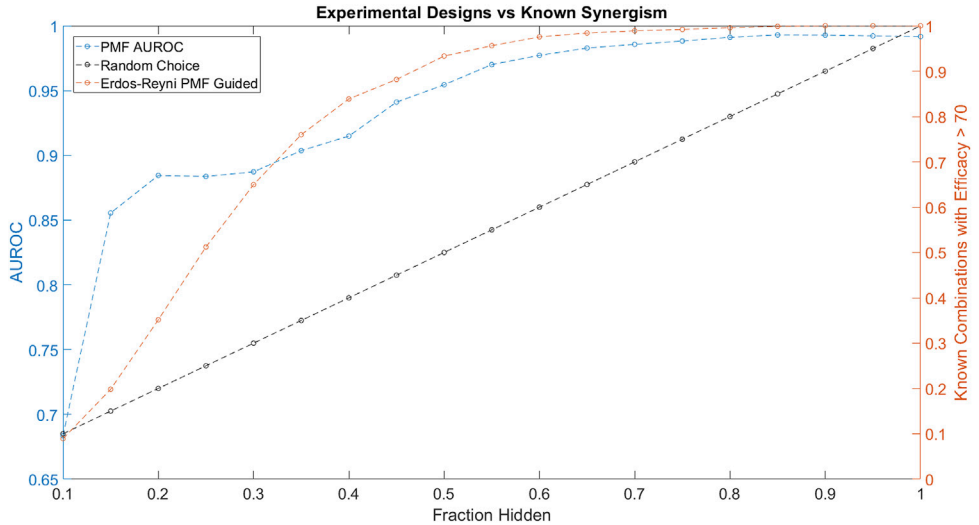

FIGURE 5 | The performance of PMF in a proposed experimental design to predict drug combinations with efficacy greater than 70 is plotted in orange and is compared against random choice plotted in black. Both the AUC of PMF's predictions in blue as well as the percentage of known efficacious drugs with efficacy greater than 70 are plotted against the known fraction of the drug-drug efficacy matrix. The experiment following random choice takes a random sample of the graph, resulting in a linear relationship between the amount of the drug-synergy matrix known and the amount of known synergistic drugs. As the procedure described above is repeated, PMF identifies more than 95% of the most efficacious combinations while only knowing 50% of the full drug efficacy matrix, much greater than random choice.

HD, and the pleiotropic nature of huntingtin makes it difficult to target directly.

Pei and coworkers reported results from a combination screen in a murine cell-based model of HD (Pei et al., 2017). Briefly, their assay used serum deprivation to induce stress in neuronal progenitor cells derived from the STHdh^{Q111} murine cell line model of HD, which has an abnormally long glutamine stretch in its huntingtin protein. The phenotypic response of the cells was then compared to that in serum-deprived cells of their isogenic wild type STHdh^{Q7}; overall, serum deprivation killed about half of the HD cells and about 5% of the wild type cells. The group evaluated 268 two-compound combinations of 32 compounds for their ability to protect against cell death. As a metric, they used "Percent Recovery," which captures the percent of HD cells that were rescued from cell death by a treatment (Pei et al., 2017).

Applying the same simulated experimental design to the HD data as we applied to the ALMANAC data, we found that PMF-guided screens identified combinations with the highest Percent Recovery much more efficiently than the rate of random chance: Over 90% of combinations with Percent Recovery over 70 were identified by testing only 70% of all available combinations (**Figure 6A**). Moreover, we found that PMF performed with nearly the same accuracy on the HD dataset as it did on similarly sized subsets of the ALMANAC data (**Figure 6B**, **Supplementary Figure 1B**). While the guided screen is more efficient than naïve guessing, the results are much weaker than on the much larger ALMANAC dataset. Starting with 10% of the 32 compound combinations known, PMF may only know a handful of combinations, and struggles until around 30% of all combinations are known.

DISCUSSION

Our results show that it is possible to use information on the effects of drug combinations to predict the effects of novel combinations. A strength of our approach is that does not require any outside knowledge of chemical structures, target profiles, or OMICS data. This lack of reliance on outside data contributes to the method's robust performance between data sets of similar sizes. Indeed, freedom from additional information augments our method's stability and flexibility: Rather than predicting the effects of combinations of drugs, it could be used for combinations of unknown substances, natural extracts, or even combinations of combinations. As such, our method may contribute to identifying mechanisms of action for novel compounds. Since PMF is lightweight and is not informed by structure or other data, it may provide a benchmark against which more complicated methods can be tested.

There are many constrained low-rank matrix approximation algorithms that could have been used other than PMF. Within this general framework, some powerful techniques include singular value decomposition (SVD) (Golub and Reinsch, 1971), principal component analysis (PCA) (Wold et al., 1987), non-negative matrix factorization (NMF) (Lee and Sebastian Seung, 1999), entropy maximization (Lezon et al., 2006; Lezon and Bahar, 2010), and deep matrix factorization (MF) (Pierre and Siebert, 2020). SVD's matrix factorization is unique and orthogonal unlike PMF. However, SVD's matrix reconstruction is a superposition of the orthogonal components with arbitrary signs, losing strong correlations that may exist and the

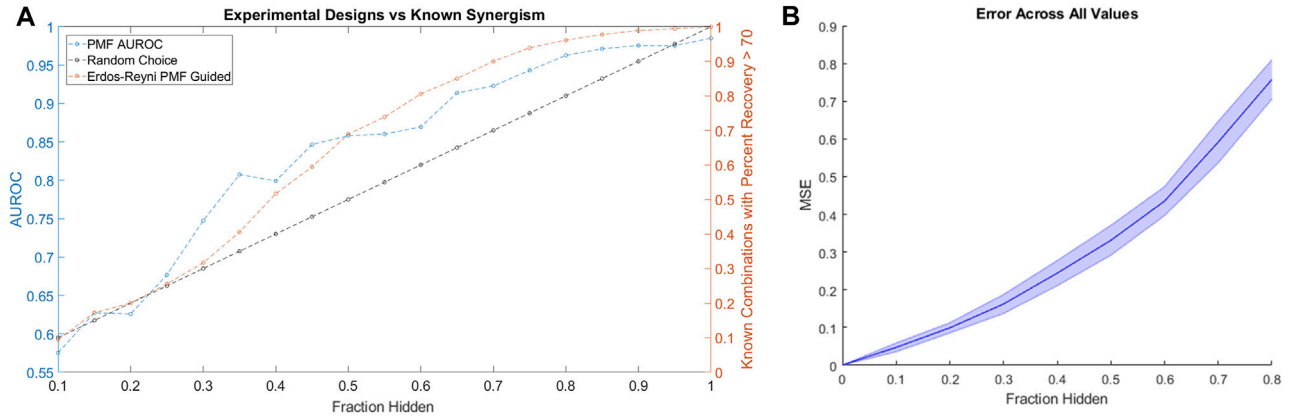

FIGURE 6 | (A) The performance of a simulated PMF guided drug screen in HD identifies all drug combinations with Percent Recovery greater than 70. Both the AUC of PMF's predictions (in blue) as well as the percentage of known efficacious drugs with efficacy greater than 70 (orange and black) are plotted against the known fraction of the drug-drug efficacy matrix. Once again, PMF guided screens outperform the rate of chance, with PMF identifying more than 90% of the most efficacious combinations while only knowing 70% of the full drug efficacy matrix. **(B)** The error of PMF in predicting all elements is plotted against the fraction hidden. PMF does as well on the smaller HD dataset as it does on smaller subsets of the ALMANAC data (**Supplementary Figure 1B**).

interpretability of the latent factor representation of PMF. Moreover, SVD has been shown to be less accurate than PMF (Salakhutdinov and Mnih, 2007), and is vulnerable to overfitting. PCA's orthogonal decomposition suffers from similar weaknesses. The parts-based decomposition of NMF has provided powerful, interpretable methods for matrix factorization in a variety of applications from text mining to gene expression. However, NMF is poorly suited to drug discovery due to its non-negativity constraint. Methods relaxing this constraint (Wang et al., 2015) may be able to provide similar results with a parts-based matrix representation as opposed to PMF's latent factor representation. Unlike PMF, which factors into only two matrices and captures a single layer of features, deep matrix factorization, inspired by the success of deep learning, aims to extract several features in a hierarchical way (Pierre and Siebert, 2020). Although many algorithms have been introduced for deep MF, it is still an emerging topic and questions of convergence, identifiability, and loss functions have not been fully explored. PMF on the contrary is well-explored algorithm with strong theoretical ground that has found success in a variety of matrix completion and collaborative filtering settings.

One limitation of PMF is that it suffers from the cold-start problem and is unable to predict the efficacy for compounds with no known values. Thus, any guided PMF assay must test at least one combination for every drug. It is also unknown how well PMF will scale to drug libraries larger than the ALMANAC. While our simulated experiment was more successful on the larger ALMANCAC data than the smaller Huntington's disease data, PMF's performance on larger drug libraries remains to be seen. We additionally note that both the ALMANAC and HD data sets employed combinations of compounds that were individually effective as monotherapies. To fully evaluate our method's utility in guiding combination screens, we will need to apply it to screens in which not all compounds are individually efficacious. That is, the proper test of the method is its application to a new screen, which is beyond the scope of this work.

CONCLUSION

We have shown that PMF can accurately impute missing values into the drug combination efficacy matrix for a screen, and that the performance of PMF does not depend on the efficacies of the drugs being tested. We further showed that PMF performs best when the input drug combination network has an Erdős-Réyni topology. Finally, we used simulated experiments to demonstrate that alternating PMF inference with experiments can efficiently identify the most efficacious two-drug combinations in a phenotypic screen.

There have been many other attempts at predicting the effects of drug combinations, and those that perform best include additional data, such as chemical structures, target profiles, or OMICS data (Wang et al., 2013; Huang et al., 2019; Menden et al., 2019). PMF has the advantage that its computation time scales linearly, and it can make accurate predictions for sparse and imbalanced data sets. Moreover, PMF is an unsupervised algorithm and by nature is easily interpretable as matrix factorizations easily provide a lens to determine relations, giving it several advantages over large deep learning networks. Our method is simpler by comparison, but it provides a baseline of performance against which more complicated prediction methods may be assessed. Indeed, not relying on additional information endows our method with flexibility: Instead of predicting the effects of combinations of drugs, it can be used to predict the effects of combinations of combinations, and we

have no reason to believe that it will perform worse on unannotated compounds. On the contrary, our method may contribute to identifying mechanisms of action for novel compounds. The very ability of PMF to predict efficacies of combinations points to hidden mechanistic similarities within the set of compounds. By interpreting the PMF in terms of underlying biochemistry, we may gain insight into the nature of disease.

DATA AVAILABILITY STATEMENT

The cancer datasets analyzed for this study can be found on the ALMANAC website (https://wiki.nci.nih.gov/display/NCIDTPdata/NCI-ALMANAC/). The HD data can be obtained from the authors. Source code is available online at https://github.com/lezonlab/pmf-drug-combo/.

AUTHOR CONTRIBUTIONS

RN and TL performed all research, analyzed all results, and wrote the manuscript.

FUNDING

This work was supported by the National Institutes of Health through grants UL1TR001857 and R56AG059612.

SUPPLEMENTARY MATERIAL

The Supplementary Material for this article can be found online at: https://www.frontiersin.org/articles/10.3389/fbinf.2021.708815/full#supplementary-material

REFERENCES

Adam, G., Rampasek, L., Safikhani, Z., Smirnov, P., Haibe-Kains, B., and Goldenberg, A. (2020). 'Machine Learning Approaches to Drug Response Prediction: Challenges and Recent Progress. *NPJ Precis Oncol.* 4, 19. doi:10.1038/s41698-020-0122-1

Aggarwal, C. C. (2016). *Recommender Systems*. London, UK): Springer International Publishing.

Assran, M., and Rabbat, M. 2020. 'On the Convergence of Nesterov's Accelerated Gradient Method in Stochastic Settings', arXiv pre-print server.

Barabási, A.-L. (2016). *Network Science*. Cambridge, England): Cambridge University Press.

Bliss, C. I. (1939). The Toxicity of Poisons Applied Jointly1. *Ann. Appl. Biol.* 26, 585–615. doi:10.1111/j.1744-7348.1939.tb06990.x

Boguñá, M., and Pastor-Satorras, R. (2003). 'Class of Correlated Random Networks with Hidden Variables. *Phys. Rev. E* 68. doi:10.1103/physreve.68.036112

Caldarelli, G., Capocci, A., De Los Rios, P., and Muñoz, M. A. (2002). 'Scale-Free Networks from Varying Vertex Intrinsic Fitness. *Phys. Rev. Lett.* 89. doi:10.1103/physrevlett.89.258702

Calzolari, D., Bruschi, S., Coquin, L., Schofield, J., Feala, J. D., Reed, J. C., et al. (2008). 'Search Algorithms as a Framework for the Optimization of Drug Combinations. *Plos Comput. Biol.* 4, e1000249. doi:10.1371/journal.pcbi.1000249

Cummings, J. L., Tong, G., and Ballard, C. (2019). Treatment Combinations for Alzheimer's Disease: Current and Future Pharmacotherapy Options. *Jad* 67, 779–794. doi:10.3233/jad-180766

Gerlee, P., Schmidt, L., Monsefi, N., Kling, T., Jornsten, R., and Nelander, S. (2013). Searching for Synergies: Matrix Algebraic Approaches for Efficient Pair Screening. *PLoS One* 8, e68598. doi:10.1371/journal.pone.0068598

Ghosn, J., Taiwo, B., Seedat, S., Autran, B., and Katlama, C. (2018). Hiv. *The Lancet* 392, 685–697. doi:10.1016/s0140-6736(18)31311-4

Golub, G. H., and Reinsch, C. (1971). *Singular Value Decomposition and Least Squares Solutions*. Springer Berlin Heidelberg.

Gough, A., Soto-Gutierrez, A., Vernetti, L., Ebrahimkhani, M. R., Stern, A. M., and Taylor, D. L. (2021). Human Biomimetic Liver Microphysiology Systems in Drug Development and Precision Medicine. *Nat. Rev. Gastroenterol. Hepatol.* 18, 252–268. doi:10.1038/s41575-020-00386-1

Holbeck, S. L., Camalier, R., Crowell, J. A., Govindharajulu, J. P., Hollingshead, M., Anderson, L. W., et al. (2017). The National Cancer Institute ALMANAC: A Comprehensive Screening Resource for the Detection of Anticancer Drug Pairs with Enhanced Therapeutic Activity. *Cancer Res.* 77, 3564–3576. doi:10.1158/0008-5472.can-17-0489

Huang, L., Brunell, D., Stephan, C., Mancuso, J., Yu, X., He, B., et al. (2019). Driver Network as a Biomarker: Systematic Integration and Network Modeling of Multi-Omics Data to Derive Driver Signaling Pathways for Drug Combination Prediction. *Bioinformatics* 35, 3709–3717. doi:10.1093/bioinformatics/btz109

Ianevski, A., Giri, A. K., Gautam, P., Kononov, A., Potdar, S., Saarela, J., et al. (2019). Prediction of Drug Combination Effects with a Minimal Set of Experiments. *Nat. Mach Intell.* 1, 568–577. doi:10.1038/s42256-019-0122-4

Julkunen, H., Cichonska, A., Gautam, P., Szedmak, S., Douat, J., Pahikkala, T., et al. (2020). 'Leveraging Multi-Way Interactions for Systematic Prediction of Pre-clinical Drug Combination Effects. *Nat. Commun.* 11, 6136. doi:10.1038/s41467-020-19950-z

Kashif, M., Andersson, C., Hassan, S., Karlsson, H., Senkowski, W., Fryknas, M., et al. (2015). '*In Vitro* Discovery of Promising Anti-cancer Drug Combinations Using Iterative Maximisation of a Therapeutic index. *Sci. Rep.* 5, 14118. doi:10.1038/srep14118

Lee, D. D., and Seung, H. S. (1999). Learning the Parts of Objects by Non-negative Matrix Factorization. *Nature* 401, 788–791. doi:10.1038/44565

Lezon, T. R., and Bahar, I. (2010). 'Using Entropy Maximization to Understand the Determinants of Structural Dynamics beyond Native Contact Topology. *Plos Comput. Biol.* 6, e1000816. doi:10.1371/journal.pcbi.1000816

Lezon, T. R., Banavar, J. R., Cieplak, M., Maritan, A., and Fedoroff, N. V. (2006). Using the Principle of Entropy Maximization to Infer Genetic Interaction Networks from Gene Expression Patterns. *Proc. Natl. Acad. Sci.* 103, 19033–19038. doi:10.1073/pnas.0609152103

Lou, Y.-R., and Leung, A. W. (2018). Next Generation Organoids for Biomedical Research and Applications. *Biotechnol. Adv.* 36, 132–149. doi:10.1016/j.biotechadv.2017.10.005

Matlock, K., Berlow, N., Keller, C., and Pal, R. (2017). 'Combination Therapy Design for Maximizing Sensitivity and Minimizing Toxicity. *BMC Bioinformatics* 18, 116. doi:10.1186/s12859-017-1523-1

Menden, M. P., Wang, D., Mason, M. J., Szalai, B., Bulusu, K. C., Guan, Y., et al. (2019). 'Community Assessment to advance Computational Prediction of Cancer Drug Combinations in a Pharmacogenomic Screen. *Nat. Commun.* 10, 2674. doi:10.1038/s41467-019-09799-2

Milgram, S. (1967). SMALL-WORLD PROBLEM. *Psychol. Today* 1, 61–67. doi:10.1037/e400002009-005

Mittal, R., Woo, F. W., Castro, C. S., Cohen, M. A., Karanxha, J., Mittal, J., et al. (2019). Organ-on-chip Models: Implications in Drug Discovery and Clinical Applications. *J. Cel Physiol* 234, 8352–8380. doi:10.1002/jcp.27729

Mokhtari, R. B., Homayouni, T. S., Baluch, N., Morgatskaya, E., Kumar, S., Das, B., et al. (2017). Combination Therapy in Combating Cancer. *Oncotarget* 8, 38022–38043. doi:10.18632/oncotarget.16723

Mulani, M. S., Kamble, E. E., Kumkar, S. N., Tawre, M. S., and Pardesi, K. R. (2019). 'Emerging Strategies to Combat ESKAPE Pathogens in the Era of Antimicrobial Resistance: A Review. *Front. Microbiol.* 10, 539. doi:10.3389/fmicb.2019.00539

Ortiz-Orendain, J., Castiello-de Obeso, S., Colunga-Lozano, L. E., Hu, Y., Maayan, N., and Adams, C. E. (2017). Antipsychotic Combinations for Schizophrenia. *Cochrane Database Syst. Rev.* 6, CD009005. doi:10.1002/14651858.CD009005.pub2

Pei, F., Li, H., Henderson, M. J., Titus, S. A., Jadhav, A., Simeonov, A., et al. (2017). 'Connecting Neuronal Cell Protective Pathways and Drug Combinations in a Huntington's Disease Model through the Application of Quantitative Systems Pharmacology. *Sci. Rep.* 7, 17803. doi:10.1038/s41598-017-17378-y

Pierre, N. G., and Siebert, X. 2020. 'Deep Matrix Factorizations', arXiv pre-print server.

Rényi, P., and Erdős, A. (1959). On Random Graphs'. *Publicationes Mathematicae (Debrecen)* 6, 290–297.

Salakhutdinov, Ruslan., and Mnih, Andriy. (2007). "Restricted Boltzmann Machines for Collaborative Filtering," in Proceedings of the 24th international conference on Machine learning - ICML '07 (Probabilistic Matrix Factorization). doi:10.1145/1273496.1273596

Silva, A., Lee, B.-Y., Clemens, D. L., Kee, T., Ding, X., Ho, C.-M., et al. (2016). Output-driven Feedback System Control Platform Optimizes Combinatorial Therapy of Tuberculosis Using a Macrophage Cell Culture Model. *Proc. Natl. Acad. Sci. USA* 113, E2172–E2179. doi:10.1073/pnas.1600812113

Singh, S., Osna, N. A., and Kharbanda, K. K. (2017). Treatment Options for Alcoholic and Non-alcoholic Fatty Liver Disease: A Review. *Wjg* 23, 6549–6570. doi:10.3748/wjg.v23.i36.6549

Skardal, A., Murphy, S. V., Devarasetty, M., Mead, I., Kang, H. W., Seol, Y. J., et al. (2017). 'Multi-tissue Interactions in an Integrated Three-Tissue Organ-On-A-Chip Platform. *Sci. Rep.* 7, 8837. doi:10.1038/s41598-017-08879-x

Söderberg, Bo. (2002). 'General Formalism for Inhomogeneous Random Graphs. *Phys. Rev. E* 66. doi:10.1103/physreve.66.066121

Stern, A. M., Schurdak, M. E., Bahar, I., Berg, J. M., and Taylor, D. L. (2016). A Perspective on Implementing a Quantitative Systems Pharmacology Platform for Drug Discovery and the Advancement of Personalized Medicine. *J. Biomol. Screen.* 21, 521–534. doi:10.1177/1087057116635818

Takahashi, T. (2019). Organoids for Drug Discovery and Personalized Medicine. *Annu. Rev. Pharmacol. Toxicol.* 59, 447–462. doi:10.1146/annurev-pharmtox-010818-021108

Wang, Jue., Guan, Naiyang., Huang, Xuhui., and Luo, Zhigang. (2015). Constraint-Relaxation Approach for Nonnegative Matrix Factorization: A Case Study, IEEE International Conference on Systems, Man, and Cybernetics. Hong Kong, China: IEEE. doi:10.1109/smc.2015.383

Wang, X., Chang, L., Wang, B., Wang, D., Li, P., Wang, L., et al. (2013). Comparative Proteomics of Thellungiella Halophila Leaves from Plants Subjected to Salinity Reveals the Importance of Chloroplastic Starch and Soluble Sugars in Halophyte Salt Tolerance. *Mol. Cell Proteomics* 12, 2174–2195. doi:10.1074/mcp.m112.022475

Watts, D. J., and Strogatz, S. H. (1998). Collective Dynamics of 'small-World' Networks. *Nature* 393, 440–442. doi:10.1038/30918

Weiss, A., Berndsen, R. H., Ding, X., Ho, C. M., Dyson, P. J., van den Bergh, H., et al. (2015). 'A Streamlined Search Technology for Identification of Synergistic Drug Combinations. *Sci. Rep.* 5, 14508. doi:10.1038/srep14508

Wold, S., Esbensen, K., and Geladi, P. (1987). Principal Component Analysis. *Chemometrics Intell. Lab. Syst.* 2, 37–52. doi:10.1016/0169-7439(87)80084-9

Zheng, W., Thorne, N., and McKew, J. C. (2013). Phenotypic Screens as a Renewed Approach for Drug Discovery. *Drug Discov. Today* 18, 1067–1073. doi:10.1016/j.drudis.2013.07.001

Zuccato, C., Valenza, M., and Cattaneo, E. (2010). Molecular Mechanisms and Potential Therapeutical Targets in Huntington's Disease. *Physiol. Rev.* 90, 905–981. doi:10.1152/physrev.00041.2009

Conflict of Interest: The authors declare that the research was conducted in the absence of any commercial or financial relationships that could be construed as a potential conflict of interest.

Publisher's Note: All claims expressed in this article are solely those of the authors and do not necessarily represent those of their affiliated organizations, or those of the publisher, the editors and the reviewers. Any product that may be evaluated in this article, or claim that may be made by its manufacturer, is not guaranteed or endorsed by the publisher.

frontiers in Bioinformatics

ORIGINAL RESEARCH
published: 03 September 2021
doi: 10.3389/fbinf.2021.731340

A Mechanistic Site-Of-Action Model: A Tool for Informing Right Target, Right Compound, And Right Dose for Therapeutic Antagonistic Antibody Programs

Georgi I. Kapitanov[1], Jeffrey R. Chabot[1], Jatin Narula[1], Mahua Roy[1], Hendrik Neubert[2], Joe Palandra[2], Vahid Farrokhi[2], Jay S. Johnson[2], Robert Webster[1] and Hannah M. Jones[1]*

[1]BioMedicine Design, Pfizer Worldwide R&D, Cambridge, MA, United States, [2]BioMedicine Design, Pfizer Worldwide R&D, Andover, MA, United States

OPEN ACCESS

Edited by:
Morgan Craig,
University of Montreal, Canada

Reviewed by:
Yanguang Cao,
University of North Carolina at Chapel Hill, United States
Patrick Glassman,
University of Pennsylvania, United States

***Correspondence:**
Georgi I. Kapitanov
georgi.kapitanov@pfizer.com

Specialty section:
This article was submitted to Drug Discovery in Bioinformatics, a section of the journal Frontiers in Bioinformatics

Received: 02 July 2021
Accepted: 23 August 2021
Published: 03 September 2021

Citation:
Kapitanov GI, Chabot JR, Narula J, Roy M, Neubert H, Palandra J, Farrokhi V, Johnson JS, Webster R and Jones HM (2021) A Mechanistic Site-Of-Action Model: A Tool for Informing Right Target, Right Compound, And Right Dose for Therapeutic Antagonistic Antibody Programs. Front. Bioinform. 1:731340. doi: 10.3389/fbinf.2021.731340

Quantitative modeling is increasingly utilized in the drug discovery and development process, from the initial stages of target selection, through clinical studies. The modeling can provide guidance on three major questions–is this the right target, what are the right compound properties, and what is the right dose for moving the best possible candidate forward. In this manuscript, we present a site-of-action modeling framework which we apply to monoclonal antibodies against soluble targets. We give a comprehensive overview of how we construct the model and how we parametrize it and include several examples of how to apply this framework for answering the questions postulated above. The utilities and limitations of this approach are discussed.

Keywords: site of action, PKPD, QSP, modeling and simulation, LC-MS

INTRODUCTION

Modeling and simulation tools have become an essential part of the drug development process (Norris et al., 2000; Lalonde et al., 2007; Barrett et al., 2008; Edginton et al., 2008; Mager and Jusko, 2008; Rajman, 2008; Jones et al., 2009; Allerheiligen, 2010; van der Graaf and Benson, 2011; Zhao et al., 2011; Jones et al., 2012a; Knight-Schrijver et al., 2016; Danhof et al., 2018; Nijsen et al., 2018). Applying quantitative analyses early in the drug discovery can be very informative for selecting and de-selecting those programs with the best/least chance of clinical success. Traditional pharmacokinetics/pharmacodynamics (PKPD) models, while still widely utilized (Meibohm and Derendorf, 1997; Derendorf and Meibohm, 1999; Rajman, 2008), have gradually given place to increased mechanistic modeling complexity, with the intent to achieve higher predictive accuracy and mechanistic insights. These mechanistic modeling techniques include systems biology (SB) (Kitano, 2005; Kohl et al., 2010; Benson et al., 2011), quantitative systems pharmacology (QSP) (Hopkins, 2008; Allerheiligen, 2010; van der Graaf and Benson, 2011; van der Graaf, 2012; Jusko, 2013; Rogers et al., 2013; Peterson and Riggs, 2015; Knight-Schrijver et al., 2016; Danhof et al., 2018; Nijsen et al., 2018; Cucurull-Sanchez et al., 2019), and physiologically based pharmacokinetics (PBPK) (Baxter et al., 1994; Andersen, 1995; Baxter et al., 1995; Hoang, 1995; Arundel, 1997; Blakey et al., 1997; Nestorov et al., 1998; Grass and Sinko, 2002; Aarons, 2005; Jones et al., 2006a; Jones et al., 2006b; Cai et al., 2006; Barton et al., 2007; Nestorov, 2007; Edginton et al., 2008; Loizou et al., 2008; Jones et al., 2009; Chabot et al., 2011; Jones et al., 2011; Jones et al., 2012a; Jones et al., 2012b; Bouzom

et al., 2012; Huang and Rowland, 2012; Rostami-Hodjegan et al., 2012; Shah and Betts, 2012; Zhao et al., 2012; Jones et al., 2013). Traditional empirical PKPD models are useful in predicting dosing and estimating pharmacology/efficacy in later stage clinical development and translation from pre-clinical animal models to humans. However, an extensive amount of pre-clinical PKPD data is needed to utilize them which limits their ability to be used to make early pre-clinical recommendations, before lead candidates are defined. In contrast, the mechanistic models, while often complex and computationally intensive, appear more suitable for overall disease and molecule modality recommendations.

Early stage biologics drug discovery programs concern themselves with three main questions: (1) is the proposed target biologically relevant and is hitting the target feasible; (2) what are the drug characteristics that would allow for biomarker modulation or efficacy; (3) what is the efficacious dose in humans? These three questions can be summarized as three components to each project: right target, right compound, right dose. Considering the high number of potential new targets, a flexible mechanistic modeling framework is needed that can be used to perform sensitivity analysis on a discrete number of parameters. This approach would quickly pinpoint gaps in knowledge that can be tested experimentally and make timely recommendations for each of the three components of project development. Therefore, for this purpose, one needs a model that is on the spectrum of complexity somewhere between the traditional PKPD and the multiscale systems biology models. We propose a site-of-action (SoA) model for assisting in the discovery and development of biologics.

The site-of-action model extends a two compartment PKPD model by including the mechanistic interactions of the drug and its target (e.g., binding, unbinding and drug-target complex clearance), the relevant properties of the target, as well as a separate compartment that models the tissues in which the disease progresses (a so-called site of action) (Brodfuehrer et al., 2014). Such a model can be implemented rapidly since it captures only the relevant biology and is expressed through a discrete number of differential equations, variables, and parameters, which allows for extensive sensitivity analysis to identify the important parameters and biological assumptions that need to be investigated further. Hence, this model should be considered a starting point from which to build out specific models of the biology of different targets, its main utility being in early stage projects.

A previous iteration of the model has been described by Tiwari et al. 2016a and used for assessing sensitivity of the projected target neutralization to target concentrations (Tiwari et al., 2016a) and antibody affinity (Tiwari, et al, 2017). The current iteration makes minor changes to the old model structure and goes into more detail in explaining the reasons for certain modeling and parameter value choices. We have implemented this approach successfully since, and, beyond the theoretical treatment in Tiwari et al. 2016a, in **Applications of SoA Model Methodology** of this manuscript will be demonstrating its utility by several real-world examples. The modeling work is highly dependent on robust assays to inform the parametrization of the model (biomeasures), which is yet another important expansion to the work presented in Tiwari et al. 2016a. We have listed the typical assays and input data used in the **Target Parameters** section. For the purposes of this article, we will focus on soluble targets. Membrane targets deserve to be covered in a separate manuscript, both in terms of the modeling approach, as well as in terms of utilizing the range of biomeasure assays and tools for supporting the modeling efforts.

MODEL STRUCTURE AND METHODS OF PARAMETRIZATION

The model is an extension of a drug-target mechanistic binding two-compartment model that accounts for the relevant disease tissue, which is referred to as site of action (SoA). Free plasma drug (with concentration D_P in plasma volume V_P) distributes into non-specific (peripheral with volume V_T) and SoA (disease-specific with volume V_S) compartments. In plasma and at the SoA, the drug binds reversibly to target protein (with concentrations T_P and T_S, respectively) to form a drug-target complex (with concentrations C_P and C_S, respectively). The binding kinetics are characterized by a second-order association (k_{on}) and first-order dissociation (k_{off}) rate constants. The model assumes target synthesis and degradation both in the central and the SoA compartments (expressed by the zero order rates $ksyn_S$, and $ksyn_P$ and first order rates k_{degTp} and k_{degTs} , respectively), target distribution between plasma and the SoA (k_{psT} and k_{spT}), and drug - target complex distribution between plasma and SoA (k_{psC} and k_{spC}) and elimination in plasma only (k_{elC}). The modeling equations are:

$$\frac{dD_P}{dt} = A + k_{sp}D_S\frac{V_S}{V_P} + k_{tp}D_T\frac{V_T}{V_P} - k_{ps}D_P - k_{pt}D_P + k_{off}C_P - k_{on}D_PT_P - k_{el}D_P \quad (1)$$

$$\frac{dD_S}{dt} = k_{ps}D_P\frac{V_P}{V_S} - k_{sp}D_S + k_{off}C_S - k_{on}D_ST_S \quad (2)$$

$$\frac{dD_T}{dt} = k_{pt}D_P\frac{V_P}{V_T} - k_{tp}D_T \quad (3)$$

$$\frac{dC_P}{dt} = k_{spC}C_S\frac{V_S}{V_P} - k_{psC}C_P + k_{on}D_PT_P - k_{off}C_P - k_{elC}C_P \quad (4)$$

$$\frac{dC_S}{dt} = k_{psC}C_P\frac{V_P}{V_S} - k_{spC}C_S + k_{on}D_ST_S - k_{off}C_S \quad (5)$$

$$\frac{dT_P}{dt} = k_{spT}T_S\frac{V_S}{V_P} - k_{psT}T_P + k_{off}C_P - k_{on}D_PT_P + k_{synP} - k_{degTp}T_P \quad (6)$$

$$\frac{dT_S}{dt} = k_{psT}T_P\frac{V_P}{V_S} - k_{spT}T_S + k_{off}C_S - k_{on}D_ST_S + k_{synS} - k_{degTs}T_P \tag{7}$$

where D_i, C_i and T_i represent the concentrations of free drug, drug-target complex, and free target in plasma ($i = P$), or SoA ($i = S$) compartment, respectively. D_T is the free drug concentration in the peripheral tissue compartment. A is the drug influx function, which is administration dependent.

A schematic of the modeling reactions is shown in **Figure 1**. **Table 1** lists the variables and parameters contained in the system of differential equations, with explanations.

The initial conditions of the variables above appear with a 0 after the subscript: D_{P0} is initial drug concentration in the plasma, T_{S0} is initial target concentration at the SoA, etc.

Table 2 presents the value of A and initial conditions related to the drug variables dependent on administration route. Other administration routes can be incorporated as well.

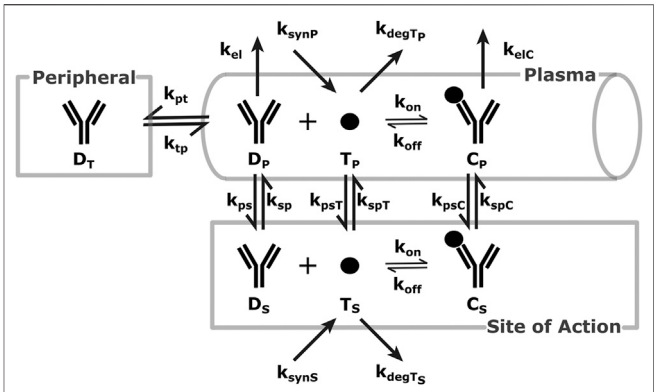

FIGURE 1 | SoA Model Scheme: A diagram describing the distribution and elimination of the mAb (denoted by D), synthesis, distribution and elimination of the target (denoted by T) and the interactions between the mAb and target and the distribution and elimination of the resulting mAb: target complex (denoted by C). Subscripts describe the compartments - p for plasma, t for peripheral tissues, s for the site of action. Detailed descriptions of all variables and parameters are in **Model Structure and Methods of Parametrization** and **Table 1**.

PARAMETER DETERMINATION

The next few sections will discuss how the different parameters are estimated and suggest typical assumptions for their values. Initial parametrization of the model may be obtained from the literature or data repositories. However, when such information is unavailable, experimental determination of key model parameters may be required. Some of the experimental methods discussed here may not be applicable, appropriate, or even possible for particular targets. A conversation among modelers, biologists, and biomeasure analysts would determine the most appropriate path to appropriate parametrization of the model.

Drug Distribution Parameters

Monoclonal antibody (mAb) PK typically shows biphasic behavior and such data can be modeled using two-compartmental models, resulting in the estimation of 4 PK parameters (e.g., $V1$, Cl, Q and $V2$) (Betts et al., 2018). A question then arises–what is the concentration of antibody at the SoA? There have been several preclinical studies that have been performed to measure concentrations in tissues relative to blood across different antibodies (Vugmeyster et al., 2008; Vugmeyster et al., 2010; Shah and Betts, 2013; Li et al., 2017; An et al., 2020). Antibodies distribute predominantly in the interstitium of tissues (Janeway and Walport, 2001), therefore the concentration ratio needs to be adjusted for the interstitial volume of the tissue of interest. Generally, the volume of the interstitium is around 1/3 of the total tissue volume (Poulin and Theil, 2002) (which includes peripheral blood and cells), unless one deals with certain specific organs like muscles or the brain (Shah and Betts, 2013). The ratio of total tissue to serum concentration for most organs in preclinical species is around 10% (Shah and Betts, 2013; Vugmeyster et al., 2010). Therefore, our recommendation is to use 30% (=10%/1/3) as a standard *ratio* parameter for non-brain and non-muscle tissue SoAs.

The following method can account for any ratio deemed appropriate for the particular project.

The calculations for the drug distribution constants presented here have two simultaneous aims: to retain mAb plasma PK and maintain the average concentration ratio (expressed as the parameter *ratio*) between the SoA and the plasma compartments (ratio of areas under the curve (AUCs) is equivalent). The following relationships are derived based on steady state analysis of total mAb concentration pharmacokinetics:

$$k_{ps} = ratio\, k_{sp}\frac{V_S}{V_P} \tag{8}$$

$$k_{pt} = \frac{Q}{V_P} - k_{ps} \tag{9}$$

$$V_T = \frac{V_P\, k_{pt}}{k_{tp}}, \tag{10}$$

where

$$k_{sp} = k_{tp} = \frac{Q}{V_2}.$$

There is an important distinction between V_2 and V_T which warrants further elaboration. Fixing the ratio of average drug concentration at the SoA vs the plasma, while preserving plasma PK, necessitates an extra degree of freedom in the calculations. Since drug concentrations in the peripheral tissue are rarely of interest, the peripheral tissue volume is a convenient (and mathematically sound) choice. However, the calculations of the drug distribution rates are done with the peripheral tissue volume of distribution from the PK parameter estimates, V_2 (see **Table 1**). In our practice, V_T is not used and peripheral mAb concentrations not tracked (as opposed to SoA concentrations), but understanding of the mathematics behind the model would

TABLE 1 | Definition of parameters used in SoA model.

Parameter	Description	Value	Units
V_P	Central compartment volume (plasma)	Drug specific	L
Q	Drug distributive clearance rate	Drug specific	L/day
Cl	Drug elimination clearance rate	Drug specific	L/day
V_S	Volume of SoA interstitial space	Tissue specific	L
V_T	Peripheral tissue volume (calculated)	Model specific	L
V_2	Peripheral tissue volume (from two-compartment PK)	Drug specific	L
D_0	Dose	Study specific	Nanomole
k_a	Rate of absorption post subcutaneous drug administration	Drug specific	1/day
F	Bioavailability post subcutaneous drug administration	Drug specific	Dimensionless
Q_{target}	Target distributive clearance rate	Target specific	L/day
$ratio$	Ratio of plasma versus SoA drug concentrations at steady state	SoA specific	Dimensionless
k_{on}	Drug-target concentration-dependent association rate	Drug specific	$nM^{-1}day^{-1}$
k_{ps}	Rate constant of drug distribution from plasma to SoA	$ratio * \frac{Q}{V_2} * \frac{V_S}{V_P}$	1/day
k_{sp}	Rate constant of drug distribution from SoA to plasma	$\frac{Q}{V_S}$	1/day
k_{pt}	Rate constant of drug distribution from plasma to peripheral tissue	$\frac{Q}{V_P} - k_{ps}$	1/day
k_{tp}	Rate constant of drug distribution from peripheral tissue to plasma	$\frac{Q}{V_2}$	1/day
k_{psT}	Rate constant of target distribution from plasma to SoA	$\frac{Q_{Target}}{V_P}$	1/day
k_{spT}	Rate constant of target distribution from SoA to plasma	Calculated to ensure target equilibrium in absence of drug	1/day
k_{psC}	Rate constant of complex distribution from plasma to SoA	k_{ps}	1/day
k_{spC}	Rate constant of complex distribution from SoA to plasma	k_{sp}	1/day
k_{el}	Rate constant of drug elimination from plasma	$\frac{Cl}{V_P}$	1/day
k_{degTp}	Rate constant of target elimination from plasma	Target specific	1/day
k_{degTs}	Rate constant of target elimination from SoA	Target specific	1/day
k_{elC}	Rate constant of complex elimination from plasma	For soluble target can be assumed = k_{el}, unless data are avalable	1/day
k_{off}	First-order dissociation rate constant of antibody	$k_{on} * K_D$	1/day
k_{synP}	Zero order target synthesis rate in plasma	Calculated to ensure target equilibrium in absence of drug	nM/day
k_{synS}	Zero order target synthesis rate in SoA	Calculated to ensure target equilibrium in absence of drug	nM/day

TABLE 2 | Expressions for ***A*** depending on route of drug administration.

Route of administration	Expression for *A*	Drug-related initial conditions
Intravenous bolus	$A = 0$	$D_{P0} = D_0$, $D_{T0} = D_{S0} = 0$
Subcutaneous	$A = D_0 * F * k_a$	$D_{P0} = D_{T0} = D_{S0} = 0$

be incomplete without V_T's explicit inclusion in the equations and the parameter set. Still, the reader's ability to use the model would not be inhibited by ignoring this extra mathematics.

Binding Parameters

If k_{on} has not been determined by a surface plasmon resonance method (Tang et al., 2010), or other methods, such as KinExA (Wani et al., 2016), k_{on} can be assumed to be $1e6\ M^{-1}s^{-1}$ (Foote and Eisen, 1995). Given a measured constant of dissociation (K_D), one can calculate k_{off} as the product of k_{on} and K_D. Drug:target interactions in the peripheral compartment and complex distribution from plasma to the peripheral compartment are typically ignored. To make binding interactions even more mechanistic, one can include step-wise binding for each of the antibody's arm. In this case the binding interactions from **Eqs 1–7** would need to be rewritten as follows:

$$\frac{dD_P}{dt} = \ldots + k_{off} C_P - 2\, k_{on} D_P T_P \tag{11}$$

$$\frac{dD_S}{dt} = \ldots + k_{off} C_S - 2\, k_{on} D_S T_S \tag{12}$$

$$\frac{dC_P}{dt} = \ldots + 2\, k_{on} D_P T_P - k_{off} C_P - k_{on} C_P T_P + 2\, k_{off} C_{P2} \tag{13}$$

$$\frac{dC_S}{dt} = \ldots + 2\, k_{on} D_S T_S - k_{off} C_S - k_{on} C_S T_S + 2\, k_{off} C_{S2} \tag{14}$$

$$\frac{dT_P}{dt} = \ldots + k_{off} C_P - 2\, k_{on} D_P T_P - k_{on} C_P T_P + 2\, k_{off} C_{P2} \tag{15}$$

$$\frac{dT_S}{dt} = \ldots + k_{off} C_S - 2\, k_{on} D_S T_S - k_{on} C_S T_S + 2\, k_{off} C_{S2} \tag{16}$$

$$\frac{dC_{P2}}{dt} = k_{spC} C_{S2} \frac{V_S}{V_P} - k_{psC} C_{P2} + k_{on} D_P T_P - k_{off} C_P - k_{elC} C_{P2} \tag{17}$$

$$\frac{dC_{S2}}{dt} = k_{psC} C_{P2} \frac{V_P}{V_S} - k_{spC} C_{S2} + k_{on} D_S T_S - k_{off} C_{S2} \tag{18}$$

For variables D_P, D_S, T_P , T_S, C_P, C_S, the only differences between **Eqs 11–18** and **Eqs 1–7** are the binding interactions, hence synthesis, distribution, and elimination reactions are replaced by ellipses for simplicity. Two new species are introduced: C_{P2} and C_{S2}, which represent the concentration of mAb bound to its target on each arm (a double complex) in plasma and the SoA, respectively. The factors of two account for the multiple ways in which an unbound antibody can engage a target, or a doubly bound antibody can release a target. Whether to include this mechanistic binding step is dependent on the biology and the requirement for this extra complexity.

Target Parameters

The target related parameters are turnover (half-life or degradation rate), synthesis rate, concentrations (both in

plasma and the SoA) and distribution rate (between the plasma and the SoA).

Estimating Target Concentrations

There are many published methods or approaches for measuring target levels both in serum and tissue (Becker and Hoofnagle, 2012), including ligand binding assays and mass spectrometry. A preferred approach, as previously highlighted due to its enhanced specificity and selectivity, is protein or peptide immunoaffinity liquid chromatography tandem mass spectrometry (IA LC-MS/MS). The method requires selection of optimal capture reagents, calibration standards and surrogate peptides for detection. In this method, proteins and/or trypsin digested peptides are enriched by anti-protein or anti-peptide antibodies or a sequential combination of both approaches. The enriched peptides are quantified using detection by nanoflow LC-MS/MS. A detailed description of this method can be found in Palandra et al. (2013) and Neubert et al. (2020). The addition of a stable isotope-labeled synthetic version of the surrogate peptide(s) prior to protein digestion reduces variables and quantitation relative to the chosen protein calibrator can be achieved. The mass spectrometric response of the endogenous peptide is compared to the analogous response for the labelled peptide in all samples, including calibrators, thereby normalizing for digestion efficiency and matrix suppression differences between the samples (Bantscheff et al., 2007). Examples of well designed, fit for purpose, sequential protein and tryptic peptide IA-LC-MS can achieve lower limit of quantitation (LLOQ) of sub 10 pg/ml (Neubert et al., 2013; Palandra et al., 2013), while protein IA and peptide IA only approaches are typically capable of achieving sub 100 pg/ml LLOQ (McAvoy et al., 2014; Zhao et al., 2018; Shuford et al., 2020).

Target expression levels vary widely depending on their biological function, disease state, tissue localization, and many other factors. For example, the growth and differentiation factor 8 (GDF-8), is present in circulation at very high expression levels of approximately 7 ng/ml in adult humans owing to its function in regulating muscle mass (Palandra et al., 2016). While targets like Interleukin-21 are not detected in human serum and can only be measured in certain human tissues such as colon tissue at an average concentration of 1 ng/g (Palandra et al., 2013). The alarmin cytokine, Interleukin-33 (IL-33) is present in circulation at approximately 20–100 pg/ml (Artru et al., 2020) and in many tissues at very elevated concentrations (200 ng/g in the lung (Cohen et al., 2015)) owing to its ubiquitous presence in the nucleus of all producing human cells. When the concentrations in a tissue homogenate are measured, the concentrations that are provided need to be adjusted for the interstitial volume of the analyzed tissue before being applied in the SoA model. Again, other methodologies have been used in some cases as driven by the protein and analytical complexities.

Estimating Target Turnover

While traditionally radio-labelling methods have been used for estimating turnover, methods based on *in-vivo* stable isotope labelling and proteomics have been established to measure physiologically relevant turnover (Bateman et al., 2006; Lindwall et al., 2006; Doherty and Whitfield, 2011; Hinkson and Elias, 2011; Lassman et al., 2014; Larance and Lamond, 2015). One of the preferred methods uses immunoaffinity enrichment of the target proteins from a stable isotope labeled amino acid tracer pulse-chase study, either from preclinical or clinical studies. Tracer incorporation in a surrogate peptide sequence is then measured by targeted mass spectrometry. The workflow and details of the study have been published (Farrokhi et al., 2018a). Once data is available for both the tracer levels and its incorporation in the protein of interest, the turnover rate is estimated using a series of models that account for the tracer's incorporation, as well as the known biological properties of the protein of interest (e.g., a shed receptor in the tissue vs cytokine released primarily in plasma). An earlier version of these models was used in Farrokhi et al. 2018a These assays are confined by the time limitations in pulse-chase durations (multiple hours or a few days) in *in vivo* studies and accurate measurement of slow turnover rates (i.e., multiple days or weeks) are not feasible or are estimated from extrapolation. Also, in some cases, measurements are not feasible due to low concentrations of the target protein. Other methodologies have also been published in the literature, (Bateman et al., 2006; Lindwall et al., 2006; Doherty and Whitfield, 2011; Hinkson and Elias, 2011; Lassman et al., 2014; Larance and Lamond, 2015), but they are likely to experience similar limitations. Physiological target turnover measurements in human is limited to only the soluble targets and turnover in SoA is estimated from soluble target when possible.

Target Synthesis Rate

Generally, once information about the target's concentrations and turnover are available, the synthesis is calculated assuming that in the absence of drug the system is at steady state. The rate constant for target distribution from the plasma to the site of action (k_{psT}) can be fixed. The rate constant for target distribution from the site of action to the plasma (k_{spT}) is derived based on the steady state levels of target in the plasma and the SoA together with k_{psT}. At steady state, synthesis rates, degradation rates, and distribution rate constants between the plasma and the SoA must be balanced to achieve known levels of target concentrations in both compartments.

Target steady state concentration in plasma prior to drug administration is defined by:

$$\frac{dT_P}{dt} = k_{synP} - T_{P0}\left(k_{degTp} + k_{psT}\right) + T_{S0}\, k_{spT}\, V_S/V_P = 0 \qquad (19)$$

Target steady state concentration at the SoA prior to drug administration is defined by:

$$\frac{dT_S}{dt} = k_{synS} - T_{S0}\left(k_{degTs} + k_{spT}\right) + T_{P0}\, k_{psT}\, V_P/V_S = 0 \qquad (20)$$

Total target synthesis in the human body (in amount, nanomoles) is defined as:

$$k_{synTot} = k_{synP}\, V_p + k_{synS}\, V_S = T_{P0}\, k_{degTp}\, V_P + T_{S0}\, k_{degTs}\, V_S \qquad (21)$$

It is rare that one has information about the ratio between target synthesis in plasma versus the SoA. This ratio is generally assumed taking into account what is known about the biology. For the remainder of this section and for the purpose of equations

and calculations, the fraction of total synthesis in the SoA is captured by the parameter *frac*.

Estimating Target Distribution

While drug distribution constants can be calculated from the PK and **Eqs 8–10** above, target rates of distribution are largely unknown. We fix k_{psT}:

$$k_{psT} = \frac{Q_{target}}{V_P}. \tag{22}$$

At an exploratory stage, we use a parameter value for Q_{target}, estimated from literature data reporting a distributive clearance rate of Albumin from Synovial joints of Rheumatoid arthritis patients (Owen et al., 1994). While this parameter value can be used in the initial stages of a project, as a project progresses, this value is explored in more detail and is updated by considering a pharmacokinetics based value for a recombinant version of the target, e.g., (Creaven et al., 1987; Banks et al., 2000; Zhang et al., 2019), or by basing Q_{target} on the molecular weight of the target (Li et al., 2017).

Since these approaches have not be largely validated and adopted, one is advised to employ sensitivity analysis regarding target distribution parameters.

If k_{psT} is fixed, assuming $k_{synS} = frac * \frac{k_{synTot}}{V_S}$ and rearranging **Eqs 19** and **22** will result in:

$$k_{spT} = frac \frac{\left(T_{P0}\, k_{degTp}\, V_P + T_{S0}\, k_{degTs}\, V_S\right)}{T_{S0}\, V_S} - k_{degTs} + \frac{T_{P0}\, V_P}{T_{S0}\, V_S} * k_{psT} \tag{23}$$

APPLICATIONS OF SITE-OF-ACTION MODEL METHODOLOGY

This section provides four examples of application of the SoA modeling structure to soluble targets. The examples are divided into the three main categories for successful use of translational modeling and simulation: right target, right compound, and right dose.

Right Target

In the pre-clinical space, especially in early project stages, it is appropriate to conduct feasibility analysis. At this stage, a successful assessment is both one that progresses a target as a part of the portfolio and eventually into the clinic, as well as one that shows that a target is infeasible from a clinical utility standpoint. Such analyses are performed to determine whether sufficient levels of target coverage can be achieved via neutralization with a monoclonal antibody and should not be confused with determining whether the target is "right" from a disease standpoint. Often these analyses are done with just in-vitro functional assays, whose utility is limited - they capture a narrow aspect of the biology and may be done in the pre-portfolio stage. Once the project is part of the portfolio, we recommend a more thorough analysis with a SoA model since more resources for modeling and biomeasures/biomarkers are available. In many cases, the required levels of target coverage for efficacy are unknown so a threshold is set, depending on the disease, competitive landscape, and other factors, often at >90% or >99% target neutralization. If the required coverage for pharmacology cannot be achieved at a commercially viable dose, project termination is recommended.

Osteopontin Example

The first example in this section is an example of the latter-targeting osteopontin for rheumatoid arthritis (RA). Osteopontin is a secreted protein from a plethora of cells, that has been implicated in a variety of biological functions, from inflammation and fibrosis, to tumorigenesis and metastasis (Ashkar et al., 2000; Lund et al., 2013; Wang et al., 2014; Liu et al., 2015; Clemente et al., 2016). The goal of the work was to assess feasibility in suppressing osteopontin for the treatment of RA. A full SoA model was not utilized in this case because, as you will see, plasma levels of osteopontin were high enough to sufficiently inform feasibility, without the need for further modeling complexity. Target turnover was estimated using a human D3-leucine pulse-chase study similar to discussed in **Estimating Target Turnover**. Target serum concentrations were measured using a nano flow liquid chromatography-tandem mass spectrometry method similar to discussed in **Estimating Target Concentrations**. Mean serum concentrations were measured at around 10 nM and half-life was estimated at around 10 min. The scenarios presented here assume a mAb interacting with a soluble target and PK parameters for the drug are in **Table 3**. For the purpose of the example, to assess the degree of target coverage (free target reduction) in plasma, two dosing regimens were explored – 300 mg SC and 1,000 mg IV, both every week. These are not commercially viable doses for RA but were selected to explore the maximum attainable coverage with a monoclonal antibody targeting osteopontin. The effect of antibody affinity on target coverage was simulated using K_D values of 1 nM, 100 pM, for both scenarios, and 10 pM for the IV dosing scenario. The results of the simulations can be seen in **Figures 2** and **3**. Ultimately, the high target levels and very fast target turnover resulted in low target trough coverage even at a non-commercially viable dosing regimens for RA. Drug affinity for the target was predicted to have little effect on the coverage, so affinity optimization would not help. Therefore, the target was determined undruggable with a regular monoclonal antibody and the project was not progressed. More detailed assessment of this target with a different modeling approach can be seen in Farrokhi et al. 2018b, where other antibody modalities were also explored.

IL-33 Example

Another feasibility example is IL-33. IL-33 is an alarmin, member of the IL-1 cytokine family, released by cells at the barrier surfaces (i.e., keratinocytes and airways epithelial cells) after disruption in the barrier function by pathogens, tissue injury, and cell death, and has been associated with atopic dermatitis and asthma (Saluja et al., 2015; Saluja et al., 2016). Asthma is the disease of choice for this example, therefore the SoA is lung. IL-33 signals through binding to ST2 and then forming a heterodimer with the IL-1

TABLE 3 | Antibody PK parameters for osteopontin feasibility analysis.

Parameter	Value (unit)	References
V_P	3.2 (L)	Betts et al. (2018)
V_2	2.2 (L)	
Cl	0.454 (L/d)	
Q	0.252 (L/d)	
k_a	0.26 (1/d)	Assumed, (Dirks and Meibohm, 2010)
F	60 (%)	

receptor (Saluja et al., 2015; Saluja et al., 2016; Griesenauer and Paczesny, 2017). ST2 can also be found in soluble form (sST2), which is a scavenger for IL-33 and constraints its signaling properties (Griesenauer and Paczesny, 2017). For the purpose of this example, our antibody competes with sST2 for binding to IL-33 in plasma. A scheme and description of the model is shown in **Figure 4**. The antibody binds IL-33 both in plasma and at the SoA. The distribution of the drug to the SoA and the periphery as well as assumptions regarding the mAb:IL-33 complex have been described earlier (see **Drug Distribution Parameters**). The target-related parameters and references used are described in **Table 4**. The mAb related parameters are described in **Table 3** and **Binding Parameters**. K_D for the purpose of this feasibility analysis was assumed to be either 100 or 10 pM - k_{on} remained fixed (see *Binding Parameters*), while k_{off} was calculated accordingly. **Figure 5** shows projected target coverage at the site of action (lung). Based on the modeling results, the 100 mg SC Q4W dose is predicted to achieve greater than 90% neutralization of IL-33 at the site of action if the affinity of the mAb is closer to 10 pM than 100 pM. While a ~10 pM affinity is challenging from an engineering perspective, design of a high-affinity antibody should be expected when targeting cytokines, especially if the ligand's binding to its natural receptor is so tight (26 pM (Palmer et al., 2008)). In this case it was concluded, using the modelling analysis, that the target should be explored further, however extensive affinity optimization will likely be required to achieve sufficient neutralization. A Matlab Simbiology model file for this example is available in the Supplement section of this article.

This early-stage feasibility analysis omits several potentially important aspects of the biology of IL-33, e.g., quick inactivation due to oxidation and proteolytic activities, and synthesis in cellular nucleus and release under inflammatory conditions (Cohen et al., 2015; Saluja et al., 2015; Griesenauer and Paczesny, 2017; Scott et al., 2018). The former can increase the apparent clearance of active IL-33 and both properties can skew the measurements of active free IL-33 in plasma and tissue. Also, considering the tight binding of IL-33 to sST2, further considerations can be made regarding the expression of membrane ST2 in the lung and the antibody's interaction with the target in a full receptor:target interaction mechanistic modeling system. Potentially, a competing vs non-competing epitope may be important for enhancing target neutralization, which could be evaluated at the next stage of mechanistic modeling - right molecule. Several anti-IL-33 molecules have already been in the clinic, and a couple have shown positive results in asthma (Anaptysbio, 2014; Regeneron Pharmaceuticals, 2019), validating the model's conclusions.

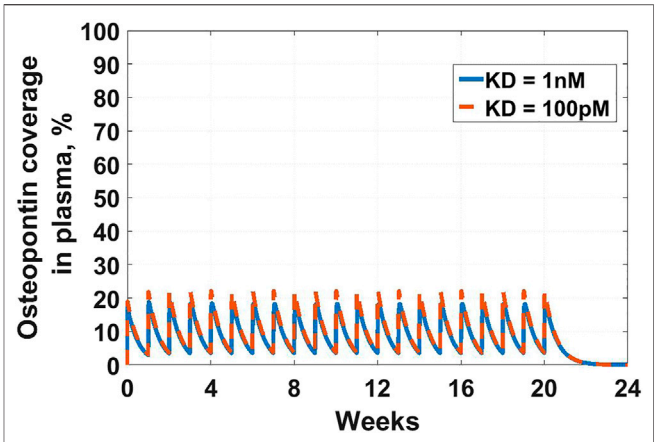

FIGURE 2 | Osteopontin coverage in plasma: Shows the projected neutralization of osteopontin after mAb administration as described in *Osteopontin Example*. Simulated dose is 300 mg SC Q1W, with two antibody affinities – K_D of 1 nM (solid blue line) and 100 pM (dashed orange line). Even peak projected neutralization is only 20%, which is unlikely to result in meaningful pharmacology.

Right Compound

Once feasibility has been established, the team delves deeper into assessing the molecular properties of the antibody necessary to neutralize the target. Most of the pharmacokinetic properties would depend on molecular assessment and there are currently few models that connect antibody molecular assessment and pharmacokinetics (Jones et al., 2019; Jones et al., 2020). Predominantly, modelers can assist the engineering team with projecting what antibody binding affinity is needed for the required level of neutralization (coverage). We use the next example of a clinical compound, to assess whether the mechanism was tested adequately and what affinity is required for improved target neutralization at a commercially viable dose.

Chemokine (C-C motif) ligand 20 (CCL20) is a chemoattractant for lymphocytes and dendritic cells in a variety of mucosal tissues (Schutyser et al., 2003). GSK3050002 is an anti-CCL20 monoclonal antibody that was tested in healthy volunteers (Bouma et al., 2017). The data presented in the study was drug, drug:target complex, and free target concentrations both in serum and in skin blister. The drug did not appear to inhibit monocytes and granulocytes activity in the skin blister model, so we decided to test whether a higher affinity antibody would be predicted to achieve higher and more sustained target coverage at the skin. For this purpose, a SoA model was constructed with skin as the SoA with the assumption that CCL20 was synthesized in the skin only and eliminated in the plasma only. Interstitial skin volume was assumed to be 1.125 L (Shah and Betts, 2012). Two-compartment PK model parameters (**Table 4**), K_D (350 pM), target half-life (15 min), plasma:skin drug concentration ratio (20%, measured), and initial CCL20 concentrations in the plasma (30 pM) were fixed based data

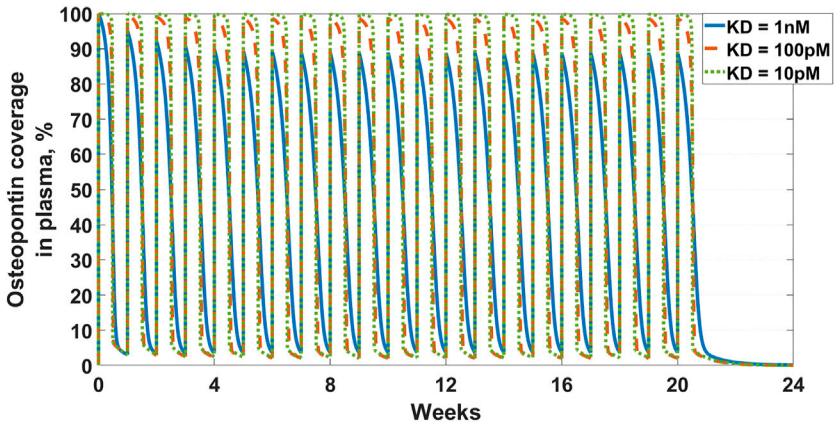

FIGURE 3 | Osteopontin coverage in plasma: Shows the projected neutralization of osteopontin after mAb administration as described in *Osteopontin Example*. Simulated dose is 1,000 mg IV Q1W, with three antibody affinities – K_D of 1 nM (solid blue line), 100 pM (dashed orange line), and 10 pM (dotted green line). All scenarios result in high peak neutralization, which is not sustained for the full duration of the dosing interval.

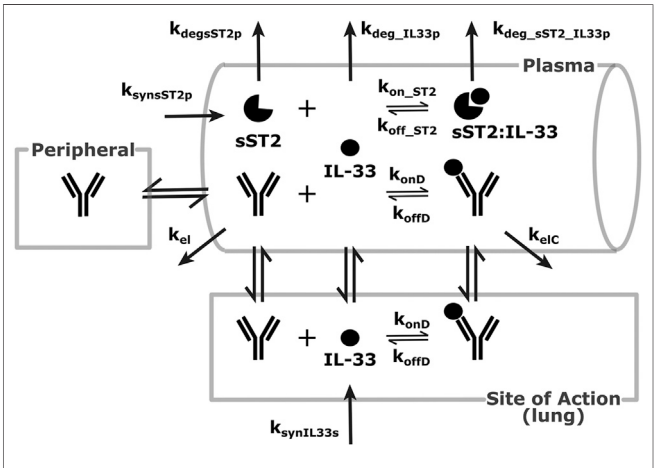

FIGURE 4 | Modeling scheme of an anti-IL-33 mAb. The general processes are similar to the default scheme described in **Figure 1**, with several details adapted to the IL-33 scenario. IL-33 is synthesized at the SoA (lung) and distributes to the plasma. There, it can bind sST2 or get eliminated. sST2 is synthesized and eliminated in plasma only. The sST2:IL-33 complex clears in the plasma.

provided in Bouma et al., 2017. Skin concentrations of CCL20 are assumed to be 10-fold higher than plasma. Under these assumptions, even a dose of 20 mg/kg is not projected to achieve 90% target reduction in the skin for more than ~ a week (**Figure 6**). At a regimen of 300 mg SC Q2W, the mAb is projected to need an affinity of 3.5 pM in order to reduce the target by 90% (**Figure 7**). This suggests that the affinity of the mAb was not tight enough and that the CCL20 mechanism was likely not adequately tested in the published clinical study.

While the general conclusion may still hold, several assumptions affect the results of the model. Some, like the synthesis of CCL20 in the skin, are reasonable given that the disease of interest is atopic dermatitis. The SoA:plasma ratio was assumed similar to the one found in IL-33 (see **Table 5**). That ratio would be target-dependent and potentially sensitivity analysis would need to be done to fully evaluate.

Right Dose

Once drug properties have been established, modeling is utilized to project a clinical efficacious dose in different patient populations. This step is important both from standpoint of selecting doses for toxicology studies and assisting in dose selection for first-in-human studies. This particular example is a *retrospective* analysis of the clinical compound IMA-026, an antagonist monoclonal antibody against IL-13 (Gauvreau et al., 2011; Kasaian et al., 2011; Tiwari et al., 2016b). IL-13 is a cytokine with demonstrated role in many inflammatory diseases, including asthma. IMA-026 is an M1 type anti-IL-13 antibody (May and Fung, 2015), which blocks IL-13 from interaction with its receptors - IL13Rα1 (signaling receptor) and IL13Rα2 (decoy receptor) (Chandriani et al., 2014). IMA-026 data in healthy volunteers (NCT00517348) has been analyzed before (Tiwari et al., 2016b), where initial IL-13 concentrations, drug affinity, and target turnover were estimated. However, we demonstrate here that the accumulation of total plasma concentration of IL-13 can be obtained without fitting any parameters by using literature references (target turnover), pre-clinical observations (drug affinity), and relevant clinical data (PK and initial target concentrations). IL-13 target turnover was estimated to be around 20 min in mice (Khodoun et al., 2007), drug K_D was 1 nM (based on internal measurements), median initial plasma IL-13 concentrations were estimated using ligand binding assay (LBA) to be around 0.06 pM for healthy volunteers and 0.12 pM for asthmatic patients, and PK parameters were estimated in Tiwari et al., 2016b. A SoA model was constructed with interstitial lung volume of 0.3 L (Shah and Betts, 2012) and SoA target concentrations of 0.03 pM in healthy volunteers and 0.4 pM in asthmatic patients (Kroegel et al., 1996). An average human bodyweight of 70 kg was assumed. **Figure 8** shows the simulation of total IL-13 accumulation using the SoA model in plasma along with the observed clinical data from the healthy

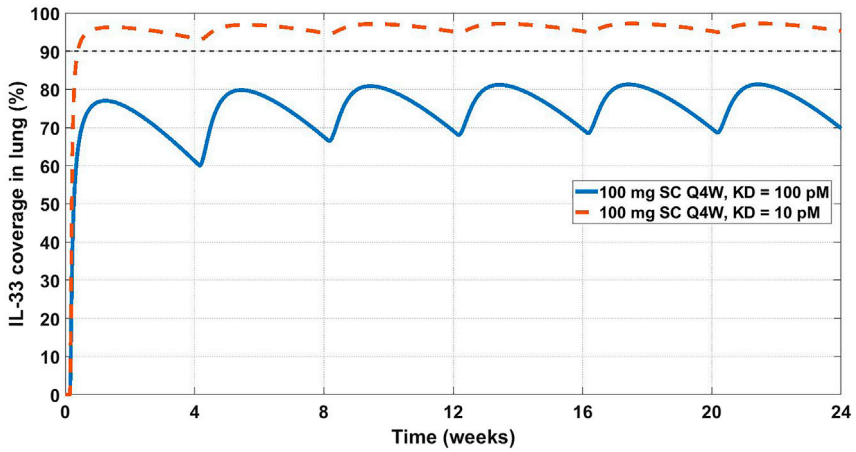

FIGURE 5 | Projected IL-33 neutralization in the lung at 100 mg SC Q4W dosing at 10 pM (dashed orange line) and 100 pM (solid blue line) drug affinities. The 90% coverage line (dashed grey) is emphasized for convenience. The model projects that a 10 pM affinity would achieve 90% IL-33 neutralization in the lung.

TABLE 4 | GSK3050002 two-compartment PK parameters (Bouma et al., 2017).

Parameter	Value (unit)	95% CI
V_P	3.63 (L)	3.44–3.83
V_2	3.19 (L)	2.89–3.52
Cl	0.475 (L/d)	0.439–0.514
Q	0.374 (L/d)	0.324–0.432

volunteer study. IMA-026 was evaluated further in an additional clinical study, NCT00725582, *Study Evaluating the Effect of IMA-026 on Allergen-Induced Late Asthma Response in Mild Asthma*. Two 2 mg/kg SC doses were administered 1 week apart.

The SoA model estimated that after 2 weeks dosing of 2 mg/kg SC Q1W the drug reached only around 8% target suppression at the site of action, while 8 weeks of dosing of 30 mg/kg SC Q1W would have achieved close to 90% coverage (**Figure 9**). Ultimately IMA-026 was abandoned since it did not show efficacy (Gauvreau et al., 2011). However, had data supporting an SoA model been available at time of the study conception, it could have projected the low coverage at 2 mg/kg and suggested either a longer duration study or a more appropriate dose for testing the mechanism. Likely, if SoA modeling had been available even earlier, an affinity maturation campaign could have been initiated to increase the affinity above 1 nM since a dose of 30 mg/kg Q1W is not commercially feasible. Suggestions for increased dose or improved affinity are corroborated by a crowd of anti-IL-13 monoclonal antibodies that have subsequently shown moderate to low efficacy in asthma (Gauvreau et al., 2011; Noonan et al., 2013; van Hartingsveldt et al., 2013; De Boever et al., 2014; Hanania et al., 2016), indicating the difficulty of achieving complete neutralization of IL-13 and/or its role as a standalone mechanism in the disease. The only anti-IL-13 mAb that has been in Phase 3 for asthma is lebrikizumab, with reported affinity of <10 pM (Ultsch et al., 2013). Lebrikizumab is currently in development for atopic dermatitis with positive results (Guttman-Yassky et al., 2020). Tralokinumab, whose affinity is reported at 58 pM (Popovic et al., 2017), has been approved for treatment of atopic dermatitis (LEO Pharma announces, 2021). The success and high affinity of both mAbs validate the model's conclusions.

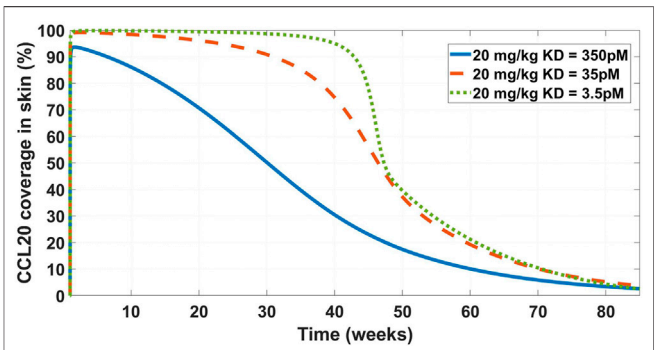

FIGURE 6 | Model projected CCL20 coverage in the skin after administration of 20 mg/kg IV bolus dose of GSK3050002. Three mAb affinity scenarios were modeled – 350 pM (solid blue line), 35 pM (dashed orange line), and 3.5 pM (dotted green line). The low coverage at the base K_D of 350 pM is consistent with observed lack of activity as described in Bouma et al. 2017.

DISCUSSION

We have presented a three compartment mechanistic model that extends a typical two-compartment model by adding a site of action - a representation of the interstitial volume of the tissue where the interactions of the protein target with the drug are expected to contribute to disease modulation. The modeling is performed through a system of ordinary differential equations and is a mechanistic representation of the interaction of the drug with the target. The framework can be used for constructing a fit-for-purpose model to evaluate whether a target is biologically relevant and hitting the target is feasible (right target), guide drug properties

TABLE 5 | List of target-related parameters used for anti-IL-33 model.

Parameter	Description	Value, units	Comments and references
IL33s_0	Initial concentration of free IL-33 at the SoA (lung)	11 pM	200 pg/mg of lung tissue in COPD or asthmatic patients (Cohen et al., 2015)
IL33p_0	Initial concentration of free IL-33 in plasma	1.5 pM	Assumed similar between asthma and allergic rhinitis – 27 pg/ml (Glück et al., 2019)
sST2_0	Initial concentration of free sST2 in plasma	27 pM	1 ng/ml in mild/moderate attack ((Oshikawa et al., 2001)), within two-fold of most other situations in Oshikawa et al. (2001) and levels in Glück et al. (2019)
sST2_IL33p_0	Initial concentration of sST2-bound IL-33 in plasma	$= k_{on\_ST2} * IL33p_0 * \frac{sST2p_0}{k_{off\_ST2} + k_{deg\_sST2\_IL33p}}$	To preserve drug-free equilibrium values
IL-33 molecular weight	To convert mass concentration into molarity	18 kDa	Palmer et al. (2008)
sST2 molecular weight	To convert mass concentration into molarity	37 kDa	Mueller and Dieplinger, (2016)
k_{deg_IL33p}	Degradation rate of IL-33 in plasma	4.2 1/day	~4 h half-life in human lung explants (Cohen et al., 2015)
k_{deg_sST2p}	Degradation rate of sST2 in plasma	2.6 1/day	6.3 h half-life (recombinant, IV administration) (Jacobs et al., 1993)
$k_{deg\_sST2\_IL33p}$	Degradation rate of sST2:IL-33 complex in plasma	$= k_{deg\_sST2p}$	Assumed
k_{on_ST2}	Association constant between IL-33 and sST2	358 1/nM/day	Palmer et al. (2008)
k_{off_ST2}	Dissociation rate between IL-33 and sST2	$= k_{on\_ST2} * K_{D\_IL33\_sST2}$	$K_{D\_IL33\_sST2}$ = 26 pM (Palmer et al., 2008)
k_{ps_IL33}	IL-33 distribution rate from plasma to SoA	0.13 1/day	See **Estimating Target Distribution**
k_{sp_IL33}	IL-33 distribution rate from SoA to plasma	$= (k_{ps\_IL33p} * IL33p_0) * \frac{V_P}{V_S * IL33s_0} + \frac{k_{syn\_IL33s}}{IL33s_0}$	To preserve drug-free equilibrium values
k_{syn_IL33s}	IL-33 synthesis rate at the SoA	$= (k_{deg\_IL33p} * IL33p_0 + k_{deg\_sST2\_IL33p} * sST2\_IL33p_0) * \frac{V_P}{V_S}$	To preserve drug-free equilibrium values
k_{syn_sST2p}	sST2 synthesis rate in plasma	$= k_{deg\_sST2p} * sST2p_0 + k_{deg\_sST2\_IL33p} * sST2\_IL33p_0$	To preserve drug-free equilibrium values

for sufficient target engagement (right compound) and inform the necessary doses for achieving the degree of target engagement required for efficacy in the clinic (right dose). While the case studies described were categorized into examples of each of these three questions, these questions are inter-linked and in practice the modelling approach addresses all three if used at an appropriate stage of the drug discovery process. Ideally at project inception, a model should be generated to explore feasibility, affinity, and PK requirements for a desired dose level. Such an approach allows drug companies to focus on programs with the highest chance of success and limit the "wasted" resources on those which are more likely to fail. Hence, our proposal is to utilize this model in the early stages of drug discovery and, if possible, validate with clinical data.

The main feature of the SoA modeling approach is its flexibility. Depending on the target, a modeler can include any number of SoA compartments, ranging from zero to including every main tissue in the human body. Along with the system of equations, we suggest two key biomeasures: target concentrations and turnover, which represent essential parameters in early stage pre-clinical work. This is evident in the examples we presented - osteopontin could not be covered at any reasonable dose or affinity because of its high abundance and turnover; IL-33 needed high affinity for high neutralization but was deemed feasible due to relatively low expression and slow turnover; CCL20 also needed high affinity and a high dose to neutralize due to fast turnover. Different targets have different associated biology and will require different strategies to overcome difficulties in neutralizing them. Hence, while for the purpose of this discussion we are focused on the modeling structure, a capable biomarkers/biomeasures group is essential for the translational research effort.

Within the SoA model framework one can implement a variety of biological complexities: downstream or upstream biomarkers, different cell types, ligand-receptor binding, etc. The SoA model facilitates their implementations but one must weigh the complexity of the model versus the questions it tries to answer. The SoA modeling approach is not appropriate for a full disease model, for that goal a more complex QSP implementation

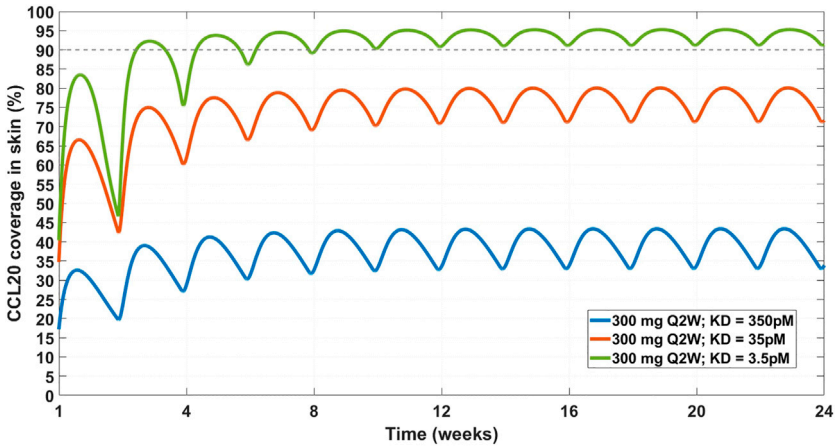

FIGURE 7 | Projected CCL20 coverage in the skin at 300 mg SC Q2W dosing regimen and varying affinity. Three affinity scenarios were simulated – 350 pM (solid blue line), 35 pM (solid orange line), and 3.5 pM (solid green line). Thin dashed grey line indicates 90% coverage, which is emphasized for convenience. The model projects that a 3.5 pM affinity is required for achieving 90% CCL20 coverage in the skin.

would be appropriate. The SoA model is also not a physiologically based pharmacokinetics (PBPK) model - if the distribution of the drug in the whole body is important for the project, a PBPK model would likely be the appropriate tool.

The SoA model, as presented here, is fit for mAb modeling with its representation of mechanistic target binding and unbinding. The model can be adjusted and has been utilized to incorporate different molecular modalities - pegylated Fab fragments, bispecific antibodies, etc.

The examples in the manuscript are focused on soluble targets, which simplified some aspects of the presentation. Membrane-bound targets often present different challenges from modeling standpoint (i.e., target-mediated drug disposition, shedding of the membrane target) and relevant biomarker and biomeasures assays (i.e., number of receptors per cell, quantifying receptor internalization). These aspects can be described in a separate manuscript but there are excellent discussions on the topic, among which Aston et al. 2011 and Grimm 2009.

There are a number of shortcomings to the SoA modeling platform. The peripheral compartment may be underutilized - the model as presented here does not include target expression and turnover in the peripheral compartment or drug:target complex distribution in and out of the peripheral compartment. The method of fixing the ratio of drug concentration in plasma vs. the SoA assumes similar

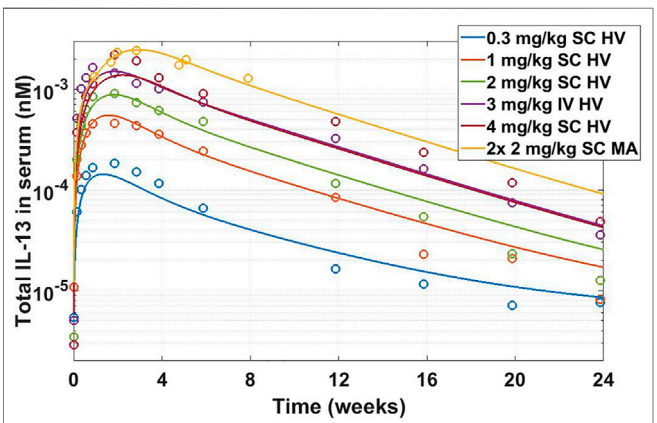

FIGURE 8 | Total IL-13 accumulation after IMA-026 administration in Phase I trial - model simulations vs published data. Different color solid lines correspond to different doses, open circles with corresponding colors are clinical data. Labels: SC, subcutaneous; IV, intravenous; HV, healthy volunteers; MA, mild asthmatics. The model reasonably captures the behavior using internal affinity measures, previously published target data, and published PK parameters for IMA-026, without fitting any parameters.

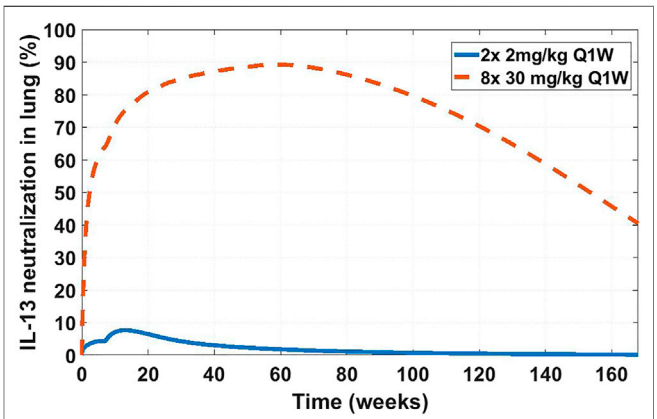

FIGURE 9 | Projected IL-13 neutralization in lung at two dosing schedules for IMA-026. Two doses of 2 mg/kg a week apart (solid blue line) was the clinically tested dose in asthma patients (NCT00725582). Eight doses of 30 mg/kg a week apart (dashed orange line) is a hypothetical clinical dose at which the projected IMA-026 coverage reaches close to 90% IL-13 neutralization in the lung. Modeling suggests that the mechanism of IL-13 neutralization was likely untested in the clinic due to low tested dose, which is projected to result in low coverage.

distribution to other previously measured antibodies. The rate of distribution of the drug into the SoA may have an effect on the target neutralization, and here it is calculated. Some of the mathematical methods may lead to non-physiological rates in order to preserve the measured concentrations at steady state. For example, the use of target distribution fixes the rate of distribution from plasma to the SoA and calculates the rate of distribution from the SoA into the plasma when assuming that the target is only synthesized in the SoA. This can lead to non-physiological differences in the plasma:SoA back and forth distribution rates. The very assumptions of target synthesis and distribution can alter the estimate of target suppression. However, despite these potential caveats of the base SoA model described in this manuscript, it is possible to adapt the framework to capture the relevant biological mechanisms as appropriate so that the sought physiological modulation can be described more accurately. Therefore, all the assumptions and calculations presented in this manuscript are just the most current iterations of ideas and are subject to scrutiny in the face of new facts and better representations.

As with all models, this framework requires validation. Early decisions can be made with sparse data and limited measurements but in order to improve confidence in the modeling results, ideally, measurements of key dynamics behaviors predicted by the model (longitudinal measurements of target engagement, free or total target levels, etc.) in relevant species with the candidate molecule or a suitable surrogate are needed for model validation. Furthermore, a retrospective validation using clinical data (external clinical data can also inform the pre-clinical model) should be performed when data is available in order to bridge the gap between theoretical and practical model projections. Some aspects of these validations include clinically-relevant disease-dependent level of target neutralization, distribution of the mAb into various types of SoA, or evaluation of the pre-clinical affinity biomeasures or functional assays and their translatability to the clinical setting. Not every project needs a site-of-action or a quantitative systems pharmacology model for successful translation from discovery to development. For the ones where understanding of the underlying pharmacology is limited, a simple exposure-response approach may be sufficient.

CONCLUSION

Ultimately, the SoA platform model is a useful framework that has allowed us to inform the progression of many successful mAb programs. In particular, we have used the model to determine the doability of targets, drug requirements for "best in class" mAbs and dosing regimens to achieve required levels of target coverage to demonstrate efficacy. This modeling approach is fully integrated in the drug discovery process with the ability to make decisions believed to be high.

DATA AVAILABILITY STATEMENT

Publicly available datasets were analyzed in this study. Available data is referenced in the article (literature references only).

AUTHOR CONTRIBUTIONS

HJ and GK conceived the concept. GK, JC, JN, and MR conducted the modeling research. HN, JP, VF, and JJ conducted the biomeasures research. RW and HJ supervised the research and manuscript. GK wrote the manuscript with support and contributions from all other authors.

SUPPLEMENTARY MATERIAL

The Supplementary Material for this article can be found online at: https://www.frontiersin.org/articles/10.3389/fbinf.2021.731340/full#supplementary-material.

REFERENCES

Aarons, L. (2005). Physiologically Based Pharmacokinetic Modelling: a Sound Mechanistic Basis Is Needed. *Br. J. Clin. Pharmacol.* 60 (6), 581–583. doi:10.1111/j.1365-2125.2005.02560.x

Allerheiligen, S. R. (2010). Next-generation Model-Based Drug Discovery and Development: Quantitative and Systems Pharmacology. *Clin. Pharmacol. Ther.* 88 (1), 135–137. doi:10.1038/clpt.2010.81

An, B., Zhang, M., Pu, J., Qu, Y., Shen, S., Zhou, S., et al. (2020). Toward Accurate and Robust Liquid Chromatography-Mass Spectrometry-Based Quantification of Antibody Biotherapeutics in Tissues. *Anal. Chem.* 92 (22), 15152–15161. doi:10.1021/acs.analchem.0c03620

Anaptysbio, I. (2014). Etokimab. Available from: https://www.anaptysbio.com/pipeline/etokimab/.

Andersen, M. E. (1995). Physiologically Based Pharmacokinetic (PB-PK) Models in the Study of the Disposition and Biological Effects of Xenobiotics and Drugs. *Toxicol. Lett.* 82-83, 341–348. doi:10.1016/0378-4274(95)03487-0

Artru, F., Bou Saleh, M., Maggiotto, F., Lassailly, G., Ningarhari, M., Demaret, J., et al. (2020). IL-33/ST2 Pathway Regulates Neutrophil Migration and Predicts Outcome in Patients with Severe Alcoholic Hepatitis. *J. Hepatol.* 72 (6), 1052–1061. doi:10.1016/j.jhep.2019.12.017

Ashkar, S., Weber, G. F., Panoutsakopoulou, V., Sanchirico, M. E., Jansson, M., Zawaideh, S., et al. (2000). Eta-1 (Osteopontin): an Early Component of Type-1 (Cell-mediated) Immunity. *Science* 287 (5454), 860–864. doi:10.1126/science.287.5454.860

Aston, P. J., Derks, G., Raji, A., Agoram, B. M., and van der Graaf, P. H. (2011). Mathematical Analysis of the Pharmacokinetic-Pharmacodynamic (PKPD) Behaviour of Monoclonal Antibodies: Predicting *In Vivo* Potency. *J. Theor. Biol.* 281 (1), 113–121. doi:10.1016/j.jtbi.2011.04.030

Banks, R. E., Forbes, M. A., Patel, P. M., Storr, M., Hallam, S., Clarke, D., et al. (2000). Subcutaneous Administration of Recombinant Glycosylated Interleukin 6 in Patients with Cancer: Pharmacokinetics, Pharmacodynamics and Immunomodulatory Effects. *Cytokine* 12 (4), 388–396. doi:10.1006/cyto.1999.0556

Bantscheff, M., Schirle, M., Sweetman, G., Rick, J., and Kuster, B. (2007). Quantitative Mass Spectrometry in Proteomics: a Critical Review. *Anal. Bioanal. Chem.* 389 (4), 1017–1031. doi:10.1007/s00216-007-1486-6

Barrett, J. S., Fossler, M. J., Cadieu, K. D., and Gastonguay, M. R. (2008). Pharmacometrics: a Multidisciplinary Field to Facilitate Critical Thinking in Drug Development and Translational Research Settings. *J. Clin. Pharmacol.* 48 (5), 632–649. doi:10.1177/0091270008315318

Barton, H. A., Chiu, W. A., Setzer, R. W., Andersen, M. E., Bailer, A. J., Bois, F. Y., et al. (2007). Characterizing Uncertainty and Variability in Physiologically Based Pharmacokinetic Models: State of the Science and Needs for Research and Implementation. *Toxicol. Sci.* 99 (2), 395–402. doi:10.1093/toxsci/kfm100

Bateman, R. J., Munsell, L. Y., Morris, J. C., Swarm, R., Yarasheski, K. E., and Holtzman, D. M. (2006). Human Amyloid-Beta Synthesis and Clearance Rates as Measured in Cerebrospinal Fluid *In Vivo*. *Nat. Med.* 12 (7), 856–861. doi:10.1038/nm1438

Baxter, L. T., Zhu, H., Mackensen, D. G., Butler, W. F., and Jain, R. K. (1995). Biodistribution of Monoclonal Antibodies: Scale-Up from Mouse to Human Using a Physiologically Based Pharmacokinetic Model. *Cancer Res.* 55 (20), 4611–4622.

Baxter, L. T., Zhu, H., Mackensen, D. G., and Jain, R. K. (1994). Physiologically Based Pharmacokinetic Model for Specific and Nonspecific Monoclonal Antibodies and Fragments in normal Tissues and Human Tumor Xenografts in Nude Mice. *Cancer Res.* 54 (6), 1517–1528.

Becker, J. O., and Hoofnagle, A. N. (2012). Replacing Immunoassays with Tryptic Digestion-Peptide Immunoaffinity Enrichment and LC-MS/MS. *Bioanalysis* 4 (3), 281–290. doi:10.4155/bio.11.319

Benson, N., Cucurull-Sanchez, L., Demin, O., Smirnov, S., and van der Graaf, P-H. (2011). Reducing Systems Biology to Practice in Pharmaceutical Company Research; Selected Case Studies. *Adv. Exp. Med. Biol.*, 736, 607–615. doi:10.1007/978-1-4419-7210-1_36

Betts, A., Keunecke, A., van Steeg, T. J., van der Graaf, P. H., Avery, L. B., Jones, H., et al. (2018). Linear Pharmacokinetic Parameters for Monoclonal Antibodies Are Similar within a Species and across Different Pharmacological Targets: A Comparison between Human, Cynomolgus Monkey and hFcRn Tg32 Transgenic Mouse Using a Population-Modeling Approach. *MAbs* 10, 751–764. doi:10.1080/19420862.2018.1462429

Blakey, G. E., Nestorov, I. A., Arundel, P. A., Aarons, L. J., and Rowland, M. (1997). Quantitative Structure-Pharmacokinetics Relationships: I. Development of a Whole-Body Physiologically Based Model to Characterize Changes in Pharmacokinetics across a Homologous Series of Barbiturates in the Rat. *J. Pharmacokinet. Biopharm.* 25 (3), 277–312. doi:10.1023/a:1025771608474

Bouma, G., Zamuner, S., Hicks, K., Want, A., Oliveira, J., Choudhury, A., et al. (2017). CCL20 Neutralization by a Monoclonal Antibody in Healthy Subjects Selectively Inhibits Recruitment of CCR6+ Cells in an Experimental Suction Blister. *Br. J. Clin. Pharmacol.* 83 (9), 1976–1990. doi:10.1111/bcp.13286

Bouzom, F., Ball, K., Perdaems, N., and Walther, B. (2012). Physiologically Based Pharmacokinetic (PBPK) Modelling Tools: How to Fit with Our Needs?. *Biopharm. Drug Dispos* 33 (2), 55–71. doi:10.1002/bdd.1767

Brodfuehrer, J., Rankin, A., Edmonds, J., Keegan, S., Andreyeva, T., Lawrence-Henderson, R., et al. (2014). Quantitative Analysis of Target Coverage and Germinal Center Response by a CXCL13 Neutralizing Antibody in a T-dependent Mouse Immunization Model. *Pharm. Res.* 31 (3), 635–648. doi:10.1007/s11095-013-1185-2

Cai, H., Stoner, C., Reddy, A., Freiwald, S., Smith, D., Winters, R., et al. (2006). Evaluation of an Integrated In Vitro-In Silico PBPK (Physiologically Based Pharmacokinetic) Model to Provide Estimates of Human Bioavailability. *Int. J. Pharm.* 308 (1-2), 133–139. doi:10.1016/j.ijpharm.2005.11.002

Chabot, J. R., Dettling, D. E., Jasper, P. J., and Gomes, B. C. (2011). Comprehensive Mechanism-Based Antibody Pharmacokinetic Modeling. *Annu. Int. Conf. IEEE Eng. Med. Biol. Soc.* 2011, 4318–4323. doi:10.1109/IEMBS.2011.6091072

Chandriani, S., DePianto, D. J., N'Diaye, E. N., Abbas, A. R., Jackman, J., Bevers, J., et al. (2014). Endogenously Expressed IL-13Rα2 Attenuates IL-13-mediated Responses but Does Not Activate Signaling in Human Lung Fibroblasts. *J. Immunol.* 193 (1), 111–119. doi:10.4049/jimmunol.1301761

Clemente, N., Raineri, D., Cappellano, G., Boggio, E., Favero, F., Soluri, M. F., et al. (2016). Osteopontin Bridging Innate and Adaptive Immunity in Autoimmune Diseases. *J. Immunol. Res.* 2016, 7675437. doi:10.1155/2016/7675437

Cohen, E. S., Scott, I. C., Majithiya, J. B., Rapley, L., Kemp, B. P., England, E., et al. (2015). Oxidation of the Alarmin IL-33 Regulates ST2-dependent Inflammation. *Nat. Commun.* 6 (1), 8327. doi:10.1038/ncomms9327

Creaven, P. J., Plager, J. E., Dupere, S., Huben, R. P., Takita, H., Mittelman, A., et al. (1987). Phase I Clinical Trial of Recombinant Human Tumor Necrosis Factor. *Cancer Chemother. Pharmacol.* 20 (2), 137–144. doi:10.1007/BF00253968

Cucurull-Sanchez, L., Chappell, M. J., Chelliah, V., Amy Cheung, S. Y., Derks, G., Penney, M., et al. (2019). Best Practices to Maximize the Use and Reuse of Quantitative and Systems Pharmacology Models: Recommendations from the United Kingdom Quantitative and Systems Pharmacology Network. *CPT Pharmacometrics Syst. Pharmacol.* 8 (5), 259–272. doi:10.1002/psp4.12381

Danhof, M., Klein, K., Stolk, P., Aitken, M., and Leufkens, H. (2018). The Future of Drug Development: the Paradigm Shift towards Systems Therapeutics. *Drug Discov. Today* 23 (12), 1990–1995. doi:10.1016/j.drudis.2018.09.002

De Boever, E. H., Ashman, C., Cahn, A. P., Locantore, N. W., Overend, P., Pouliquen, I. J., et al. (2014). Efficacy and Safety of an anti-IL-13 mAb in Patients with Severe Asthma: a Randomized Trial. *J. Allergy Clin. Immunol.* 133 (4), 989–996. doi:10.1016/j.jaci.2014.01.002

Derendorf, H., and Meibohm, B. (1999). Modeling of Pharmacokinetic/Pharmacodynamic (PK/PD) Relationships: Concepts and Perspectives. *Pharm. Res.* 16 (2), 176–185. doi:10.1023/a:1011907920641

Dirks, N. L., and Meibohm, B. (2010). Population Pharmacokinetics of Therapeutic Monoclonal Antibodies. *Clin. Pharmacokinet.* 49 (10), 633–659. doi:10.2165/11535960-000000000-00000

Doherty, M. K., and Whitfield, P. D. (2011). Proteomics Moves from Expression to Turnover: Update and Future Perspective. *Expert Rev. Proteomics* 8 (3), 325–334. doi:10.1586/epr.11.19

Edginton, A. N., Theil, F. P., Schmitt, W., and Willmann, S. (2008). Whole Body Physiologically-Based Pharmacokinetic Models: Their Use in Clinical Drug Development. *Expert Opin. Drug Metab. Toxicol.* 4 (9), 1143–1152. doi:10.1517/17425255.4.9.1143

Farrokhi, V., Chabot, J. R., Neubert, H., and Yang, Z. (2018). Assessing the Feasibility of Neutralizing Osteopontin with Various Therapeutic Antibody Modalities. *Sci. Rep.* 8 (1), 7781. doi:10.1038/s41598-018-26187-w

Farrokhi, V., Chen, X., and Neubert, H. (2018). Protein Turnover Measurements in Human Serum by Serial Immunoaffinity LC-MS/MS. *Clin. Chem.* 64 (2), 279–288. doi:10.1373/clinchem.2017.272922

Foote, J., and Eisen, H. N. (1995). Kinetic and Affinity Limits on Antibodies Produced during Immune Responses. *Proc. Natl. Acad. Sci. U S A.* 92 (5), 1254–1256. doi:10.1073/pnas.92.5.1254

Gauvreau, G. M., Boulet, L. P., Cockcroft, D. W., Fitzgerald, J. M., Carlsten, C., Davis, B. E., et al. (2011). Effects of Interleukin-13 Blockade on Allergen-Induced Airway Responses in Mild Atopic Asthma. *Am. J. Respir. Crit. Care Med.* 183 (8), 1007–1014. doi:10.1164/rccm.201008-1210OC

Glück, J., Rymarczyk, B., Jura-Szołtys, E., and Rogala, B. (2019). Serum Levels of Interleukin 33 and its Receptor ST2 in Patients Treated with Subcutaneous Allergen Immunotherapy in Intermittent Allergic Rhinitis. *Cent. Eur. J. Immunol.* 44 (2), 214–217.

Grass, G. M., and Sinko, P. J. (2002). Physiologically-based Pharmacokinetic Simulation Modelling. *Adv. Drug Deliv. Rev.* 54 (3), 433–451. doi:10.1016/s0169-409x(02)00013-3

Griesenauer, B., and Paczesny, S. (2017). The ST2/IL-33 Axis in Immune Cells during Inflammatory Diseases. *Front. Immunol.* 8, 475. doi:10.3389/fimmu.2017.00475

Grimm, H. P. (2009). Gaining Insights into the Consequences of Target-Mediated Drug Disposition of Monoclonal Antibodies Using Quasi-Steady-State Approximations, *J. Pharmacokinet. Pharmacodyn*, 36, 1573–8744. doi:10.1007/s10928-009-9129-5

Guttman-Yassky, E., Blauvelt, A., Eichenfield, L. F., Paller, A. S., Armstrong, A. W., Drew, J., et al. (2020). Efficacy and Safety of Lebrikizumab, a High-Affinity Interleukin 13 Inhibitor, in Adults with Moderate to Severe Atopic Dermatitis: A Phase 2b Randomized Clinical Trial. *JAMA Dermatol.* 156 (4), 411–420. doi:10.1001/jamadermatol.2020.0079

Hanania, N. A., Korenblat, P., Chapman, K. R., Bateman, E. D., Kopecky, P., Paggiaro, P., et al. (2016). Efficacy and Safety of Lebrikizumab in Patients with Uncontrolled Asthma (LAVOLTA I and LAVOLTA II): Replicate, Phase 3, Randomised, Double-Blind, Placebo-Controlled Trials. *Lancet Respir. Med.* 4 (10), 781–796. doi:10.1016/S2213-2600(16)30265-X

Hinkson, I. V., and Elias, J. E. (2011). The Dynamic State of Protein Turnover: It's about Time. *Trends Cel Biol.* 21 (5), 293–303. doi:10.1016/j.tcb.2011.02.002

Hoang, K. (1995). Physiologically Based Pharmacokinetic Models: Mathematical Fundamentals and Simulation Implementations. *Toxicol. Lett.* 79 (1-3), 99–106. doi:10.1016/0378-4274(95)03361-n

Hopkins, A. L. (2008). Network Pharmacology: the Next Paradigm in Drug Discovery. *Nat. Chem. Biol.* 4 (11), 682–690. doi:10.1038/nchembio.118

Huang, S. M., and Rowland, M. (2012). The Role of Physiologically Based Pharmacokinetic Modeling in Regulatory Review. *Clin. Pharmacol. Ther.* 91 (3), 542–549. doi:10.1038/clpt.2011.320

Jacobs, C. A., Beckmann, M. P., Mohler, K., Maliszewski, C. R., Fanslow, W. C., and Lynch, D. H. (1993). Pharmacokinetic Parameters and Biodistribution of Soluble Cytokine Receptors. *Int. Rev. Exp. Pathol.* 34 Pt B, 123–135. doi:10.1016/b978-0-12-364935-5.50013-4

Janeway, C. A., Jr, and Walport, M. (2001). *Immunobiology: The Immune System in Health and Disease*. 5th ed. New York: Garland Science.

Jones, H. M., Barton, H. A., Lai, Y., Bi, Y. A., Kimoto, E., Kempshall, S., et al. (2012). Mechanistic Pharmacokinetic Modeling for the Prediction of Transporter-Mediated Disposition in Humans from sandwich Culture Human Hepatocyte Data. *Drug Metab. Dispos* 40 (5), 1007–1017. doi:10.1124/dmd.111.042994

Jones, H. M., Dickins, M., Youdim, K., Gosset, J. R., Attkins, N. J., Hay, T. L., et al. (2012). Application of PBPK Modelling in Drug Discovery and Development at Pfizer. *Xenobiotica* 42 (1), 94–106. doi:10.3109/00498254.2011.627477

Jones, H. M., Gardner, I. B., Collard, W. T., Stanley, P. J., Oxley, P., Hosea, N. A., et al. (2011). Simulation of Human Intravenous and Oral Pharmacokinetics of 21 Diverse Compounds Using Physiologically Based Pharmacokinetic Modelling. *Clin. Pharmacokinet.* 50 (5), 331–347. doi:10.2165/11539680-000000000-00000

Jones, H. M., Gardner, I. B., and Watson, K. J. (2009). Modelling and PBPK Simulation in Drug Discovery. *AAPS J.* 11 (1), 155–166. doi:10.1208/s12248-009-9088-1

Jones, H. M., Mayawala, K., and Poulin, P. (2013). Dose Selection Based on Physiologically Based Pharmacokinetic (PBPK) Approaches. *AAPS J.* 15 (2), 377–387. doi:10.1208/s12248-012-9446-2

Jones, H. M., Parrott, N., Jorga, K., and Lavé, T. (2006). A Novel Strategy for Physiologically Based Predictions of Human Pharmacokinetics. *Clin. Pharmacokinet.* 45 (5), 511–542. doi:10.2165/00003088-200645050-00006

Jones, H. M., Parrott, N., Ohlenbusch, G., and Lavé, T. (2006). Predicting Pharmacokinetic Food Effects Using Biorelevant Solubility media and Physiologically Based Modelling. *Clin. Pharmacokinet.* 45 (12), 1213–1226. doi:10.2165/00003088-200645120-00006

Jones, H. M., Tolsma, J., Zhang, Z., Jasper, P., Luo, H., Weber, G. L., et al. (2020). A Physiologically-Based Pharmacokinetic Model for the Prediction of "Half-Life Extension" and "Catch and Release" Monoclonal Antibody Pharmacokinetics. *CPT Pharmacometrics Syst. Pharmacol.* 9 (9), 534–541. doi:10.1002/psp4.12547

Jones, H. M., Zhang, Z., Jasper, P., Luo, H., Avery, L. B., King, L. E., et al. (2019). A Physiologically-Based Pharmacokinetic Model for the Prediction of Monoclonal Antibody Pharmacokinetics from *In Vitro* Data. *CPT Pharmacometrics Syst. Pharmacol.* 8 (10), 738–747. doi:10.1002/psp4.12461

Jusko, W. J. (2013). Moving from Basic toward Systems Pharmacodynamic Models. *J. Pharm. Sci.* 102 (9), 2930–2940. doi:10.1002/jps.23590

Kasaian, M. T., Raible, D., Marquette, K., Cook, T. A., Zhou, S., Tan, X. Y., et al. (2011). IL-13 Antibodies Influence IL-13 Clearance in Humans by Modulating Scavenger Activity of IL-13Rα2. *J. Immunol.* 187 (1), 561–569. doi:10.4049/jimmunol.1100467

Khodoun, M., Lewis, C. C., Lewis, C., Yang, J. Q., Orekov, T., Potter, C., et al. (2007). Differences in Expression, Affinity, and Function of Soluble (s)IL-4Ralpha and sIL-13Ralpha2 Suggest Opposite Effects on Allergic Responses. *J. Immunol.* 179 (10), 6429–6438. doi:10.4049/jimmunol.179.10.6429

Kitano, H. (2005). International Alliances for Quantitative Modeling in Systems Biology. *Mol. Syst. Biol.* 1, 2005–0007. doi:10.1038/msb4100011

Knight-Schrijver, V. R., Chelliah, V., Cucurull-Sanchez, L., and Le Novère, N. (2016). The Promises of Quantitative Systems Pharmacology Modelling for Drug Development. *Comput. Struct. Biotechnol. J.* 14, 363–370. doi:10.1016/j.csbj.2016.09.002

Kohl, P., Crampin, E. J., Quinn, T. A., and Noble, D. (2010). Systems Biology: an Approach. *Clin. Pharmacol. Ther.* 88 (1), 25–33. doi:10.1038/clpt.2010.92

Kroegel, C., Julius, P., Matthys, H., Virchow, J. C., and Luttmann, W. (1996). Endobronchial Secretion of Interleukin-13 Following Local Allergen challenge in Atopic Asthma: Relationship to Interleukin-4 and Eosinophil Counts. *Eur. Respir. J.* 9 (5), 899–904. doi:10.1183/09031936.96.09050899

Lalonde, R. L., Kowalski, K. G., Hutmacher, M. M., Ewy, W., Nichols, D. J., Milligan, P. A., et al. (2007). Model-based Drug Development. *Clin. Pharmacol. Ther.* 82 (1), 21–32. doi:10.1038/sj.clpt.6100235

Larance, M., and Lamond, A. I. (2015). Multidimensional Proteomics for Cell Biology. *Nat. Rev. Mol. Cel Biol.* 16, 269–280. doi:10.1038/nrm3970

Lassman, M. E., McAvoy, T., Lee, A. Y., Chappell, D., Wong, O., Zhou, H., et al. (2014). Practical Immunoaffinity-Enrichment LC-MS for Measuring Protein Kinetics of Low-Abundance Proteins. *Clin. Chem.* 60 (9), 1217–1224. doi:10.1373/clinchem.2014.222455

Leo Pharma announces European Commission Approval of Adtralza® (Tralokinumab) as the First and Only Treatment Specifically Targeting IL-13 for Adults with Moderate-To-Severe Atopic Dermatitis [press release]. 2021.

Li, Z., Krippendorff, B. F., and Shah, D. K. (2017). Influence of Molecular Size on the Clearance of Antibody Fragments. *Pharm. Res.* 34 (10), 2131–2141. doi:10.1007/s11095-017-2219-y

Lindwall, G., Hsieh, E. A., Misell, L. M., Chai, C. M., Turner, S. M., and Hellerstein, M. K. (2006). Heavy Water Labeling of Keratin as a Non-invasive Biomarker of Skin Turnover *In Vivo* in Rodents and Humans. *J. Invest. Dermatol.* 126 (4), 841–848. doi:10.1038/sj.jid.5700189

Liu, Y., Cao, L., Chen, R., Zhou, X., Fan, X., Liang, Y., et al. (2015). Osteopontin Promotes Hepatic Progenitor Cell Expansion and Tumorigenicity via Activation of β-Catenin in Mice. *Stem Cells* 33 (12), 3569–3580. doi:10.1002/stem.2072

Loizou, G., Spendiff, M., Barton, H. A., Bessems, J., Bois, F. Y., d'Yvoire, M. B., et al. (2008). Development of Good Modelling Practice for Physiologically Based Pharmacokinetic Models for Use in Risk Assessment: the First Steps. *Regul. Toxicol. Pharmacol.* 50 (3), 400–411. doi:10.1016/j.yrtph.2008.01.011

Lund, S. A., Wilson, C. L., Raines, E. W., Tang, J., Giachelli, C. M., and Scatena, M. (2013). Osteopontin Mediates Macrophage Chemotaxis via α4 and α9 Integrins and Survival via the α4 Integrin. *J. Cel Biochem.* 114 (5), 1194–1202. doi:10.1002/jcb.24462

Mager, D. E., and Jusko, W. J. (2008). Development of Translational Pharmacokinetic-Pharmacodynamic Models. *Clin. Pharmacol. Ther.* 83 (6), 909–912. doi:10.1038/clpt.2008.52

May, R. D., and Fung, M. (2015). Strategies Targeting the IL-4/IL-13 Axes in Disease. *Cytokine* 75 (1), 89–116. doi:10.1016/j.cyto.2015.05.018

McAvoy, T., Lassman, M. E., Spellman, D. S., Ke, Z., Howell, B. J., Wong, O., et al. (2014). Quantification of Tau in Cerebrospinal Fluid by Immunoaffinity Enrichment and Tandem Mass Spectrometry. *Clin. Chem.* 60 (4), 683–689. doi:10.1373/clinchem.2013.216515

Meibohm, B., and Derendorf, H. (1997). Basic Concepts of Pharmacokinetic/pharmacodynamic (PK/PD) Modelling. *Int. J. Clin. Pharmacol. Ther.* 35 (10), 401–413.

Mueller, T., and Dieplinger, B. (2016). Soluble ST2 and Galectin-3: What We Know and Don't Know Analytically. *EJIFCC* 27 (3), 224–237.

Nestorov, I. (2007). Whole-body Physiologically Based Pharmacokinetic Models. *Expert Opin. Drug Metab. Toxicol.* 3 (2), 235–249. doi:10.1517/17425255.3.2.235

Nestorov, I. A., Aarons, L. J., Arundel, P. A., and Rowland, M. (1998). Lumping of Whole-Body Physiologically Based Pharmacokinetic Models. *J. Pharmacokinet. Biopharm.* 26 (1), 21–46. doi:10.1023/a:1023272707390

Neubert, H., Muirhead, D., Kabir, M., Grace, C., Cleton, A., and Arends, R. (2013). Sequential Protein and Peptide Immunoaffinity Capture for Mass Spectrometry-Based Quantification of Total Human β-nerve Growth Factor. *Anal. Chem.* 85 (3), 1719–1726. doi:10.1021/ac303031q

Neubert, H., Shuford, C. M., Olah, T. V., Garofolo, F., Schultz, G. A., Jones, B. R., et al. (2020). Protein Biomarker Quantification by Immunoaffinity Liquid Chromatography-Tandem Mass Spectrometry: Current State and

Future Vision. *Clin. Chem.* 66 (2), 282–301. doi:10.1093/clinchem/hvz022

Nijsen, M. J. M. A., Wu, F., Bansal, L., Bradshaw-Pierce, E., Chan, J. R., Liederer, B. M., et al. (2018). Preclinical QSP Modeling in the Pharmaceutical Industry: An IQ Consortium Survey Examining the Current Landscape. *CPT Pharmacometrics Syst. Pharmacol.* 7 (3), 135–146. doi:10.1002/psp4.12282

Noonan, M., Korenblat, P., Mosesova, S., Scheerens, H., Arron, J. R., Zheng, Y., et al. (2013). Dose-ranging Study of Lebrikizumab in Asthmatic Patients Not Receiving Inhaled Steroids. *J. Allergy Clin. Immunol.* 132 (3), 567–e12. doi:10.1016/j.jaci.2013.03.051

Norris, D. A., Leesman, G. D., Sinko, P. J., and Grass, G. M. (2000). Development of Predictive Pharmacokinetic Simulation Models for Drug Discovery. *J. Control. Release* 65 (1-2), 55–62. doi:10.1016/s0168-3659(99)00232-1

Oshikawa, K., Kuroiwa, K., Tago, K., Iwahana, H., Yanagisawa, K., Ohno, S., et al. (2001). Elevated Soluble ST2 Protein Levels in Sera of Patients with Asthma with an Acute Exacerbation. *Am. J. Respir. Crit. Care Med.* 164 (2), 277–281. doi:10.1164/ajrccm.164.2.2008120

Owen, S. G., Francis, H. W., and Roberts, M. S. (1994). Disappearance Kinetics of Solutes from Synovial Fluid after Intra-articular Injection. *Br. J. Clin. Pharmacol.* 38 (4), 349–355. doi:10.1111/j.1365-2125.1994.tb04365.x

Palandra, J., Finelli, A., Zhu, M., Masferrer, J., and Neubert, H. (2013). Highly Specific and Sensitive Measurements of Human and Monkey Interleukin 21 Using Sequential Protein and Tryptic Peptide Immunoaffinity LC-MS/MS. *Anal. Chem.* 85 (11), 5522–5529. doi:10.1021/ac4006765

Palandra, J., Quazi, A., Fitz, L., Rong, H., Morris, C., and Neubert, H. (2016). Quantitative Measurements of GDF-8 Using Immunoaffinity LC-MS/MS. *Proteomics Clin. Appl.* 10 (5), 597–604. doi:10.1002/prca.201500112

Palmer, G., Lipsky, B. P., Smithgall, M. D., Meininger, D., Siu, S., Talabot-Ayer, D., et al. (2008). The IL-1 Receptor Accessory Protein (AcP) Is Required for IL-33 Signaling and Soluble AcP Enhances the Ability of Soluble ST2 to Inhibit IL-33. *Cytokine* 42 (3), 358–364. doi:10.1016/j.cyto.2008.03.008

Peterson, M. C., and Riggs, M. M. (2015). FDA Advisory Meeting Clinical Pharmacology Review Utilizes a Quantitative Systems Pharmacology (QSP) Model: A Watershed Moment?. *CPT Pharmacometrics Syst. Pharmacol.* 4 (3), e00020–92. doi:10.1002/psp4.20

A Multi-Compartmental Model Generally Applicable to Physiologically-Based Pharmacokinetics,"P. H. Arundel in *3rd IFAC Symposium; Modelling and Control in Biomedial Systems* (UK: University of Warwick).

Popovic, B., Breed, J., Rees, D. G., Gardener, M. J., Vinall, L. M., Kemp, B., et al. (2017). Structural Characterisation Reveals Mechanism of IL-13-Neutralising Monoclonal Antibody Tralokinumab as Inhibition of Binding to IL-13Rα1 and IL-13Rα2. *J. Mol. Biol.* 429 (2), 208–219. doi:10.1016/j.jmb.2016.12.005

Poulin, P., and Theil, F. P. (2002). Prediction of Pharmacokinetics Prior to *In Vivo* Studies. 1. Mechanism-Based Prediction of Volume of Distribution. *J. Pharm. Sci.* 91 (1), 129–156. doi:10.1002/jps.10005

Rajman, I. (2008). PK/PD Modelling and Simulations: Utility in Drug Development. *Drug Discov. Today* 13 (7), 341–346. doi:10.1016/j.drudis.2008.01.003

Regeneron Pharmaceuticals, I. (2019). Regeneron and Sanofi Announce Positive Topline Phase 2 Results for IL-33 Antibody in Asthma June 21, 2019. Available from: https://investor.regeneron.com/news-releases/news-release-details/regeneron-and-sanofi-announce-positive-topline-phase-2-results/ (Acessed on June 21, 2019).

Rogers, M., Lyster, P., and Okita, R. (2013). NIH Support for the Emergence of Quantitative and Systems Pharmacology. *CPT: Pharmacometrics Syst. Pharmacol.* 2 (4), 37. doi:10.1038/psp.2013.13

Rostami-Hodjegan, A., Tamai, I., and Pang, K. S. (2012). Physiologically Based Pharmacokinetic (PBPK) Modeling: it Is Here to Stay!. *Biopharm. Drug Dispos* 33 (2), 47–50. doi:10.1002/bdd.1776

Saluja, R., Khan, M., Church, M. K., and Maurer, M. (2015). The Role of IL-33 and Mast Cells in Allergy and Inflammation. *Clin. Transl Allergy* 5 (1), 33. doi:10.1186/s13601-015-0076-5

Saluja, R., Zoltowska, A., Ketelaar, M. E., and Nilsson, G. (2016). IL-33 and Thymic Stromal Lymphopoietin in Mast Cell Functions. *Eur. J. Pharmacol.* 778, 68–76. doi:10.1016/j.ejphar.2015.04.047

Schutyser, E., Struyf, S., and Van Damme, J. (2003). The CC Chemokine CCL20 and its Receptor CCR6. *Cytokine Growth Factor. Rev.* 14 (5), 409–426. doi:10.1016/s1359-6101(03)00049-2

Scott, I. C., Majithiya, J. B., Sanden, C., Thornton, P., Sanders, P. N., Moore, T., et al. (2018). Interleukin-33 Is Activated by Allergen- and Necrosis-Associated Proteolytic Activities to Regulate its Alarmin Activity during Epithelial Damage. *Sci. Rep.* 8 (1), 3363. doi:10.1038/s41598-018-21589-2

Shah, D. K., and Betts, A. M. (2013). Antibody Biodistribution Coefficients: Inferring Tissue Concentrations of Monoclonal Antibodies Based on the Plasma Concentrations in Several Preclinical Species and Human. *MAbs* 5 (2), 297–305. doi:10.4161/mabs.23684

Shah, D. K., and Betts, A. M. (2012). Towards a Platform PBPK Model to Characterize the Plasma and Tissue Disposition of Monoclonal Antibodies in Preclinical Species and Human. *J. Pharmacokinet. Pharmacodyn* 39 (1), 67–86. doi:10.1007/s10928-011-9232-2

Shuford, C. M., Johnson, J. S., Thompson, J. W., Holland, P. L., Hoofnagle, A. N., and Grant, R. P. (2020). More Sensitivity Is Always Better: Measuring Sub-clinical Levels of Serum Thyroglobulin on a μLC-MS/MS System. *Clin. Mass Spectrom.* 15, 29–35. doi:10.1016/j.clinms.2020.01.001

Tang, Y., Zeng, X., and Liang, J. (2010). Surface Plasmon Resonance: An Introduction to a Surface Spectroscopy Technique. *J. Chem. Educ.* 87 (7), 742–746. doi:10.1021/ed100186y

Tiwari, A., Abraham, A. K., Harrold, J. M., Zutshi, A., and Singh, P. (2017). Optimal Affinity of a Monoclonal Antibody: Guiding Principles Using Mechanistic Modeling, *AAPS J.*, 19, 1550–7416. doi:10.1208/s12248-016-0004-1

Tiwari, A., Kasaian, M., Heatherington, A. C., Jones, H. M., and Hua, F. (2016). A Mechanistic PK/PD Model for Two anti-IL13 Antibodies Explains the Difference in Total IL-13 Accumulation Observed in Clinical Studies. *MAbs* 8 (5), 983–990. doi:10.1080/19420862.2016.1172151

Tiwari, A., Luo, H., Chen, X., Singh, P., Bhattacharya, I., Jasper, P., et al. (2016). Assessing the Impact of Tissue Target Concentration Data on Uncertainty in *In Vivo* Target Coverage Predictions. *CPT Pharmacometrics Syst. Pharmacol.* 5 (10), 565–574. doi:10.1002/psp4.12126

Ultsch, M., Bevers, J., Nakamura, G., Vandlen, R., Kelley, R. F., Wu, L. C., et al. (2013). Structural Basis of Signaling Blockade by Anti-IL-13 Antibody Lebrikizumab. *J. Mol. Biol.* 425 (8), 1330–1339. doi:10.1016/j.jmb.2013.01.024

van der Graaf, P. H., and Benson, N. (2011). Systems Pharmacology: Bridging Systems Biology and Pharmacokinetics-Pharmacodynamics (PKPD) in Drug Discovery and Development. *Pharm. Res.* 28 (7), 1460–1464. doi:10.1007/s11095-011-0467-9

van der Graaf, P. H. (2012). CPT: Pharmacometrics and Systems Pharmacology. *CPT Pharmacometrics Syst. Pharmacol.* 1 (9), e8–e. doi:10.1038/psp.2012.8

van Hartingsveldt, B., Nnane, I. P., Bouman-Thio, E., Loza, M. J., Piantone, A., Davis, H. M., et al. (2013). Safety, Tolerability and Pharmacokinetics of a Human Anti-interleukin-13 Monoclonal Antibody (CNTO 5825) in an Ascending Single-Dose First-In-Human Study. *Br. J. Clin. Pharmacol.* 75 (5), 1289–1298. doi:10.1111/j.1365-2125.2012.04477.x

Vugmeyster, Y., DeFranco, D., Szklut, P., Wang, Q., and Xu, X. (2010). Biodistribution of [125I]-Labeled Therapeutic Proteins: Application in Protein Drug Development beyond Oncology. *J. Pharm. Sci.* 99 (2), 1028–1045. doi:10.1002/jps.21855

Vugmeyster, Y., Szklut, P., Tchistiakova, L., Abraham, W., Kasaian, M., and Xu, X. (2008). Preclinical Pharmacokinetics, Interspecies Scaling, and Tissue Distribution of Humanized Monoclonal anti-IL-13 Antibodies with Different IL-13 Neutralization Mechanisms. *Int. Immunopharmacol* 8 (3), 477–483. doi:10.1016/j.intimp.2007.12.004

Wang, X., Lopategi, A., Ge, X., Lu, Y., Kitamura, N., Urtasun, R., et al. (2014). Osteopontin Induces Ductular Reaction Contributing to Liver Fibrosis. *Gut* 63 (11), 1805–1818. doi:10.1136/gutjnl-2013-306373

Wani, T. A., Zargar, S., Wakil, S. M., and Darwish, I. A. (2016). New Analytical Application of Antibody-Based Biosensor in Estimation of Thyroid-Stimulating Hormone in Serum. *Bioanalysis* 8 (7), 625–632. doi:10.4155/bio-2015-0034

Zhang, T. T., Ma, J., Durbin, K. R., Montavon, T., Lacy, S. E., Jenkins, G. J., et al. (2019). Determination of IL-23 Pharmacokinetics by Highly Sensitive Accelerator Mass Spectrometry and Subsequent Modeling to Project IL-23 Suppression in Psoriasis Patients Treated with Anti-IL-23 Antibodies. *AAPS J.* 21 (5), 82. doi:10.1208/s12248-019-0352-8

Zhao, P., Rowland, M., and Huang, S. M. (2012). Best Practice in the Use of Physiologically Based Pharmacokinetic Modeling and Simulation to Address Clinical Pharmacology Regulatory Questions. *Clin. Pharmacol. Ther.* 92 (1), 17–20. doi:10.1038/clpt.2012.68

Zhao, P., Zhang, L., Grillo, J. A., Liu, Q., Bullock, J. M., Moon, Y. J., et al. (2011). Applications of Physiologically Based Pharmacokinetic (PBPK) Modeling and Simulation during Regulatory Review. *Clin. Pharmacol. Ther.* 89 (2), 259–267. doi:10.1038/clpt.2010.298

Zhao, Y., Liu, G., Kwok, S., Jones, B. R., Liu, J., Marchisin, D., et al. (2018). Highly Selective and Sensitive Measurement of Active Forms of FGF21 Using Novel Immunocapture Enrichment with LC-MS/MS. *Bioanalysis* 10 (1), 23–33. doi:10.4155/bio-2017-0208

Conflict of Interest: All authors are current or former employees of Pfizer Inc.

Publisher's Note: All claims expressed in this article are solely those of the authors and do not necessarily represent those of their affiliated organizations, or those of the publisher, the editors and the reviewers. Any product that may be evaluated in this article, or claim that may be made by its manufacturer, is not guaranteed or endorsed by the publisher.

frontiers in Pharmacology

ORIGINAL RESEARCH
published: 24 December 2021
doi: 10.3389/fphar.2021.786078

Translational Pharmacokinetic–Pharmacodynamic Modeling of NaV1.7 Inhibitor MK-2075 to Inform Human Efficacious Dose

Jeanine E. Ballard[1], Parul S. Pall[2], Joshua Vardigan[2], Fuqiang Zhao[3], Marie A. Holahan[3], Xiaoping Zhou[2], Nina Jochnowitz[2], Richard L. Kraus[2], Rebecca M. Klein[2], Darrell A. Henze[2], Andrea K. Houghton[2], Christopher S. Burgey[4], Christopher Gibson[1] and Arie Struyk[5]*

[1]Pharmacokinetics Pharmacodynamics and Drug Metabolism, Merck & Co. Inc., Kenilworth, NJ, United States, [2]Neuroscience Pharmacology, Merck & Co. Inc., Kenilworth, NJ, United States, [3]Translational Imaging Biomarkers, Merck & Co. Inc., Kenilworth, NJ, United States, [4]Discovery Chemistry, Merck & Co. Inc., Kenilworth, NJ, United States, [5]Translational Medicine, Merck & Co. Inc., Kenilworth, NJ, United States

OPEN ACCESS

Edited by:
Tristan Scott Maurer, Pfizer, United States

Reviewed by:
Vivaswath S. Ayyar, Janssen Research and Development, United States
David Hackos, Genentech, Inc., United States

***Correspondence:**
Jeanine E. Ballard
jeanine_ballard@merck.com

Specialty section:
This article was submitted to Experimental Pharmacology and Drug Discovery, a section of the journal Frontiers in Pharmacology

Received: *29 September 2021*
Accepted: *17 November 2021*
Published: *24 December 2021*

Citation:
Ballard JE, Pall PS, Vardigan J, Zhao F, Holahan MA, Zhou X, Jochnowitz N, Kraus RL, Klein RM, Henze DA, Houghton AK, Burgey CS, Gibson C and Struyk A (2021) Translational Pharmacokinetic–Pharmacodynamic Modeling of NaV1.7 Inhibitor MK-2075 to Inform Human Efficacious Dose. Front. Pharmacol. 12:786078. doi: 10.3389/fphar.2021.786078

MK-2075 is a small-molecule selective inhibitor of the NaV1.7 channel investigated for the treatment of postoperative pain. A translational strategy was developed for MK-2075 to quantitatively interrelate drug exposure, target modulation, and the desired pharmacological response in preclinical animal models for the purpose of human translation. Analgesics used as a standard of care in postoperative pain were evaluated in preclinical animal models of nociceptive behavior (mouse tail flick latency and rhesus thermode heat withdrawal) to determine the magnitude of pharmacodynamic (PD) response at plasma concentrations associated with efficacy in the clinic. MK-2075 was evaluated in those same animal models to determine the concentration of MK-2075 required to achieve the desired level of response. Translation of MK-2075 efficacious concentrations in preclinical animal models to a clinical PKPD target in humans was achieved by accounting for species differences in plasma protein binding and *in vitro* potency against the NaV1.7 channel. Estimates of human pharmacokinetic (PK) parameters were obtained from allometric scaling of a PK model from preclinical species and used to predict the dose required to achieve the clinical exposure. MK-2075 exposure–response in a preclinical target modulation assay (rhesus olfaction) was characterized using a computational PKPD model which included a biophase compartment to account for the observed hysteresis. Translation of this model to humans was accomplished by correcting for species differences in PK NaV1.7 potency, and plasma protein binding while assuming that the kinetics of distribution to the target site is the same between humans and rhesus monkeys. This enabled prediction of the level of target modulation anticipated to be achieved over the dosing interval at the projected clinical efficacious human dose. Integration of these efforts into the early development plan informed clinical study design and decision criteria.

Keywords: NaV1.7, nociception, pain, modeling, PKPD, MK-2075

INTRODUCTION

A critical component of drug discovery and development is gaining an understanding of the relationship between drug exposure, target engagement or modulation at the site of action, and the desired pharmacological response (Bueters et al., 2015; Wong et al., 2017). The ability to interrelate these three components using a combination of clinical and preclinical information as early as possible in a drug discovery setting can increase the probability of achieving clinical success at a reasonable dose (Morgan et al., 2012). A recent analysis of the general correlation between *in vitro* potency and clinically efficacious unbound *in vivo* exposure has highlighted a variable relationship across therapeutic areas, target types, and mechanisms of action, and this emphasizes the importance of accounting for contributing factors such as target-specific pharmacology and turnover kinetics, drug distribution to the site of action, and *in vitro* assay conditions (Jansson-Löfmark et al., 2020). Therefore, it is important to develop a strategy to quantitatively integrate *in vitro* potency, exposure at the site of action, time course of biomarker response, and efficacy from preclinical models to predict clinical activity.

The objective of the work described herein was to develop a translational strategy for NaV1.7 inhibitor MK-2075 which would improve the likelihood of achieving therapeutically relevant target modulation in the clinic within the anticipated safety margins and to inform on the study design for pharmacodynamic (PD) endpoints. NaV1.7 has human genetic and preclinical validation for involvement in acute and chronic pain. Humans with genetic mutations leading to a loss of function (LOF) of the NaV1.7 channel have a congenital indifference to pain and anosmia while a gain of function mutations can result in pain syndromes such as primary erythromelalgia (Dib-Hajj et al., 2007; Weiss et al., 2011). Pharmacological inhibition of NaV1.7 channels in nonhuman primates has demonstrated a similar phenotype to humans with a genetic loss of NaV1.7 function, including hyposmia and analgesia (Kraus et al., 2021). While drugs with sodium channel–blocking activity such as carbamazepine have demonstrated some utility in pain treatment, their nonselective nature contributes to dose-limiting adverse effects (Tanelian and Victory, 1995; Dick et al., 2007; Moulin et al., 2014). MK-2075 is a small-molecule selective inhibitor of the NaV1.7 channel investigated for the potential treatment of postoperative pain.

The translational workflow for MK-2075 included benchmarking preclinical nociception assays with the clinical standard of care (SOC), characterization of MK-2075 preclinical PKPD and *in vitro* potency, scaling of preclinical pharmacokinetic (PK) and PD parameters to predict human clinical dose, and prediction of target modulation biomarker PD in humans at the anticipated efficacious dose (**Figure 1**). These efforts were integrated into a translational strategy enabling definition of the PKPD targets for MK-2075 in acute postoperative pain and prediction of efficacious human dose to achieve the PKPD target. The results of this work were used to identify a compound with reasonable probability of success to test inhibition of NaV1.7 as a mechanism for pain mitigation in the clinic. In addition, clinical assessment of olfaction was proposed to evaluate NaV1.7 target modulation in healthy volunteers, so translation of target modulation PD from rhesus olfaction measured by functional magnetic resonance imaging (fMRI)

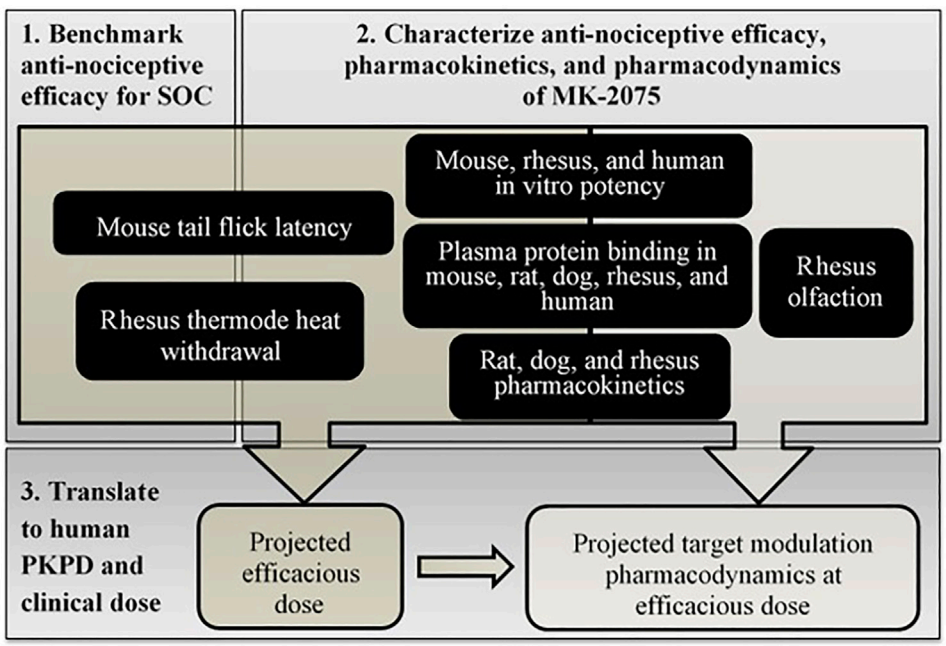

FIGURE 1 | Schematic of step-wise workflow for translational PKPD of MK-2075 for prediction of dose and target modulation in humans.

was used to inform early clinical study design and clinical decision criteria.

MATERIALS AND METHODS

In Vitro NaV1.7 Potency

The intrinsic potency for inhibition of NaV1.7 from humans, rhesus monkeys, and mice was determined *in vitro*. Whole-cell sodium currents were recorded from a recombinant human embryonic kidney 293 cell line stably overexpressing either the human, mouse, or rhesus NaV1.7 channels using a manual patch clamp. Recording solutions comprised of the following (in mM): internal solution: 30 CsCl, 5 HEPES, 10 EGTA, 120 CsF, 5 NaF, 2 $MgCl_2$, pH = 7.3 with CsOH; and external solution: 150 NaCl, 5 KCl, 2 $CaCl_2$, 1 $MgCl_2$, 10 HEPES, 12 dextrose, pH = 7.3 with NaOH. Pipettes were fabricated from borosilicate glass using a Sutter P-97 micropipette puller to an open tip resistance of 1–2 MΩ. Cells were voltage clamped at −60 mV for cell detection and sealing. At the start of the procedure, a voltage curve and an inactivation curve were run for each cell to determine the voltage at which 50% of the channels reside in the inactivated state ($V_{0.5inact}$). The voltage curve was used to determine if the cell was adequately clamped; cells with currents larger than 10 nA or with space clamp issues were not used further. For the hyperpolarized state protocol, the holding potential was set to 20 mV negative of $V_{0.5inact}$. A pulse train consisting of consecutive double pulses, an 8-s hyperpolarizing pre-pulse to −120 mV followed by a test pulse to −10 mV was applied at a frequency of 0.1 Hz. First, vehicle (0.3% DMSO) was added to establish a baseline measurement. MK-2075 was added after the baseline was established. Cells were exposed to MK-2075 for 5 min at a holding potential of 20 mV negative to $V_{0.5inact}$ during which time no pulsing occurred. The cells were then exposed to the same hyperpolarized voltage protocol described above. A washout was performed to measure recovery of the sodium currents from inhibition. At least 3 concentrations of MK-2075 were tested with 3–5 replicates per concentration.

In Vitro Plasma Protein Binding

Plasma protein binding was determined across species at a MK-2075 concentration of 1 or 2.5 μM using equilibrium dialysis against 100 mM PBS buffer with a 12–14 kDa threshold semipermeable membrane. After 4–6 h of incubation on a single-plate rotator at 37°C inside a CO_2 chamber maintained at 5% CO_2, aliquots of plasma and buffer were analyzed using LC-MS/MS. The fraction unbound in plasma ($f_{u,p}$) was calculated as the ratio of MK-2075 concentration in buffer to that in plasma. Recovery of greater than 80% total MK-2075 from the assay was determined to confirm stability of the compound over the duration of the incubation.

In Vivo Pharmacokinetics and Bioanalytical Methods

All animal studies were conducted according to the NIH Guide for the Care and Use of Laboratory Animals, and all protocols were reviewed and approved by the Institutional Animal Care and Use Committee at Merck & Co., Inc, Kenilworth, NJ, USA. The PK data for MK-2075 in the Wistar Han rat, beagle dog, and rhesus monkey were obtained following 2-h intravenous (IV) infusions. Doses administered were 1 mg/kg in 5% Captisol in rats, 0.4 mg/kg in 30% Captisol in dogs, and 2 mg/kg in 5% Captisol in monkeys. The dose levels in rats and monkeys were selected to achieve concentrations similar to the anticipated target clinical exposure based on the data from the preliminary low dose (0.05 mg/kg) IV bolus studies. Lower IV infusion doses were selected for dogs due to historical evidence of emesis and trembling with structural analogs of MK-2075. The blood samples were collected into EDTA tubes and centrifuged to obtain plasma prior to storage at −20°C until bioanalysis. The plasma samples were prepared for analysis using a protein precipitation technique, and the supernatant was analyzed by LC-MS/MS.

A two-compartment PK model with first-order elimination from the central compartment (differential equations (1) and (2)) was fit to preclinical plasma concentration–time data from rats, dogs, and monkeys separately in Phoenix 64 (Build 8.1.0.3530) to obtain the mean and standard error (SE) of the PK parameters *CL*, *V1*, *V2*, and *CLD*, as well as the correlation matrix for these parameters.

$$V1 * \frac{dC}{dt} = -CL * C - CLD * C + CLD * C2 \quad (1)$$

$$V2 * \frac{dC2}{dt} = CLD * C - CLD * C2 \quad (2)$$

where *CL* is the clearance from the central compartment, and *CLD* is the distributional clearance between the central and peripheral compartments. *V1* is the apparent volume of the central compartment, and *V2* is the apparent volume of the peripheral compartment. *C* is the concentration in the central compartment, and *C2* is the concentration in the peripheral compartment.

Mouse Tail Flick Latency Methods and Modeling Strategy

In vivo antinociceptive activity was determined preclinically in a mouse tail flick latency study for two SOC agents for postoperative pain, morphine and tramadol, and the NaV1.7 inhibitor MK-2075 in a blinded and randomized design. Evaluation of antinociceptive activity was based on treatment-mediated increase in time to withdraw from a thermal stimulus. Briefly, BALB/c male mice were gently restrained and a focused infrared beam of radiant heat (Ugo Basilo, Italy) applied to a point approximately 2.5 cm from the tip of the tail. The intensity of the thermal stimulus was adjusted to provide an average baseline response of 3–5 s. The time taken for the mice to withdraw their tail from the heat stimulus was determined as the tail flick latency. To prevent tissue injury for the animals a cutoff time was set at 15 s. Mice not responding within the cutoff time were removed from the apparatus and assigned a latency of 15 s. After a baseline response was obtained, the mice were dosed

(SC, in a volume of 10 ml/kg) with either vehicle or with the test compound. The tail flick responses were then measured at 40, 60, and 80 min after vehicle or compound administration. The drug concentration in the plasma was determined from the blood samples collected from the test animals at the end of the study (1–1.5 h postinjection).

The graphical analysis of the exposure–response relationship over time for a structural analog of MK-2075 showed no apparent hysteresis (data not shown). Therefore, a sigmoidal E_{max} model assuming a direct effect (**Eq. 3**) was fit to the tail flick latency measured at the last time point, either 60 or 80 min, as a function of the terminal total plasma concentration in Phoenix 64 (Build 8.1.0.3530) to estimate an *in vivo* potency (EC_{50}) for MK-2075. The value of E_{max} was set equivalent to the difference between the latency threshold of 15 s (i.e., the maximum time for the application of the stimulus) and the model estimated baseline (E_0).

$$E = E_0 + \frac{E_{max} * C^h}{EC_{50^h} + C^h} \quad (3)$$

where, E is the total time to tail flick following thermal stimulation, E_0 is the baseline tail flick latency in the absence of drug, and E_{max} is the maximum achievable effect level. EC_{50} is defined as the concentration required to increase the time to tail flick by 50% of the maximum achievable latency, C is the total plasma concentration measured at termination of the study, and h is the hill coefficient describing the steepness of the exposure–response relationship.

Rhesus Thermode Heat Withdrawal Methods and Modeling Strategy

In vivo antinociceptive potency of MK-2075 was determined preclinically in the rhesus thermode heat withdrawal study based on treatment-mediated decrease in magnitude of behavioral response to a thermal stimulus on the forearm. Rhesus thermode heat withdrawal was measured by brief application of heat delivered to the forearm of rhesus macaque as described by Vardigan et al. (2018) and Kraus et al. (2021). Briefly, four test temperatures: 44°C, 46°C, 48°C, and 50°C were delivered randomly and repeated six times per session. The investigator rated the intensity of arm withdrawal evoked by heat stimuli on a scale from 0 to 2 (0: no movement, 1: a single movement, and 2: multiple movements of the test arm). The average response from the six replicate stimuli per temperature was reported. Experiments were performed 30 min following subcutaneous injection of vehicle or drug at two to four dose levels. Blood samples were collected 1 h following dosing for the measurement of drug concentration in the plasma.

An inhibitory E_{max} model assuming direct effect was fit to the heat response score data at a temperature of 46°C as a function of terminal total plasma concentration in Phoenix 64 (Build 8.1.0.3530):

$$E = E_0 * 1 - \frac{C}{IC_{50} + C} \quad (4)$$

where E is the measured heat response score following thermal stimulation at 46°C, and E_0 is the baseline response to thermal stimulus in the absence of drug. C is the total plasma concentration measured at the end of the study, and IC_{50} is defined as the concentration required to decrease the response score by 50%.

Rhesus fMRI Olfaction Methods and Modeling Strategy

The detailed methods of fMRI of olfaction including animal preparation, experiment setup, anesthesia protocol, odor stimulation, MRI measurement, and data analysis have been described previously (Zhao et al., 2015). Briefly, odorant-induced olfaction in the olfactory bulb (OB) of anesthetized rhesus monkeys was monitored by multiple fMRI measurements made during a 4-h experiment session. Following 1 h of baseline measurement, MK-2075 was administered by IV route as a loading dose followed by 1 h of infusion at four dose levels. Multiple fMRI measurements of odorant-induced olfaction were made over the 1-h infusion period and 2-h washout period following termination of the infusion. Blood samples were collected at the end of the infusion for measurement of drug concentrations in the plasma by LC-MS/MS following protein precipitation.

Rhesus fMRI data was processed to determine percentage inhibition of olfaction over time (Ballard et al., 2020). Briefly, the time course of the fMRI signals was first obtained by averaging the time courses of all the activated pixels within the OB for each fMRI measurement, then the time courses from three consecutive fMRI measurements were averaged to yield one fMRI response for olfaction quantification. A total of 15 fMRI measurements performed during each 1-h block of the 4-h experiment session yielded 5 fMRI responses. A change in olfaction was expressed as percentage inhibition of the averaged fMRI responses following MK-2075 administration relative to the averaged fMRI responses during the 1-h baseline period before compound delivery.

Percentage inhibition of olfaction fMRI by NaV1.7 inhibitors as a function of exposure has been evaluated for time dependence in a previous publication (Ballard et al., 2020). The observed hysteresis was assumed to be a result of a distributional delay to the effect site, and a PKPD model with a biophase compartment (Ce) was utilized to account for the time delay between exposure and response.

While multiple measurements of olfaction inhibition by fMRI were obtained throughout the 4-h study period (~12-min intervals), sampling for PK during the study was not feasible since the animal was isolated inside the fMRI machine. However, a single blood sample was collected from each animal at the end of the infusion to obtain a measure of the plasma concentration achieved in individual animals. In order to estimate the concentration–time profile over the entire study period in each individual animal, population PK parameters from a two-compartment model fit (**Eqs. 1, 2**) of MK-2075 concentration–time profile in the rhesus monkeys were determined from satellite IV infusion studies at 2 and 8 mg/kg

(n = 3/dose). Post-hoc estimates of *CL*, *V1*, *V2*, and *CLD* were then obtained for individual subjects using population parameter estimates with interindividual variability from the population PK model anchored by the measured plasma concentration at the end of infusion for animals in the study.

The predicted exposure and observed response profile over time was used to fit a PD model with an effect-compartment in Phoenix 64 (Build 8.1.0.3530). The model structure contains a hypothetical compartment for concentrations at the site of effect with a first-order distribution rate constant *ke0* (**Eq. 5**). The PD model structure is a modification of the $E_{\max}$ model to incorporate concentrations in the effect-compartment (*Ce*) as the exposure term which drives the response (**Eq. 6**).

$$\frac{dCe}{dt} = ke0^{*}Cp - ke0^{*}Ce \tag{5}$$

$$E = E_0 + \frac{E_{max}{}^{*}Ce}{EC_{50} + Ce} \tag{6}$$

In Vivo Exposure–Response Post Processing

To facilitate visualization of the exposure–response relationship across preclinical assays, the PD response in each assay was converted to percent maximum possible effect (%MPE) using **Equation 7**.

$$\%MPE = \frac{(max - baseline) - (max - observed)}{(max - baseline)}{}^{*}100 \tag{7}$$

To account for species differences in both plasma protein binding and intrinsic activity on the target, measured total plasma concentrations ($C_{p,total}$) were multiplied by the measured species-specific fraction unbound in the plasma ($f_{u,p}$) and then divided by the measured species-specific *in vitro* NaV1.7 IC_{50} value. Therefore, the exposure term *C* in **Equations 3, 4** becomes a derived dimensionless scalar for unbound plasma concentration relative to *in vitro* potency as in **Equation 8**.

$$In\,Vivo/In\,Vitro\,Scalar = \frac{C_{p,total}{}^{*}f_{u,p}}{in\,vitro\,IC_{50}} \tag{8}$$

Respectively, the ratio of unbound plasma concentration relative to *in vitro* potency required to achieve 50% effect in the preclinical *in vivo* assays can be derived by substituting IC_{50} or EC_{50} for $C_{p,total}$ in **Equation 8**.

Projection of Human Pharmacokinetics, Pharmacodynamics, and Efficacious Dose

The MK-2075 human PK parameters, namely, clearance and volume of distribution, were predicted from preclinical data using allometric scaling. The resulting PK parameters were then integrated with the preclinical PKPD model output to predict the dose required to achieve a target plasma concentration anticipated to be efficacious in the reduction of postoperative pain.

Pharmacokinetics

Human clearance and volume of distribution for MK-2075 were predicted using allometric scaling of two-compartment PK parameters obtained from rats, dogs, and monkeys, using an internal web-based application employing R script which enables incorporation and visualization of the impact of experimental uncertainty on the predicted dose and PK profile (Lindauer et al., 2014).

Elimination in preclinical species was balanced between metabolic and non–metabolic (renal or biliary excretion) pathways as determined from metabolite profiling of excreta in bile duct cannulated animals (unpublished data). Poor *in vitro* metabolic turnover and involvement of hepatic uptake and biliary efflux transporters in elimination resulted in an underestimation of *in vivo* metabolic clearance in preclinical species, precluding the use of *in vitro* biochemical data to predict human clearance (unpublished data). Therefore, allometric scaling was selected as the appropriate prediction method for human clearance. Unbound metabolic clearance was predicted by allometric scaling using Tang's coefficients (Tang et al., 2007). Non-metabolic unbound clearance (*CL*) and intercompartmental distribution CL (*CLD*) were scaled using fixed exponent allometry with the standard exponent of 0.75, and unbound body weight–normalized volumes (*V1* and *V2*) were scaled with the fixed exponent of 1.

Pharmacodynamics

The relationship between *in vitro* potency and *in vivo* potency determined from the mouse tail flick and rhesus thermode assays as described above was used to calculate a concentration target to achieve 50% effect in humans. The measured *in vitro* human NaV1.7 IC_{50} was multiplied by the derived *in vivo*/*in vitro* scalars and divided by the measured free fraction in the human plasma in order to translate to a total plasma concentration target for MK-2075 in humans. The biophase PKPD model used to characterize the exposure–response in the rhesus fMRI olfaction assay was subsequently used to predict the target modulation time course in humans at the anticipated clinical efficacious dose. Translation of this model to humans was accomplished by correcting for species differences in PK, *in vitro* potency, and plasma protein binding, while assuming that the kinetics of distribution to the target site and *in vitro* to *in vivo* translation of the NaV1.7 potency were the same between humans and rhesus monkeys. The mean and SE for individual parameter estimates, *ke0* and EC_{50}, were used along with the correlation matrix to simulate uncertainty in the resulting PD profile within the human PK prediction application.

Efficacious Dose

The human PK prediction application generates a distribution of predicted human PK and PD parameters derived from the uncertainty in measured experimental data as described by Lindauer et al. (2014). Subsequently, 1,000 Monte-Carlo simulations were conducted at each dose level to generate the human concentration–time profiles while sampling from these

TABLE 1 | Comparison of preclinical potency and clinical minimum efficacious concentration (MEC) for SOC analgesics.

SOC analgesic	Clinical MEC[a] (μM), mean (range)	Mouse tail flick EC_{50} (μM), mean ± SE
Morphine	0.074 (0.032–0.116)[b]	0.14 ± 0.03
Tramadol	1.092 (0.077–3.744)[c]	1.13 ± 0.08

[a]*MEC is defined as the trough plasma concentration measured just prior to patient-controlled administration of a subsequent dose of analgesic.*
[b]Clinical Pharmacokinetics *7: 266–279 (1982) (Dahlstrom, Tamsen, Paalzow, & Hartvig, 1982).*
[c]The Clinical Journal of Pain, *6: 212–220 (1990) (Lehmann, Kratzenberg, Schroederbark, & Horrichshaermeyer, 1990).*

parameter distributions, which results in a median-predicted profile with an associated confidence interval (CI) for each simulated dose level. Based on predicted human PK, preliminary simulations of various IV dose levels and infusion durations were explored to identify a dosing regimen which could achieve and sustain the PK target described above while also remaining below the exposure limits derived from preclinical toxicology studies. Ultimately, a dosing regimen consisting of a single IV infusion over a duration of 8 h was used for clinical dose and PD profile predictions.

RESULTS

Benchmarking Preclinical Antinociceptive Response With Clinical SOC Analgesics

Benchmarking antinociceptive response in preclinical assays for acute pain (mouse tail flick and rhesus thermode) with marketed SOC drugs was conducted to support the relevance of each assay for the target indication and provide a framework for PD target selection (**Table 1**). Total trough plasma concentrations following efficacious doses of the SOC analgesics used clinically to treat postoperative pain, namely, morphine, tramadol, and fentanyl, were obtained from the literature (Dahlstrom et al., 1982; Lehmann et al., 1990). The clinically efficacious concentrations were compared to the *in vivo* potency obtained from sigmoidal E_{max} modeling of the mouse tail flick latency data. Both SOC drugs, morphine and tramadol, achieved approximately 50% of the maximum possible effect in mouse tail flick latency at clinical efficacious concentrations (**Figure 2**), suggesting that the EC_{50}

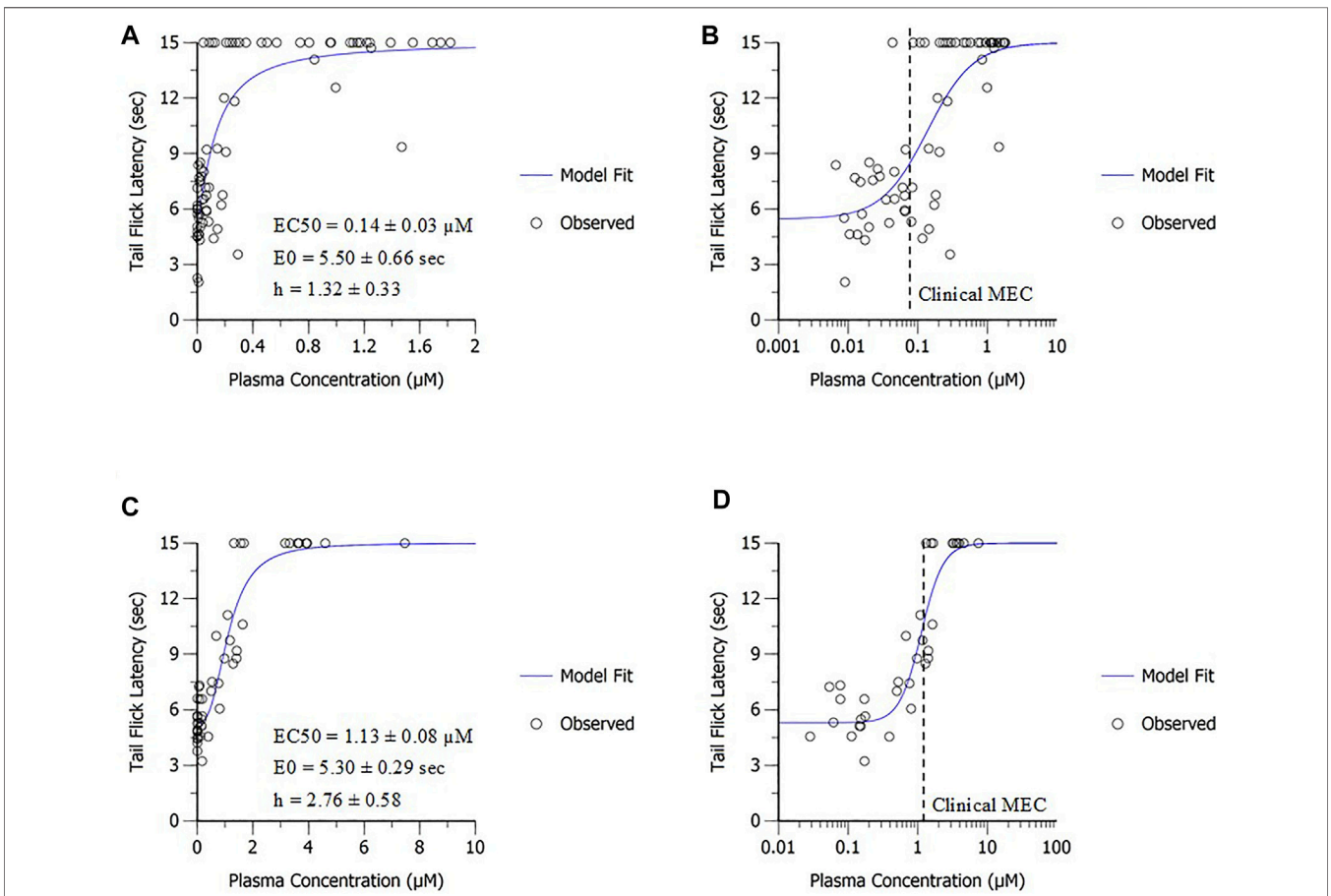

FIGURE 2 | *In vivo* potency derived from the mouse tail flick latency assay for SOC postoperative pain therapeutics. Data are presented on **(A)** linear and **(B)** semi-log scale for morphine and **(C)** linear and **(D)** semi-log scale for tramadol.

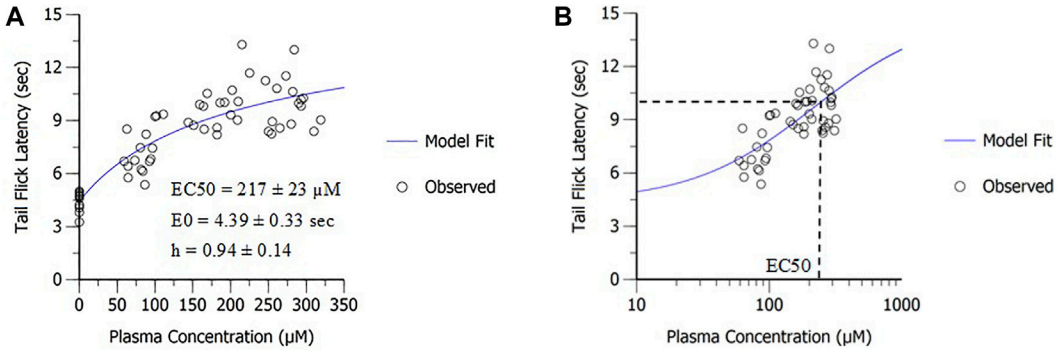

FIGURE 3 | *In vivo* potency of MK-2075 was derived from the mouse tail flick latency assay as depicted in **(A)** linear scale and **(B)** semi-log scale.

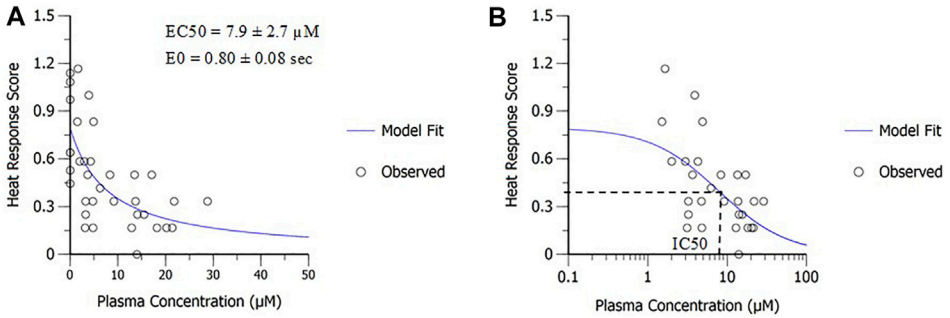

FIGURE 4 | *In vivo* potency of MK-2075 derived from the rhesus thermode heat withdrawal assay at 46°C as depicted in **(A)** linear scale and **(B)** semi-log scale.

obtained in this assay for MK-2075 would be a reasonable exposure to the target in the clinic. Evaluation of morphine, tramadol, and fentanyl in the rhesus thermode heat withdrawal assay of nociception and correlation to clinical efficacious concentration has been described previously, and IC_{50} determined from this model aligned well with the clinical minimum efficacious concentration for postoperative pain (Vardigan et al., 2018). Therefore, concentrations of MK-2075 achieving a response of 50% inhibition in the rhesus thermode assay is expected to be an appropriate target for postoperative pain in humans.

MK-2075 Preclinical PKPD and Translation to Clinical Exposure Targets

PD modeling was applied to determine *in vivo* potency of MK-2075 in preclinical nociception assays (mouse tail flick and rhesus thermode) and the NaV1.7 target modulation assay (fMRI olfaction). The sigmoidal E_{max} model fit of the MK-2075 exposure–response in mouse tail flick latency resulted in an *in vivo* potency (EC_{50}) of 217 ± 23 μM (mean ± SE), baseline latency (E_0) of 4.4 ± 0.3 s, and the Hill coefficient of 0.94 ± 0.14 (**Figure 3**). The inhibitory E_{max} model fit of the MK-2075 exposure–response in rhesus thermode heat withdrawal at a temperature of 46°C resulted in an IC_{50} of 7.9 ± 2.7 μM (mean ± SE) and a baseline response score (E_0) of 0.80 ± 0.08 (**Figure 4**).

There was a substantial shift in the *in vivo* potency of MK-2075 obtained from the mouse tail flick assay relative to the rhesus thermode assay (**Figure 5A**). The expression of exposure–response in terms of the intrinsic potency–normalized unbound exposure results in improved alignment across species (**Figure 5B**) and a consistent ratio of unbound plasma concentrations (approximately twofold) over *in vitro* NaV1.7 IC_{50} to achieve 50% MPE in both the mouse and rhesus nociception assays (**Table 2**).

A population PK model based on IV infusion in conscious rhesus monkeys adequately captured the MK-2075 concentrations observed in the anesthetized rhesus monkeys in fMRI olfaction studies (**Figure 6A**). Concentration–time predictions based on post-hoc PK analysis from anesthetized subjects enabled fitting of individual PD data. Incorporation of a biophase compartment to account for distributional delay corrected the hysteresis observed in the exposure–response data and adequately captured the time course of treatment-mediated inhibition of olfaction (**Figure 6B**). The resulting effect compartment EC_{50} was 10.3 ± 1.9 μM with a *ke0* of 2.1 ± 0.5 h^{-1}. The measured exposure–response at the end of a 1-h infusion, when *Ce* and *Cp* were near equilibrium, aligns well with the results from the rhesus thermode assay (**Figure 7**).

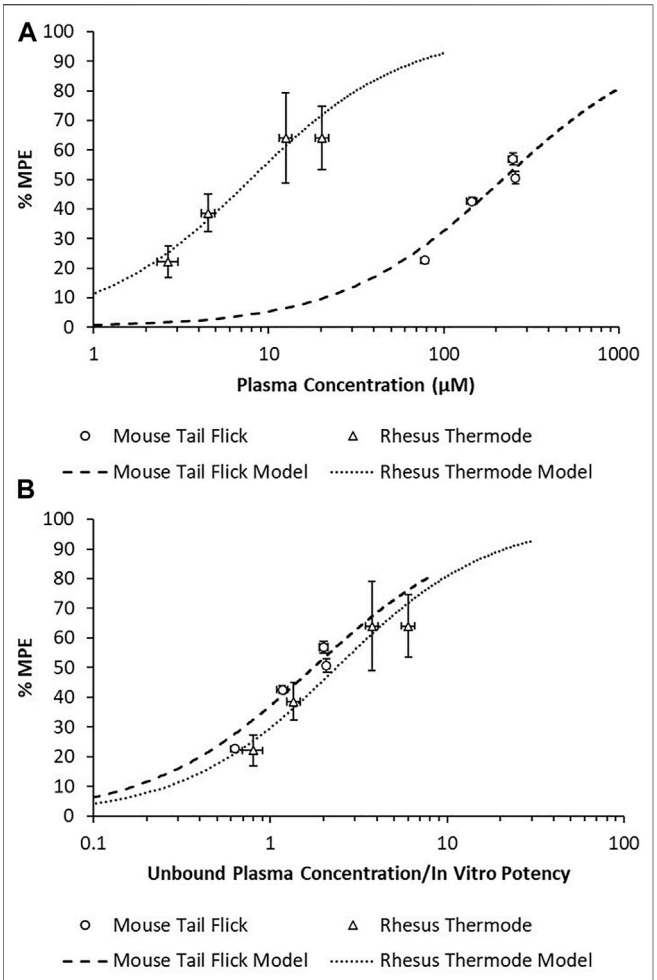

FIGURE 5 | Overlay of MK-2075 exposure–response in the mouse tail flick latency and rhesus thermode heat withdrawal assays of nociception using **(A)** total plasma concentration and **(B)** unbound plasma concentration normalized by *in vitro* potency.

The measured *in vitro* human NaV1.7 IC_{50} of MK-2075 was 0.149 μM, and a free fraction of 0.067 was measured in the human plasma. The application of the *in vivo*/*in vitro* scalars derived from the mouse tail flick and rhesus thermode assays to human *in vitro* NaV1.7 potency and correction for plasma protein binding results in a predicted clinical efficacious total plasma concentration of 3.9–5.3 μM (0.26–0.36 μM unbound, 1.75- to 2.37-fold over the *in vitro* NaV1.7 IC_{50}) for MK-2075 in postoperative pain. The achievement of the upper bound of this predicted concentration range (5.3 μM) was selected as the clinical PK target and used to project efficacious human doses.

Projection of MK-2075 Human Pharmacokinetics, Pharmacodynamics, and Efficacious Dose

A two-compartment PK model with IV administration adequately captured the concentration–time profile observed in rats, dogs, and monkeys following a 2-h IV infusion (**Figure 8**). The resulting parameter estimates with SE and CV% are presented in **Table 3**. The consistent biphasic nature of the PK profile in preclinical species led us to assume that a two-compartment PK model structure would also be appropriate for humans.

The predicted human PK parameters from allometric scaling from rats, dogs, and monkeys, including uncertainty in the prediction due to variability in the measured input parameters, are presented in **Table 4**. The low clearance and long half-life contributed to a relatively long time to reach steady state with IV infusion administration. In early clinical studies, the concentration needs to be sustained above the PK target for a period of time sufficient to allow evaluation of the PD response. In order to achieve target concentrations for the desired duration (~1 h) within the overall exposure and maximum concentration limits for safety, a long duration (8-h) IV infusion was required.

The projected dose to achieve the target median plasma concentration of 5.3 μM for at least 1 h was 50 mg over an 8-h infusion with a 90% CI of 45–55 mg (**Figure 9A**). This dose level corresponds to the median total plasma concentrations of 5.3–5.5 μM between 7 and 8 h and an AUC_{0-24h} of 56 μM·h (90% CI of 51–61 μM·h) (**Figure 9B**). Translation of the PKPD modeling results from rhesus olfaction indicates that the anticipated median target modulation achievable within the last hour of an 8-h infusion at 6.25 mg/h (50 mg total dose) in humans would be 43% inhibition (90% CI of 37–53%) (**Figure 10A**). Doses ranging from 20 to 80 mg infused over 8 h are projected to achieve average total plasma concentrations of 2.1–8.6 μM in the last hour of infusion and anticipated to produce 24–55% average inhibition of olfaction (**Figure 10B**).

DISCUSSION

Based on clinical benchmarking with marketed SOC analgesics, concentrations eliciting 50% inhibition in the rhesus thermode heat withdrawal assay and the mouse tail flick are associated with postoperative pain mitigation in the clinic, and 50% inhibition is therefore a reasonable PD target to test the effectiveness of

TABLE 2 | Correction of MK-2075 *in vivo* potency for species-specific plasma protein binding and intrinsic NaV1.7 potency.

Species/assay	*In vivo* EC_{50} or IC_{50} (μM)	Plasma fraction unbound ($f_{u,p}$)	*In vitro* NaV1.7 IC_{50} (μM)	$\frac{\text{In Vivo}}{\text{In Vitro}}$ Scalar
Mouse tail flick	217	0.026	3.228	1.75
Rhesus thermode	7.9	0.077	0.257	2.37

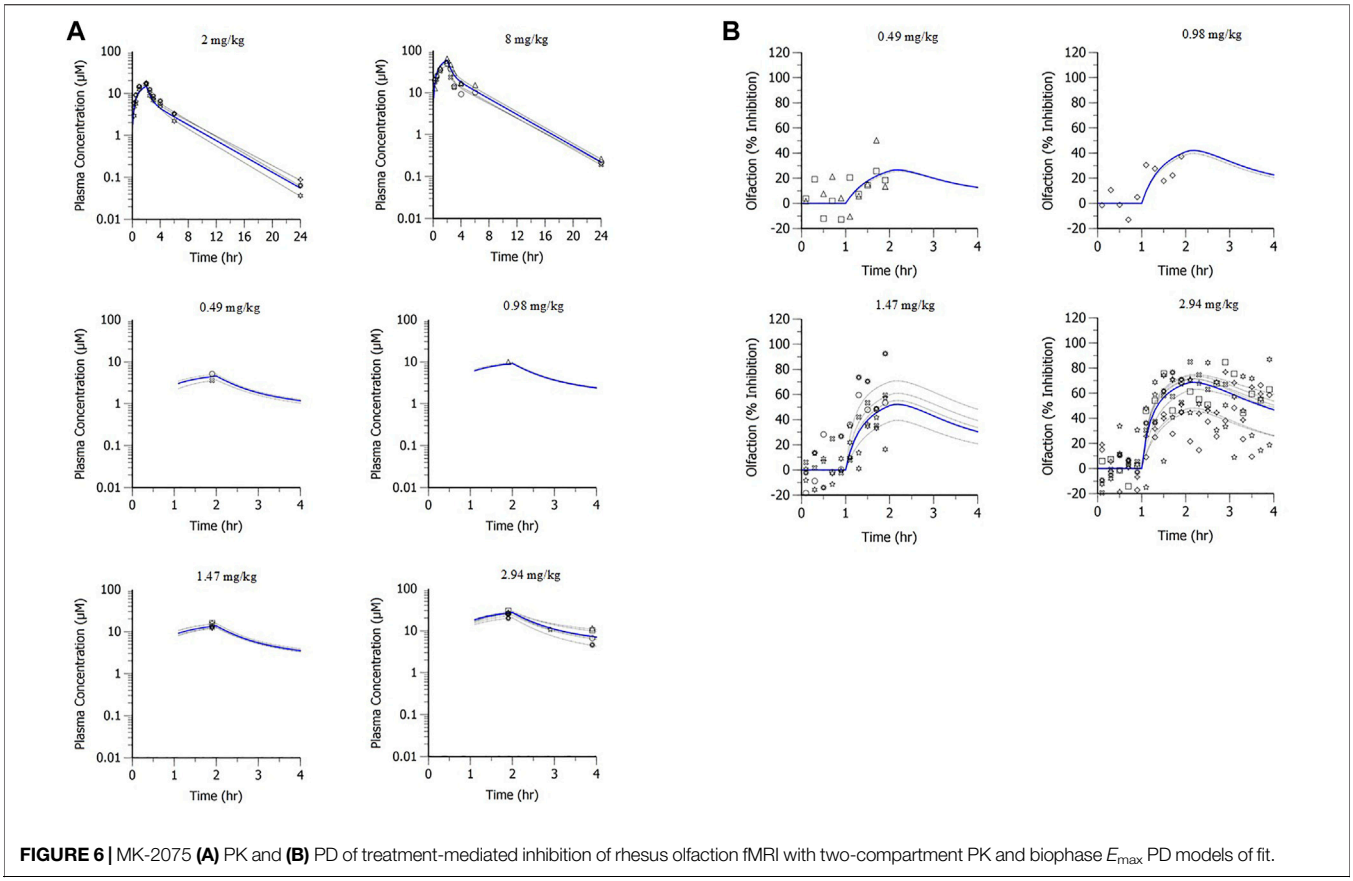

FIGURE 6 | MK-2075 **(A)** PK and **(B)** PD of treatment-mediated inhibition of rhesus olfaction fMRI with two-compartment PK and biophase E_{max} PD models of fit.

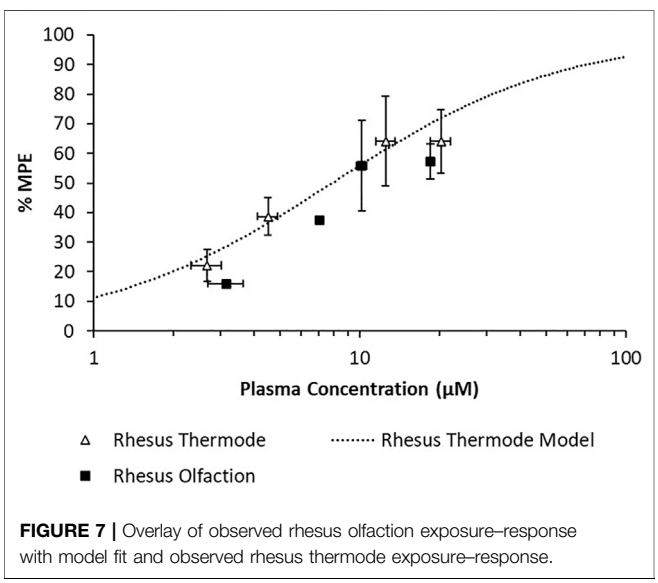

FIGURE 7 | Overlay of observed rhesus olfaction exposure–response with model fit and observed rhesus thermode exposure–response.

inhibition of NaV1.7 in acute pain. The quantitative models of MK-2075 exposure–response with normalization for species differences in plasma protein binding and *in vitro* potency established an understanding of the *in vitro* to *in vivo* translation of target potencies. This enables translation of PD response in preclinical species to humans when species differences exist in target potency, plasma fraction unbound, and PK. Integration of *in vitro* human NaV1.7 potency and plasma protein binding into these models provided a prediction of the total plasma concentration PK target of 5.3 μM (0.36 μM unbound, 2.4-fold over the *in vitro* NaV1.7 IC_{50}) for MK-2075 in postoperative pain. Allometric scaling of preclinical PK parameters and translation of a biophase PKPD model based on rhesus olfaction with correction for species differences in potency and plasma protein binding was used to predict human PK, PD, and dose regimen. The anticipated target modulation achieved by 8 h following an infusion of 50 mg total dose to humans was projected to be ~40–50% inhibition. The results of this model-based analysis of preclinical PKPD and translation to human PKPD and dose projections described herein were used to identify a compound with sufficient PK and safety profile to test the NaV1.7 inhibition mechanism in humans and aid the clinical study design and inform decision criteria in the early clinical development plan.

The quantitative translation of preclinical PKPD and antinociceptive activity to anticipated human PKPD and efficacious dose requires some assumptions and therefore will have some inherent limitations. A critical assumption in the benchmarking analysis is that there are no meaningful species difference in intrinsic potency for each of these SOC compounds against their biological target. Since the benchmarking analysis

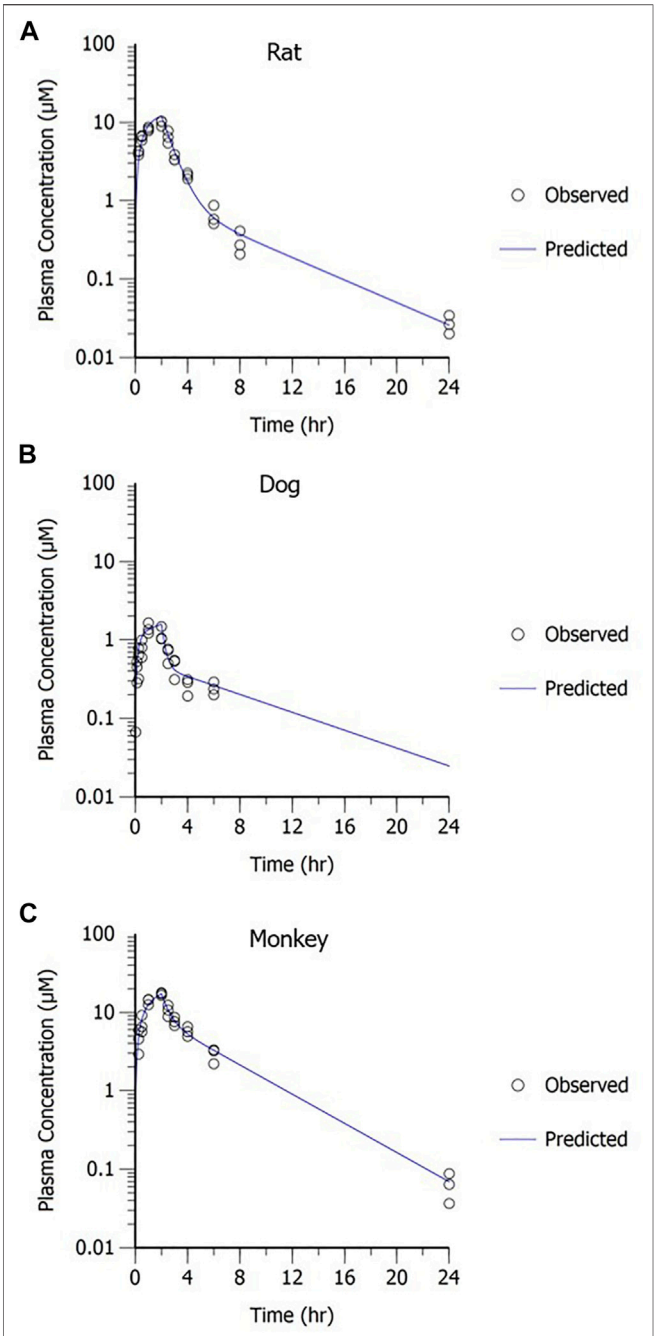

FIGURE 8 | MK-2075 concentration–time profile in **(A)** rat, **(B)** dog, and **(C)** monkey with two-compartment PK model fit.

was conducted with drugs acting on a different biological target than MK-2075, an assumption was required that the observed translation of response in the preclinical nociception assay to clinical efficacy will be independent of the mechanism and is therefore applicable to the inhibition of NaV1.7. The potential for potency differences depending on the type of pain stimulus must also be considered. Bankar et al. (2018) demonstrated a shift in potency between a thermal stimulus assay using a hot plate and the traditional assays for inflammatory or neuropathic pain for NaV1.7 antagonists.

TABLE 3 | MK-2075 preclinical PK parameters from two-compartment model fit of concentration–time data in rat, dog, and monkey.

Species	Parameter	Estimate	SE	CV%
Wistar Han rat	V1 (L/kg)	0.072	0.006	8.3
	CL (L/hr/kg)	0.068	0.003	4.5
	V2 (L/kg)	0.066	0.008	12.3
	CLD (L/hr/kg)	0.013	0.002	16.8
Beagle dog	V1 (L/kg)	0.092	0.013	14.4
	CL (L/hr/kg)	0.149	0.009	5.8
	V2 (L/kg)	0.649	0.071	10.9
	CLD (L/hr/kg)	0.197	0.029	14.9
Rhesus monkey	V1 (L/kg)	0.096	0.010	11.0
	CL (L/hr/kg)	0.067	0.003	4.1
	V2 (L/kg)	0.133	0.015	11.6
	CLD (L/hr/kg)	0.073	0.020	26.8

TABLE 4 | Predicted human PK parameters of MK-2075 represented as median and 90% CI.

PK parameter	Median predicted value	90% confidence interval
CL (ml/min/kg)	0.402	0.368–0.440
V1 (L/kg)	0.063	0.055–0.071
V2 (L/kg)	0.130	0.114–0.148
CLD (ml/min/kg)	0.312	0.256–0.382
Terminal T1/2 (h)	9.5	8.9–10.1
Effective T1/2 (h)	5.5	5.2–6.0

Multiple structural analogs of MK-2075 have been evaluated in a mouse formalin paw assay demonstrating 90% inhibition of behavioral response to formalin stimulus at unbound concentrations approximately equal to the *in vitro* potency (Roecker et al., 2021). This represents a substantial leftward shift from a value of unbound EC_{50} approximately twofold over *in vitro* potency for thermal stimulus in the mouse tail flick assay, and it is consistent with the results obtained by Bankar et al., suggesting that NaV1.7 inhibitors may require greater target engagement to elicit antinociceptive effects in assays of acute nociception compared to assays of inflammatory/persistent nociception.

Another important consideration in the interpretation of the mouse tail flick latency results is a potential for species-specific selectivity profiles. While MK-2075 has robust selectivity for human NaV1.7 over the other isoforms such as NaV1.6 and NaV1.5 (>500-fold, manuscript in preparation), the selectivity profile for the mouse isoforms of the sodium ion channel has not been evaluated. Given the substantial shift in NaV1.7 potency between humans and mice, it is possible that selectivity for the NaV1.7 isoform is reduced in rodents. Therefore, at the high unbound concentrations of MK-2075 required for inhibition in the mouse tail flick assay, pharmacological activity at other NaV isoforms cannot be ruled out.

The direct-effect PD models selected for fitting of mouse tail flick latency and rhesus thermode heat withdrawal data assume that there is no hysteresis in the PKPD relationship. While graphical analysis of the mouse tail flick latency measured at different time points with structural analogs supports this assumption, the exposure–response data in rhesus thermode studies consisted of only a single time point concentration measurement at study termination, prohibiting the

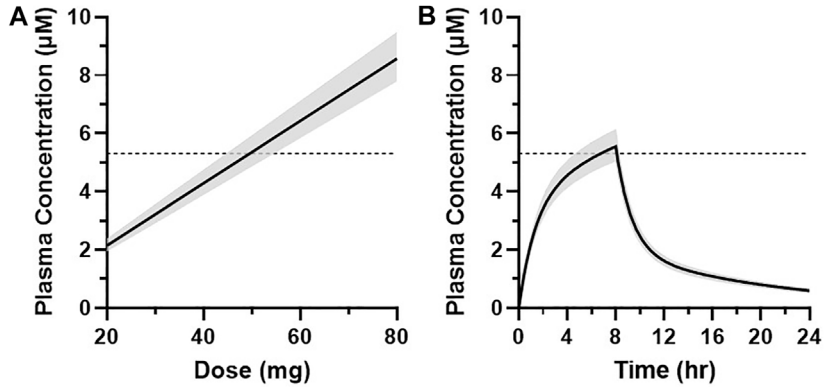

FIGURE 9 | (A) Graphical representation of the simulated plasma concentration (median ± 90% CI) at 7 h after the start of infusion at multiple dose levels in humans. **(B)** Simulated MK-2075 plasma concentration over time (median ± 90% CI) at a predicted dose of 50 mg infused intravenously over 8 h. Dashed horizontal line represents the target plasma concentration of 5.3 μM.

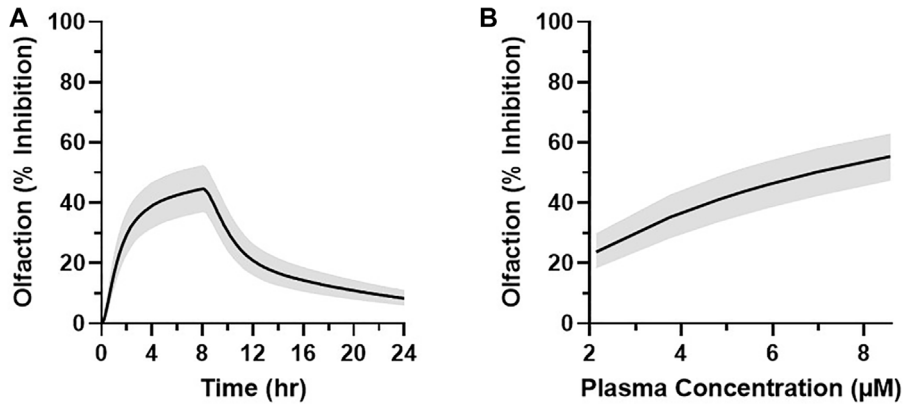

FIGURE 10 | (A) Simulated MK-2075 percent olfactory response inhibition over time (median ± 90% CI) at a predicted dose of 50 mg infused intravenously over 8 h in humans. **(B)** Graphical representation of the simulated olfaction inhibition response (median ± 90% CI) at 7 h after the start of infusion as a function of the simulated plasma concentration of MK-2075 at 7 h after doses of 20, 35, 45, 50, 55, 65, and 80 mg.

evaluation of potential for hysteresis. A key assumption in the rhesus olfaction PKPD model is that hysteresis is presumed to be a result of slightly delayed distribution to the target site due to the poor permeability of MK-2075. This assumption was informed by PKPD analysis with other NaV1.7 inhibitors, indicating that the extent of hysteresis is compound dependent and can likely be attributed to poor permeability causing slow distribution into the nerves (Ballard et al., 2020). The distribution rate constant (*ke0*) for the site of action in humans is assumed to be equivalent to that in rhesus monkeys.

Lastly, inhibition of olfaction as measured by fMRI is anticipated to be a relevant marker of target modulation based on the genetic evidence of both anosmia and loss of pain sensation in individuals with the NaV1.7 LOF mutation. While concordance was observed between inhibition of olfaction and heat withdrawal score in the rhesus assays with MK-2075, it is reasonable to consider that the magnitude of restriction at the blood–nerve barrier could be different at the peripheral nerves in the forearm than at the olfactory epithelium. There are structural differences identified in the blood–nerve barrier along different regions of the olfactory receptor neurons as well as differences in the tight junction protein occludin relative to the blood–nerve barrier in typical peripheral nerves such as the sciatic nerve (Hussar et al., 2002) (Tserentsoodol et al., 1999). A quantitative relationship between treatment-mediated inhibition of olfaction and reduction in pain sensation has not yet been established in the clinic. A recent clinical study with a NaV1.7 inhibitor, GDC-0276, monitored reduced sense of smell (hyposmia) as a potential biomarker of on-target pharmacology (Rothenberg et al., 2019). While a couple of incidents of hyposmia were reported, the authors conclude that due to a lack of an exposure-related pattern, the findings do not support impaired sense of smell as a biomarker. However, it is unclear if the relatively low unbound plasma concentrations obtained in this study achieved sufficient target engagement at the site of action to inhibit olfaction. The authors

themselves acknowledge that further study will be needed to define the exposures required to achieve on-target PD effects.

In summary, MK-2075 administered as a continuous IV infusion of 50 mg over an 8-h duration is projected to achieve sufficient NaV1.7 target engagement to further evaluate the potential of this target for treatment of pain indications. Benchmarking the desired preclinical antinociceptive response against clinical SOC for acute postoperative pain and establishing the *in vitro* to *in vivo* potency relationship for MK-2075 in both the mouse and rhesus assays afforded a data-driven PKPD target for the clinic. The quantitative integration of intrinsic potency against the human NaV1.7 target, predicted unbound exposure in the plasma, and distribution to the site of action using mathematical PKPD modeling enabled projection of clinically efficacious dose and simulation of anticipated PD profile of olfaction as a potential target modulation biomarker.

DATA AVAILABILITY STATEMENT

The raw data supporting the conclusions of this article will be made available by the authors, without undue reservation.

ETHICS STATEMENT

The animal study was reviewed and approved by Institutional Animal Care and Use Committee.

AUTHOR CONTRIBUTIONS

The corresponding author JB conducted data analysis, wrote and edited the manuscript, and contributed to the design of experiments. PP, JV, FZ, MH, XZ, and NJ designed and conducted *in vivo* experiments and contributed to the writing of the article. RLK and RMK designed and conducted *in vitro* experiments and contributed to the writing of the article. DH, AH, and CB contributed to the design of the experiments and editing of the manuscript. CG and AS contributed to the writing and editing of the manuscript.

FUNDING

This study was funded by Merck & Co., Inc.

REFERENCES

Ballard, J. E., Pall, P., Vardigan, J., Zhao, F., Holahan, M. A., and Kraus, R. (2020). Application of Pharmacokinetic-Pharmacodynamic Modeling to Inform Translation of *In Vitro* NaV1.7 Inhibition to *In Vivo* Pharmacological Response in Non-human Primate. *Pharm. Res.* 37, 181. doi:10.1007/s11095-020-02914-9

Bankar, G., Goodchild, S., Howard, S., Nelkenbrecher, K., Waldbrook, M., and Dourado, M. (2018). Selective NaV1.7 Antagonists With Long Residence Time Show Improved Efficacy Against Inflammatory and Neuropathic Pain. *Cel Rep.* 24, 3133–3145. doi:10.1016/j.celrep.2018.08.063

Bueters, T., Gibson, C., and Visser, S. (2015). Optimization of Human Dose Prediction by Using Quantitative and Translational Pharmacology in Drug Discovery. *Future Med. Chem.* 7 (17), 2351–2369. doi:10.4155/fmc.15.143

Dahlstrom, B., Tamsen, A., Paalzow, L., and Hartvig, P. (1982). Patient-Controlled Analgesic Therapy .4. Pharmacokinetics and Analgesic Plasma-Concentrations of Morphine. *Clin. Pharmacokinet.* 7 (3), 266–279. doi:10.2165/00003088-198207030-00006

Dib-Hajj, S., Cummins, T., Black, J., and Waxman, S. (2007). From Genes to Pain: Na(v)1.7 and Human Pain Disorders. *Trends Neurosciences.* 30 (11), 555–563. doi:10.1016/j.tins.2007.08.004

Dick, I., Brochu, R., Purohit, Y., Kaczorowski, G., Martin, W., and Priest, B. (2007). Sodium Channel Blockade May Contribute to the Analgesic Efficacy of Antidepressants. *J. Pain.* 8 (4), 315–324. doi:10.1016/j.jpain.2006.10.001

Hussar, P., Tserentsoodol, N., Koyama, H., Yokoo-Sugawara, M., Matsuzaki, T., Takami, S., et al. (2002). The Glucose Transporter GLUT1 and the Tight Junction Protein Occludin in Nasal Olfactory Mucosa. *Chem. Senses.* 27 (1), 7–11. doi:10.1093/chemse/27.1.7

Jansson-Löfmark, R., Hjorth, S., and Gabrielsson, J. (2020). Does *In Vitro* Potency Predict Clinically Efficacious Concentrations? *Clin. Pharmacol. Ther.* 108 (2), 298–305. doi:10.1002/cpt.1846

Kraus, R., Zhao, F., Pall, P., Zhou, D., Vardigan, J., and Danziger, A. (2021). Na(v) 1.7 Target Modulation and Efficacy Can Be Measured in Nonhuman Primate Assays. *Sci. Translational Med.* 13. doi:10.1126/scitranslmed.aay1050

Lehmann, K., Kratzenberg, U., Schroederbark, B., and Horrichshaermeyer, G. (1990). Postoperative Patient-Controlled Analgesia With Tramadol - Analgesic Efficacy and Minimum Effective Concentrations. *Clin. J. Pain.* 6 (3), 212–220. doi:10.1097/00002508-199009000-00008

Lindauer, A. Y., Guo, K., Lee, B., Ivashina, J., and Deshmukh, S. (2014). A Tool for First-In-Human PK Prediction Incorporating Experimental Uncertainty. *PAGE.* 23. Available at: Abstr 3171. www.page-meeting.org/?abstract=3171

Morgan, P., Van Der Graaf, P., Arrowsmith, J., Feltner, D., Drummond, K., Wegner, C., et al. (2012). Can the Flow of Medicines Be Improved? Fundamental Pharmacokinetic and Pharmacological Principles Toward Improving Phase II Survival. *Drug Discov. Today.* 17 (9-10), 419–424. doi:10.1016/j.drudis.2011.12.020

Moulin, D., Boulanger, A., Clark, A., Clarke, H., Dao, T., and Finley, G. (2014). Pharmacological Management of Chronic Neuropathic Pain: Revised Consensus Statement From the Canadian Pain Society. *Pain Res. Management.* 19 (6), 328–335. doi:10.1155/2014/754693

Roecker, A. J., Layton, M. E., Pero, J. E., Kelly, M. J., Greshock, T. J., and Kraus, R. L. (2021). Discovery of Arylsulfonamide Nav1.7 Inhibitors: IVIVC, MPO Methods, and Optimization of Selectivity Profile. *ACS Med. Chem. Lett.* 12, 1038–1049. doi:10.1021/acsmedchemlett.1c00218

Rothenberg, M., Tagen, M., Chang, J., Boyce-Rustay, J., Friesenhahn, M., and Hackos, D. (2019). Safety, Tolerability, and Pharmacokinetics of GDC-0276, a Novel Na(V)1.7 Inhibitor, in a First-In-Human, Single- and Multiple-Dose Study in Healthy Volunteers. *Clin. Drug Invest.* 39 (9), 873–887. doi:10.1007/s40261-019-00807-3

Tanelian, D. L., and Victory, R. A. (1995). Sodium Channel-Blocking Agents: Their Use in Neuropathic Pain Conditions. *Pain Forum.* 4 (2), 75–80. doi:10.1016/s1082-3174(11)80001-2

Tang, H., Hussain, A., Leal, M., Mayersohn, M., and Fluhler, E. (2007). Interspecies Prediction of Human Drug Clearance Based on Scaling Data From One or Two Animal Species. *Drug Metab. Disposition.* 35 (10), 1886–1893. doi:10.1124/dmd.107.016188

Tserentsoodol, N., Shin, B.-C., Koyama, H., Suzuki, T., and Takata, K. (1999). Immunolocalization of Tight Junction Proteins, Occludin and ZO-1, and Glucose Transporter GLUT1 in the Cells of the Blood-Nerve Barrier. *Arch. Histology Cytol.* 62 (5), 459–469. doi:10.1679/aohc.62.459

Vardigan, J., Houghton, A., Lange, H., Adarayan, E., Pall, P., and Ballard, J. (2018). Pharmacological Validation of a Novel Nonhuman Primate Measure of thermal Responsivity With Utility for Predicting Analgesic Effects. *J. Pain Res.* 11, 735–741. doi:10.2147/JPR.S152879

Weiss, J., Pyrski, M., Jacobi, E., Bufe, B., Willnecker, V., and Schick, B. (2011). Loss-of-Function Mutations in Sodium Channel Na(v)1.7 Cause Anosmia. *Nature.* 472, 186–190. doi:10.1038/nature09975

Wong, H., Bohnert, T., Damian-Lordache, V., Gibson, C., Hsu, C.-P., and Krishnatry, A. S. (2017). Translational Pharmacokinetic-Pharmacodynamic Analysis in the Pharmaceutical Industry: an IQ Consortium PK-PD Discussion Group Perspective. *Drug Discov. Today.* 22, 1447–1459. doi:10.1016/j.drudis.2017.04.015

Zhao, F., Holahan, M. A., Houghton, A. K., Hargreaves, R., Evelhoch, J. L., Winkelmann, C. T., et al. (2015). Functional Imaging of Olfaction by CBV fMRI Inmonkeys: Insight into the Role of Olfactory Bulb in Habituation. *NeuroImage.* 106, 364–372. doi:10.1016/j.neuroimage.2014.12.001

Conflict of Interest: The authors JB, PP, JV, FZ, MH, XZ, NJ, RLK, RMK, DH, AH, CB, CG, and AS were employed by the company of Merck and Co., Inc. during the period of this work and may hold stock in those companies.

Publisher's Note: All claims expressed in this article are solely those of the authors and do not necessarily represent those of their affiliated organizations, or those of the publisher, the editors, and the reviewers. Any product that may be evaluated in this article, or claim that may be made by its manufacturer, is not guaranteed or endorsed by the publisher.

frontiers in Pharmacology

ORIGINAL RESEARCH
published: 18 February 2022
doi: 10.3389/fphar.2022.837744

Development and Evaluation of Competitive Inhibitors of Trastuzumab-HER2 Binding to Bypass the Binding-Site Barrier

*Brandon M. Bordeau, Lubna Abuqayyas, Toan D. Nguyen, Ping Chen and Joseph P. Balthasar**

Department of Pharmaceutical Sciences, School of Pharmacy and Pharmaceutical Sciences, University at Buffalo, Buffalo, NY, United States

Our group has developed and experimentally validated a strategy to increase antibody penetration in solid tumors through transient inhibition of antibody-antigen binding. In prior work, we demonstrated that 1HE, an anti-trastuzumab single domain antibody that transiently inhibits trastuzumab binding to HER2, increased the penetration of trastuzumab and increased the efficacy of ado-trastuzumab emtansine (T-DM1) in HER2+ xenograft bearing mice. In the present work, 1HE variants were developed using random mutagenesis and phage display to enable optimization of tumor penetration and efficacy of trastuzumab-based therapeutics. To guide the rational selection of a particular 1HE mutant for a specific trastuzumab-therapy, we developed a mechanistic pharmacokinetic (PK) model to predict within-tumor exposure of trastuzumab/T-DM1. A pharmacodynamic (PD) component was added to the model to predict the relationship between intratumor exposure to T-DM1 and the corresponding therapeutic effect in HER2+ xenografts. To demonstrate the utility of the competitive inhibition approach for immunotoxins, PK parameters specific for a recombinant immunotoxin were incorporated into the model structure. Dissociation half-lives for variants ranged from 1.1 h (for variant LG11) to 107.9 h (for variant HE10). Simulations predicted that 1HE co-administration can increase the tumor penetration of T-DM1, with inhibitors with longer trastuzumab binding half-lives relative to 1HE (15.5 h) further increasing T-DM1 penetration at the expense of total tumor uptake of T-DM1. The PK/PD model accurately predicted the response of NCI-N87 xenografts to treatment with T-DM1 or T-DM1 co-administered with 1HE. Model predictions indicate that the 1HE mutant HF9, with a trastuzumab binding half-life of 51.1 h, would be the optimal inhibitor for increasing T-DM1 efficacy with a modest extension in the median survival time relative to T-DM1 with 1HE. Model simulations predict that LG11 co-administration will dramatically increase immunotoxin penetration within all tumor regions. We expect that the mechanistic model structure and the wide range of inhibitors developed in this work will enable optimization of trastuzumab-cytotoxin penetration and efficacy in solid tumors.

Keywords: binding site barrier, ADC tumor pharmacokinetics/pharmacodynamics, T-DM1, modeling and simulation, antibody

OPEN ACCESS

Edited by:
David Z. D'Argenio, University of Southern California, United States

Reviewed by:
Zinnia P. Parra-Guillen, University of Navarra, Spain
Bernd Meibohm, University of Tennessee Health Science Center (UTHSC), United States

****Correspondence:***
Joseph P. Balthasar
jb@buffalo.edu

Specialty section:
This article was submitted to Experimental Pharmacology and Drug Discovery, a section of the journal Frontiers in Pharmacology

Received: *17 December 2021*
Accepted: *27 January 2022*
Published: *18 February 2022*

Citation:
Bordeau BM, Abuqayyas L, Nguyen TD, Chen P and Balthasar JP (2022) Development and Evaluation of Competitive Inhibitors of Trastuzumab-HER2 Binding to Bypass the Binding-Site Barrier. Front. Pharmacol. 13:837744. doi: 10.3389/fphar.2022.837744

1 INTRODUCTION

There is substantial interest in the development of strategies to increase monoclonal antibody (mAb) uptake and distribution in solid tumors (Bordeau and Balthasar, 2021). The uptake and penetration of mAb within tumors is limited due to several pathophysiological characteristics and biological phenomena associated with tumors, including high tumor interstitial fluid pressure, dense extracellular matrix development, an abnormal vasculature network, and by the "binding site barrier" (BSB) (Jain and Baxter, 1988; Netti et al., 2000; Pluen et al., 2001; Bordeau and Balthasar, 2021). The BSB was first described in 1990 by Fujimori et al. (1990), Juweid et al. (1992) and has since been characterized through experimental investigations and through application of mathematical modeling and simulation (Saga et al., 1995; Thurber et al., 2007; Thurber et al., 2008; Thurber and Wittrup, 2008; Lee and Tannock, 2010; Thurber and Weissleder, 2011a; Thurber and Weissleder, 2011b). Briefly, following extravasation, mAb rapidly binds to cellular antigens, concentrating antibodies at sites near blood vessels and decreasing the extent of within-tumor mAb distribution. Due to this barrier, high-affinity antibodies demonstrate heterogenous distribution within tumors, with high concentrations of antibody at sites near tumor capillaries, and with little or no antibody distribution to distant sites (i.e., >20 μm from tumor capillaries). Recently, there has been renewed interest in the BSB due to the apparent impact of poor tumor penetration on the anti-tumor effects of mAb-cytotoxin conjugates. Radioimmunoconjugates with alpha-emitting radionuclides can kill a cancer cell with 1–10 emissions (Thurber et al., 2007), recombinant immunotoxins (RITs) can achieve cell killing with ~1,000 bound toxins (Kreitman and Pastan, 1998), and high-potency antibody-drug conjugates (ADCs) may be effective following internalization of <1,000 ADC molecules. Commonly, tumor antigen density exceeds 10^6 antigens/cell. Heterogenous intra-tumoral ADC distribution, consistent with the BSB, can lead to an overkilling effect for cells in close proximity to blood vessels at the expense of subtherapeutic ADC exposure for the majority of tumor cells which are distant from blood vessels. The BSB can substantially limit therapeutic efficacy, particularly for highly-toxic antibody therapies where the maximum tolerated dose is far below levels needed to saturate the tumor antigen.

Trastuzumab, an anti-HER2 mAb, is currently employed as the targeting vector within two FDA-approved ADCs, ado-trastuzumab emtansine (T-DM1) and fam-trastuzumab deruxtecan-nxki. A third trastuzumab-based ADC, trastuzumab duocarmazine, is in late-stage clinical trials (Rinnerthaler et al., 2019). As the first FDA-approved mAb for solid tumor indications, trastuzumab has been widely used for characterizing the impact of the BSB on mAb and ADC efficacy. For example, using a physiologically-based pharmacokinetic model, Cilliers et al. predicted that, in high HER2 expressing tumors, current clinical doses of T-DM1 result in poor tumor penetration and predicted that the co-administration of unconjugated (i.e., "naked") mAb with T-DM1 would increase the fraction of tumor cells that are exposed to lethal T-DM1 concentrations (Cilliers et al., 2016; Khera et al., 2018). In an NCI-N87 xenograft mouse model that is insensitive to trastuzumab, co-administration of naked trastuzumab with T-DM1 significantly enhanced T-DM1 efficacy (Cilliers et al., 2018). Similar observations were presented by Singh et al., who employed pharmacokinetic-pharmacodynamic (PK-PD) modeling to demonstrate a synergistic interaction between naked trastuzumab and T-DM1 in NCI-N87 xenograft bearing mice (Singh et al., 2020). Both groups highlighted several limitations of the mAb co-administration strategy including 1) the optimal dose ratio of naked mAb to ADC varies based on tumor antigen expression, 2) ADC binding at smaller metastatic sites may be outcompeted by naked mAb, and 3) tumors with high antigen expression and poor vascularity require grams of naked antibody to effectively saturate tumor antigen, which may not be feasibly administered clinically (Cilliers et al., 2018; Singh et al., 2020).

Our laboratory has developed an alternative method to increase the tumor penetration of anti-tumor antibodies through transient, competition inhibition of mAb-tumor binding. For example, when trastuzumab is engaged with a competitive inhibitor of HER2 binding, the within-tumor distribution of the antibody is not hindered by the BSB. Following dissociation from the inhibitor within the tumor milieu, trastuzumab is free to bind to tumor cell-associated HER2, including at sites distant from blood vessels. In our prior work, an anti-idiotype single domain antibody, 1HE, was employed as a model inhibitor of trastuzumab-HER2 binding (Bordeau et al., 2021). Administration of 1HE with a 2 mg/kg dose of trastuzumab to mice bearing SKOV3 xenografts increased the penetration distance of trastuzumab from tumor vasculature by 40%, and in NCI-N87 xenograft bearing mice, the co-administration of 1HE with a 1.8 mg/kg dose of T-DM1 increased the median time of survival from 29 to 42 days (Bordeau et al., 2021).

Development of competitive inhibitors with a range of binding characteristics may yield optimal agents for application to the varying trastuzumab-based conjugates (ado-trastuzumab emtansine, fam-trastuzumab deruxtecan-nxki, trastuzumab duocarmazine, etc.). In the present work, we take steps to extend the competitive inhibition strategy through the development of 1HE mutants with altered trastuzumab binding half-lives. To support the identification of ideal inhibitors, we developed a semi-mechanistic mathematical model to predict the impact of competitive inhibition on antibody and antibody-conjugate distribution and efficacy.

2 MATERIALS AND METHODS

2.1 Antibodies, Mice, and Tumor Cell-Line

Trastuzumab and T-DM1 were purchased from Millard Fillmore Memorial Hospital (Amherst, NY). The gastric carcinoma cell-line NCI-N87 was a generous gift from Dr. Dhaval K. Shah and was authenticated by short tandem repeat profiling by the American Type Culture Collection (ATCC, Manassas, VA) and tested negative for mycoplasma in January of 2021.

2.2 Phage Library Construction

One nanogram of 1HE DNA with NdeI and XhoI restriction digestion overhangs was used as the template DNA for error-prone polymerase chain reaction (PCR). PCR primers were designed with sFiI restriction digest overhangs for ligation of the PCR product into the pComb3XSS phagemid plasmid (Addgene, Cambridge, MA). Error-prone PCR product was obtained following 14-cycles of denaturation at 94°C for 1 min, annealing at 52°C for 1 min, and extension at 68°C for 3 min with a final 10-minute extension. PCR product (1 μg) was ligated into the pComb3XSS phagemid (2.4 μg) and transfected into TG1 *E. coli* cells (Lucigen, Middleton, WI) through electroporation. Following electroporation, transformed bacteria were serially diluted up to 10^4 and spread over lysogeny broth (LB) agar plates supplemented with 2% glucose and 100 μg/ml ampicillin. Remaining transformed bacteria were spread onto four 245 mm square dishes containing LB agar with 2% glucose and 100 μg/ml ampicillin. The next day the library size was determined through colony counting and the bacteria from the 245 mm plates scrapped and inoculated into 8 mls of LB with 8 mls of 40% sterile glycerol. The library was stored in aliquots at −80°C.

2.3 Phage Isolation

An aliquot of the phage library was removed from −80°C and inoculated into 60 ml of 2xYT medium with 100 μg/ml ampicillin and 2% glucose. The inoculated medium was grown at 37°C to a 600 nm optical density of 0.4–0.6. Subsequently, 10 ml of the 2xYT culture was transferred to a 50 ml conical tube and 1 μl of CM13 helper phage (Antibody Design Laboratories, San Diego, CA) added with a 1-hour incubation at 37°C in a shaker incubator. Infected cells were pelleted by centrifugation at 2,800 rotational centrifugal force (RCF) for 10 min. Pelleted cells were re-suspended in 50 ml of 2×YT media with 100 μg/ml ampicillin and 50 μg/ml kanamycin and incubated overnight at 30°C in a shaker incubator. The following day, the culture was centrifuged for 15 min at 3,200 RCF to pellet TG1 cells. The media supernatant was decanted into two 50 ml conical tubes, 6 ml of 20% (wt/v) PEG6000/2.5 M NaCl solution were added, and conical tubes were placed in ice for 30-minute. Precipitated phage was pelleted by centrifugation at 10,000 RCF for 20 min. Pelleted phage were re-suspended in 1 ml of PBS and centrifuged for 1.5 min at 16,000 RCF in a microcentrifuge to pellet any residual bacteria. Phage concentration was determined prior to panning *via* a titration method. Briefly, phage was serially diluted by factors of 10 in 2×YT media, and 10 μl of each dilution added to 90 μl of TG1 cells in mid-log phase growth with a subsequent 15-minute incubation at 37°C. Infected TG1 cells from each dilution were spread on LB agar plates with 100 μg/ml ampicillin and 2% glucose and plates incubated overnight at 37°C. Phage concentration was determined by counting colonies on the plate with the highest dilution of phage that grew between 20 and 200 bacterial colonies.

2.4 Phage Biopanning

Trastuzumab was chemically conjugated to Dynabeads following manufacturer recommendations (Thermo Fisher Scientific, Waltham, MA). Prior to panning, trastuzumab modified beads were blocked with 2% milk in phosphate buffered saline pH 7.4 (PBS) for 1 h. Two panning strategies were used to isolate low- and high-affinity binders, relative to 1HE. For the first round of panning, the phage library was diluted 100-fold (8.2×10^{11} phages/ml) into a 0.2% milk PBS solution and incubated with trastuzumab modified beads for 1 h. Following incubation, beads were washed five times for 5 minutes with PBS. Following washing, a 5 μM solution of 1HE in PBS was added and incubated for 2 h. For the low-affinity panning method, the supernatant, following the 2-hour incubation with 1HE, was removed, and phages amplified in TG1 cells. The panning was repeated identically, with the amplified phage from the previous round for two additional rounds. For the high-affinity panning strategy, following the 2-hour dissociation and supernatant removal, trastuzumab modified beads were incubated with a 100 mM glycine pH 2.0 buffer for 10 minutes. Subsequently, the eluate was removed and neutralized with the addition of 75 μl of 1 M TRIS-HCL pH 9. The output titer was amplified, and two additional pannings performed with a 24-hour and a 72-hour dissociation, for the second and third round, respectively, in a PBS buffer with 5 μM 1HE. The final output titer was infected into TG1 cells, incubated at 37°C for 2 h, with 50 μg/ml ampicillin added 1 h into incubation. Subsequently, phage infected TG1 cells were pelleted by centrifugation, lysed, and phage DNA purified using a plasmid purification kit. Purified phage DNA from the high-affinity panning was transformed into the *E. coli* strain BL21DE3 (New England Biolabs, Ipswich, MA), serially diluted, spread onto LB agar plates with 100 μg/ml ampicillin, and grown overnight at 37°C. Purified phage DNA from the low-affinity panning was digested with XhoI and NdeI restriction enzymes and separated from the Pcomb3XSS plasmid through agarose gel electrophoresis and purified using a gel extraction and purification kit. Low-affinity mutant DNA was ligated into the expression plasmid pET22b(+) (Millipore-Sigma, Burlington, MA) and transformed into the *E. coli* strain SHuffle (New England Biolabs, Ipswich, MA). Transformed cells were spread onto an LB agar plate with 100 μg/ml ampicillin and grown overnight at 30°C.

2.5 Phage Screening

A master plate was established by inoculating single SHuffle or BL21DE3 bacterial colonies into the wells of a 96 well plate with 200 μl of LB medium with 100 ug/ml ampicillin, and 20% glycerol and grown overnight at 30°C. The following day, 20 μl of overnight growth media from each well was inoculated into individual wells of a deep well plate with 1 ml of LB, and the starter plate stored at −80°C. The expression plate was grown in a shaker incubator at 300 rpm at 37°C for BL21DE3 or 30°C for SHuffle cells to an optical density at 600 nm of 0.4–0.8. Expression was induced with the addition of 1 mM isopropyl β-d1-thiogalactopyranoside (IPTG) and incubated overnight at 16°C and 300 rotations per minute (RPM). The next day bacterial cells were pelleted by centrifugation at 3,900 RCF for 15 min. Following centrifugation, the culture media was removed, and 100 μl of BugBuster® (Millipore-Sigma, Burlington, MA) with 10 mg/ml lysozyme, and a 1:1,000 dilution of Benzonase®

(Millipore-Sigma, Burlington, MA) was added to each well, and bacterial pellets resuspended by pipetting. Cells were incubated with lysis buffer for 15 min at room temperature on a shaker platform at 300 rpm. NUNC Maxisorb plates (Thermo Scientific, Waltham, MA) were incubated with 250 µl of 4 µg/ml trastuzumab in a 20 mM disodium phosphate buffer (pH unadjusted) overnight. The following day, enzyme-linked immunosorbent assay (ELISA) plates were blocked with the addition of 250 µl of a 1% bovine serum albumin (BSA) solution for 1 h. The bacterial lysate from the expression plate was diluted 10-fold in a 0.1% BSA solution, and 25 µl added to individual wells of an ELISA plate containing 225 µl of PBS. The plate was incubated with diluted lysate for 1 h and then washed four times, with 250 µl of phosphate-buffered 0.05% Tween-20 (wash buffer). For the high-affinity clones, ELISA screening was run in duplicate wells. Following binding, a well for each colony was incubated in PBS, and another well for each colony incubated with 1 µM 1HE to prevent rebinding for 40 h. After 40 h, the wells were washed four times with wash buffer and 250 µl of a 1:2,000 dilution of an anti-hemagglutinin alkaline phosphatase (AP) conjugated secondary antibody (Millipore Sigma, Burlington, MA) in 0.1% BSA PBS added to each well and incubated for 1 h on a shaker incubator at 300 RPM. Following incubation, wells were washed three times with wash buffer and two times with distilled water (dH_2O). 250 µl of 4 mg/ml para-nitrophenyl phosphate (PnPP) in a 10 mM diethanolamine pH 9.8 buffer was added to each well, and the change in absorbance at 405 nm monitored using a SpectraMax 340PC plate reader (Molecular Devices, San Jose, CA) for 10 min at 30-second intervals. An estimate for the trastuzumab binding half-life for each clone was calculated using the half-life equation using the signal from the PBS well as time = 0 and the signal from the well incubated with 1HE as time = 40 h. For the low-affinity panning clones, a similar approach to estimate binding half-life was used. Individual clones were run in triplicate, with a 3-hour and a 6-hour dissociation time point. In addition, 500 µM of trastuzumab was added to block rebinding for the 3- and 6-hour timepoints and a 1:5,000 dilution of an anti-hexahistidine tag AP secondary antibody (Abcam, Cambridge, United Kingdom) used for detection.

2.6 Sequencing

Following the screening protocol, 11 Colonies from the low-affinity panning and 13 colonies from the high-affinity panning were selected for DNA sequencing. Mutants were grown in 10 ml of LB media with 100 µg/ml ampicillin overnight at 37°C for BL21DE3 cells or 30°C for SHuffle cells. The next day, cells were pelleted, lysed, and DNA purified using a plasmid purification kit. DNA concentration was determined using a nanodrop and diluted to 100 ng/ml. Low-affinity clones in the Pet22b vector were sequenced using T7 promoter primers, and high-affinity clones were sequenced using pComb3FOR and pComb3REV primers. Sanger sequencing was completed at the Roswell Park sequencing core facility (Buffalo, NY).

2.7 Dissociation Rate Constant Screening

1HE mutants were selected from the DNA sequencing results for characterization of the trastuzumab dissociation rate constant. Individual mutants were expressed and purified using a nickel chromatography resin. Nunc Immobilizer Amino (Thermo Fisher Scientific, Waltham, MA) plates were incubated with 100 µl of 5 µg/ml of trastuzumab in a 100 mM disodium phosphate pH 8 buffer overnight. The following day, unreacted sites were blocked with 10 mM ethanolamine in a 100 mM sodium bicarbonate buffer pH 9.5 for 1 h. Purified mutants were incubated for 1 h and subsequently washed three times with wash buffer. Following washing, 0.1% BSA PBS solution was added to the initial timepoint wells. Wells containing the low-affinity mutants were incubated in a buffer with 500 nM trastuzumab, and the high-affinity mutants were incubated in a buffer with 1 µM of purified 1HE. Trastuzumab or 1HE was added to prevent rebinding of the 1HE mutants to trastuzumab, following dissociation. Trastuzumab was included in the low-affinity mutant screening to capture dissociated mutants to prevent rebinding to immobilized trastuzumab. 1HE was used for the high affinity mutant screening to block binding sites on immobilized trastuzumab (following dissociation of 1HE variants). Of note, the high-affinity mutants contained a c-terminal hemagglutinin (HA) tag whereas free 1HE did not; therefore, high affinity mutants bound to trastuzumab could be detected using an anti-HA antibody with dissociated mutants being outcompeted for rebinding to trastuzumab by 1HE. The concentrations of free 1HE and trastuzumab that were spiked into the wells were at a large molar excess (~100×) relative to immobilized trastuzumab to ensure efficient blockade of dissociated mutant rebinding by either 1) free 1HE outcompeting dissociated high-affinity 1HE mutants rebinding to immobilized trastuzumab or 2) free trastuzumab outcompeting immobilized trastuzumab for rebinding to the low affinity 1HE mutants. At individual time points, the buffer was removed by pipetting, the wells were washed three times with wash buffer, and 0.1% BSA PBS added. At the terminal time point, all wells were washed three times with wash buffer, and secondary antibodies added at the dilutions listed above for 1 h at room temperature. Following secondary incubation, plates were washed three times with wash buffer and three times with dH_2O. 250 µl of 4 mg/ml PnPP in a 10 mM diethanolamine pH 9.8 buffer was added to each well, and absorbance values read for 10 min at 30-second intervals. The change in absorbance per minute for each well, which is a measure of 1HE mutants bound to immobilized trastuzumab, was divided by the average change in absorbance per minute for the initial time point wells, and the resulting dissociation curves fit to a monoexponential decay function in GraphPad Prism 7 (GraphPad, San Diego, CA). Each time point was run in triplicate for each mutant.

2.8 Cell Cytotoxicity Assay

NCI-N87 cells were seeded at a density of 5,000 cells per well of a 96-well U-bottom plate (Corning Inc., Corning, NY). Following overnight incubation, the culture media was removed using a needle vacuum aspiration method and 200 µl of fresh media with a range of T-DM1 concentrations was added to individual wells. Each T-DM1 concentration was run in triplicate on each plate, with plates run in triplicate. Spent media was removed and replaced with fresh T-DM1 dilutions daily for a total

TABLE 1 | Calculated PK/PD sphere model parameters.

Parameter	Abbreviation	Value	Units	Source
Width of tumor layer	W	1.5E-3	cm	IVR/5
Tumor layer A volume	Va	1.4E-11	L	$4/3\pi W^3/10^3$
Tumor layer B volume	Vb	9.9E-11	L	$4/3\pi(2W)^3/10^3$-Va
Tumor layer C volume	Vc	2.7E-10	L	$4/3\pi(3W)^3/10^3$-Va-Vb
Tumor layer D volume	Vd	5.2E-10	L	$4/3\pi(4W)^3/10^3$-Va-Vb-Vc
Tumor layer E volume	Ve	8.6E-10	L	$4/3\pi(5W)^3/10^3$-Va-Vb-Vc-Vd
Interstitial volume A	VaVF	3.4E-12	L	Va×VF
Interstitial volume B	VbVF	2.4E-11	L	Vb×VF
Interstitial volume C	VcVF	6.5E-11	L	Vc×VF
Interstitial volume D	VdVF	1.3E-10	L	Vd×VF
Interstitial volume E	VeVF	2.1E-10	L	Ve×VF
Inhibitor diffusion coefficient	D2	5.1E-2	cm^2/h	Stokes-Einstein
Vascular volume	VV	2.1E-10	mL	TVF×$4/3\pi(5W)^3$
Vascular radius	VR	3.7E-10	cm	$(3/(4\pi)VV)^{1/3}$
Vascular surface area	VSA	1.7E-4	cm^2	$4\pi VR^2$
Vascular PS coefficient TmAb	PSpa	1.7E-10	L/h	P1×VSA/10^3
Vascular PS coefficient 1HE	PSpa2	2.9E-10	L/h	P2×VSA/10^3
Surface area layer A	SAa	2.8E-5	cm^2	$4\pi W^2$
Surface area layer B	SAb	1.1E-4	cm^2	$4\pi(2W)^2$
Surface area layer C	SAc	2.5E-4	cm^2	$4\pi(3W)^2$
Surface area layer D	SAd	4.5E-4	cm^2	$4\pi(4W)^2$
Distribution clearance TmAb A-B	CLdAB	8.9E-9	L/h	D1×SAa/(10^3×W)
Distribution clearance TmAb B-C	CLdBC	3.5E-8	L/h	D1×SAb/(10^3×W)
Distribution clearance TmAb C-D	CLdCD	8.0E-8	L/h	D1×SAc/(10^3×W)
Distribution clearance TmAb D-E	CLdDE	1.4E-7	L/h	D1×SAd/(10^3×W)
Distribution clearance 1HE A-B	CLdAB2	9.6E-7	L/h	D2×SAa/(10^3×W)

PS, permeability surface area coefficient; TmAb, trastuzumab.

Volumes A–E represent layer volumes for the disposition model. Volumes A2–E2 represent the starting tumor layer volumes for the tumor growth model for a tumor with a starting volume of 250 mm^3. VF, D2, P1, P2, IVD values and definitions are provided in ***Table 2****.*

treatment duration of 6-days. On the sixth day, media with 1 mg/ml 3-(4,5-dimethylthiazol-2-yl)-2,5-diphenyltetrazolium bromide (MTT) (Sigma, St. Louis, MO) was added to individual wells and incubated for 2 h. Subsequently, 100 ul of a 10% SDS 0.01 M HCl solution was added and incubated overnight to solubilize the formazan crystals. Following solubilization, plates were read at 550 nm to measure formazan dye with normalization at a wavelength of 690 nm using a SpectraMax 340PC plate reader (Molecular Devices, San Jose, CA). The viable cell fraction was determined by dividing the normalized absorbance for T-DM1 treated wells to untreated control wells on the same plate.

2.9 Sphere Pharmacokinetic Model Development

A pharmacokinetic model, previously used by our laboratory to predict the effect of anti-vascular endothelial growth factor (VEGF) therapy on topotecan tumor uptake (Shah et al., 2009), was adapted for predicting the impact competitive inhibition would have on trastuzumab and T-DM1 tumor disposition. Systemic concentrations of trastuzumab/T-DM1 and inhibitor were simulated with a 2-compartment model with tumor distribution modeled using a concentric sphere with five well-mixed sub-compartments of equal width (Sphere model). Previously observed plasma pharmacokinetics for trastuzumab and 1HE, in non-tumor bearing mice (Bordeau et al., 2021), were fit to a 2-compartment model using Adapt 5 (BMSR, Los Angeles, CA) (D'Argenio et al., 2009), assuming a mouse bodyweight of 25 g. Model fits for trastuzumab and 1HE are provided in **Supplementary Figures 1 and 2** and the fit parameter values and coefficient of variation percentages are provided in **Supplementary Table 1**. The tumor model represents mAb uptake and distribution from a single tumor blood vessel with an inter-vessel radius (IVR) of 75 μm (Baish et al., 1996; Thurber and Dane Wittrup, 2012). The center compartment of the tumor, layer A, is the point of extravasation for antibody through the vasculature into the tumor space. Upon entry, trastuzumab can bind HER2, diffuse to tumor layer B, or redistribute back into the plasma. Trastuzumab is modeled to enter tumor layers B-E *via* diffusion through connected sub-compartments. Several simplifying assumptions were made for this proof-of-concept investigation, including homogenous tumor antigen expression, no antigen shedding, and diffusion as the only transport mechanism for mAb through the interstitial space. Diffusion was considered to be the only transport mechanism within the tumor interstitial space as high tumor interstitial pressure, resulting from poor lymphatic drainage and high vasculature permeability, eliminates the pressure gradient that drives fluid to flow from the tumor vasculature to the lymphatic system (Jain and Baxter, 1988; Thurber et al., 2008) Tumor layer volume and surface area values were calculated based on the equations for a sphere, assuming a density of 1 g/ml, and can be found in **Table 1**. For calculating the individual layer volumes, the radius was equal to the width of the layer (15 μm) plus the width of any previous layers. For example the volume of layer C is equal to $4/3 \times \pi \times$

TABLE 2 | Experimentally determined PK/PD sphere model parameters.

Parameter		Value	Units	Source
T-DM1 clearance	CL1	1.0E-5	L/h	—
T-DM1 distribution clearance	CLd1	8.4E-5	L/h	—
T-DM1 central volume	V1	2.1E-3	L	—
T-DM1 peripheral volume	V2	2.2E-3	L	—
1HE clearance	CL2	1.9E-2	L/h	—
1HE distribution clearance	CLd2	5.2E-3	L/h	—
1HE central volume	V3	2.3E-3	L	—
1HE peripheral volume	V4	6.6E-3	L	—
T-DM1 deconjugation	CLdec	1.5E-5	L/h	Bender et al. (2014); Singh et al. (2016)
DM1 Conjugation Ratio	DAR	3.5	—	
kon 1HE:T-DM1	konl	0.89	$nM^{-1}\ h^{-1}$	Bordeau et al. (2021)
koff 1HE:T-DM1	koffl	0.04	h^{-1}	-
MAb diffusion	D1	4.7E-4 (1.7E-4)	cm^2/h	Berk et al. (1997); Netti et al. (2000); Pluen et al. (2001)
MAb Vasculature permeability	P1	1.0E-3 (4.3E-4)	cm/h	Yuan et al. (1995); Yuan et al. (1996); Dellian et al. (2000)
Vasculature permeability 1HE	P2	1.7E-3	cm/h	Yuan et al. (1995)
Tumor Vasculature Fraction	TVF	0.12 (0.04)	—	Vogel, (1965); Fallowfield, (1989); Baxter et al. (1994); Henderson et al. (2000); Chen et al. (2017)
Intervessel Radius	IVR	75	μm	Cilliers et al. (2016)
Hematocrit	Hct	0.45	—	Green, (1966)
Void Volume Fraction	VF	0.24	—	Schmidt and Wittrup, (2009)
kon Tmab:HER2	konA	2.6	$nM^{-1}\ h^{-1}$	Bostrom et al. (2011)
koff TmAb:HER2	koffA	1.3	h^{-1}	Bostrom et al. (2011)
kon DM1:tubulin	kond	0.018	$nM^{-1}\ h^{-1}$	Shah et al. (2012)
koff DM1:tubulin	koffd	0.55	1/h	Shah et al. (2012)
Cell Volume	—	5	pL	Erickson et al. (2012); Goldmacher et al. (2015)
DM1 Loss Rate	kloss	0.14	h^{-1}	Khera et al. (2018)
Tubulin Concentration	Tub	14,750	nM	Goldmacher et al. (2015)
HER2 internalization rate	kint	4.9E-2 (3.3E-2)	h^{-1}	Worthylake et al. (1999); Austin et al. (2004); Maass et al. (2016); Nessler et al. (2020)
HER2 Expression	—	1.5E6 (2.8E5)	Rec/cell	Hendriks et al. (2013); Onsum et al. (2013); Li et al. (2016)
HER2 tumor concentration	Ag0	2075	nM	—
Tumor growth rate	kgex	3E-3 (1E-3)	h^{-1}	—
Maximum kill rate constant	Kkill	0.014	h^{-1}	Menezes et al. (2020)
DM1 conc. for 50% of Kkill	Km	800	nM	Menezes et al. (2020)
Minimum conc. for killing	—	120	nM	Menezes et al. (2020)
RIT Clearance	—	1.3E-3	L/h	Bauss et al. (2016)
RIT Central Volume	—	9.8E-4	L	Bauss et al. (2016)
RIT Diffusion Rate	—	9.0E-5	cm^2/h	Chen et al. (2008)
RIT vascular permeability	—	1.8E-3	cm/h	Chen et al. (2008)

Abbreviations: kon, Association rate constant; koff, Dissociation rate constant.
DM1 = T-DM1 catabolites, e.g., lysine-mcc-DM1, conc., concentration; Rec, receptors; IVR, tumor inter-vessel radius.

$(45\ \mu m)^3$ minus the volume that is accounted for by layers A and B. Trastuzumab permeability, diffusion coefficients, HER2 tumor concentration, and internalization kinetics were obtained from the literature and are provided with references in **Table 2**. The diffusion coefficient for the inhibitor was calculated using the Stokes-Einstein equation, using the molecular radius of a sdAb (Bhunia et al., 2015), and the vascular permeability coefficient for the inhibitor was based on the permeability of a 25 kilodalton (kDa) antibody fragment (Yuan et al., 1995). The volume transfer rate constant between plasma and Layer A was calculated using the permeability surface area product, with tumor vasculature surface area per unit volume calculated using reported values for tumor blood volumes and the equations for a sphere. Diffusion clearance (CLd) between connected tumor layers was calculated using the equation CLd = D × SA/W where D is the diffusion coefficient, SA the surface area of a tumor layer, and W the width of a tumor layer. The interstitial volume of tumor layers A–E was calculated as the product of the void fraction times the total volume of each layer. To accurately capture target mediated disposition of mAb, plasma exchange with tumor was scaled from a single vessel, represented by the sphere model, to a whole tumor, using the ratio of the whole tumor volume/sphere tumor volume (TVs), as shown in differential equations CP1, CP2, CP3. The value of TVs is time-dependent and increases along with tumor growth. Bivalent trastuzumab binding to 1HE and HER2 was added to accurately capture the impact of 1HE on T-DM1 tumor distribution. Deconjugation clearance (CLdec) of T-DM1 to free trastuzumab was included to capture the decline in the drug antibody ratio (DAR) over time (Bender et al., 2014; Singh et al., 2016). A simplifying assumption was made that deconjugated trastuzumab does not bind free 1HE. To ensure the model was mass-balanced, simulations that included tumor growth included a loss term that was equal to the growth rate for each tumor equation, except for the equation for HER2. All simulations were conducted in Berkley-Madonna Version 9. All model parameters that were calculated can be found in **Table 1**, and model parameters that were obtained from in-house or previously reported experimental observations can be found in

Table 2. Model equations for the systemic pharmacokinetics of T-DM1, 1HE, and trastuzumab and the differential equations for tumor layer A are provided beneath the subsequent methods section. Differential equations for tumor layers B-E are identical in structure to A, apart from there being no antibody exchange with the vasculature and diffusion transport only occurring between connected sub-compartments.

2.10 T-DM1 Pharmacodynamic Model

A mechanism-based pharmacodynamic model was developed to consider tumor cell killing following T-DM1 internalization and degradation. DM1 metabolites transport out of the lysosome and out of the cell with a rate constant (kloss) reported by Khera et al. (2018). In the cell cytosol, DM1 metabolites can bind to tubulin or be effluxed from the cell. Tubulin DM1 binding rate constants were obtained from the report by Shah et al. which was used to characterize MMAE tubulin-binding (Shah et al., 2012); however, the ratio of the koff/kon values (30 nM) is close to the experimentally determined DM1-tubulin equilibrium dissociation constant (K_D: 11–31 nM) (Goldmacher et al., 2015; Menchon et al., 2018). The intracellular tubulin concentration was obtained from a report by Goldmacher et al. and is an average of four cancer cell lines (Goldmacher et al., 2015). A simplifying assumption was made that DM1 metabolites, which are charged and show poor membrane permeability, do not reflux back into cells. This assumption is consistent with a modeling analysis by Khera et al. that predicted rapid tumor clearance of DM1 metabolites following cellular efflux (Khera et al., 2018). Tubulin bound DM1 drives cell-killing which is modeled using a Hill function, with a maximum killing rate constant (Kkill), a half-maximum concentration (Km) and minimum tubulin bound DM1 concentration to achieve cell-killing of 120 nM as reported by Menzenes et al. (2020). The minimum concentration required for cell-killing was coded using a conditional if then statement with Kkill set to a value of 0 when intracellular DM1 concentrations are less than 120 nM. *In-vitro* cell or tumor growth was included in the model equations with growth causing dilution of bound ADC, or intracellular DM1 concentration. The growth dilution function was set to a value of 0 when the number of cells or tumor volume was less than its initial conditions to prevent artificial concentration of ADC/DM1. An *in vitro* model was developed and predictions for intracellular DM1 catabolites accumulation and ADC catabolism were compared to data reported by Erickson et al. (2012). Data were digitized using WebPlotDigitizer (Ankit Rohatgi, Pacifica, CA, United States, Version 4.5 https://automeris.io/WebPlotDigitizer). Model predictions for NCI-N87 growth and killing *in vitro* were made and compared to the results obtained from the *in vitro* NCI-N87 cell cytotoxicity experiments. Subsequently, the *in vitro* PD model was incorporated into the sphere PK model to predict NCI-N87 xenograft growth/killing following administration of T-DM1. The PK/PD sphere model has two tumor spaces, the first represents T-DM1 disposition around a single tumor vessel, and the second represents tumor growth and killing. The concentration of intracellular DM1 in individual layers of the disposition model drives the killing function in individual layers of the growth model. The initial volumes for each layer in the growth model is the product of the scaling factor (TVs) multiplied by the calculated volume for each layer that is provided in **Table 1**. Monte Carlo simulations (n = 1,000) with variability on the tumor growth rate (mean: 0.003 h^{-1}, SD: 0.001 h^{-1}, range 0.006–0.00125 h^{-1}) and on the initial tumor volume (mean: 250–310 mm^3, SD: 44 mm^3, range = 200–400 mm^3) were completed to predict NCI-N87 tumor volumes at the indicated dosing conditions. Model equations for the pharmacodynamic component of layer A are provided below (CTA12-CTA13, A1).

2.11 Systemic Pharmacokinetics

CP1: Central Compartment Concentration of free T-DM1

$$\frac{dCP1}{dt} = \frac{Cld}{V1} \times (CT1 - CP1) - \frac{Cl1}{V1} \times CP1 - \frac{CLdec}{V1} \times CP1 + TVs \frac{PSpa}{V1} \times (1 - Hct) \times (CTA1 - CP1) + koffI \times CP2 - konI \times CP1 \times CP4 \times \frac{V3}{V1}$$

CT1: Peripheral Compartment Concentration of Free T-DM1

$$\frac{dCT1}{dt} = \frac{Cld}{V2} \times (CP1 - CT1) + koffI \times CT2 - konI \times CT1 \times CT4 \times \frac{V4}{V2}$$

CP2: Central Compartment Concentration of TDM1-1HE

$$\frac{dCP2}{dt} = \frac{Cld}{V1} \times (CT2 - CP2) - \frac{Cl1}{V1} \times CP2 - \frac{CLdec}{V1} \times CP2 + TVs \times \frac{PSpa}{V1} \times (1 - Hct) \times (CTA2 - CP2) - koffI \times CP2 + koffI \times CP3 + konI \times CP1 \times CP4 \times \frac{V3}{V1} - konI \times CP2 \times CP4 \times \frac{V3}{V1}$$

CT2: Peripheral Compartment Concentration of TDM1-1HE

$$\frac{dCT2}{dt} = \frac{Cld}{V2} \times (CP2 - CT2) - koffI \times CT2 + koffI \times CT3 + konI \times CT1 \times CT4 \times \frac{V4}{V2} - konI \times CT2 \times CT4 \times \frac{V4}{V2}$$

CP3: Central Compartment Concentration of TDM1-(1HE)2

$$\frac{dCP3}{dt} = \frac{Cld}{V1} \times (CT3 - CP3) - \frac{Cl1}{V1} \times CP3 - \frac{CLdec}{V1} \times CP3 + TVs\frac{PSpa}{V1} \times (1 - Hct) \times (CTA3 - CP3) - koffI \times CP3 + konI \times CP2 \times CP4 \times \frac{V3}{V1}$$

CT3: Peripheral Compartment Concentration of TDM1-(1HE)2

$$\frac{dCT3}{dt} = \frac{Cld}{V2} \times (CP3 - CT3) - koffI \times CT3 + konI \times CT2 \times CT4 \times \frac{V4}{V2}$$

CP4: Central Compartment Concentration of free 1HE

$$\frac{dCP4}{dt} = \frac{Cld2}{V3} \times (CT4 - CP4) - \frac{Cl2}{V3} \times CP4 + TVs\frac{PSpa2}{V3} \times (1 - Hct) \times (CTA4 - CP4) + koffI \times CP2 \times \frac{V1}{V3} + koffI \times CP3 \times \frac{V1}{V3} - konI \times CP1 \times CP4 \times \frac{V1}{V3} - konI \times CP2 \times CP4 \times \frac{V1}{V3}$$

CT4: Peripheral Compartment Concentration of free 1HE

$$\frac{dCT4}{dt} = \frac{Cld2}{V4} \times (CP4 - CT4) + koffI \times CT2 \times \frac{V2}{V4} + koffI \times CT3 \times \frac{V2}{V4} - konI \times CT1 \times CT4 \times \frac{V2}{V4} - konI \times CT2 \times CT4 \times \frac{V2}{V4}$$

CP5: Central Compartment Concentration of Trastuzumab

$$\frac{dCP5}{dt} = \frac{Cld}{V1} \times (CT5 - CP5) - \frac{Cl1}{V1} \times CP5 + \frac{CLdec}{V1} \times CP1 + \frac{CLdec}{V1} \times CP2 + \frac{CLdec}{V1} \times CP3 + TVs\frac{PSpa}{V1} \times (1 - Hct) \times (CTA - CP5)$$

CT5: Peripheral Compartment Concentration of Trastuzumab

$$\frac{dCT5}{dt} = \frac{Cld}{V2} \times (CP5 - CT5)$$

2.12 Tumor Layer A

CTA1: Concentration of free TDM1 in Layer A

$$\frac{dCTA1}{dt} = \frac{PSpa}{VaVF} \times (1 - Hct) \times (CP1 - CTA1) + CTA2 \times koffI - konI \times CTA1 \times CTA4 - konA \times CTA1 \times CTA6 + koffA \times CTA7 - \frac{CldAB}{VaVF} \times (CTA1 - CTB1)$$

CTA2: Concentration of free TDM1-1HE in Layer A

$$\frac{dCTA2}{dt} = \frac{PSpa}{VaVF} \times (1 - Hct) \times (CP2 - CTA2) - CTA2 \times koffI + CTA3 \times koffI + konI \times CTA1 \times CTA4 - konI \times CTA2 \times CTA4 - konA \times CTA2 \times CTA6 + koffA \times CTA9 - \frac{CldAB}{VaVF} \times (CTA2 - CTB2)$$

CTA3: Concentration of free TDM1-(1HE2) in Layer A

$$\frac{dCTA3}{dt} = \frac{PSpa}{VaVF} \times (1 - Hct) \times (CP3 - CTA3) - CTA3 \times koffI + konI \times CTA2 \times CTA4 - \frac{CldAB}{VaVF} \times (CTA3 - CTB3)$$

CTA4: Concentration of free 1HE in Layer A

$$\frac{dCTA4}{dt} = \frac{PSpa2}{VaVF} \times (1 - Hct) \times (CP4 - CTA4) + CTA2 \times koffI + CTA3 \times koffI + koffI \times CTA9 - konI \times CTA1 \times CTA4 - konI \times CTA2 \times CTA4 - konI \times CTA7 \times CTA4 - \frac{CldAB2}{VaVF} \times (CTA4 - CTB4)$$

CTA5: Concentration of free trastuzumab in Layer A

$$\frac{dCTA5}{dt} = \frac{PSpa}{VaVF} \times (1 - Hct) \times (CP5 - CTA5) - konA \times CTA5 \times CTA6 + koffA \times CTA10 - \frac{CldAB}{VaVF} \times (CTA5 - CTB5)$$

CTA6: Concentration of free HER2 in Layer A

$$\frac{dCTA6}{dt} = ksyn - kint \times CTA6 - konA \times CTA6 \times CTA1 - konA \times CTA6 \times CTA2 - konA \times CTA6 \times CTA5 - konA \times CTA7 \times CTA6 - konA \times CTA10 \times CTA6 + koffA \times CTA7 + koffA \times CTA8 + koffA \times CTA9 + koffA \times CTA10 + koffA \times CTA11$$

CTA7: Concentration of TDM1-HER2 in Layer A

$$\frac{dCTA7}{dt} = -kint \times CTA7 + konA \times CTA6 \times CTA1 - konA \times CTA6 \times CTA7 - konI \times CTA7 \times CTA4 - koffA \times CTA7 + koffA \times CTA8 + koffI \times CTA9$$

CTA8: Concentration of TDM1-(HER2)2 in Layer A

$$\frac{dCTA8}{dt} = -kint \times CTA8 + konA \times CTA6 \times CTA7 - koffA \times CTA8$$

CTA9: Concentration of TDM1:1HE-HER2 in Layer A

$$\frac{dCTA9}{dt} = -kint \times CTA9 + konA \times CTA6 \times CTA2 + konI \times CTA7 \times CTA4 - koffA \times CTA9 - koffI \times CTA9$$

CTA10: Concentration of Trastuzumab-HER2 in Layer A

$$\frac{dCTA10}{dt} = -kint \times CTA10 + konA \times CTA6 \times CTA5 - konA \times CTA10 \times CTA6 - koffA \times CTA10 + koffA \times CTA11$$

CTA11: Concentration of Trastuzumab-(HER2)2 in Layer A

$$\frac{dCTA11}{dt} = -kint \times CTA11 + konA \times CTA6 \times CTA10 - koffA \times CTA11$$

CTA12: Concentration of intracellular T-DM1 in Layer A

$$\frac{dCTA12}{dt} = kint \times \left(\frac{VF}{1-VF}\right) \times (CTA7 + CTA8 + CTA9) - kloss \times CTA12$$

CTA13: Concentration of intracellular DM1 in Layer A

$$\frac{dCTA13}{dt} = kloss \times CTA12 \times DAR - kloss \times CTA13 - konD \times CTA13 \times (Tub - CTA14) + koffD \times CTA14$$

CTA14: Concentration of Tubulin bound DM1 in Layer A

$$\frac{dCTA14}{dt} = konD \times CTA13 \times (Tub - CTA14) - koffD \times CTA14$$

A1: Volume of Tumor layer A

$$\frac{dA1}{dt} = kgex \times A1 - A1 \times \frac{kkill \times (CTA14)}{Km + (CTA14)}$$

Initial Conditions CTA6 = Ag0, A1 = Va×TVs, All other differential equations initial conditions = 0.

3 RESULTS

3.1 1HE Mutants

Following panning, 96 colonies from the low-affinity panning and 88 colonies from the high-affinity panning were screened using ELISA to estimate the half-life of trastuzumab binding for each colony. ELISA results were used to select individual colonies over a range of trastuzumab binding half-lives for DNA sequencing. All the sequenced colonies had at least one mutation from the parent sequence of 1HE. Two mutation "hot-spots" were observed for both the low and high-affinity mutants from the parent DNA. Five of the 11 low-affinity mutants had mutations in the center of complementary determining region two (CDR2), with four having mutations at aspartate 56 (D56). Of the thirteen sequenced colonies from the high-affinity panning, four shared an identical mutation of threonine 103 to alanine (T103A) in CDR3. None of the four colonies with the shared T103A mutations had identical sequences, indicating the mutants originated from different parent phages. Three low-affinity and four high-affinity mutants were selected to estimate the dissociation rate constant from trastuzumab using the covalent ELISA method described in the methods section. Dissociation curves and monoexponential decline fittings for individual clones are shown in **Figure 1**, with clones from the high affinity panning starting with the letter H and clones from the low affinity panning starting with the letter L. Best-fit dissociation rate constants (koff) and estimated half-lives of trastuzumab binding (determined as the quotient of 0.693/koff) are provided in the inset of **Figure 1**. LG11 with mutations of G10D, S31G, D56V had the fastest dissociation rate with a trastuzumab binding half-life of 1.1 h. HE10 with the mutations L18Q and T103A had the slowest dissociation rate with an estimated trastuzumab binding half-life of 107.9 h. The monoexponential decay function reasonably captured the decline in ELISA signal across timepoints for the mutants. Several early timepoints deviate from the fitting which may be attributed to heterogeneity in either the immobilized trastuzumab (i.e., partially occluded binding sites) or the expressed and purified 1HE mutants (e.g., due to partial degradation, etc.). The present results are consistent with assessments of 1HE and trastuzumab binding and dissociation, as measured by ELISA and surface plasmon resonance, in our prior work (Bordeau et al., 2021). The estimated binding half-life of 1HE for trastuzumab using the covalent ELISA method was 15.5 h, which is close to the value of 12.2 h that was determined using a radiolabeled dissociation method described previously (Bordeau et al., 2021). The covalent ELISA method provides a relative affinity ranking of the 1HE mutants, and further characterization to ensure the accuracy of the estimated dissociation rate and to evaluate potential changes in the trastuzumab association rate constant may be pursued using surface plasmon resonance binding analysis.

3.2 Trastuzumab Tumor Uptake

To evaluate if the sphere model structure and parameters accurately characterized total antibody uptake, 1,000 Monte Carlo simulations were completed to predict trastuzumab tumor concentrations following a 1 mg/kg intravenous dose. A schematic representation of the major components of the model is provided in **Figure 2**. Parameter variability was included on the antibody tumor vasculature permeability rate (mean: 0.001 cm h^{-1}, SD: 0.00043 cm h^{-1}, range 0.002–0.005 cm h^{-1}), tumor blood volume fraction (mean: 0.12, SD: 0.04, range 0.07–0.2), antibody

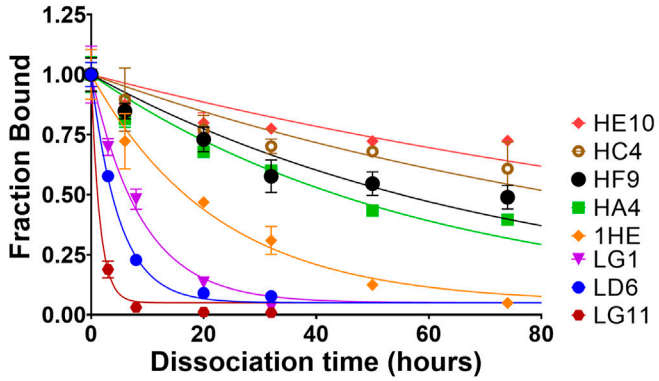

1HE Mutants Dissociation Rates

Mutant	Point mutation	koff (HR^{-1})	$T_{1/2}$ (HR)
LG11	G10D, S31G, D56V	6.5E-1	1.1
LD6	D56N	2.0E-1	3.5
LG1	N54D, D56G	1.1E-1	6.2
1HE	WT	4.5E-2	15.5
HA4	T58A	1.7E-2	40.6
HF9	D105E	1.4E-2	51.1
HC4	T103A, Q117L	8.9E-03	78.3
HE10	L18Q, T103A	6.4E-03	107.9

FIGURE 1 | 1HE Mutant Trastuzumab Dissociation Rates. (Top left) Plotted is the fractional change in absorbance over time for 1HE mutants that are bound to trastuzumab that is covalently linked to wells of an ELISA plate. Points represent the mean of samples in triplicate with standard deviation error bars. Lines represent the best-fit monoexponential decay for individual mutants. The estimated dissociation rate (koff), the corresponding dissociation half-life and the point mutations relative to wildtype (WT) 1HE for each mutant are provided in the top right inset.

diffusion rate (mean: 0.00047 cm^2 h^{-1}, SD: 0.00017 cm^2 h^{-1}, range 0.0003–0.0007 cm^2 h^{-1}), HER2 antigens per cell (mean: 1.5E6, SD: 2.8E5) and HER2 internalization/degradation rate (mean: 0.049 h^{-1}, SD: 0.033 h^{-1}, range 0.027–0.12 h^{-1}). Our laboratory previously characterized trastuzumab uptake in nude mice bearing HER2+ xenografts of the human ovarian cancer cell line SKOV3 following a 1 mg/kg dose (Abuqayyas and Balthasar, 2012), and this data was used to evaluate model prediction accuracy. The model output for trastuzumab tumor concentration was the sum of both free and HER2 bound trastuzumab in each layer multiplied by the volume of the corresponding layer divided by the total volume of all tumor layers. The median of the Monte Carlo simulations reasonably captured the observed trastuzumab tumor concentration-time profile with a trend for overprediction; however, all observed concentrations fell within the simulation range (**Figure 3**).

3.3 Simulations Predicting the Effect of Co-Administered 1HE on Within-Tumor Distribution of T-DM1

Figures 4A,B show the sphere model predicted concentrations of T-DM1 bound to HER2, in each tumor layer, following T-DM1 administration alone (**Figure 4A**) or T-DM1 administrated in complex with 1HE (**Figure 4B**). T-DM1 administered alone leads to maximum concentrations of 246, 216, 88, 11, and 1 nM for tumor layers A-E. T-DM1 administered with 1HE results in maximum concentrations of 160, 119, 32, 12, and 8 nM for tumor layers A-E. Qualitatively, the simulation values are similar to our published experimental observations, where we observed a several-fold increase in trastuzumab fluorescence with 1HE co-administration starting ~50 µm from the tumor vasculature (Bordeau et al., 2021). Due to the limitations of fluorescence imaging, a direct quantitative comparison of the simulated data to our prior fluorescence imaging data is limited. **Figure 4C** provides the cumulative total percent of T-DM1 delivered per gram of each tumor layer, which is the percent of T-DM1 eliminated by HER2 internalization in a tumor layer divided by the tumor layer volume in ml. The percent of the injected dose/gram (%ID/G) values for T-DM1/T-DM1:1HE respectively are Layer A: 1,615.4/1,479.2, Layer B: 828.7/673.1, Layer C: 224.0/143.1, Layer D: 27.1/33.4, Layer E: 3.2/18.2, whole tumor: 102.9/90.0. A sensitivity analysis was completed to determine parameters leading to the most significant change in the quotient of T-DM1 delivered to layer E with/without 1HE co-administration (**Figure 4D**). When adjusted by 10%, parameters representing the tumor tumor inter-vessel radius (IVR), tumor antigen concentration, mAb diffusion rate constant, and mAb association rate constant (kon) led to the largest changes in layer E exposure to T-DM1.

3.4 Impact of Inhibitor Dissociation Half-Life on T-DM1 Tumor Distribution

Monte Carlo simulations (n = 1,000) were completed across a range of inhibitor dissociation half-lives. Parameter variability was identical to the trastuzumab tumor uptake simulations. **Figure 5** shows the cumulative %ID/G of T-DM1 delivered for layers A-E (total tumor uptake) and layer E alone. The total tumor uptake of T-DM1 is negligibly changed by competitive inhibitors with a binding half-life up to ~10 h, whereas inhibitors with a trastuzumab binding half-life >20 h decrease total tumor uptake by >15%. The median value of total T-DM1 delivered to layer E increases by more than 50% at inhibitor half-lives ≥1 h and reaches a maximum increase of 770% at a half-life of 69.3 h.

3.5 *In-Vitro* T-DM1 Efficacy Simulations

The T-DM1 efficacy model, which makes considerations for DM1-tubulin binding and target cell killing was compared to *in vitro* data to evaluate model accuracy. A schematic of the model structure is provided in **Figure 6A**. To validate model parameters for T-DM1 metabolism, DM1-tubulin binding, and DM1 cellular efflux, simulated profiles for ADC catabolism and intracellular DM1 concentrations were compared to digitized

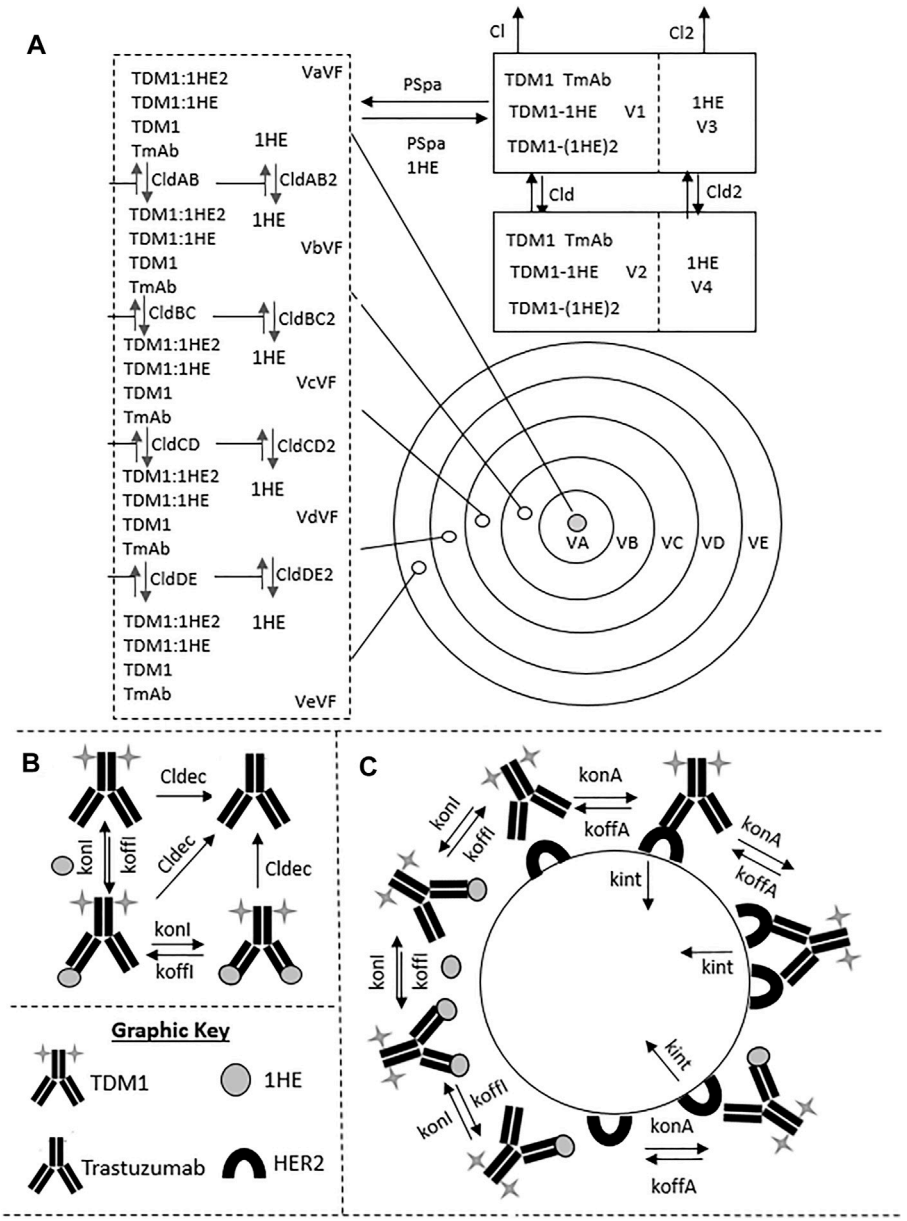

FIGURE 2 | Pharmacokinetic Sphere Model Structure. A graphic representation of the sphere model structure is shown. Panel **(A)** shows the distribution processes of T-DM1, T-DM1:1HE, T-DM1:(1HE)2, 1HE, and Trastuzumab. T-DM1, T-DM1:1HE, T-DM1:(1HE)2, and trastuzumab share distribution parameters from the central and peripheral compartments and share transport rates into and out of the tumor space. Unbound 1HE has unique distribution, clearance, and tumor uptake parameters. Panel **(B)** shows the binding processes between T-DM1 and 1HE that occur within the two-compartment model that represents the systemic disposition of mAb. Shown in section **(B)** is the deconjugation clearance of T-DM1 to free trastuzumab. Panel **(C)** represents the binding processes occurring within each individual tumor layer. Free arms of T-DM1 or T-DM1:1HE can bind free cellular HER2 and can either dissociate or be internalized into the cell layer. Deconjugated trastuzumab can also bind HER2 in each tumor layer but is not explicitly shown due to space limitations. Parameter definitions and values are provided in **Tables 1** and **2**.

data reported by Erickson et al. (2012). The simulations captured the observed profiles for DM1 metabolite accumulation (**Figure 6B**) and percent ADC catabolized (**Figure 6C**) reasonably well, with a slight overprediction of the DM1 metabolites between 3 and 8 h and an underprediction of the percent of the ADC catabolized. These contradictory results may be due to an unaccounted-for intermediate product (i.e., partially catabolized ADC) that was not included in the model, or not detected by the original authors HPLC assay (Erickson et al., 2012). Target cell killing is included in the model and is driven by a Hill function that is dependent on the concentration of DM1 that is bound to intracellular tubulin. The T-DM1 specific parameter values for Kkill and Km were previously reported by Menezes et al. (2020) and were evaluated in our model structure by comparing predictions that were made using these values and experimental data for NCI-N87 cell

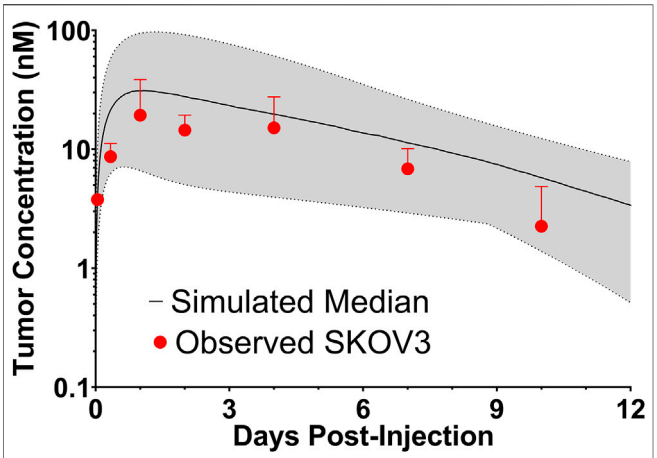

FIGURE 3 | Observed and Sphere Model Predicted Tumor Concentrations. Shown is the median (solid black line) and range (gray shaded region) of 1,000 Monte Carlo simulations for total trastuzumab uptake in HER2+ xenografts following a 1 mg/kg IV bolus. In red is the observed uptake of trastuzumab in SKOV3 xenografts following IV injection of trastuzumab with a tracer dose of ^{125}I-trastuzumab. Individual timepoints represent the mean of three xenografts with a standard deviation error bar.

growth and killing following T-DM1 treatment. Model simulations for the fraction of viable cells, which is equal to the quotient of the number of cells with T-DM1 treatment divided by the number of cells without treatment, overlaid well with the observed NCI-N87 cytotoxicity data (**Figure 6D**), supporting the use of these parameter values despite the differences between the model structure that is used here in comparison to the model structure used by Menezes et al. (2020).

3.6 *In-Vivo* T-DM1 Efficacy Simulations

Simulations to predict NCI-N87 xenograft tumor volume over time and the median time for tumors to reach a volume of 1,200 mm^3 (survival time) following an intravenous dose of PBS, 10 mg/kg trastuzumab, 1.8 mg/kg TDM1, and 1.8 mg/kg T-DM1:1HE were completed and compared to our previously observed data (Bordeau et al., 2021). As each tumor layer has unique growth/killing equations the total tumor volume was equal to the sum of the individual simulated tumor layer volumes. 1,000 Monte Carlo simulations with variability on the tumor growth rate (mean: 0.003 h^{-1}, SD: 0.001 h^{-1}, range 0.006–0.00125 h^{-1}) and initial tumor volume (mean: 250–310 mm^3, SD: 44 mm^3, range = 200–400 mm^3) were completed for each dose condition. The mean tumor volume for each dose group was set to the observed mean for the individual groups (PBS control: 255 mm^3, Trastuzumab: 288 mm^3, TDM1: 312 mm^3, TDM1:1HE: 309 mm^3). Simulation results and observed tumor volumes over time are plotted in **Figure 7**. Both the PBS and 10 mg/kg trastuzumab simulations accurately captured the observed data, with several of the observed tumor volumes exceeding the 75% quartile at early time points. The median predicted survival time for PBS and trastuzumab was 21 and 20 days, respectively, and the observed median survival time was 22 and 18 days. The predicted 1.8 mg/kg T-DM1 and T-DM1:1HE tumor profiles were well captured, except for several xenografts in the 1.8 mg/kg dose group growing faster than the simulation prediction. The model predicts a greater tumor volume regression for T-DM1 treated tumors approximately 10 days after injection and approximately 15–20 days following T-DM1:1HE administration; however, the median tumor volumes following tumor regression are accurately captured. The simulated median survival time is 29 days for 1.8 mg/kg T-DM1 and 40 days for 1.8 mg/kg T-DM1:1HE, close to the observed times of 29 and 42 days for T-DM1 and T-DM1:1HE, respectively. To predict if any of the 1HE mutants would further enhance T-DM1 efficacy, simulations were completed, without growth variability, using the mutant-specific dissociation rate constants provided in **Figure 1**. Mutants HA4 and HF9 with trastuzumab binding half-lives of 40.6 and 51.1 h are predicted to modestly increase T-DM1 efficacy, with extensions in the simulated median survival time from 39 days for T-DM1:1HE to 42 days for T-DM1:HA4 or HF9 (**Figure 8**).

3.7 Immunotoxin Simulations

To explore the use of competitive inhibitors for optimizing the within-tumor distribution of immunotoxins, the sphere model was modified with previously reported pharmacokinetic parameters for a recombinant immunotoxin (RIT) (Bauss et al., 2016). Recombinant immunotoxins commonly utilize antibody fragments to target protein toxins, such as pseudomonas exotoxin, to cancer cells (Pastan et al., 2006). Antibody fragments lack the Fc domain of intact antibodies and as a result, have dramatically altered plasma pharmacokinetic profiles. Notably, the clearance value that was used for the RIT is ~100× greater than the clearance rate that was used for T-DM1. Tumor distribution of a theoretical trastuzumab-based RIT was simulated at a dose of 140 μg/kg, which is the maximum tolerated dose for an anti-mesothelin RIT that is currently being evaluated in clinical trials (Hassan et al., 2020). Prior work has demonstrated that a threshold of ~1,000 RITs bound per cell is required for cell killing (Kreitman and Pastan, 1998). **Figure 9A** shows the simulated number of HER2 antigens that are bound by RIT per cell for each layer of the sphere model when RIT is administered alone. Layers A and B exceed the therapeutic threshold, whereas layers C, D and E (representing 93.6% of the total tumor volume) are below the threshold. As a result of the rapid systemic clearance of RIT, co-administration of a high-affinity inhibitor with an inhibition half-life that is much greater than the plasma half-life of RIT would decrease total tumor uptake of RIT, similar to the results observed for T-DM1 in **Figure 5**. Therefore, we simulated the impact of the fastest dissociating 1HE mutant (LG11) with a binding half-life of 1.1 h (**Figure 9B**). LG11 co-administration is predicted to increase the number of RITs bound per cell in all tumor layers above the threshold, with layer E predicted to achieve a maximum of ~1,200 RITs/cell.

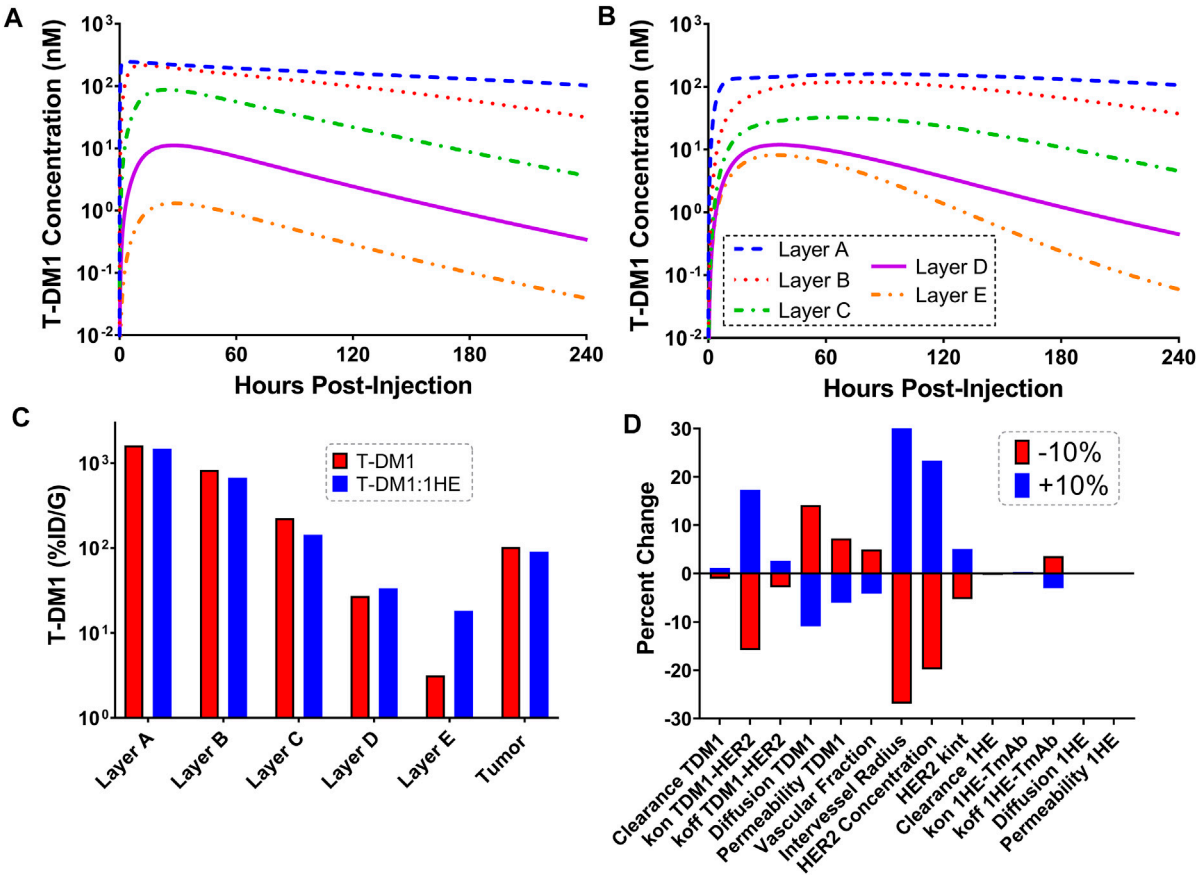

FIGURE 4 | Simulated T-DM1 Distribution with and without 1HE Co-administration. Shown are sphere model simulations for the concentration of T-DM1 bound to HER2 antigen in individual tumor layers over time for T-DM1 administered alone **(A)** or for T-DM1 that is co-administered with 1HE **(B)**. **(C)** Shown is the percent of T-DM1 that is internalized per gram of tumor tissue for each tumor layer with and without 1HE co-administration. **(D)** Sensitivity analysis indicates that the percent of T-DM1 that is internalized in layer E when mAb is administered with 1HE/without 1HE is most sensitive to the intervessel radius, tumor antigen concentration, mAb association rate constant (mAb kon), and mAb diffusion rate constant.

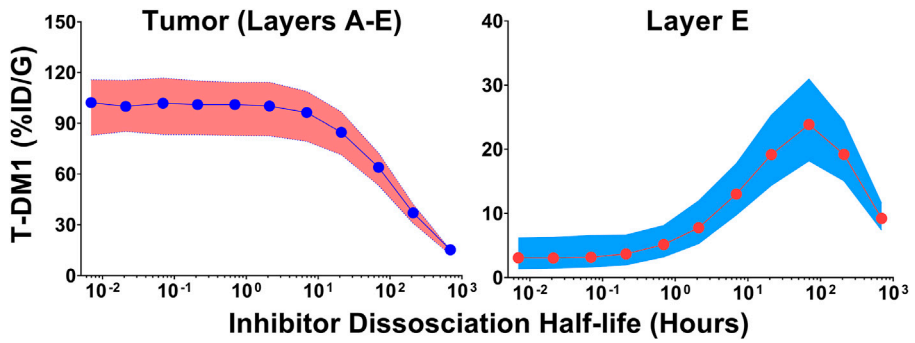

FIGURE 5 | Impact of Inhibitor Binding Half-life on T-DM1 Tumor Distribution. The total percent of T-DM1 that binds to HER2 and is internalized over time, for all tumor layers or for layer E alone, as a function of a co-administered inhibitors half-life is shown. Points represent the median of 1,000 Monte Carlo simulations with the shaded regions representing the first and third quartile of the simulations.

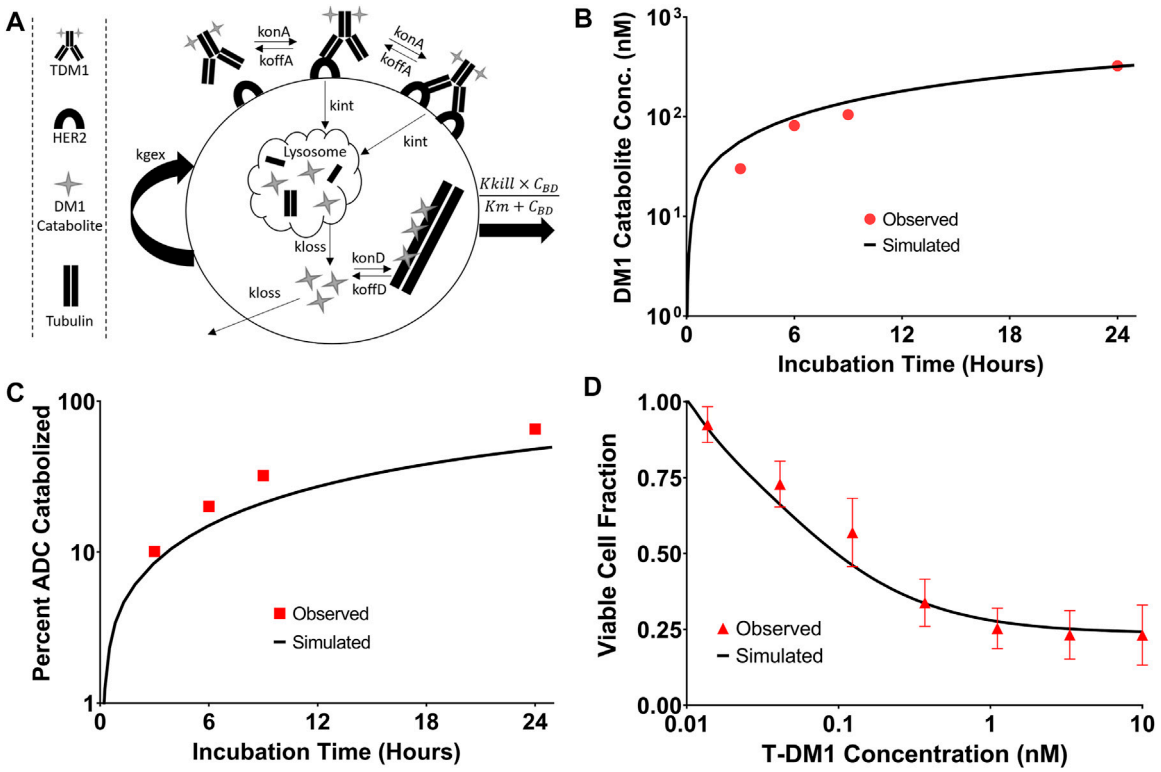

FIGURE 6 | T-DM1 Pharmacodynamic Model: **(A)** A graphic representation of model additions to capture T-DM1 cell killing is provided. Following internalization DM1 catabolites enter the cytosol from the lysosome and either bind to tubulin or are eliminated from the cell. DM1 bound tubulin drives the cell killing hill function. **(B)** represents the *in vitro* model simulations (solid black lines) for accumulation of DM1 catabolites in BT474EEI cells following a 24-hour incubation with T-DM1 in comparison to the data observed by Erickson et al. in red. **(C)** Demonstrates the simulations for the percent of T-DM1 catabolized over time in comparison to the data observed by Erickson et al. **(D)** Model simulations for the fraction of viable NCI-N87 cells treated with T-DM1 in comparison to an untreated control. Red points represent the mean of three assays with standard deviation error bars.

4 DISCUSSION

In the present work, error-prone PCR and phage display were used to develop and isolate variants of 1HE with trastuzumab dissociation rate constants between 0.0064 and 0.65 h^{-1}. The 1HE mutants may be used in strategies to bypass the binding site barrier, enabling improved tumor distribution for a range of trastuzumab-based constructs, and enabling translation of our competitive inhibition strategy beyond pre-clinical animal models. To guide the selection of an optimum inhibitor, simulations were conducted with representation of a solid tumor as a collection of concentric spheres of five sub-compartments. Antibody extravasation within tumors was defined to occur at a peri-vascular site (represented by Layer A in the model), and mAb could then diffuse to distant sites as represented by Layers B-E. Many similar models have been utilized in the past to characterize mAb uptake and penetration into tumors. Jain and Baxter used a spherical model structure to explore the impact of elevated interstitial fluid pressure (IFP) on mAb tumor distribution (Jain and Baxter, 1988). Jain and Baxter predicted that the high IFP in the center of solid tumors restricts mAb extravasation; therefore, most mAb enters the tumor from vessels in the periphery where IFP is lower. As a result, mAb needs to diffuse larger distances than the inter-vessel diameter, which may take many hours or several days (Jain and Baxter, 1988). Fujimori et al. used a sphere model with a well-vascularized outer shell to predict mAb penetration from the outer layer to the tumor core as a function of mAb affinity (Fujimori et al., 1990). This seminal work led to the prediction of the existence of a binding site barrier that limits high-affinity mAb distribution in solid tumors (Fujimori et al., 1990). Significant contributions to the understanding of factors that contribute to the heterogeneous distribution of mAb in solid tumors have been made through a series of publications by the Wittrup group (Graff and Wittrup, 2003; Thurber et al., 2007; Thurber et al., 2008; Thurber and Wittrup, 2008; Schmidt and Wittrup, 2009; Rhoden and Wittrup, 2012; Thurber and Dane Wittrup, 2012). Mathematical predictions combined with experimental studies led to the proposal of two criteria to predict mAb tumor distribution: the clearance modulus and the Thiele modulus (Graff and Wittrup, 2003; Thurber et al., 2008; Thurber and Wittrup, 2008). The clearance modulus is the ratio of the time to saturate tumor antigen to the plasma clearance time (Thurber et al., 2008). The time to saturate tumor antigen, for a high-affinity mAb, is a function of the diffusion rate (or when vessel permeability is rate-limiting, the extravasation rate), inter-vessel radius, and tumor antigen concentration (Thurber et al., 2008). The clearance time is the weighted

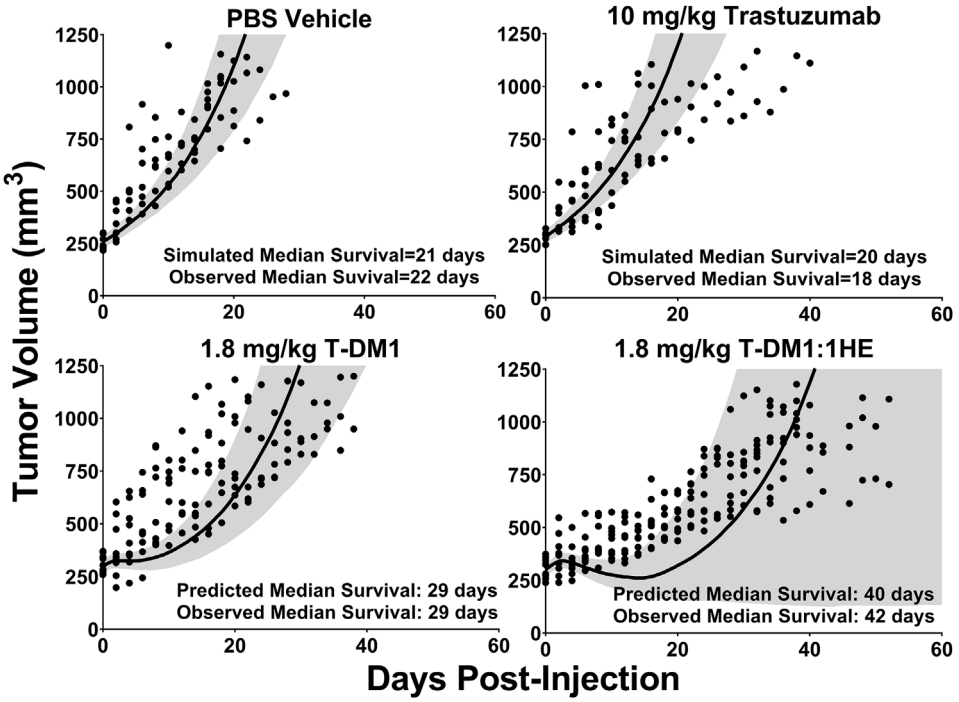

FIGURE 7 | Observed and Predicted Tumor Volumes after a 1.8 mg/kg T-DM1 Dose. PK/PD Model Predictions for the tumor volume of NCI-N87 xenografts over time following a single dose of PBS, 10 mg/kg trastuzumab, 1.8 mg/kg T-DM1, and 1.8 mg/kg T-DM1:1HE. Solid black lines represent the median tumor volume of 1,000 simulations, and the shaded area represents the first and third quartiles. Solid circles represent an individual tumor volume measurement for a single xenograft at one timepoint.

average half-life of mAb in the plasma (Thurber et al., 2008). The Thiele modulus makes considerations for target-mediated elimination and is the ratio of the time to saturate antigen to the characteristic time of endocytosis (Thurber et al., 2008). mAbs have slow clearance rates, conducive to antigen saturation; however, penetration is significantly hampered by target mediated elimination, with receptor turnover allowing peri-vasculature cells to consume a significant fraction of mAbs that enter the tumor. The sensitivity analysis of the sphere model (**Figure 4D**) predicts that T-DM1 penetration to layer E is most influenced by inter-vessel distance, tumor antigen expression, antibody diffusion rate, and trastuzumab-HER2 association rate. These results are consistent with expectations based on intuition. The intervessel distance and mAb diffusion rate are determinants of the length of time required for T-DM1 to traverse the intervessel distance. The HER2 concentration and trastuzumab-HER2 association rate constant determine the length of time T-DM1 can diffuse prior to binding HER2. As mAb-antigen binding is a second order process, the interstitial concentration of mAb will also impact the penetration distance. **Figure 3** demonstrates that the sphere model accurately characterizes total trastuzumab SKOV3 xenograft tumor concentrations using parameter values obtained across many different xenografts and HER2+ cell-lines. Further improvements in model predictions may be obtained through consideration of cell-line specific HER2 expression/internalization rate and cell-line specific xenograft physiology (e.g., vascularity). Additionally, for some mAbs, the rate of antigen dissociation can significantly impact tumor penetration, as rapidly dissociating mAbs have several chances to diffuse through the tumor interstitial space prior to target mediated elimination. For trastuzumab, sphere model predictions are relatively insensitive to the HER2 dissociation rate constant, indicating that upon binding, a large fraction of HER2 bound trastuzumab is internalized and degraded prior to dissociation.

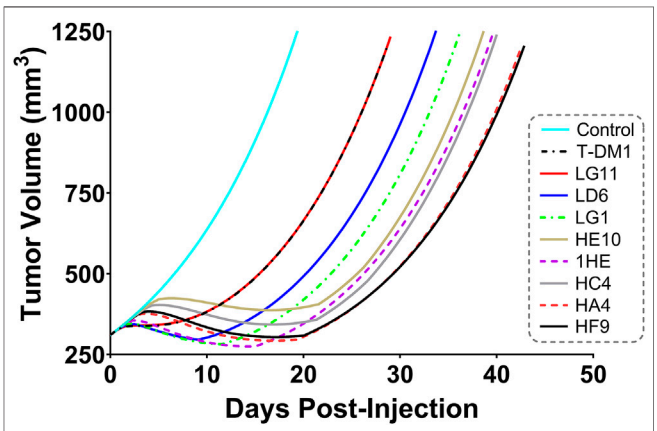

FIGURE 8 | Predicted Impact of 1HE Mutants on T-DM1 Efficacy. PK/PD model predictions for the impact of the 1HE mutants characterized in **Figure 1** on T-DM1 efficacy in NCI-N87 xenografts following a single 1.8 mg/kg dose of T-DM1.

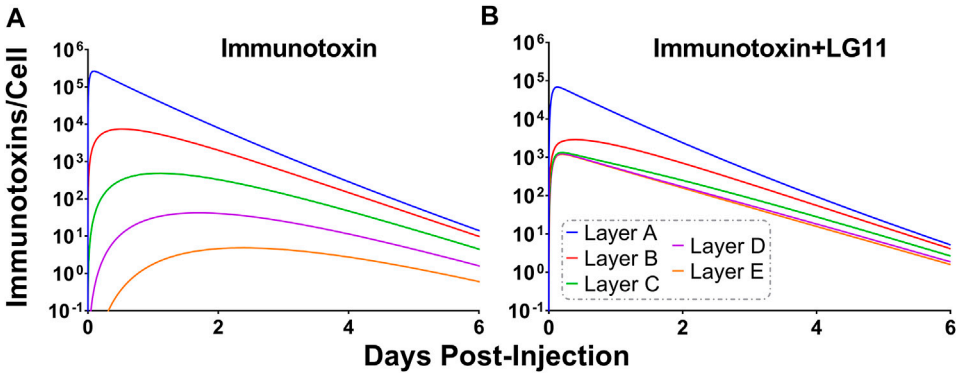

FIGURE 9 | Impact of LG11 on Immunotoxin Tumor Distribution. **(A)** Simulations considering immunotoxin specific pharmacokinetic parameters demonstrate limited tumor penetration following a 0.14 mg/kg dose. Tumor layers C, D, and E are below the 1,000 antigens/cell threshold necessary for tumor cell killing **(B)** Co-administration of immunotoxin with the LG11 mutant (1.1 h trastuzumab binding half-life) results in all tumor layers exceeding 1,000 antigens/cell.

The initial sphere model simulations were performed to identify an inhibitor dissociation half-life that would improve tumor distribution without significantly impacting the total tumor uptake of T-DM1. The dissociation half-life was considered the prime metric, as the competitive inhibition strategy may be most conveniently applied in the circumstance where the inhibitor can be administered with ADC on the same dosing schedule (i.e., same dosing frequency). Upon administration, inhibitor-bound ADC needs to extravasate and diffuse throughout the tumor tissue prior to inhibitor dissociation. Low-affinity inhibitors, with rapid dissociation rates, do not provide an inhibition window long enough for ADCs to extravasate and diffuse throughout the tumor interstitial space. Conversely, for slowly dissociating inhibitors, the inhibition window can be too long, leading to a significant fraction of ADC being eliminated in complex with an inhibitor, decreasing total tumor uptake. Based on model predictions, inhibitors with a binding half-life between 10 and 70 h (**Figure 5**) can increase Layer E exposure to T-DM1 by ≥5×, with total tumor uptake decreasing by ≥15% for inhibitor half-lives greater than 20 h. As the distribution benefit gained from a high-affinity inhibitor may supersede any decrease in total tumor uptake, a quantitative framework to evaluate the relationship between T-DM1 distribution and efficacy was required. Toward this aim, the sphere model was adapted to predict the impact of 1HE on T-DM1 efficacy in NCI-N87 xenografts. Significant work has been done to mathematically characterize T-DM1 efficacy by several groups (Singh et al., 2016; Khera et al., 2018; Menezes et al., 2020; Singh et al., 2020), and all of the parameters that were required to modify the sphere model were found in these prior publications. The PK/PD sphere model was able to accurately capture our previously observed efficacy data for T-DM1 and T-DM1:1HE at a single dose of 1.8 mg/kg. The best 1HE mutant for increasing T-DM1 efficacy was predicted to be HF9 (**Figure 8**), with an inhibition half-life of 51.1 h. This result highlights the need to consider a dynamic component to modeling and simulation as HF9 is predicted to decrease total tumor uptake of T-DM1 by >25%. When T-DM1 is administered alone, perivasculature tumor regions are exposed to T-DM1 in excess of that necessary to achieve a therapeutic effect, therefore the dose of T-DM1 that is "wasted" due to the overkilling effect is predicted to have a greater impact on overall efficacy than an inhibitor with a long half-life of binding, such as HF9, that may decrease total tumor uptake. Notably, when T-DM1 is administered alone, ~50% of the total T-DM1 delivered to the tumor is accounted for by tumor layers A and B despite these layers representing only 6.4% of the total tumor volume. The model-based predictions that suggest that an 8% increase in median survival may be obtained with HF9 co-administration with T-DM1, relative to 1HE, were not experimentally validated. A follow up study to validate the model simulations would require a group size of ~300 mice to achieve a statistical power of 80% to detect the 8% predicted increase in median survival time given the ~30% variability in NCI-N87 xenograft tumor growth.

Although model predictions indicate that the 1HE mutants we identified here would not substantially improve T-DM1 efficacy in xenograft-bearing mice, relative to 1HE, we believe these mutants will be superior to 1HE when applied in other circumstances. For example, in humans, the plasma half-life of antibodies and ADCs are several-fold longer than in mice. In addition, human tumors are less vascularized (Lauk et al., 1989) and have greater extracellular matrix development (Cybulska et al., 2018) in comparison to mouse xenograft models. Therefore, a longer window of inhibition may be necessary to allow antibodies to extravasate and diffuse into human tumors. A circumstance in which an inhibitor with a shorter binding half-life may be beneficial is in the case of a potent trastuzumab conjugate with rapid plasma elimination. For example, a single-chain variable fragment of trastuzumab has been used to target the ribosome-inactivating protein, pseudomonas exotoxin (Sokolova et al., 2017; Lee et al., 2019). Immunotoxin conjugates have short plasma half-lives (~1 h) and are highly cytotoxic, with approximately 1,000 bound molecules leading to cell death (Kreitman and Pastan, 1998; Bauss et al., 2016). Sphere model simulations using previously reported plasma pharmacokinetics of an immunotoxin in mice (Bauss et al., 2016) indicate a 1HE mutant with a binding half-life of ~1 h would decrease the dose required to achieve the 1,000 bound antigens/cell threshold in layer E of the sphere model by ~50-fold.

As immunotoxins commonly have dose-limiting toxicities (Alewine et al., 2015), the competitive inhibition strategy is likely to be facilely scaled to improve immunotoxin efficacy. Interestingly, a theoretical modeling analysis by Pak et al. predicted that shed antigen may improve recombinant immunotoxin efficacy, as shed-antigen bound immunotoxin can penetrate deeper into solid tumors (mechanistically analogous to the competitive inhibition approach described here) (Pak et al., 2012). To experimentally validate model predictions, the efficacy of an anti-mesothelin immunotoxin was compared in tumor models with low and high rates of mesothelin shedding. In contrast to model predictions, immunotoxin efficacy was decreased in the high shed antigen model (Awuah et al., 2016). The decreased efficacy may result from enhanced plasma elimination of shed mesothelin-bound immunotoxin. Enhanced plasma elimination of mAb, when bound to a soluble antigen, has been observed previously by our group, with co-administration of recombinant carcinoembryonic antigen (CEA) leading to a ~2-fold increase in plasma elimination of the anti-CEA mAb T84.66, decreasing total tumor exposure of T84.66 in a CEA positive xenograft mouse model by 55% (Abuqayyas, 2012). Enhanced elimination of anti-CEA mAb was also reported recently by Iwano et al., with the observation that mAb engineered to have preferential binding for membrane CEA, can in part, overcome shed antigen mediated elimination (Iwano et al., 2019). Additionally, the recombinant immunotoxins utilized to validate model simulations were reported to have a half-life of approximately 1 h (Bauss et al., 2016), therefore, shed antigen which is continuously being produced may lead to a significant fraction of immunotoxin being eliminated in the inhibited form, decreasing total tumor cell uptake. Shed HER2 was not included in the sphere model, however, it would be interesting to extend the model to evaluate any relationship between HER2 shedding and the impact of competitive inhibitors on trastuzumab tumor disposition.

The 1HE mutants identified in the current study span a wide range of dissociation rates constants; however, additional constructs with specific binding affinities or enhanced stability may be necessary. Only a fraction of the total clones from the low- and high-affinity master plates were chosen for DNA sequencing, and only a fraction of the clones that were sequenced were characterized using the covalent ELISA dissociation assay. Therefore, many additional clones with unique sequences and unique trastuzumab binding affinities are likely to be found among our unscreened colonies. The sequences that have been identified, and characterized, provide information on the paratopes of 1HE that are responsible for trastuzumab binding. The center of CDR2 appears to be critical for high-affinity binding to trastuzumab, as most of the clones with faster dissociation rates have mutations at ^{59}NGDST^{63}. Alvarez-Rueda et al. reported the CDR2 residues ^{59}NGDST^{63} as being similar to the HER2 motif ^{571}NGS^{573}, which is part of a region of HER2 that is bound by trastuzumab (Alvarez-Rueda et al., 2009). Therefore, if necessary, 1HE mutants with faster dissociation rate constants may be rationally designed through site-directed mutagenesis at the ^{54}NGDST^{58} motif of CDR2. Alvarez-Rueda et al., also reported that the CDR3 sequence ^{103}TGDGHRADY^{111}, showed identity to the HER2 epitope ^{575}TCFGPEADQ^{583} at four positions; however, based on the crystal structure of trastuzumab in complex in with HER2, only the A and D residues are likely to interact with trastuzumab (Alvarez-Rueda et al., 2009). Consistent with the A and D residues being critical for trastuzumab binding, none of the sequenced colonies had mutations at these residues. Threonine 103 was observed to be a common mutation site among the mutants with slower dissociation rate constants, relative to wild-type 1HE. Specifically, six mutants had mutations of threonine to alanine, serine, or isoleucine. Identification of these critical mutation "hot-spots" will support the rational design of competitive inhibitors or allow informed selection of 1HE colonies for further characterization, following DNA sequencing.

In the present work, we have developed competitive inhibitors of trastuzumab: HER2 binding with binding dissociation half-lives between 1.1 and 108 h. These constructs will be used to further the development of our competitive inhibition strategy to bypass the binding site barrier. Here we demonstrate that modeling and simulation using mechanistic models can be used to support the rationale selection of a competitive inhibitor for optimization of trastuzumab-cytotoxin conjugate efficacy.

DATA AVAILABILITY STATEMENT

The raw data supporting the conclusions of this article will be made available by the authors, without undue reservation.

ETHICS STATEMENT

The animal study was reviewed and approved by the University at Buffalo Institutional Animal Care and Use Committee.

AUTHOR CONTRIBUTIONS

All authors contributed to the development and review of the manuscript. JB and BB contributed to conceptualization of the project. BB, TN, PC, and LA contributed to data collection. BB and TN developed the phage library. PC and BB characterized 1HE mutants. LA performed the SKOV3 experimental work. LA and BB performed modeling and simulation work.

FUNDING

This work was supported by the National Cancer Institute of the National Institutes of Health (grant numbers CA204192 and CA246785) and by the Center for Protein Therapeutics.

SUPPLEMENTARY MATERIAL

The Supplementary Material for this article can be found online at: https://www.frontiersin.org/articles/10.3389/fphar.2022.837744/full#supplementary-material

REFERENCES

Abuqayyas, L., and Balthasar, J. P. (2012). Application of PBPK Modeling to Predict Monoclonal Antibody Disposition in Plasma and Tissues in Mouse Models of Human Colorectal Cancer. *J. Pharmacokinet. Pharmacodyn* 39, 683–710. doi:10.1007/s10928-012-9279-8

Abuqayyas, L. (2012). *Evaluation of the Mechanistic Determinants for IgG Exposure in Tissues, Pharmaceutical Sciences*. Buffalo, NY: University at Buffalo.

Alewine, C., Hassan, R., and Pastan, I. (2015). Advances in Anticancer Immunotoxin Therapy. *Oncologist* 20, 176–185. doi:10.1634/theoncologist.2014-0358

Alvarez-Rueda, N., Ladjemi, M. Z., Béhar, G., Corgnac, S., Pugnière, M., Roquet, F., et al. (2009). A Llama Single Domain Anti-idiotypic Antibody Mimicking HER2 as a Vaccine: Immunogenicity and Efficacy. *Vaccine* 27, 4826–4833. doi:10.1016/j.vaccine.2009.05.067

Austin, C. D., De Mazière, A. M., Pisacane, P. I., van Dijk, S. M., Eigenbrot, C., Sliwkowski, M. X., et al. (2004). Endocytosis and Sorting of ErbB2 and the Site of Action of Cancer Therapeutics Trastuzumab and Geldanamycin. *Mol. Biol. Cel* 15, 5268–5282. doi:10.1091/mbc.e04-07-0591

Awuah, P., Bera, T. K., Folivi, M., Chertov, O., and Pastan, I. (2016). Reduced Shedding of Surface Mesothelin Improves Efficacy of Mesothelin-Targeting Recombinant Immunotoxins. *Mol. Cancer Ther.* 15, 1648–1655. doi:10.1158/1535-7163.MCT-15-0863

Baish, J. W., Gazit, Y., Berk, D. A., Nozue, M., Baxter, L. T., and Jain, R. K. (1996). Role of Tumor Vascular Architecture in Nutrient and Drug Delivery: an Invasion Percolation-Based Network Model. *Microvasc. Res.* 51, 327–346. doi:10.1006/mvre.1996.0031

Bauss, F., Lechmann, M., Krippendorff, B. F., Staack, R., Herting, F., Festag, M., et al. (2016). Characterization of a Re-engineered, Mesothelin-Targeted Pseudomonas Exotoxin Fusion Protein for Lung Cancer Therapy. *Mol. Oncol.* 10, 1317–1329. doi:10.1016/j.molonc.2016.07.003

Baxter, L. T., Zhu, H., Mackensen, D. G., and Jain, R. K. (1994). Physiologically Based Pharmacokinetic Model for Specific and Nonspecific Monoclonal Antibodies and Fragments in normal Tissues and Human Tumor Xenografts in Nude Mice. *Cancer Res.* 54, 1517–1528.

Bender, B., Leipold, D. D., Xu, K., Shen, B. Q., Tibbitts, J., and Friberg, L. E. (2014). A Mechanistic Pharmacokinetic Model Elucidating the Disposition of Trastuzumab Emtansine (T-DM1), an Antibody-Drug Conjugate (ADC) for Treatment of Metastatic Breast Cancer. *AAPS J.* 16, 994–1008. doi:10.1208/s12248-014-9618-3

Berk, D. A., Yuan, F., Leunig, M., and Jain, R. K. (1997). Direct *In Vivo* Measurement of Targeted Binding in a Human Tumor Xenograft. *Proc. Natl. Acad. Sci. U S A.* 94, 1785–1790. doi:10.1073/pnas.94.5.1785

Bhunia, D., Chowdhury, R., Bhattacharyya, K., and Ghosh, S. (2015). Fluorescence Fluctuation of an Antigen-Antibody Complex: Circular Dichroism, FCS and smFRET of Enhanced GFP and its Antibody. *Phys. Chem. Chem. Phys.* 17, 25250–25259. doi:10.1039/c5cp04908c

Bordeau, B. M., and Balthasar, J. P. (2021). Strategies to Enhance Monoclonal Antibody Uptake and Distribution in Solid Tumors. *Cancer Biol. Med.* 18, 649–664. doi:10.20892/j.issn.2095-3941.2020.0704

Bordeau, B. M., Yang, Y., and Balthasar, J. P. (2021). Transient Competitive Inhibition Bypasses the Binding Site Barrier to Improve Tumor Penetration of Trastuzumab and Enhance T-DM1 Efficacy. *Cancer Res* 81, 4145–4154. doi:10.1158/0008-5472.can-20-3822

Bostrom, J., Haber, L., Koenig, P., Kelley, R. F., and Fuh, G. (2011). High Affinity Antigen Recognition of the Dual Specific Variants of Herceptin Is Entropy-Driven in Spite of Structural Plasticity. *PLoS One* 6, e17887. doi:10.1371/journal.pone.0017887

Chen, H., Tong, X., Lang, L., Jacobson, O., Yung, B. C., Yang, X., et al. (2017). Quantification of Tumor Vascular Permeability and Blood Volume by Positron Emission Tomography. *Theranostics* 7, 2363–2376. doi:10.7150/thno.19898

Chen, K. C., Kim, J., Li, X., and Lee, B. (2008). Modeling Recombinant Immunotoxin Efficacies in Solid Tumors. *Ann. Biomed. Eng.* 36, 486–512. doi:10.1007/s10439-007-9425-4

Cilliers, C., Guo, H., Liao, J., Christodolu, N., and Thurber, G. M. (2016). Multiscale Modeling of Antibody-Drug Conjugates: Connecting Tissue and Cellular Distribution to Whole Animal Pharmacokinetics and Potential Implications for Efficacy. *AAPS J.* 18, 1117–1130. doi:10.1208/s12248-016-9940-z

Cilliers, C., Menezes, B., Nessler, I., Linderman, J., and Thurber, G. M. (2018). Improved Tumor Penetration and Single-Cell Targeting of Antibody-Drug Conjugates Increases Anticancer Efficacy and Host Survival. *Cancer Res.* 78, 758–768. doi:10.1158/0008-5472.CAN-17-1638

Cybulska, M., Olesinski, T., Goryca, K., Paczkowska, K., Statkiewicz, M., Kopczynski, M., et al. (2018). Challenges in Stratifying the Molecular Variability of Patient-Derived Colon Tumor Xenografts. *Biomed. Res. Int.* 2018, 2954208. doi:10.1155/2018/2954208

D'Argenio, D. Z., Schumitzky, A., and Wang, X. (2009). *ADAPT 5 User's Guide: Pharmacokinetic/Pharmacodynamic Systems Analysis Software*. Los Angeles, CA: Biomedical Simulations Resource

Dellian, M., Yuan, F., Trubetskoy, V. S., Torchilin, V. P., and Jain, R. K. (2000). Vascular Permeability in a Human Tumour Xenograft: Molecular Charge Dependence. *Br. J. Cancer* 82, 1513–1518. doi:10.1054/bjoc.1999.1171

Erickson, H. K., Lewis Phillips, G. D., Leipold, D. D., Provenzano, C. A., Mai, E., Johnson, H. A., et al. (2012). The Effect of Different Linkers on Target Cell Catabolism and Pharmacokinetics/Pharmacodynamics of Trastuzumab Maytansinoid Conjugates. *Mol. Cancer Ther.* 11, 1133–1142. doi:10.1158/1535-7163.MCT-11-0727

Fallowfield, M. E. (1989). Vascular Volume in B16 Allografts and Human Melanoma Xenografts Estimated by Means of Hoechst 33342. *J. Pathol.* 157, 249–252. doi:10.1002/path.1711570312

Fujimori, K., Covell, D. G., Fletcher, J. E., and Weinstein, J. N. (1990). A Modeling Analysis of Monoclonal Antibody Percolation through Tumors: a Binding-Site Barrier. *J. Nucl. Med.* 31, 1191–1198.

Goldmacher, V. S., Audette, C. A., Guan, Y., Sidhom, E. H., Shah, J. V., Whiteman, K. R., et al. (2015). High-affinity Accumulation of a Maytansinoid in Cells via Weak Tubulin Interaction. *PLoS One* 10, e0117523. doi:10.1371/journal.pone.0117523

Graff, C. P., and Wittrup, K. D. (2003). Theoretical Analysis of Antibody Targeting of Tumor Spheroids: Importance of Dosage for Penetration, and Affinity for Retention. *Cancer Res.* 63, 1288–1296. Available at: https://cancerres.aacrjournals.org/content/63/6/1288

Green, E. L. (1966). *Biology of the Laboratory Mouse*. New York: Dover Publications, inc..

Hassan, R., Alewine, C., Mian, I., Spreafico, A., Siu, L. L., Gomez-Roca, C., et al. (2020). Phase 1 Study of the Immunotoxin LMB-100 in Patients with Mesothelioma and Other Solid Tumors Expressing Mesothelin. *Cancer* 126, 4936–4947. doi:10.1002/cncr.33145

Henderson, E., Sykes, J., Drost, D., Weinmann, H. J., Rutt, B. K., and Lee, T. Y. (2000). Simultaneous MRI Measurement of Blood Flow, Blood Volume, and Capillary Permeability in Mammary Tumors Using Two Different Contrast Agents. *J. Magn. Reson. Imaging* 12, 991–1003. doi:10.1002/1522-2586(200012)12:6<991:aid-jmri26>3.0.co;2-1

Hendriks, B. S., Klinz, S. G., Reynolds, J. G., Espelin, C. W., Gaddy, D. F., and Wickham, T. J. (2013). Impact of Tumor HER2/ERBB2 Expression Level on HER2-Targeted Liposomal Doxorubicin-Mediated Drug Delivery: Multiple Low-Affinity Interactions lead to a Threshold Effect. *Mol. Cancer Ther.* 12, 1816–1828. doi:10.1158/1535-7163.MCT-13-0180

Iwano, J., Shinmi, D., Masuda, K., Murakami, T., and Enokizono, J. (2019). Impact of Different Selectivity between Soluble and Membrane-Bound Forms of Carcinoembryonic Antigen (CEA) on the Target-Mediated Disposition of Anti-CEA Monoclonal Antibodies. *Drug Metab. Dispos* 47, 1240–1246. doi:10.1124/dmd.119.088179

Jain, R. K., and Baxter, L. T. (1988). Mechanisms of Heterogeneous Distribution of Monoclonal Antibodies and Other Macromolecules in Tumors: Significance of Elevated Interstitial Pressure. *Cancer Res.* 48, 7022–7032.

Juweid, M., Neumann, R., Paik, C., Perez-Bacete, M. J., Sato, J., van Osdol, W., et al. (1992). Micropharmacology of Monoclonal Antibodies in Solid Tumors: Direct Experimental Evidence for a Binding Site Barrier. *Cancer Res.* 52, 5144–5153.

Khera, E., Cilliers, C., Bhatnagar, S., and Thurber, G. M. (2018). Computational Transport Analysis of Antibody-Drug Conjugate Bystander Effects and Payload Tumoral Distribution: Implications for Therapy. *Mol. Syst. Des. Eng.* 3, 73–88. doi:10.1039/C7ME00093F

Kreitman, R. J., and Pastan, I. (1998). Accumulation of a Recombinant Immunotoxin in a Tumor *In Vivo*: Fewer Than 1000 Molecules Per Cell Are Sufficient for Complete Responses. *Cancer Res.* 58, 968–975.

Lauk, S., Zietman, A., Skates, S., Fabian, R., and Suit, H. D. (1989). Comparative Morphometric Study of Tumor Vasculature in Human Squamous Cell Carcinomas and Their Xenotransplants in Athymic Nude Mice. *Cancer Res.* 49, 4557–4561.

Lee, C. M., and Tannock, I. F. (2010). The Distribution of the Therapeutic Monoclonal Antibodies Cetuximab and Trastuzumab within Solid Tumors. *BMC Cancer* 10, 255. doi:10.1186/1471-2407-10-255

Lee, S., Park, S., Nguyen, M. T., Lee, E., Kim, J., Baek, S., et al. (2019). A Chemical Conjugate between HER2-Targeting Antibody Fragment and Pseudomonas Exotoxin A Fragment Demonstrates Cytotoxic Effects on HER2-Expressing Breast Cancer Cells. *BMB Rep.* 52, 496–501. doi:10.5483/bmbrep.2019.52.8.250

Li, J. Y., Perry, S. R., Muniz-Medina, V., Wang, X., Wetzel, L. K., Rebelatto, M. C., et al. (2016). A Biparatopic HER2-Targeting Antibody-Drug Conjugate Induces Tumor Regression in Primary Models Refractory to or Ineligible for HER2-Targeted Therapy. *Cancer Cell* 29, 117–129. doi:10.1016/j.ccell.2015.12.008

Maass, K. F., Kulkarni, C., Betts, A. M., and Wittrup, K. D. (2016). Determination of Cellular Processing Rates for a Trastuzumab-Maytansinoid Antibody-Drug Conjugate (ADC) Highlights Key Parameters for ADC Design. *AAPS J.* 18, 635–646. doi:10.1208/s12248-016-9892-3

Menchon, G., Prota, A. E., Lucena-Agell, D., Bucher, P., Jansen, R., Irschik, H., et al. (2018). A Fluorescence Anisotropy Assay to Discover and Characterize Ligands Targeting the Maytansine Site of Tubulin. *Nat. Commun.* 9, 2106. doi:10.1038/s41467-018-04535-8

Menezes, B., Cilliers, C., Wessler, T., Thurber, G. M., and Linderman, J. J. (2020). An Agent-Based Systems Pharmacology Model of the Antibody-Drug Conjugate Kadcyla to Predict Efficacy of Different Dosing Regimens. *AAPS J.* 22, 29. doi:10.1208/s12248-019-0391-1

Nessler, I., Cilliers, C., and Thurber, G. M. (2020). Practical Guide for Quantification of *In Vivo* Degradation Rates for Therapeutic Proteins with Single-Cell Resolution Using Fluorescence Ratio Imaging. *Pharmaceutics* 12, 132. doi:10.3390/pharmaceutics12020132

Netti, P. A., Berk, D. A., Swartz, M. A., Grodzinsky, A. J., and Jain, R. K. (2000). Role of Extracellular Matrix Assembly in Interstitial Transport in Solid Tumors. *Cancer Res.* 60, 2497–2503. Available at: https://cancerres.aacrjournals.org/content/60/9/2497.article-info

Onsum, M. D., Geretti, E., Paragas, V., Kudla, A. J., Moulis, S. P., Luus, L., et al. (2013). Single-cell Quantitative HER2 Measurement Identifies Heterogeneity and Distinct Subgroups within Traditionally Defined HER2-Positive Patients. *Am. J. Pathol.* 183, 1446–1460. doi:10.1016/j.ajpath.2013.07.015

Pak, Y., Zhang, Y., Pastan, I., and Lee, B. (2012). Antigen Shedding May Improve Efficiencies for Delivery of Antibody-Based Anticancer Agents in Solid Tumors. *Cancer Res.* 72, 3143–3152. doi:10.1158/0008-5472.CAN-11-3925

Pastan, I., Hassan, R., FitzGerald, D. J., and Kreitman, R. J. (2006). Immunotoxin Therapy of Cancer. *Nat. Rev. Cancer* 6, 559–565. doi:10.1038/nrc1891

Pluen, A., Boucher, Y., Ramanujan, S., McKee, T. D., Gohongi, T., di Tomaso, E., et al. (2001). Role of Tumor-Host Interactions in Interstitial Diffusion of Macromolecules: Cranial vs. Subcutaneous Tumors. *Proc. Natl. Acad. Sci. U S A.* 98, 4628–4633. doi:10.1073/pnas.081626898

Rhoden, J. J., and Wittrup, K. D. (2012). Dose Dependence of Intratumoral Perivascular Distribution of Monoclonal Antibodies. *J. Pharm. Sci.* 101, 860–867. doi:10.1002/jps.22801

Rinnerthaler, G., Gampenrieder, S. P., and Greil, R. (2019). HER2 Directed Antibody-Drug-Conjugates beyond T-DM1 in Breast Cancer. *Int. J. Mol. Sci.* 20, 1115. doi:10.3390/ijms20051115

Saga, T., Neumann, R. D., Heya, T., Sato, J., Kinuya, S., Le, N., et al. (1995). Targeting Cancer Micrometastases with Monoclonal Antibodies: a Binding-Site Barrier. *Proc. Natl. Acad. Sci. U S A.* 92, 8999–9003. doi:10.1073/pnas.92.19.8999

Schmidt, M. M., and Wittrup, K. D. (2009). A Modeling Analysis of the Effects of Molecular Size and Binding Affinity on Tumor Targeting. *Mol. Cancer Ther.* 8, 2861–2871. doi:10.1158/1535-7163.MCT-09-0195

Shah, D. K., Haddish-Berhane, N., and Betts, A. (2012). Bench to Bedside Translation of Antibody Drug Conjugates Using a Multiscale Mechanistic PK/PD Model: a Case Study with Brentuximab-Vedotin. *J. Pharmacokinet. Pharmacodyn* 39, 643–659. doi:10.1007/s10928-012-9276-y

Shah, D. K., Shin, B. S., Veith, J., Tóth, K., Bernacki, R. J., and Balthasar, J. P. (2009). Use of an Anti-vascular Endothelial Growth Factor Antibody in a Pharmacokinetic Strategy to Increase the Efficacy of Intraperitoneal Chemotherapy. *J. Pharmacol. Exp. Ther.* 329, 580–591. doi:10.1124/jpet.108.149443

Singh, A. P., Guo, L., Verma, A., Wong, G. G., Thurber, G. M., and Shah, D. K. (2020). Antibody Coadministration as a Strategy to Overcome Binding-Site Barrier for ADCs: a Quantitative Investigation. *AAPS J.* 22, 28. doi:10.1208/s12248-019-0387-x

Singh, A. P., Maass, K. F., Betts, A. M., Wittrup, K. D., Kulkarni, C., King, L. E., et al. (2016). Evolution of Antibody-Drug Conjugate Tumor Disposition Model to Predict Preclinical Tumor Pharmacokinetics of Trastuzumab-Emtansine (T-DM1). *AAPS J.* 18, 861–875. doi:10.1208/s12248-016-9904-3

Sokolova, E., Guryev, E., Yudintsev, A., Vodeneev, V., Deyev, S., and Balalaeva, I. (2017). HER2-specific Recombinant Immunotoxin 4D5scFv-PE40 Passes through Retrograde Trafficking Route and Forces Cells to Enter Apoptosis. *Oncotarget* 8, 22048–22058. doi:10.18632/oncotarget.15833

Thurber, G. M., and Dane Wittrup, K. (2012). A Mechanistic Compartmental Model for Total Antibody Uptake in Tumors. *J. Theor. Biol.* 314, 57–68. doi:10.1016/j.jtbi.2012.08.034

Thurber, G. M., Schmidt, M. M., and Wittrup, K. D. (2008). Antibody Tumor Penetration: Transport Opposed by Systemic and Antigen-Mediated Clearance. *Adv. Drug Deliv. Rev.* 60, 1421–1434. doi:10.1016/j.addr.2008.04.012

Thurber, G. M., and Weissleder, R. (2011b). A Systems Approach for Tumor Pharmacokinetics. *PLoS One* 6, e24696. doi:10.1371/journal.pone.0024696

Thurber, G. M., and Weissleder, R. (2011a). Quantitating Antibody Uptake *In Vivo*: Conditional Dependence on Antigen Expression Levels. *Mol. Imaging Biol.* 13, 623–632. doi:10.1007/s11307-010-0397-7

Thurber, G. M., and Wittrup, K. D. (2008). Quantitative Spatiotemporal Analysis of Antibody Fragment Diffusion and Endocytic Consumption in Tumor Spheroids. *Cancer Res.* 68, 3334–3341. doi:10.1158/0008-5472.CAN-07-3018

Thurber, G. M., Zajic, S. C., and Wittrup, K. D. (2007). Theoretic Criteria for Antibody Penetration into Solid Tumors and Micrometastases. *J. Nucl. Med.* 48, 995–999. doi:10.2967/jnumed.106.037069

Vogel, A. W. (1965). Intratumoral Vascular Changes with Increased Size of a Mammary Adenocarcinoma: New Method and Results. *J. Natl. Cancer Inst.* 34, 571–578.

Worthylake, R., Opresko, L. K., and Wiley, H. S. (1999). ErbB-2 Amplification Inhibits Down-Regulation and Induces Constitutive Activation of Both ErbB-2 and Epidermal Growth Factor Receptors. *J. Biol. Chem.* 274, 8865–8874. doi:10.1074/jbc.274.13.8865

Yuan, F., Chen, Y., Dellian, M., Safabakhsh, N., Ferrara, N., and Jain, R. K. (1996). Time-dependent Vascular Regression and Permeability Changes in Established Human Tumor Xenografts Induced by an Anti-vascular Endothelial Growth Factor/vascular Permeability Factor Antibody. *Proc. Natl. Acad. Sci. U S A.* 93, 14765–14770. doi:10.1073/pnas.93.25.14765

Yuan, F., Dellian, M., Fukumura, D., Leunig, M., Berk, D. A., Torchilin, V. P., et al. (1995). Vascular Permeability in a Human Tumor Xenograft: Molecular Size Dependence and Cutoff Size. *Cancer Res.* 55, 3752–3756.

Conflict of Interest: BB reports a patent for PCT/US 2020/050159 pending. JB reports a patent for PCT/US 2020/050159 pending. JB has served as a consultant to Genentech and Roche (on issues unrelated to the present work). In addition, JB serves as the Director of the University at Buffalo Center for Protein Therapeutics, which is supported by an industry consortium. Through the consortium, JB has received research support, for work unrelated to this report, from Abbvie, Amgen, CSL-Behring, Eli Lilly, Genentech, GSK, Janssen, Merck and Sanofi. During the course of this work, JB has received consulting fees from companies involved with the development of cancer therapies, including: Abbvie, Amgen, Eli Lilly, Merck, and Pfizer.

The remaining authors declare that the research was conducted in the absence of any commercial or financial relationships that could be construed as a potential conflict of interest.

Publisher's Note: All claims expressed in this article are solely those of the authors and do not necessarily represent those of their affiliated organizations, or those of the publisher, the editors and the reviewers. Any product that may be evaluated in this article, or claim that may be made by its manufacturer, is not guaranteed or endorsed by the publisher.

frontiers in Pharmacology

REVIEW
published: 24 February 2022
doi: 10.3389/fphar.2022.856961

Physiological Considerations for Modeling *in vivo* Antibody-Target Interactions

Tyler Dunlap[1] *and Yanguang Cao*[1,2]*

[1]Division of Pharmacotherapy and Experimental Therapeutics, Eshelman School of Pharmacy, University of North Carolina at Chapel Hill, Chapel Hill, NC, United States, [2]Lineberger Comprehensive Cancer Center, School of Medicine, University of North Carolina at Chapel Hill, Chapel Hill, NC, United States

The number of therapeutic antibodies in development pipelines is increasing rapidly. Despite superior success rates relative to small molecules, therapeutic antibodies still face many unique development challenges. There is often a translational gap from their high target affinity and specificity to the therapeutic effects. Tissue microenvironment and physiology critically influence antibody-target interactions contributing to apparent affinity alterations and dynamic target engagement. The full potential of therapeutic antibodies will be further realized by contextualizing antibody-target interactions under physiological conditions. Here we review how local physiology such as physical stress, biological fluid, and membrane characteristics could influence antibody-target association, dissociation, and apparent affinity. These physiological factors in the early development of therapeutic antibodies are valuable toward rational antibody engineering, preclinical candidate selection, and lead optimization.

Keywords: physiological factors, therapeutic antibody, target binding, receptor occupancy, MIDD, modeling and simulation

OPEN ACCESS

Edited by:
Rui Li,
Pfizer, United States

Reviewed by:
Robert Kelley,
Genentech, Inc., United States
Mahua Roy,
Pfizer, United States

***Correspondence:**
Yanguang Cao
yanguang@unc.edu

Specialty section:
This article was submitted to Experimental Pharmacology and Drug Discovery, a section of the journal Frontiers in Pharmacology

Received: *17 January 2022*
Accepted: *10 February 2022*
Published: *24 February 2022*

Citation:
Dunlap T and Cao Y (2022) Physiological Considerations for Modeling in vivo Antibody-Target Interactions. Front. Pharmacol. 13:856961. doi: 10.3389/fphar.2022.856961

INTRODUCTION

In 1984, the first therapeutic monoclonal antibody was approved by the U.S. Food and Drug Administration (FDA). In 2021, the 100th antibody was approved just 6 years following approval of the 50th (Mullard, 2021). This trend highlights the accelerating interest and clinical application of antibody-based therapeutics. The ability to modulate cell-surface and soluble targets with high affinity and specificity make these molecules attractive therapeutic modalities. With a phase I to approval success rate of approximately 22% (Kaplon and Reichert, 2019), nearly double that of small molecule drugs, drug developers are increasingly shifting their focus toward protein drug development (Kaplon et al., 2020). Although antibodies and small molecule drugs share similar clinical development paths, antibody-based therapeutics present unique challenges from the early stage of candidate selection to the late stage of therapeutic confirmation (Tang and Cao, 2021).

Bringing a therapeutic antibody to market requires a team of scientists across multiple disciplines closely collaborating in all stages of development. At the early stage, after the therapeutic target for an indication is selected, decisions must be made regarding the design format, affinity requirement, feasibility of efficacious doses, and candidates for subsequent stages. Rational lead optimization and candidate selection are critical tasks in early drug development and can differentiate success and failure in clinical stages. Antibody engineering provides means for controlling a candidate's half-life, affinity, and biological activity (Chiu et al., 2019). Computational modeling and simulation can be helpful to explore these engineered parameters before comprehensive experimental evaluation and

thereby provide early insights for antibody engineering. The iterative learn and confirm paradigm between antibody engineering and computational modeling exemplifies model informed drug development (MIDD) in preclinical drug development, which seeks to leverage mathematical and statistical models to optimize drug development processes. In the preclinical stage, one critical MIDD task is to evaluate plausible ranges of target binding affinity and clinically feasible doses likely to achieve adequate target engagement.

Antibody-target interactions take place within specific tissue environments with characteristic physiological attributes. The physiology of these local environment critically influences antibody-target interactions resulting in apparent affinity alterations and heterogenous target engagement. Contextualizing these *in vivo* interactions by integrating local physiological factors beyond those commonly considered in physiologically based pharmacokinetic (PBPK) models could enhance model prediction fidelity and boost confidence in early-stage decisions (Cao et al., 2013; Cao and Jusko, 2014). For instance, if the binding rate between antibody and target is high, association and dissociation are primarily restricted by the diffusion rate of antibody to or away from the target in the local tissue and cellular environment. In this case, the apparent rate of association and dissociation will become context-dependent, not directly reflective of the intrinsic reaction rate. Incorporating this kind of physiological intuition into early-stage models depicting antibody-target interactions could yield insights toward optimal antibody design and affinity thresholds. MIDD approaches should leverage knowledge of tissue microenvironment and local physiology to guide preclinical candidate selection, antibody design, and lead optimization. Here we briefly review how physiological factors can influence antibody-target engagement and demonstrate these concepts toward optimizing preclinical decision-making processes.

ANTIBODY-TARGET INTERACTIONS

Antibody-Target Affinity: *In Vitro* Approaches and Problems

Surface plasmon resonance (SPR) is a label-free technique to measure the kinetics of molecular interactions and has become the standard for *in vitro* characterization of antibody-target binding (Olaru et al., 2015). An extension of this technology is SPR imaging which directly measures cell surface antibody-antigen binding kinetics and can be used to estimate binding affinity and antigen density (Zhang et al., 2020). Major advantages to this technique are that interacting species need not be labeled and binding events can be visualized in real-time, allowing for measurement of association and dissociation rates. Inherent problems to this method include mass transport limitations and surface site heterogeneity. Strategies for analyzing SPR data to account for these complexities are reviewed elsewhere (Schuck and Zhao, 2010). In addition, flow cytometry has also become an approach applied to assess antibody-target engagement in blood cells and tissue-derived cell samples (Moulard and Ozoux, 2016).

The slow dissociation rate of antibodies from their target necessitates relatively long incubation times to reach equilibrium compared to small molecule drugs. Equilibrium states are, by definition, invariant with time; thus, determining accurate estimates requires the demonstration of negligible change in product and reactant amounts over time. For therapeutic antibodies with pM or nM affinities, it takes hours, even days, to reach binding equilibrium with their targets. However, nearly 90% of reported incubation times for equilibrium constants in a survey by Jarmoskaite et al. were an hour or less (Jarmoskaite et al., 2020). Jarmoskaite et al. provide two recommendations for establishing confidence in reported equilibrium constants, publishing the time to equilibrium and demonstrating that the dissociation constant is not susceptible to titration (Jarmoskaite et al., 2020). Furthermore, while a single equilibrium constant is often reported for ligand-receptor interactions, association and dissociation are concentration- and context-dependent (Berkers et al., 1992). Individual equilibrium estimates likely reflect the mean of a distribution of experimental values calculated for a given reaction (Reverbi and Reverbi, 2007). The inherent uncertainty in reported values warrant careful consideration when using published rate constants in models depicting target engagement, as commonly done in pharmacokinetic (PK) and pharmacodynamic (PD) models. Reporting statistical metrics, such as the standard error or coefficient of variation of parameter estimates derived from experimental data should be encouraged and may promote greater appreciation for the uncertainty in calculated rate constants.

Equilibrium rate constants (e.g., K_D) are used, in essence, to summarize ligand-receptor engagement. While an affinity summary metric is theoretically useful, understanding both the association (k_{on}), and dissociation (k_{off}) rates are essential for *in vivo* characterization of antibody-target interactions. These rate constants describe the microkinetic relationship between individual antibody domains and corresponding binding domains on the target. The "intrinsic" value to these rate constants may be estimated through *in vitro* techniques, such as SPR. However, these values do not reflect binding under physiological conditions. Understanding antibody-target interactions under physiological conditions is necessary for developing accurate foresight into the potential efficacy of preclinical antibody candidates; yet remains largely uncharacterized at the very early stage. A schematic representation of concepts depicting how the microenvironment and local physiology can influence antibody-target interactions is shown in **Figure 1**.

Factors Affecting Antibody Avidity

In solution, the probability of antibody-target interactions is largely dependent upon the relative concentrations and diffusion rates of the two species (Arrhenius, 1889): with a theoretical upper limit around $10^9\ Mol^{-1}s^{-1}$ in the absence of steric hindrance. The probability of complex formation is also influenced by bond activation energies and the orientation of the

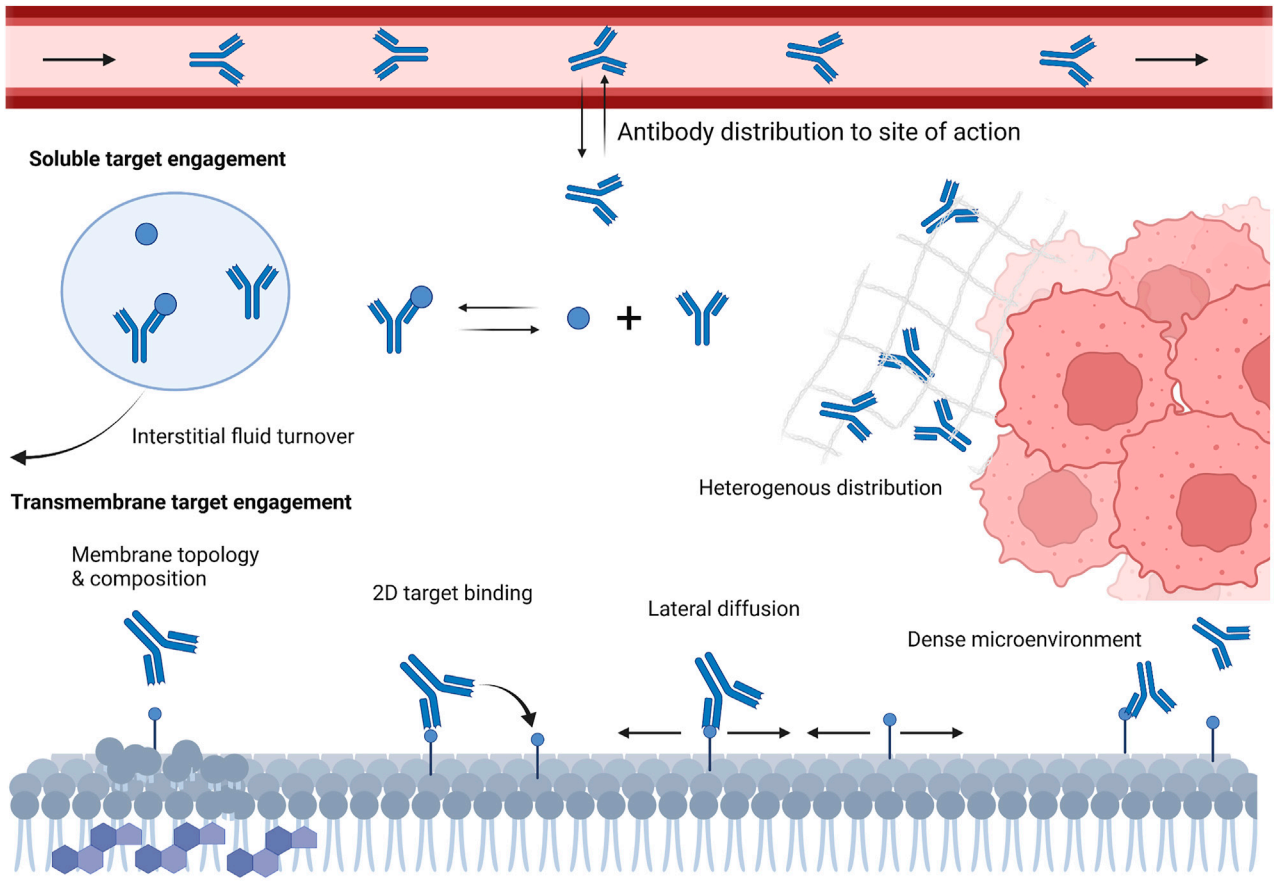

FIGURE 1 | Schematic representation of various local microenvironment and physiological factors that can influence antibody-target engagement *in vivo*. These factors include antibody slow and poor distribution into target tissues, interstitial fluid turnover, restricted antibody diffusion in dense microenvironment, cell membrane topology and composition, and target density and lateral diffusivity.

species when they encounter (Wigner, 1932; Eyring, 1935). The k_{on} and k_{off} essentially summarize this information and characterize the likelihood of complex formation following physical interaction and the stability of bonds formed, respectively. Engineered increases to k_{on} (faster association rates) result in faster complex formation while decreases to k_{off} (slower off-binding rates) result in a more stable complex. The ratio between these rates (k_{off}/k_{on}) is used to describe the overall affinity (i.e., K_D) of the interaction. Notably, affinity is determined by the relative difference in these rate constants, not by their individual magnitudes. While affinity can be easily estimated from *in vitro* techniques, *in vivo* affinities can be profoundly different (Fujimori et al., 1989; Sharkey et al., 1990; Shockley et al., 1992). Antibody-target interactions demonstrate that cooperativity, dimensionality, multivalency, diffusivity, and local physiology contribute to the overall affinity of an interaction. These phenomena orchestrate complex engagement dynamics that are difficult to recapitulate *in vitro*. Avidity, also referred to as "functional affinity", depicts the affinity of two species in their native environment by accounting for synergistic/antagonistic physical properties and environmental influences (Erlendsson and Teilum, 2020). Avidity is conceptually intuitive but challenging to predict. There is no single quantity that can be described as "the avidity" of an interaction because the value is context-dependent (Kaufman and Jain, 1992). Discrepancies between *in vitro* affinity and *in vivo* avidity highlight the poorly understood influence of the microenvironment on molecular interactions.

An often-overlooked factor influencing the avidity of an interaction is the geometry of the physiological space in which the species interact (Coombs and Goldstein, 2004). Cells and tissues are highly compartmentalized ecosystems often spatially restricted across multiple dimensions. This dimensionality reduction can influence the k_{on} and k_{off} of an interaction in many ways. For example, diffusion of antibodies adhered to the cell membrane and transmembrane targets are confined to two dimensions (i.e., laterally on the cell surface) and further restricted by other macromolecules, membrane rigidity, tight junctions, etc. The diffusion rate of bound antibodies on lymphocytes has been estimated to be approximately 10^{-10} cm^2/s (Elson et al., 1976), nearly four orders of magnitude lower than the diffusion constant in solution. These hindrances influence the avidity between two species by reducing molecular dispersion on the cell surface after dissociation events, thereby promoting rebinding (Mosquera et al., 2020). Rebinding can

contribute to apparent increases in k_{on}, or decreases in k_{off}, between molecules *in vivo* (Vauquelin and Charlton, 2013). Coombs and Goldstein propose the effects of hindered diffusion (i.e., diffusion through a dense microenvironment) can be approximated by calculating a modulated rate constant considering the compartment dimensions, flux, and diffusion coefficients of the interacting species (Coombs and Goldstein, 2004).

Target Engagement and Antibody Efficacy Metrics

A critical element to PD theory is the receptor occupancy model (Hill, 1909), based on the premise that receptor engagement will translate to modulation of downstream biology and that PD effect is closely related to the fraction of receptors engaged. Models extending receptor occupancy to account for complex signaling phenomena such as fractional occupancy, constitutive activity, and nonlinear transduction have been developed to further appreciate the complexity of drug action (Buchwald, 2019). Widely accepted models depicting various antibody PD mechanisms remain largely undeveloped.

A variety of antibody formats can be used to bind targets, block signaling, stimulate receptor internalization/degradation, deliver cytotoxic payloads, and more. Given this mechanistic diversity, the traditional implementation of receptor occupancy theory may be inappropriate for antibody efficacy assessment. Oftentimes, efficacy could be driven by maximizing the number of antibody-target complexes, minimizing free target levels, or maximizing bivalent bound antibodies. For antibodies that work through antibody-dependent cellular cytotoxicity (ADCC), efficacy may not be directly related to the fraction of receptors engaged, but rather to the successful initiation of subsequent effector mechanisms (Meyer et al., 2014; Wang et al., 2015; Weiskopf and Weissman, 2015). Rituximab is one such example where the density and persistence of antibody-target complex may be more therapeutically relevant than the fraction of targets engaged (Cragg et al., 2003; Maloney, 2005; Rouge et al., 2020). Bivalent bound rituximab to its CD20 target is related to a stronger ADCC effect than monovalent bound antibodies (Cragg et al., 2003). Conversely, minimum target concentration, regardless of complex abundance, is a reliable predictor of drug effect for antibodies, like infliximab, working through neutralization of soluble antigens (Tracey et al., 2008). Similarly, for antibody-drug conjugates, intracellular delivery of payload through endocytosis is most relevant to therapeutic effect (Birrer et al., 2019). We should differentiate antibodies acting as agonists versus antagonists. The therapeutic efficacy appears to be more related to target engagement for agonist antibodies than antagonists do. Generally, antibody mechanism of action and target turnovers should guide appropriate drug characteristics and dosing strategies. If target turnover within target tissues is fast (i.e., rapid production), enduring antibody concentrations to neutralize newly produced antigens, or a "C_{min}" approach, with relatively frequent dosing are likely preferable for strong efficacy. If target turnover is relatively slow, additional dosing will not translate into increased efficacy once a target is engaged. Thus, a "C_{max}" approach with large, infrequent doses may be sufficient.

Association and dissociation kinetics influence target engagement and, thereby, influence subsequent initiation of effector functions. Effector cell cytotoxicity can be mediated through a multitude of mechanisms including: ADCC, antibody-dependent cellular phagocytosis, or initiation of the complement cascade (Meyer et al., 2014; Wang et al., 2015; Weiskopf and Weissman, 2015; Yang et al., 2019). Importantly, effector cell engagement is related to immune complex stability, primarily determined by the ratio of antibody-antigen in the complex and avidity of individual bonds (Diebolder et al., 2014). The stoichiometry of the Fab domain target binding interaction also contributes to stable immune complex formation and is crucial for effective initiation of effector functions (Pierson et al., 2007; Tajima et al., 2011; Lux et al., 2013; Strasser et al., 2019). Furthermore, the antibody Fc domain can influence the avidity of an antibody-target interaction (Abboud et al., 2010; Bournazos et al., 2014). Additional molecular features correlated with effector cell engagement include the recognized epitope, target affinity, binding orientation, and elbow angle of the antibody (Hughes-Jones, 1977; Teeling et al., 2006; Tang et al., 2007).

The diversity in antibody mechanisms of action continues to increase with increasing use of novel design formats, such as bispecific or trispecific antibodies (Wu and Demarest, 2019). Novel design formats and increasingly complex PD warrant new approaches for quantifying antibody-target interactions. Target engagement metrics, beyond fraction of targets engaged, are needed to facilitate rational selection of preclinical antibody therapeutics (Kambayashi et al., 2019).

Target Engagement and Antibody Spatial Distribution

Conventional PK models typically assume uniform drug distribution within a given tissue as well as proportional uptake and loss from the tissue with respect to plasma concentrations. However, antibody distribution within tissues, a process affected by transvascular permeability, local target expression, target affinity, cellular internalization, and the extracellular environment (Eikenes et al., 2004; Thurber et al., 2008a), is known to be very heterogeneous. Within tissue microenvironment, antibody diffusion is related to its size and interaction with other macromolecules and structures (Reiten et al., 2008; Cilliers et al., 2016). The diffusion coefficient of an antibody in solution, without consideration for the environmental architecture, may provide unrealistic expectations for the molecule's ability to traverse a physiological space (Davies Cde et al., 2002). Techniques, such as fluorescence correlation spectroscopy, have been used to explore antibody diffusion and protein-protein interactions in biological matrices (Lagerkvist et al., 2001; Hung et al., 2019). Antibody diffusivity in the body can range from relatively unrestricted (e.g., in plasma) to severely hindered in densely packed physiological spaces (e.g., solid tumors and brain). When

relatively unrestricted, the upper rate limit of diffusion will be rate limiting to the probability of species engagement. In these situations, increasing k_{on} beyond this theoretical rate limit will not increase the probability of species interaction. Engineering efforts should therefore focus on optimizing k_{off} to promote stable target binding.

If the target exists exclusively within densely packed physiological spaces (e.g., tumor microenvironment), only a small fraction of antibody molecules may access the area (Netti et al., 2000; Davies Cde et al., 2002). However, once accessed, the residence time of the molecule may be increased by the restrictive environment, thereby contributing to apparent increases in target affinity (Vauquelin, 2016; Tang and Cao, 2020). The density of extracellular matrices within tumor tissues can also be very heterogeneous creating a diverse landscape surrounding transmembrane targets. (Davies et al., 1997). Distinct microenvironment and high interstitial pressure, in conjunction with antibody target binding characteristics, likely contribute to the spatial heterogeneity of antibody distribution within tumor tissues (Fujimori et al., 1989; Weinstein and Van Osdol, 1992; Flessner et al., 2005; Baker et al., 2008; Tang and Cao, 2020). Accumulation and retention of cetuximab within relatively stroma-rich tissue regions has been shown even after systemic antibody has been eliminated (Tang and Cao, 2020). Heterogeneous distribution of trastuzumab, with higher levels of target-bound drug found in transverse tumor tissue, has also been observed (Baker et al., 2008).

The binding site barrier effect is a widely acknowledged concept in which high-affinity antibodies show strong perivascular distribution within tumor tissues (Fujimori et al., 1989). The theory suggests an inverse relationship between antibody-target affinity and antibody tissue penetration and may result in nonlinear PK behavior through target mediated drug disposition (Mager and Jusko., 2001). In the absence of target saturation, high target density and high affinity binding create a PK sink in which antibody diffusion through the tissue becomes significantly restricted (Weinstein and Van Osdol., 1992). This phenomenon may be exacerbated by bivalent binding, reduced dimensionality, and other factors that promote rebinding events (e.g., cross-arm binding efficiency, high k_{on}, dense microenvironment). Collectively, heterogeneous antibody distribution within tumor tissues could affect treatment outcomes by promoting survival and resistance of unexposed cells.

ANTIBODY-SOUBLE TARGET INTERACTIONS

Biological Fluid Turnover

Targeting soluble, pathologically relevant targets (e.g., TNFα, IL-17, and IL-1β) have been a common strategy for therapeutic antibodies, particularly for treating autoimmune diseases (Hafeez et al., 2018). Soluble targets may exist in the circulation or be largely confined to a pathologically relevant tissue compartment. An important consideration for these targets is the turnover rate of biological fluid within the tissues. Interstitial fluid (ISF) turnover is the efficiency of lymphatic drainage in tissues. Significant variability in ISF turnovers have been shown between tissue types, and the physiological processes underpinning this turnover may be affected by diseases (Petrova and Koh, 2020). ISF turnover affects antibody-target engagement, binding equilibrium, as well as antibody-target complex accumulation (Li et al., 2018). The influence of ISF turnover on target binding kinetics for varying antibodies have been demonstrated previously (Li et al., 2018). This may explain why antibodies that bind the same target with similar affinities demonstrate different degrees of efficacy among disease states (e.g., Crohn's Disease, Rheumatoid Arthritis, and Ankylosing Spondylitis).

When ISF turnover in the diseased tissue is relatively fast, the time for antibodies and targets to engage before being washed away is limited. Maximizing target suppression through lowering k_{off} becomes increasingly challenging because rapid fluid turnover may prevent antibodies from reaching equilibrium with their targets. Tissues with higher ISF turnover rates generally experience more robust target suppression, partly due to greater antibody convections into these tissues (Li et al., 2018). Additionally, this could be, in part, attributable to the efficient removal of antibody-target complexes promoting reaction kinetics toward target suppression and complex formation. In these situations, antibodies with high k_{on} (fast binders) are preferred to promote engagement of as many targets as possible before the species are washed away. Lowering k_{off} beyond the ISF turnover may become futile, and an affinity ceiling exists. Simulations demonstrating the relative efficacy of adalimumab, etanercept, and infliximab on TNF-alpha target suppression under various ISF turnover conditions is shown in **Figure 2**.

When the fluid turnover rate is slow, stable binding antibodies (low k_{off}) demonstrate greater target suppression than fast binders (high k_{on}). However, the reaction equilibrium may shift toward dissociation due to antibody-target complex accumulation (Li et al., 2018). Soluble-target binding antibodies lead to free target suppression but also serve as a target reservoir, protecting it from endogenous degradation and potentially extending plasma half-life. Increasing complex concentrations may promote a shift in reaction equilibrium toward complex dissociation, thereby reducing target suppression efficacy (Ternant et al., 2022). In tissues with slow ISF turnover, such as solid tumors, antibody distribution is also limited due to poor convection (Thurber et al., 2008b). Low distribution and complex accumulation present dual challenges for developing therapeutic antibodies for indications associated with tissues with slow ISF turnover. This may partially explain the lack of success in developing therapeutic antibodies targeting soluble targets in solid tumors, even though several pathologically validated targets exist, such as the transforming growth factor-β (Syed, 2016). Four situations in which fast or stable binders would be preferrable for optimizing target suppression are shown in

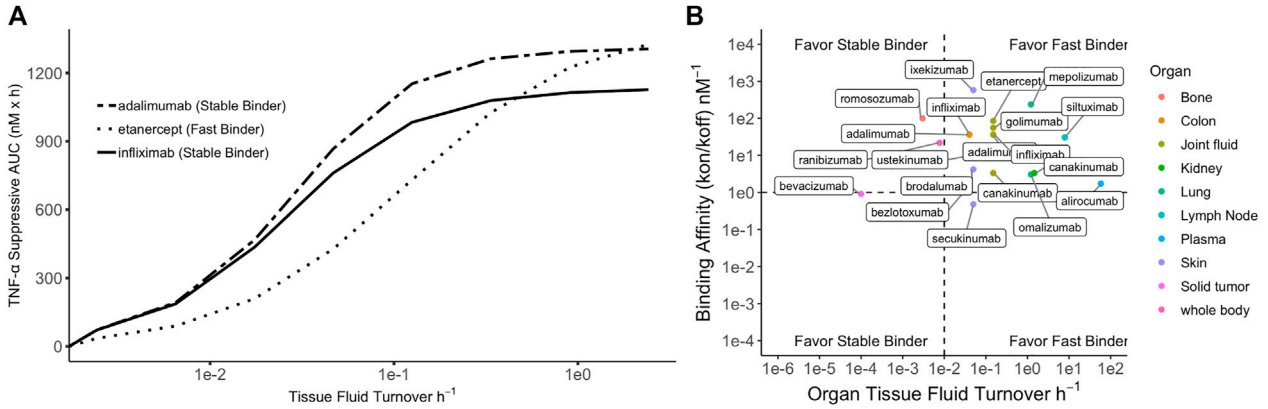

FIGURE 2 | Simulated relationship between tissue fluid turnover and TNF-α suppression by three anti-TNF-α biologics. Simulation was performed using binding constants of each biologic to soluble TNF-a at their therapeutic doses. **(A)** For tissues with low fluid turnover, stable binders are favored but high affinity could contribute to accumulation of antibody-target complex; for tissues with high fluid turnover, fast binders are generally favored but lowering k_{off} beyond fluid turnover rate produces a plateau effect (i.e., affinity ceiling). **(B)** Summary of 27 licensed antibodies (Li et al., 2018) that bind soluble ligands for treatment of various diseases. Four scenarios proposed based on target binding affinity and tissue fluid turnover rate.

Figure 2 and are overlayed with licensed antibodies and the ISF turnover rate of their site of action.

Antibody-CNS Target Engagement

Historically, accessing the central nervous system (CNS) with monoclonal antibodies has been challenging. Antibody concentrations in the cerebrospinal fluid (CSF) and brain ISF are typically on the order of 0.1% of plasma concentrations (Bard et al., 2012; Sevigny et al., 2016; Wang et al., 2018; Gustavsson et al., 2020). Given their poor CNS penetration, antibodies with high target affinity that elicit therapeutic effects at low concentrations are desirable for CNS targets (Tolar et al., 2020). Target selection may be limited if significant target suppression is needed for therapeutic effect. Pathological factors with low baseline levels and slow production rates may be more suitable for targeting when developing antibody therapies for CNS diseases.

Antibody-target engagement in the brain is further complicated by dynamic fluid exchange and a diverse extracellular environment (Cserr, 1988; Sykova and Nicholson, 2008; Brinker et al., 2014). Past estimates for CSF and ISF turnover in the brain are called into question due to the difficulty of measuring solute transport (Brinker et al., 2014). CSF turnover is generally greater than ISF turnover, which may have implications for antibody distribution and target engagement (Brinker et al., 2014). If the target exists predominantly in the ISF, antibody-target complex formation rate may be restricted by complex accumulation promoting reaction kinetics toward dissociation (Li et al., 2018). Furthermore, convective transport of antibodies may be constrained by the convolution of brain interstitial paths. Movement of antibodies inside the brain parenchyma has been estimated to be less than 1 mm per day (Raghavan et al., 2016). Rubenstein et al. observed that after intrathecal administration, rituximab, was cleared from the CSF slower than the rate of bulk flow (Rubenstein et al., 2003). The relatively slow convection rate of antibodies in CSF increases the chances of equilibrium bindings between antibodies and the cognate targets, which may realize the potential of antibodies with high binding affinity. The complexities of fluid transport and macromolecular diffusion within the brain remain largely unresolved.

ANTIBODY-TRANSMEMBRANE TARGET INTERACTIONS

Many therapeutic targets are transmembrane proteins (e.g., EGFR, HER-2, and PD-1). These molecules face spatial and diffusional constraints, unlike soluble targets (Elson et al., 1976; Bell, 1978). The binding intricacies of transmembrane targets create engagement dynamics across time and space significantly more complex than soluble targets, particularly for bivalent antibodies. Bivalent antibody binding to a transmembrane target is a complex, two-step process that cannot be viewed as two independent monovalent steps. For example, dissociation of a bivalently bound antibody is not a first-order process, like monovalent binding. Mathematical modeling of bivalent binding at the cell surface is further complicated by dimensionality reductions, macromolecular diffusivity, antibody cross-arm binding efficiency (Kareva et al., 2018), and cell membrane characteristics.

Cell Line Considerations

An essential consideration for any preclinical model is the validity of the cell line as a representative system for the cell/tissue of interest. This is particularly important in oncology, where each cancer cell phenotype deviates from normal host cells. Association rates between specific antibody-transmembrane targets can vary substantially between cell lines for

therapeutically relevant targets, such as human epidermal growth factor receptor 2 (HER2) and epidermal growth factor receptor (EGFR), by up to an order of magnitude (Bjorkelund et al., 2011; Barta et al., 2012). The disparity in binding characteristics between cell lines may be due to differences in cell surface topology causing variability in k_{on} and k_{off} between antibody and target (Hu et al., 2013). Molecular dynamic simulations suggest the affinity of two-dimensional binding may be inversely related to the relative roughness of the cell surface, presumably due to nanoscale fluctuations in membrane shape causing macromolecular repulsion between the ligand and membrane (Hu et al., 2013). In addition to receptor expression, cell pathophysiology can influence membrane composition and contribute to heterogeneous binding (Nagy et al., 2002; Pereira et al., 2018; Zhang et al., 2019). Notably, increased cholesterol content of some breast cancer cell lines has been shown to decrease membrane fluidity and alter HER2 cell surface distribution and internalization rate (Zhang et al., 2019). When macromolecular diffusion rates at the cell surface are small, as for receptors in a viscous membrane, apparent association and dissociation rates will be reduced (Bell, 1978).

Antibody-Transmembrane Target Binding

When an antibody binds a transmembrane target, the molecule becomes anchored to the membrane creating an effective local concentration of antibody at the cell surface. This regional concentration promotes subsequent interaction with additional targets on the cell surface (Kaufman and Jain, 1992; Pluckthon and Pack., 1997; Kramer and Karpen., 1998; Sengers et al., 2016). This local interaction between antibody-target complex and free target increases the apparent affinity of the interaction and promotes ligand rebinding. Rebinding refers to the propensity for an antibody/antibody-target complex and target to re-associate after dissociation and can contribute to significant affinity alterations, particularly for membrane-bound targets. Rebinding is a highly localized process and can refer to the re-association of primary targets or secondary target binding. In the example above, the apparent association rate of secondary binding events is increased by forced proximity of the target and the free binding arm of the antibody (Sengers et al., 2016). These secondary rebinding events are also related to antibody cross-arm binding efficiency, which measures an antibody free arm's ability to engage targets at suboptimal binding distances (Harms et al., 2014). After initial target binding, the monovalent complex free arm undergoes a dynamic search process for a free target that becomes increasingly operative with greater hinge flexibility and decreasing molecular size. Hinge flexibility governs the arm's propensity to engage targets at suboptimal binding distances, while the size of the molecule contributes to steric interactions and diffusivity on the membrane (De Michele et al., 2016; Sengers et al., 2016). Inclusion of a cross-arm binding efficiency parameter in preclinical models incorporates two phenomena: antibody-target complex adhered to the cell surface are restricted to a quasi-two-dimensional space, and free-arm binding is limited by rotational, torsional, and bending freedom of the antibody hinge region (Harms et al., 2014). This parameter has been suggested to be useful for rational selection of preclinical candidates (Harms et al., 2014).

Translational and rotational diffusion in two dimensions has been shown to differ greatly compared to three-dimensional diffusion (Saffman and Delbruck, 1975), thus in the event of dissociation, the two species are likely to interact again. In densely packed tissues, such as tumor microenvironments, diffusion of dissociated antibodies away from the target on the cell surface can be inhibited, promoting primary antibody rebinding events (Vauquelin, 2016). The surrounding extracellular matrix may similarly influence k_{on} and k_{off} (Morgan et al., 1998). Hindering the free three-dimensional diffusion of antibodies away from the cell surface results in prolonged "apparent" target occupancy and rebinding propensity may be directly related to the k_{on} of the interaction (Vauquelin, 2016). In microenvironment that promote target rebinding, increasing k_{on} can influence target occupancy similarly to decreasing k_{off}, providing increased flexibility for antibody engineering strategies. Historically, structural antibody engineering to increase k_{on} has been more challenging relative to reducing k_{off}. Although difficult, structural modifications to both the antibody-target binding domain and non-binding regions have been used to increase the association rate of antibodies or peptides to their target by order of magnitude or more (Fukunaga and Tsumoto., 2013; Muguruma et al., 2019).

IMPORTANCE OF MONOVALENT-BIVALENT BINDING MODES

Bivalent Binding-Concentration Relationships

The predominant binding mode (i.e., monovalent vs. bivalent) is critical to overall antibody selectivity, distribution, and effector function. The relative concentrations of antibodies and targets critically influence the likelihood of bivalent binding (Zuckier et al., 2000). When target density on the cell membrane is sufficient for antibodies to engage multiple targets, the proportion of bivalently bound antibodies is likely to increase with increasing target density (Zuckier et al., 2000), assuming uniform target distribution on the cell surface, which is not always the case (Wehrman et al., 2006; Byrne et al., 2020). Similarly, when antibody concentrations are low relative to the target, most target molecules on the cell surface are unoccupied and available for antibody binding, assuming little competition from endogenous ligand. A high proportion of antibodies at the cell surface will be bivalently bound under these conditions. In contrast, monovalent bound antibodies will become increasingly prevalent at relatively high antibody concentrations, as antibodies must compete for the free target. These conditions favor monovalent binding and diminishing increases in bivalent engagement with increasing antibody concentration. De Michele et al., suggest antibody size also plays a role in promoting bivalent binding by keeping neighboring molecules at a distance through steric interactions thus ensuring targets within reach of the antibody's free arm are unoccupied (De Michele et al., 2016).

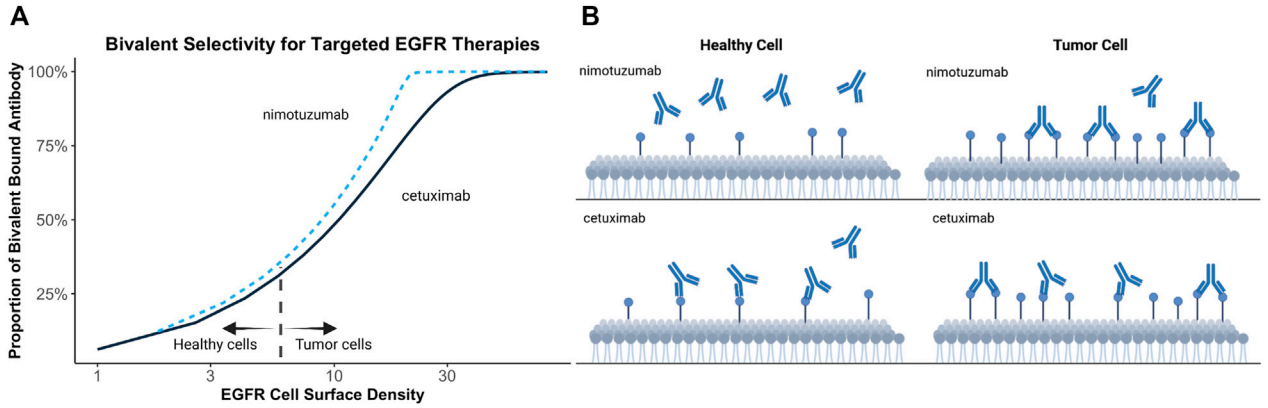

FIGURE 3 | Simulated relationship between target expression and bivalent selectivity. **(A)** Simulation of select EGFR targeted therapies, nimotuzumab ($K_D = 2.1 \times 10^{-8}$ mol/L; $k_{on} = 5.2 \times 10^4$ (s mol/L)$^{-1}$; $k_{off} = 1.1 \times 10^{-3}$ s^{-1}) and cetuximab ($K_D = 1.8 \times 10^{-9}$ mol/L; $k_{on} = 3.1 \times 10^6$ (s mol/L)$^{-1}$; $k_{off} = 5.8 \times 10^{-3}$ s^{-1}) between EGFR expression and maximum proportion of bivalent complex formed. **(B)** Low affinity of nimotuzumab relative to cetuximab prevents accumulation of antibody on healthy cells. Increasing target density promotes bivalent binding and retention of antibody on tumor cells.

Work by Bondza et al. demonstrates the influence of free antibody concentration on bivalent binding stability (Bondza et al., 2020). Increasing free antibody concentrations contribute to an increased apparent k_{off}, (i.e., reduced binding stability) for monovalent-bound complexes because bivalent binding events must compete with free antibodies for unoccupied targets. In their study, the apparent k_{off} for both rituximab and obinutuzumab differed approximately threefold in tested concentration ranges despite similar antibody affinities. The authors posited that obinutuzumab's increased k_{off}, relative to rituximab, led to more dynamic bivalent target binding than for rituximab, demonstrating an important point: antibodies with similar affinities can display significant differences in their predominant binding mode depending on the relative magnitude of their k_{on} and k_{off}. The implications for these concentration-binding-mode relationships are varying bivalent-monovalent ratios of bound antibody on cells/tissues depending on the relative concentration of antibody and target and antibody-target binding characteristics. If bivalent binding stability is advantageous, engineered reductions in k_{off} may be used to promote increased bivalent binding.

Bivalent Binding and Antibody Selectivity

Bivalent binding can be leveraged to facilitate antibody selectivity for cells upregulating therapeutic targets. Increasing antibody k_{off} has been recognized as a strategy to promote selective binding to cells upregulating targets, such as HER2 (Slaga et al., 2018). Bivalent binding on disease-associated tissue is promoted by increased target density, avoiding exceedingly high local antibody concentrations, improved cross-arm binding efficiency, and a rebinding-promoting microenvironment. Increased selectivity for disease-associated cells, has also been proposed to explain the differing toxicity profiles of targeted EGFR therapies (Garrido et al., 2011). EGFR is commonly upregulated in human epithelial cancers and is present in healthy tissues (London and Gallo, 2020). Targeted EGFR therapies often demonstrate toxicity associated with on-target off-tumor target binding (Lacouture, 2006; Izzedine et al., 2010). Garrido et al. postulated that nimotuzumab demonstrates a reduced adverse effect profile relative to other EGFR-targeting therapies, such as cetuximab, due to its intermediate affinity for EGFR (Garrido et al., 2011). Monovalent binding of nimotuzumab was prevalent but not efficient to elicit pharmacological actions in cells with low EGFR expressions. Conversely, monovalent cetuximab binding was efficient to trigger pharmacological actions at all examined EGFR densities. This theory may explain why a ten-fold reduction in EGFR affinity of nimotuzumab compared to cetuximab leads to selective binding in tumor tissue while sparing healthy tissues, thereby reducing adverse effects (Garrido et al., 2011). Simulations in **Figure 3** demonstrate the relationship between kinetic rate constants and antibody selectivity for select EGFR targeted therapies, cetuximab and nimotuzumab. The steep slope of nimotuzumab with increasing cell surface target density in **Figure 3** demonstrates a sharply increasing proportion of bivalent bound antibody with increasing target concentrations due to an intermediate affinity promoting greater selectivity.

Bispecific Antibodies

As of January 2022, only four bispecific antibody (BsA) products have been approved. However, over 85 bispecific agents were in clinical development in 2019 (Labrijn et al., 2019) suggesting a potential influx of BsA formats in coming years. BsA can be used to bind two targets on the same cell (cis-) or different cells (trans-, i.e., bridge two cells). The ability of BsA to modulate multiple targets may prove advantageous for addressing multifactorial diseases, such as cancer, where target pathway dysregulation, upregulation of alternative pathways, and crosstalk between pathways can lead to treatment resistance (Wu et al., 2015; Thakur et al., 2018). For targets on the same cell, much of the antibody-transmembrane interaction material above applies to BsA; however, antibody affinity must be optimized concerning two targets (Staflin et al., 2020). When density of the therapeutic target is low, an anchoring strategy may be used if other ligands

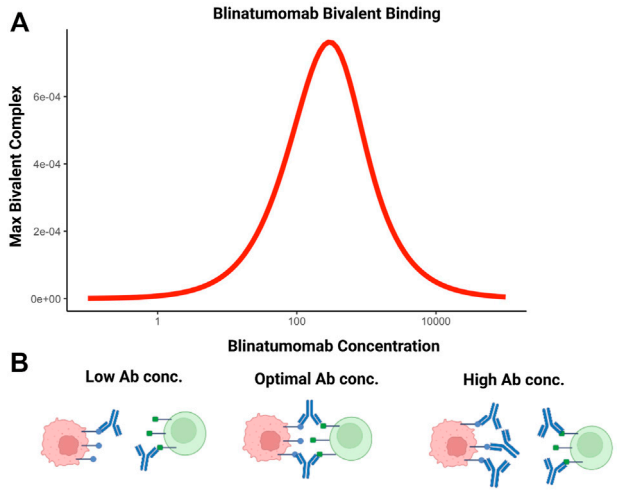

FIGURE 4 | The bell-shaped concentration-effect curves for bispecific T-cell engaging antibodies. **(A)** Simulated relationship between blinatumomab concentration and maximum amount of bivalent complex formed. **(B)** At suboptimal concentrations of bispecific antibodies, bivalent complex formation is limited by the number of bispecific molecules. At optimal concentrations, the number of bivalent complexes formed is maximized. Above the optimal concentration range, target saturation leads to inefficient crosslinking and bivalent complex formation is limited. This condition reduces cell-cell engagement and, potentially, therapeutic efficacy.

on the cell surface are highly expressed relative to the target. Antibody selectivity can be increased up to 100-fold (Harms et al., 2014) through this strategy if relative concentration conditions between the two targets are met. When expressed in equal proportions, or the anchor target is under-expressed relative to therapeutic target, a bispecific anchor strategy provides only slight advantage over two monoclonal antibodies (Harms et al., 2014). Provided concentration conditions are met, this strategy can improve the selectivity and specificity of the antibody for disease-specific cells, thereby reducing on-target off-site adverse effects. Grugan et al. demonstrate use of an anti-EGFR/c-Met BsA, amivantamab, toward modulating multiple cell surface targets and show binding of one of the two targets is critical to Fc effector function engagement (Grugan et al., 2017).

BsA can also be used to facilitate cell-cell interactions. For example, blinatumomab, the first in class bispecific T-cell engager molecule is used to promote interaction between T cells and CD19-expressing tumor cells (Einsele et al., 2020). Efficacy of this molecule is based on maximizing the number of bivalent bound complexes; achieved through optimal antibody concentration. The relationship between maximum number of bivalent complexes and increasing antibody concentration is demonstrated by a bell-shape (Betts et al., 2019; Schropp et al., 2019). This phenomenon is attributable to target saturation at higher antibody concentrations. Increasing monovalent complexes compete for targets available for crosslinking, interfering with bivalent complex formation and is depicted in **Figure 4**.

When used to mediate a bridging strategy between a ligand and receptor attached to cell surfaces, the reaction kinetics will be much different compared to the two species in solution. In this situation, bivalent binding rates are not reflective of interaction affinities, but more generally, the relative rates of cross-linking and intercellular encounter since only adjacent cells can facilitate bivalent binding. Mathematical modeling and experimental interpretation of these reactions is complicated by quantifying the likelihood of cell-cell interaction and potential for additional molecular interactions (e.g., carbohydrates, lectins) between cells contributing to bond avidity (Bell, 1978).

CONCLUSION

The number of antibodies and other protein-based therapeutics on the market is increasing rapidly (Kaplon et al., 2020). Despite improved success rates relative to small molecule drugs, the full potential of these molecules will be further realized through rigorous characterization of their *in vivo* target engagement. Additionally, identifying lead drug candidates with optimal target engagement within the tissue/cellular context is paramount to minimizing futile resource allocation in drug development programs. Extensive evidence indicates that the engagement dynamics for antibody-target interactions in living systems differ considerably from that observed *in vitro*. Insight into how the native microenvironment and local physiology influence antibody-target interactions could improve preclinical evaluation, lead optimization, and translation of preclinical candidates to clinical development. Notable takeaways from this work include 1) SPR technologies can serve as a rational basis for antibody screening, but affinity estimates should be used with caution in modeling and simulations depicting target engagement; 2) implementation of local tissue/cellular microenvironment and physiology in preclinical antibody-target engagement models could improve our understanding of *in vivo* antibody-target interactions; 3) antibody physical characteristics, microenvironment, and antibody-target interactions influence the predominant antibody binding mode and can be leveraged to modulate antibody selectivity, distribution, and effector function. Here we briefly reviewed how the interplay between physiological factors and the kinetics of association/dissociation for an antibody-target interaction can influence their engagement *in vivo*. We hope to draw attention to the knowledge gap surrounding the characterization of antibody-target interactions in living systems and demonstrate the relevance of this information to preclinical candidate selection and optimization processes.

AUTHOR CONTRIBUTIONS

Conceptualization YC; investigation and analysis TD and YC; writing-original draft preparation TD; writing-review and editing YC; supervision YC; funding acquisition YC. All authors have read and agreed to the published version of the manuscript.

FUNDING

This study was funded by National Institute of Health (GM119661).

REFERENCES

Abboud, N., Chow, S. K., Saylor, C., Janda, A., Ravetch, J. V., Scharff, M. D., et al. (2010). A Requirement for FcγR in Antibody-Mediated Bacterial Toxin Neutralization. *J. Exp. Med.* 207, 2395–2405. doi:10.1084/jem.20100995

Arrhenius, S. (1889). Über die Reaktionsgeschwindigkeit bei der Inversion von Rohrzucker durch Säuren. *Z. Phys. Chem. (Leipzig)* 4U, 226–248. doi:10.1515/zpch-1889-0416

Baker, J. H., Lindquist, K. E., Huxham, L. A., Kyle, A. H., Sy, J. T., and Minchinton, A. I. (2008). Direct Visualization of Heterogeneous Extravascular Distribution of Trastuzumab in Human Epidermal Growth Factor Receptor Type 2 Overexpressing Xenografts. *Clin. Cancer Res.* 14, 2171–2179. doi:10.1158/1078-0432.CCR-07-4465

Bard, F., Fox, M., Friedrich, S., Seubert, P., Schenk, D., Kinney, G. G., et al. (2012). Sustained Levels of Antibodies against Aβ in Amyloid-Rich Regions of the CNS Following Intravenous Dosing in Human APP Transgenic Mice. *Exp. Neurol.* 238, 38–43. doi:10.1016/j.expneurol.2012.07.022

Barta, P., Malmberg, J., Melicharova, L., Strandgård, J., Orlova, A., Tolmachev, V., et al. (2012). Protein Interactions with HER-Family Receptors Can Have Different Characteristics Depending on the Hosting Cell Line. *Int. J. Oncol.* 40, 1677–1682. doi:10.3892/ijo.2011.1307

Bell, G. I. (1978). Models for the Specific Adhesion of Cells to Cells. *Science* 200, 618–627. doi:10.1126/science.347575

Berkers, J. A., Van Bergen En Henegouwen, P. P., and Boonstra, J. (1992). The Effects of Receptor Density and Cell Shape on Epidermal Growth Factor Binding. *J. Recept Res.* 12, 71–100. doi:10.3109/10799899209066025

Betts, A., Haddish-Berhane, N., Shah, D. K., Van Der Graaf, P. H., Barletta, F., King, L., et al. (2019). Correction to: A Translational Quantitative Systems Pharmacology Model for CD3 Bispecific Molecules: Application to Quantify T Cell-Mediated Tumor Cell Killing by P-Cadherin LP DART®. *Aaps j* 21, 73. doi:10.1208/s12248-019-0348-4

Birrer, M. J., Moore, K. N., Betella, I., and Bates, R. C. (2019). Antibody-Drug Conjugate-Based Therapeutics: State of the Science. *J. Natl. Cancer Inst.* 111, 538–549. doi:10.1093/jnci/djz035

Björkelund, H., Gedda, L., and Andersson, K. (2011). Comparing the Epidermal Growth Factor Interaction with Four Different Cell Lines: Intriguing Effects Imply strong Dependency of Cellular Context. *PLoS One* 6, e16536. doi:10.1371/journal.pone.0016536

Bondza, S., Ten Broeke, T., Nestor, M., Leusen, J. H. W., and Buijs, J. (2020). Bivalent Binding on Cells Varies between Anti-CD20 Antibodies and Is Dose-dependent. *MAbs* 12, 1792673. doi:10.1080/19420862.2020.1792673

Bournazos, S., Klein, F., Pietzsch, J., Seaman, M. S., Nussenzweig, M. C., and Ravetch, J. V. (2014). Broadly Neutralizing Anti-HIV-1 Antibodies Require Fc Effector Functions for *In Vivo* Activity. *Cell* 158, 1243–1253. doi:10.1016/j.cell.2014.08.023

Brinker, T., Stopa, E., Morrison, J., and Klinge, P. (2014). A New Look at Cerebrospinal Fluid Circulation. *Fluids Barriers CNS* 11, 10. doi:10.1186/2045-8118-11-10

Buchwald, P. (2019). A Receptor Model with Binding Affinity, Activation Efficacy, and Signal Amplification Parameters for Complex Fractional Response versus Occupancy Data. *Front. Pharmacol.* 10, 605. doi:10.3389/fphar.2019.00605

Byrne, P. O., Hristova, K., and Leahy, D. J. (2020). EGFR Forms Ligand-independent Oligomers that Are Distinct from the Active State. *J. Biol. Chem.* 295, 13353–13362. doi:10.1074/jbc.RA120.012852

Cao, Y., Balthasar, J. P., and Jusko, W. J. (2013). Second-generation Minimal Physiologically-Based Pharmacokinetic Model for Monoclonal Antibodies. *J. Pharmacokinet. Pharmacodyn* 40 (5), 597–607. doi:10.1007/s10928-013-9332-2

Cao, Y., and Jusko, W. J. (2014). Incorporating Target-Mediated Drug Disposition in a Minimal Physiologically-Based Pharmacokinetic Model for Monoclonal Antibodies. *J. Pharmacokinet. Pharmacodyn* 41 (4), 375–387. doi:10.1007/s10928-014-9372-2

Chiu, M. L., Goulet, D. R., Teplyakov, A., and Gilliland, G. L. (2019). Antibody Structure and Function: The Basis for Engineering Therapeutics. *Antibodies* 8, 55. doi:10.3390/antib8040055

Cilliers, C., Guo, H., Liao, J., Christodolu, N., and Thurber, G. M. (2016). Multiscale Modeling of Antibody-Drug Conjugates: Connecting Tissue and Cellular Distribution to Whole Animal Pharmacokinetics and Potential Implications for Efficacy. *Aaps j* 18, 1117–1130. doi:10.1208/s12248-016-9940-z

Coombs, D., and Goldstein, B. (2004). Effects of the Geometry of the Immunological Synapse on the Delivery of Effector Molecules. *Biophys. J.* 87, 2215–2220. doi:10.1529/biophysj.104.045674

Cragg, M. S., Morgan, S. M., Chan, H. T., Morgan, B. P., Filatov, A. V., Johnson, P. W., et al. (2003). Complement-mediated Lysis by Anti-CD20 mAb Correlates with Segregation into Lipid Rafts. *Blood* 101, 1045–1052. doi:10.1182/blood-2002-06-1761

Cserr, H. F. (1988). Role of Secretion and Bulk Flow of Brain Interstitial Fluid in Brain Volume Regulation. *Ann. N y Acad. Sci.* 529, 9–20. doi:10.1111/j.1749-6632.1988.tb51415.x

Davies, C. D., Müller, H., Hagen, I., Gårseth, M., and Hjelstuen, M. H. (1997). Comparison of Extracellular Matrix in Human Osteosarcomas and Melanomas Growing as Xenografts, Multicellular Spheroids, and Monolayer Cultures. *Anticancer Res.* 17, 4317–4326.

Davies, Cde. L., Berk, D. A., Pluen, A., and Jain, R. K. (2002). Comparison of IgG Diffusion and Extracellular Matrix Composition in Rhabdomyosarcomas Grown in Mice versus *In Vitro* as Spheroids Reveals the Role of Host Stromal Cells. *Br. J. Cancer* 86, 1639–1644. doi:10.1038/sj.bjc.6600270

De Michele, C., De Los Rios, P., Foffi, G., and Piazza, F. (2016). Simulation and Theory of Antibody Binding to Crowded Antigen-Covered Surfaces. *Plos Comput. Biol.* 12, e1004752. doi:10.1371/journal.pcbi.1004752

Diebolder, C. A., Beurskens, F. J., De Jong, R. N., Koning, R. I., Strumane, K., Lindorfer, M. A., et al. (2014). Complement Is Activated by IgG Hexamers Assembled at the Cell Surface. *Science* 343, 1260–1263. doi:10.1126/science.1248943

Eikenes, L., Bruland, Ø. S., Brekken, C., and Davies, Cde. L. (2004). Collagenase Increases the Transcapillary Pressure Gradient and Improves the Uptake and Distribution of Monoclonal Antibodies in Human Osteosarcoma Xenografts. *Cancer Res.* 64, 4768–4773. doi:10.1158/0008-5472.CAN-03-1472

Einsele, H., Borghaei, H., Orlowski, R. Z., Subklewe, M., Roboz, G. J., Zugmaier, G., et al. (2020). The BiTE (Bispecific T-Cell Engager) Platform: Development and Future Potential of a Targeted Immuno-Oncology Therapy across Tumor Types. *Cancer* 126, 3192–3201. doi:10.1002/cncr.32909

Elson, E. L., Schlessinger, J., Koppel, D. E., Axelrod, D., and Webb, W. W. (1976). Measurement of Lateral Transport on Cell Surfaces. *Prog. Clin. Biol. Res.* 9, 137–147.

Erlendsson, S., and Teilum, K. (2020). Binding Revisited-Avidity in Cellular Function and Signaling. *Front. Mol. Biosci.* 7, 615565. doi:10.3389/fmolb.2020.615565

Eyring, H. (1935). The Activated Complex in Chemical Reactions. *J. Chem. Phys.* 3, 107–115. doi:10.1063/1.1749604

Flessner, M. F., Choi, J., Credit, K., Deverkadra, R., and Henderson, K. (2005). Resistance of Tumor Interstitial Pressure to the Penetration of Intraperitoneally Delivered Antibodies into Metastatic Ovarian Tumors. *Clin. Cancer Res.* 11, 3117–3125. doi:10.1158/1078-0432.CCR-04-2332

Fujimori, K., Covell, D. G., Fletcher, J. E., and Weinstein, J. N. (1989). Modeling Analysis of the Global and Microscopic Distribution of Immunoglobulin G, F(ab')2, and Fab in Tumors. *Cancer Res.* 49, 5656–5663.

Fukunaga, A., and Tsumoto, K. (2013). Improving the Affinity of an Antibody for its Antigen via Long-Range Electrostatic Interactions. *Protein Eng. Des. Sel* 26 (12), 773–780. doi:10.1093/protein/gzt053

Garrido, G., Tikhomirov, I. A., Rabasa, A., Yang, E., Gracia, E., Iznaga, N., et al. (2011). Bivalent Binding by Intermediate Affinity of Nimotuzumab: a Contribution to Explain Antibody Clinical Profile. *Cancer Biol. Ther.* 11, 373–382. doi:10.4161/cbt.11.4.14097

Grugan, K. D., Dorn, K., Jarantow, S. W., Bushey, B. S., Pardinas, J. R., Laquerre, S., et al. (2017). Fc-mediated Activity of EGFR X C-Met Bispecific Antibody JNJ-61186372 Enhanced Killing of Lung Cancer Cells. *MAbs* 9, 114–126. doi:10.1080/19420862.2016.1249079

Gustavsson, T., Syvänen, S., O'callaghan, P., and Sehlin, D. (2020). SPECT Imaging of Distribution and Retention of a Brain-Penetrating Bispecific Amyloid-β Antibody in a Mouse Model of Alzheimer's Disease. *Transl Neurodegener* 9, 37. doi:10.1186/s40035-020-00214-1

Hafeez, U., Gan, H. K., and Scott, A. M. (2018). Monoclonal Antibodies as Immunomodulatory Therapy against Cancer and Autoimmune Diseases. *Curr. Opin. Pharmacol.* 41, 114–121. doi:10.1016/j.coph.2018.05.010

Harms, B. D., Kearns, J. D., Iadevaia, S., and Lugovskoy, A. A. (2014). Understanding the Role of Cross-Arm Binding Efficiency in the Activity of Monoclonal and Multispecific Therapeutic Antibodies. *Methods* 65, 95–104. doi:10.1016/j.ymeth.2013.07.017

Hill, A. V. (1909). The Mode of Action of Nicotine and Curari, Determined by the Form of the Contraction Curve and the Method of Temperature Coefficients. *J. Physiol.* 39, 361–373. doi:10.1113/jphysiol.1909.sp001344

Hu, J., Lipowsky, R., and Weikl, T. R. (2013). Binding Constants of Membrane-Anchored Receptors and Ligands Depend Strongly on the Nanoscale Roughness of Membranes. *Proc. Natl. Acad. Sci. U S A.* 110, 15283–15288. doi:10.1073/pnas.1305766110

Hughes-Jones, N. C. (1977). Functional Affinity Constants of the Reaction between 125I-Labelled C1q and C1q Binders and Their Use in the Measurement of Plasma C1q Concentrations. *Immunology* 32, 191–198.

Hung, J. J., Zeno, W. F., Chowdhury, A. A., Dear, B. J., Ramachandran, K., Nieto, M. P., et al. (2019). Self-diffusion of a Highly Concentrated Monoclonal Antibody by Fluorescence Correlation Spectroscopy: Insight into Protein-Protein Interactions and Self-Association. *Soft matter* 15 (33), 6660–6676. doi:10.1039/c9sm01071h

Izzedine, H., Bahleda, R., Khayat, D., Massard, C., Magné, N., Spano, J. P., et al. (2010). Electrolyte Disorders Related to EGFR-Targeting Drugs. *Crit. Rev. Oncol. Hematol.* 73, 213–219. doi:10.1016/j.critrevonc.2009.03.012

Jarmoskaite, I., Alsadhan, I., Vaidyanathan, P. P., and Herschlag, D. (2020). How to Measure and Evaluate Binding Affinities. *Elife* 9. doi:10.7554/eLife.57264

Kambayashi, Y., Fujimura, T., Hidaka, T., and Aiba, S. (2019). Biomarkers for Predicting Efficacies of Anti-PD1 Antibodies. *Front. Med. (Lausanne)* 6, 174. doi:10.3389/fmed.2019.00174

Kaplon, H., Muralidharan, M., Schneider, Z., and Reichert, J. M. (2020). Antibodies to Watch in 2020. *MAbs* 12, 1703531. doi:10.1080/19420862.2019.1703531

Kaplon, H., and Reichert, J. M. (2019). Antibodies to Watch in 2019. *MAbs* 11, 219–238. doi:10.1080/19420862.2018.1556465

Kareva, I., Zutshi, A., and Kabilan, S. (2018). Guiding Principles for Mechanistic Modeling of Bispecific Antibodies. *Prog. Biophys. Mol. Biol.* 139, 59–72. doi:10.1016/j.pbiomolbio.2018.08.011

Kaufman, E. N., and Jain, R. K. (1992). Effect of Bivalent Interaction upon Apparent Antibody Affinity: Experimental Confirmation of Theory Using Fluorescence Photobleaching and Implications for Antibody Binding Assays. *Cancer Res.* 52, 4157–4167.

Kramer, R. H., and Karpen, J. W. (1998). Spanning Binding Sites on Allosteric Proteins with Polymer-Linked Ligand Dimers. *Nature* 395, 710–713. doi:10.1038/27227

Lacouture, M. E. (2006). Mechanisms of Cutaneous Toxicities to EGFR Inhibitors. *Nat. Rev. Cancer* 6, 803–812. doi:10.1038/nrc1970

Lagerkvist, A. C., Földes-Papp, Z., Persson, M. A., and Rigler, R. (2001). Fluorescence Correlation Spectroscopy as a Method for Assessment of Interactions between Phage Displaying Antibodies and Soluble Antigen. *Protein Sci.* 10 (8), 1522–1528. doi:10.1110/ps.5701

Li, X., Jusko, W. J., and Cao, Y. (2018). Role of Interstitial Fluid Turnover on Target Suppression by Therapeutic Biologics Using a Minimal Physiologically Based Pharmacokinetic Model. *J. Pharmacol. Exp. Ther.* 367, 1–8. doi:10.1124/jpet.118.250134

London, M., and Gallo, E. (2020). Epidermal Growth Factor Receptor (EGFR) Involvement in Epithelial-Derived Cancers and its Current Antibody-Based Immunotherapies. *Cell Biol Int* 44, 1267–1282. doi:10.1002/cbin.11340

Lux, A., Yu, X., Scanlan, C. N., and Nimmerjahn, F. (2013). Impact of Immune Complex Size and Glycosylation on IgG Binding to Human FcγRs. *J. Immunol.* 190, 4315–4323. doi:10.4049/jimmunol.1200501

Mager, D. E., and Jusko, W. J. (2001). General Pharmacokinetic Model for Drugs Exhibiting Target-Mediated Drug Disposition. *J. Pharmacokinet. Pharmacodyn* 28 (6), 507–532. doi:10.1023/a:1014414520282

Maloney, D. G. (2005). Concepts in Radiotherapy and Immunotherapy: Anti-CD20 Mechanisms of Action and Targets. *Semin. Oncol.* 32, S19–S26. doi:10.1053/j.seminoncol.2005.01.010

Meyer, S., Leusen, J. H., and Boross, P. (2014). Regulation of Complement and Modulation of its Activity in Monoclonal Antibody Therapy of Cancer. *MAbs* 6, 1133–1144. doi:10.4161/mabs.29670

Morgan, C. L., Newman, D. J., Burrin, J. M., and Price, C. P. (1998). The Matrix Effects on Kinetic Rate Constants of Antibody-Antigen Interactions Reflect Solvent Viscosity. *J. Immunol. Methods* 217, 51–60. doi:10.1016/s0022-1759(98)00092-1

Mosqueira, A., Camino, P. A., and Barrantes, F. J. (2020). Antibody-induced Crosslinking and Cholesterol-Sensitive, Anomalous Diffusion of Nicotinic Acetylcholine Receptors. *J. Neurochem.* 152, 663–674. doi:10.1111/jnc.14905

Moulard, M., and Ozoux, M. L. (2016). How Validated Receptor Occupancy Flow Cytometry Assays Can Impact Decisions and Support Drug Development. *Cytometry B Clin. Cytom* 90, 150–158. doi:10.1002/cyto.b.21320

Muguruma, K., Fujita, K., Fukuda, A., Kishimoto, S., Sakamoto, S., Arima, R., et al. (2019). Kinetics-Based Structural Requirements of Human Immunoglobulin G Binding Peptides. *ACS omega* 4 (11), 14390–14397. doi:10.1021/acsomega.9b01104

Mullard, A. (2021). FDA Approves 100th Monoclonal Antibody Product. *Nat. Rev. Drug Discov.* 20, 491–495. doi:10.1038/d41573-021-00079-7

Nagy, P., Vereb, G., Sebestyén, Z., Horváth, G., Lockett, S. J., Damjanovich, S., et al. (2002). Lipid Rafts and the Local Density of ErbB Proteins Influence the Biological Role of Homo- and Heteroassociations of ErbB2. *J. Cel Sci* 115, 4251–4262. doi:10.1242/jcs.00118

Netti, P. A., Berk, D. A., Swartz, M. A., Grodzinsky, A. J., and Jain, R. K. (2000). Role of Extracellular Matrix Assembly in Interstitial Transport in Solid Tumors. *Cancer Res.* 60, 2497–2503.

Olaru, A., Bala, C., Jaffrezic-Renault, N., and Aboul-Enein, H. Y. (2015). Surface Plasmon Resonance (SPR) Biosensors in Pharmaceutical Analysis. *Crit. Rev. Anal. Chem.* 45, 97–105. doi:10.1080/10408347.2014.881250

Pereira, P. M. R., Sharma, S. K., Carter, L. M., Edwards, K. J., Pourat, J., Ragupathi, A., et al. (2018). Caveolin-1 Mediates Cellular Distribution of HER2 and Affects Trastuzumab Binding and Therapeutic Efficacy. *Nat. Commun.* 9, 5137. doi:10.1038/s41467-018-07608-w

Petrova, T. V., and Koh, G. Y. (2020). Biological Functions of Lymphatic Vessels. *Science* 369. doi:10.1126/science.aax4063

Pierson, T. C., Xu, Q., Nelson, S., Oliphant, T., Nybakken, G. E., Fremont, D. H., et al. (2007). The Stoichiometry of Antibody-Mediated Neutralization and Enhancement of West Nile Virus Infection. *Cell Host Microbe* 1, 135–145. doi:10.1016/j.chom.2007.03.002

Plückthun, A., and Pack, P. (1997). New Protein Engineering Approaches to Multivalent and Bispecific Antibody Fragments. *Immunotechnology* 3, 83–105. doi:10.1016/s1380-2933(97)00067-5

Raghavan, R., Brady, M. L., Rodríguez-Ponce, M. I., Hartlep, A., Pedain, C., and Sampson, J. H. (2006). Convection-enhanced Delivery of Therapeutics for Brain Disease, and its Optimization. *Neurosurg. Focus* 20, E12. doi:10.3171/foc.2006.20.4.7

Reitan, N. K., Juthajan, A., Lindmo, T., and De Lange Davies, C. (2008). Macromolecular Diffusion in the Extracellular Matrix Measured by Fluorescence Correlation Spectroscopy. *J. Biomed. Opt.* 13, 054040. doi:10.1117/1.2982530

Reverberi, R., and Reverberi, L. (2007). Factors Affecting the Antigen-Antibody Reaction. *Blood Transfus.* 5, 227–240. doi:10.2450/2007.0047-07

Rougé, L., Chiang, N., Steffek, M., Kugel, C., Croll, T. I., Tam, C., et al. (2020). Structure of CD20 in Complex with the Therapeutic Monoclonal Antibody Rituximab. *Science* 367 (6483), 1224–1230. doi:10.1126/science.aaz9356

Rubenstein, J. L., Combs, D., Rosenberg, J., Levy, A., Mcdermott, M., Damon, L., et al. (2003). Rituximab Therapy for CNS Lymphomas: Targeting the Leptomeningeal Compartment. *Blood* 101, 466–468. doi:10.1182/blood-2002-06-1636

Saffman, P. G., and Delbrück, M. (1975). Brownian Motion in Biological Membranes. *Proc. Natl. Acad. Sci. U S A.* 72, 3111–3113. doi:10.1073/pnas.72.8.3111

Schropp, J., Khot, A., Shah, D. K., and Koch, G. (2019). Target-Mediated Drug Disposition Model for Bispecific Antibodies: Properties, Approximation, and Optimal Dosing Strategy. *CPT Pharmacometrics Syst. Pharmacol.* 8, 177–187. doi:10.1002/psp4.12369

Schuck, P., and Zhao, H. (2010). The Role of Mass Transport Limitation and Surface Heterogeneity in the Biophysical Characterization of Macromolecular Binding Processes by SPR Biosensing. *Methods Mol. Biol.* 627, 15–54. doi:10.1007/978-1-60761-670-2_2

Sengers, B. G., Mcginty, S., Nouri, F. Z., Argungu, M., Hawkins, E., Hadji, A., et al. (2016). Modeling Bispecific Monoclonal Antibody Interaction with

Two Cell Membrane Targets Indicates the Importance of Surface Diffusion. *MAbs* 8, 905–915. doi:10.1080/19420862.2016.1178437

Sevigny, J., Chiao, P., Bussière, T., Weinreb, P. H., Williams, L., Maier, M., et al. (2016). The Antibody Aducanumab Reduces Aβ Plaques in Alzheimer's Disease. *Nature* 537, 50–56. doi:10.1038/nature19323

Sharkey, R. M., Gold, D. V., Aninipot, R., Vagg, R., Ballance, C., Newman, E. S., et al. (1990). Comparison of Tumor Targeting in Nude Mice by Murine Monoclonal Antibodies Directed against Different Human Colorectal Cancer Antigens. *Cancer Res.* 50, 828s–834s.

Shockley, T. R., Lin, K., Sung, C., Nagy, J. A., Tompkins, R. G., Dedrick, R. L., et al. (1992). A Quantitative Analysis of Tumor Specific Monoclonal Antibody Uptake by Human Melanoma Xenografts: Effects of Antibody Immunological Properties and Tumor Antigen Expression Levels. *Cancer Res.* 52, 357–366.

Slaga, D., Ellerman, D., Lombana, T. N., Vij, R., Li, J., Hristopoulos, M., et al. (2018). Avidity-based Binding to HER2 Results in Selective Killing of HER2-Overexpressing Cells by Anti-her2/cd3. *Sci. Transl Med.* 10, 5775. doi:10.1126/scitranslmed.aat5775

Staflin, K., Zuch De Zafra, C. L., Schutt, L. K., Clark, V., Zhong, F., Hristopoulos, M., et al. (2020). Target Arm Affinities Determine Preclinical Efficacy and Safety of Anti-her2/cd3 Bispecific Antibody. *JCI Insight* 5, 757. doi:10.1172/jci.insight.133757

Strasser, J., De Jong, R. N., Beurskens, F. J., Wang, G., Heck, A. J. R., Schuurman, J., et al. (2019). Unraveling the Macromolecular Pathways of IgG Oligomerization and Complement Activation on Antigenic Surfaces. *Nano Lett.* 19, 4787–4796. doi:10.1021/acs.nanolett.9b02220

Syed, V. (2016). TGF-β Signaling in Cancer. *J. Cel Biochem* 117, 1279–1287. doi:10.1002/jcb.25496

Syková, E., and Nicholson, C. (2008). Diffusion in Brain Extracellular Space. *Physiol. Rev.* 88, 1277–1340. doi:10.1152/physrev.00027.2007

Tajima, N., Takai, M., and Ishihara, K. (2011). Significance of Antibody Orientation Unraveled: Well-Oriented Antibodies Recorded High Binding Affinity. *Anal. Chem.* 83, 1969–1976. doi:10.1021/ac1026786

Tang, Y., and Cao, Y. (2021). Modeling Pharmacokinetics and Pharmacodynamics of Therapeutic Antibodies: Progress, Challenges, and Future Directions. *Pharmaceutics* 13 (3). doi:10.3390/pharmaceutics13030422

Tang, Y., and Cao, Y. (2020). Modeling the Dynamics of Antibody-Target Binding in Living Tumors. *Sci. Rep.* 10, 16764. doi:10.1038/s41598-020-73711-y

Tang, Y., Lou, J., Alpaugh, R. K., Robinson, M. K., Marks, J. D., and Weiner, L. M. (2007). Regulation of Antibody-dependent Cellular Cytotoxicity by IgG Intrinsic and Apparent Affinity for Target Antigen. *J. Immunol.* 179, 2815–2823. doi:10.4049/jimmunol.179.5.2815

Teeling, J. L., Mackus, W. J., Wiegman, L. J., Van Den Brakel, J. H., Beers, S. A., French, R. R., et al. (2006). The Biological Activity of Human CD20 Monoclonal Antibodies Is Linked to Unique Epitopes on CD20. *J. Immunol.* 177, 362–371. doi:10.4049/jimmunol.177.1.362

Ternant, D., Pfister, M., Le Tilly, O., Mulleman, D., Picon, L., Willot, S., et al. (2022). Infliximab Treatment Does Not Lead to Full TNF-α Inhibition: A Target-Mediated Drug Disposition Model. *Clin. Pharmacokinet.* 61 (1), 143–154. doi:10.1007/s40262-021-01057-3

Thakur, A., Huang, M., and Lum, L. G. (2018). Bispecific Antibody Based Therapeutics: Strengths and Challenges. *Blood Rev.* 32, 339–347. doi:10.1016/j.blre.2018.02.004

Thurber, G. M., Schmidt, M. M., and Wittrup, K. D. (2008a). Antibody Tumor Penetration: Transport Opposed by Systemic and Antigen-Mediated Clearance. *Adv. Drug Deliv. Rev.* 60, 1421–1434. doi:10.1016/j.addr.2008.04.012

Thurber, G. M., Schmidt, M. M., and Wittrup, K. D. (2008b). Factors Determining Antibody Distribution in Tumors. *Trends Pharmacol. Sci.* 29, 57–61. doi:10.1016/j.tips.2007.11.004

Tolar, M., Abushakra, S., Hey, J. A., Porsteinsson, A., and Sabbagh, M. (2020). Aducanumab, Gantenerumab, BAN2401, and ALZ-801-The First Wave of Amyloid-Targeting Drugs for Alzheimer's Disease with Potential for Near Term Approval. *Alzheimers Res. Ther.* 12, 95. doi:10.1186/s13195-020-00663-w

Tracey, D., Klareskog, L., Sasso, E. H., Salfeld, J. G., and Tak, P. P. (2008). Tumor Necrosis Factor Antagonist Mechanisms of Action: a Comprehensive Review. *Pharmacol. Ther.* 117, 244–279. doi:10.1016/j.pharmthera.2007.10.001

Vauquelin, G., and Charlton, S. J. (2013). Exploring Avidity: Understanding the Potential Gains in Functional Affinity and Target Residence Time of Bivalent and Heterobivalent Ligands. *Br. J. Pharmacol.* 168, 1771–1785. doi:10.1111/bph.12106

Vauquelin, G. (2016). Effects of Target Binding Kinetics on *In Vivo* Drug Efficacy: Koff , Kon and Rebinding. *Br. J. Pharmacol.* 173, 2319–2334. doi:10.1111/bph.13504

Wang, Q., Delva, L., Weinreb, P. H., Pepinsky, R. B., Graham, D., Veizaj, E., et al. (2018). Monoclonal Antibody Exposure in Rat and Cynomolgus Monkey Cerebrospinal Fluid Following Systemic Administration. *Fluids Barriers CNS* 15, 10. doi:10.1186/s12987-018-0093-6

Wang, W., Erbe, A. K., Hank, J. A., Morris, Z. S., and Sondel, P. M. (2015). NK Cell-Mediated Antibody-dependent Cellular Cytotoxicity in Cancer Immunotherapy. *Front. Immunol.* 6, 368. doi:10.3389/fimmu.2015.00368

Wehrman, T. S., Raab, W. J., Casipit, C. L., Doyonnas, R., Pomerantz, J. H., and Blau, H. M. (2006). A System for Quantifying Dynamic Protein Interactions Defines a Role for Herceptin in Modulating ErbB2 Interactions. *Proc. Natl. Acad. Sci. U S A.* 103, 19063–19068. doi:10.1073/pnas.0605218103

Weinstein, J. N., and Van Osdol, W. (1992). Early Intervention in Cancer Using Monoclonal Antibodies and Other Biological Ligands: Micropharmacology and the "binding Site Barrier". *Cancer Res.* 52, 2747s–2751s.

Weiskopf, K., and Weissman, I. L. (2015). Macrophages Are Critical Effectors of Antibody Therapies for Cancer. *MAbs* 7, 303–310. doi:10.1080/19420862.2015.1011450

Wigner, E. (1932). Über das Überschreiten von Potentialschwellen bei chemischen Reaktionen. *Z. Phys. Chem. Abt. B* 19B, 203–216. doi:10.1515/zpch-1932-1920

Wu, J., Fu, J., Zhang, M., and Liu, D. (2015). Blinatumomab: a Bispecific T Cell Engager (BiTE) Antibody against CD19/CD3 for Refractory Acute Lymphoid Leukemia. *J. Hematol. Oncol.* 8, 104. doi:10.1186/s13045-015-0195-4

Wu, X., and Demarest, S. J. (2019). Building Blocks for Bispecific and Trispecific Antibodies. *Methods* 154, 3–9. doi:10.1016/j.ymeth.2018.08.010

Yang, Y., Yeh, S. H., Madireddi, S., Matochko, W. L., Gu, C., Pacheco Sanchez, P., et al. (2019). Tetravalent Biepitopic Targeting Enables Intrinsic Antibody Agonism of Tumor Necrosis Factor Receptor Superfamily Members. *mAbs* 11 (6), 996–1011. doi:10.1080/19420862.2019.1625662

Zhang, J., Li, Q., Wu, Y., Wang, D., Xu, L., Zhang, Y., et al. (2019). Cholesterol Content in Cell Membrane Maintains Surface Levels of ErbB2 and Confers a Therapeutic Vulnerability in ErbB2-Positive Breast Cancer. *Cell Commun Signal* 17, 15. doi:10.1186/s12964-019-0328-4

Zhang, P., Ma, G., Dong, W., Wan, Z., Wang, S., and Tao, N. (2020). Plasmonic Scattering Imaging of Single Proteins and Binding Kinetics. *Nat. Methods* 17, 1010–1017. doi:10.1038/s41592-020-0947-0

Zuckier, L. S., Berkowitz, E. Z., Sattenberg, R. J., Zhao, Q. H., Deng, H. F., and Scharff, M. D. (2000). Influence of Affinity and Antigen Density on Antibody Localization in a Modifiable Tumor Targeting Model. *Cancer Res.* 60, 7008–7013.

Conflict of Interest: The authors declare that the research was conducted in the absence of any commercial or financial relationships that could be construed as a potential conflict of interest.

Publisher's Note: All claims expressed in this article are solely those of the authors and do not necessarily represent those of their affiliated organizations, or those of the publisher, the editors and the reviewers. Any product that may be evaluated in this article, or claim that may be made by its manufacturer, is not guaranteed or endorsed by the publisher.

frontiers in Pharmacology

BRIEF RESEARCH REPORT
published: 03 March 2022
doi: 10.3389/fphar.2022.836925

Predictive Simulations in Preclinical Oncology to Guide the Translation of Biologics

Shujun Dong[1], *Ian Nessler*[1], *Anna Kopp*[1], *Baron Rubahamya*[1] *and Greg M. Thurber*[1,2,3]*

[1]Department of Chemical Engineering, University of Michigan, Ann Arbor, MI, United States, [2]Department of Biomedical Engineering, University of Michigan, Ann Arbor, MI, United States, [3]Rogel Cancer Center, University of Michigan, Ann Arbor, MI, United States

Preclinical *in vivo* studies form the cornerstone of drug development and translation, bridging *in vitro* experiments with first-in-human trials. However, despite the utility of animal models, translation from the bench to bedside remains difficult, particularly for biologics and agents with unique mechanisms of action. The limitations of these animal models may advance agents that are ineffective in the clinic, or worse, screen out compounds that would be successful drugs. One reason for such failure is that animal models often allow clinically intolerable doses, which can undermine translation from otherwise promising efficacy studies. Other times, tolerability makes it challenging to identify the necessary dose range for clinical testing. With the ability to predict pharmacokinetic and pharmacodynamic responses, mechanistic simulations can help advance candidates from *in vitro* to *in vivo* and clinical studies. Here, we use basic insights into drug disposition to analyze the dosing of antibody drug conjugates (ADC) and checkpoint inhibitor dosing (PD-1 and PD-L1) in the clinic. The results demonstrate how simulations can identify the most promising clinical compounds rather than the most effective *in vitro* and preclinical *in vivo* agents. Likewise, the importance of quantifying absolute target expression and antibody internalization is critical to accurately scale dosing. These predictive models are capable of simulating clinical scenarios and providing results that can be validated and updated along the entire development pipeline starting in drug discovery. Combined with experimental approaches, simulations can guide the selection of compounds at early stages that are predicted to have the highest efficacy in the clinic.

Keywords: antibody drug conjugate, Checkpoint inhibitors, Thiele modulus, Predictive pharmokinetics, tissue penetration

OPEN ACCESS

Edited by:
Salvatore Salomone, University of Catania, Italy

Reviewed by:
Shawn C Owen, The University of Utah, United States
Antje-Christine Walz, Roche, Switzerland

***Correspondence:**
Greg M. Thurber
gthurber@umich.edu

Specialty section:
This article was submitted to Experimental Pharmacology and Drug Discovery, a section of the journal Frontiers in Pharmacology

Received: *16 December 2021*
Accepted: *04 February 2022*
Published: *03 March 2022*

Citation:
Dong S, Nessler I, Kopp A, Rubahamya B and Thurber GM (2022) Predictive Simulations in Preclinical Oncology to Guide the Translation of Biologics. Front. Pharmacol. 13:836925. doi: 10.3389/fphar.2022.836925

INTRODUCTION

The design of next-generation biologics for cancer therapy has dramatically changed the drug development landscape by enabling greater control over the specificity of one (or more) molecular interaction(s) within the patient. Meanwhile, this increased complexity has made it more difficult to identify the requisite properties needed for clinical success, particularly because sophisticated therapies have multiple points of failure. Traditionally, animal experiments have been utilized for guidance on the manifold factors that impact *in vivo* and clinical efficacy. However, despite widely accepted limitations of animal results in predicting clinical outcomes, these discrepancies have

become more acute with recent therapies. The result is a majority of Phase II and Phase III clinical trials ending in failure (Lowenstein and Castro, 2009).

Using antibody-drug conjugates (ADCs) to illustrate this point, different types of animal experiments are needed to gauge efficacy and toxicity. Non-human primates are often used to estimate toxicity since the targeting antibodies typically don't cross-react with mouse antigens and expression levels are different in rodent species. Ocular toxicity, which can limit dosing from the cytotoxic small molecule payload on ADCs, may only clearly show up in rabbit models (Zhao et al., 2018). For efficacy, mouse cells are often less sensitive to ADC payloads, so human xenograft models are typically used to measure response. To examine contributions from the immune system, however, humanized or syngeneic mouse models are needed, which usually require additional engineering of the animal system. This lack of a single model to incorporate these factors exists on top of other long-standing challenges: animal species/strain differences in metabolic pathways, faster clearance in animals than humans, and immune differences between species (Bracken, 2009; Van Norman, 2019).

To bridge such gaps between *in vitro* and *in vivo* as well as animal experiments and human trials, computational approaches, such as predictive mechanistic modelling, are needed (Denayer et al., 2014). To be clear, animal data is still essential for the drug development pipeline at the present time (e.g., to predict safety/toxicity in humans). However, computational approaches are necessary to integrate this data in a quantitative manner to make informed decisions. There have been innumerable published mechanistic models which utilize the *in vitro* and/or *in vivo* results to elucidate mechanisms and to evaluate and predict efficacy in animal experiments or clinical trials. For example, some of these models focus on micro-physiological systems, such as 3-D cell culture (organoids/spheroids) (Groh et al., 2014; Hubbard et al., 2017; Cartaxo et al., 2020; Khera et al., 2021). Others include the macroscopic system, such as utilization of multi-compartment physiologically-based pharmacokinetic models (Baxter et al., 1995; Cao and Jusko, 2012; Cao et al., 2013; Groh et al., 2014). These can be expanded to combine the macroscopic features (e.g., systemic clearance and tumor uptake) with the microscopic distribution or simplified to focus on the most critical features (Cao and Jusko, 2012; Cao et al., 2013).

Sophisticated models can include many detailed mechanisms to enhance the preclinical to clinical translation of drug efficacy. For example, models for checkpoint inhibitors take experimental data including plasma clearance, organ biodistribution, tissue heterogeneity, and cellular binding to capture drug disposition (Deng et al., 2016). Li et al., 2021 started from a minimal physiologically based pharmacokinetic model by Cao et al., 2013 and applied it to pembrolizumab to predict intra-tumoral target engagement and optimal dosing (Cao et al., 2013; Li et al., 2021). For ADCs, drug processing at the cellular level plays a central role in payload release and distribution. The development of ADC models involves more complicated local metabolism/degradation features, including antibody interaction with cell surface antigens, antigen induced internalization, lysosomal degradation and release and passive diffusion of payloads (Shah et al., 2012; Cao et al., 2013; Shah et al., 2014; Cilliers et al., 2016; Singh et al., 2016). Compartmental models are sometimes inadequate to capture the heterogeneity in distribution, and 'distributed parameter' models are needed that capture spatial differences in drug concentration, often using penetration distance from blood vessels as a central metric (Eikenberry, 2009; Cilliers et al., 2016; Khera et al., 2018; Burton et al., 2019). More recently, hybrid agent-based models capture not only the gradients in ADC delivery, but also the heterogeneity of vessel distribution and nonuniformity of the tumor cells (e.g., heterogeneous target expression, drug sensitivity), providing more reliable prediction to clinical efficacy (Menezes et al., 2020). These models each have their strengths and limitations.

Utilization of mechanistic simulations enables insight and prediction of the processing of drugs in humans, from compartmental uptake to tissue and cellular drug distribution and efficacy. Modeling can be employed throughout the drug development pipeline, starting during the discovery phase and continuing through preclinical *in vitro* and *in vivo* testing into the clinic. These predictions can play a crucial role in avoiding poorly designed preclinical experiments and forecasting clinical trial outcomes. Importantly, these predictions should be independent from the *in vivo* experiments themselves, allowing comparison between *in silico* and experimental outcomes. The model can be refined for minor differences during development. For example, the predicted clinical dosing, initially based on archived human tissue samples, could be adjusted if the target expression is upregulated in response to treatment. In contrast, major discrepancies can signal a need to invest in further research to determine why a drug is behaving unexpectedly to avoid issues further down the pipeline, as shown in **Figure 1A**.

The FDA recently appealed to sponsors to determine the optimal dose instead of relying on the maximum tolerated dose (MTD) before pivotal trials. They pointed out that some MTDs lay in the over-saturating regime, producing unnecessary toxicity. Optimal dosage is often achieved when drugs are evenly distributed throughout the target compartment and saturate all targeted receptors to achieve maximum cellular response. From this perspective, drug metabolism at the cellular level, including binding, receptor internalization, recycling or degradation, combined with systemic clearance, is the determinant factor for estimating drug saturation and efficacy with most biologics.

In this work, we analyze the dosing of two classes of agents important in cancer therapy: antibody drug conjugates and PD-1/PD-L1 checkpoint inhibitors. These agents represent two cases lying far apart on the tolerability/receptor engagement scale. ADCs, with their potent payloads that can result in high toxicity, are often administered at sub-saturating doses (near the MTD) that just approach full receptor engagement at their maximum concentration (C_{max}). Changes in the design impact both the MTD and receptor saturation, and agents with tolerable doses close to saturation have shown success in the clinic. In contrast, checkpoint inhibitors are generally well-tolerated antagonists which can be given at super-saturating doses. These agents are capable of maintaining full saturation even at

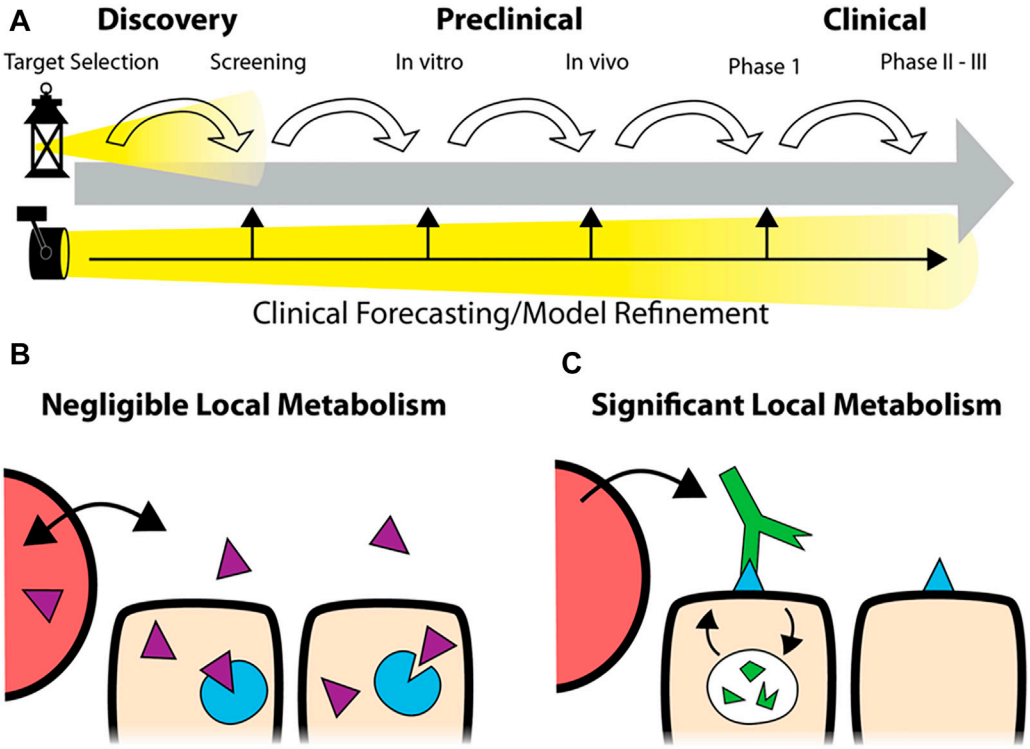

FIGURE 1 | Predictive Simulations in Development. Rather than focusing on each step in the pipeline **(A)**, top, robust simulations of drug distribution can be employed at the earliest stages of development to forecast clinical application. During development, the predictions can be refined to improve the accuracy of the forecast or identify discrepancies (A, bottom). While predictive models for small molecule drugs typically assume tissue concentrations proportional to the plasma concentration due to fast distribution **(B)**, the local metabolism/degradation of biologics and slow tissue penetration require alternative approaches for accurate predictions **(C)**.

the trough plasma concentrations (C_{min}). However, without an MTD "limit," selecting a recommended Phase II dose is difficult when the relationship between dose and efficacy is unclear (Li et al., 2021). In both cases, drug design and optimal dosing are key determinants of clinical success but challenging to identify during development. Computational tools, including simplified analysis of tumor target saturation, can provide useful insight. Some of the simplest and most predictive models can be employed early in drug development, prior to animal studies, to help guide the drug design for later stages of development. Specifically, we focus on local therapeutic degradation, which plays a central role in drug design and dosing but is often underemphasized relative to other PK metrics like plasma clearance half-life, binding affinity, and area under the curve (AUC) also used for small molecules (**Figures 1B,C**). Here, we utilize a previously reported dimensionless number ((Thurber et al., 2007a; Thurber et al., 2008; Wittrup et al., 2012), the Thiele modulus, to analyze the level of tumor saturation for both agents.

METHODS

Thiele Modulus Definition

For this simplified approach, we utilize the dimensionless group, the Thiele Modulus derived for antibody pharmacokinetics (Thurber et al., 2008; Thurber and Wittrup, 2008; Wittrup et al., 2012), to describe the relative receptor saturation by accounting for tumor clearance versus delivery. While the analysis is valid for different geometries, it is defined here for a Krogh cylinder representation with the blood vessel surface area (S) to tumor volume (V): (Thurber and Dane Wittrup, 2012):

$$\frac{S}{V} = \frac{2R_{cap}}{R_{Krogh}^2}$$

The Thiele Modulus predicts tissue saturation by comparing the rate of vascular extravasation with endocytic consumption/degradation (Thurber et al., 2007b; Thurber et al., 2008). For high affinity antibodies (which simplifies the generalized expression for a range in antibody affinity, provided in the **Supplementary Material**), the expression for the Thiele Modulus is:

$$\Phi^2 = \frac{k_e R_{Krogh}^2 \left([Ag]/\mathcal{E} \right)}{D\left(\frac{[Ab]}{1+(1/Bi)}\right)}$$

$$Bi = \frac{2PR_{cap}}{D\varepsilon}$$

where k_e is the rate constant of internalization which also represents the rate of endocytosis; R_{Krogh} is the radius of the cylinder; $[Ag]$ is the concentration of available antigen receptors (see note in

TABLE 1 | A summary of package insert doses and targets of five FDA approved ADCs and seven checkpoint inhibitors.

Name	Target	Internalization half-life (hr)	Target expression (receptors/cell)	Package insert dose	C_{max} (10^{-6}M)	C_{trough} (10^{-6}M)	PS/V (s^{-1})
Trodelvy	Trop-2	4.06	250,000 Yuan et al. (1995), Zhang et al. (2016)	10 mg/kg D1 and D8 of 21 days cycle	1.73	~0	6E-6 Yuan et al. (1995)
Kadcyla	Her2	7 Maass et al. (2016)	1,000,000 Onsum et al. (2013)	3.6 mg/kg Q3W	0.639	0.0168	Zhang et al. (2016)
Enhertu (IHC3+)	Her2	7	1,000,000 Onsum et al. (2013)	5.4 mg/kg Q3W	1.01	0.0787	
Enhertu (IHC2+)	Her2	7	100,000	5.4 mg/kg Q3W	1.01	0.0682	
Padcev	Nectin-4	18 Yuan et al. (1995) Zhang et al. (2016)	115,000	1.25 mg/kg D1, D8 and D15 of 28 days cycle	0.284	0.0682	
Mirvetuximab soravtansine	FR-alpha	32	1,000,000 (Forster et al. (2007)	6 mg/kg Q3W	1.09	0.0540	
Tivdak	Tissue factor (TF)	3.7 Yuan et al. (1995) Zhang et al. (2016)	112,000 Yuan et al. (1995) Zhang et al. (2016)	2 mg/kg Q3W	0.355	0.00933	
Nivolumab	PD-1	36 Lindauer et al. (2017)	5,600	240 mg Q2W	0.594	0.39 Bi et al. (2019)	6E-6 ((Yuan et al.,
Pembrolizumab				200 mg Q3W	0.495	0.156 Jacobs et al. (2021)	1995; Zhang et al., 2016)
Cemiplimab				350 mg Q3W	0.866	0.382 Kitano et al. (2021)	6E-6 Yuan et al. (1995)
Dostarlimab	PD-L1	35 ((Heskamp et al., 2015)	134,000	500 mg Q3W	1.24	0.278 ((Kasherman et al. (2020)	Zhang et al. (2016)
	PD-L1		134,000				
Atezolizumab		35 (Heskamp et al. (2015)		1200 mg Q3W	2.97	2.01 Mizugaki et al. (2016)	
Avelumab				800 mg Q2W	1.98	0.301 Doi et al. (2019)	

supplemental data when more than 1 cell type expresses the target); $[Ab]$ is the plasma concentration of antibody; D is the antibody interstitial diffusivity in tumor tissue; P is the antibody permeability through capillary; ε is the tumor void fraction, and R_{cap} is the radius of capillary (Thurber et al., 2007b). For most antibodies, diffusion is much faster than extravasation/permeability, resulting in a small Biot number (Bi) (Thurber and Dane Wittrup, 2012). Therefore, the expression can be simplified to

$$\Phi^2 = \frac{k_e R_{Krogh}^2 [Ag]}{2PR_{cap}[Ab]} = \frac{k_e [Ag]}{\left(PS/V\right)[Ab]}$$

Both the Biot number and Thiele modulus are dimensionless groups derived from partial differential equation models of drug distribution; therefore, the units in these expressions must cancel out. For the Thiele modulus, a faster rate of endocytosis/degradation prevents the antibodies from reaching distant tissue, resulting in limited drug penetration and unsaturated antigen receptors ($\Phi^2 > 1$). Under such circumstances, increasing the antibody dose can improve tumor uptake as well as drug distribution via increasing $[Ab]$. On the other hand, where saturation is achievable ($\Phi^2 < 1$), increasing the dose may maintain saturation for longer times but have limited improvement in tissue penetration.

RESULTS

The simplified yet predictive early-stage approach for the dosing of biologics using the Thiele modulus was applied to both ADCs and checkpoint inhibitors. The antibodies/ADCs considered here distribute as "high affinity" antibodies due to avidity and high antigen expression [where K_d values of 270 nM are sometimes needed to increase tissue penetration) (Rudnick et al., 2011). Likewise, lower affinity can impact internalization (Zwaagstra et al., 2019), but intrinsic receptor internalization rates are a good first approximation (Nessler et al., 2020a). A more generalized version of the Thiele modulus can describe the low affinity cases (supplemental data). ADCs are sophisticated pro-drugs that utilize a tumor targeted antibody conjugated to a potent, typically cytotoxic, payload via a cleavable or non-cleavable linker. Following intravenous administration, they circulate in the blood, are taken up in the tumor (and healthy tissue), extravasate, diffuse to their target, bind and internalize, and release their small molecule payload. The payload can then target the original cell or in the case of bystander payloads, diffuse to nearby cells. In contrast, checkpoint inhibitors block cell surface proteins which modulate immune responses and can prevent T-cells from attacking cancer cells. Instead of toxicity limitations preventing dose escalation, as is often the case for ADCs, checkpoint inhibitors don't reach an MTD, making it difficult to determine the optimal clinical dose. Despite these major differences, the same delivery principles can be applied to both biologics to provide insight into therapeutic design and dosing.

Thiele Modulus of Successful ADCs Are Close to 1

The doses for five FDA-approved solid tumor ADCs, mirvetuximab soravtansine, and seven checkpoint inhibitors

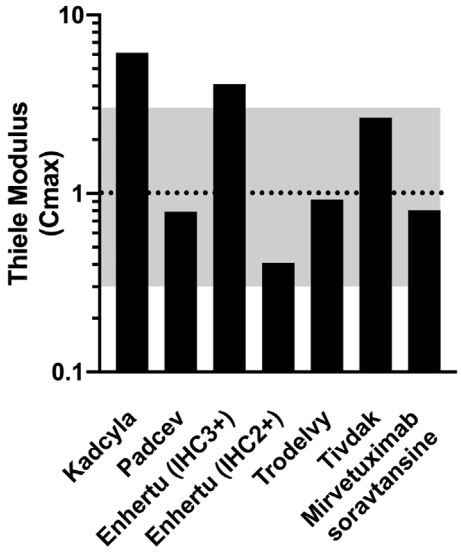

FIGURE 2 | Thiele Modulus of Approved Solid Tumor ADCs and Mirvetuximab soravtansine. Values for most recent agents are close to one indicating a balance between tumor uptake and local metabolism.

are summarized in **Table 1**. Other values needed to calculate the Thiele modulus are also included in the table. The expression of PD-1/PD-L1 (tumor cells, tumor-resident T-cells and macrophages) and nectin-4 were measured to complete the table.

The Thiele modulus was calculated from the values listed in **Table 1** along with the antigen expression and internalization rate constants reported in **Supplemental Table S1**. The Thiele modulus of ADCs are close to one (**Figure 2**), indicating that endocytic consumption is not significantly faster or slower than vascular extravasation. This results in dosing that approaches saturation ($\Phi^2 = 1$) for many of the ADCs.

The Thiele modulus of Padcev and Mirvetuximab soravtansine is slightly lower than 1, indicating the dose is sufficient to overcome binding and internalization within the tumor. The antigen expression of Nectin-4 on T47D cells is lower than HER2 and Trop2, and an 18 h estimated internalization half-life (**Supplementary Table S1**) allows ADC molecules to quickly occupy the receptor binding sites on cell surface before they are internalized. The Thiele modulus of Mirvetuximab soravtansine is below 1 due to the low FR-internalization and recycling rate (Monteiro et al., 2020; Ponte et al., 2021). Although there's an antibody-dependent downmodulation of TF surface expression, the Thiele modulus of Tivdak is greater than 1, consistent with heterogeneous distribution of tissue factor antibodies seen in some animal models (de Goeij et al., 2015; Koga et al., 2015). Additionally, the internalization and recycling of Tivdak is not significantly affected by binding with factor VIIa, with a half-life of 3.7 h measured by Hamik et al., 1999 (Hamik et al., 1999; Mandal et al., 2006; Breij et al., 2014; de Goeij et al., 2015). TROP2 is both highly expressed and rapidly internalized, but the high tolerability and dosing of Trodelvy helps overcome this large sink (Okajima et al., 2021). Finally, the first solid tumor ADC, Kadcyla, has a value significantly greater than one, higher than all other ADCs examined. In contrast, the higher tolerability of Enhertu allows larger dosing, resulting in a lower Thiele modulus. For patients with lower HER2 expression (IHC 2+), the Thiele modulus drops below one, balancing delivery to high and moderate expressors.

Thiele Modulus of Checkpoint Inhibitors Are Less Than 0.1 Indicating Super-saturation

The binding affinity and plasma clearance of approved checkpoint inhibitors vary widely in the clinic (**Figures 3A,B**). Models that assume tissue concentration is proportional to the plasma concentration (e.g., **Figure 1B**) indicate dosing should be related to these parameters, but there is not a correlation between approved immune checkpoint inhibitors and affinity or plasma clearance. The dosing more closely corresponds to local binding and metabolism in the tumor (**Figure 3C**). The Thiele modulus of PD-1 and PD-L1 inhibitors at their C_{max} and C_{trough} is shown in **Figure 3D**. A lower C_{trough} results in an increased Thiele modulus; however, the values are still less than 0.1 for almost all agents, indicating that PD-1 and PD-L1 proteins are saturated throughout the tumor during treatment at the FDA approved dose. With low tumor degradation due to slow checkpoint antigen internalization, the doses of PD-1 targeted antibodies are super-saturating even at the trough concentrations, i.e. $\Phi^2 \ll 1$, while leaving a safety margin of 10-fold ($\Phi^2 \ll 0.1$) for these drugs (e.g., a patient with 10-fold lower tumor vascularization would still have $\Phi^2 < 1$). Due to a greater expression of PD-L1 and faster clearance, the doses of Avelumab give a Thiele modulus above 0.1 at the trough concentration but are still able to saturate the tumor.

DISCUSSION

By integrating data from across the drug development pipeline, computational models can help identify therapeutics that will be successful in the clinic rather than simply focused on the next step in development (**Figure 1A**). As more data are gathered, clinical and preclinical predictions can be refined from values based on drug structure and target properties alone (discovery phase) to incorporate *in vitro* experiments, *in vivo* results, and clinical trial data. Accurate predictions build confidence in the compound while inaccurate predictions indicate a need to better understand the system before (or while) proceeding. In fact, an inaccurate prediction can be one of the most valuable contributions of a simulation since it highlights a misunderstanding of the drug pharmacokinetics and/or response.

In addition to experimental results, some underlying fundamental principles can assist in guiding drug design and dosing. Analogous to principles such as Lipinski's Rule of Five (Ro5) for small molecules, the Thiele modulus for biologics can provide early insight into dosing and potential delivery limitations. Values greater or less than one don't indicate a drug will fail. However, it can motivate additional investigation into whether receptor engagement and dosing are optimally suited for clinical success. Orally available small

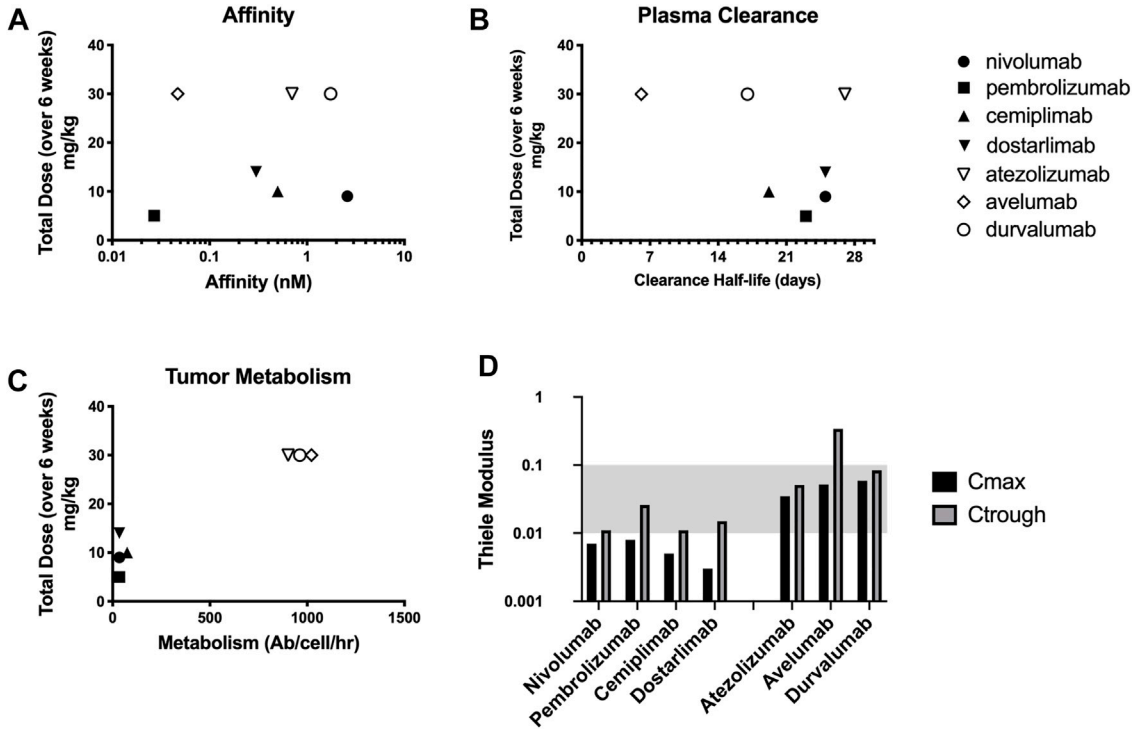

FIGURE 3 | Checkpoint inhibitors vary widely in target affinity **(A)** and plasma clearance **(B)** relative to dosing. However, the doses correspond more closely with the local tumor degradation/metabolism of the drug **(C)**. Thiele Modulus of 7 different checkpoint inhibitors calculated at both C_{max} and C_{trough} showing supersaturating doses **(D)**.

molecule drug pharmacokinetics are usually dominated by their oral absorption (related to the Ro5) versus systemic clearance (usually centrally controlled by liver metabolism). In contrast, intravenously delivered cancer biologics are often driven by their plasma concentration (C_{min} and C_{max}), vascular permeability, and local degradation (e.g., cellular expression, internalization, and degradation). The ratio of these values yields the Thiele modulus for biologics, which determines the saturation level in the tumor. Because receptor occupancy is not a static number, C_{min} and C_{max} can be used to estimate if the drug reaches all cells at the maximum concentration (important for cytotoxic delivery) or maintains full receptor occupancy at the minimum (important for antagonism of immune checkpoints). For example, an ADC with a Thiele modulus >1 may indicate the potency/DAR is too high to allow sufficient dosing to achieve tumor penetration and efficacy at a clinically tolerated dose, pointing to a reduction in potency/DAR to improve the therapeutic window. Likewise, a checkpoint inhibitor with a Thiele modulus <1 is unlikely to benefit significantly from an increase in dose since tumor target saturation is already achieved.

In fact, many of the clinical failures with ADCs point to mismatched potencies resulting in limited tissue penetration. In addition to flagging potential delivery challenges, the Thiele modulus could help identify compounds or dosing schemes that may ultimately prove more effective in the clinic based on delivery considerations, preventing them from being prematurely cut from the development pipeline. For example, the high tolerability of Trodelvy allows large dosing, improving tissue penetration into the tumor with a low Thiele modulus. However, the hydrolysable linker makes it difficult to determine an *in vitro* IC50 due to contributions from the released payload before internalization - yet it results in an effective drug (Goldenberg et al., 2015). Similarly, the *in vivo* data from Enhertu in a CT26-HER2 xenograft showed negligible efficacy due to lower sensitivity of mouse cells to the payload, yet the higher dosing and bystander payload help drive deeper tissue penetration than Kadcyla (Iwata et al., 2018). For checkpoint inhibitors, the clinical dosing of pembrolizumab was debated internally given an early signal in dose response. However, the simulations indicated receptor saturation at the lower doses, which ultimately prevailed with additional data (Patnaik et al., 2015; Elassaiss-Schaap et al., 2017).

For ADCs, the Thiele modulus varies between 0.5 and 10 with most new ADCs close to 1. The first ADC for solid tumors, Kadcyla, has the highest value. This provides an example where the analysis can raise flags but still allow successful development (similar to some successful small molecules breaking Lipinski's Ro5). Other mechanisms, such as HER2 signaling blockade or Fc-effector function of the trastuzumab antibody, may contribute to Kadcyla's success. Enhertu has a lower Thiele modulus due to a higher antibody dose, but it's still greater than 1. Interestingly, Enhertu has also shown efficacy in lower expressing tumors. For these cases, its Thiele modulus for HER2+ tumors is closer to optimum. The bystander payload, where Dxd released from

Enhertu can diffuse deeper into the tumor, may contribute to its efficacy at higher expression levels (IHC 3+) while saturating doses in lower expression tumors maintain effectiveness (IHC 2+). For Trodelvy and Padcev, these agents have faster plasma clearance than the other ADCs. While this may lower the exposure (e.g. AUC), a combination of high dosing and/or lower receptor expression enables them to reach most receptors for efficacy. Notably, most Thiele modulus values are not significantly less than 1, either, due to dosing limitations from the toxicity of the payload. In fact, values much less than 1 would lower the therapeutic index by increasing toxicity from the higher payload dose without a significant increase in efficacy.

Efficient internalization is critical for ADC success but can also lead to poor tissue penetration (Nessler et al., 2020b). Therefore, it's necessary to balance the net internalization (which includes recycling) and expression level with tolerability, dosing, and potency. In fact, a lot can be gleaned from the expression and internalization rates for approved agents. For example, literature reports of the internalization rate for Nectin-4 indicate an ~18 h half-life with 10^5 receptors/cell, which is one of the lowest rates of uptake for the 5 solid tumor approved ADCs (M-Rabet et al., 2017). Correspondingly, Padcev has one of the highest potencies in terms of combined payload and DAR (DAR 4, MMAE) among these ADCs. On the other extreme of these approvals, Trodelvy has both higher expression (between 10^5 and 10^6 Trop2/cell) and much faster internalization (4.06 h half-life) (Cardillo et al., 2015). It also has the lowest potency payload (SN38) which is only partially compensated by the higher DAR (DAR 8)—hence greater tolerability and higher dosing. Finally, Kadcyla and Enhertu are in-between, with higher expression than Nectin 4 but slower internalization than Trop2 (Austin et al., 2004). Both utilize moderate payloads and DARs, with Dxd and DM1 having greater potency than SN38 but less than MMAE. Comparing these two HER2-targeting constructs, the lower potency of Dxd is only partially compensated by higher DAR (DAR 8 for Dxd vs DAR 3.5 for DM1 on Kadcyla), resulting in greater tolerability/dosing of Enhertu. Overall, the higher expression and faster internalized targets are paired with lower potency ADCs (a product of payload potency and DAR), which enables higher dosing for better tissue penetration. This balance between intrinsic payload potency/DAR, expression, internalization, and dose results in most approved ADCs with a Thiele modulus close to 1.

The situation is very different for checkpoint inhibitors, but the same fundamental principles apply. The Thiele modulus of PD-1 and PD-L1 inhibitors at their maximum concentrations are all below 0.01 and 0.1, respectively. Even at lower trough concentrations, all except the fastest clearing agents are still below 0.1, indicating supersaturation of the receptor. In most early phase development trials, data reported on pharmacodynamic properties of PD-1 and PD-L1 inhibitors suggest that a MTD dosing scheme supersaturates receptors. In fact, the MTD is often not reached with checkpoint inhibitors in clinical trials (Brahmer et al., 2010; Herbst et al., 2014; Powles et al., 2014; Sehgal et al., 2020). Studies by Topalian et al., 2012 and Agrawal et al., 2016 have shown that with a dose of nivolumab at 0.1–0.3 mg/kg, which is about ten-fold lower than the approved dose (**Table 1**), maximal occupancy of PD-1 receptors can be achieved (Topalian et al., 2012; Agrawal et al., 2016). Data collected by Song et al., 2015 also indicated that soluble PD-L1 receptors were fully saturated in a majority of patients treated with durvalumab at 0.3 mg/kg every 2 weeks (Song et al., 2015). A similar result has been observed by Antonia et al., 2019 where complete soluble PD-L1 suppression is achieved (Antonia et al., 2019).

Supersaturating doses may be acceptable for agents that are well-tolerated, but the higher doses of checkpoint inhibitors do come at a cost. These doses not only increase the expense of treatment but can exacerbate anti-drug antibody (ADA) responses, particularly for agents that are designed to increase immune responses (Hock et al., 2015; Davda et al., 2019; Enrico et al., 2020). The situation raises some important drug development questions. Current dosing provides a 10X or greater 'safety margin' (i.e. dosing above tumor saturation) according to this analysis. The result is consistent with a relatively flat dose response curve at these levels (e.g., atezolizumab (Boswell et al., 2019)). What cost (in terms of ADA risk and material price for all patients) is acceptable for additional benefit in a subset of patients (such as those with poorly vascularized tumors that require a higher dose)?

Ironically, higher dosing can not only increase the risk of ADA but simultaneously overcome the same problem. For example, atezolizumab has been reported to induce ADA responses in 39.1% of the safety-evaluable patients, but the large dose appears to also prevent an impact on efficacy (Davda et al., 2019). Systemic exposure of atezolizumab is lower in ADA-positive patients due to enhanced clearance, but there was no significant impact on efficacy. Therefore, even with a good understanding of receptor occupancy, outstanding questions remain. Is it better to utilize lower doses to prevent ADA responses or higher doses to overcome the problem? Is an ADA response impairing drug efficacy and/or an indication that the immune system has been activated? The best answer will depend on the specific drug, but analysis of dosing and receptor occupancy with these trade-offs are important to consider.

Another uncommon feature of checkpoint inhibitors is tumor versus healthy tissue target saturation. Typically, antibodies saturate receptors in healthy tissue at lower doses than the tumor (enabling strategies such as preblocking healthy tissue) (Boswell et al., 2019). This occurs due to healthy tissue having a combination of higher and more uniform vascularization, better convection and lymphatic drainage (versus impaired convection from elevated interstitial pressure in tumors), and often lower target expression relative to tumors (Jain et al., 2007; Zhang et al., 2016). A collection of permeability and S/V values for healthy tissues has been published by Zhang et al. (Zhang et al., 2016) and can be used to predict healthy tissue saturation. However, compartmental/PBPK models are better suited for analyzing healthy tissue uptake (Mager and Jusko, 2001). Healthy tissue saturation often coincides with achieving linear plasma pharmacokinetics, where the dose is high enough to saturate receptors (reducing targeted mediated drug disposition, TMDD) such that the clearance rate becomes constant and plasma

concentrations are proportional to dose (Patnaik et al., 2015). Linear pharmacokinetic profiles have been observed during treatment with most checkpoint inhibitors at 1 mg/kg (0.3 mg/kg for pembrolizumab (Patnaik et al., 2015; Elassaiss-Schaap et al., 2017); 0.1 mg/kg for nivolumab (Patnaik et al., 2015; Elassaiss-Schaap et al., 2017); 1 mg/kg for atezolizumab (Stroh et al., 2017; Sehgal et al., 2020), cemiplimab (Yang et al., 2021), and avelumab (Heery et al., 2015) and 3 mg/kg for the PD-L1 inhibitor durvalumab (Patnaik et al., 2015; Elassaiss-Schaap et al., 2017), implying that the approved doses saturate normal tissues. In contrast, predictions indicate tumor saturation occurs at much lower doses primarily due to lower target expression (the product of immune cell count and receptors/cell) in tumors where cancer cells often outnumber tumor infiltrating lymphocytes. Interestingly, this enables the possibility for tumor specific inhibition, where a lower dose saturates lymphocytes in the tumor without saturating the receptor in tissues with much denser receptor concentration (e.g., lymph nodes).

Finally, receptor expression is not static. Upon treatment with anti-PD-1 and anti-PD-L1 therapies, Vilain et al., 2017 showed an infiltration of PD-1+ T-cells in tumor, as well as upregulation of tumoral PD-L1 and macrophage PD-L1 of responders (Vilain et al., 2017). There's also a large amount of literature addressing the regulation of PD-L1 expression in cancer cells mediated by cytokines or transcriptional pathways (Tremblay-LeMay et al., 2018). A relatively high dose of checkpoint inhibitors can compensate for upregulation of antigens and prolong the duration of an effective treatment. This is an example of where literature values and *in vitro* estimates of target expression from the discovery phase can be updated with preclinical *in vivo* data or *ex vivo* clinical data to further refine the clinical predictions. Quantitative measurements of animal and clinical expression are essential. With absolute receptor expression levels (rather than semi-quantitative metrics like IHC or H-scores), computational models can offer advantages over animal models by tailoring the results to the clinic. For example, the level of vascularization has a significant impact on PS/V and therefore delivery. Computational models can vary the PS/V values to those seen in the clinic (or even a particular tumor type or patient) rather than a given animal model. Additionally, by varying the S/V, this analysis can also be applied to healthy tissue for the prediction of therapeutic window.

As the biologics used to treat cancer increase in complexity, it is important to develop computational methods alongside animal experiments to better predict clinical outcomes. The fact that animal experiments can give opposite results depending on their design (e.g., a high or low DAR is more effective depending on the dose used) means that the preclinical outcomes are not necessarily providing fundamental insight into how the drug will behave in the clinic but rather how the drug behaves in that specific experiment (Nessler et al., 2021). Computational predictions, grounded in experimental data, can help translate how these results will manifest in patients for better decision-making during development.

In conclusion, the success of biologics in cancer therapy not only relies on the biology of the target but equally on forecasting the dosing and drug design for clinical efficacy. Mechanistic computational models can predict how drugs will translate from the discovery to *in vitro*, *in vivo*, and clinical stages. This includes simple and robust metrics, such as the Thiele modulus derived from computational models, that can provide insight into how currently successful drugs are behaving and guide the design and dosing of future therapeutics.

DATA AVAILABILITY STATEMENT

The original contributions presented in the study are included in the article/**Supplementary Material**, further inquiries can be directed to the corresponding author.

ETHICS STATEMENT

The animal study was reviewed and approved by Institutional Animal Care and Use Committee (IACUC) at the University of Michigan.

AUTHOR CONTRIBUTIONS

Proposed the research (SD, IN, GT), conducted experiments (IN, AK, BR), performed analysis (SD, IN, GT), wrote the paper (SD, IN, GT), revised paper (SD, IN, AK, BR, GT).

SUPPLEMENTARY MATERIAL

The Supplementary Material for this article can be found online at: https://www.frontiersin.org/articles/10.3389/fphar.2022.836925/full#supplementary-material

REFERENCES

Agrawal, S., Feng, Y., Roy, A., Kollia, G., and Lestini, B. (2016). Nivolumab Dose Selection: Challenges, Opportunities, and Lessons Learned for Cancer Immunotherapy. *J. Immunother. Cancer* 4, 72. doi:10.1186/s40425-016-0177-2

Antonia, S. J., Balmanoukian, A., Brahmer, J., Ou, S. I., Hellmann, M. D., Kim, S. W., et al. (2019). Clinical Activity, Tolerability, and Long-Term Follow-Up of Durvalumab in Patients with Advanced NSCLC. *J. Thorac. Oncol.* 14 (10), 1794–1806. doi:10.1016/j.jtho.2019.06.010

Austin, C. D., De Mazière, A. M., Pisacane, P. I., van Dijk, S. M., Eigenbrot, C., Sliwkowski, M. X., et al. (2004). Endocytosis and Sorting of ErbB2 and the Site of Action of Cancer Therapeutics Trastuzumab and Geldanamycin. *Mol. Biol. Cel* 15 (12), 5268–5282. doi:10.1091/mbc.e04-07-0591

Baxter, L. T., Zhu, H., Mackensen, D. G., Butler, W. F., and Jain, R. K. (1995). Biodistribution of Monoclonal Antibodies: Scale-Up from Mouse to Human Using a Physiologically Based Pharmacokinetic Model. *Cancer Res.* 55 (20), 4611–4622.

Bi, Y., Liu, J., Furmanski, B., Zhao, H., Yu, J., Osgood, C., et al. (2019). Model-informed Drug Development Approach Supporting Approval of the 4-week (Q4W) Dosing Schedule for Nivolumab (Opdivo) across Multiple Indications: a

Regulatory Perspective. *Ann. Oncol.* 30 (4), 644–651. doi:10.1093/annonc/mdz037

Boswell, C. A., Yadav, D. B., Mundo, E. E., Yu, S. F., Lacap, J. A., Fourie-O'Donohue, A., et al. (2019). Biodistribution and Efficacy of an Anti-TENB2 Antibody-Drug Conjugate in a Patient-Derived Model of Prostate Cancer. *Oncotarget* 10 (58), 6234–6244. doi:10.18632/oncotarget.27263

Bracken, M. B. (2009). Why Animal Studies Are Often Poor Predictors of Human Reactions to Exposure. *J. R. Soc. Med.* 102 (3), 120–122. doi:10.1258/jrsm.2008.08k033

Brahmer, J. R., Drake, C. G., Wollner, I., Powderly, J. D., Picus, J., Sharfman, W. H., et al. (2010). Phase I Study of Single-Agent Anti-programmed Death-1 (MDX-1106) in Refractory Solid Tumors: Safety, Clinical Activity, Pharmacodynamics, and Immunologic Correlates. *J. Clin. Oncol.* 28 (19), 3167–3175. doi:10.1200/JCO.2009.26.7609

Breij, E. C., de Goeij, B. E., Verploegen, S., Schuurhuis, D. H., Amirkhosravi, A., Francis, J., et al. (2014). An Antibody-Drug Conjugate that Targets Tissue Factor Exhibits Potent Therapeutic Activity against a Broad Range of Solid Tumors. *Cancer Res.* 74 (4), 1214–1226. doi:10.1158/0008-5472.CAN-13-2440

Burton, J. K., Bottino, D., and Secomb, T. W. (2019). A Systems Pharmacology Model for Drug Delivery to Solid Tumors by Antibody-Drug Conjugates: Implications for Bystander Effects. *AAPS J.* 22 (1), 12. doi:10.1208/s12248-019-0390-2

Cao, Y., Balthasar, J. P., and Jusko, W. J. (2013). Second-generation Minimal Physiologically-Based Pharmacokinetic Model for Monoclonal Antibodies. *J. Pharmacokinet. Pharmacodyn* 40 (5), 597–607. doi:10.1007/s10928-013-9332-2

Cao, Y., and Jusko, W. J. (2012). Applications of Minimal Physiologically-Based Pharmacokinetic Models. *J. Pharmacokinet. Pharmacodyn* 39 (6), 711–723. doi:10.1007/s10928-012-9280-2

Cardillo, T. M., Govindan, S. V., Sharkey, R. M., Trisal, P., Arrojo, R., Liu, D., et al. (2015). Sacituzumab Govitecan (IMMU-132), an Anti-trop-2/sn-38 Antibody-Drug Conjugate: Characterization and Efficacy in Pancreatic, Gastric, and Other Cancers. *Bioconjug. Chem.* 26 (5), 919–931. doi:10.1021/acs.bioconjchem.5b00223

Cartaxo, A. L., Almeida, J., Gualda, E. J., Marsal, M., Loza-Alvarez, P., Brito, C., et al. (2020). A Computational Diffusion Model to Study Antibody Transport within Reconstructed Tumor Microenvironments. *BMC bioinformatics* 21 (1), 529. doi:10.1186/s12859-020-03854-2

Cilliers, C., Guo, H., Liao, J., Christodolu, N., and Thurber, G. M. (2016). Multiscale Modeling of Antibody-Drug Conjugates: Connecting Tissue and Cellular Distribution to Whole Animal Pharmacokinetics and Potential Implications for Efficacy. *AAPS J.* 18 (5), 1117–1130. doi:10.1208/s12248-016-9940-z

Davda, J., Declerck, P., Hu-Lieskovan, S., Hickling, T. P., Jacobs, I. A., Chou, J., et al. (2019). Immunogenicity of Immunomodulatory, Antibody-Based, Oncology Therapeutics. *J. Immunother. Cancer* 7 (1), 105. doi:10.1186/s40425-019-0586-0

de Goeij, B. E., Satijn, D., Freitag, C. M., Wubbolts, R., Bleeker, W. K., Khasanov, A., et al. (2015). High Turnover of Tissue Factor Enables Efficient Intracellular Delivery of Antibody-Drug Conjugates. *Mol. Cancer Ther.* 14 (5), 1130–1140. doi:10.1158/1535-7163.MCT-14-0798

Denayer, T., Stöhr, T., and Roy, M. V. (2014). Animal Models in Translational Medicine: Validation and Prediction. *New Horizons Translational Med.* 2 (1), 5–11. doi:10.1016/j.nhtm.2014.08.001

Deng, R., Bumbaca, D., Pastuskovas, C. V., Boswell, C. A., West, D., Cowan, K. J., et al. (2016). Preclinical Pharmacokinetics, Pharmacodynamics, Tissue Distribution, and Tumor Penetration of Anti-PD-L1 Monoclonal Antibody, an Immune Checkpoint Inhibitor. *mAbs* 8 (3), 593–603. doi:10.1080/19420862.2015.1136043

Doi, T., Iwasa, S., Muro, K., Satoh, T., Hironaka, S., Esaki, T., et al. (2019). Phase 1 Trial of Avelumab (Anti-PD-L1) in Japanese Patients with Advanced Solid Tumors, Including Dose Expansion in Patients with Gastric or Gastroesophageal junction Cancer: the JAVELIN Solid Tumor JPN Trial. *Gastric Cancer* 22 (4), 817–827. doi:10.1007/s10120-018-0903-1

Eikenberry, S. (2009). A Tumor Cord Model for Doxorubicin Delivery and Dose Optimization in Solid Tumors. *Theor. Biol. Med. Model.* 6 (1), 16. doi:10.1186/1742-4682-6-16

Elassaiss-Schaap, J., Rossenu, S., Lindauer, A., Kang, S. P., de Greef, R., Sachs, J. R., et al. (2017). Using Model-Based "Learn and Confirm" to Reveal the Pharmacokinetics-Pharmacodynamics Relationship of Pembrolizumab in the KEYNOTE-001 Trial. *CPT Pharmacometrics Syst. Pharmacol.* 6 (1), 21–28. doi:10.1002/psp4.12132

Enrico, D., Paci, A., Chaput, N., Karamouza, E., and Besse, B. (2020). Antidrug Antibodies against Immune Checkpoint Blockers: Impairment of Drug Efficacy or Indication of Immune Activation. *Clin. Cancer Res.* 26 (4), 787–792. doi:10.1158/1078-0432.CCR-19-2337

Forster, M. D., Ormerod, M. G., Agarwal, R., Kaye, S. B., and Jackman, A. L. (2007). Flow Cytometric Method for Determining Folate Receptor Expression on Ovarian Carcinoma Cells. *Cytometry A* 71 (11), 945–950. doi:10.1002/cyto.a.20456

Goldenberg, D. M., Cardillo, T. M., Govindan, S. V., Rossi, E. A., and Sharkey, R. M. (2015). Trop-2 Is a Novel Target for Solid Cancer Therapy with Sacituzumab Govitecan (IMMU-132), an Antibody-Drug Conjugate (ADC). *Oncotarget* 6 (26), 22496–22512. doi:10.18632/oncotarget.4318

Groh, C. M., Hubbard, M. E., Jones, P. F., Loadman, P. M., Periasamy, N., Sleeman, B. D., et al. (2014). Mathematical and Computational Models of Drug Transport in Tumours. *J. R. Soc. Interf.* 11 (94), 20131173. doi:10.1098/rsif.2013.1173

Hamik, A., Setiadi, H., Bu, G., McEver, R. P., and Morrissey, J. H. (1999). Down-regulation of Monocyte Tissue Factor Mediated by Tissue Factor Pathway Inhibitor and the Low Density Lipoprotein Receptor-Related Protein. *J. Biol. Chem.* 274 (8), 4962–4969. doi:10.1074/jbc.274.8.4962

Heery, C. R., O'Sullivan Coyne, G. H., Marte, J. L., Singh, H., Cordes, L. M., Madan, R. A., et al. (2015). Pharmacokinetic Profile and Receptor Occupancy of Avelumab (MSB0010718C), an Anti-PD-L1 Monoclonal Antibody, in a Phase I, Open-Label, Dose Escalation Trial in Patients with Advanced Solid Tumors. *J. Clin. Oncol.* 33 (15_Suppl. l), 3055. doi:10.1200/jco.2015.33.15_suppl.3055()

Herbst, R. S., Soria, J. C., Kowanetz, M., Fine, G. D., Hamid, O., Gordon, M. S., et al. (2014). Predictive Correlates of Response to the Anti-PD-L1 Antibody MPDL3280A in Cancer Patients. *Nature* 515 (7528), 563–567. doi:10.1038/nature14011

Heskamp, S., Hobo, W., Molkenboer-Kuenen, J. D., Olive, D., Oyen, W. J., Dolstra, H., et al. (2015). Noninvasive Imaging of Tumor PD-L1 Expression Using Radiolabeled Anti-PD-L1 Antibodies. *Cancer Res.* 75 (14), 2928–2936. doi:10.1158/0008-5472.CAN-14-3477

Hock, M. B., Thudium, K. E., Carrasco-Triguero, M., and Schwabe, N. F. (2015). Immunogenicity of Antibody Drug Conjugates: Bioanalytical Methods and Monitoring Strategy for a Novel Therapeutic Modality. *AAPS J.* 17 (1), 35–43. doi:10.1208/s12248-014-9684-6

Hubbard, M. E., Jove, M., Loadman, P. M., Phillips, R. M., Twelves, C. J., and Smye, S. W. (2017). Drug Delivery in a Tumour Cord Model: a Computational Simulation. *R. Soc. Open Sci.* 4 (5), 170014. doi:10.1098/rsos.170014

Iwata, T. N., Ishii, C., Ishida, S., Ogitani, Y., Wada, T., and Agatsuma, T. (2018). A HER2-Targeting Antibody-Drug Conjugate, Trastuzumab Deruxtecan (DS-8201a), Enhances Antitumor Immunity in a Mouse Model. *Mol. Cancer Ther.* 17 (7), 1494–1503. doi:10.1158/1535-7163.MCT-17-0749

Jacobs, C. R., Rapoport, B. L., Chan, S. W., Ruff, P., Arance, A. M., Mujika, K., et al. (2021). KEYNOTE-555 Cohort B: Efficacy, Safety, and PK of Pembrolizumab (Pembro) 400 Mg Every 6 Weeks (Q6W) as 1L Therapy for Advanced Melanoma. *J. Clin. Oncol.* 39 (15_Suppl. l), 9541. doi:10.1200/jco.2021.39.15_suppl.9541

Jain, R. K., Tong, R. T., and Munn, L. L. (2007). Effect of Vascular Normalization by Antiangiogenic Therapy on Interstitial Hypertension, Peritumor Edema, and Lymphatic Metastasis: Insights from a Mathematical Model. *Cancer Res.* 67 (6), 2729–2735. doi:10.1158/0008-5472.CAN-06-4102

Kasherman, L., Ahrari, S., and Lheureux, S. (2020). Dostarlimab in the Treatment of Recurrent or Primary Advanced Endometrial Cancer. *Future Oncol.* 17 (8), 877–892. doi:10.2217/fon-2020-0655

Khera, E., Cilliers, C., Bhatnagar, S., and Thurber, G. M. (2018). Computational Transport Analysis of Antibody-Drug Conjugate Bystander Effects and Payload Tumoral Distribution: Implications for Therapy. *Mol. Syst. Des. Eng.* 3 (1), 73–88. doi:10.1039/c7me00093f

Khera, E., Cilliers, C., Smith, M. D., Ganno, M. L., Lai, K. C., Keating, T. A., et al. (2021). Quantifying ADC Bystander Payload Penetration with Cellular Resolution Using Pharmacodynamic Mapping. *Neoplasia* 23 (2), 210–221. doi:10.1016/j.neo.2020.12.001

Kitano, S., Shimizu, T., Koyama, T., Ebata, T., Iwasa, S., Kondo, S., et al. (2021). Dose Exploration Results from Phase 1 Study of Cemiplimab, a Human Monoclonal Programmed Death (PD)-1 Antibody, in Japanese Patients with Advanced Malignancies. *Cancer Chemother. Pharmacol.* 87 (1), 53–64. doi:10.1007/s00280-020-04161-6

Koga, Y., Manabe, S., Aihara, Y., Sato, R., Tsumura, R., Iwafuji, H., et al. (2015). Antitumor Effect of Antitissue Factor Antibody-MMAE Conjugate in Human Pancreatic Tumor Xenografts. *Int. J. Cancer* 137 (6), 1457–1466. doi:10.1002/ijc.29492

Li, T. R., Chatterjee, M., Lala, M., Abraham, A. K., Freshwater, T., Jain, L., et al. (2021). Pivotal Dose of Pembrolizumab: A Dose-Finding Strategy for Immuno-Oncology. *Clin. Pharmacol. Ther.* 110 (1), 200–209. doi:10.1002/cpt.2170

Lindauer, A., Valiathan, C. R., Mehta, K., Sriram, V., De Greef, R., Elassaiss-Schaap, J., et al. (2017). Translational Pharmacokinetic/Pharmacodynamic Modeling of Tumor Growth Inhibition Supports Dose-Range Selection of the Anti-PD-1 Antibody Pembrolizumab. *CPT Pharmacometrics Syst. Pharmacol.* 6 (1), 11–20. doi:10.1002/psp4.12130

Lowenstein, P. R., and Castro, M. G. (2009). Uncertainty in the Translation of Preclinical Experiments to Clinical Trials. Why Do Most Phase III Clinical Trials Fail. *Curr. Gene Ther.* 9 (5), 368–374. doi:10.2174/156652309789753392

M-Rabet, M., Cabaud, O., Josselin, E., Finetti, P., Castellano, R., Farina, A., et al. (2017). Nectin-4: a New Prognostic Biomarker for Efficient Therapeutic Targeting of Primary and Metastatic Triple-Negative Breast Cancer. *Ann. Oncol.* 28 (4), 769–776. doi:10.1093/annonc/mdw678

Maass, K. F., Kulkarni, C., Betts, A. M., and Wittrup, K. D. (2016). Determination of Cellular Processing Rates for a Trastuzumab-Maytansinoid Antibody-Drug Conjugate (ADC) Highlights Key Parameters for ADC Design. *AAPS J.* 18 (3), 635–646. doi:10.1208/s12248-016-9892-3

Mager, D. E., and Jusko, W. J. (2001). General Pharmacokinetic Model for Drugs Exhibiting Target-Mediated Drug Disposition. *J. Pharmacokinet. Pharmacodyn* 28 (6), 507–532. doi:10.1023/a:1014414520282

Mandal, S. K., Pendurthi, U. R., and Rao, L. V. (2006). Cellular Localization and Trafficking of Tissue Factor. *Blood* 107 (12), 4746–4753. doi:10.1182/blood-2005-11-4674

Menezes, B., Cilliers, C., Wessler, T., Thurber, G. M., and Linderman, J. J. (2020). An Agent-Based Systems Pharmacology Model of the Antibody-Drug Conjugate Kadcyla to Predict Efficacy of Different Dosing Regimens. *AAPS J.* 22 (2), 29. doi:10.1208/s12248-019-0391-1

Mizugaki, H., Yamamoto, N., Murakami, H., Kenmotsu, H., Fujiwara, Y., Ishida, Y., et al. (2016). Phase I Dose-Finding Study of Monotherapy with Atezolizumab, an Engineered Immunoglobulin Monoclonal Antibody Targeting PD-L1, in Japanese Patients with Advanced Solid Tumors. *Invest. New Drugs* 34 (5), 596–603. doi:10.1007/s10637-016-0371-6

Monteiro, C. A. P., Oliveira, A. D. P. R., Silva, R. C., Lima, R. R. M., Souto, F. O., and Baratti, M. O. (2020). Evaluating Internalization and Recycling of Folate Receptors in Breast Cancer Cells Using Quantum Dots. *J. Photochem. Photobiol. B* 209, 111918. doi:10.1016/j.jphotobiol.2020.111918

Nessler, I., Cilliers, C., and Thurber, G. M. (2020). Practical Guide for Quantification of In Vivo Degradation Rates for Therapeutic Proteins with Single-Cell Resolution Using Fluorescence Ratio Imaging. *Pharmaceutics* 12 (2), 12. doi:10.3390/pharmaceutics12020132

Nessler, I., Khera, E., Vance, S., Kopp, A., Qiu, Q., Keating, T. A., et al. (2020). Increased Tumor Penetration of Single-Domain Antibody-Drug Conjugates Improves In Vivo Efficacy in Prostate Cancer Models. *Cancer Res.* 80 (6), 1268–1278. doi:10.1158/0008-5472.CAN-19-2295

Nessler, I., Menezes, B., and Thurber, G. M. (2021). Key Metrics to Expanding the Pipeline of Successful Antibody-Drug Conjugates. *Trends Pharmacol. Sci.* 42 (10), 803–812. doi:10.1016/j.tips.2021.07.005

Okajima, D., Yasuda, S., Maejima, T., Karibe, T., Sakurai, K., Aida, T., et al. (2021) Datopotamab Deruxtecan, a Novel TROP2-Directed Antibody–Drug Conjugate, Demonstrates Potent Antitumor Activity by Efficient Drug Delivery to Tumor Cells. *Mol. Cancer Ther.* 20 2329–2340. doi:10.1158/1535-7163.MCT-21-0206

Onsum, M. D., Geretti, E., Paragas, V., Kudla, A. J., Moulis, S. P., Luus, L., et al. (2013). Single-Cell Quantitative HER2 Measurement Identifies Heterogeneity and Distinct Subgroups within Traditionally Defined HER2-Positive Patients. *Am. J. Pathol.* 183 (5), 1446–1460. doi:10.1016/j.ajpath.2013.07.015

Patnaik, A., Kang, S. P., Rasco, D., Papadopoulos, K. P., Elassaiss-Schaap, J., Beeram, M., et al. (2015). Phase I Study of Pembrolizumab (MK-3475; Anti-PD-1 Monoclonal Antibody) in Patients with Advanced Solid Tumors. *Clin. Cancer Res.* 21 (19), 4286–4293. doi:10.1158/1078-0432.CCR-14-2607

Ponte, J. F., Lanieri, L., Khera, E., Laleau, R., Ab, O., Espelin, C., et al. (2021). Antibody Co-administration Can Improve Systemic and Local Distribution of Antibody-Drug Conjugates to Increase In Vivo Efficacy. *Mol. Cancer Ther.* 20 (1), 203–212. doi:10.1158/1535-7163.MCT-20-0451

Powles, T., Eder, J. P., Fine, G. D., Braiteh, F. S., Loriot, Y., Cruz, C., et al. (2014). MPDL3280A (Anti-PD-L1) Treatment Leads to Clinical Activity in Metastatic Bladder Cancer. *Nature* 515 (7528), 558–562. doi:10.1038/nature13904

Rudnick, S. I., Lou, J., Shaller, C. C., Tang, Y., Klein-Szanto, A. J., Weiner, L. M., et al. (2011). Influence of Affinity and Antigen Internalization on the Uptake and Penetration of Anti-HER2 Antibodies in Solid Tumors. *Cancer Res.* 71 (6), 2250–2259. doi:10.1158/0008-5472.CAN-10-2277

Sehgal, K., Costa, D. B., and Rangachari, D. (2020). Extended-Interval Dosing Strategy of Immune Checkpoint Inhibitors in Lung Cancer: Will it Outlast the COVID-19 Pandemic. *Front. Oncol.* 10, 1193. doi:10.3389/fonc.2020.01193

Shah, D. K., Haddish-Berhane, N., and Betts, A. (2012). Bench to Bedside Translation of Antibody Drug Conjugates Using a Multiscale Mechanistic PK/PD Model: a Case Study with Brentuximab-Vedotin. *J. Pharmacokinet. Pharmacodyn* 39 (6), 643–659. doi:10.1007/s10928-012-9276-y

Shah, D. K., King, L. E., Han, X., Wentland, J. A., Zhang, Y., Lucas, J., et al. (2014). A Priori prediction of Tumor Payload Concentrations: Preclinical Case Study with an Auristatin-Based anti-5T4 Antibody-Drug Conjugate. *AAPS J.* 16 (3), 452–463. doi:10.1208/s12248-014-9576-9

Singh, A. P., Maass, K. F., Betts, A. M., Wittrup, K. D., Kulkarni, C., King, L. E., et al. (2016). Evolution of Antibody-Drug Conjugate Tumor Disposition Model to Predict Preclinical Tumor Pharmacokinetics of Trastuzumab-Emtansine (T-DM1). *AAPS J.* 18 (4), 861–875. doi:10.1208/s12248-016-9904-3

Song, X., Pak, M., Chavez, C., Liang, M., Lu, H., Schwickart, M., et al. (2015). Pharmacokinetics and Pharmacodynamics of MEDI4736, a Fully Human Anti-programmed Death Ligand 1 (PD-L1) Monoclonal Antibody, in Patients with Advanced Solid Tumors. *J. Clin. Oncol.* 33 (15_Suppl. l), e14009 doi:10.1200/jco.2015.33.15_suppl.e14009()

Stroh, M., Winter, H., Marchand, M., Claret, L., Eppler, S., Ruppel, J., et al. (2017). Clinical Pharmacokinetics and Pharmacodynamics of Atezolizumab in Metastatic Urothelial Carcinoma. *Clin. Pharmacol. Ther.* 102 (2), 305–312. doi:10.1002/cpt.587

Thurber, G. M., and Dane Wittrup, K. (2012). A Mechanistic Compartmental Model for Total Antibody Uptake in Tumors. *J. Theor. Biol.* 314, 57–68. doi:10.1016/j.jtbi.2012.08.034

Thurber, G. M., Schmidt, M. M., and Wittrup, K. D. (2008). Antibody Tumor Penetration: Transport Opposed by Systemic and Antigen-Mediated Clearance. *Adv. Drug Deliv. Rev.* 60 (12), 1421–1434. doi:10.1016/j.addr.2008.04.012

Thurber, G. M., and Wittrup, K. D. (2008). Quantitative Spatiotemporal Analysis of Antibody Fragment Diffusion and Endocytic Consumption in Tumor Spheroids. *Cancer Res.* 68, 3334–3341. doi:10.1158/0008-5472.CAN-07-3018

Thurber, G. M., Zajic, S. C., and Wittrup, K. D. (2007). Theoretic Criteria for Antibody Penetration into Solid Tumors and Micrometastases. *J. Nucl. Med.* 48 (6), 995–999. doi:10.2967/jnumed.106.037069

Thurber, G. M., Zajic, S. C., and Wittrup, K. D. (2007). Theoretic Criteria for Antibody Penetration into Solid Tumors and Micrometastases. *J. Nucl. Med.* 48 (6), 995–999. doi:10.2967/jnumed.106.037069

Topalian, S. L., Hodi, F. S., Brahmer, J. R., Gettinger, S. N., Smith, D. C., McDermott, D. F., et al. (2012). Safety, Activity, and Immune Correlates of Anti-PD-1 Antibody in Cancer. *N. Engl. J. Med.* 366 (26), 2443–2454. doi:10.1056/NEJMoa1200690

Tremblay-LeMay, R., Rastgoo, N., and Chang, H. (2018). Modulating PD-L1 Expression in Multiple Myeloma: an Alternative Strategy to Target the PD-1/pd-L1 Pathway. *J. Hematol. Oncol.* 11 (1), 46. doi:10.1186/s13045-018-0589-1

Van Norman, G. A. (2019). Limitations of Animal Studies for Predicting Toxicity in Clinical Trials. *JACC: Basic Translational Sci.* 4 (7), 845–854. doi:10.1016/j.jacbts.2019.10.008

Vilain, R. E., Menzies, A. M., Wilmott, J. S., Kakavand, H., Madore, J., Guminski, A., et al. (2017). Dynamic Changes in PD-L1 Expression and Immune Infiltrates Early during Treatment Predict Response to PD-1 Blockade in Melanoma. *Clin. Cancer Res.* 23 (17), 5024–5033. doi:10.1158/1078-0432.CCR-16-0698

Wittrup, K. D., Thurber, G. M., Schmidt, M. M., and Rhoden, J. J. (2012). Practical Theoretic Guidance for the Design of Tumor-Targeting Agents. *Methods Enzymol.* 503, 255–268. doi:10.1016/B978-0-12-396962-0.00010-0

Yang, F., Paccaly, A. J., Rippley, R. K., Davis, J. D., and DiCioccio, A. T. (2021). Population Pharmacokinetic Characteristics of Cemiplimab in Patients with Advanced Malignancies. *J. Pharmacokinet. Pharmacodyn* 48 (4), 479–494. doi:10.1007/s10928-021-09739-y

Yuan, F., Dellian, M., Fukumura, D., Leunig, M., Berk, D. A., Torchilin, V. P., et al. (1995). Vascular Permeability in a Human Tumor Xenograft: Molecular Size Dependence and Cutoff Size. *Cancer Res.* 55 (17), 3752–3756.

Zhang, L., Bhatnagar, S., Deschenes, E., and Thurber, G. M. (2016). Mechanistic and Quantitative Insight into Cell Surface Targeted Molecular Imaging Agent Design. *Sci. Rep.* 6 (1), 25424. doi:10.1038/srep25424

Zhao, H., Atkinson, J., Gulesserian, S., Zeng, Z., Nater, J., Ou, J., et al. (2018). Modulation of Macropinocytosis-Mediated Internalization Decreases Ocular Toxicity of Antibody-Drug Conjugates. *Cancer Res.* 78 (8), 2115–2126. doi:10.1158/0008-5472.CAN-17-3202

Zwaagstra, J. C., Sulea, T., Baardsnes, J., Radinovic, S., Cepero-Donates, Y., Robert, A., et al. (2019). Binding and Functional Profiling of Antibody Mutants Guides Selection of Optimal Candidates as Antibody Drug Conjugates. *PLoS One* 14 (12), e0226593. doi:10.1371/journal.pone.0226593

Conflict of Interest: The authors declare that the research was conducted in the absence of any commercial or financial relationships that could be construed as a potential conflict of interest.

Publisher's Note: All claims expressed in this article are solely those of the authors and do not necessarily represent those of their affiliated organizations, or those of the publisher, the editors, and the reviewers. Any product that may be evaluated in this article, or claim that may be made by its manufacturer, is not guaranteed or endorsed by the publisher.

frontiers | Frontiers in Pharmacology

PERSPECTIVE
published: 12 April 2022
doi: 10.3389/fphar.2022.860881

Navigating Between Right, Wrong, and Relevant: The Use of Mathematical Modeling in Preclinical Decision Making

Anna Kondic[1], Dean Bottino[2], John Harrold[3], Jeffrey D. Kearns[4], CJ Musante[5], Aleksandrs Odinecs[1], Saroja Ramanujan[6], Jangir Selimkhanov[5†] and Birgit Schoeberl[4]*

[1]Nektar Therapeutics, San Francisco, CA, United States, [2]Takeda Development Center Americas, Inc. (TDCA), Lexington, MA, United States, [3]Seagen Inc., South San Francisco, CA, United States, [4]Novartis Institutes for BioMedical Research Inc., Cambridge, MA, United States, [5]Pfizer Worldwide Research Development and Medical, Cambridge, MA, United States, [6]Genentech Inc., South San Francisco, CA, United States

OPEN ACCESS

Edited by:
Salvatore Salomone,
University of Catania, Italy

Reviewed by:
Lucia Gozzo,
University of Catania, Italy
Hana Maria Dobrovolny,
Texas Christian University, United States
Kien Wei Siah,
Massachusetts Institute of Technology, United States

***Correspondence:**
Anna Kondic
annageorgievakondic@gmail.com

†Present Address:
Takeda Development Center Americas,
Inc., San Diego, CA, United States

Specialty section:
This article was submitted to Experimental Pharmacology and Drug Discovery, a section of the journal Frontiers in Pharmacology

Received: 23 January 2022
Accepted: 16 March 2022
Published: 12 April 2022

Citation:
Kondic A, Bottino D, Harrold J, Kearns JD, Musante CJ, Odinecs A, Ramanujan S, Selimkhanov J and Schoeberl B (2022) Navigating Between Right, Wrong, and Relevant: The Use of Mathematical Modeling in Preclinical Decision Making. Front. Pharmacol. 13:860881. doi: 10.3389/fphar.2022.860881

The goal of this mini-review is to summarize the collective experience of the authors for how modeling and simulation approaches have been used to inform various decision points from discovery to First-In-Human clinical trials. The article is divided into a high-level overview of the types of problems that are being aided by modeling and simulation approaches, followed by detailed case studies around drug design (Nektar Therapeutics, Genentech), feasibility analysis (Novartis Pharmaceuticals), improvement of preclinical drug design (Pfizer), and preclinical to clinical extrapolation (Merck, Takeda, and Amgen).

Keywords: model-informed decision making, predictive modeling, translational modeling, modeling case studies, research and preclinical development

1 INTRODUCTION

The goal of this article is to provide a targeted perspective on how modeling and simulation approaches have been used to inform various decision points during the 'R' phase of Research and Development, namely from discovery to First-In-Human clinical trials. It is worth mentioning that the full adoption of modeling and simulation approaches in pharma has historically lagged compared to other industries, where products are routinely simulated even before being built. The reasons for that could largely be grouped in two main categories: technical and institutional. The first group is much easier to explain: lack of appropriate quantitative measurements and computational power to inform the development of adequate models was, in fact, true 20 years ago. However, this is much less of an issue today. The second category relates to biological complexity. Mathematical modeling and computer simulations have been an essential part of product development in just about every branch of science, engineering, and technology. The application of such approaches to reverse-engineer biology and to "design" novel therapies has been hindered by the lack of a pre-existing mathematical description of the broad range of biology involved and the common belief that the complexities of human health are too intractable to be addressed by computer models. The gradual change from resistance to acceptance by pharma and biotech companies has been aided by three factors: 1) success stories, such as the use of population pharmacokinetic/pharmacodynamic (PK/PD) models for dose selection or the widespread the use of physiologically-based PD (PBPK) models to assess drug-drug interactions in silico, 2) the wider availability of diverse data that are challenging to fully understand in the absence of integration into mathematical models, and 3) external pressure on the industry to accelerate development timelines and reduce potential late stage failures. All three factors have been

recognized and supported by changes in regulatory policy. The FDA MIDD (Model-Informed-Drug-Development) program is a prime example of how regulators value the power of mathematical models and what they can bring to drug development. The creation of dedicated modeling functions within pharmaceutical and biotech companies has led to an increased investment and adoption of modeling approaches to inform decisions within R&D. While most of the investment has traditionally occurred in modeling of the clinical development stages, the insight that mathematical models can impact the design of novel therapeutics and allow us to anticipate the clinical experiences through early simulation of potential human scenarios have led to an increased investment in preclinical modeling and simulation activities.

To illustrate the value of such approaches in pre-clinical stages of R&D, our cross-institutional team of authors has aimed to provide here concrete examples where we have used quantitative approaches to impact decisions in these early stages. We decided that this approach, while more colloquial in nature, would be a nice complement to existing papers in the literature providing details around specific modeling methodology. We hope that the reader will find this collection of examples informative and thought-provoking. We have been privileged to be part of institutions and teams that worked on interesting and challenging problems. We have also been lucky to live in times of increased biological understanding and technology developments. But, most importantly, we live in times when society demands that our industry lives up to the promise of personalized medicine—understanding the etiology of disease for any given patient and finding solutions that will work for that patient. Albert Einstein once said: "Learn from yesterday, live for today, hope for tomorrow. The important thing is not to stop questioning". He also famously said: "Everything should be made simple, but not simpler". We hope that by cataloging our experiences, we provide simple examples that helps streamline future uses of models in preclinical drug development.

The organization of this paper is as follows. We begin by providing a high-level summary or enumeration for the types of problems in the preclinical stage of drug development that might benefit from quantitative approaches. Then we proceed to provide a more detailed description of a case study that illustrates an approach to such a problem from our experience in our various organizations. Finally, we finish with a few words of reflections and hopes for the future.

2 HIGH-LEVEL SUMMARY OF DECISIONS BENEFITING FROM QUANTITATIVE APPROACHES

We work in a highly regulated industry in which development of new investigational medicines must comply with high standards to ensure that we understand the anticipated safety of the proposed interventions prior to bringing them into the clinic. Furthermore, the high cost of R&D necessitates continuous consideration of the probability of clinical success with respect to risk-benefit tradeoffs. Per FDA guidance (https://www.fda.gov/patients/drug-development-process/step-2-preclinical-research), the first two steps of the drug development process are 1) discovery and development, and 2) preclinical research. A key objective that arises in these stages is to identify a promising therapeutic target that can help alter the course of human disease or treat symptoms. We then screen among the different possible drug candidates to select the most promising candidate based on the interplay between several factors including: pharmacological activity for potential efficacy; Absorption, Distribution, Metabolism, and Excretion (ADME), and pharmacokinetic (PK) properties; side effects (toxicity); and how a particular modality compares with existing treatments. It is necessary to address these objectives while balancing resource constraints with the goal to progress further potentially promising programs while ending those that are less promising ones as early as possible. There are ample opportunities for quantitative approaches to be used to aid the decision making at this stage.

Our list of decisions supported by modeling in the discovery space is presented below:

1) Target or modality assessment:
   a) Feasibility assessment
   b) Competitive evaluation
   c) Repurposing of existing targets and molecules
2) Rational Drug Design and Compound Selection
   a) Desired drug property optimization
   b) Molecule generation and selection
3) Preclinical study design
4) Toxicology assessment (organ-specific)
5) Interspecies translation and clinical regimen design
   a) Clinical Study Design: PKPD, safety, efficacy
   b) Animal rule for translation-based approval

Before going to the specifics of the case studies, we wanted to acknowledge that they do not cover all aspects in the list above. For example, multiple publications cover topic (Brown et al., 2003) with examples of renal (Thomas, 2019), hepatic (Watkins, 2020), and cardiac toxicities (Amuzescu et al., 2021). In addition, while modeling can be a useful tool for the repurposing of existing molecules in new diseases, this topic is not covered in this paper [for published considerations on the topic the reader should consider (Pushpakom et al., 2019; Gozzo et al., 2020; Verbaanderd et al., 2020)].

3 DETAILED CASE STUDIES

3.1 Novartis: Novel Modality and Feasibility Analysis

Novartis regularly applies modeling and simulation to assess the potential of new therapeutic concepts at early stages of drug discovery to inform Go/No-Go decisions and therapeutic design. Here, we describe a model-informed molecular design exploration and feasibility assessment of a theoretical antibody intended to treat obesity-related disorders. Obesity is becoming increasingly common, and the available treatment options do not fully address this problem (Mullican and Rangwala, 2018; Tsai et al., 2018). The therapeutic potential of GFRAL agonism with GDF15 has been demonstrated preclinically with multiple approaches. Mice and monkeys on a

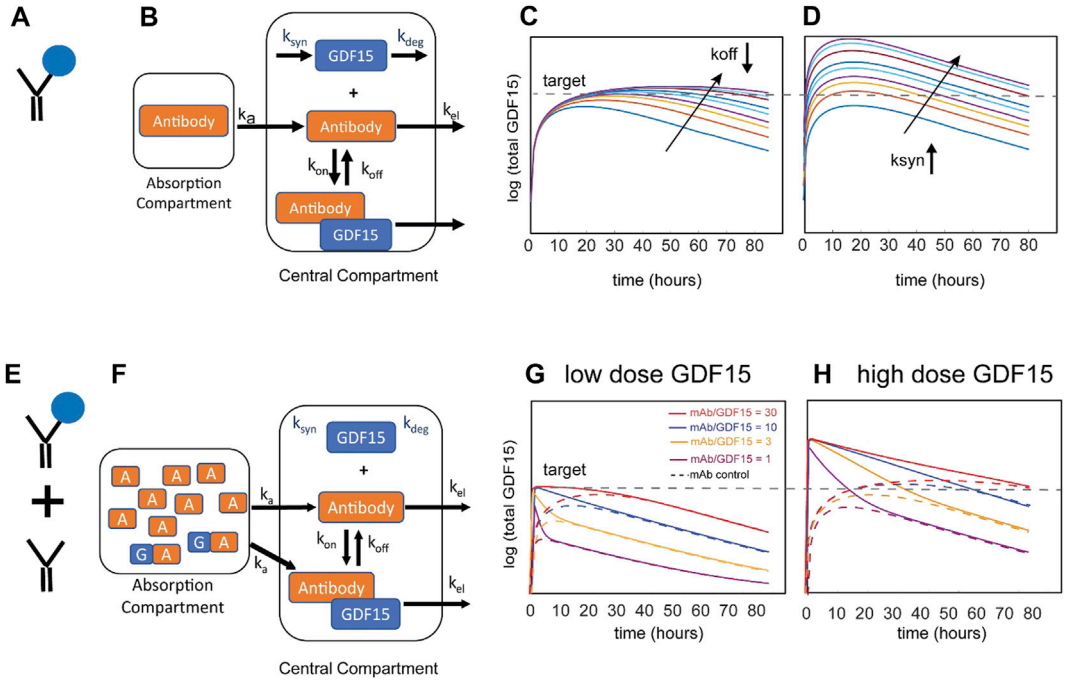

FIGURE 1 | Schematic of the model for the Novartis case study and resulting simulations. Stabilization of endogenous GDF15 ligand via binding to therapeutic antibody **(A)** can be described with a one-compartment model **(B)**. Results of local parameter scans for increasing the stability of the GDF15:antibody complex **(C)** and increasing the pool of endogenous GDF15 **(D)**. The arrows represent rate constant modifiers from 1ù to 1/25ù (decreasing k_{off}) or 1ù to 25ù (increasing ksyn), respectively. Administration of a mixture of stabilizing therapeutic antibody and recombinant GDF15 **(E)** can be described by the same one-compartment model **(F)**. Simulations of different mixture compositions with a low **(G)** or high **(H)** dose of exogenous GDF15. Shown in the solid lines are four ratios of antibody to GDF15 (30:1, 10:1, 3:1, 1:1 or equimolar). The stippled lines represent an antibody-only control for each of the four compositions.

high-fat diet treated with either AAVhu-GDF15, recombinant GDF15, or a scFc-GDF15 fusion lost about 10–24% of their body weight over 5–6 weeks and showed reductions in key metabolic parameters (Xiong et al., 2018). However, the use of recombinant GDF15 as a therapeutic is limited by its short serum half-life of less than 3 h in human (Zorzi et al., 2019).

In this example, the therapeutic antibody was proposed to bind to endogenous GDF15 to extend its half-life (**Figure 1A**) as an alternative to exogenous GDF15 approaches. The mechanistic hypothesis is that pharmacological stabilization of GDF15 with a non-antagonist antibody should increase circulating levels and thereby drive sustained GFRAL signaling, reduction in food intake, and weight loss. The Novartis team employed a small mechanistic PK/PD model for subcutaneous administration (**Figure 1B**) with a structure similar to published models of antibody-ligand traps (Davda and Hansen, 2010). Standard monoclonal antibody (mAb) PK parameters for cynomolgus monkeys and human were assumed. The drug PK, dosing regimen, affinity of the antibody:GDF15 complex, and patient-to-patient variability of baseline GDF15 levels (Brown et al., 2003) were explored to maximize the amount of circulating GDF15:mAb and to assess whether sufficiently high total GDF15 concentrations can be achieved.

Representative simulation results in **Figure 1C** show the impact of binding affinity on total GDF15 (by decreasing the antibody dissociation constant k_{off} at a constant dose). The simulations show that increasing the binding affinity does not meaningfully increase GDF15 Cmax but instead extends the time above threshold. This system behavior can be explained by the pool of total GDF15 quickly saturating despite free antibody being in excess. The GDF15 synthesis rate is the most sensitive parameter and predicted to increase GDF15 Cmax and time over threshold (**Figure 1D**). Subsequent consideration of synthesis rates derived from baseline GDF15 levels in patients revealed an increase of up to ~100-fold (data not shown), suggesting that this concept may not be viable for most patients to achieve the 100-to-1000-fold increase identified as an efficacious threshold for the scFv-GDF15 fusion (Xiong et al., 2018).

The modeling analysis was extended to consider an alternative therapeutic approach that is less dependent on patient GDF15 levels: a mixture of free antibody and antibody pre-complexed with recombinant GDF15 (**Figure 1E**). This mixture allows the administration of recombinant GDF15 in excess over endogenous GDF15 levels and thus decouples the therapeutic from patient-specific levels of baseline GDF15. The same PK/PD model with different initial conditions was used to explore different ratios (**Figure 1F**). Since the antibody dose and amount of recombinant GDF15 can be modulated, it is theoretically possible to achieve much higher Cmax with no time delay and to "control" the time over threshold. In **Figure 1G** the impact of a low dose of GDF15 is shown. Looking at the total GDF15 concentration time course, a 1:1 ratio of mAb and GDF15 results in a sharp peak and behaves over time similarly to the mAb control that binds endogenous

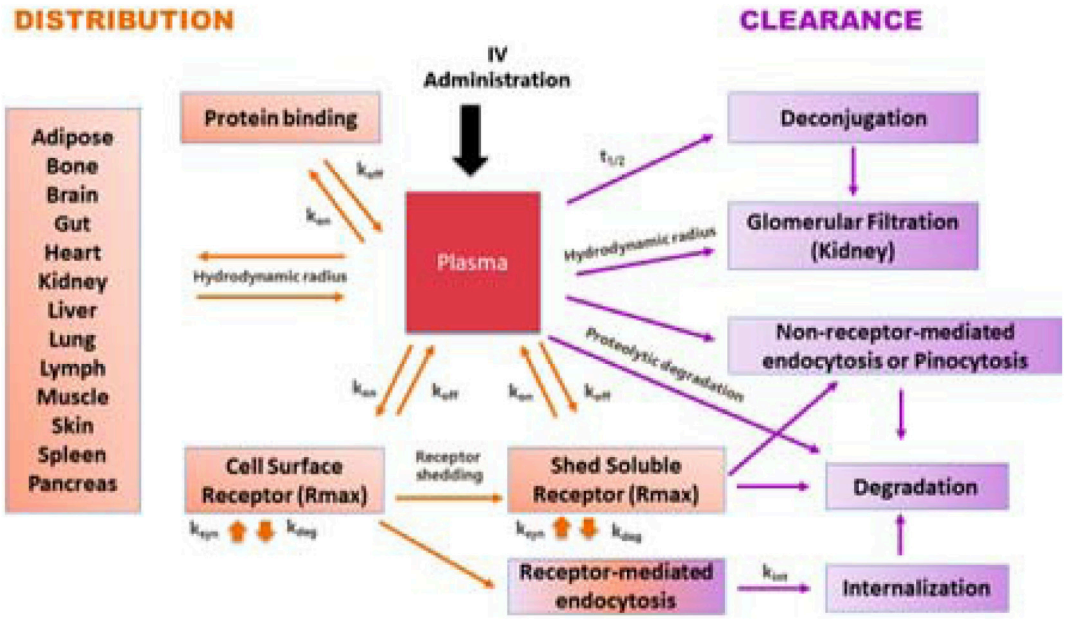

FIGURE 2 | A schematic representation of a general modeling framework incorporating key processed involved in the disposition and clearance of PEGylated cytokines.

GDF15. As the ratio of mAb to GDF15 increases, the concentration time course of total GDF15 can be modulated to achieve sustained GDF15 levels. **Figure 1H** demonstrates that at a high dose of GDF15 precomplexed with antibody the time over threshold can now be extended from hours to weeks. To summarize, the amount of GDF15 and the mAb to GDF15 ratio allows for a lot of flexibility to modulate the shape of the total GDF15 concentration-time course. As a research tool, it allows to gain a deep understanding of what pharmacokinetic features like Cmax or time over threshold drive weight loss which ultimately informs the design of an optimized therapeutic.

3.2 Nektar Therapeutics: Rational Drug Design

To systematically address questions in its portfolio of PEGylated cytokines (PEG = polyethylene glycol), Nektar created a predictive modeling platform in Simcyp™ PBPK Simulator (Certara, Inc., Princeton, New Jersey, USA) based on first principles. The PBPK modeling module for protein- based therapeutics in Simcyp™ is well established and continues to evolve by integrating new information. Its goal is to predict disposition and clearance for protein-based therapeutics. **Figure 2** provides a brief overview of the processes impacting the disposition and clearance of large molecules and can be adapted for individual programs and molecules. This is important, because the framework is no longer just a system of equations but contains parameter values that have been derived based on experimental data. As such, the model has become an integrated database that can b used to guide experiments and aid dose, dosing regimen, and candidate selection.

Distribution to tissues is governed by permeability, partition, and binding to cell surface receptors. Key pathways contributing to clearance include glomerular filtration, pinocytosis, degradation, and internalization of receptor-bound molecules, (depending on the conjugation chemistry) release of PEG molecules. Understanding the physical-chemical characteristics, receptor binding kinetics (association and disassociation constants k_{on} and k_{off}) and fate of receptor complex are important for development of a predictive model.

A PEGylated cytokine has larger hydrodynamic radius than its parent molecule. Experimental measurement of hydrodynamic radius during the drug design stage is not always practical. Therefore, we developed an artificial neuronal network model to estimate the hydrodynamic radius of a PEGylated cytokine based on the PEG molecular weight, the protein molecular weight, the PEGylated cytokine molecular weight, and the percent of PEG in the PEGylated cytokine. During the drug development stage, techniques such as Dynamic Light Scattering can be used to experimentally determine the hydrodynamic radius. Knowing the hydrodynamic radius of a PEGylated cytokine conjugate allowed us to simulate the amount of PEGylated conjugate eliminated by glomerular filtration. The biologics module in Simcyp™ is based on the two-pore theory; a cut off for glomerular filtration to molecules with a hydrodynamic radius larger than 6 nm. With this restriction, molecules with higher hydrodynamic radius, such as cytokines with molecular weight in a range of 10–30 kDa PEGylated with 60 kDa PEG or 50 kDa cytokine dimers, trimers, and tetramers PEGylated with 40 kDa PEG are not expected to be eliminated by glomerular filtration.

In addition to glomerular filtration, target-mediated drug disposition (TMDD) contributes to elimination of all cytokines.

Standard receptor binding parameters such as k_{on} and k_{off} can be experimentally determined *in vitro*. The maximum achievable binding can be assumed to be the same for a given cytokine, whether PEGylated or not; it can be estimated using published PK profiles and the binding properties for the cytokine of interest. After a PEGylated cytokine binds to its receptor, the drug-target complex has two pathways: some molecules will dissociate, and some will undergo subsequent internalization and endocytosis. The receptors for some cytokines, such as IL-1, IL-2, and TNF-alpha, are shed, and interactions with the soluble receptors need to be considered. The Simcyp™ biologics module can be used to implement the interaction of cytokines with soluble receptors, which can result in dissociation or degradation.

In instances when the PEG-conjugates exceed the glomerular filtration cutoff value, the relative contribution of non-receptor-mediated endocytosis or pinocytosis in their elimination increases. The reference CL through pinocytosis is ~0.01 L/h, which is the reported CL value for Cimzia® (Cimzia Full prescribing information, 2017). Cimzia® is a humanized antigen-binding 50 kDa fragment (Fab') of a monoclonal antibody that has been conjugated to a 40 kDa PEG. The hydrodynamic radius of this 90 kDa PEG-conjugate prevents glomerular filtration and TMDD was reported not to contribute to its clearance. Hence, the observed clearance values for Cimzia® provide a good estimate for the magnitude of clearance by pinocytosis, a constant, non-saturable process. Alterative methodologies for estimating rate of pinocytosis (e.g., expanding the *in vitro* pinocytosis rate in endothelial cells to the whole body), generate values within 3 times the Cimzia® reference value. For PEGylated molecules with conjugation chemistries that release PEG molecules *in vivo*, PK profile predictions require estimation of the PEG release rate, which can be directly measured or obtained by fitting a parameter to experimental data.

In summary, the modeling platform used by Nektar Therapeutics considers key molecular attributes such as hydrodynamic volume and receptor binding kinetics. This platform can be used to evaluate the impact of different PEGylation strategies on PK, thus contributing to rational drug design and informing decisions in the preclinical stages of R8D.

3.3 Genentech: Molecule Design and Compound Selection

Modeling can have meaningful impact early in the R&D process when used to compare alternate mechanisms for antagonizing a target to inform molecule generation and selection. In one such example, Genentech was exploring an antibody-based approach to targeting the protease tryptase in the lung for treatment of asthma and allergic airway disease. Tryptase is assembled into an active tetrameric molecule within acidic granules of mast cells and released in this active tetrameric form during degranulation. At extracellular pH, the tetramer dissociates relatively quickly into four inactive but longer-lived monomers; the combined effects of 4:1 stoichiometry and increased stability render the inactive monomer more abundant physiologically than the active tetramer. The molecule team had developed a destabilizing antibody that bound and rapidly disassembled the tetramer, but also bound the monomer with similar binding kinetics. Due to concerns that unproductive binding to the more abundant monomeric form would reduce drug availability, the team was also generating tetramer-selective antibodies, although these formed stabilizing complexes with the tetramer, inhibiting their physiological dissociation. Thus, a mechanistic PKPD model was developed and applied to quantitatively compare the ability molecules with these different Mode of Action (MoA) to neutralize tryptase activity in the lung (**Figure 3**).

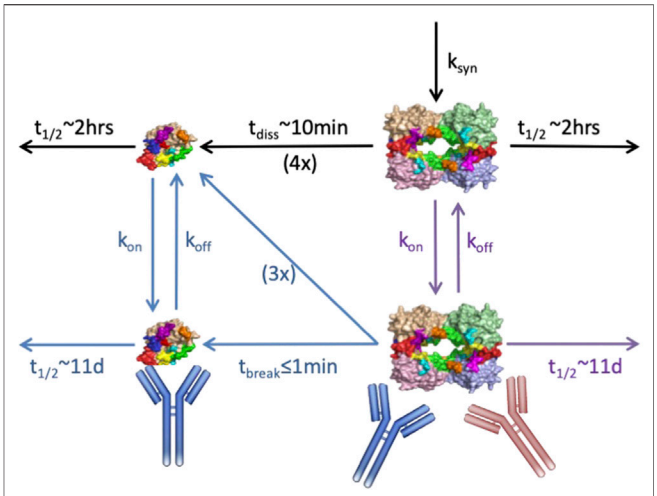

FIGURE 3 | Schematic of anti-tryptase PKPD model with lung compartment shown. Mechanisms represented include: tryptase tetramer secretion in the lung, physiological dissociation of tetramer to four monomers, antibody binding to/dissociation from the monomeric, and tetrameric forms, as appropriate, and binding induced disruption *vs.* stabilization of the tetramer. Black arrows represent physiological mechanisms; red antibody/ arrows pertain to tetramer-selective stabilizing molecule; blue antibody/ arrows pertain to destabilizing molecule; purple arrows pertain to both. Standard two-compartment systemic/peripheral nonspecific PK augmented by binding to monomer in the serum, and drug partitioning to lung were also included in the model but are not shown.

The modeling results indicated a clear advantage of the destabilizing antibody under various scenarios for systemic and lung tryptase concentrations, despite the molecule's nonproductive binding to inactive monomer (Chen et al., 2020). The quantitative simulations highlighted that tetramer destabilization leads to efficient reduction in the active species across the dose-regimens and concentration scenarios evaluated, superior to that achieved by the stabilizing antibody. Further, because binding-induced destabilization occurs even faster than antibody dissociation, a relatively fast dissociation rate (i.e., a higher k_{off} and K_D) can reduce unproductive engagement of drug with monomer without compromising tetramer inhibition. For the stabilizing antibody however, the model suggested >10x lower K_D molecules would be needed for near-comparable inhibition due to the need to continuously engage target. These simulations drove the decision to focus on development of the destabilizing antibody without further affinity improvements, saving significant time and money on antibody campaigns and optimization. The molecule was advanced and is now under clinical evaluation. Notably, the initial model structure also was expanded in subsequent PKPD efforts to capture nonhuman primate data and

to then project and interpret clinical PKPD, thus enabling integration of knowledge and data alongside development, and providing value beyond its initial application to molecule design/selection.

3.4 Pfizer: Improvement of Preclinical Study Design for Obesity Target Using Model Informed Drug Development

Preclinical program decisions in drug discovery often rely on results from a set of key studies. In the following example, Pfizer illustrated how modeling and simulation can help increase confidence in conclusions that are based on results coming from such studies by informing their design.

The discovery and development of novel therapies for the treatment of obesity is challenging, often due to lack of clinical efficacy. A key to bringing the best possible anti-obesity therapies to the clinic is based on effective preclinical efficacy evaluation of anti-obesity targets. This evaluation is dependent on the understanding of the inter- and intra-animal variability of key endpoints, such as food intake and body composition, to aid in study design, and the proper interpretation of results. To address this, the team leveraged a model-based power analysis to propose guidelines for endpoint selection and study size to inform *in vivo* preclinical study design for anti-obesity programs.

Specifically, Selimkhanov et al. (2017) fit a published physiologically based (PB) model of energy balance (Guo and Hall, 2009; Guo and Hall, 2011) that describes the feedbacks and interrelationships between efficacy endpoints typically measured in weight loss studies to individual C57BL/6 mouse's longitudinal data (Guo and Hall, 2009; Guo and Hall, 2011). The resulting statistical model described intra and inter subject variability that could be observed in a typical mouse study as well as the response of key endpoints to changes in metabolic energy balance. The statistical model was then used to simulate a typical study design with a hypothetical anorectic agent in order to estimate various endpoint effect sizes and variances. Using model-predicted effect sizes and variances, the team was then able to calculate the number of animals necessary to achieve sufficient statistical power for different endpoints.

The results of the analysis indicated that food intake variability is driven primarily by day-to-day intra-animal variability, whereas body weight and fat mass variability were driven primarily by differences between animals, important factors to consider in endpoint selection. Moreover, the analysis highlighted the need for caution when interpreting results from small preclinical studies that are not statistically powered for a given endpoint. As an example, in a simulated food intake reduction study powered to detect a change in body weight, the team found that the study also was sufficiently powered to detect a change in cumulative food intake; however, the study was underpowered to detect changes in other common endpoints, such as fat mass, fat- free mass, and single day food intake. In summary, model-based approaches such as this may be utilized to inform preclinical study design parameters, such as sample size and endpoint selection, as well as to aid in the proper interpretation of results for improved preclinical efficacy evaluations.

3.5 Translational Modeling in Oncology

The goal in this class of problems is to inform a possible dosing regimen in the clinic using data that typically comes from tumor-bearing or syngeneic mice. One of the goals is to build these models in such a way that they can continue incorporating new data, decreasing the uncertainty of the model predictions.

3.5.1 Merck

In the case of dinacyclib, a selective CDK1,4 small molecule inhibitor, different doses were studied in a Phase 1 setting yielding information on the pharmacokinetics, pharmacodynamics and safety of the drug, as well as the tolerability of the drug. there was a clear picture for dose limiting toxicity, based on the phase 1 clinical data (Nemunaitis et al., 2013; Mita et al., 2017). Information on the shape of dose response curves in tumor-bearing mice for different tumor types was also available (Mehrara et al., 2007). The task was to use this information and combine it with the data being generated from a satellite PK study (Booher et al., 2014) to determine the width the therapeutic window would be for this molecule.

1) The translation on the PK side was done by using a hybrid PBPK model with a tumor compartment using data from both preclinical and clinical studies, while accounting for any differences in plasma protein binding.
2) On the PD side, the dataset consisted of 1) tumor growth curves for the different tumor types and corresponding dose levels for tumor bearing mice and 2) an epidemiological dataset that described the observed tumor doubling times for different tumor types in patients, reporting on the variability. Starting from the doses inducing dose limiting toxicities (DLT-s), the translational model was then used to simulate dose-exposure-response scenarios providing a simple guide for further clinical investigations.

3.5.2 Takeda

A similar approach was taken by Takeda (Bottino et al., 2019) where a methodology was developed to determine the most appropriate dose and dosing regimen for novel oncology combination, consisting of two small molecules, inhibiting the PI3Kα, and mTOR pathways. As above, this modeling framework utilizes preclinical anti-tumor activity data and phase 1 clinical toxicity data, but for two, rather than a single molecule. The principal methodology, set up as a two-dimensional constrained optimization problem can be described in the following steps:

- Modeled observed antitumor activity as a function of drug concentration. All doses were converted to human-equivalent free fraction-corrected exposures (as in the Merck example).
- This methodology depends on clinical toxicity data, using bivariate logistic regression. One can make a point that quantitative systems toxicology models can be used to extrapolate preclinical data should this information be not available. Maximum tolerated exposure (MTE) curve in this case was defined as the set of exposures predicted to result in 25% probability of DLT.

- The MTE curve was then overlaid on the preclinically determined efficacy surface to see which tolerable concentration pair maximized the anti-tumor activity and doses that led to the optimal concentrations were back calculated.

3.6 Amgen: Translational Modeling - Application of Animal Rule

For some indications it is not feasible or ethical to conduct clinical trials to evaluate the efficacy of therapeutics. Development of therapeutic interventions for these indications can utilize the Animal Rule where efficacy is established in a well-controlled animal study using an animal model that best represents the indication of interest (US Food and Drug Administration, 2019). These pivotal studies will establish the efficacy of the therapeutic as well as the exposures and other metrics associated with that level of efficacy. Because it is not possible to verify the efficacy of the therapy in human subjects, it is important to establish that the human dosing is likely to achieve or exceed efficacy metrics in the preclinical species.

The approval of granulocyte colony stimulating factor treatments (G-CSF), filgrastim and pegfilgrastim, for the treatment of acute radiation syndrome (ARS) provides an example of the challenges associated with combining preclinical and clinical data together to identify the proper dosing under the Animal Rule. ARS results from acuate exposure to high doses of radiation leading to myelosuppression. As a result, individuals develop neutropenia and are exposed to opportunistic infections that can lead to increased mortality. Treatment with G-CSF can stimulate the production of granulocytes and reduce the duration of neutropenia after a hematopoietic injury. Two pivotal studies were sponsored by the National Institute of Allergy and Infectious Disease and conducted by the University of Maryland (Farese et al., 2013; Hankey et al., 2015). These establish the reduced duration of neutropenia and survival benefit of G-CSF treatment in non-human primates (NHP) exposed to lethal amounts of radiation. Because of their historic use in the treatment of chemotherapy induced neutropenia (CIN) there is substantial clinical data relating G-CSF treatment to exposures and neutrophil response in humans.

A series of models were developed to predict the effects of radiation and potential benefits G-CSF treatment on survival in humans. PK and ANC response data from healthy volunteers and patients (adults and pediatrics) with CIN were used to develop a mechanistic model. This accurately characterized the interplay of target-mediated disposition of both filgrastim and pegfilgrastim and the stimulation of ANC production in response to treatment (Melhem et al., 2018). This model allowed for the characterization of the underlying dynamics of granulocyte homeostasis as well as the impact of neutrophils on G-CSF PK. Two separate models were developed in parallel from the pivotal ARS NHP studies (Harrold et al., 2020a). The first model characterized granulopoiesis and radiation injury in NHPs. This effort utilized the same structural model of granulopoiesis from the human model. Next a time to event model was used to predict overall survival (OS) using the observed ANC profiles. Next these models were combined: Granulopoiesis and the disposition of filgrastim and pegfilgrastim from the human model was merged with the models of radiation injury and survival benefit in NHPs (Harrold et al., 2020b). The resulting model was calibrated using historical survival data in humans exposed to radiation to characterize the untreated response. Simulations were then used to evaluate the potential survival benefits of different G-CSF treatment regimens and the impact of delaying treatment.

4 CONCLUDING REMARKS

In this manuscript, we have detailed illustrative case studies from our experience that highlight how modeling and simulation is used to inform decision making in discovery and preclinical development. These examples only scratch the surface of this evolving modeling landscape which includes additional categories beyond the case studies here, for example, computational chemistry and structural biology, systems toxicology, and more. Nevertheless, there are some important high-level learnings that apply across various model applications:

1) Collaborative efforts between modelers and experimental scientists are key to creation of pragmatic models to influence decisions.
2) Models should come with clearly stated assumptions and relevant context of use.
3) Inaccurate model prediction from a well-designed and developed model should not be interpreted as an error, but rather an indication of a key knowledge gap.
4) Building models as integrated knowledge frameworks usually pays dividends to answer more than one question and inform development of multiple therapies in the portfolio.

In a field with continuously evolving technologies, data, and knowledge, we hope that the future will bring many more examples of impactful decision making from industry and academia, consortia efforts and government research.

DATA AVAILABILITY STATEMENT

Publicly available datasets were analyzed in this study. This data can be found here: na.

AUTHOR CONTRIBUTIONS

AK wrote the general text and was responsible for the write up of the Merck case study. The rest of the authors appear in alphabetical order and were responsible for the write up and review of their corresponding case studies and review/revision of the integrated manuscript.

ACKNOWLEDGMENTS

For the Pfizer study, CM and JS would like to acknowledge W. Clay Thompson as a primary contributor to the Pfizer published research. For the Merck study, AK would like to acknowledge Junghoon Lee and Alwin Schuller for the close collaboration on the design and analysis of the preclinical study. For the Genentech example, SR acknowledges Jeff Lutman and Tangsheng Yi for

collaboration and review of the model biology and predictions, AK and AO would like to thank Ute Hoch, Jacqueline Gibbons, and Jonathan Zalevsky for careful review and helpful suggestions for the Nektar Therapeutics case study. BS and JK would like to acknowledge the contributions of Hong Liu from from the Novartis Institutes for BioMedical Research (NIBR).

REFERENCES

Amuzescu, B., Airini, R., Epureanu, F. B., Mann, S. A., Knott, T., and Radu, B. M. (2021). Evolution of Mathematical Models of Cardiomyocyte Electrophysiology. *Math. Biosciences* 334, 2021.

Booher, R. N., Hatch, H., and Dolinski, B. M. (2014). MCL1 and BCL-xL Levels in Solid Tumors Are Predictive of Dinaciclib-Induced Apoptosis. *PLoS One* 9 (10), e108371. doi:10.1371/journal.pone.0108371

Bottino, D. B., Patel, M., Kadakia, E., Zhou, J., Patel, C., Neuwirth, R., et al. (2019). Dose Optimization for Anticancer Drug Combinations: Maximizing Therapeutic Index via Clinical Exposure-Toxicity/Preclinical Exposure-Efficacy Modeling. *Clin. Cancer Res.* 25, 6633–6643. doi:10.1158/1078-0432.CCR-18-3882

Brown, D. A., Ward, R. L., Buckhaults, P., Liu, T., Romans, K. E., Hawkins, N. J., et al. (2003). MIC-1 Serum Level and Genotype: Associations with Progress and Prognosis of Colorectal Carcinoma. *Clin. Cancer Res. Off. J. Am. Assoc. Cancer Res.* 9 (7), 2642–2650.

Chen, X., Mark, D., Jackman, J., JamesKoerber, T., Maun, H. R., Kathila, R., et al. (2020). *Anti-Tryptase Antibodies, Composition Thereof, and Uses Thereof*. US Patent, 2020.

Cimzia Full prescribing information (2020). available from: https://www.accessdata.fda.gov/drugsatfda_docs/label/2017/125160s270lbl.pdf.

Davda, J. P., and Hansen, R. J. (2010). Properties of a General PK/PD Model of Antibody-Ligand Interactions for Therapeutic Antibodies that Bind to Soluble Endogenous Targets. *MAbs* 2 (5), 576–588. doi:10.4161/mabs.2.5.12833

Farese, A. M., Cohen, M. V., Katz, B. P., Smith, C. P., Gibbs, A., Cohen, D. M., et al. (2013). Filgrastim Improves Survival in Lethally Irradiated Nonhuman Primates. *Radiat. Res.* 179 (1), 89–100. doi:10.1667/RR3049.1

Gozzo, L., Longo, L., Vitale, D. C., and Drago, F. (2020). The Regulatory Challenges for Drug Repurposing during the Covid-19 Pandemic: The Italian Experience. *Front. Pharmacol.* 11, 588132. doi:10.3389/fphar.2020.588132

Guo, J., and Hall, K. D. (2009). Estimating the Continuous-Time Dynamics of Energy and Fat Metabolism in Mice. *Plos Comput. Biol.* 5 (9), e1000511. doi:10.1371/journal.pcbi.1000511

Guo, J., and Hall, K. D. (2011). Predicting Changes of Body Weight, Body Fat, Energy Expenditure and Metabolic Fuel Selection in C57BL/6 Mice. *PLoS One* 6 (1), e15961. doi:10.1371/journal.pone.0015961

Hankey, K. G., Farese, A. M., Blaauw, E. C., Gibbs, A. M., Smith, C. P., Katz, B. P., et al. (2015). Pegfilgrastim Improves Survival of Lethally Irradiated Nonhuman Primates. *Radiat. Res.* 183 (6), 643–655. doi:10.1667/RR13940.1

Harrold, J., Gisleskog, P. O., and Delor, I. (2020). Quantification of Radiation Injury on Neutropenia and the Link between Absolute Neutrophil Count Time Course and Overall Survival in Nonhuman Primates Treated with G-CSF. *Pharm. Res.* 37, 102. doi:10.1007/s11095-020-02839-3

Harrold, J., Gisleskog, P. O., Perez-Ruixo, J. J., Delor, I., Chow, A., Jacqmin, P., et al. (2020). Prediction of Survival Benefit of Filgrastim in Adult and Pediatric Patients with Acute Radiation Syndrome. *Clin. Transl Sci.* 13, 807–817. doi:10.1111/cts.12777

Mehrara, E., Forssell-Aronsson, E., and Ahlman, H. (2007). Specific Growth Rate versus Doubling Time for Quantitative Characterization of Tumor Growth Rate. *Cancer Res.* 67, 3970–3975. doi:10.1158/0008-5472.CAN-06-3822

Melhem, M., Delor, I., Perez-Ruixo, J. J., Harrold, J., Chow, A., Wu, L., et al. (2018). Pharmacokinetic-pharmacodynamic Modelling of Neutrophil Response to G-CSF in Healthy Subjects and Patients with Chemotherapy-Induced Neutropenia. *Br. J. Clin. Pharmacol.* 84 (5), 911–925. doi:10.1111/bcp.13504

Mita, M. M., Mita, A. C., Moseley, J. L., Poon, J., Small, K. A., Jou, Y. M., et al. (2017). Phase 1 Safety, Pharmacokinetic and Pharmacodynamic Study of the Cyclin-dependent Kinase Inhibitor Dinaciclib Administered Every Three Weeks in Patients with Advanced Malignancies. *Br. J. Cancer* 117 (9), 1258–1268. doi:10.1038/bjc.2017.288

Mullican, S. E., and Rangwala, S. M. (2018). Uniting GDF15 and GFRAL: Therapeutic Opportunities in Obesity and beyond. *Trends Endocrinol. Metab.* 29 (8), 560–570. doi:10.1016/j.tem.2018.05.002

Nemunaitis, J. J., Small, K. A., Kirschmeier, P., Zhang, D., Zhu, Y., Jou, Y. M., et al. (2013). A First-In-Human, Phase 1, Dose-Escalation Study of Dinaciclib, a Novel Cyclin-dependent Kinase Inhibitor, Administered Weekly in Subjects with Advanced Malignancies. *J. Transl Med.* 11, 259. doi:10.1186/1479-5876-11-259

Pushpakom, S., Iorio, F., Eyers, P. A., Escott, K. J., Hopper, S., Wells, A., et al. (2019). Drug Repurposing: Progress, Challenges and Recommendations. *Nat. Rev. Drug Discov.* 18 (1), 41–58. doi:10.1038/nrd.2018.168

Selimkhanov, J., Thompson, W. C., Guo, J., Hall, K. D., and Musante, C. J. (2017). A Quantitative Analysis of Statistical Power Identifies Obesity End Points for Improved *In Vivo* Preclinical Study Design. *Int. J. Obes. (Lond)* 41, 1306–1309. doi:10.1038/ijo.2017.93

Thomas, S. R. (2019). Mathematical Models for Kidney Function Focusing on Clinical Interest. *Morphologie* 103 (Issue 343), 161–168. doi:10.1016/j.morpho.2019.10.043

Tsai, V. W. W., Husaini, Y., Sainsbury, A., Brown, D. A., and Breit, S. N. (2018). The MIC-1/gdf15-GFRAL Pathway in Energy Homeostasis: Implications for Obesity, Cachexia, and Other Associated Diseases. *Cell Metab* 28 (3), 353–368. doi:10.1016/j.cmet.2018.07.018

Us Food and Drug Administration (2019). *Product Development under the Animal Rule: Guidance for Industry*. Bethesda, MD: U.S. Department of Health and Human Services. Available from: https://www.fda.gov/downloads/drugs/guidances/ucm399217.pdf.

Verbaanderd, C., Rooman, I., Meheus, L., and Huys, I. (2020). On-Label or Off-Label? Overcoming Regulatory and Financial Barriers to Bring Repurposed Medicines to Cancer Patients. *Front. Pharmacol.* 10, 1664. doi:10.3389/fphar.2019.01664

Watkins, P. B. (2020). Quantitative Systems Toxicology Approaches to Understand and Predict Drug-Induced Liver Injury. *Clin. Liver Dis.* 24 (1), 49–60. doi:10.1016/j.cld.2019.09.003

Xiong, Y., Walker, K., and Min, X. (2018). Erratum for the Research Article: "Long-Acting MIC-1/GDF15 Molecules to Treat Obesity: Evidence from Mice to Monkeys" by Y. Xiong, K. Walker, X. Min, C. Hale, T. Tran, R. Komorowski, J. Yang, J. Davda, N. Nuanmanee, D. Kemp, X. Wang, H. Liu, S. Miller, K. J. Lee, Z. Wang, M. M. Véniant. *Sci. Transl Med.* 10, 456. doi:10.1126/scitranslmed.aav1069

Zorzi, A., Linciano, S., and Angelini, A. (2019). Non-covalent Albumin-Binding Ligands for Extending the Circulating Half-Life of Small Biotherapeutics. *Medchemcomm* 10 (7), 1068–1081. doi:10.1039/c9md00018f

Conflict of Interest: At present, AK and AO are employees of Nektar Therapeutics; CJM works at Pfizer, JS and DB at Takeda, BS and JK are employees of Novartis, JH works at Seattle Genetics and SR at Genentech. The Merck, Pfizer and Amgen case studies are based on previously published work when AK, JS and JH were at those companies. For each case study, all non-contributing authors declare that the research was conducted in the absence of any commercial or financial relationships that could be construed as a potential conflict of interest.

Publisher's Note: All claims expressed in this article are solely those of the authors and do not necessarily represent those of their affiliated organizations, or those of the publisher, the editors and the reviewers. Any product that may be evaluated in this article, or claim that may be made by its manufacturer, is not guaranteed or endorsed by the publisher.

frontiers | Frontiers in Pharmacology

ORIGINAL RESEARCH
published: 19 April 2022
doi: 10.3389/fphar.2022.855743

Mathematical Modeling of Complement Pathway Dynamics for Target Validation and Selection of Drug Modalities for Complement Therapies

Loveleena Bansal[1], Eva-Maria Nichols[2], Daniel P. Howsmon[3], Jessica Neisen[2], Christina M. Bessant[2], Fraser Cunningham[2], Sebastien Petit-Frere[2], Steve Ludbrook[2] and Valeriu Damian[1]*

[1]Systems Modeling and Translational Biology, Computational Sciences, GSK, Upper Providence, Collegeville, PA, United States, [2]Immunology Research Unit, GSK, Stevenage, United Kingdom, [3]Department of Chemical and Biological Engineering, Rensselaer Polytechnic Institute, Troy, NY, United States

OPEN ACCESS

Edited by:
Salvatore Salomone,
University of Catania, Italy

Reviewed by:
Kirill Peskov,
Modeling and Simulation Decisions, Russia
Giulia Palermo,
University of California, Riverside, United States
Xaria Li,
The University of Queensland, Australia

***Correspondence:**
Loveleena Bansal
loveleena.x.bansal@gsk.com

Specialty section:
This article was submitted to Experimental Pharmacology and Drug Discovery, a section of the journal Frontiers in Pharmacology

Received: 15 January 2022
Accepted: 14 March 2022
Published: 19 April 2022

Citation:
Bansal L, Nichols E-M, Howsmon DP, Neisen J, Bessant CM, Cunningham F, Petit-Frere S, Ludbrook S and Damian V (2022) Mathematical Modeling of Complement Pathway Dynamics for Target Validation and Selection of Drug Modalities for Complement Therapies. Front. Pharmacol. 13:855743. doi: 10.3389/fphar.2022.855743

Motivation: The complement pathway plays a critical role in innate immune defense against infections. Dysregulation between activation and regulation of the complement pathway is widely known to contribute to several diseases. Nevertheless, very few drugs that target complement proteins have made it to the final regulatory approval because of factors such as high concentrations and dosing requirements for complement proteins and serious side effects from complement inhibition.

Methods: A quantitative systems pharmacology (QSP) model of the complement pathway has been developed to evaluate potential drug targets to inhibit complement activation in autoimmune diseases. The model describes complement activation *via* the alternative and terminal pathways as well as the dynamics of several regulatory proteins. The QSP model has been used to evaluate the effect of inhibiting complement targets on reducing pathway activation caused by deficiency in factor H and CD59. The model also informed the feasibility of developing small-molecule or large-molecule antibody drugs by predicting the drug dosing and affinity requirements for potential complement targets.

Results: Inhibition of several complement proteins was predicted to lead to a significant reduction in complement activation and cell lysis. The complement proteins that are present in very high concentrations or have high turnover rates (C3, factor B, factor D, and C6) were predicted to be challenging to engage with feasible doses of large-molecule antibody compounds (≤20 mg/kg). Alternatively, complement fragments that have a short

Abbreviations: aHUS, atypical hemolytic uremic syndrome; AP, alternative pathway; C34b*, cell surface binding site; Cn, clusterin; CR1, complement receptor type 1; DAF, decay accelerating factor or CD55; FB, factor B; FD, factor D; FH, factor H; FI, factor I; FP, factor P or Properdin; FPn, Properdin oligomer; GPE, guinea pig erythrocytes; K_D, drug affinity; LM-Ab, large-molecule antibody; MAC, membrane attack complex; P*, Properdin binding site; PNH, paroxysmal nocturnal hemoglobinuria; QSP, quantitative systems pharmacology; SA, sialic acid; SLE, systemic lupus erythematosus; SM, small molecule; TE, target engagement; TMDD, target-mediated drug disposition; ULQ, upper limit of quantitation; Vd, volume of distribution; Vn, vitronectin.

half-life (C3b, C3bB, and C3bBb) were predicted to be challenging or infeasible to engage with small-molecule compounds because of high drug affinity requirements (>1 nM) for the inhibition of downstream processes. The drug affinity requirements for disease severity reduction were predicted to differ more than one to two orders of magnitude than affinities needed for the conventional 90% target engagement (TE) for several proteins. Thus, the QSP model analyses indicate the importance for accounting for TE requirements for achieving reduction in disease severity endpoints during the lead optimization stage.

Keywords: complement pathway, mathematical modeling, Quantitative Systems Pharmacology, drug modality selection, target validation, dose prediction

1 INTRODUCTION

The complement system forms an important component of innate immunity by providing the first line of defense against infections. It is composed of several proteins produced mainly by the liver or expressed on the surface of the cells. The complement proteins participate in a cascade that forms large protein complexes on the cell surface, opsonizing and killing the target cell. The tight regulation of the pathway through various regulatory proteins and cell surface receptors protects the host cells against complement-mediated cell death, and there exists a fine balance between complement activation and regulation. However, dysregulation of the complement pathway due to protein deficiencies or genetic mutations can unfavorably tip the balance (Morgan and Harris, 2015) toward over-activation, leading to autoimmune diseases or under-activation increasing susceptibility to infections.

The complement system is widely known to contribute to the pathology of several diseases and is an active area of drug development. However, despite a wealth of knowledge on the complement cascade and its components, very few drugs have made it to the final regulatory approval (Harris, 2018). The presence of multiple regulatory and activating proteins, the high abundance and turnover rate of most complement proteins, as well as serious side effects from complement inhibition are just some of the emerging factors that make drug development extremely challenging for therapies targeting complement proteins. Thus, there is a critical need for the investigation of efficacious and cost-effective complement modulatory therapies for patients.

Quantitative systems pharmacology (QSP) is an *in silico* modeling approach that combines the knowledge of disease processes with drug mechanisms to evaluate targets and drug candidates for modulating disease severity and biological pathways (Sorger et al., 2011). It is now widely used in the pharmaceutical industry to estimate drug efficacy, clinical doses, biomarker responses, and patient stratification (Nijsen et al., 2018). To take a step toward overcoming the challenges in developing drugs targeting the complement pathway, we have developed a comprehensive QSP model describing complement activation *in vivo* in humans *via* alternative and terminal pathways. The model contains several variables representing complement proteins, protein complexes, cleavage products, and intermediates participating in biochemical processes across the plasma and surface of host cells.

There have been a few previous reports of mathematical modeling for the complement pathway. The previous models have lacked sufficient details for a comprehensive description of the pathway or translation of modeling results from *in vitro* to *in vivo* activation of the complement system in humans. The first attempts at mathematical descriptions of the pathway included simplified descriptions of the complex dynamics in key aspects of complement activation such as the amplification loop (Reeve and Woo, 1982) in the alternative pathway and formation of the membrane attack complex (MAC) (Hirayama et al., 1996). Korotaevskiy et al. (2009) developed a combined mathematical model of classical, alternative, and terminal pathways of the complement system; however, the impact of complement regulators and the differentiation between pathway activation on the cell surface *versus* in the plasma were not included. Over the years, more comprehensive models have been developed (Zewde et al., 2016; Zewde and Morikis, 2018; Tille et al., 2020; Zewde et al., 2021) with descriptions of the plasma and cell surface regulators. However, these models have included simplified descriptions of the dynamics of regulators such as Properdin, clusterin, and vitronectin which do not capture all regulatory effects. In a recent modeling assessment (Zewde et al., 2021), an integrated systems biology model for all the three complement pathways, alternative, classical, and lectin, has also been developed for modeling the complement response against pathogens such as N. meningitidis. The focus in this study is on evaluating target proteins in the alternative and terminal pathways with a mechanistic description of complement over-activation observed in autoimmune diseases. Moreover, the previous modeling assessments have not evaluated the effect of several complement proteins as potential targets for drug development, and the evaluation of drug dosing requirements for human clinical trials has also not been conducted.

The computational complement pathway model or simply the "complement model" or "QSP model" developed in this study comprehensively describes the dynamics of complement activation through the alternative and terminal pathways. The tick-over and amplification of the alternative pathway have been described in plasma and on the surface of erythrocytes, respectively. An *in silico* description of the lysis of host cells due to complement over-activation has been modeled due to the formation of the MAC *via* the terminal pathway. The complement model also includes an expanded and more

physiologically relevant description of the plasma and cell surface regulatory proteins such as Properdin or factor P (FP), clusterin, vitronectin, CD59, complement receptor type 1 (CR1), CD55 or decay-accelerating factor (DAF), factor H (FH), and factor I (FI). For refining the model dynamics and estimating the kinetic parameters, several published and in-house *in vitro* datasets were used for validation of the dynamics of alternative and terminal pathways.

The model simulations, *via* reduction in FH and CD59, reflect the mechanistic basis of complement activation in diseases such as atypical hemolytic uremic syndrome (aHUS) and paroxysmal nocturnal hemoglobinuria (PNH). These fundamental representations of simulated disease states have been used for evaluating the effect of potential complement targets on reducing disease severity *via* downstream biomarkers (e.g., C3a, C5a, and MAC) and the lysis of erythrocytes.

A number of drug candidates are currently in development across the pharmaceutical industry (Harris, 2018; Mastellos et al., 2019; Zelek et al., 2019) for targeting complement proteins. Several complement proteins such as C3, factor B (FB), factor D (FD), C5, C6, and C7 are present in the blood at extremely high concentrations (~mg/ml) and/or have fast turnover rates (Harris, 2018) as compared to most other targets in inflammatory diseases, such as cytokines (~pg/ml). This poses challenges around the feasibility of dosing enough for drugs to engage the target and risk of potential side effects due to it. Thus, we have evaluated drug doses needed for small-molecule and large-molecule antibody drugs to engage complement proteins to provide "dosing tractability" estimates within feasible dose ranges of these two modalities.

There are also short-lived intermediate proteins in the complement pathway (e.g., C3b, C3bB, and C3/C5 convertases) formed due to proteolytic cleavage and conformational changes. These cleavage products have not been fully explored in the pharmaceutical industry but represent promising drug targets due to their low concentrations and the potential of engaging them with lower drug doses. Therefore, an assessment of the dosing tractability was performed for these novel targets as well. Additionally, since higher doses of drug candidates may be compensated by lower, that is, more potent drug affinities to attain the required level of target engagement and *vice versa*, an assessment of both the dose levels and drug affinities for target engagement has been done. These evaluations have been used to guide the drug development for complement therapeutics during early target validation and lead optimization phases to support assessments such as modality selection, dosing tractability, and effects of target engagement on complement pathway endpoints.

In **Section 2**, the development of the complement pathway model with alternative and terminal pathways as well as the dynamics of regulatory proteins has been described. This section also describes the methods for preclinical *in vitro* assays that were used for validating the QSP model dynamics. **Section 3** shows the simulation results for the complement model starting with the comparisons with preclinical data. After validation of the pathway dynamics with *in vitro* data, the model has been further validated by predicting the effect of deficiency in regulatory proteins on the pathway activation *in vivo* in humans which have been observed in several complement-driven disease pathologies. Furthermore, an analysis of the effect of inhibiting potential drug targets on reducing complement activation is shown to identify promising targets for drug development. In addition to reducing the disease severity, the tractability of the targets due to their drug dosing and affinity requirements has been analyzed to provide a comprehensive evaluation of developing drugs targeting complement proteins and intermediates. **Section 4** discusses the key results obtained in this work, the scope of the analysis conducted, model limitations, and thoughts on further explorations for future work using the computational modeling approach.

2 METHODS

2.1 Mathematical Model Development

The complement model describes pathway activation in plasma and on the surface of erythrocytes *via* the alternative and terminal pathways. The model consists of 311 state variables and 139 kinetic parameters. The processes included in the computational model are detailed in the following sections and presented in **Figure 1**. A summary of the model variables, reactions, parameter values, their sources, and ordinary differential equations (ODEs) is provided in supplementary files. The reaction fluxes have been derived using mass action kinetics for most processes and Michaelis–Menten kinetics for enzymatic reactions. All the model development and simulation work have been carried out using the SimBiology toolbox in MATLAB 2019a (Mathworks).

2.1.1 Alternative Pathway and Its Regulators

2.1.1.1 Tickover reactions

The tickover reactions in the alternative pathway provide a sustained low level of complement activation in plasma which can get amplified if a pathogen or cell surface is detected by the complement proteins. The alternative pathway is initiated by the spontaneous hydrolysis of the thioester in C3, forming $C3(H_2O)$ in the plasma or "fluid" phase. $C3(H_2O)$ can then bind with FB, generating $C3(H_2O)B$. There are conflicting reports (Pryzdial and Isenman, 1988; Bexborn et al., 2008) regarding the relative affinity of FB for $C3(H_2O)$ and C3b. Because of this discrepancy, the model assumes that $C3(H_2O)$ and C3b bind with FB with the same binding rate constants. FD cleaves $C3(H_2O)B$ producing the tickover convertases $C3(H_2O)Bb$ and Ba. Once activated, $C3(H_2O)Bb$ can cleave C3, producing C3a and C3b with a reactive thioester denoted as C3b(meta) in the model. The kinetic efficiency of the fluid convertase $C3(H_2O)Bb$ is assumed to be half of C3bBb (based on (Pangburn and Müller-Eberhard, 1986; Bexborn et al., 2008)). Since studies on particle-bound and cobra venom factor convertases indicate that the non-catalytic subunit of the convertase only affects its K_m (Tille et al., 2020), the model uses the k_{cat} reported for C3bBb and modifies the K_m to match experimental observations for the kinetic efficiency.

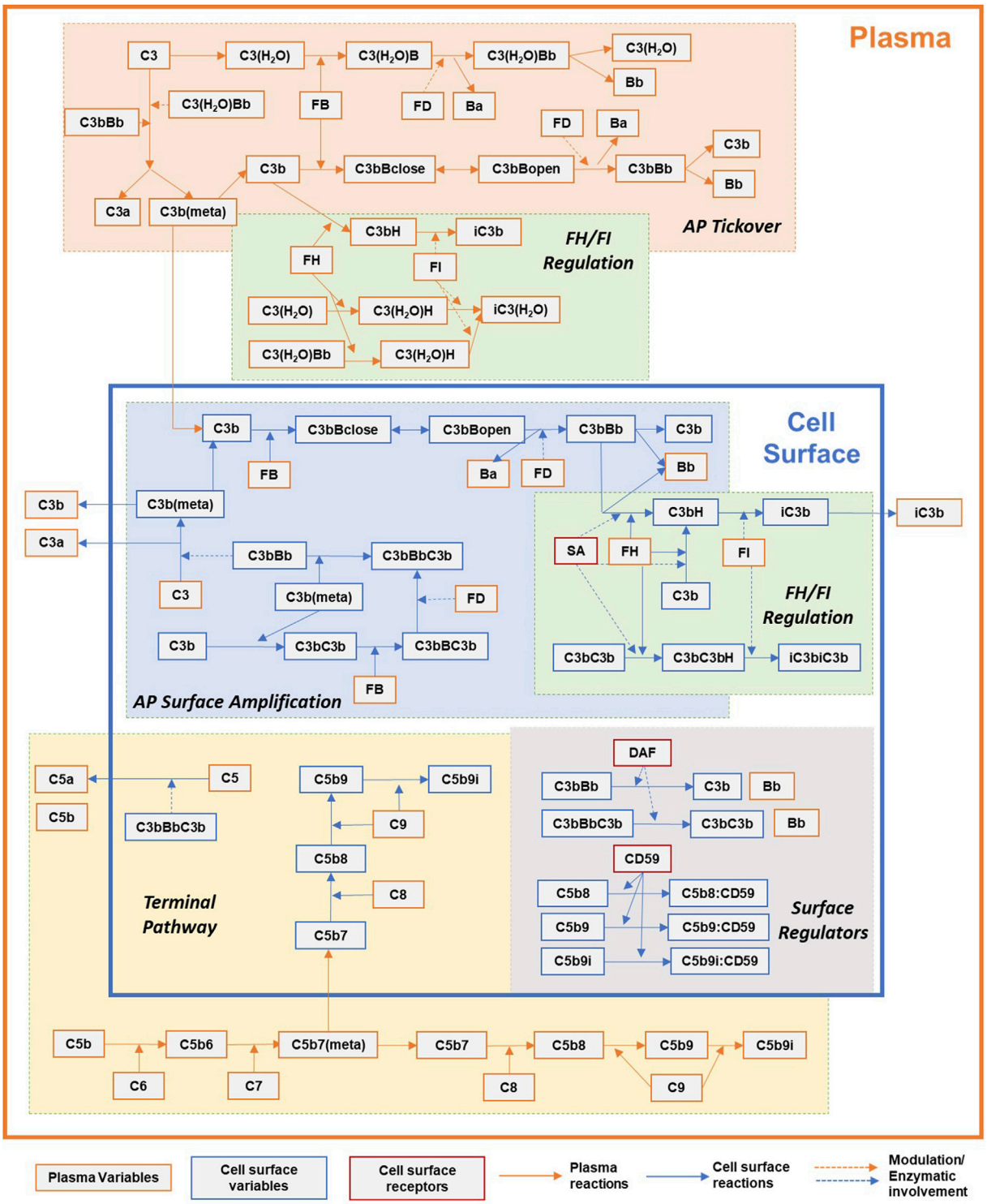

FIGURE 1 | Simplified overview of the processes in the complement pathway model for plasma and cell surface reactions. Key processes shown here: alternative pathway (AP) tickover, regulation by FH and FI in plasma and cell surface, AP surface amplification, terminal pathway, and surface regulators: sialic acid, DAF, and CD59. Dynamics for binding of complement proteins to Properdin are not included here for simplicity and represented separately in **Figure 2**. Other key processes included in the model but not shown here: dynamics of regulation by CR1, clusterin, and vitronectin.

The metastable thioester of C3b(meta) either binds to the cell surface or gets inactivated in plasma. If the metastable thioester decays before it binds to the cell surface, it can still participate in the fluid-phase reactions described for C3(H_2O) by first binding with FB and then FH (Volanakis, 1990). The products of these reactions are cleaved by FD and FI. Surface plasmon resonance (SPR) studies of C3b binding to FB have revealed a two-state conformational change model (Harris et al., 2005; Hourcade and Mitchell, 2011) for the proconvertase C3bB which has been adopted in the model for both plasma and cell surface reactions. C3b binds with FB to form a "closed C3bB," denoted as C3bBclose, which undergoes a rapid conformation change to form C3bBopen (following the notation in (Torreira et al., 2009)) which is then cleaved by FD to form C3bBb. The parameters for this conformation change are assumed to be the average of the parameter values estimated from multiple studies (Hourcade and Mitchell, 2011). The fluid-phase C3bBb can cleave C3, generating more C3a and C3b(meta) in the surrounding fluid. The C3-convertase is very unstable, and the Bb domain can irreversibly disassociate with a half-life of approximately 1.5 min (Pangburn and Müller-Eberhard, 1986). The isolated Bb has been shown to lose 99% of its activity toward C3 after decay of the C3-convertase (Fishelson and Müller-Eberhard, 1984); thus, the model assumes that Bb does not participate in any other reactions in the complement cascade.

2.1.1.2 Regulation by Factor H and Factor I

In plasma, C3(H_2O) can bind to FH, generating C3(H_2O)H. This represents the first point of regulation in the alternative pathway as the binding to FH competes with the binding to FB and further activation. FI can cleave C3(H_2O)H, releasing FH and the inactive product iC3(H_2O). FH also binds with C3b, creating the complex C3bH in the fluid and on the cell surface. The model assumes that FH binds to C3b with a slightly higher affinity than that of C3(H_2O) based on the parameter fitting with internal data (data not shown). Unlike the FH reactions in the fluid phase, the cell surface reaction depends on the quality of the surface, usually attributed to the presence of sialic acid (SA) residues, and studies have shown (Kazatchkine et al., 1979) that the affinity of FH for C3b in the absence of SA is significantly lower, which has been accounted by the model by adding a linear effect of SA residues on FH binding with C3b. FI can cleave C3b to iC3b in the presence of a cofactor such as FH or CR1, and then subsequently to C3c and C3dg.

2.1.1.3 Surface Amplification

Amplification of the alternative pathway can occur on suitable cell surfaces. Although the thioester of C3b appears to have little preference for various cell surface moieties (Müller-Eberhard, 1988), regulation by soluble FH and membrane-bound receptors classify cells as activators or non-activators of the alternative pathway. Cell surface-bound C3b occupies binding sites denoted as C34b* in the model. As in the fluid phase, surface-bound C3b interacts with fluid-phase FB to form the proconvertase closed and open confirmations, and then with FD to form the C3-convertase C3bBb. Cell surface C3-convertase is also assumed to be unstable with a half-life of 1.5 min as modeled for the fluid phase.

On the surface, C3bBb further cleaves C3 and perpetuates the amplification loop of the alternative pathway. However, since the convertase is bound to the surface, the extremely labile C3b(meta) generated near the surface has a higher probability of binding that surface. C3b(meta) also interacts with C3bBb to form the C5-convertase, C3bBbC3b. Furthermore, C3b(meta) can bind to the α-chain of the surface-bound C3b (Hong et al., 1991, p. 199), generating C3b dimers on the surface. C3b dimers are also assumed to interact with fluid-phase FB and FD to form surface-bound C5-convertase.

2.1.1.4 Role of Properdin

Properdin or factor P (FP) is the only known positive regulator of the alternative pathway. In plasma, FP exists as a mixture of head-to-tail dimers, trimers, and tetramers (Smith et al., 1984). It is assumed that the Properdin oligomers provide two, three, and four binding sites, respectively, on dimers, trimers, and tetramers for C3b binding and *de novo* assembly of the C3-convertase. The quantitative implementation for the role of Properdin in the activation of the alternative pathway is based on the model proposed by Hourcade (2006). In addition to the stabilization of the C3 and C5-convertase, Properdin promotes the association of C3b to FB, binds to the surface-bound C3b or other ligands, and uses its unoccupied binding sites as receptors for nascent C3b and preformed C3-proconvertase and convertase. The binding of Properdin to the surface of erythrocytes is assumed to be fully dependent on the initial deposition of C3b in line with recent studies (Harboe et al., 2004), and its controversial role as a pattern-recognition molecule with direct binding to cell surfaces is not taken into account in the model.

The effective number of C3b binding sites on a Properdin oligomer was estimated using the weighted average of the ratios of the oligomers (dimers, trimers, and tetramers) and is approximately 3 ((22*2 + 52*3 + 28*4)/(22 + 52+28) = 3.06). The oligomer, denoted as FPn in the model, binds to surface-bound C3b, C3bBclose, C3bBopen, C3bBb, or iC3b, and generates two additional binding sites (P*) on the cell surface for convertase assembly (**Figure 2**). C3b and its complexes, in plasma as well as on the cell surface, can bind with P* and continue the assembly of the C3-convertase. FPn is assumed to behave in a similar manner in plasma and provides three binding sites to C3b, its complexes, and inactive cleavage products. The binding affinity of C3b to Properdin is more than the order of the magnitude higher than FB (0.0345 μM (DiScipio, 1981)) with a stable half-life of 23 min. Furthermore, Properdin binds to C3-proconvertases and convertases better than how it binds to C3b (association rate constant assumed 2.5 and 15 times that of C3b, respectively, inferred from the study by Hourcade (2006). All Properdin-bound proteins participate in the same reactions as non-Properdin proteins for binding or cleavage by FB, FD, FH, FI, and other regulators, however, with different kinetic rate constants in some reactions. Properdin-bound C3b associates five times faster with FB than nascent C3b (Hourcade, 2006) and with a reduced affinity with FH (Medicus et al., 1976). The kinetic rate constants for all subsequent interactions with P* are assumed to be the same as the 1st binding event to the oligomer FPn. Although steric hindrance might lower the binding rates for the

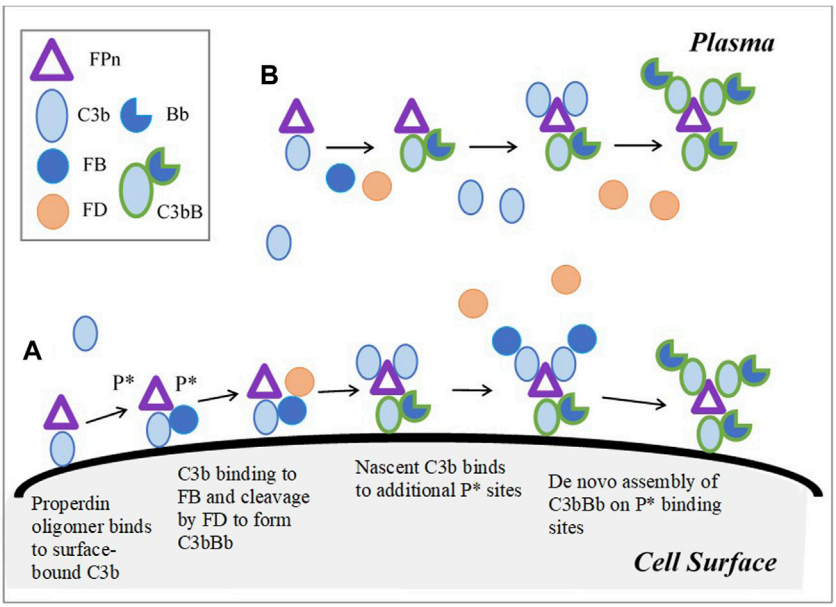

FIGURE 2 | Model implementation for Properdin dynamics in plasma and cell surface (expanded based on Figure 6 in Hourcade (2006)). **(A)** Cell surface: Properdin binds to surface bound C3b and C3-proconvertases, C- convertase, or iC3b, and provides two additional sites P* for the *de novo* assembly of the convertase. FPn binding to only surface-bound C3b is shown in the figure for simplicity. Similarly, in addition to C3b-P* binding, C3 proconvertase–C3bB, C3b-convertase, and iC3b can occupy P* sites. **(B)** Plasma: C3b or its complexes and cleavage products bind to three binding sites on FPn, leading to convertase assembly. Unlike on cell surface, P* does not contribute to amplification of the pathway through additional binding sites in plasma; however, complement activation in plasma is enhanced by Properdin due to increased binding between C3bP and FB, and stabilization of C3-convertase.

2^{nd} and 3^{rd} binding events, or alternatively, the cross-linking effect on C3bBb binding to multiple Properdin-binding sites may progressively increase the stabilization of the convertase (Alcorlo et al., 2013), these effects are not considered in the model.

The availability of multiple binding sites on Properdin oligomers for the assembly of the C3-convertases as well as reactions with several plasma and surface-bound proteins leads to rapid amplification, and it is a key component of complement activation.

2.1.2 Terminal Pathway and its Regulators

The terminal pathway is initiated by the cleavage of C5 to C5a and C5b by the alternative pathway C5-convertase. C5a is a potent, short-lived anaphylatoxin and C5b can bind to C6 and perpetuate the formation of the MAC that causes cell lysis. However, only a portion of the newly generated C5b binds to C6 forming C5b6 before its binding site degrades. Since C5b6 is a stable complex, the model assumes the formation of this complex as irreversible. The newly generated C5b6 can bind to C7, creating the C5b-7(meta) complex that possesses a meta-stable binding site for the surface of the target cell.

The metastable binding site of C5b-7(meta) can either bind to the target membrane or become inactive in the solution. C5b-7(meta) deposition on the surface is inhibited by clusterin (Cn), vitronectin (Vn), and C8 in the plasma. The C5b-7 complexes that have lost the ability to bind to the cell surface are collectively denoted here as soluble MACs or SC5b-9 complexes. The formation of C5b-7 on the surface of a target cell represents a key point of regulation in the terminal cascade. Once bound to the target surface, C5b-7 can bind to C8 and up to 16 C9 units, forming MACs of various sizes denoted in the model as C5b-9_i (where $1 \le i \le 16$). The binding rate of C9 molecules to C5b-8 and C5b-9_i is assumed to be equal based on literature evidence (Müller-Eberhard, 1988). The accumulation of MACs (C5b-9i) causes cell lysis as a function of MAC per cell surface (MAC/cell) and a cell-dependent parameter "K_m_lysis," which denotes the number of MAC per cell that leads to 50% cell lysis.

The formation of C5b-9 complexes on the surface is inhibited by the membrane-bound regulator CD59, and it acts by inhibiting the C5b-8-catalyzed insertion of C9 into the lipid bilayer (Meri et al., 1990). CD59 is widely expressed in different cell types, including erythrocytes (Holguin et al., 1989a; Sugita et al., 1988), and is missing or reduced in PNH (Holguin et al., 1989b), causing the lysis of erythrocytes. CD59 binds tightly to the C9 binding site on C5b-8 and on C5b-9_i, thus competing with and inhibiting the binding of subsequent C9 units. Meri et al. (1990) estimated the number of CD59 to be 25,000 per human erythrocyte.

Clusterin and vitronectin bind to C5b-7(meta) and prevent its binding to the cell surface inhibiting MAC formation and subsequent cell lysis. C5b-7(meta) bound to Cn and Vn in the fluid phase, denoted as C5b-7:Cn and C5b-7:Vn, and can continue to bind to C8 and C9 to assemble soluble MACs. In addition, Cn and Vn bind to C5b-8 and C5b-9_i both in the fluid and on the cell surface to prevent binding to C9 and inhibit C9 polymerization (Preissner et al., 1989; Tschopp et al., 1993; Hadders et al., 2012). The affinity of Cn for binding to C5b-8 and C5b-9_i has been adopted based on a previous modeling work (Korotaevskiy et al., 2009). In the absence of quantitative

TABLE 1 | Complement protein levels in healthy state in humans and their half-lives.

Protein	MW	Serum concentration[a] (micromole/L)			Half-life	Half-life references
	(kDa)				(hour)	
		Min	Max	Average	*Unless specified*	
C3	185	5.405	8.108	6.486	49–69	Sliwinski and Zvaifler (1972)
C5	190	0.289	0.595	0.395	34.65	Alper and Rosen (1984)
C6	105	0.514	0.686	0.610	30–50 min	Schaller et al. (2008)
C7	92.4	0.530	0.758	0.606	61	Schaller et al. (2008)
C8	151	0.331	0.530	0.364	48	Assumed
C9	71	0.662	0.986	0.845	48	Assumed
FB	93	1.828	2.774	2.151	34.65	Alper and Rosen (1984)
FD	24	0.042	0.083	0.058	0.87	Pascual et al. (1988)
FH	155	1.613	3.639	3.226	6 days	Licht et al. (2005)
FI	88	0.386	0.386	0.386	45	Møller Rasmussen et al. (1988)
FP[b]	53	0.094	0.283	0.094	73.2	Alper and Rosen (1984)
Vn	70	2.857	5.714	6.786	48	Assumed
Cn	80	3.125	5.250	3.750	48	Assumed

[a]*"Human Complement Proteins." https://www.complementtech.com/catalog/human-complement- proteins/ (accessed Jun. 15, 2017).*
[b]*FP, trimer concentration (FPn) = 0.094/3 = 0.031 μmol/L.*

estimates for kinetic rate constants for vitronectin, the same values are adopted as for clusterin.

2.1.3 Other Regulatory Effects

FH and FI are prominent negative regulators of the alternative pathway. In addition to binding with C3b to prevent the C3-convertase assembly, FH accelerates the decay of C3-convertases of the alternative and classical pathways (Seya et al., 1985; Bernet et al., 2004). Based on literature data (Weiler et al., 1976), the presence of FH reduces the half-life of nascent and FP-stabilized convertases by almost 4 and 2.5 times, respectively. As discussed previously, FH and FI also compete with FB for binding to C3b(meta) and lead to its cleavage into inactive C3b products such as iC3b, C3dg, and C3c.

Similar to FH, the surface receptor CR1 serves as a cofactor for the FI-mediated cleavage of C3b while also accelerating the decay of the alternative pathway convertases. Low levels of CR1 are associated with autoimmune diseases such as systemic lupus erythematosus and rheumatoid arthritis. Furthermore, the different CR1 isoforms appear to contribute to the decay acceleration and FI-mediated cleavage to a similar degree (Seya et al., 1985); therefore, different isoforms are not considered in the model.

The alternative pathway convertases are also degraded by DAF or CD55. Unlike CR1, DAF does not serve as a cofactor for FI-mediated cleavage. The effect of DAF on the decay of C3-convertase has been included based on the literature studies (Harris et al., 2005) on both cell surface and plasma in the model.

2.1.4 Baseline Complement Model Simulation

The baseline simulation of the complement model represents a human *in vivo* "healthy state" without any disease pathologies and captures the healthy levels of major complement proteins within the known ranges. The levels of complement proteins and their serum half-lives are summarized in **Table 1**. For complement proteins where data on half-life were not available, a 2-day half-life has been assumed based on the known ranges of the half-lives for other complement proteins. The synthesis rates of proteins were estimated to maintain the healthy levels in baseline simulations.

2.2 Methods for *In Vitro* Complement Assays

2.2.1 Alternative Pathway Assays

The generation of C3a, Ba, and iC3b, in the presence and absence of FP, was measured in an *in vitro* assay using purified alternative pathway components (all purchased from Complement Technologies, Tyler, Texas, United States). C3 (final 300 μg/ml), C3b (final 5 μg/ml), factor B (final 50 μg/ml), factor D (final 350 ng/ml), factor H (final 125 μg/ml), and factor I (final 8.5 μg/ml) were mixed in an assay buffer (PBS/14 mM $MgCl_2$) in the presence or absence of Properdin (1.25 μg/ml) and placed in a 37°C water bath. Samples were removed at each time point (5, 10, 15, 30, and 45min; 1, 1.5, 2, and 3 h) and placed in a fresh tube containing 2 μl of 10x stopping solution (100 mM EDTA/100 μM GSK3528001A, a small-molecule factor B inhibitor) and placed on wet ice. The samples were diluted 1/5 with PBS and stored at −80°C until cleavage fragment analysis. C3a was measured using the Complement C3a Human ELISA Kit (Invitrogen, BMS 2089, lot: 123684009), and the samples were further diluted 1/75 in the kit sample diluent. Ba was measured using the MicroVue Ba fragment EIA (Quidel, A034, lot: 064580) and the samples were further diluted 1/500 in the kit sample diluent. A custom sandwich ELISA (method in **Supplementary Material**) was developed to measure iC3b using neo-epitope specific monoclonal antibodies (capture: antihuman C3 clone bH6; detection: antihuman C3dg/iC3b/C3g clone 9; both Hycult).

All complement proteins (human biological samples) for this and other assays were sourced ethically, and their research use was in accordance with the terms of the informed consents under an IRB/EC approved protocol.

2.2.2. Terminal pathway assays

The titration of purified C5b6, C7, C8, and C9 was performed in a reactive lysis system using guinea pig erythrocytes. For each assay

plate (C7, C8, and C9 titrations), 2 ml of guinea pig erythrocytes (supplied in Alsever's solution, TCS Biosciences) were washed in PBS and pelleted (500xg, 5 min). After aspiration of the supernatant, 120 µl of the cell pellet were suspended in 6 ml C5b6 in PBS (1 µg/ml) and incubated for 5 min at 37°C in a water bath. For the C8 and C9 titrations, C7 (1 µg/ml) was added directly to the C5b6-coated erythrocytes to generate C5b7-coated erythrocytes and incubated for 15 min at 37°C, followed by two washes with PBS. C8 (or C9) was serial-diluted in wells of a round-bottom polypropylene plate (50 µl per well), and C9 (or C8) was diluted to 3 µg/ml (or 1 µg/ml) and 50 µl added to the relevant wells in the serial-dilution plates for C8 (or C9). 50 µl of C5b-7-coated erythrocytes were then added to each well and the reactions incubated on a plate shaker for 30 min at 37 °C. For the C7 titration, C7 was diluted to 10 µg/ml, serial-diluted in the wells of a round-bottom polypropylene plate and 200 µl of suspended C5b6-coated erythrocytes added to each well, and the plates were covered and incubated for 15 min at 37°C, followed by two washes in PBS and the resuspension of the pellets in 150 µl PBS. 50µl of the cells were then transferred to a fresh plate containing 100 µl of C8 and C9 (at 1 and 3 µg/ml, respectively), and the reactions were incubated on a plate shaker for 30 min at 37°C. Cells mixed with 100 µl H_2O/0.01% Triton-x-100 (Sigma-Aldrich) or 100 µl PBS only were used as 100% lysis and background lysis control, respectively. After incubation, the plates were centrifuged for 5 min at 1000xg, the 100 µl supernatant was transferred to a microtiter plate, and the absorbance was read at 540 nm. For analysis, the background lysis was subtracted from all samples, and the percentage lysis relative to the 100% lysis control was calculated.

2.3 Validation of the Complement Model Simulations

The complement model dynamics were validated using *in vitro* assay data for the alternative and terminal pathways as well as patient disease state data. A "unit testing" approach was used for validating the QSP model dynamics as model sub-components were compared with different datasets separately. A schematic for model simulations for *in vitro* and *in vivo* data is shown in **Figure 3**. The *in vitro* assays can be conducted using purified complement proteins with or without target cells where the activation of the pathway is measured using proteolytic cleavage products such as C3a, Ba, iC3b, and cell hemolysis. To simulate the *in vitro* assays, the synthesis and degradation reactions in the MATLAB SimBiology model were set as "inactive" to create a "closed system." If the cells were not used in the assay, all the reactions for cell surface variables were also set as "inactive," resulting in a simplified "fluid phase tickover" model. The initial conditions in the model were set as the concentrations of the purified proteins or cells used in the *in vitro* assays, and the rest of the state variables were set to 0. After any washing step in the assays with cells, the fluid compartment concentrations are set to 0, while the cell surface concentrations are unaffected before the next protocol step is simulated. The model was simulated for the assay protocols, and the time-course of cleavage fragments or cell hemolysis was compared against experimental data.

The overall validation of the model dynamics has also been performed against data for disease pathologies and drug treatments for completeness. Thus, varied representations of the same complement pathway model, for example, fluid-phase model, closed system, or human *in vivo* system, supported model validation across several data types with parameter values kept the same across all the representations.

3 MATHEMATICAL MODELING RESULTS

3.1 Model Validation With *In Vitro* Data

3.1.1 Alternative Pathway Assays

The dynamics of tickover reactions in the complement model was assessed based on the literature data (Pangburn et al., 1981) for the decay of C3 hemolytic activity due to spontaneous hydrolysis alone, with purified proteins FB and FD, and with FB, FD, FH, and FI. Aligned with the literature data, the hemolytic activity of C3 due to spontaneous hydrolysis was predicted to decline at a slow rate (**Figure 4A**), and in the presence of FB and FD, all C3 hemolytic activity was lost within minutes (**Figure 4B**). However, the regulatory activity of FH and FI in addition to FB and FD led to the controlled decay of C3 hemolytic activity, but it was faster than that due to hydrolysis alone. The value of the parameter for only the forward binding rate of C3b to FB was adjusted within the literature reported values (1.74–4.74 L/(micromole*minute)) to match the experimental data.

The complement pathway fluid-phase tickover model was also compared with GSK *in vitro* data for the pathway activation *via* the formation of cleavage products C3a, Ba, and iC3b. There is a significant increase in C3a, Ba, and iC3b due to complement activation in the assay, and the model predictions match with the observed data for C3a and Ba for both the experimental conditions with and without FP (**Figure 5**). The model predicted that the levels of iC3b will be above the ULQ which was also observed in the assay. The value of the parameter for only the forward binding rate of C3b to FH was adjusted within the values from the literature (6.08–66.48 L/(micromole*minute)) to match the experimental data. The mechanistic model captures the increased pathway activation in the presence of FP (**Figure 5B**) without any further changes in the parameter values or mechanistic implementation of FP dynamics.

Please note that the model parameters were not fitted against the *in vitro* data. The model was able to describe the *in vitro* datasets by adjusting the parameter values within their known ranges, thus validating the model implementation of the complement processes and literature derived kinetic parameters. Moreover, there is also variability observed between the experimental datasets. The *in vitro* AP assays are rapid reactions, and there are several factors that can cause variability. These factors include small differences in the manual addition of reactants, addition of stop solution, temperature, thawing of proteins, and the presence of small

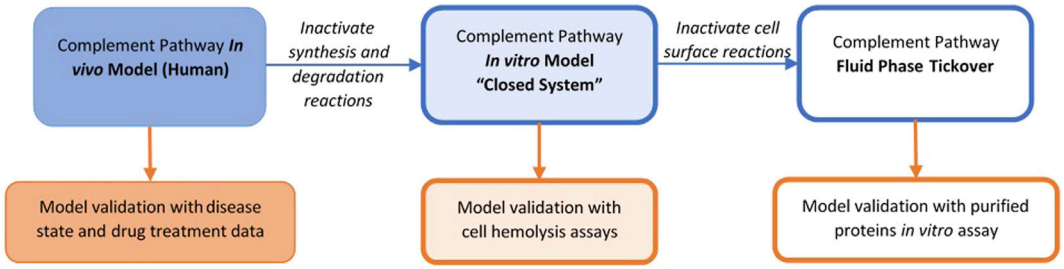

FIGURE 3 | Representations of the complement model for validation with different datasets.

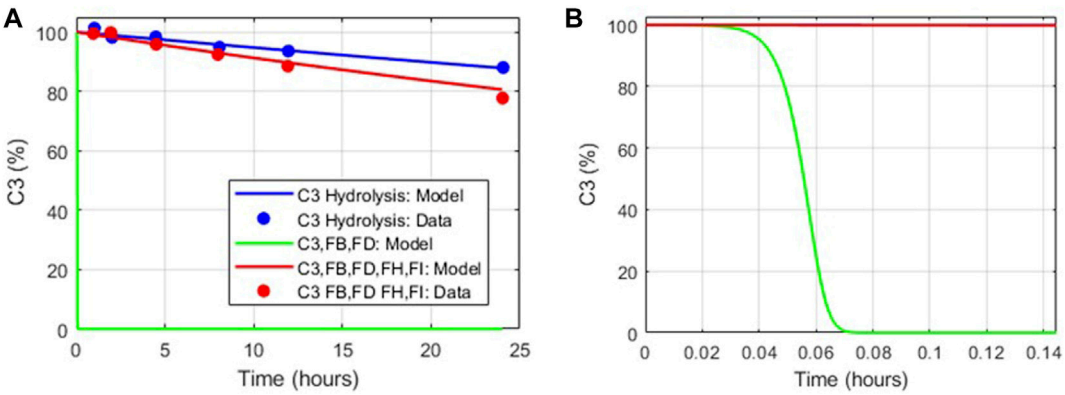

FIGURE 4 | Comparison of the tickover complement model dynamics with *in vitro* data (Pangburn et al., 1981). **(A)** Model simulations match *in vitro* data for C3 hydrolysis alone (blue), with FB, FD added (green) and with FH, FI, FB, and FD added (red). **(B)** Zoomed in view of model simulations for decay in C3 hemolytic activity in the presence of FB, FD (green).

amounts of aggregate. The experiments included were also performed on different days.

3.1.2 Terminal Pathway Assays

There is increased lysis of guinea pig erythrocytes (GPE) observed in terminal pathway assays due to the formation of the MAC on the cell surface by the action of terminal pathway proteins derived from human plasma. The *in vitro* complement model captures the level of hemolysis observed in GPE due to the titration of the levels of C5b6, C7, C8, and C9 complement proteins in terminal pathway assays (**Figure 6**). The cell-dependent parameter "K_m_lysis" was determined to be 0.5 for GPE based on the C5b6 hemolysis assay and kept the same for all other terminal pathway titrations. These assays provide a comprehensive validation of the parameters in the terminal pathway of the model.

The experimental system used for the *in vitro* terminal pathway lysis is a rapid lysis system using GPE. The guinea pig cells are used instead of human erythrocytes as they are void of cell surface regulators that would control human terminal pathway proteins. Healthy human erythrocytes would not lyse effectively. As the experimental system is very sensitive, variation between experiments can be derived from cell batches, small differences in cell number, or time of the cells in storage. The experiments shown were also performed on different days.

3.2 Model Simulations for Humans

In addition to unit testing of the complement pathways with *in vitro* data, the overall model simulations were also compared against human *in vivo* data for the validation of the model dynamics.

3.2.1 Model Validation With Patient Disease States

Deficiency or mutations in regulators of the complement pathway have been implicated in several diseases. Cell surface regulators (CR1, DAF/CD55, and CD59) and FH in plasma were reduced in the complement model to assess the effects on pathway activation *via* an increase in complement fragments, soluble and surface MACs, and lysis of cells. The cell surface regulators were reduced by 99%, representing almost the complete loss of function, and FH was reduced by 50% of their baseline values to simulate their deficiencies or mutations observed in autoimmune diseases (Iida et al., 1982; Rougier et al., 1998; Brodsky, 2014).

Model simulations show that reduction in CR1 leads to a significant increase in the surface and plasma levels of iC3b (**Figure 7**) because it acts as a cofactor for factor I-mediated cleavage of C3b and C3-convertases. An increase in iC3b and other C3 fragments may contribute to complement-driven immune activation in diseases such as systemic lupus erythematosus (SLE) where patients have reduced levels of

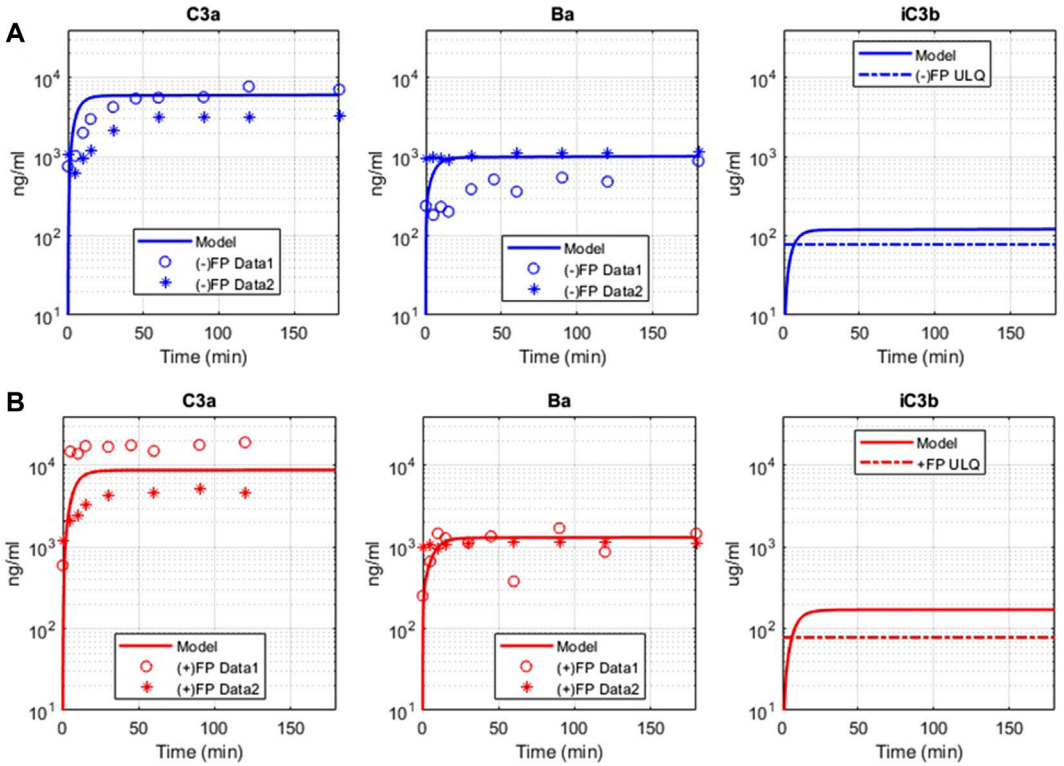

FIGURE 5 | Comparison of model simulations with GSK *in vitro* assay data for alternative pathway. Model results are denoted by solid line, and the assay results are from two sets of independent, identical experiments, denoted as "Data 1" (o) and "Data 2" (*). **(A)** Model simulation and *in vitro* data for alternative pathway assay without Properdin (–) FP for C3a, Ba, iC3b. **(B)** Model simulation and *in vitro* data for alternative pathway assay with Properdin (+)FP for C3a, Ba, and iC3b.

CR1 in erythrocytes (Iida et al., 1982). In fact, the model also predicts a negative linear correlation between the levels of CR1 receptors with deposition of C3 fragments on erythrocytes (**Figure 8A**) similar to the relationship reported in the literature for SLE patients (Ross et al., 1985).

Reduction in CD59 leads to two to three orders of magnitude increase in surface MACs (**Figure 8B**) and soluble MACs (data not shown), causing significant lysis of erythrocytes (~20%) (**Figure 8C**). These simulations are aligned with increased lysis of erythrocytes observed in PNH disease where erythrocytes are highly vulnerable to complement-mediated lysis due to a reduction, or absence, of CD59 and DAF/CD55. However, model simulations show that reduction in DAF does not cause an increase in the MAC or lysis (**Figure 8B,C**) but may contribute to inflammation through some increase in complement fragments such as C5a (**Figure 7**). In line with these modeling results, it has been reported that the reduction in CD59 contributes more to PNH pathogenesis than DAF as there are patients with DAF deficiency but normal CD59 expression who do not have clinically evident hemolytic disease (Wilcox et al., 1991; DeZern and Brodsky, 2015).

A reduction in FH causes a significant increase in several complement fragments, MACs, and cell lysis (**Figure 7**, **Figure 8**). Modeling results also show a reduction in other complement proteins such as C3 and FB due to an increased consumption from the persistent activation of the alternative pathway (**Figure 8D**). The consumption of complement proteins increases significantly at higher FH deficiency levels. These results are consistent with complement protein deficiencies observed in diseases linked to FH mutations such as aHUS, glomerulopathies, and acute infections (C3: 5–68% and FB: 35–100% of normal (Nielsen et al., 1989; Vogt et al., 1995; Rougier et al., 1998)), where FH levels or function vary from 0 to 40% of normal levels.

It is interesting to note that CD59 and FH deficiencies have the strongest effects on cell lysis, which is seen in PNH and aHUS patients where CD59 deficiency and FH deficiency, respectively, have been indicated. FH deficiency also causes an increase in complement fragments (C3a, Ba, iC3b, C5a, *etc.*) which drive inflammatory processes such as immune cell attraction, opsonization, and phagocytosis of host cells, leading to worsening of autoimmune diseases in addition to lysis of host cells.

3.2.2 Effect of Complement Targets on Disease States

The effect of potential drug treatments for reducing disease severity driven by complement pathway activation was evaluated using the computational model. CD59 and FH reduction leads to significant amount of cell lysis, and increase in complement fragments and MAC proteins. Complement model simulations for CD59 and FH reduction represent a semi-mechanistic way of simulating PNH and aHUS disease

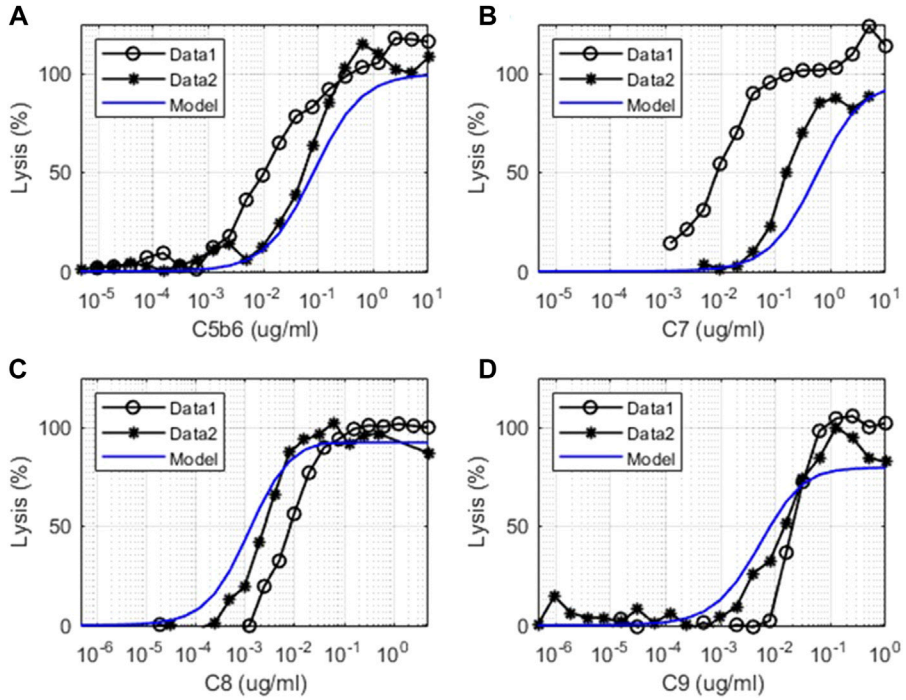

FIGURE 6 | Comparison of model simulations with *in vitro* assay data for terminal pathways. Model simulation results are denoted by solid blue line, and the terminal pathway assay results are from two sets of independent, identical experiments denoted as "Data 1" (o) and "Data 2" (*). Dose–response of cell lysis is shown for different concentrations of **(A)** C5b6 (μg/ml), **(B)** C7 (μg/ml), **(C)** C8 (μg/ml), and **(D)** C9 (μg/ml).

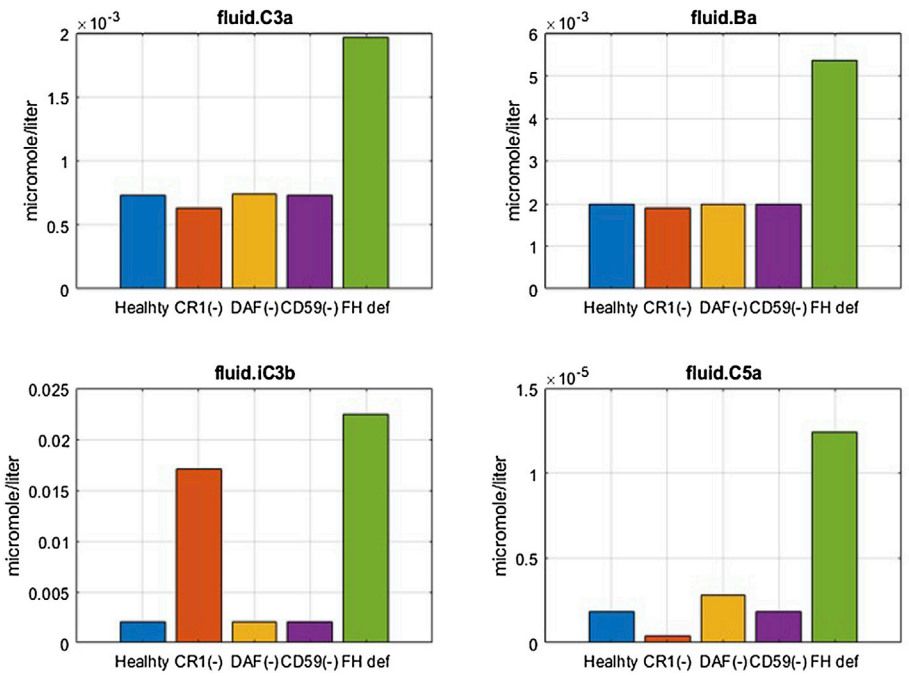

FIGURE 7 | Effect of 99% reduction in cell surface regulators, CR1, DAF, and CD59, and 50% reduction in fluid phase regulator FH on complement fragments C3a, Ba, iC3b, and C5a.

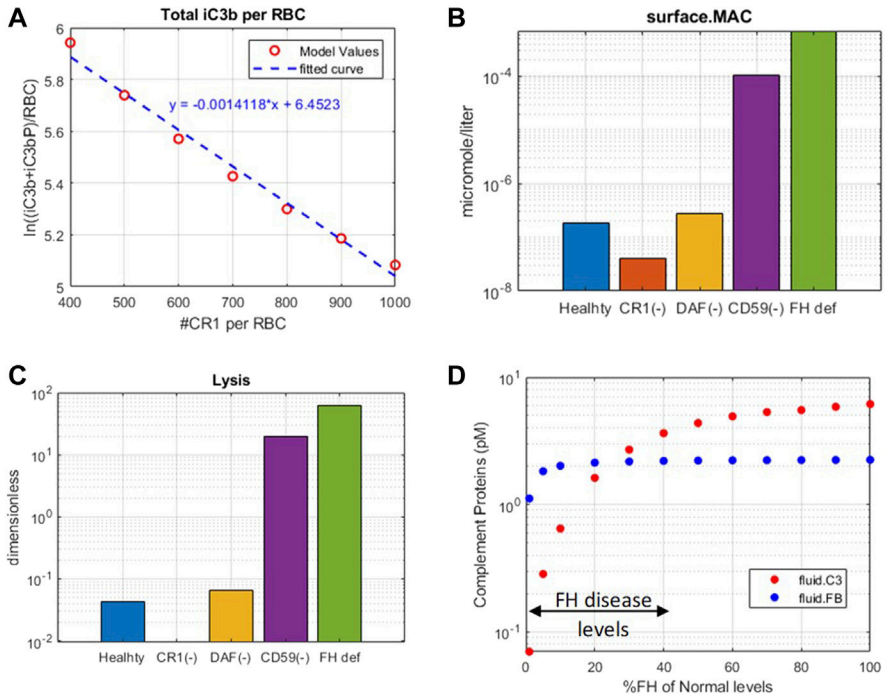

FIGURE 8 | Complement model predictions for **(A)** correlation between iC3b + iC3bP deposition on erythrocytes and levels of CR1, **(B)** surface MAC, **(C)** lysis of host erythrocytes due to 99% reduction in CR1, DAF, and CD59 and 50% reduction in fluid-phase regulator FH, and **(D)** consumption of complement proteins C3 and FB due to FH deficiency ranging from 0 to 99%.

pathologies, respectively. QSP model simulations were used for assessing the effect of potential treatments to reduce the complement activation for these pathologies by reducing the levels of key complement proteins and fragments to 10 and 1% of the normal levels, that is, 90% and 99% inhibition, respectively, from the baseline, which are the typical levels of target inhibition aimed during drug development. CD59 reduction was assumed to be at 99% of its baseline value, and FH reduction at 40% of the baseline aligned with a reduction in function or levels observed in diseases (Rougier et al., 1998; Brodsky, 2014).

For complement activation driven by CD59 reduction, significant lysis of erythrocytes was observed, but there is no increase in upstream biomarkers such as C3a and C5a (**Figure 9**). For reducing this activation, 90% inhibition of C3, FB, FD, C5, C6, FP, C3b, C3Bb, and C3-convertase (C3bBb and C3bBbP) leads to a significant reduction in cell lysis (**Figure 9C**). Moreover, C6 levels needed to be reduced by 99% for complete reduction in cell lysis which may be infeasible with real-world drug compounds. Modulation of alternative pathway proteins C3, FB, FD, C3b, C3bB, and C3-convertase also reduces the complement fragments C3a (**Figure 9A**), iC3b, and Ba (data not shown); however, it may not be important for PNH disease as the levels of these inflammatory mediators were not predicted to be elevated in comparison to healthy control.

For reducing complement activation due to FH deficiency, drug compounds targeting C3, FB, C5, FP, C3b, C3bB, and C3 convertase are predicted to be efficacious in reducing disease severity (**Figure 10**). While 99% inhibition of FD, C6, and C7 is also predicted to reduce cell lysis, it may be infeasible from a drug-development perspective due to high drug dosing requirements. In addition, C6 and C7 inhibition does not lead to a reduction in alternative pathway fragments and may provide only partial efficacy in reducing complement-driven immune activation in aHUS.

As expected, reduction in terminal pathway proteins C6, C7, C8, and C9 does not lead to a reduction in alternative pathway biomarkers such as C3a, C5a (**Figure 9**, **Figure 10**), iC3b, and Ba (data not shown). It is also interesting to note that the inhibition of alternative pathway cleavage fragments C3b, C3bB, and C3-convertase has a stronger effect on C5a and cell lysis than that of C3a in plasma. This is because reduction in these alternative pathway fragments shifts the contribution of C3 cleavage from C3-convertase C3bBb to the fluid tickover convertase C3(H_2O) Bb, thus still maintaining the production of C3a in plasma but causing a reduction in C5a which is formed by the cleavage of C5 by C5-convertase on the cell surface downstream of surface C3-convertase.

3.2.3 Dosing Tractability of Complement Targets

The simulations in **Sections 3.2.1** and **3.2.2** assume sustained inhibition of targets for a prolonged duration. These assessments are invaluable for providing a preliminary assessment for target validation efforts in drug discovery. However, the sustained high level of target inhibition cannot be attained with real-world drugs because of factors such as rapid metabolism of the drugs *in vivo*,

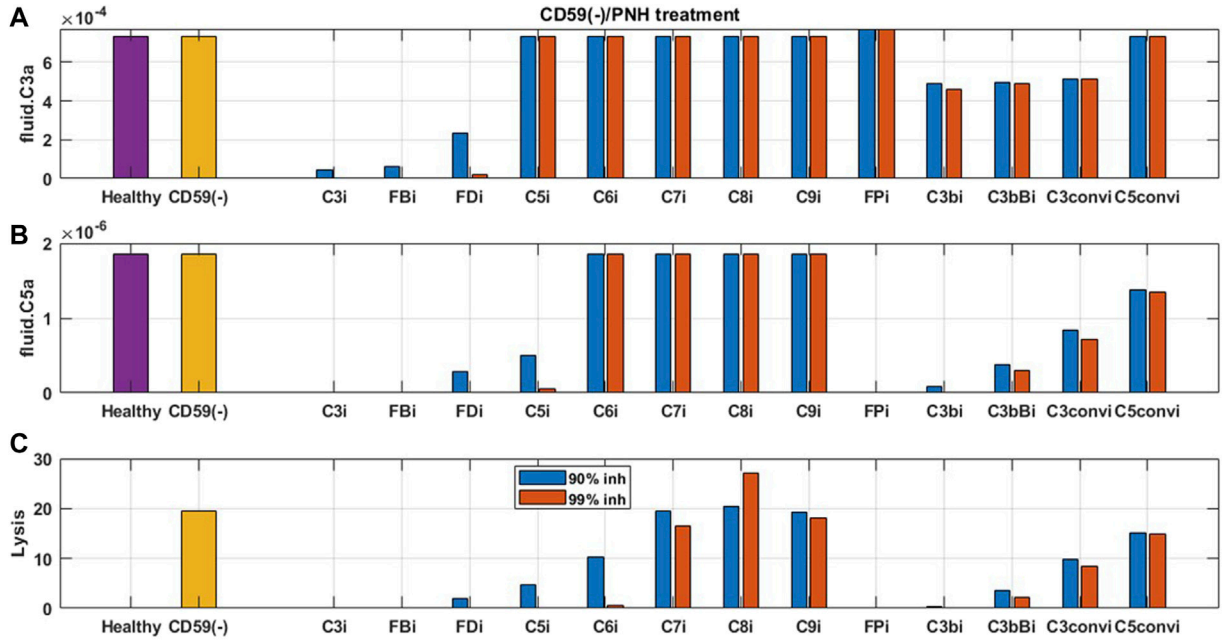

FIGURE 9 | Model predictions for the effect of 90 and 99% inhibition of complement proteins (C3, FB, FD, C5, C6, C7, C8, C9, FP, C3b, C3bB, C3-convertase (C3conv), and C5-convertase (C5conv)) on complement activation driven by CD59 deficiency or knockout such as in PNH disease.

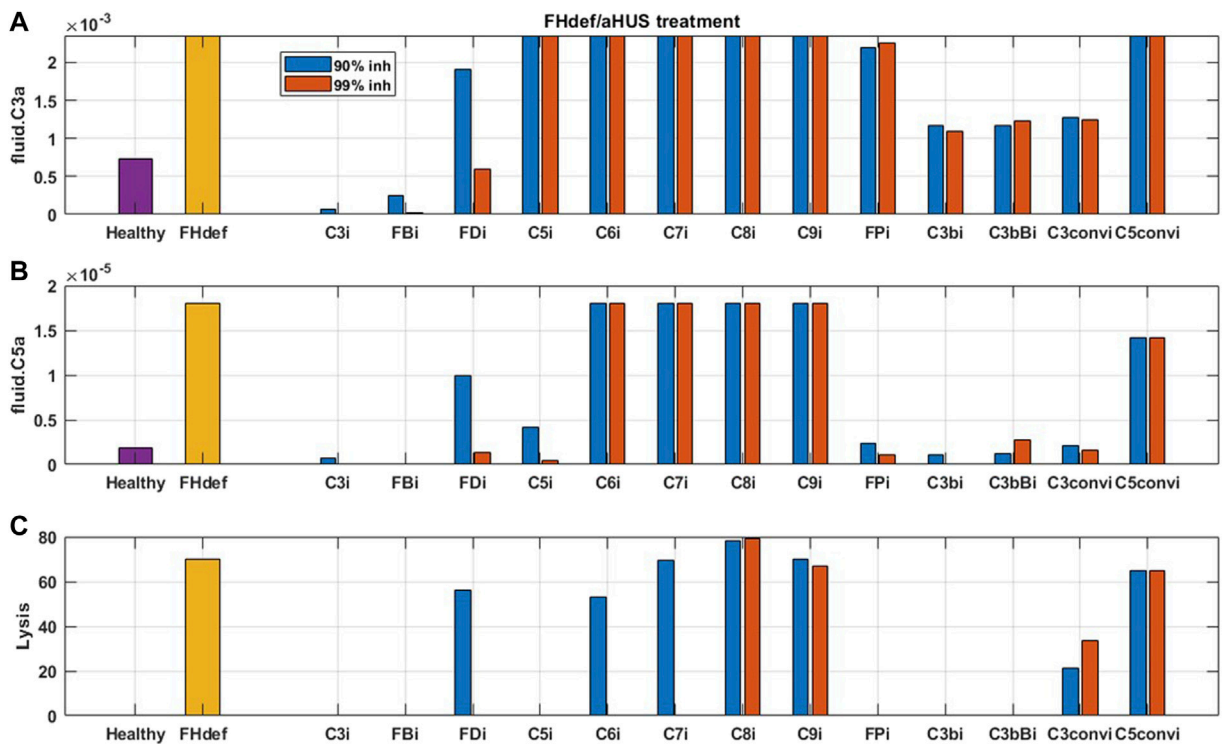

FIGURE 10 | Model predictions for the effect of 90 and 99% inhibition of complement proteins (C3, FB, FD, C5, C6, C7, C8, C9, FP, C3b, C3bB, C3-convertase (C3conv), and C5-convertase (C5conv)) on complement activation driven by 40% FH deficiency such as in aHUS.

TABLE 2 | PK model and parameters for small molecules and large-molecule antibodies.

	Unit	Small molecule	Large molecule-ab
PK model type		2-compartment	1-compartment
Absorption rate (Ka)	1/hr	3.0	5.0
Elimination rate (K10)	1/hr	0.11 (half-life: 6.3 h)	1.03e-3(half-life: 28 days)
Distribution parameter K12	1/hr	0.53	
Distribution parameter K21	1/hr	0.39	
Volume of distribution (Vd)	L/kg or L	0.54 L/kg	5 L
Bioavailability (F)		0.95	1.0
Affinity (K_D)	MM	1e-3	1e-6
Drug kon	1/μM/min	6e+3	60
Molecular weight	Da	390 Da	150,000
Body weight	kg	70	70
Feasible dose range	mg or mg/kg	<= 100 mg	<=20 mg/kg
Dosing frequency		Once daily	Biweekly (two weeks)

limits on drug doses due to toxicity effects, and inconvenience of frequent IV/SC dosing. We have evaluated the feasibility of developing drug modalities targeting specific complement proteins by assessing the dose levels and affinities needed for small molecules (SMs) and large-molecule antibody (LM-Ab) compounds to maintain reduction in free complement target levels and pathway activation. The PK parameters and affinities are assumed the same as a GSK's tool FB inhibitor compound for the SM modality and for a typical "good" LM-Ab compound based on published PK parameters for known mAbs (Zhao et al., 2012; Ovacik and Lin, 2018) (**Table 2**). Note that additional modalities such as peptides, other Ab fragments, and pro-drugs were not considered for simplicity but can also be evaluated using the respective PK parameters and dose levels.

The information on drugs in development (Mastellos et al., 2019; Zelek et al., 2019) is overlaid on dosing tractability predictions performed using the computational model (**Figure 12**). Several complement proteins that are present in very high concentrations or have high synthesis/turnover rates (e.g., C3, FB, FD, and C6) are challenging to block in plasma with LM-Ab compounds (**Figure 12B**) as the drug doses in molar amounts needed for target engagement would be higher than the feasible dose ranges (≤20 mg/kg). This also leads to faster drug clearance due to target-mediated drug disposition (TMDD) for LM-Abs. The inability to engage FD for the entire dosing interval of two weeks even with doses of 20 mg/kg of an antibody is shown in **Figure 11D**. Note that the feasible subcutaneous doses of LM-Ab drugs are even lower, usually <5 mg/kg, and may further restrict the target inhibition that can be attained for complement targets. On the other hand, since high molar amounts of SMs for target engagement can be administered with relatively low dose levels in milligrams due to low molecular weights, SM modalities can be used to block high-concentration complement proteins with low doses. This is illustrated using the compliment model for FD and C5 where ≥ 99% inhibition is attained for an SM dose of only 10 mg (**Figures 11A, B**).

The complement proteins that have a short half-life (e.g., C3b, C3bB, and C3bBb) were predicted to be challenging or infeasible to engage with SM compounds (**Figure 12A**). These short-lived proteins are quickly consumed or degraded in the complement pathway and thus require higher drug affinities for engagement within their short life span and for competing with other proteins in the pathway. Since affinities of SMs are lower than those of LM-Ab compounds, it is challenging to attain higher target engagement for complement fragment targets with SMs as shown for C3-convertase (**Figure 11C**) where only 50% engagement is attained even at the highest SM dose of 100 mg. Additionally, since the plasma levels of C3-convertase are lower, it makes the convertase an ideal target for LM-Ab modality (**Figure 11F**).

Several complement proteins (e.g., C5, C7, Properdin, and C5-convertases) are predicted to have dosing tractability by both small and large molecules with appropriate ranges for target concentrations, turnover, and half-lives. C5 target has the only approved antibody drug, eculizumab, as well as SM assets in development, indicating the tractability by SM/LM-Ab modalities as also predicted by the complement pathway model (**Figures 11B,E**). Although the approved doses needed for the LM-Ab drug eculizumab are high for PNH and aHUS indications, they still lie within the "feasible" ranges assumed in this study.

3.2.4 Drug Affinities Needed for Target Engagement

A nominal drug affinity has been assumed for SMs and LM-Ab compounds for dose assessments in **Section 3.2.3** at 1 nM and 1p.m., respectively. These values are at the upper limit of the feasible affinities for these modalities. Lower drug affinities may be compensated by administering higher doses of drug candidates to attain the required level of target engagement. However, since there are limits on the highest dose range for each modality, lower drug potencies can only be compensated to a certain extent. Thus, the QSP model was used to predict the minimum drug affinity that can still lead to 90% target engagement at the highest feasible dose for SM/LM-Ab compounds. This provides an estimate of the drug affinity that can be aimed during lead optimization of compounds to attain high levels of target engagement for the drug modalities.

The drug affinity requirements for 90% target engagement (TE) may be different from the affinity required for 90% reduction in the disease severity because of the pathway dynamics. This is because the level of TE required for reduction in disease severity may be much higher or lower than the customary 90% TE assumption. Thus, affinities needed for a 90% reduction in cell lysis have been estimated

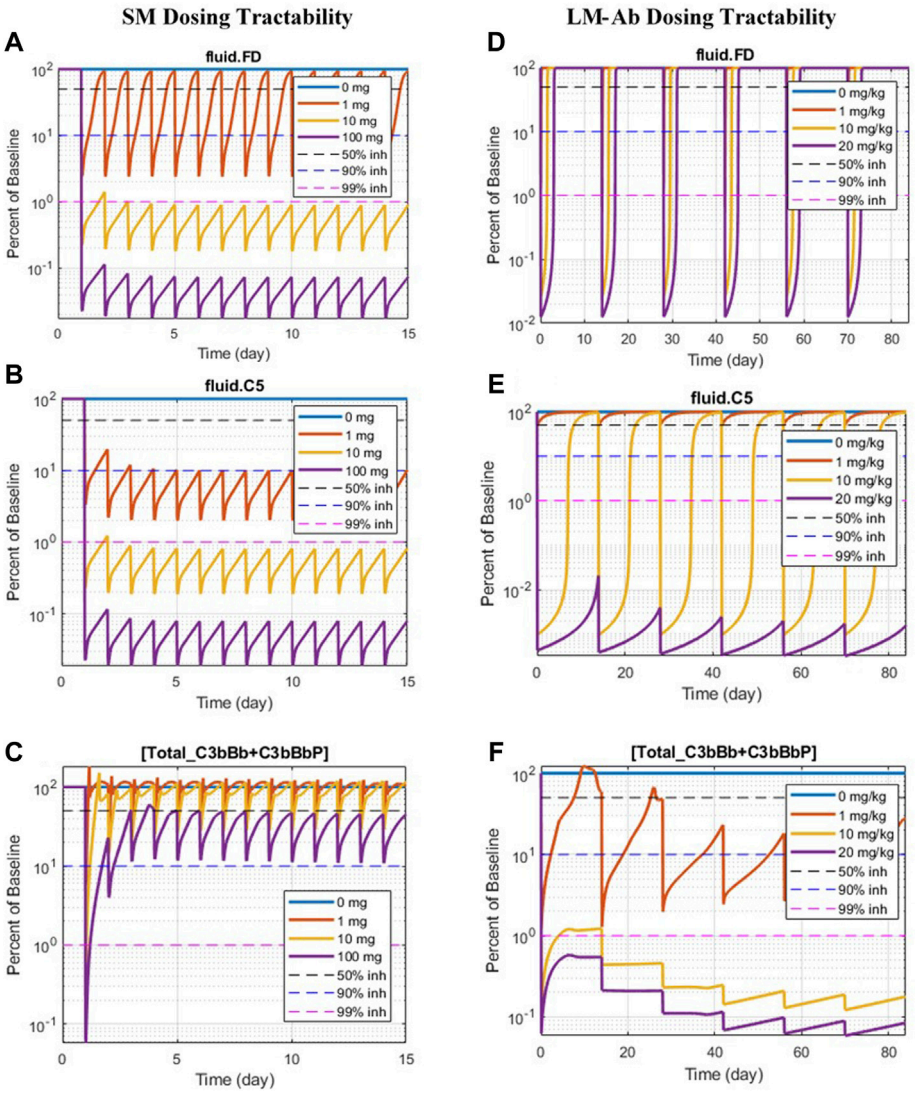

FIGURE 11 | Doses of SM/LM-Ab compounds needed for engaging complement proteins. Free complement protein levels are shown for different doses of SM (0, 1, 10, and 100 mg) and LM-Ab (0, 1, 10, and 20 mg/kg). Dashed lines: 50% inhibition (black), 90% inhibition (blue), 99% inhibition (pink) from baseline. Solid lines: % free target from the baseline at different dose levels. **(A,D)** Blocking of FD; **(B,C)** blocking of C5; **(C,F)** blocking of C3-convertases (C3bBb + C3bBbP).

separately. For example, the SM affinity required for 90% inhibition of FD at the highest feasible dose of 100 mg is ~0.1 μM (**Figure 13A**). But the level of FD inhibition required for reducing cell lysis by 90% is much higher at ~99%, pushing the SM affinity estimated to ~0.01 μM, that is, 10-fold higher for reducing disease severity (**Figure 13B**).

The drug affinity requirements for complement targets vary significantly due to differences in half-lives, concentrations, and competition of drug binding with other proteins in the complement pathway. For SM modality, complement proteins C3, FB, C5, C6, and FD required affinities around 10–100 nM for 90% TE, but affinity required for 90% reduction in cell lysis was almost an order of magnitude more potent for C5, FD, and C6 (**Figure 13C**). Additionally, C3 and C5-convertases needed more potent sub-nanomolar affinity SM compounds for both TE and cell lysis.

For LM-Ab modality, C3/C5-convertases, C5, and C7 are on the lower end of the drug affinity range of ≤1 nM for 90% TE (**Figure 13D**). But the affinity needed for cell lysis *via* C7 inhibition is 100 times more potent than the affinity required for just 90% TE indicating C7 inhibition of 99.9%, or more is required to reduce disease severity. C3bBclose/open forms need ~0.1 p.m. affinity for TE; however, the impact of cell lysis seems to be prominent at even lower affinities for the "closed" form of C3bB.

4 DISCUSSION

A comprehensive QSP model describing complement activation through alternative and terminal pathways has been developed in

	C3	FB	FD	C5	C6	C7	FP	C3b	C3bB open	C3bB close	C3bBb	C3bBb -C3b
A) Small molecule		✓	✓	O								
B) Large Molecule-Ab			×	★	O		O					

Feasible	>90% target inhibition for SM dose <= 100 mg, LM-Ab dose <=20 mg/kg
Challenging	50-90% target inhibition for entire dosing interval or >90% inhibition for at least half of the dosing interval at maximum feasible dose
Infeasible	<50% target inhibition in the desired dose range

★	Approved drug
✓	In clinical development – positive data
O	In clinical/ preclinical development
×	Terminated

FIGURE 12 | Model predictions for dosing tractability of complement proteins for SM and LM-Ab drugs.

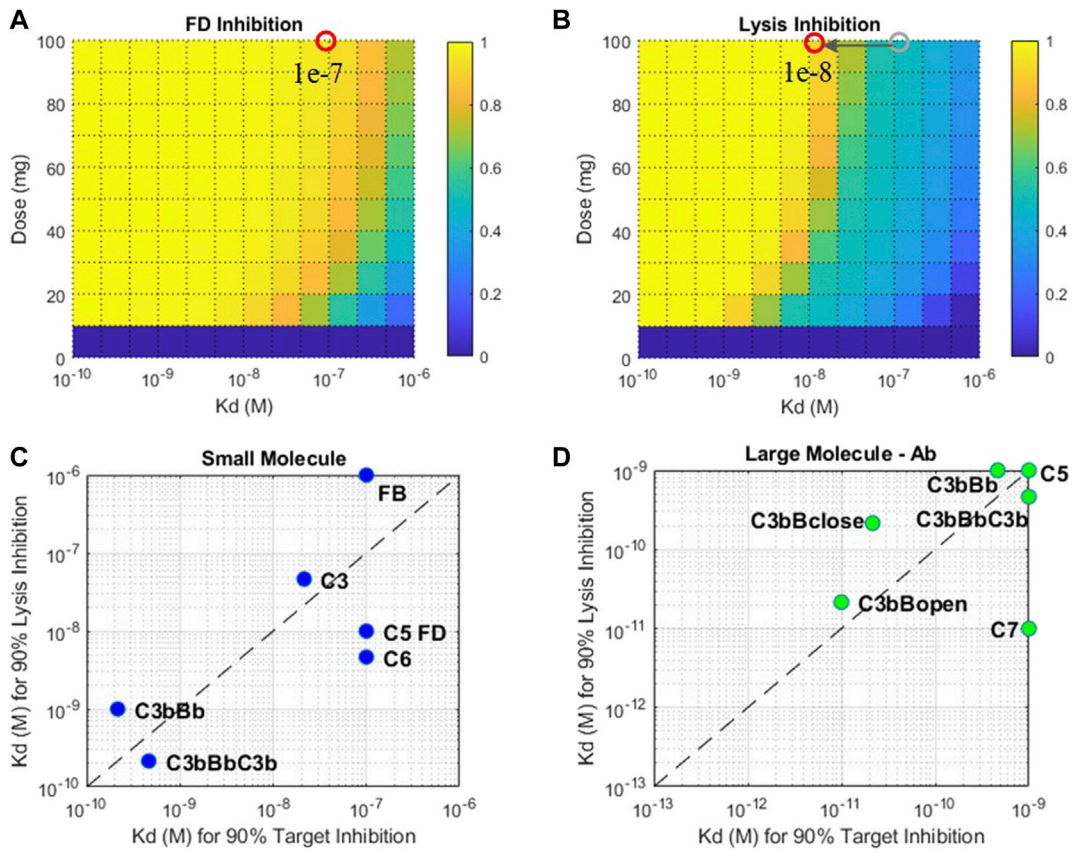

FIGURE 13 | Fractional inhibition in **(A)** FD and **(B)** cell lysis at different affinities (K_D) and doses of a SM modality. Drug affinities required for 90% target inhibition versus 90% cell lysis inhibition for **(C)** small-molecule and **(D)** large-molecule Ab modalities. Plots **(C)** and **(D)**: only the select targets that attain 90% TE and cell lysis are shown. The affinity ranges tested for SM modality—1 μM-0.1 nM and LM-Ab modality 1nM-0.1p.m. Affinity requirements predicted to be on the edges of the plots may be lower than the ranges tested.

this work. The complement model differentiates between the pathway activation dynamics in plasma and on the cell surface. The model also includes a detailed description of several plasma and cell-surface regulatory proteins such as Properdin, clusterin, vitronectin, CD59, CR1, DAF, FH, and FI. The effect of Properdin has been described on the stabilization of the C3 and C5-convertase, on promoting the association of C3b to FB as well as its binding to the surface-bound C3b or other ligands, and using the unoccupied Properdin oligomer-binding sites as receptors for nascent C3b and preformed C3-proconvertase/convertase. This work provides, to date, the most comprehensive mathematical implementation for Properdin stoichiometry and its effect on alternative pathway activation based on available experimental evidence.

The complement model was validated using published or in-house GSK data from *in vitro* assays of alternative/terminal pathways and patient data on disease states. A "unit testing" approach was utilized where separate validation was done for different components of the complex complement model such as alternative pathway, terminal pathway, fluid-phase tickover, a closed *in vitro* system with cells, and overall *in vivo* dynamics. This provided an integrated computational and experimental workflow for the utilization of a variety of preclinical and clinical data for model predictions. It also allowed better management of model complexity and higher confidence in the predictions of the combined model as several datasets were used for calibration and validation of model dynamics.

To assess the effect of drug targets in disease pathologies, a reduction in FH and CD59 was used as a proximate mechanistic description of complement activation in aHUS and PNH, respectively. The effect of complement targets on downstream biomarkers and cell lysis was assessed for these simulated disease states in the QSP model. One limitation of the complement model developed in this study is that it considers the lysis of RBCs only, but in autoimmune diseases such as aHUS, other host cells such as platelets would also be lysed in additional to RBCs (Raina et al., 2019). Nevertheless, model simulations provide a preliminary way of understanding the effect of deficiency of complement proteins, their role in autoimmune diseases, and potential treatments to reduce complement activation. Detailed mechanistic models for a more exact assessment of specific complement-driven diseases can be developed in the future.

For reducing the complement activation due to CD59 reduction in aHUS, 90% inhibition of C3, FB, FD, C5, C6, FP, C3b, C3Bb, and C3-convertase (C3bBb and C3bBbP) was predicted to lead to a significant reduction in cell lysis. For inhibiting complement activation due to FH deficiency, drug compounds targeting C3, FB, C5, FP, C3b, C3bB, and C3-convertase at 90% inhibition are predicted to be efficacious in reducing disease severity. Several of these complement proteins, such as C5, FB, FD, C6, and FP, have either approved treatments targeting them (e.g., anti-C5 eculizumab) or drugs in preclinical or clinical stages of development (Mastellos et al., 2019; Zelek et al., 2019). The modeling results further highlighted the complement fragments or intermediates such as C3b, C3bB, and C3-convertases as potential targets for drug development. These assessments were extensively used to support target validation for complement programs in GSK and provided an early assessment of efficacy for improving severity in complement-driven diseases.

A few other targets were also predicted to inhibit complement activation driven by CD59 and FH deficiency, however at a sustained target engagement requirement of 99% inhibition which posed uncertainty around feasibility of dosing high drug amounts to maintain high target inhibitions. Thus, an assessment of the dosing requirements for complement proteins using small/large-molecule modalities was also warranted. Small- and large-molecule Ab compounds, with PK properties that lie within the feasible range for these modalities, were simulated to provide estimates for the feasibility of dosing with these modalities. These assessments were initiated around the target validation phase of drug development to support target selection based on not only the reduction in disease severity but also dosing feasibility. The modeling results were also used to inform lead discovery efforts for pursuing the right modality for a target.

Key trends emerged from the QSP assessment, which were used to guide the selection of target–modality pairs for drug development. Complement proteins that are present in very high concentrations or have high synthesis/turnover rates (e.g., C3, FB, FD, and C6) are challenging to block in the plasma with LM-Ab compounds as the drug doses in molar amounts needed for target engagement compared with the total target would be higher than their feasible dose range (≤20 mg/kg). Because of high dosing requirements for target inhibition in plasma, strategies for localized dosing in the tissues, for example, intravitreous delivery of FD-targeting mAb lampalizumab in the eye (Mastellos et al., 2019), have been adopted. However, lampalizumab failed to achieve its primary endpoint in Phase 3 clinical trials for age-related macular degeneration (AMD) (Holz et al., 2018), and the specific reasons for failure due to drug bioavailability or efficacy are yet to be addressed.

The complement model simulations also predict that SM compounds are ideal for maintaining sustained target engagement for high concentration complement proteins due to the low molecular weights and high molar amounts per mg of SM doses. However, the complement proteins/fragments that have a short half-life (e.g., C3b, C3bB, and C3bBb) were predicted to be challenging or infeasible to engage with SM compounds due to a high drug affinity requirement to "catch" the target before consumption in the pathway. LM-Ab compounds which have higher affinities were able to engage these targets within their feasible dose ranges and are ideal candidates for targeting short-lived complement fragments or complexes.

Another limitation of this study is that the early dose estimates are based on "typical" PK and affinities for drug modalities. These preliminary estimates should be refined during lead optimization as the specific PK properties of drug candidates become available. Modalities such as peptides were not assessed here for simplicity; however, the principles discussed in this work can be applied for the assessment of several modalities. Also, only systemic dosing was considered; however, it may be feasible to attain target engagement in a specific organ/tissue with localized dosing even though significant target engagement overall in plasma may not be feasible due to high target amounts.

In addition to feasible doses for modality selection, another aspect explored in this work was the estimation of drug affinities needed for engaging the complement proteins. During lead optimization, attaining the right level of drug affinity is extremely critical for success in later studies to demonstrate the required level of target engagement. In addition, the drug affinity requirements for 90% target engagement (TE) may be different from affinity requirements for 90% reduction in disease severity if the level of TE required for disease modulation is much higher or lower than the usually targeted 90% level. Thus, an assessment of affinity requirements for TE and cell lysis was done separately, and significant differences in the affinity requirements were observed for targets. For SM modality, complement proteins C3, FB, C5, C6, and FD required affinities around 10–100 nM for 90% TE, but the K_D required for 90% reduction in cell lysis was almost an order of magnitude higher for C5, FD, and C6. Similarly, for LM-Ab modality, drug affinity requirements for C7 are on the lower end of the drug affinity range of ≤1 nM for 90% TE, but the K_D needed for cell lysis is 100 times more potent. These analyses indicate the importance for accounting for both TE and biomarker/severity endpoints for affinity predictions at the lead optimization stage to prevent the termination of the compounds in later stages of development and improve their probability of success.

The kinetic parameters in the complement model have been set based on literature references, and for parameters without direct literature evidence, the values were assumed based on similar biological processes or proteins. An assessment of the impact of parameter variability in the QSP model using virtual patients and virtual populations (Klinke, 2008; Schmidt et al., 2013; Allen et al., 2016) is beyond the scope of the present assessment and will be covered in future publications. The focus in this work was to provide guidelines for target validation and lead optimization of complement targets and related modalities in early discovery rather than a precise estimate of variability in clinical responses from modulating complement proteins. Thus, assessments have focused on simulating proximate disease states for aHUS and PNH for potential complement targets and doses/affinities for common drug modalities. A detailed assessment of variability in response to biological patient variability and clinical response will be part of further work using the complement model.

DATA AVAILABILITY STATEMENT

The raw data supporting the conclusion of this article will be made available by the authors, without undue reservation.

AUTHOR CONTRIBUTIONS

LB and DH developed the computational model and performed the *in silico* simulation work. E-MN, JN, and CB planned and performed the *in vitro* experimental work. LB and E-MN wrote the manuscript. LB and VD conceived the study and supervised all the findings of this work. LB, E-MN, DH, FC, SL, and VD contributed to discussion and interpretation of the results. All the authors reviewed and contributed to the final manuscript.

SUPPLEMENTARY MATERIAL

The Supplementary Material for this article can be found online at: https://www.frontiersin.org/articles/10.3389/fphar.2022.855743/full#supplementary-material

REFERENCES

Alcorlo, M., Tortajada, A., Rodríguez de Córdoba, S., and Llorca, O. (2013). Structural Basis for the Stabilization of the Complement Alternative Pathway C3 Convertase by Properdin. *Proc. Natl. Acad. Sci. U S A.* 110, 13504–13509. doi:10.1073/pnas.1309618110

Allen, R. J., Rieger, T. R., and Musante, C. J. (2016). Efficient Generation and Selection of Virtual Populations in Quantitative Systems Pharmacology Models. *CPT Pharmacometrics Syst. Pharmacol.* 5, 140–146. doi:10.1002/psp4.12063

Alper, C. A., and Rosen, F. S. (1984). "Metabolism of Radiolabelled Complement Proteins in Health and Disease," in *Pathophysiology of Plasma Protein Metabolism* (Heidelberg, Germany: Springer Link), 195–220. doi:10.1007/978-1-349-06680-3_10

Bernet, J., Mullick, J., Panse, Y., Parab, P. B., and Sahu, A. (2004). Kinetic Analysis of the Interactions between Vaccinia Virus Complement Control Protein and Human Complement Proteins C3b and C4b. *J. Virol.* 78, 9446–9457. doi:10.1128/JVI.78.17.9446-9457.2004

Bexborn, F., Andersson, P. O., Chen, H., Nilsson, B., and Ekdahl, K. N. (2008). The Tick-Over Theory Revisited: Formation and Regulation of the Soluble Alternative Complement C3 Convertase (C3(H2O)Bb). *Mol. Immunol.* 45, 2370–2379. doi:10.1016/j.molimm.2007.11.003

Brodsky, R. A. (2014). Paroxysmal Nocturnal Hemoglobinuria. *Blood* 124, 2804–2811. doi:10.1182/blood-2014-02-522128

DeZern, A. E., and Brodsky, R. A. (2015). Paroxysmal Nocturnal Hemoglobinuria: a Complement-Mediated Hemolytic Anemia. *Hematol. Oncol. Clin. North. Am.* 29, 479–494. doi:10.1016/j.hoc.2015.01.005

DiScipio, R. G. (1981). The Binding of Human Complement Proteins C5, Factor B, Beta 1H and Properdin to Complement Fragment C3b on Zymosan. *Biochem. J.* 199, 485–496. doi:10.1042/bj1990485

Fishelson, Z., and Müller-Eberhard, H. J. (1984). Residual Hemolytic and Proteolytic Activity Expressed by Bb after Decay-Dissociation of C3b,Bb. *J. Immunol.* 132, 1425–1429.

Hadders, M. A., Bubeck, D., Roversi, P., Hakobyan, S., Forneris, F., Morgan, B. P., et al. (2012). Assembly and Regulation of the Membrane Attack Complex Based on Structures of C5b6 and sC5b9. *Cell Rep* 1, 200–207. doi:10.1016/j.celrep.2012.02.003

Harboe, M., Ulvund, G., Vien, L., Fung, M., and Mollnes, T. E. (2004). The Quantitative Role of Alternative Pathway Amplification in Classical Pathway Induced Terminal Complement Activation. *Clin. Exp. Immunol.* 138, 439–446. doi:10.1111/j.1365-2249.2004.02627.x

Harris, C. L., Abbott, R. J., Smith, R. A., Morgan, B. P., and Lea, S. M. (2005). Molecular Dissection of Interactions between Components of the Alternative Pathway of Complement and Decay Accelerating Factor (CD55). *J. Biol. Chem.* 280, 2569–2578. doi:10.1074/jbc.M410179200

Harris, C. L. (2018). Expanding Horizons in Complement Drug Discovery: Challenges and Emerging Strategies. *Semin. Immunopathol.* 40, 125–140. doi:10.1007/s00281-017-0655-8

Hirayama, H., Yoshii, K., Ojima, H., Kawai, N., Gotoh, S., and Fukuyama, Y. (1996). Linear Systems Analysis of Activating Processes of Complement

System as a Defense Mechanism. *BioSystems* 39, 173–185. doi:10.1016/0303-2647(96)01617-6

Holguin, M. H., Fredrick, L. R., Bernshaw, N. J., Wilcox, L. A., and Parker, C. J. (1989a). Isolation and Characterization of a Membrane Protein from normal Human Erythrocytes that Inhibits Reactive Lysis of the Erythrocytes of Paroxysmal Nocturnal Hemoglobinuria. *J. Clin. Invest.* 84, 7–17. doi:10.1172/JCI114172

Holguin, M. H., Wilcox, L. A., Bernshaw, N. J., Rosse, W. F., and Parker, C. J. (1989b). Relationship between the Membrane Inhibitor of Reactive Lysis and the Erythrocyte Phenotypes of Paroxysmal Nocturnal Hemoglobinuria. *J. Clin. Invest.* 84, 1387–1394. doi:10.1172/JCI114311

Holz, F. G., Sadda, S. R., Busbee, B., Chew, E. Y., Mitchell, P., Tufail, A., et al. (2018). Efficacy and Safety of Lampalizumab for Geographic Atrophy Due to Age-Related Macular DegenerationEfficacy and Safety of Lampalizumab for Geographic Atrophy Due to Age-Related Macular Degeneration: Chroma and Spectri Phase 3 Randomized Clinical Trials. *JAMA Ophthalmol.* 136, 666–677. doi:10.1001/jamaophthalmol.2018.1544

Hong, K., Kinoshita, T., Pramoonjago, P., Kim, Y. U., Seya, T., and Inoue, K. (1991). Reconstitution of C5 Convertase of the Alternative Complement Pathway with Isolated C3b Dimer and Factors B and D. *J. Immunol.* 146, 1868–1873.

Hourcade, D. E., and Mitchell, L. M. (2011). Access to the Complement Factor B Scissile Bond Is Facilitated by Association of Factor B with C3b Protein. *J. Biol. Chem.* 286, 35725–35732. doi:10.1074/jbc.M111.263418

Hourcade, D. E. (2006). The Role of Properdin in the Assembly of the Alternative Pathway C3 Convertases of Complement. *J. Biol. Chem.* 281, 2128–2132. doi:10.1074/jbc.M508928200

Iida, K., Mornaghi, R., and Nussenzweig, V. (1982). Complement Receptor (CR1) Deficiency in Erythrocytes from Patients with Systemic Lupus Erythematosus. *J. Exp. Med.* 155, 1427–1438. doi:10.1084/jem.155.5.1427

Kazatchkine, M. D., Fearon, D. T., and Austen, K. F. (1979). Human Alternative Complement Pathway: Membrane-Associated Sialic Acid Regulates the Competition between B and Beta1 H for Cell-Bound C3b. *J. Immunol.* 122, 75–81.

Klinke, D. J. (2008). Integrating Epidemiological Data into a Mechanistic Model of Type 2 Diabetes: Validating the Prevalence of Virtual Patients. *Ann. Biomed. Eng.* 36, 321–334. doi:10.1007/s10439-007-9410-y

Korotaevskiy, A. A., Hanin, L. G., and Khanin, M. A. (2009). Non-linear Dynamics of the Complement System Activation. *Math. Biosci.* 222, 127–143. doi:10.1016/j.mbs.2009.10.003

Licht, C., Weyersberg, A., Heinen, S., Stapenhorst, L., Devenge, J., Beck, B., et al. (2005). Successful Plasma Therapy for Atypical Hemolytic Uremic Syndrome Caused by Factor H Deficiency Owing to a Novel Mutation in the Complement Cofactor Protein Domain 15. *Am. J. Kidney Dis.* 45, 415–421. doi:10.1053/j.ajkd.2004.10.018

Mastellos, D. C., Ricklin, D., and Lambris, J. D. (2019). Clinical Promise of Next-Generation Complement Therapeutics. *Nat. Rev. Drug Discov.* 18, 707–729. doi:10.1038/s41573-019-0031-6

Medicus, R. G., Götze, O., and Müller-Eberhard, H. J. (1976). Alternative Pathway of Complement: Recruitment of Precursor Properdin by the Labile C3/C5 Convertase and the Potentiation of the Pathway. *J. Exp. Med.* 144, 1076–1093. doi:10.1084/jem.144.4.1076

Meri, S., Morgan, B. P., Davies, A., Daniels, R. H., Olavesen, M. G., Waldmann, H., et al. (1990). Human Protectin (CD59), an 18,000-20,000 MW Complement Lysis Restricting Factor, Inhibits C5b-8 Catalysed Insertion of C9 into Lipid Bilayers. *Immunology* 71, 1–9.

Møller Rasmussen, J., Teisner, B., Jepsen, H. H., Svehag, S. E., Knudsen, F., Kirstein, H., et al. (1988). Three Cases of Factor I Deficiency: the Effect of Treatment with Plasma. *Clin. Exp. Immunol.* 74, 131–136.

Morgan, B. P., and Harris, C. L. (2015). Complement, a Target for Therapy in Inflammatory and Degenerative Diseases. *Nat. Rev. Drug Discov.* 14, 857–877. doi:10.1038/nrd4657

Müller-Eberhard, H. J. (1988). Molecular Organization and Function of the Complement System. *Annu. Rev. Biochem.* 57, 321–347. doi:10.1146/annurev.bi.57.070188.001541

Nielsen, H. E., Christensen, K. C., Koch, C., Thomsen, B. S., Heegaard, N. H., and Tranum-Jensen, J. (1989). Hereditary, Complete Deficiency of Complement Factor H Associated with Recurrent Meningococcal Disease. *Scand. J. Immunol.* 30, 711–718. doi:10.1111/j.1365-3083.1989.tb02480.x

Nijsen, M. J. M. A., Wu, F., Bansal, L., Bradshaw-Pierce, E., Chan, J. R., Liederer, B. M., et al. (2018). Preclinical QSP Modeling in the Pharmaceutical Industry: An IQ Consortium Survey Examining the Current Landscape. *CPT Pharmacometrics Syst. Pharmacol.* 7, 135–146. doi:10.1002/psp4.12282

Ovacik, M., and Lin, K. (2018). Tutorial on Monoclonal Antibody Pharmacokinetics and its Considerations in Early Development. *Clin. Transl. Sci.* 11, 540–552. doi:10.1111/cts.12567

Pangburn, M. K., and Müller-Eberhard, H. J. (1986). The C3 Convertase of the Alternative Pathway of Human Complement. Enzymic Properties of the Bimolecular Proteinase. *Biochem. J.* 235, 723–730. doi:10.1042/bj2350723

Pangburn, M. K., Schreiber, R. D., and Müller-Eberhard, H. J. (1981). Formation of the Initial C3 Convertase of the Alternative Complement Pathway. Acquisition of C3b-like Activities by Spontaneous Hydrolysis of the Putative Thioester in Native C3. *J. Exp. Med.* 154, 856–867. doi:10.1084/jem.154.3.856

Pascual, M., Steiger, G., Estreicher, J., Macon, K., Volanakis, J. E., and Schifferli, J. A. (1988). Metabolism of Complement Factor D in Renal Failure. *Kidney Int.* 34, 529–536. doi:10.1038/ki.1988.214

Preissner, K. P., Podack, E. R., and Müller-Eberhard, H. J. (1989). SC5b-7, SC5b-8 and SC5b-9 Complexes of Complement: Ultrastructure and Localization of the S-Protein (Vitronectin) within the Macromolecules. *Eur. J. Immunol.* 19, 69–75. doi:10.1002/eji.1830190112

Pryzdial, E. L., and Isenman, D. E. (1988). A Thermodynamic Study of the Interaction between Human Complement Components C3b or C3(H2O) and Factor B in Solution. *J. Biol. Chem.* 263, 1733–1738. doi:10.1016/s0021-9258(19)77937-x

Raina, R., Krishnappa, V., Blaha, T., Kann, T., Hein, W., Burke, L., et al. (2019). Atypical Hemolytic-Uremic Syndrome: An Update on Pathophysiology, Diagnosis, and Treatment. *Ther. Apher. Dial.* 23, 4–21. doi:10.1111/1744-9987.12763

Reeve, J., and Woo, P. M. (1982). Steady State Relations between Control Proteins Regulating the Formation of the Alternative Pathway C3 Convertase. *Immunology* 46, 859–866.

Ross, G. D., Yount, W. J., Walport, M. J., Winfield, J. B., Parker, C. J., Fuller, C. R., et al. (1985). Disease-associated Loss of Erythrocyte Complement Receptors (CR1, C3b Receptors) in Patients with Systemic Lupus Erythematosus and Other Diseases Involving Autoantibodies And/or Complement Activation. *J. Immunol.* 135, 2005–2014.

Rougier, N., Kazatchkine, M. D., Rougier, J. P., Fremeaux-Bacchi, V., Blouin, J., Deschenes, G., et al. (1998). Human Complement Factor H Deficiency Associated with Hemolytic Uremic Syndrome. *J. Am. Soc. Nephrol.* 9, 2318–2326. doi:10.1681/ASN.V9122318

Schaller, J., Gerber, S., Kaempfer, U., Lejon, S., and Trachsel, C. (2008). *Human Blood Plasma Proteins: Structure and Function*. Hoboken, NY: John Wiley & Sons.

Schmidt, B. J., Casey, F. P., Paterson, T., and Chan, J. R. (2013). Alternate Virtual Populations Elucidate the Type I Interferon Signature Predictive of the Response to Rituximab in Rheumatoid Arthritis. *BMC Bioinformatics* 14, 221. doi:10.1186/1471-2105-14-221

Seya, T., Holers, V. M., and Atkinson, J. P. (1985). Purification and Functional Analysis of the Polymorphic Variants of the C3b/C4b Receptor (CR1) and Comparison with H, C4b-Binding Protein (C4bp), and Decay Accelerating Factor (DAF). *J. Immunol.* 135, 2661–2667.

Sliwinski, A. J., and Zvaifler, N. J. (1972). Decreased Synthesis of the Third Component of Complement (C3) in Hypocomplementemic Systemic Lupus Erythematosus. *Clin. Exp. Immunol.* 11, 21–29.

Smith, C. A., Pangburn, M. K., Vogel, C. W., and Müller-Eberhard, H. J. (1984). Molecular Architecture of Human Properdin, a Positive Regulator of the Alternative Pathway of Complement. *J. Biol. Chem.* 259, 4582–4588. doi:10.1016/s0021-9258(17)43086-9

Sorger, P. K., Allerheiligen, S. R., Abernethy, D. R., Altman, R. B., Brouwer, K. L., Califano, A., et al. (2011). "Quantitative and Systems Pharmacology in the post-genomic Era: New Approaches to Discovering Drugs and Understanding Therapeutic Mechanisms," in Presented at the An NIH white paper by the QSP workshop group, Bethesda, 1–48. NIH Bethesda.

Sugita, Y., Nakano, Y., and Tomita, M. (1988). Isolation from Human Erythrocytes of a New Membrane Protein Which Inhibits the Formation of Complement

Transmembrane Channels. *J. Biochem.* 104, 633–637. doi:10.1093/oxfordjournals.jbchem.a122524

Tille, A., Lehnert, T., Zipfel, P. F., and Figge, M. T. (2020). Quantification of Factor H Mediated Self vs. Non-self Discrimination by Mathematical Modeling. *Front. Immunol.* 11, 1911. doi:10.3389/fimmu.2020.01911

Torreira, E., Tortajada, A., Montes, T., Rodríguez de Córdoba, S., and Llorca, O. (2009). Coexistence of Closed and Open Conformations of Complement Factor B in the Alternative Pathway C3bB(Mg2+) Proconvertase. *J. Immunol.* 183, 7347–7351. doi:10.4049/jimmunol.0902310

Tschopp, J., Chonn, A., Hertig, S., and French, L. E. (1993). Clusterin, the Human Apolipoprotein and Complement Inhibitor, Binds to Complement C7, C8 Beta, and the B Domain of C9. *J. Immunol.* 151, 2159–2165.

Vogt, B. A., Wyatt, R. J., Burke, B. A., Simonton, S. C., and Kashtan, C. E. (1995). Inherited Factor H Deficiency and Collagen Type III Glomerulopathy. *Pediatr. Nephrol.* 9, 11–15. doi:10.1007/BF00858956

Volanakis, J. E. (1990). "Participation of C3 and its Ligands in Complement Activation," in *The Third Component of Complement, Current Topics in Microbiology and Immunology*. Editor J. D. Lambris (Heidelberg, Germany: Springer-Verlag), 1–21. doi:10.1007/978-3-642-74977-3_1

Weiler, J. M., Daha, M. R., Austen, K. F., and Fearon, D. T. (1976). Control of the Amplification Convertase of Complement by the Plasma Protein beta1H. *Proc. Natl. Acad. Sci. U. S. A.* 73, 3268–3272. doi:10.1073/pnas.73.9.3268

Wilcox, L. A., Ezzell, J. L., Bernshaw, N. J., and Parker, C. J. (1991). Molecular Basis of the Enhanced Susceptibility of the Erythrocytes of Paroxysmal Nocturnal Hemoglobinuria to Hemolysis in Acidified Serum. *Blood* 78, 820–829. doi:10.1182/blood.v78.3.820.bloodjournal783820

Zelek, W. M., Xie, L., Morgan, B. P., and Harris, C. L. (2019). Compendium of Current Complement Therapeutics. *Mol. Immunol.* 114, 341–352. doi:10.1016/j.molimm.2019.07.030

Zewde, N., Jr, Gorham, R. D., Dorado, A., and Morikis, D. (2016). Quantitative Modeling of the Alternative Pathway of the Complement System. *PLOS ONE* 11, e0152337. doi:10.1371/journal.pone.0152337

Zewde, N., and Morikis, D. (2018). A Computational Model for the Evaluation of Complement System Regulation under Homeostasis, Disease, and Drug Intervention. *PLOS ONE* 13, e0198644. doi:10.1371/journal.pone.0198644

Zewde, N. T., Hsu, R. V., Morikis, D., and Palermo, G. (2021). Systems Biology Modeling of the Complement System under Immune Susceptible Pathogens. *Front. Phys.* 9. doi:10.3389/fphy.2021.603704

Zhao, L., Ren, T. H., and Wang, D. D. (2012). Clinical Pharmacology Considerations in Biologics Development. *Acta Pharmacol. Sin.* 33, 1339–1347. doi:10.1038/aps.2012.51

Conflict of Interest: LB, E-MN, JN, CB, FC, S-PF, SL and VD were employed GSK.

The remaining author declares that the research was conducted in the absence of any commercial or financial relationships that could be construed as a potential conflict of interest.

Publisher's Note: All claims expressed in this article are solely those of the authors and do not necessarily represent those of their affiliated organizations, or those of the publisher, the editors and the reviewers. Any product that may be evaluated in this article, or claim that may be made by its manufacturer, is not guaranteed or endorsed by the publisher.

frontiers | Frontiers in Pharmacology

ORIGINAL RESEARCH
published: 25 April 2022
doi: 10.3389/fphar.2022.862291

Minimal Physiologically-Based Pharmacokinetic (mPBPK) Metamodeling of Target Engagement in Skin Informs Anti-IL17A Drug Development in Psoriasis

Vivaswath S. Ayyar[1†], *Jong Bong Lee*[1†], *Weirong Wang*[1], *Meghan Pryor*[1], *Yanli Zhuang*[1], *Thomas Wilde*[1] *and An Vermeulen*[1,2*]

[1]Janssen Research & Development, LLC, Spring House, PA, United States, [2]Janssen R & D, Division of Janssen Pharmaceutica NV, Beerse, Belgium

OPEN ACCESS

Edited by:
Rui Li,
Pfizer, United States

Reviewed by:
Patrick Glassman,
University of Pennsylvania, United States
Tyler Dunlap,
University of North Carolina at Chapel Hill, United States

***Correspondence:**
An Vermeulen
avermeul@its.jnj.com

[†]*These authors have contributed equally to this work*

Specialty section:
This article was submitted to Experimental Pharmacology and Drug Discovery, a section of the journal Frontiers in Pharmacology

Received: *25 January 2022*
Accepted: *16 March 2022*
Published: *25 April 2022*

Citation:
Ayyar VS, Lee JB, Wang W, Pryor M, Zhuang Y, Wilde T and Vermeulen A (2022) Minimal Physiologically-Based Pharmacokinetic (mPBPK) Metamodeling of Target Engagement in Skin Informs Anti-IL17A Drug Development in Psoriasis. Front. Pharmacol. 13:862291. doi: 10.3389/fphar.2022.862291

The pharmacologic effect(s) of biotherapeutics directed against soluble targets are driven by the magnitude and duration of free target suppression at the tissue site(s) of action. Interleukin (IL)-17A is an inflammatory cytokine that plays a key role in the pathogenesis of psoriasis. In this work, clinical trial data from two monoclonal antibodies (mAbs) targeting IL-17A for treatment of psoriasis (secukinumab and ixekizumab) were analyzed simultaneously to quantitatively predict their target engagement (TE) profiles in psoriatic skin. First, a model-based meta-analysis (MBMA) for clinical responses was conducted separately for each drug based on dose. Next, a minimal physiologically-based pharmacokinetic (mPBPK) model was built to assess skin site IL-17A target engagement for ixekizumab and secukinumab simultaneously. The mPBPK model captured the observed drug PK, serum total IL-17A, and skin drug concentration-time profiles reasonably well across the different dosage regimens investigated. The developed mPBPK model was then used to predict the average TE (i.e., free IL-17A suppression) in skin achieved over a 12-weeks treatment period for each drug following their respective regimens and subsequently assess the TE-efficacy response relationship. It was predicted that secukinumab achieved 98.6% average TE in the skin at 300 mg q4w SC while ixekizumab achieved 99.9% average TE under 160 mg (loading) followed by 80 mg q2w SC. While direct quantification of free IL-17A levels at the site of action is technically challenging, integrated mPBPK-MBMA approaches offer quantitative predictions of free IL-17A levels at the site of action to facilitate future drug development via IL-17A suppression in psoriasis.

Keywords: IL-17A, MBMA, mPBPK, psoriasis, target engagement, translational medicine, secukinumab, ixekizumab

INTRODUCTION

Psoriasis is a chronic autoimmune and inflammatory skin disease characterized by red, itchy, and scaly skin patches. According to the World Psoriasis Day consortium, psoriasis affects over 125 million people worldwide (https://www.psoriasis.org/psoriasis-statistics/; date accessed: 03/05/2022). Many cytokines and immune cells have been identified to promote the disease initiation and propagation (Schon and Boehncke, 2005); among those, the Interleukin (IL)-23/T helper (Th) 17/IL-17 immune pathways play pivotal roles (Lima and Kimball, 2010). IL-17A is an inflammatory

cytokine secreted by Th17 cells and is reported to play a key role in the pathogenesis of psoriasis (Krueger et al., 2012; Martin et al., 2013). In psoriatic patients, both IL-23 and IL-17 exhibit elevated expression in lesional skin sites (Arican et al., 2005). Upon release, IL-17A signals various cells in the skin, such as keratinocytes, which are activated to produce downstream mediators reported to be elevated in psoriatic skin (Harper et al., 2009; Brembilla et al., 2018). Drugs targeting the IL-17A cytokine and its signaling pathway have shown effectiveness in treatment of psoriasis and other immune disorders (Martin et al., 2013; Brembilla et al., 2018). There are two marketed monoclonal antibodies (mAbs) that specifically target the IL-17A cytokine: secukinumab and ixekizumab. Both compounds offer safe and effective treatment for psoriasis patients (Blauvelt, 2016; Frieder et al., 2018).

The pharmacologic effect(s) of biotherapeutics directed against soluble targets are driven by the magnitude and duration of free target suppression at the site of action *in vivo* (Zheng et al., 2015; Chen et al., 2016; Ayyar et al., 2021a). However, the relationship between *in vivo* target/pathway blockade at the target site and clinical improvement in disease severity warrants further study. Population PK models of diverse mAbs, including anti-IL17A mAbs (secukinumab and ixekizumab), using serum total PK data in psoriasis patients have been reported. Further, exposure-response and/or semi-mechanistic PK/PD models linking mAb PK to PD endpoints have been established (Zhu et al., 2009; Bruin et al., 2017; Yao et al., 2018; Jackson et al., 2022). However, relationships developed using such models may not be readily extrapolated to other therapies against the same target, owing to differing PK/biodistribution characteristics, target binding affinities, and/or biophysical properties. Knowledge of the magnitude and duration of target engagement required to achieve the desired therapeutic benefit can be useful to facilitate discovery and development of future therapies. The minimal physiologically-based pharmacokinetic (mPBPK) model, first proposed by Cao and Jusko (Cao et al., 2013), is a commonly used approach to quantitatively assess the drug exposure and target engagement at the tissue site of action. A typical mPBPK model for a mAb comprises a central (plasma) compartment, lumped "tight" and "leaky" compartments (assigned based on tissue vascular endothelial permeabilities), and a lymph compartment connected by lymphatic flow. It inherits the key advantages of a whole-body PBPK model by using physiologically relevant parameters while focusing only on the tissue of interest hence being easier to implement (Ayyar and Jusko, 2020). With specific tissue PK and target dynamics data to inform the model, target-mediated drug disposition (TMDD) kinetics can be incorporated into the central circulation and/or the specific tissue compartments, as exemplified previously in preclinical studies (Chen et al., 2016; Chen et al., 2018; Zheng et al., 2020a). To our knowledge, an approach integrating mPBPK modeling of human PK and IL-17A TE data with observed clinical response (e.g., disease score) has not been reported thus far.

The present work sought to develop a mPBPK model to predict free IL-17A neutralization in skin for secukinumab and ixekizumab and quantitatively relate it with clinical response rates based on 75% reduction in the Psoriasis Area and Severity Index (PASI) score (PASI75) and 90% reduction in PASI score (PASI90). To this end, clinical trial data from both antibodies were analyzed using model-based meta-analysis (MBMA) coupled with drug-target binding affinity, clinical PK, IL-17A TE with relevant physiological parameters (using mPBPK-TE modeling) to quantitatively predict TE needed to inform future drug development targeting the IL-17A pathway.

MATERIALS AND METHODS

Data Source

All data used in this study were collected from published literature or data published within regulatory reviews. Data from placebo-controlled randomized clinical trials conducted in psoriasis patients evaluating clinical response were included (**Table 1**). In addition, a phase 1 exploratory study measuring skin biodistribution was also included (Leonardi et al., 2012; Papp et al., 2013; Rich et al., 2013; Langley et al., 2014; FDA, 2015; Mrowietz et al., 2015; Dragatin et al., 2016; FDA, 2016; Papp et al., 2018).

Model-Based Meta-Analysis

MBMA was performed by non-linear regression of the trial level data. A 75% or greater reduction in the PASI score (PASI75) and 90% or greater reduction in PASI score (PASI90) after 12 weeks of treatment were used as clinical efficacy measurements as these were the common endpoints for secukinumab and ixekizumab. The response rate was adjusted by subtracting the placebo response from the active drug arm response for each study. A dose-based MBMA was conducted using the total dose administered during the 12 weeks divided by the total duration (12 weeks) to obtain dose per unit time (mg/week). Additionally, a TE-based MBMA was conducted based on the average inhibition of IL-17A during the 12 weeks based on the simulation.

The equation used for the MBMA model was:

$$Response = E_0 + \frac{x^{hill} \cdot (E_{max} - E_0)}{x^{hill} + E_{50}^{hill}} \quad (1)$$

where, x is dose or TE, E_0 is baseline response, E_{max} is maximum response, and E_{50} is dose or TE needed for 50% of maximum response and *hill* is the Hill coefficient. This MBMA fitted a trendline that described the overall trend of the clinical datasets (see **Figures 2**, **6**).

Minimal Physiologically-Based Pharmacokinetic–Target Engagement Model

A mPBPK model incorporating features of TMDD (Chen et al., 2018) was adapted to characterize the interrelationships between secukinumab/ixekizumab and free and total IL-17 in psoriasis patients. The model sought to describe the whole-body physiology and drug-specific characteristics in a minimal

TABLE 1 | Randomized placebo-controlled clinical trials of secukinumab and ixekizumab in psoriasis patients included in the analyses.

Study Description	Treatment Groups (up to week 12)	N*	References
Secukinumab			
Phase II			
Proof of Concept	3 mg/kg IV single dose Placebo	36	FDA (2015)
Low dose-ranging	25 mg SC q4w 75 mg SC q4w 150 mg SC q4w Placebo	125	Papp et al., 2013
High dose-ranging	3 mg/kg IV single dose 10 mg/kg IV single dose 10 mg/kg IV Wk 0, 2, 4 Placebo	100	Rich et al., 2013
Dose regimen finding	150 mg SC single dose 150 mg SC q4w 150 mg SC Wk 0, 1, 2, 4 Placebo	404	Rich et al., 2013
Phase III			
ERASURE	150 mg SC Wk 0, 1, 2, 3, 4; q4w	734	Langley et al., 2014
FIXTURE	300 mg SC Wk 0, 1, 2, 3, 4; q4w	974	Langley et al., 2014
FEATURE	Placebo	176	FDA (2015)
JUCTURE		181	FDA (2015)
Ixekizumab			
Phase I			
Dose-escalation	15 mg IV at Wk 0, 2, 4 5 mg SC at Wk 0, 2, 4 15 mg SC at Wk 0, 2, 4 50 mg SC at Wk 0, 2, 4 150 mg SC at Wk 0, 2, 4 Placebo	46	FDA (2016)
Phase II			
Dose-ranging	10 mg SC at Wk 0, 2, 4, 8 25 mg SC at Wk 0, 2, 4, 8 75 mg SC at Wk 0, 2, 4, 8 150 mg SC at Wk 0, 2, 4, 8 Placebo	141	Leonardi et al., 2012
Phase III			
UNCOVER-1	160 mg SC at Wk 0; 80 mg SC q2w	1,296	Papp et al., 2018
UNCOVER-2	160 mg SC at Wk 0; 80 mg SC q4w	866	
UNCOVER-3	PBO	964	

**Excludes participants enrolled in active comparator arms.*

manner (**Figure 1**). Compartments representing serum, lymph, skin, muscle, and an absorption depot were incorporated. Other organs were lumped into a "leaky" compartment, where "leaky" refers to the permeability of the vascular endothelial structure of these tissues. Since skin and muscle together account for ~90% of total body mass of "tight" organs, an additional "tight" compartment lumping other organs was excluded. Circulation of secukinumab and ixekizumab was assumed to depend predominantly on lymphatic flow and paravascular convection (Cao et al., 2013). Although interaction between the antibody and IL-17A would occur ubiquitously, this process was simplified to occur in skin and serum compartments only (Zheng et al., 2020a). Similarly, distributary circulation of IL-17A and the drug-target complex were not modeled explicitly; instead, their dynamics in serum and in skin were considered locally (Chen et al., 2018). The elimination rate constant for free ligands, especially soluble cytokines, is typically substantially faster than that of mAb-bound ligand (Davda and Hansen, 2010). As such, when ligand becomes bound to the mAb and takes on the disposition properties of the mAb, there is a rapid and measurable increase in total ligand concentrations (Davda and Hansen, 2010). Consistently, identical elimination rate constants for mAb-IL17A complexes and free mAb were assumed to jointly characterize serum total mAb and total target (free IL-17A+ complex) concentrations. Equations describing the model are listed in Supplementary Materials.

A naïve pooled approach was used for model fitting, as available data from trial reports were at a group level. For model simulation, the population mean of the parameter estimates was used. Clinically approved dose regimens of secukinumab and ixekizumab were simulated and free IL-17A in skin was predicted as a measure of target engagement for each drug.

Data Analysis and Software

The data were extracted as mean values from published graphs by computer digitization (WebPlotDigitizer, version 4.1; https://automeris.io/WebPlotDigitizer). NONMEM version 7.4 (Icon Development Solutions, Ellicott City, MD, United States) was used for mPBPK model fitting and parameter estimation. The model code is provided as Supplementary Material. The First-Order Conditional Estimation method with Interaction (FOCE-i) was applied. Since mean data were analyzed, inter-individual variability (IIV) was not considered and the variance–covariance matrix was fixed to 0. A proportional error model was used to describe the residual error. Model performance was evaluated by goodness-of-fit plots and objective function values (OFV). MBMA and mPBPK model simulations were performed in R (Comprehensive R Network version 3.6.3 [www.r-project.org]). The non-linear least squares function (nls) provided in the stats package (version 3.6.3) was used for MBMA and the mrgsolve package (version 0.10.0) was used for mPBPK model simulations.

RESULTS

Model-Based Meta-Analysis Based on Secukinumab and Ixekizumab Doses

MBMA conducted for secukinumab and ixekizumab based on dose (mg/week) is shown in **Figure 2**. Two dose regimens of secukinumab are approved for the treatment of psoriasis: 150 or 300 mg SC at Weeks 0, 1, 2, 3 followed by q4w from Week 4 onwards. The MBMA showed that the 300 mg dose regimen yielded higher PASI75 and PASI90 responses than the 150 mg dose regimen. Moreover, the trendline constructed by model fitting predicted that there may be a continuously increasing trend when the dose is increased even further from the 300 mg dose regimen, which is more apparent with the more stringent endpoint of PASI90.

For ixekizumab, only one dose regimen is approved for the treatment of psoriasis: 160 mg SC at Week 0 followed by 80 mg SC q2w from Week 2 onwards. Four different dose levels (10, 25, 75 or 150 mg SC at Week 0, 2, 4 and 8) were tested in the Phase 2 study, which showed obvious dose-response for both PASI75 and PASI90 (**Figure 2**). Phase 3 studies of ixekizumab tested both 80 mg SC q4w and q2w following the initial induction dosing for which the results are shown. The q2w regimen yielded slightly higher PASI75 and PASI90 responses. Nonetheless, the fitted trendline indicated that further increasing the dose may achieve marginally higher efficacy. Note that the dose-response curves for secukinumab and ixekizumab do not overlap, signifying the involvement of additional determinants (beyond mAb dose)

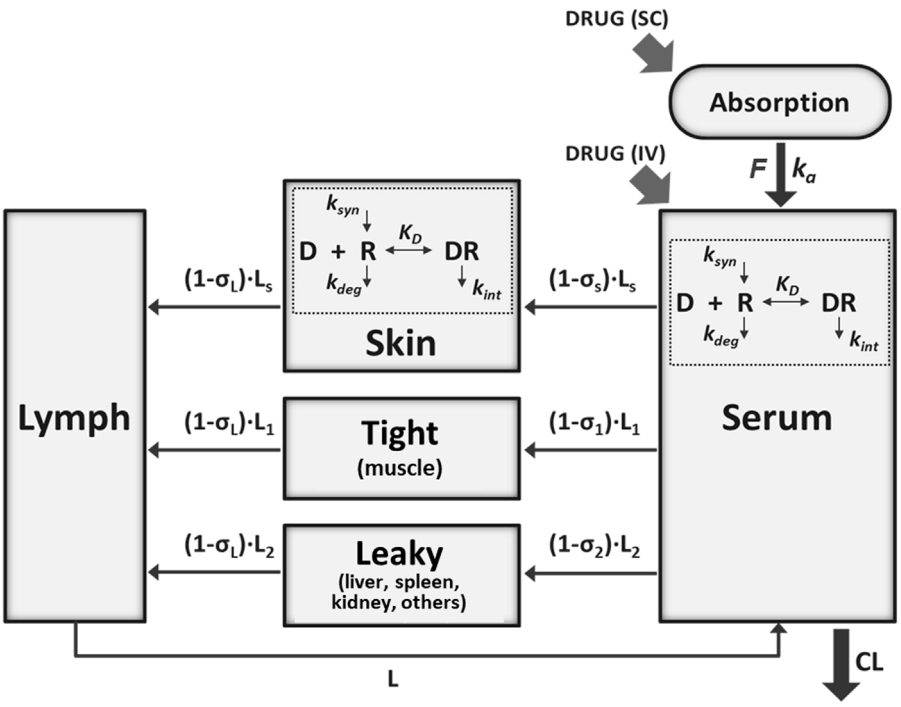

FIGURE 1 | Schematic of the minimal physiologically-based pharmacokinetic (mPBPK) model for secukinumab and ixekizumab incorporating IL-17 binding in serum and skin. See **Table 2** for model parameter values.

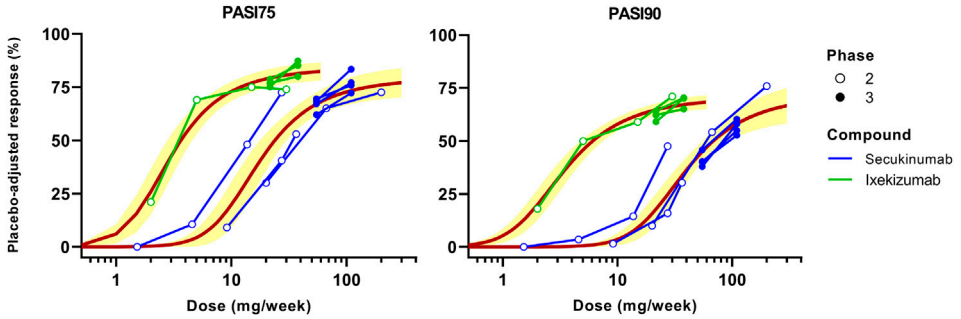

FIGURE 2 | Dose-based model-based meta-analysis (MBMA) of clinical trial results for secukinumab and ixekizumab. Average dose (mg/week) was calculated based on total administered dose over 12 weeks. Clinical response 12 weeks after the initial dose was used as efficacy endpoint. Solid lines represent model-fitted trendline, whereas symbols indicate observed mean data. The observed mean data from individual clinical studies are connected. Shaded bands depict the 95% CI around the regression curves.

that may be incorporated to jointly model the dose-exposure-TE-clinical response relationship for these therapies.

Minimal Physiologically-Based Pharmacokinetic Modeling to Assess IL-17A TE

The mPBPK model for secukinumab and ixekizumab IL-17A TE was developed by fitting data reported from clinical trials conducted in psoriasis patients (**Table 1**). The model simultaneously captured the observed secukinumab serum concentration-time profiles following IV (3 and 10 mg/kg) and SC (25–300 mg) doses across various dosing regimens (**Figures 3A–C**). In the secukinumab proof-of-concept study (FDA, 2015), both serum secukinumab PK and serum total IL-17A (i.e., antibody-bound IL-17A and free IL-17A) were measured and well-characterized by the model (**Figures 3D,E**). In an exploratory biodistribution study (Dragatin et al., 2016), both serum and skin secukinumab concentrations were profiled. The mPBPK model simultaneously captured these observed data well (**Figures 3F,G**).

Similarly, available serum ixekizumab concentration-time profiles were also well captured by the mPBPK model (**Figure 4**). The physiological flows/volumes, parameters relating to IL-17A dynamics, and drug-target binding affinities were fixed to reported values as summarized in **Table 2**. Parameter estimates for SC bioavailability (F) and the first-order absorption rate constant (k_a) for secukinumab and ixekizumab were fixed based on population PK model-derived estimates (Bruin et al., 2017; Jackson et al., 2022), whereas free mAb clearances (CL) were re-estimated using the mPBPK model and were found to be reasonably similar to previous estimates of total CL for secukinumab (0.19 L/day) and ixekizumab (0.29 L/day) (Bruin et al., 2017; Jackson et al., 2022). Parameters related to IL-17A were kept identical between secukinumab and ixekizumab. The elimination rate constants for free IL-17A in serum and skin were fixed to values determined previously (Zheng et al., 2020b). Consistent with physiological expectation, the elimination rate constant for free IL-17A in serum was much faster compared to that in skin (**Table 2**). Selected parameters such as free mAb CL, elimination rate constant for serum total IL-17A (i.e., secukinumab-bound IL-17A and free IL-17A) (k_{int}), and reflection coefficients for skin ($\sigma_{s,skin}$) and leaky compartments ($\sigma_{2,leaky}$) were estimated upon simultaneous fitting of all observed data with acceptable precision (**Table 2**).

The developed mPBPK model was used to simulate free IL-17A suppression in skin following approved dose regimens of secukinumab and ixekizumab. The simulated profiles in **Figure 5A** show that free IL-17A concentrations were lowered by 2-3 orders of magnitude following treatment with secukinumab or ixekizumab, and greater skin free IL-17A suppression is predicted after ixekizumab treatment, driven by its higher binding affinity for IL-17A compared with secukinumab (**Table 2**). Consistently, skin concentrations of total (free + bound) IL-17A increased substantially above baseline, reaching a steady-state maximum around 2–3 weeks following either secukinumab or ixekizumab at their respective doses (**Figure 5B**).

Target Engagement Model-Based Meta-Analysis

A TE-based MBMA was subsequently conducted based on the predicted average free IL-17A lowering in skin over 12 weeks, accounting for differences in dose regimen (doses, frequencies, and induction dosing), drug PK, and drug-target binding affinity between secukinumab and ixekizumab. **Figure 6** depicts the MBMA results based on PASI75 (left) and PASI90 (right) for both secukinumab and ixekizumab. Of interest, unlike the dose-based MBMA, the same relationship between skin free IL-17A suppression, and clinical efficacy could be applied successfully to the majority of both secukinumab and ixekizumab data. The approved dose regimen of secukinumab (300 mg q4w SC) was predicted to achieve 98.6% average TE over 12 weeks. The approved dose regimen of ixekizumab (160 mg at week 0 followed by 80 mg q2w SC) was predicted to achieve 99.9% average TE over 12 weeks.

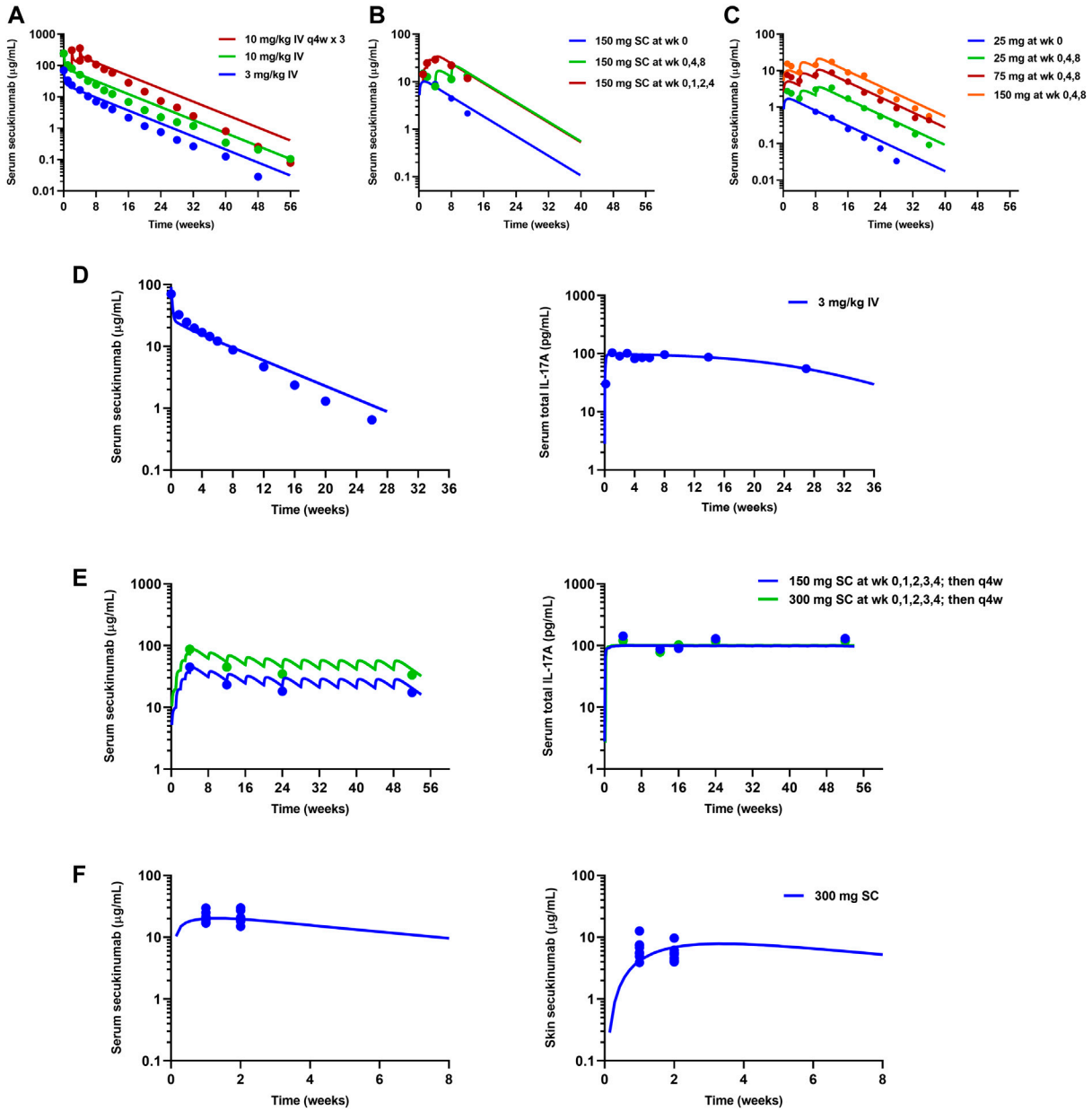

FIGURE 3 | Model fitting of observed mean data in clinical trials for secukinumab. Refer to **Table 1** for details on each clinical study. **(A)** High dose-ranging study (Rich et al., 2013). **(B)** SC dose regimen-finding study (Rich et al., 2013). **(C)** SC low dose-ranging study (Papp et al., 2013). **(D)** Proof-of-concept study (FDA, 2015). **(E)** Phase 3 studies (Langley et al., 2014; FDA, 2015). **(F)** Exploratory biodistribution study (Dragatin et al., 2016). Solid lines represent model-fitted profiles, whereas symbols indicate observed mean data.

DISCUSSION

This work aimed to quantitatively identify the extent of TE of IL-17A in skin needed to achieve a clinical response comparable to existing antibody therapies (i.e., secukinumab and ixekizumab). MBMA of clinical trial data for two marketed anti-IL-17A drugs was coupled with mPBPK modeling to understand the relationship between IL-17A suppression in skin and clinical efficacy in psoriasis patients. Routinely employed population-based PK and exposure-response models typically relate total serum or plasma concentrations to clinical responses (Bruin et al., 2017; Jackson et al., 2022). Such models are highly useful for informing dose optimization, quantifying inter-subject variability, and identifying clinically meaningful covariates

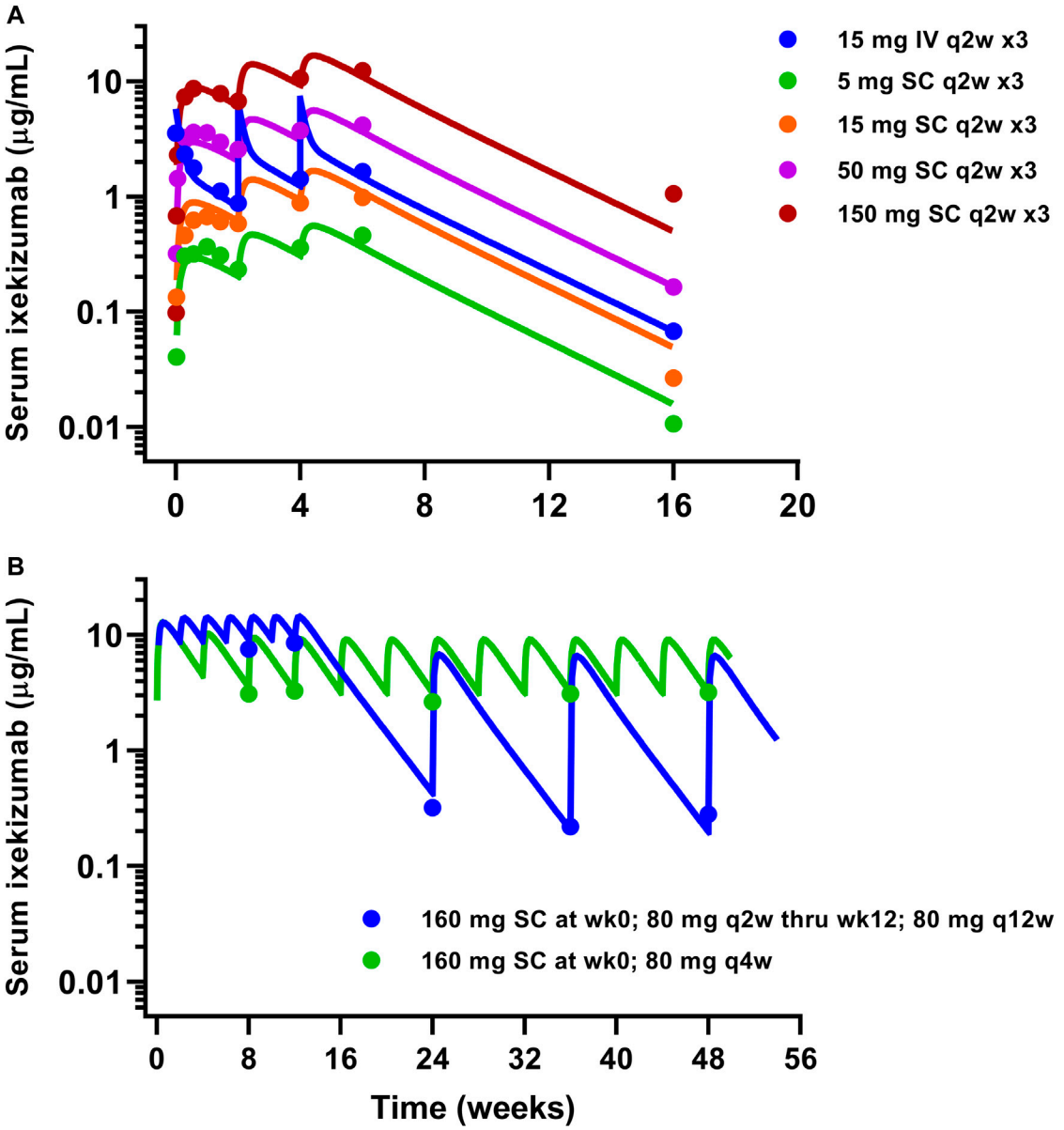

FIGURE 4 | Model fitting of observed ixekizumab mean serum PK data. **(A)** Phase 1 study (FDA, 2016). **(B)** Phase 3 studies (Papp et al., 2018). Solid lines represent model-fitted profiles, whereas symbols indicate observed mean data.

(Ayyar and Jusko, 2020). However, it is well recognized, for neutralizing agents, that additional factors such as tissue biodistribution and target binding affinity are major determinants governing the magnitude and duration of free target suppression (and relatedly, clinical efficacy) at the site of action. Incorporating such aspects using a mPBPK-TE-MBMA modeling approach, a main focus of this effort, is expected to strengthen the predictability of clinical response across different IL-17-targeting agents.

First, MBMA was conducted based on average dose administered per week (mg/week) over 12 weeks (**Figure 2**). The analysis showed that dose regimens of secukinumab may not have reached the plateau, especially for the more stringent endpoint of PASI90. However, ixekizumab appeared to have approached the plateau of the dose-response curve. The dose-based MBMA results are difficult to interpret across anti-IL-17A drugs due to different characteristics including differing dose regimens, binding affinities, and pharmacokinetics.

To address this challenge, a mPBPK model was developed and applied to account for the different characteristics of the two mAbs and predict the tissue site TE achieved by each drug at their

TABLE 2 | Summary of mPBPK model parameters and estimates.

Parameter		Unit	Value (RSE%)[a]		Source[c]
			Secukinumab	Ixekizumab	
Clearance (*CL*)		L/day	0.154 (3.3%)	0.379 (8.0%)	
SC Bioavailability (*F*)		—	0.729	0.81	[1, 9, 10]
Absorption rate constant (k_a)		1/day	0.18	0.24	[1, 9, 10]
Lymph flow rate	***L*, total**	L/day	2.9		[2]
	***L*$_s$, skin**	L/day	0.247		[2, 3]
	***L*$_1$, muscle**	L/day	0.71		[2, 3]
	***L*$_2$, leaky tissue**	L/day	1.943		[2]
Volume of distribution	***V*$_p$, plasma**	L	2.6		[2]
	***V*$_2$, leaky tissue**	L	4.37		[2]
	***V*$_s$, skin**	L	1.81		[2, 3]
	***V*$_1$, muscle**	L	6.3		[2, 3]
	***V*$_L$, lymph**	L	2.6		[2]
k_{deg} IL-17A	**Skin**	1/day	2.44		$k_{deg,skin} = k_{syn}/baseline_{skin}$
	Plasma	1/day	45.5		[4]
k_{int} complex	**Skin**	1/day	0.34		2.5 x Ls/Vs. [5]
	Plasma	1/day	1.24 (6.4%)	1.24[b]	
baseline IL-17A	**Skin**	pM	0.28		[6]
	Plasma	pM	0.015		[6]
k_{syn} IL-17A		pM/day	0.683		$k_{syn} = k_{deg,plasma}$ x $baseline_{plasma}$
K_D		pM	129	1.8	[7]
Reflection co-efficient	**σ_s, skin**	—	0.630 (7.0%)	0.63[b]	
	σ_1, muscle	—	0.95		[2, 8]
	σ_2, leaky	—	0.363 (14.2%)	0.524 (17.4%)	
	σ_L, lymph	—	0.2		[2]

[a]*Parameters estimated by mPBPK, modeling are indicated with RSE% shown in parentheses.*
[b]*Parameter assumed to be the same as for secukinumab.*
[c]*References: [1] (Bruin et al., 2017); [2] (Cao et al., 2013); [3] (Shah and Betts, 2012); [4] (Zheng et al., 2020); [5] (Chen et al., 2016); [6] (Dragatin et al., 2016); [7] (Adams et al., 2020); [8] (Chen et al., 2018); [9] (FDA, 2015); [10] (FDA, 2016).*

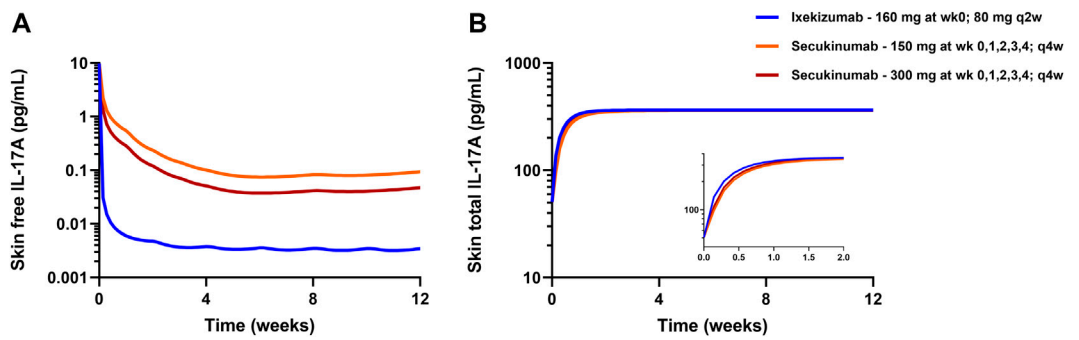

FIGURE 5 | mPBPK model-predicted free IL-17A lowering **(A)** and total IL-17A **(B)** in psoriatic skin following secukinumab or ixekizumab. Solid lines represent model simulations.

respective dose regimens. Our groups have demonstrated the utility of mPBPK and mechanistic PK-TE-PD models for various biotherapeutics and targets with preclinical and translational applications (Chen et al., 2016; Chen et al., 2018; Jiang et al., 2020; Zheng et al., 2020a; Ayyar et al., 2021a; Ayyar et al., 2021b). In this study, a combined mPBPK-MBMA approach was taken to jointly examine clinical data from Phase 1-3 studies of secukinumab and ixekizumab. The drug- and system-parameters were either fixed based on reported values or were estimated based on observed clinical data including serum and skin drug concentrations and serum total IL-17A concentrations (**Table 2**).

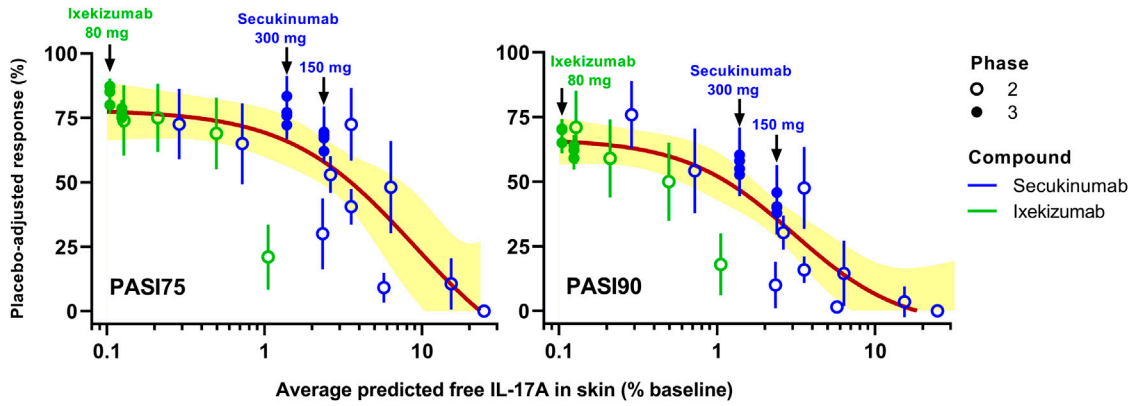

FIGURE 6 | Simulated target engagement (TE)-based model-based meta-analysis (MBMA) of clinical trial results for secukinumab and ixekizumab. Average TE was calculated based on the concentration of free IL-17A over 12 weeks. Clinical response 12 weeks after the initial dose was used as efficacy endpoint. The two approved dose regimens of secukinumab and the approved dose regimen of ixekizumab are marked with arrows on the graphs. Solid lines represent model-fit, whereas symbols indicate observed placebo-adjusted clinical responses. Shaded bands depict the 95% CI around the TE-PASI regression curves.

The skin site IL-17A TE predicted by the mPBPK model was combined with the MBMA for secukinumab and ixekizumab (**Figure 6**). Clear trends were observed between both PASI75 and PASI90 and IL-17A TE (% lowering of free IL-17A from baseline) for secukinumab and ixekizumab together. The 300 mg SC dose regimen of secukinumab achieved less IL-17A TE compared to ixekizumab. Consistently, it appeared to have reached near-maximal effect for PASI75 but not for PASI90. On the other hand, the approved dose regimen of ixekizumab was predicted to reach 99.9% TE, i.e., lowering the free IL-17A to 0.1% of baseline, and ixekizumab was reported to have reached higher PASI75 and PASI90 responses. The TE predicted by the mPBPK modeling identified the TE differences for the two drugs: 98.6% average TE was predicted for the 300 mg dose regimen of secukinumab and 99.9% average TE for ixekizumab over a 12-weeks treatment period, and this implies that skin site free IL-17A was lowered to 1.4 and 0.1% of the baseline, respectively. Of note, in contrast with **Figure 2**, where the PASI response was plotted against mAb doses, a single nonlinear sigmoidal function (**Eq. 1**) related PASI response and free IL-17A in skin to adequately capture the majority of Phase 2 and Phase 3 response data collected for both mAbs. This confirms that the PASI/IL-17A relationship should be mAb-independent, and that the minor deviations are likely due to uncertainties in skin free IL-17 prediction. This finding exemplifies the mechanistic insight gained using the proposed mPBPK-TE approach over the more empirical MBMA based on dose alone, which required separate relationships to analyze secukinumab and ixekizumab data independently.

While the developed mPBPK model with TMDD kinetics provided a good description of the observed data, it is important to note some limitations and assumptions in the current approach. First, there are no tissue site IL-17A TE data being reported and very limited serum TE data to support the mPBPK model development; therefore, model estimation of IL-17A target related parameters (including turnover and route of clearance) may still possess some uncertainty. Hence, relative differences in the model-predicted free IL-17A lowering in skin between secukinumab and ixekizumab may be more reliable for decision-making compared to absolute predicted values. The estimation of drug-specific reflection coefficients ($\sigma_{2,leaky}$) between secukinumab and ixekizumab was based on observed PK data for both compounds. There could be a mechanistic reason for the difference, e.g., differences in charge or IgG subtype, which could impact capillary permeability or tissue binding resulting in an apparent difference in $\sigma_{2,\ leaky}$ between secukinumab and ixekizumab. Though potential impacts from other technical issues, e.g., PK assay or sampling times cannot be ruled out, the correlation between PASI and model predicted free IL-17A (**Figure 6**) supported the overall credibility of the model estimates. Fixing a majority of mPBPK parameter values *a priori* enables the model to predict tissue disposition but confers less flexibility to best characterize or "fit" multiple serum PK datasets simultaneously. Such constraints imposed on one or more parameters could have contributed to the modest underestimation of serum concentrations at early time points following IV secukinumab. (**Figure 3D**). The model assumes that the production of IL-17A remains constant throughout the course of treatment. However, since many biomarkers, including Th17 cells (Aguilar-Flores et al., 2020), IL-17 signature genes (Chiricozzi et al., 2016), and serum IL-17 (Chen et al., 2013) are positively correlated with disease severity, this assumption may not hold true, especially upon long-term treatment. In the TE-based MBMA, results from a small number of secukinumab and ixekizumab Phase 2 studies deviated notably from the overall PASI75/90-TE relationship. Though the exact cause of these deviations is not known, potential differences in target dynamics as a function of treatment duration may have contributed. Tissue-specific ISF turnover rates can impact the binding kinetics between antibodies and soluble targets to varying degrees, depending upon their rate constants of association (k_{on}) and dissociation (k_{off}) (Li et al., 2018). This work involved the comparison of the target binding profiles of two approved mAbs (with broadly differing affinities) within skin, a tissue with relatively higher

ISF turnover rate (Li et al., 2018). Interestingly, Li et al. showed that both secukinumab and ixekizumab possess substantially fast k_{on} rates (4.1×10^5 1/Ms and 7.5×10^6 1/Ms, respectively) (Liu et al., 2016), which is favored for targeting within high ISF turnover tissues. This may reconcile why the current model, despite assuming equilibrium-based binding, performed satisfactorily in relating PASI response with predicted % free IL-17A for both drugs jointly. Nonetheless, tissue-specific ISF turnover and drug-target binding kinetics were not considered in the current model; this can be evaluated in the future to further strengthen and refine our modeling approach. Although it is challenging to obtain tissue samples from clinical studies, and it can be technically challenging to directly measure the lowering of free target with rapid turnover following treatment with mAbs (Zheng et al., 2015), any such data, even sparse, would allow significant improvement in the mPBPK model to better characterize the relationship between tissue site TE and clinical outcomes.

The current mPBPK model and TE-based analysis offers several advantages to inform forward- and reverse-translation in drug development as it 1) enables a mechanism- and physiology-based integration of multiple clinical datasets within a single framework, 2) can identify the extent of TE needed to exert comparable clinical responses to those seen with existing therapies, and 3) provide quantitative simulations to optimize drug-specific characteristics, including target binding affinity and clearance, for novel compounds in the discovery and preclinical stages sought to improve upon current therapies. Finally, the mechanistic nature of this model also enables utilization of physiologically relevant findings to other similar therapies.

CONCLUSION

Clinical trial data from secukinumab and ixekizumab were analyzed quantitatively and simultaneously using MBMA and mPBPK modeling. The approach predicted the skin site TE achieved by the two drugs and the overall trend in the TE-clinical response relationship. By virtue of deriving several parameter values from (best available) sources in the literature, there is uncertainty associated with certain model components (e.g., tissue site IL-17A TE) in the absence of *in vivo* measurements. As such, it is important to restate that the main purpose of this work is to guide decision making for future drug development and the model predictions be updated as newer data emerge. While direct quantification of free IL-17A levels is challenging during treatment, the findings from this study reveal the value to assess tissue site TE and provide quantitative predictions to facilitate future drug development via IL-17A suppression in psoriasis.

DATA AVAILABILITY STATEMENT

The original contributions presented in the study are included in the article/**Supplementary Material**, further inquiries can be directed to the corresponding author.

AUTHOR CONTRIBUTIONS

Conception and design: VA, JL, WW, MP, and TW. Acquisition of data: VA, JL, MP, and TW. Analysis and interpretation of data: VA, JL, WW, AV, and YZ Manuscript review and editing: all authors.

FUNDING

This work was supported by Janssen Research and Development, LLC.

SUPPLEMENTARY MATERIAL

The Supplementary Material for this article can be found online at: https://www.frontiersin.org/articles/10.3389/fphar.2022.862291/full#supplementary-material

REFERENCES

Adams, R., Maroof, A., Baker, T., Lawson, A. D. G., Oliver, R., Paveley, R., et al. (2020). Bimekizumab, a Novel Humanized IgG1 Antibody that Neutralizes Both IL-17A and IL-17F. *Front. Immunol.* 11, 1894. doi:10.3389/fimmu.2020.01894

Aguilar-Flores, C., Castro-Escamilla, O., Ortega-Rocha, E. M., Maldonado-García, C., Jurado-Santa Cruz, F., Pérez-Montesinos, G., et al. (2020). Association of Pathogenic Th17 Cells with the Disease Severity and its Potential Implication for Biological Treatment Selection in Psoriasis Patients. *Mediators Inflamm.* 2020, 8065147. doi:10.1155/2020/8065147

Arican, O., Aral, M., Sasmaz, S., and Ciragil, P. (2005). Serum levels of TNF-alpha, IFN-gamma, IL-6, IL-8, IL-12, IL-17, and IL-18 in patients with active psoriasis and correlation with disease severity. *Mediators Inflamm.* 2005, 273–279.

Ayyar, V. S., Jaiprasart, P., Geist, B., Huang Devine, Z., Case, M., Hazra, A., et al. (2021a). Translational PK/PD and Model-Informed Development of JNJ-67842125, a Fab Reversal Agent for JNJ-64179375, a Long-Acting Thrombin Inhibitor. *Br. J. Pharmacol.* 178, 3943–3958. doi:10.1111/bph.15533

Ayyar, V. S., and Jusko, W. J. (2020). Transitioning from Basic toward Systems Pharmacodynamic Models: Lessons from Corticosteroids. *Pharmacol. Rev.* 72, 414–438. doi:10.1124/pr.119.018101

Ayyar, V. S., Song, D., Zheng, S., Carpenter, T., and Heald, D. L. (2021b). Minimal Physiologically Based Pharmacokinetic-Pharmacodynamic (mPBPK-PD) Model of GalNAc-Conjugated siRNA Disposition and Gene Silencing in Preclinical Species and Humans. *J. Pharmacol. Exp. Ther.* 379 (2), 134–146. JPET-AR-2021-000805. doi:10.1124/jpet.121.000805

Blauvelt, A. (2016). Ixekizumab: a New anti-IL-17A Monoclonal Antibody Therapy for Moderate-To Severe Plaque Psoriasis. *Expert Opin. Biol. Ther.* 16 (2), 255–263. doi:10.1517/14712598.2016.1132695

Brembilla, N. C., Senra, L., and Boehncke, W. H. (2018). The IL-17 Family of Cytokines in Psoriasis: IL-17A and beyond. *Front. Immunol.* 9, 1682. doi:10.3389/fimmu.2018.01682

Bruin, G., Loesche, C., Nyirady, J., and Sander, O. (2017). Population Pharmacokinetic Modeling of Secukinumab in Patients with Moderate to Severe Psoriasis. *J. Clin. Pharmacol.* 57 (7), 876–885. doi:10.1002/jcph.876

Cao, Y., Balthasar, J. P., and Jusko, W. J. (2013). Second-generation Minimal Physiologically-Based Pharmacokinetic Model for Monoclonal Antibodies. *J. Pharmacokinet. Pharmacodyn* 40 (5), 597–607. doi:10.1007/s10928-013-9332-2

Chen, B., Deng, Y., Tan, Y., Qin, J., and Chen, L. B. (2013). Association between Severity of Knee Osteoarthritis and Serum and Synovial Fluid Interleukin 17 Concentrations. *J. Int. Med. Res.* 42 (1), 138–144. doi:10.1177/0300060513501751

Chen, X., Jiang, X., Doddareddy, R., Geist, B., Mcintosh, T., Jusko, W. J., et al. (2018). Development and Translational Application of a Minimal Physiologically Based Pharmacokinetic Model for a Monoclonal Antibody against Interleukin 23 (IL-23) in IL-23-Induced Psoriasis-like Mice. *J. Pharmacol. Exp. Ther.* 365 (1), 140–155. doi:10.1124/jpet.117.244855

Chen, X., Jiang, X., Jusko, W. J., Zhou, H., and Wang, W. (2016). Minimal Physiologically-Based Pharmacokinetic (mPBPK) Model for a Monoclonal Antibody against Interleukin-6 in Mice with Collagen-Induced Arthritis. *J. Pharmacokinet. Pharmacodyn* 43 (3), 291–304. doi:10.1007/s10928-016-9472-2

Chiricozzi, A., Suárez-Fariñas, M., Fuentes-Duculan, J., Cueto, I., Li, K., Tian, S., et al. (2016). Increased Expression of Interleukin-17 Pathway Genes in Nonlesional Skin of Moderate-To-Severe Psoriasis Vulgaris. *Br. J. Dermatol.* 174 (1), 136–145. doi:10.1111/bjd.14034

Davda, J. P., and Hansen, R. J. (2010). Properties of a General PK/PD Model of Antibody-Ligand Interactions for Therapeutic Antibodies that Bind to Soluble Endogenous Targets. *MAbs* 2 (5), 576–588. doi:10.4161/mabs.2.5.12833

Dragatin, C., Polus, F., Bodenlenz, M., Calonder, C., Aigner, B., Tiffner, K. I., et al. (2016). Secukinumab Distributes into Dermal Interstitial Fluid of Psoriasis Patients as Demonstrated by Open Flow Microperfusion. *Exp. Dermatol.* 25 (2), 157–159. doi:10.1111/exd.12863

FDA, U. (2016). "Clinical Pharmacology and Biopharmaceutics Review(s) - Ixekizumab," in *Application Numer: 125521Orig1s000* (Silver Spring, MD: Center for Drug Evaluation and Research).

FDA, U. (2015). "Clinical Pharmacology and Biopharmaceutics Review(s) - Secukinumab," in *Application Numer: 125504Orig1s000* (Silver Spring, MD: Center for Drug Evaluation and Research).

Frieder, J., Kivelevitch, D., and Menter, A. (2018). Secukinumab: a Review of the anti-IL-17A Biologic for the Treatment of Psoriasis. *Ther. Adv. Chronic Dis.* 9 (1), 5–21. doi:10.1177/2040622317738910

Harper, E. G., Guo, C., Rizzo, H., Lillis, J. V., Kurtz, S. E., Skorcheva, I., et al. (2009). Th17 Cytokines Stimulate CCL20 Expression in Keratinocytes *In Vitro* and *In Vivo*: Implications for Psoriasis Pathogenesis. *J. Invest. Dermatol.* 129 (9), 2175–2183. doi:10.1038/jid.2009.65

Jackson, K., Chua, L., Velez De Mendizabal, N., Pitou, C., Rodriguez Capriles, C., Paller, A. S., et al. (2022). Population Pharmacokinetic and Exposure-Efficacy Analysis of Ixekizumab in Paediatric Patients with Moderate-To-Severe Plaque Psoriasis (IXORA-PEDS). *Br. J. Clin. Pharmacol.* 88 (3), 1075–1086. doi:10.1111/bcp.15034

Jiang, X., Chen, X., Jaiprasart, P., Carpenter, T. J., Zhou, R., and Wang, W. (2020). Development of a Minimal Physiologically-Based Pharmacokinetic/pharmacodynamic Model to Characterize Target Cell Depletion and Cytokine Release for T Cell-Redirecting Bispecific Agents in Humans. *Eur. J. Pharm. Sci.* 146, 105260. doi:10.1016/j.ejps.2020.105260

Krueger, J. G., Fretzin, S., Suárez-Fariñas, M., Haslett, P. A., Phipps, K. M., Cameron, G. S., et al. (2012). IL-17A Is Essential for Cell Activation and Inflammatory Gene Circuits in Subjects with Psoriasis. *J. Allergy Clin. Immunol.* 130 (1), 145–154. doi:10.1016/j.jaci.2012.04.024

Langley, R. G., Elewski, B. E., Lebwohl, M., Reich, K., Griffiths, C. E., Papp, K., et al. (2014). Secukinumab in Plaque Psoriasis-Rresults of Two Phase 3 Trials. *N. Engl. J. Med.* 371 (4), 326–338. doi:10.1056/NEJMoa1314258

Leonardi, C., Matheson, R., Zachariae, C., Cameron, G., Li, L., Edson-Heredia, E., et al. (2012). Anti-interleukin-17 Monoclonal Antibody Ixekizumab in Chronic Plaque Psoriasis. *N. Engl. J. Med.* 366 (13), 1190–1199. doi:10.1056/NEJMoa1109997

Li, X., Jusko, W. J., and Cao, Y. (2018). Role of Interstitial Fluid Turnover on Target Suppression by Therapeutic Biologics Using a Minimal Physiologically Based Pharmacokinetic Model. *J. Pharmacol. Exp. Ther.* 367 (1), 1–8. doi:10.1124/jpet.118.250134

Lima, H. C., and Kimball, A. B. (2010). Targeting IL-23: insights into the pathogenesis and the treatment of psoriasis. *Indian J Dermatol* 55, 171–175.

Liu, L., Lu, J., Allan, B. W., Tang, Y., Tetreault, J., Chow, C. K., et al. (2016). Generation and Characterization of Ixekizumab, a Humanized Monoclonal Antibody that Neutralizes interleukin-17A. *J. Inflamm. Res.* 9, 39–50. doi:10.2147/JIR.S100940

Martin, D. A., Towne, J. E., Kricorian, G., Klekotka, P., Gudjonsson, J. E., Krueger, J. G., et al. (2013). The Emerging Role of IL-17 in the Pathogenesis of Psoriasis: Preclinical and Clinical Findings. *J. Invest. Dermatol.* 133 (1), 17–26. doi:10.1038/jid.2012.194

Mrowietz, U., Leonardi, C. L., Girolomoni, G., Toth, D., Morita, A., Balki, S. A., et al. (2015). Secukinumab Retreatment-As-Needed versus Fixed-Interval Maintenance Regimen for Moderate to Severe Plaque Psoriasis: A Randomized, Double-Blind, Noninferiority Trial (SCULPTURE). *J. Am. Acad. Dermatol.* 73 (1), 27–e1. doi:10.1016/j.jaad.2015.04.011

Papp, K. A., Langley, R. G., Sigurgeirsson, B., Abe, M., Baker, D. R., Konno, P., et al. (2013). Efficacy and Safety of Secukinumab in the Treatment of Moderate-To-Severe Plaque Psoriasis: a Randomized, Double-Blind, Placebo-Controlled Phase II Dose-Ranging Study. *Br. J. Dermatol.* 168 (2), 412–421. doi:10.1111/bjd.12110

Papp, K. A., Leonardi, C. L., Blauvelt, A., Reich, K., Korman, N. J., Ohtsuki, M., et al. (2018). Ixekizumab Treatment for Psoriasis: Integrated Efficacy Analysis of Three Double-Blinded, Controlled Studies (UNCOVER-1, UNCOVER-2, UNCOVER-3). *Br. J. Dermatol.* 178 (3), 674–681. doi:10.1111/bjd.16050

Rich, P., Sigurgeirsson, B., Thaci, D., Ortonne, J. P., Paul, C., Schopf, R. E., et al. (2013). Secukinumab Induction and Maintenance Therapy in Moderate-To-Severe Plaque Psoriasis: a Randomized, Double-Blind, Placebo-Controlled, Phase II Regimen-Finding Study. *Br. J. Dermatol.* 168 (2), 402–411. doi:10.1111/bjd.12112

Schön, M. P., and Boehncke, W. H. (2005). Psoriasis. New England Journal of Medicine. 352, 1899–1912.

Shah, D. K., and Betts, A. M. (2012). Towards a Platform PBPK Model to Characterize the Plasma and Tissue Disposition of Monoclonal Antibodies in Preclinical Species and Human. *J. Pharmacokinet. Pharmacodyn* 39 (1), 67–86. doi:10.1007/s10928-011-9232-2

Yao, Z., Hu, C., Zhu, Y., Xu, Z., Randazzo, B., Wasfi, Y., et al. (2018). Population Pharmacokinetic Modeling of Guselkumab, a Human IgG1λ Monoclonal Antibody Targeting IL-23, in Patients with Moderate to Severe Plaque Psoriasis. *J. Clin. Pharmacol.* 58 (5), 613–627. doi:10.1002/jcph.1063

Zheng, S., Mcintosh, T., and Wang, W. (2015). Utility of Free and Total Target Measurements as Target Engagement and Efficacy Biomarkers in Biotherapeutic Development-Oopportunities and Challenges. *J. Clin. Pharmacol.* 55 (Suppl. 3), S75–S84. doi:10.1002/jcph.357

Zheng, S., Niu, J., Geist, B., Fink, D., Xu, Z., Zhou, H., et al. (2020a). A Minimal Physiologically Based Pharmacokinetic Model to Characterize colon TNF Suppression and Treatment Effects of an Anti-TNF Monoclonal Antibody in a Mouse Inflammatory Bowel Disease Model. *MAbs* 12 (1), 1813962. doi:10.1080/19420862.2020.1813962

Zheng, S., Shen, F., Jones, B., Fink, D., Geist, B., Nnane, I., et al. (2020b). Characterization of Concurrent Target Suppression by JNJ-61178104, a Bispecific Antibody against Human Tumor Necrosis Factor and interleukin-17A. *MAbs* 12 (1), 1770018. doi:10.1080/19420862.2020.1770018

Zhu, Y., Hu, C., Lu, M., Liao, S., Marini, J. C., Yohrling, J., et al. (2009). Population Pharmacokinetic Modeling of Ustekinumab, a Human Monoclonal Antibody Targeting IL-12/23p40, in Patients with Moderate to Severe Plaque Psoriasis. *J. Clin. Pharmacol.* 49 (2), 162–175. doi:10.1177/0091270008329556

Conflict of Interest: VA, JL, WW, MP, YZ, TW, and AV are current or past employees of Janssen Research and Development, LLC and may be shareholders of Johnson and Johnson, of which Janssen Research and Development, LLC is a wholly owned subsidiary.

Publisher's Note: All claims expressed in this article are solely those of the authors and do not necessarily represent those of their affiliated organizations, or those of the publisher, the editors and the reviewers. Any product that may be evaluated in this article, or claim that may be made by its manufacturer, is not guaranteed or endorsed by the publisher.

frontiers | Frontiers in Pharmacology

ORIGINAL RESEARCH
published: 02 May 2022
doi: 10.3389/fphar.2022.837261

An *in silico* Model of T Cell Infiltration Dynamics Based on an Advanced *in vitro* System to Enhance Preclinical Decision Making in Cancer Immunotherapy

*Thomas D. Lewin *, Blandine Avignon, Alessio Tovaglieri, Lauriane Cabon, Nikolche Gjorevski and Lucy G. Hutchinson*

Roche Pharma Research and Early Development, Roche Innovation Center, Basel, Switzerland

Cancer immunotherapy often involves the use of engineered molecules to selectively bind and activate T cells located within tumour tissue. Fundamental to the success of such treatments is the presence or recruitment of T cells localised within the tumour microenvironment. Advanced organ-on-a-chip systems provide an *in vitro* setting in which to investigate how novel molecules influence the spatiotemporal dynamics of T cell infiltration into tissue, both in the context of anti-tumour efficacy and off-tumour toxicity. While highly promising, the complexity of these systems is such that mathematical modelling plays a crucial role in the quantitative evaluation of experimental results and maximising the mechanistic insight derived. We develop a mechanistic, mathematical model of a novel microphysiological *in vitro* platform that recapitulates T cell infiltration into epithelial tissue, which may be normal or transformed. The mathematical model describes the spatiotemporal dynamics of infiltrating T cells in response to chemotactic cytokine signalling. We integrate the model with dynamic imaging data to optimise key model parameters. The mathematical model demonstrates a good fit to the observed experimental data and accurately describes the distribution of infiltrating T cells. This model is designed to complement the *in vitro* system; with the potential to elucidate complex biological mechanisms, including the mode of action of novel therapies and the drivers of safety events, and, ultimately, improve the efficacy-safety profile of T cell-targeted cancer immunotherapies.

Keywords: cancer immunotherapy, T cell infiltration, *in vitro* cell systems, mathematical modelling, spatio—temporal analysis

OPEN ACCESS

Edited by:
Morgan Craig,
University of Montreal, Canada

Reviewed by:
Vasileios Vavourakis,
University of Cyprus, Cyprus
Paul Valle,
Instituto Tecnológico de Tijuana, Mexico

****Correspondence:***
Thomas D. Lewin
thomas.lewin.tl1@roche.com

Specialty section:
This article was submitted to Experimental Pharmacology and Drug Discovery, a section of the journal Frontiers in Pharmacology

Received: *16 December 2021*
Accepted: *11 March 2022*
Published: *02 May 2022*

Citation:
Lewin TD, Avignon B, Tovaglieri A, Cabon L, Gjorevski N and Hutchinson LG (2022) An in silico Model of T Cell Infiltration Dynamics Based on an Advanced in vitro System to Enhance Preclinical Decision Making in Cancer Immunotherapy. Front. Pharmacol. 13:837261. doi: 10.3389/fphar.2022.837261

1 INTRODUCTION

In the last decade, cancer immunotherapy (CIT) has emerged as one of the most rapidly advancing and promising fields in the research and development of cancer treatments (Mellman et al., 2011; Couzin-Frankel, 2013; Farkona et al., 2016). Such treatments often involve the use of engineered molecules to selectively bind and activate T cells located within the tumour tissue in order to harness their cytotoxic potential. The presence or recruitment of T cells within the target tissue is crucial to the mode of action of such treatments (Zhang et al., 2019). Thus, a deep understanding of the

processes driving T cell trafficking and tissue infiltration and how these are modulated by novel CIT molecules is key to the development of new drugs to reduce the high rate of attrition which results from a lack of efficacy or adverse effects *in vivo* (Havel et al., 2019; Martins et al., 2019). However, observing these dynamics at a high resolution using *in vivo* animal models may be technically challenging. Such models may also fail to be translationally predictive in the clinic as a consequence of genetic differences, with more complex molecules often not cross-reactive with pre-clinical species (Husain and Ellerman, 2018; Olson et al., 2018; Wagar et al., 2018). Aligning with the principle of the "3 Rs" for the refinement, reduction and replacement of animal models (Guhad, 2005), such considerations motivate the development of advanced *in vitro* cell systems towards more controllable, predictive platforms in which to test the pharmacodynamic effects of novel drugs and reduce the emphasis on *in vivo* animal experiments.

We set out to address this gap by building the first *in vitro* system that permits physiologically relevant, basal infiltration of T cells into engineered three-dimensional (3D) intestinal mucosa. We further increased the physiological relevance and predictive capacity of the model by incorporating a resident immune compartment. The multiple components that constitute the model—primary intestinal epithelium, resident immune cells and matched circulating T cells—enable us to introduce controlled modulations that can allow for a simplified representation of variations in patient physiological status within the system, such as chronic inflammation, common asymptomatic infections, microbiome changes, autoimmune susceptibilities or even tissue damage, and immune reprogramming due to cancer or chemotherapy. While T cells are principally responsible for the effects on the epithelium (given the mode of action of TCBs), we cannot exclude the contribution of other immune cell types (B cells, monocytes, NK cells) in the pharmacodynamic effects in both efficacy and safety, even if it is indirect by way of soluble factors, for example. As such, our *in vitro* models incorporate the whole compartment, rather than only T cells (Kerns et al., 2021). Consequently, the experimental data and subsequent analysis presented in this paper consider the infiltration of the PBMC population as a whole.

The control and tractability provided by the platform enables in-depth quantitative analyses of the mechanisms that underlie the observed outcomes. However, the multiple components within the system are interdependent and interact with each other in a complex manner resulting in spatiotemporal dynamics that can be challenging to analyse in a manner that fully utilises the extent of the available data to understand the underlying biology. Mathematical modelling has the potential to enhance the insight gained from such systems and elucidate complex, interrelated biological mechanisms and, ultimately, provide more quantitative predictions. Cellular movement, interactions, and signalling processes have been modelled extensively to mechanistically explore these phenomena using a variety of modelling approaches (DiMilla et al., 1991; Dallon and Othmer, 1997; Matzavinos et al., 2004; Anderson, 2005; Di Costanzo et al., 2015; McLennan et al., 2015). In particular, the chemotactic response has received a lot of attention to understand the directed movement of cell populations and organisms in response to chemical stimuli (Painter et al., 2000; Horstmann, 2003). Among these approaches, variations on the classical system of partial differential equations (PDEs) first formulated by Keller and Segel (1971) have been successfully used to describe the dynamics of a variety of cell populations in different biological contexts (Hillen and Painter, 2009; Painter, 2019). The ability of these systems to mechanistically describe how the distribution of cell populations may evolve spatially and temporally makes them an attractive choice of framework for modelling the rich imaging data which may be collected from advanced *in vitro* cell systems.

There are numerous established techniques which are routinely employed for fitting mathematical models to experimental data. However, these may often be computationally expensive involving large numbers of model simulations; including, but not limited to, Monte Carlo Markov Chain (MCMC) methods, particle swarm optimizers, and differential evolution and genetic algorithms (Storn and Price, 1997; Jin, 2005; Poli et al., 2007; Qin et al., 2009; Gelman et al., 2014). For PDE model systems there are two key considerations which may hinder the use of these approaches, namely, the computational complexity of solving a PDE system numerically and the dimension of the model parameter space to be explored. Surrogate-based optimisation algorithms leverage an approximation of the solution to the full model which may be simulated cheaply in order to perform global optimisation using the aforementioned approaches (Wang and Shan, 2007; Viana et al., 2014). Such methods are routinely used in other fields such as engineering in manufacturing, automotive, and aerospace applications (Wang and Shan, 2007; Laurenceau and Sagaut, 2008; Haftka et al., 2016; Bergh et al., 2020) but their use for complex modelling of biological processes are limited to just a few examples in the literature (Afraites and Bellouquid, 2014; Li et al., 2016; Grenier et al., 2018).

In this paper we present a novel microphysiological system that recapitulates immune cell infiltration into gut epithelial tissue and develop a mathematical model of the *in vitro* system to mechanistically describe the dynamics of infiltrating cells observed experimentally. We combine features from a number of surrogate-based optimisation algorithms and develop a workflow to efficiently explore the model parameter space to fit the model to the spatiotemporal experimental data. We use *in silico* simulations of the mathematical model to analyse the imaging data from the *in vitro* model under a range of experimental conditions to explore how the dynamics of T cell infiltration are altered in the presence of a cytotoxic T cell bispecific antibody (TCB) compared to control, non-toxic conditions.

2 MATERIALS AND METHODS

2.1 *In vitro* System

To construct the *in vitro* model, we leverage the multicompartment design of the Organoplate (Mimetas BV, Netherlands)—a microfluidic device containing 40 three-channel chips

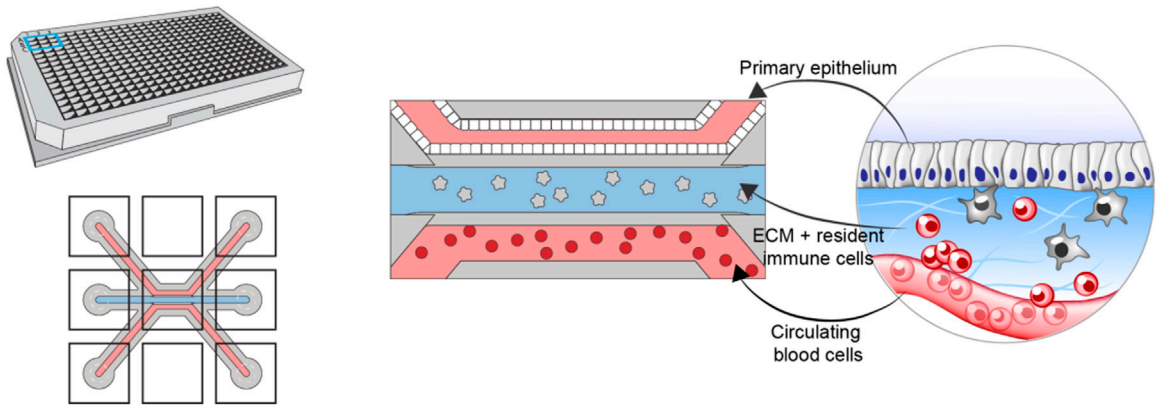

FIGURE 1 | Schematic showing the design and layout of the Mimetas Organoplate chip and the components comprising each of the three channels of each well—primary gut epithelium in the top channel, extracellular matrix and resident immune cells in the middle channel, and peripheral blood mononuclear cells in the bottom channel.

(**Figure 1**). The three channels of each chip are delimited *via* a phase guide promoting the formation of distinct microenvironments within each channel while permitting cellular movement between channels [further details of the chip design can be found in (Gjorevski et al., 2020)]. The top (luminal) channel is used to form an intestinal tube using Caco-2 colonocytes. The middle channel is used to create the stromal compartment of the intestine, by incorporating primary monocyte-derived macrophages, embedded in collagen-based extracellular matrix (Gjorevski et al., 2020). The bottom (basal) channel is used to introduce circulating peripheral blood mononuclear cells (PBMCs), including effector T-cells. Importantly, the same pool of PBMCs is used to generate the resident macrophages, thus ensuring matched resident, and peripheral immune compartments.

A tool HLA-restricted T cell bispecific antibody (hereafter toxic TCB), D66-ESK, known to result in broad T-cell mediated killing of HLA-A2-expressing target cells (Augsberger et al., 2021) is used to test whether recreating the cellular and architectural complexity of an immune-responsive intestinal mucosa would allow us to recapitulate the damaging apoptotic effects and investigate the resulting influence on T cell infiltration. A non-targeting, CD3-only binding TCB (hereafter control TCB), DP47, was used as a control expected to yield no toxicity. TCBs, along with PBMCs, were introduced using the basal channel, mimicking systemic delivery in the clinic.

In this paper we present results using resident macrophages that were characterised as an M1 phenotype to provide a pro-inflammatory stimulus and promote T cell migration (Gjorevski et al., 2020). Our dataset comprises 16 different experiments of which 8 were performed in the presence of the control TCB, DP47, and 8 included the cytotoxic TCB, D66-ESK.

The course of each experiment was imaged at 2 h intervals to capture the dynamics of infiltrating PBMCs. Images were acquired using an Opera Phoenix (PerkinElmer) with a 5X objective. The images contain a bright-field and two fluorescent channels (488: Caspase 3/7 green and 555: Cell Tracker red) in a 14 planes z-stack. We analysed the multi-channel images utilizing the Fiji (Schindelin et al., 2012) distribution of ImageJ (Rueden et al., 2017). We opened the images with the Bio formats plugin (Linkert et al., 2010) and reduced the image dimensionality projecting the maximum intensity of the z-planes. We select the area of the image corresponding to the Mimetas Organoplate chip middle and upper compartments utilizing the bright-field channel. To do this we manually defined a region of interest based on the bright-field channel with the ROI-manager tool and cropped the multi-channel images accordingly.

We then quantified the fluorescently labelled immune cells present in the middle and upper chip compartments based on the fluoresce channel. To achieve this we converted the images to a binary mask applying the default auto-threshold method. Additionally, we separated touching nuclei with watershed segmentation. From this segmented image we analysed the particle amount, area, coordinates, and morphology with the Analyze Particles tool. The tabular results were then exported for the *in silico* modelling.

The image analysis algorithm may fail to separate some cells which are closely clumped together. We handle this by incorporating a post-processing step in which cell areas above a threshold size are assumed to be multiple cells occupying the same location, with the number of cells determined by rounding to the nearest multiple of the threshold size. We choose a threshold of $50\,\mu m^2$ under the assumption that a PBMC is typically less than $10\,\mu m$ in diameter. This is such that regions above $75\,\mu m^2$ in area ($\sim 10\mu m$ in diameter) are assumed to comprise more than one cell and rounded up. The spatial distribution of infiltrating PBMCs at each time point is summarised by dividing the region of interest into 20 bins of equal size and counting the number of cells identified in each bin.

2.2 Mathematical Model

We propose a reaction-diffusion-chemotaxis system of partial differential equations (PDEs) to describe the evolution of a continuous PBMC density. The infiltration of PBMCs is assumed to be influenced by the micro-environment in the different channels of the *in vitro* system and responds to

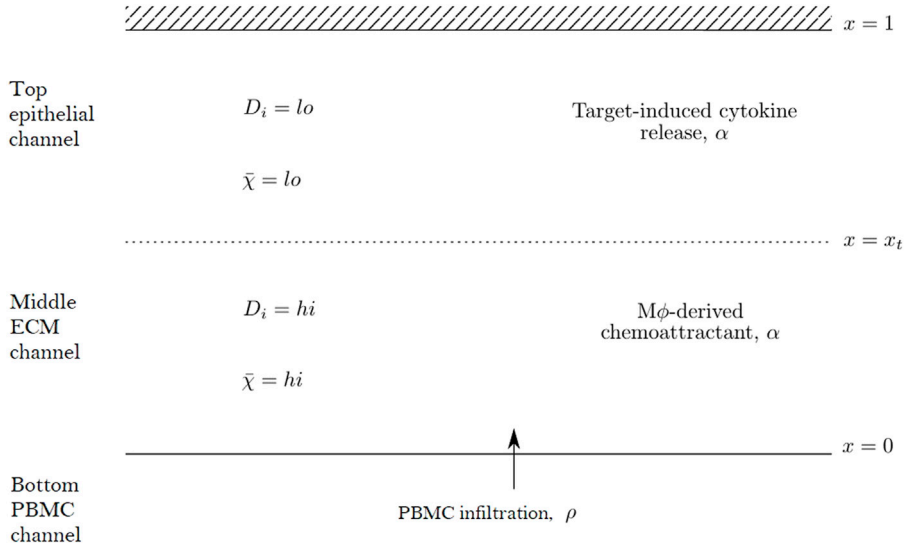

FIGURE 2 | Schematic diagram of the mathematical domain used to model the PBMC infiltration dynamics in the top two channels of the Mimetas Organoplate chip. The interface with the bottom channel is given by $x = 0$, while $x = x_t$ denotes the interface between the middle and top channels. The diffusivity parameters, D_i, and chemotactic sensitivity, $\tilde{\chi}$, vary spatially as given by **Eq. 4**, with cells moving more freely in the middle channel corresponding to higher (hi *vs.* lo) parameter values. Cytokine production may occur in both channels *via* two distinct mechanisms.

cytokine-mediated chemotactic cues. For simplicity, we assume that we may neglect any horizontal movement of PBMCs parallel to the boundaries of each channel and that the infiltration dynamics may be captured considering a single spatial dimension in the forward direction as cells travel across the different channels within the system. We thus describe the dynamics in space, x, and time, t, of two constituent species within our mathematical model system: the PBMC density, $\rho(x, t)$, and the concentration of a generic chemoattractant, $\alpha(x, t)$. We focus on capturing the dynamics of infiltrating PBMCs and thus consider a domain including the middle matrix channel and top epithelial tissue channel. PBMCs enter the domain at $x = 0$ from the PBMC channel while the boundary $x = 1$ corresponds to the top of the epithelial tissue channel, with the transition between the matrix and tissue channels denoted by $x = x_t \in (0, 1)$. A schematic representation of this domain is shown in **Figure 2**.

The reaction-diffusion-chemotaxis system governing the evolution of the PBMC density, ρ, and chemoattractant concentration, α, may thus be written as:

$$\frac{\partial \rho}{\partial t} = \frac{\partial}{\partial x}\left(D_\rho(x)\frac{\partial \rho}{\partial x}\right) - \frac{\partial}{\partial x}\left(\chi(x,\alpha)\rho\frac{\partial \alpha}{\partial x}\right) - \xi\rho, \tag{1}$$

$$\frac{\partial \alpha}{\partial t} = \frac{\partial}{\partial x}\left(D_\alpha(x)\frac{\partial \alpha}{\partial x}\right) + \underbrace{\eta_1 \mathbb{1}_{\{x \le x_t\}}}_{\text{Production from macrophages}} + \overbrace{\eta_2 \rho \mathbb{1}_{\{x \ge x_t\}}}^{\text{Target-induced release}} - \kappa\rho\alpha - \nu\alpha, \tag{2}$$

where $\mathbb{1}_A$ denotes the indicator function on the set A.

The interactions between the species in our model describe the dynamics of PBMC infiltration as influenced by a resident immune compartment and the additional effects of drug-target interactions in the epithelial tissue. The production of the chemical species α captures the influence of the resident immune compartment in the matrix channel. Here we do not explicitly model the resident macrophages, instead assuming a uniform distribution throughout the matrix and thus uniform rate of production of α in $0 < x < x_t$ given by η_1. This mechanism thus represents a pro-inflammatory, macrophage-derived, chemotactic stimulus within our system. If the experimental conditions include the presence of a TCB, for example, then drug-target interactions may occur upon infiltrating PBMCs reaching the tissue channel. This may result in apoptotic epithelial cell death and induce cytokine release, acting as a source of α in the top channel. For simplicity we similarly do not model epithelial cell density directly but again assume a uniform distribution such that cytokine release of α occurs at a rate, η_2 proportional to the PBMC density, ρ, in $x_t < x < 1$. This assumption is of course a simplification and may break down at later times in the case of widespread apoptosis. The cytokines represented by α are assumed to degrade with rate ν and may be taken up by PBMCs with rate, κ. Diffusion throughout the domain is assumed to occur with the spatially varying diffusion coefficient, $D_\alpha(x)$.

PBMCs are assumed to infiltrate in response to the chemotactic gradient of α. Based upon the empirical observations that cytokine expression increases throughout the time course of the experiments while the total number of infiltrating PBMCs saturates, we are motivated to consider a "receptor law" formulation for the chemotactic sensitivity, $\chi(x, \alpha)$, given by

$$\chi(x,\alpha) = \frac{\tilde{\chi}(x)k}{(k+\alpha)^2}. \tag{3}$$

This well-established and characterised functional form captures the observed behaviour that for large concentrations individual cells may not be able to resolve gradients of the chemoattractant and thus may no longer respond to the chemotactic signal (Painter et al., 2000). In addition to chemotaxis, the cells may also move in an unbiased, diffusive manner. Since we here consider a one-dimensional domain, we also introduce a sink term proportional to the local cell density to account for the small number of cells which are observed to move horizontally and leave the region of interest captured by the image analysis.

Aside from the different mechanisms of cytokine release previously described, we also capture differences between the two channels in the ability of the species to move across each part of the domain. More specifically, it is assumed that cells may move and cytokines may diffuse more freely through the matrix channel than they may penetrate the epithelial tissue. These differences manifest themselves in the form of piece-wise constant diffusion and chemotaxis coefficients, $D_\rho(x)$, $D_\alpha(x)$ and $\tilde{\chi}(x)$, which are defined by

$$D_\rho(x) = \begin{cases} \bar{D}_\rho & 0 < x < x_t \\ \bar{D}_\rho \Big/ \mu_\rho & x_t < x < 1, \end{cases}$$

$$D_\alpha(x) = \begin{cases} \bar{D}_\alpha & 0 < x < x_t \\ \bar{D}_\alpha \Big/ \mu_\alpha & x_t < x < 1, \end{cases} \quad \tilde{\chi}(x) = \begin{cases} \bar{\chi} & 0 < x < x_t \\ \bar{\chi} \Big/ \mu_\rho & x_t < x < 1, \end{cases} \tag{4}$$

for μ_ρ, $\mu_\alpha > 1$, where $\bar{D}_\rho$, $\bar{D}_\alpha$ and $\bar{\chi}$ are scalar parameters for the motility coefficients. Thus the diffusion and chemotaxis coefficients are higher (c.f. "hi" in **Figure 2**) in the middle channel than in the top channel (c.f. "lo" in **Figure 2**).

It remains to specify appropriate initial and boundary conditions to close the system given by **Eqs. 1**, **2**. For the boundary at the top of the tissue channel at $x = 1$ we prescribe no flux conditions for ρ and α given by:

$$D_\rho \frac{\partial \rho}{\partial x} - \chi \frac{\partial \alpha}{\partial x} \rho \Big|_{x=1} = 0, \quad \frac{\partial \alpha}{\partial x}\Big|_{x=1} = 0. \tag{5}$$

The boundary at $x = 0$, however, does not represent a solid boundary of the *in vitro* system, but rather the interface between the bottom PBMC channel and the middle compartment representing the ECM. As a consequence of the experimental observation that very few PBMCs infiltrate in the absence of macrophages in the system, we assume that the initial infiltration of PBMCs into the matrix channel is driven by chemotaxis. The total flux of PBMCs into the domain at $x = 0$ is thus proportional to the chemotactic signal from α which may be written as:

$$-D_\rho \frac{\partial \rho}{\partial x} + \chi \frac{\partial \alpha}{\partial x} \rho = \chi \frac{\partial \alpha}{\partial x} \tilde{\rho}, \tag{6}$$

where $\tilde{\rho}$ represents the assumed constant source of PBMCs in the bottom channel. The cytokine species α is able to diffuse across the interface at $x = 0$ and so we prescribe a diffusive flux out of the domain proportional to the concentration such that

$$\frac{\partial \alpha}{\partial x} = \zeta \alpha. \tag{7}$$

The *in vitro* system is initialised with the pool of PBMCs contained within the bottom channel. The resident immune compartment is present at the start of the experiment and provides the chemotactic stimulus for PBMC infiltration. We therefore assume a non-zero, steady state initial condition for the concentration of α due to the production by the macrophages in the matrix channel. Initial conditions for the PBMC density, ρ, and the cytokine concentration, α, throughout the domain are thus given by:

$$\rho(x, 0) = 0, \qquad \alpha(x, 0) = \bar{\alpha}(x), \tag{8}$$

where $\bar{\alpha}(x)$ satisfies

$$\frac{\partial}{\partial x}\left(D_\alpha(x) \frac{\partial \bar{\alpha}}{\partial x} \right) + \eta_1 \mathbb{1}_{\{x \le x_t\}} - \nu \bar{\alpha} = 0. \tag{9}$$

Eqs. 1–9 completely describe our spatiotemporal mathematical model of PBMC infiltration in the *in vitro* system. We note that this model is similar to that proposed by Alt and Lauffenburger (Lauffenburger and Kennedy, 1983; Alt and Lauffenburger, 1987) for modelling T cell infiltration *in vivo*. We simulate the solution of our model using a finite volume numerical scheme, of which more details may be found in the **Supplementary Material**.

2.3 Parameter Optimisation Framework

In order to integrate the mathematical model developed in **Section 2.2** with the *in vitro* experimental data of PBMC infiltration, we require a framework to efficiently explore the model parameter space. In this section we present a summary of the key ideas of the optimisation methodology used in this paper, which is summarised by the pseudo-code in Algorithm 1. Please see the **Supplementary Material** and the references therein for a more detailed explanation.

Kriging, also known as Gaussian process modelling, is a method of statistically interpolating data to build a response surface (Sacks et al., 1989). First introduced by Jones et al. (1998) based on ideas developed by Sacks et al. (1989), the key idea of surrogate-based optimisation is to leverage the Kriging surrogate for computationally-intensive global optimisation to minimise the number of calls to numerically simulate the true function. In brief, a typical Kriging-based optimization algorithm proceeds by first building an initial Kriging model based on a random sample of the parameter space [e.g., Latin hypercube sample (LHS)]. Subsequent iterations involve the use of a differential evolution (DE) global optimisation algorithm (Storn and Price, 1997) on the Kriging model to identify the best next point to sample based on a metric of expected improvement (EI) over the current minimum. The true model is then solved at the identified point and the Kriging model correspondingly updated. The algorithm iterates until either a convergence tolerance is met or a pre-determined computational budget is exceeded.

In our framework, we incorporate additional features from a number of existing algorithms to improve the speed and

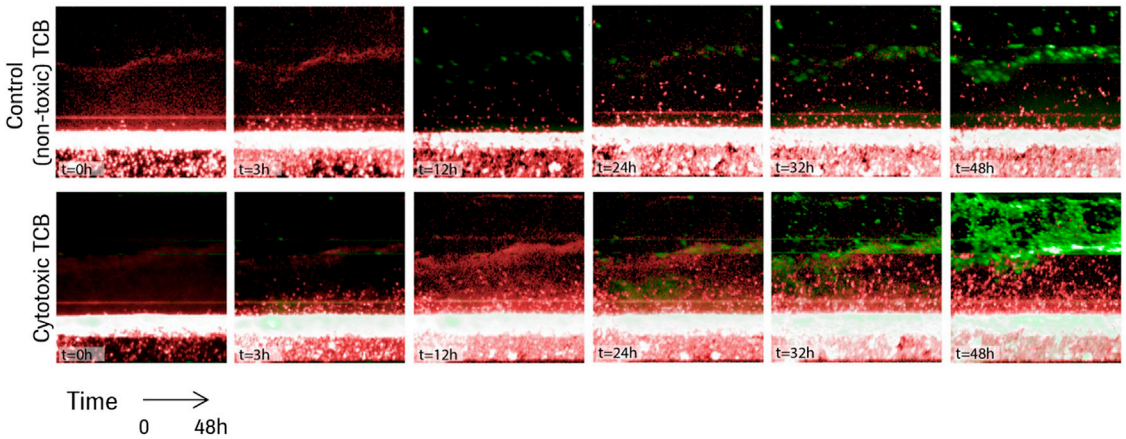

FIGURE 3 | Time lapse images for the first 48 h of two representative experiments in the presence of a control TCB, DP47 (top), and in the presence of a cytotoxic TCB, D66-ESK (bottom). Infiltrating PBMCs are tracked in red while apoptotic epithelial cells are imaged in green.

convergence of the algorithm to the global optimum. These features include parallelisation (Zhan et al., 2017), additional sampling criteria (Sacher et al., 2018; Xing et al., 2020), and domain size reduction (Xing et al., 2020).

Algorithm 1 Kriging-based optimisation workflow.

```
1   Generate LHS sample of p_init parameter sets, simulate model and calculate residual error
    metric.
2   while iter < iter_min and ϵ > tol do
        while p < p_max do
2.1         Build kriging model from sampled parameter sets.
2.2         Build SVM classifier for infeasible regions of parameter space.
2.3         for i = 1, ..., k do
                Determine ith new point to sample maximising the Pseudo-EI criterion/a using a
                DE algorithm.
                Generate LHS sample of l additional local points around new point.
            end
            Simulate model for k(l + 1) new parameter sets in parallel.
            Calculate residual errors and add to sample.
        end
3       if iter < iter_min and ϵ > tol then
            Reduce size of design space in each dimension and retain already sampled points for
            initialisation of next iteration.
        end
    end
4   Build final kriging approximation.
```

The PBMC distribution at each time point is characterised from the *in vitro* data by splitting the domain into equally sized bins and counting the number of cells identified in each. Correspondingly, we also numerically integrate the solution for PBMC density across each bin. We calculate the sum of squares distance between each bin count and the solution summed over all time points to give the distance metric to be minimised as the objective function for the optimisation algorithm.

3 RESULTS

3.1 Recapitulating T Cell Infiltration *in vitro*

A series of time lapse images for two representative experiments are shown in **Figure 3**, one in the presence of the non-toxic, control TCB, DP47, and one in the presence of the cytotoxic TCB, D66-ESK. A video of the time lapse imaging for an experiment in cytotoxic TCB conditions can be found in the online **Supplementary Material**. From a visual comparison, it is evident that the *in vitro* system recapitulates differences in both PBMC infiltration and epithelial cell apoptosis between the two conditions. Soon after TCB treatment, as observed in the snapshot at 3 h in **Figure 3**, lymphocytes began infiltrating the ECM compartment, likely also guided by cytokines produced by the resident macrophages. Within 48 h, however, toxic TCB treatment resulted in substantially higher PBMC infiltration compared with the control TCB. Moreover, in the toxic TCB-treated *in vitro* model, PBMC infiltration culminated with massive epithelial cell killing *via* apoptosis, which is consistent with mechanisms of T cell cytotoxicity.

We use our image analysis pipeline to identify infiltrating PBMCs and quantify precisely these observations. We visualise how the extent of PBMC infiltration at 48 h differs between the control TCB and cytotoxic TCB conditions in **Figure 4**. In **Figure 4A** we confirm that significantly more PBMCs have migrated into the top two channels after 48 h in conditions in the presence of the cytotoxic TCB. Across the 16 experiments in our dataset, a mean of 582.13 cells are identified in the D66-ESK conditions compared to 237.63 cells in the DP47 conditions. However, if we visualise how these populations of infiltrating PBMCs are distributed throughout the system we observe very little difference between the two conditions (**Figure 4B**). The majority of infiltrating cells are spread throughout the middle ECM channel with a mean distance travelled of 109.81 and 119.20 μm for the DP47 and D66-ESK conditions, respectively. The leading cells that travel the furthest and reach the interface with the top epithelial channel at 350 μm appear to cluster close to the interface and do not significantly penetrate through this epithelial barrier.

3.2 Mathematical Model Fitting to Data

The ability of the mathematical model given by **Eqs. 1–9** to describe the observed dynamics is assessed by fitting the model to

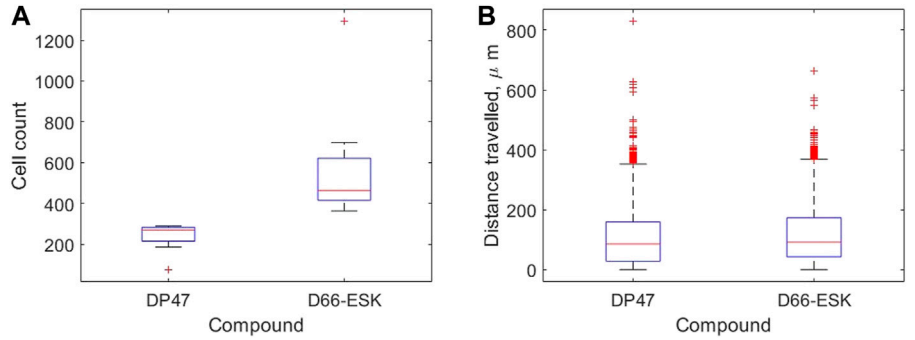

FIGURE 4 | Summaries of PBMC infiltration data at 48 h grouped by compound. **(A)** The total number of infiltrating cells. **(B)** The distribution of distances travelled per infiltrating cell away from the interface with the bottom channel in μm.

the experimental data. We consider each well of the plate to be a different experiment and separately optimise the model fit to each dataset in turn. In each case the optimisation framework described in **Section 2.3** is used to identify the parameter set which best describes the data. An example of a good fit to the data is shown in **Figure 5** whereby the model well describes the dynamics of infiltrating PBMCs *in vitro*. In this particular case the experiment was performed in the presence of 10 μg/ml of the control TCB, DP47. The surface in **Figure 5A** represents the model solution for the PBMC density, ρ, as it evolves in space and time. The red points summarising the cell counts of infiltrating PBMCs identified in the imaging data lie close to the solution surface and are evenly distributed around it. From the model solution we can see that the infiltration dynamics comprise an initial infiltration phase, lasting ~24 h, during which PBMCs infiltrate the system, migrate through the middle ECM channel and begin to accumulate at the interface with the epithelial tissue. The first cells reach the interface with the epithelial cell channel and start to accumulate around 12–15 h into the experiment. Subsequently, a steady state distribution profile is reached with few cells penetrating the epithelial channel beyond the cellular interactions at the interface. A more granular time lapse showing the comparison between the simulated cell distributions and the data is shown in **Figure 5B**.

We note, however, that while our imaging dataset provides good resolution on the PBMC infiltration dynamics throughout the time course of the experiment, we lack information on the cytokine expression in each channel and how it changes over time. Consequently some model parameters are not identifiable with respect to the current dataset. This is most obviously seen when we consider the boundary conditions given by **Eqs. 6**, **7**. Using **Eq. 7**, the right hand side of **Eq. 6** becomes $\chi(0,\alpha)\zeta\tilde{\rho}\alpha$. Consequently, in the absence of cytokine data, we would anticipate that the parameters ζ and $\tilde{\rho}$ are not identifiable. We may verify this by fixing all other model parameters to those used in **Figure 5** and exploring the $(\tilde{\rho},\zeta)$-subspace. In **Figure 6** we visualise the contours of this subspace with respect to model fit to the data. As might be expected from the equations, we observe a reciprocal relationship between $\tilde{\rho}$ and ζ which gives rise to parameter combinations with equally good fits.

3.3 The Influence of Cytotoxic TCBs

While we may not make any concrete statements based on the identified parameter values arising from our parameter fitting as a result of the unidentifiability of a number of model parameters, we may still more broadly interpret the ability of the mathematical model and the proposed mechanisms to describe the *in vitro* infiltration dynamics in the data based on the quality of fit. In **Figure 5**, we presented an example of data from a single experiment to which the model provides a good fit. However, as might be expected, there is variability in both the experimental data and, correspondingly, the quality of the model fit to the data. Our dataset includes experiments performed under a variety of experimental conditions, in particular in the presence of either a control, non-toxic TCB, DP47, or a cytotoxic TCB, D66-ESK. In **Figure 7A** we visualise the results of the parameter optimisation grouped by compound. When grouped by compound we observe that the mathematical model consistently describes the conditions in the presence of the control TCB, DP47, better than those treated with the cytotoxic TCB, D66-ESK, in absolute terms.

To further investigate the discrepancies between the mathematical model and the data in the D66-ESK treated conditions we consider each residual to the data in space, x, and time, t. We sum the values for each residual across all experiments performed in the presence of D66-ESK and visualise the results as a heatmap in (x, t)-space in **Figure 7B**. The dark blue area of the heatmap near (x, t)=(0,0) corresponds to the initial infiltration phase with large negative residuals corresponding to a significant overestimation of the early dynamics by the model simulations. By contrast, the predominantly green colours at later times represent a relatively good fit of the model to the data. As discussed in **Section 3.1**, the presence of D66-ESK results in an increase in the number of infiltrating PBMCs compared to the DP47 conditions. In order to optimise the fit to the data, the model simulations closely match the distribution profile at later times when more cells are present in the system at the expense of capturing the initial infiltration phase. The inability of the model to capture both phases with a single parameter set suggests that the increased infiltration observed with the cytotoxic TCB does

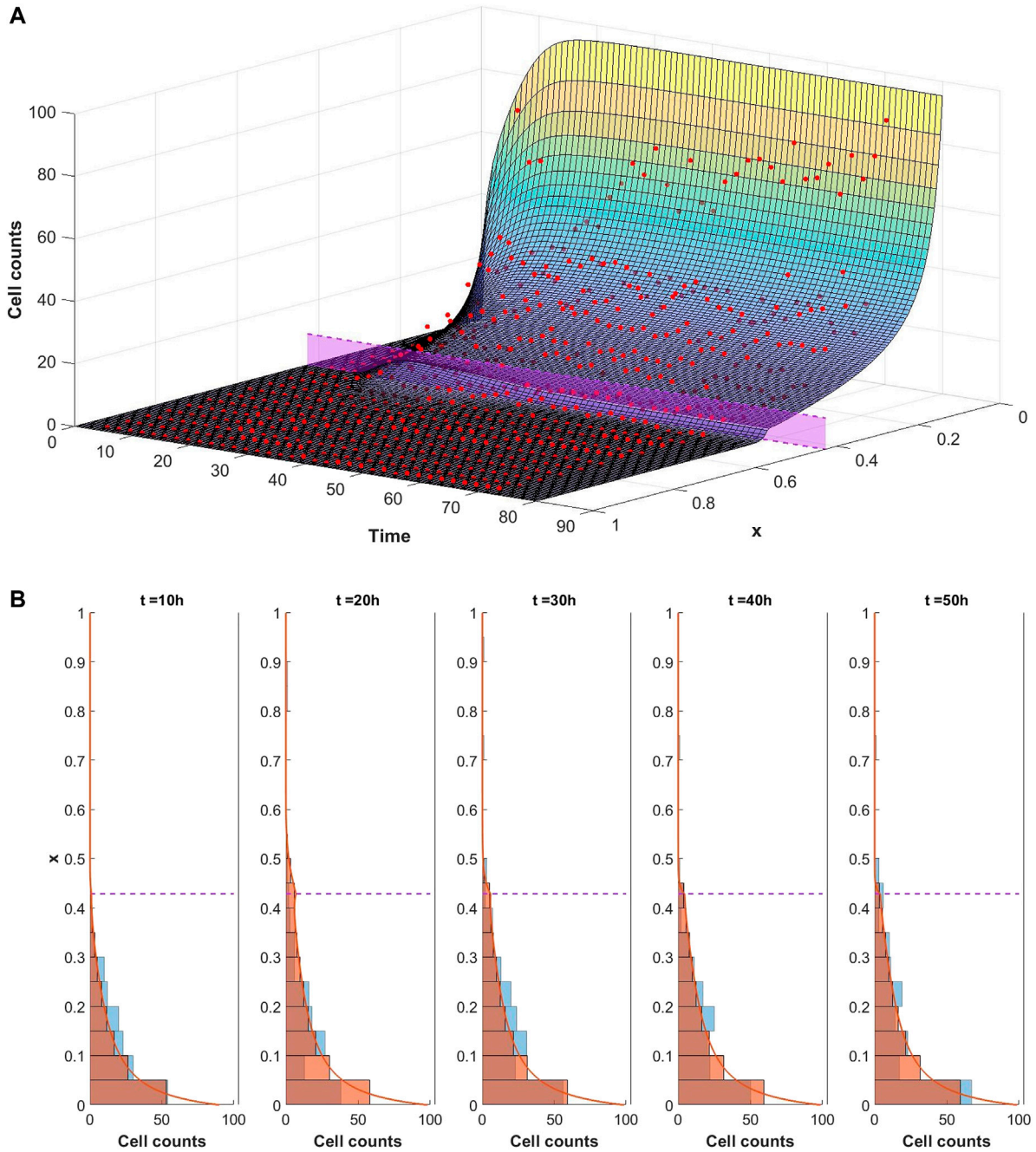

FIGURE 5 | (A) Visualisation of the mathematical model exhibiting a good fit to the experimental data for conditions with 10 μg/ml of DP47. The cell counts for each bin at each time point are shown by the red dots. The model is simulated up to 80 h using the optimal parameters found using Algorithm 1 (given in **Supplementary Table S2** in the supplementary material). The solution surface for the PBMC density, ρ, is scaled to account for the bin width and overlaid with the data points. The purple region denotes the position of the interface between the middle and top channels of the *in vitro* system. **(B)** Comparison of simulated cell count distributions (red bars) in 10 h intervals with experimental data (blue bars) for the same data and simulation shown in **Figure 5**. The scaled simulated PBMC density ρ is overlaid for reference (red line).

not arise as simply an amplification of the mechanisms present in the control TCB conditions.

The distinction between the dynamics observed in the presence of the cytotoxic TCB versus the control TCB is further highlighted when we plot the difference between the aggregated D66-ESK data points and the aggregated DP47 data points (**Figure 7C**). It is evident that there is very little difference in the early dynamics between the two conditions

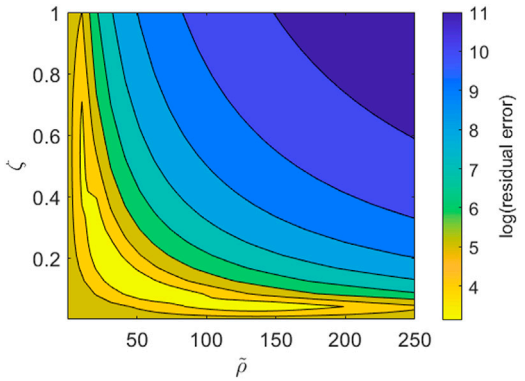

FIGURE 6 | Contour plot for the parameter subspace of the pool size of PBMCs, $\tilde{\rho} \in [0, 250]$, and the cytokine outflux rate, $\zeta \in [0, 1]$. The contours represent the quality of fit to the data shown in **Figure 5** as given by the sum of squares residual error and is shown on a log scale. All other model parameters are fixed to those used for the simulation in **Figure 5**.

with a notable increase in infiltration in the cytotoxic TCB conditions occurring after approximately 12 h. We note that this discrepancy appears to coincide with the progress of the first infiltrating cells. This suggests that the second, increased infiltration phase in the D66-ESK dynamics may result from the effects of target engagement by the first infiltrating PBMCs mediated by a chemotactic signal that is distinct from that provided by the resident macrophages in the ECM channel. Consequently, PBMCs are able to first moderately infiltrate in response to a pro-inflammatory stimulus, and subsequently increase infiltration upon target engagement.

4 DISCUSSION

In this paper, we have presented a novel microphysiological system which recapitulates the dynamics of infiltrating T cells into tissues. The *in vitro* model includes the effects of a resident immune compartment and exhibits observable differences in the dynamics in the presence of different immune modulatory compounds. The multiple components that constitute the *in vitro* model—primary intestinal epithelium, resident immune cells and matched circulating T-cells—enable us to introduce controlled modulations that can allow for a simplified representation of variations in patient physiological status within the system, such as chronic inflammation, common asymptomatic infections, microbiome changes, autoimmune susceptibilities or even tissue damage, and immune reprogramming due to cancer or chemotherapy. Thus, we created a complex immune-competent model of the intestine, and the first to incorporate T-cell infiltration as a crucial step of the cancer immunity cycle. We also demonstrated the model's competence to recapitulate TCB-mediated T-cell activation and epithelial cell killing. As such, our system provides a highly promising setting in which to test new drugs and provide predictions for safety and efficacy *in vivo*.

Live imaging of the *in vitro* system allows for the observation of such dynamics at a high temporal resolution. Image analysis techniques can provide a rich dataset for quantitative analysis of the complex biological processes involved. Simple analysis of the imaging data confirmed greater infiltration of PBMCs was oberved in the presence of a cytotoxic TCB at 48 h when compared to control, non-toxic conditions. No significant difference, however, was observed in the distribution of distances travelled by infiltrating PBMCs between the two conditions. In both scenarios, infiltrates were spread throughout the middle matrix channel with cells observed to accumulate upon reaching the interface with the epithelial cells. When in the presence of the cytotoxic TCB this target-engagement with the epithelial cells was observed to trigger apoptosis.

However, reduction of the complete, spatiotemporal dataset to summary statistics in this manner, does not utilise the data to its full extent or maximise the insight which may be gained into the spatiotemporal dynamics. To that end, we developed a mathematical model to describe the infiltration of PBMCs in response to chemotactic signals pertaining to the particular geometry and components of our *in vitro* system. We implemented a surrogate-based optimisation algorithm in order to fit the model to the experimental data. We observed that the model may provide a good description of the PBMC infiltration dynamics and can characterise an initial infiltration phase that subsequently settles to a steady state distribution of PBMCs throughout the system whereby infiltrating cells are spread throughout the middle, matrix channel but do not significantly penetrate the top, epithelial tissue channel.

Inspection of the model equations and subsequent analysis of a subspace of the full parameter space revealed that the model is not practically identifiable with respect to the current imaging data. This limits the extent to which we may make quantitative conclusions about specific parameters and the magnitude of influence of different processes. We thus have identified that additional data is necessary to further inform the mathematical model in order to ultimately make more quantitative predictions. In particular, the ability to robustly estimate the model parameters may allow for further, quantitative understanding for the TCB dose dependence on the infiltration dynamics, for example. Although not available for the experimental data presented here, it is feasible to measure cytokine readouts at discrete timepoints within the top and bottom channels of each well. As such, the use of the current model to inform the design of future experiments is an important avenue for future work. The model may be used to inform the types of data which should be measured as well as identifying the most informative time points at which to sample. This is of particular relevance for cytokine readouts which may not be continuously monitored as for the imaging data and are therefore more costly to sample.

By analysing the quality of fit of the mathematical model to the data we identified differences between the conditions in the presence of a cytotoxic TCB, D66-ESK, versus a control, non-toxic TCB, DP47. The discrepancies between the model and data with the cytotoxic TCB do not arise simply as a result of uniformly increased numbers of infiltrating PBMCs. Under the hypothesised mechanisms described by the model, in order to achieve the large numbers of infiltrating PBMCs at steady state at later times, the initial infiltration phase must also necessarily be accelerated. This is evident in the heatmap of the residuals in the cytotoxic TCB

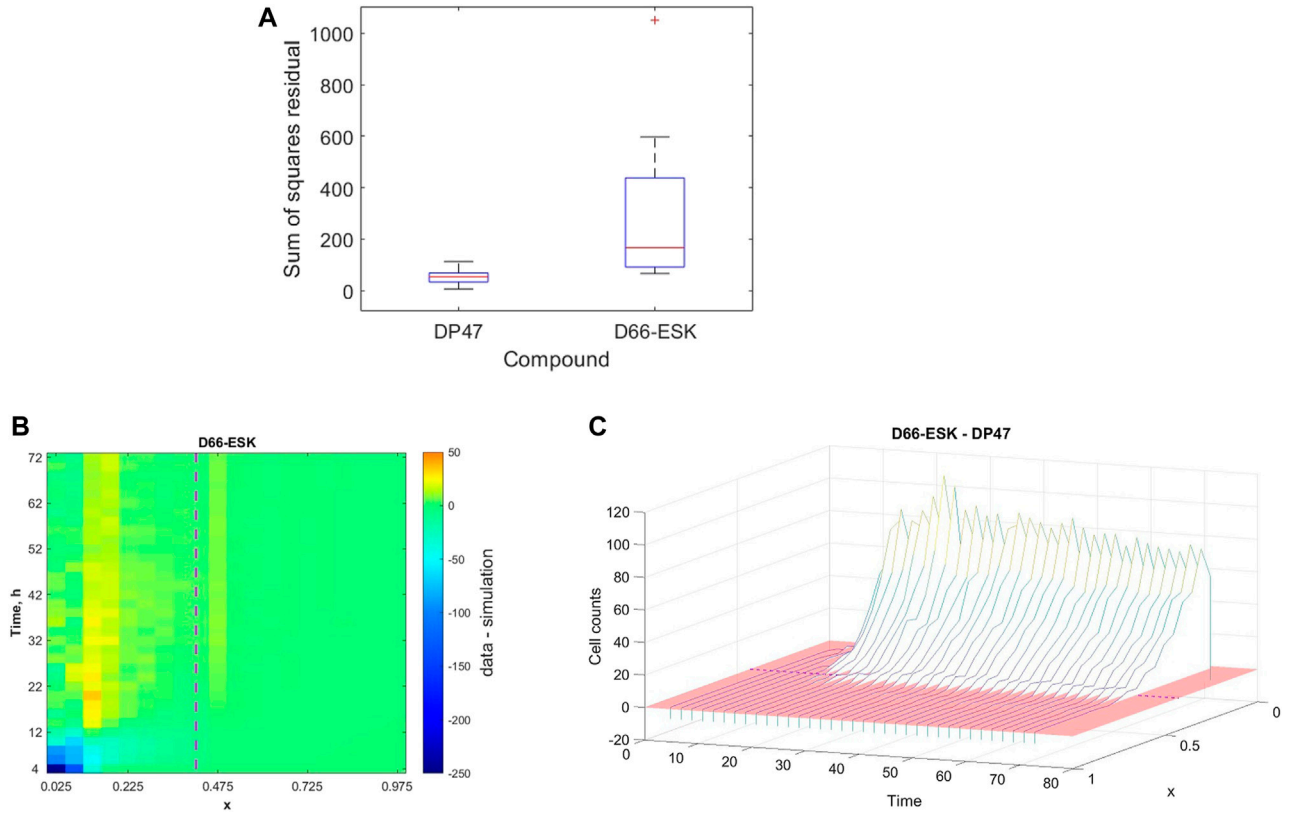

FIGURE 7 | (A) Boxplots showing the distribution of the best model fits to the data across all experimental conditions separated by compound between the control TCB, DP47, and the cytotoxic TCB, D66-ESK. **(B)** Heatmap of the discrepancy between the model simulations and the data for each data point aggregated across all conditions in the presence of D66-ESK. The purple dashed line marks the position of the interface between the middle and top channels. **(C)** Waterfall plot showing the difference in distribution of infiltrating PBMCs at each time point between the D66-ESK conditions and the DP47 conditions. The red region shows the plane where the difference in cell count is zero. The location of the interface between the middle and top channels of the plate is marked by the purple dashed line.

conditions whereby the model fit is compromised with a significant overestimation of the initial dynamics in order to accomodate the steady state profile. Further analysis of the differences between the control and cytotoxic TCB conditions showed that in both cases the initial phase is almost identical, with acceleration of the dynamics in the cytotoxic TCB case occurring after ~10–12 h coincident with the first PBMCs reaching the interface with the epithelial cell channel. The relatively poor fit of the model to these dynamics suggests that the cytokine signalling as a result of this target engagement must act as a distinct chemotactic cue for the infiltrating PBMCs, rather than as an amplification of the existing, initial chemotactic trigger provided by the resident macrophages. Extending the model to account for these mechanisms will further increase the complexity of the system. An exploration of these model dynamics for the cytotoxic TCB conditions is an important area of future work in combination with further experiments to supplement data available for model calibration as discussed above.

In this paper we focus on PBMC infiltration dynamics towards epithelial tissue and thus, for simplicity, we model the cellular distribution in a single spatial dimension perpendicular to the direction of each channel of the *in vitro* system. The model equations naturally generalise to higher dimensions, and simulations of such are an avenue for future work in order to validate the work presented in this paper and subsequent extrapolation to geometries beyond that imposed by the *in vitro* system considered here. By contrast, typical pharmacokinetic/pharmacodynamic (PKPD) models used in drug development context are often formulated as systems of ODEs. It is likely feasible to reduce the mathematical model in this paper to an ODE description of the total number of infiltrating PBMCs in the manner presented by Alt and Lauffenburger (1987). Such an analysis would facilitate integration of these dynamics with commonly-used PKPD modelling frameworks.

The *in vitro* system, experimental data, mathematical model and analysis presented in this paper may be used provide insight and understanding of the spatiotemporal dynamics of PBMC infiltration and how they are influenced by novel immune-modulatory compounds. This is of fundamental interest for understanding the interrelated signalling mechanisms involved. However, perhaps of more importance for drug development, is the potential for these systems to predict the consequent apoptosis induced by target-engagement with these compounds in both a safety and an efficacy context. Thus, an important future extension of the current modelling will be to incorporate a description of the epithelial cell population to investigate the influence of the spatiotemporal infiltration dynamics on target-mediated cell death with the aim of

quantitative *in vivo* predictions for the safety and efficacy of novel cancer immunotherapy drugs.

In conclusion, mathematical approaches to modelling *in vitro* systems, such as the one presented in this paper, can aid in the design and analysis of complex experiments representing *in vivo* biology, provide insights into interrelated biological mechanisms and, ultimately, provide more quantitative predictions to develop safe, efficacious drugs.

DATA AVAILABILITY STATEMENT

The raw data supporting the conclusion of this article will be made available by the authors, without undue reservation.

AUTHOR CONTRIBUTIONS

NG performed the *in vitro* experiments. BA and AT performed the image data analysis. TL performed the mathematical modelling and wrote the manuscript. TL, LC, NG, and LH were involved in the design of the study. All authors reviewed and approved the final manuscript.

ACKNOWLEDGMENTS

The authors would like to thank Margery Rousseille, Miro Eigenmann, and Benjamin Ribba for their helpful discussions on this work.

SUPPLEMENTARY MATERIAL

The Supplementary Material for this article can be found online at: https://www.frontiersin.org/articles/10.3389/fphar.2022.837261/full#supplementary-material

Supplementary Video S1 | Time lapse of in vitro PBMC infiltration in the presence of a cytotoxic TCB, D66-ESK. Infiltrating PBMCs are tracked in red while apoptotic epithelial cells are imaged in green.

REFERENCES

Afraites, L., and Bellouquid, A. (2014). Global Optimization Approaches to Parameters Identification in Immune Competition Model. *Commun. Appl. Ind. Maths.* 5 (0). ISSN 2038-0909. doi:10.1685/journal.caim.466

Alt, W., and Lauffenburger, D. A. (1987). Transient Behavior of a Chemotaxis System Modelling Certain Types of Tissue Inflammation. *J. Math. Biol.* 24 (6), 691–722. ISSN 0303-6812URL http://link.springer.com/10.1007/BF00275511. doi:10.1007/BF00275511

Anderson, A. R. (2005). A Hybrid Mathematical Model of Solid Tumour Invasion: The Importance of Cell Adhesion. *Math. Med. Biol.* 22 (2), 163–186. ISSN 14778599. doi:10.1093/imammb/dqi005

Augsberger, C., Hänel, G., Xu, W., Pulko, V., Hanisch, L. J., Augustin, A., et al. (2021). Targeting Intracellular WT1 in AML with a Novel RMF-peptide-MHC-specific T-Cell Bispecific Antibody. *Blood* 138, 2655–2669. ISSN 0006-4971. doi:10.1182/blood.2020010477

Bergh, J., Snedden, G., and Reddy, D. (2020). Development of an Automated Non-axisymmetric Endwall Contour Design System for the Rotor of a 1-stage Research Turbine - Part 1: System Design. *Proc. Inst. Mech. Eng. A: J. Power Energ.* 234 (5), 565–581. ISSN 0957-6509. URL http://journals.sagepub.com/doi/10.1177/0957650919876730. doi:10.1177/0957650919876730

Couzin-Frankel, J. (2013). Breakthrough of the Year 2013. Cancer Immunotherapy. *Science* 342 (6165), 1432–1433. ISSN 0036-8075. URL https://www.science.org/doi/10.1126/science.342.6165.1432. doi:10.1126/science.342.6165.1432

Dallon, J. C., and Othmer, H. G. (1997). A Discrete Cell Model with Adaptive Signalling for Aggregation of *Dictyostelium discoideum*. *Philos. Trans. R. Soc. Lond. B Biol. Sci.* 352 (1351), 391–417. ISSN 09628436. doi:10.1098/rstb.1997.0029

Di Costanzo, E., Natalini, R., and Preziosi, L. (2015). A Hybrid Mathematical Model for Self-Organizing Cell Migration in the Zebrafish Lateral Line. *J. Math. Biol.* 71 (1), 171–214. ISSN 14321416. doi:10.1007/s00285-014-0812-9

DiMilla, P. A., Barbee, K., and Lauffenburger, D. A. (1991). Mathematical Model for the Effects of Adhesion and Mechanics on Cell Migration Speed. *Biophys. J.* 60 (1), 15–37. ISSN 00063495. doi:10.1016/S0006-3495(91)82027-6

Farkona, S., Diamandis, E. P., and Blasutig, I. M. (2016). Cancer Immunotherapy: The Beginning of the End of Cancer? *BMC Med.* 14 (1), 73–18. ISSN 17417015. doi:10.1186/s12916-016-0623-510.1186/s12916-016-0623-5

Gelman, A., Carlin, J. B., Stern, H. S., and Rubin, D. B. (2014). *Bayesian Data Analysis*. New York, NY: Chapman and Hall/CRC. ISBN 978-1-4398-9820-8.

Gjorevski, N., Avignon, B., Gérard, R., Cabon, L., Roth, A. B., Bscheider, M., et al. (2020). Neutrophilic Infiltration in Organ-On-A-Chip Model of Tissue Inflammation. *Lab. Chip* 20 (18), 3365–3374. ISSN 14730189. doi:10.1039/d0lc00417k

Grenier, E., Helbert, C., Louvet, V., Samson, A., and Vigneaux, P. (2018). Population Parametrization of Costly Black Box Models Using Iterations Between SAEM Algorithm and Kriging. *Comp. Appl. Math.* 37 (1), 161–173. ISSN 18070302. doi:10.1007/s40314-016-0337-5

Guhad, F. (2005). Introduction to the 3Rs (Refinement, Reduction and Replacement). *Contemp. Top. Lab. Anim. Sci.* 44 (2), 58–59. ISSN 10600558.

Haftka, R. T., Villanueva, D., and Chaudhuri, A. (2016). Parallel Surrogate-Assisted Global Optimization with Expensive Functions - a Survey. *Struct. Multidisc. Optim.* 54 (1), 3–13. ISSN 16151488. doi:10.1007/s00158-016-1432-310.1007/s00158-016-1432-3

Havel, J. J., Chowell, D., and Chan, T. A. (2019). The Evolving Landscape of Biomarkers for Checkpoint Inhibitor Immunotherapy. *Nat. Rev. Cancer* 19 (3), 133–150. ISSN 14741768. doi:10.1038/s41568-019-0116-x10.1038/s41568-019-0116-x

Hillen, T., and Painter, K. J. (2009). A User's Guide to PDE Models for Chemotaxis. *J. Math. Biol.* 58 (1-2), 183–217. ISSN 03036812. doi:10.1007/s00285-008-0201-3

Horstmann, D. (2003). From 1970 until Present : the Keller-Segel Model in Chemotaxis and its Consequences. *Jahresbericht der Deutschen Mathematiker-Vereinigung* 105 (3), 103–165. ISSN 0012-0456.

Husain, B., and Ellerman, D. (2018). Expanding the Boundaries of Biotherapeutics with Bispecific Antibodies. *BioDrugs* 32 (5), 441–464. ISSN 1179190X. doi:10.1007/s40259-018-0299-910.1007/s40259-018-0299-9

Jin, Y. (2005). A Comprehensive Survey of Fitness Approximation in Evolutionary Computation. *Soft Comput.* 9 (1), 3–12. ISSN 1432-7643. doi:10.1007/s00500-003-0328-5

Jones, D. R., Schonlau, M., and Welch, W. J. (1998). Efficient Global Optimization of Expensive Black-Box Functions. *J. Glob. Optimization* 13, 455–492. doi:10.1023/A:1008306431147

Keller, E. F., and Segel, L. A. (1971). Model for Chemotaxis. *J. Theor. Biol.* 30 (2), 225–234. ISSN 0022-5193. doi:10.1016/0022-5193(71)90050-6

Kerns, S. J., Belgur, C., Petropolis, D., Kanellias, M., Barrile, R., Sam, J., et al. (2021). Human Immunocompetent Organ-On-Chip Platforms Allow Safety Profiling of Tumor-Targeted T-Cell Bispecific Antibodies. *Elife* 10, e67106. doi:10.7554/eLife.67106

Lauffenburger, D. A., and Kennedy, C. R. (1983). Localized Bacterial Infection in a Distributed Model for Tissue Inflammation. *J. Math. Biol.* 16 (2), 141–163. ISSN 0303-6812. URL http://link.springer.com/10.1007/BF00276054. doi:10.1007/BF00276054

Laurenceau, J., and Sagaut, P. (2008). Building Efficient Response Surfaces of Aerodynamic Functions with Kriging and Cokriging. *AIAA J.* 46 (2), 498–507. ISSN 0001-1452. URL https://arc.aiaa.org/doi/10.2514/1.32308. doi:10.2514/1.32308

Li, H., Gu, J., Wang, M., Zhao, D., Li, Z., Qiao, A., et al. (2016). Multi-objective Optimization of Coronary Stent Using Kriging Surrogate Model. *Biomed. Eng. Online* 15 (S2), 148. ISSN 1475-925XURL http://biomedical-engineering-online.biomedcentral.com/articles/10.1186/s12938-016-0268-9. doi:10.1186/s12938-016-0268-9

Linkert, M., Rueden, C. T., Allan, C., Burel, J. M., Moore, W., Patterson, A., et al. (2010). Metadata Matters: Access to Image Data in the Real World. *J. Cel. Biol.* 189 (5), 777–782. ISSN 1540-8140. URL https://rupress.org/jcb/article/189/5/777/35828/Metadata-matters-access-to-image-data-in-the-real. doi:10.1083/jcb.201004104

Martins, F., Sofiya, L., Sykiotis, G. P., Lamine, F., Maillard, M., Fraga, M., et al. (2019). Adverse Effects of Immune-Checkpoint Inhibitors: Epidemiology, Management and Surveillance. *Nat. Rev. Clin. Oncol.* 16 (9), 563–580. ISSN 17594782. doi:10.1038/s41571-019-0218-010.1038/s41571-019-0218-0

Matzavinos, A., Chaplain, M. A., and Kuznetsov, V. A. (2004). Mathematical Modelling of the Spatio-Temporal Response of Cytotoxic T-Lymphocytes to a Solid Tumour. *Math. Med. Biol.* 21 (1), 1–34. ISSN 14778599. doi:10.1093/imammb/21.1.1

McLennan, R., Schumacher, L. J., Morrison, J. A., Teddy, J. M., Ridenour, D. A., Box, A. C., et al. (2015). Neural Crest Migration Is Driven by a Few Trailblazer Cells with a Unique Molecular Signature Narrowly Confined to the Invasive Front. *Development* 142 (11), 2014–2025. ISSN 14779129. doi:10.1242/dev.117507

Mellman, I., Coukos, G., and Dranoff, G. (2011). Cancer Immunotherapy Comes of Age. *Nature* 480 (7378), 480–489. ISSN 14764687. doi:10.1038/nature10673

Olson, B., Li, Y., Lin, Y., Liu, E. T., and Patnaik, A. (2018). Mouse Models for Cancer Immunotherapy Research. *Cancer Discov.* 8 (11), 1358–1365. ISSN 21598290. doi:10.1158/2159-8290.CD-18-0044

Painter, K. J., Maini, P. K., and Othmer, H. G. (2000). Development and Applications of a Model for Cellular Response to Multiple Chemotactic Cues. *J. Math. Biol.* 41 (4), 285–314. ISSN 03036812. doi:10.1007/s002850000035

Painter, K. J. (2019). Mathematical Models for Chemotaxis and Their Applications in Self-Organisation Phenomena. *J. Theor. Biol.* 481, 162–182. ISSN 10958541. doi:10.1016/j.jtbi.2018.06.019

Poli, R., Kennedy, J., and Blackwell, T. (2007). Particle Swarm Optimization. *Swarm Intell.* 1 (1), 33–57. ISSN 1935-3820. doi:10.1007/s11721-007-0002-0

Qin, A. K., Huang, V. L., and Suganthan, P. N. (2009). Differential Evolution Algorithm with Strategy Adaptation for Global Numerical Optimization. *IEEE Trans. Evol. Computat.* 13 (2), 398–417. doi:10.1109/tevc.2008.927706

Rueden, C. T., Schindelin, J., Hiner, M. C., DeZonia, B. E., Walter, A. E., Arena, E. T., et al. (2017). ImageJ2: ImageJ for the Next Generation of Scientific Image Data. *BMC Bioinformatics* 18 (1), 529. ISSN 1471-2105. URL http://www.ncbi.nlm.nih.gov/pubmed/29187165 http://www.pubmedcentral.nih.gov/articlerender.fcgi?artid=PMC5708080. doi:10.1186/s12859-017-1934-z

Sacher, M., Duvigneau, R., Le Maître, O., Durand, M., Berrini, É., Hauville, F., et al. (2018). A Classification Approach to Efficient Global Optimization in Presence of Non-computable Domains. *Struct. Multidisc Optim* 58 (4), 1537–1557. ISSN 16151488. doi:10.1007/s00158-018-1981-810.1007/s00158-018-1981-8

Sacks, J., Welch, W. J., Mitchell, T. J., and Wynn, H. P. (1989). Design and Analysis of Computer Experiments. *Statist. Sci.* 4 (4), 409–423. ISSN 0883-4237. URL http://projecteuclid.org/euclid.ss/1177012413. doi:10.1214/ss/1177012413

Schindelin, J., Arganda-Carreras, I., Frise, E., Kaynig, V., Longair, M., Pietzsch, T., et al. (2012). Fiji: An Open-Source Platform for Biological-Image Analysis. *Nat. Methods* 9 (7), 676–682. ISSN 1548-7105. URL http://www.ncbi.nlm.nih.gov/pubmed/22743772 http://www.pubmedcentral.nih.gov/articlerender.fcgi?artid=PMC3855844. doi:10.1038/nmeth.2019

Storn, R., and Price, K. (1997). Differential Evolution – A Simple and Efficient Heuristic for Global Optimization Over Continuous Spaces. *J. Glob. Optimization* 11 (44), 11341–11359. ISSN 1573-2916. URL https://link.springer.com/article/10.1023/A:1008202821328. doi:10.1023/A:1008202821328

Viana, F. A. C., Simpson, T. W., Balabanov, V., and Toropov, V. (2014). Special Section on Multidisciplinary Design Optimization: Metamodeling in Multidisciplinary Design Optimization: How Far Have We Really Come? *AIAA J.* 52 (4), 670–690. ISSN 0001-1452. URL https://arc.aiaa.org/doi/10.2514/1.J052375. doi:10.2514/1.J052375

Wagar, L. E., Difazio, R. M., and Davis, M. M. (2018). Advanced Model Systems and Tools for Basic and Translational Human Immunology. *Genome Med.* 10 (1), 73–14. ISSN 1756994X. doi:10.1186/s13073-018-0584-8

Wang, G. G., and Shan, S. (2007). Review of Metamodeling Techniques in Support of Engineering Design Optimization. *J. Mech. Des.* 129 (4), 370–380. ISSN 1050-0472, URL https://asmedigitalcollection.asme.org/mechanicaldesign/article/129/4/370/466824/Review-of-Metamodeling-Techniques-in-Support-of. doi:10.1115/1.2429697

Xing, J., Luo, Y., and Gao, Z. (2020). A Global Optimization Strategy Based on the Kriging Surrogate Model and Parallel Computing. *Struct. Multidisc. Optim.* 62, 405–417. doi:10.1007/s00158-020-02495-6

Zhan, D., Qian, J., and Cheng, Y. (2017). Pseudo Expected Improvement Criterion for Parallel EGO Algorithm. *J. Glob. Optim.* 68 (3), 641–662. ISSN 15732916. URL https://link.springer.com/article/10.1007/s10898-016-0484-7. doi:10.1007/s10898-016-0484-7

Zhang, J., Endres, S., and Kobold, S. (2019). Enhancing Tumor T Cell Infiltration to Enable Cancer Immunotherapy. *Immunotherapy* 11 (3), 201–213. ISSN 17507448. doi:10.2217/imt-2018-0111

Conflict of Interest: The authors declare that the research was conducted in the absence of any commercial or financial relationships that could be construed as a potential conflict of interest.

frontiers | Frontiers in Pharmacology

ORIGINAL RESEARCH
published: 08 June 2022
doi: 10.3389/fphar.2022.864768

Early Feasibility Assessment: A Method for Accurately Predicting Biotherapeutic Dosing to Inform Early Drug Discovery Decisions

*Diana H. Marcantonio†, Andrew Matteson†, Marc Presler†, John M. Burke, David R. Hagen, Fei Hua and Joshua F. Apgar**

Applied BioMath, LLC, Concord, MA, United States

The application of model-informed drug discovery and development (MID3) approaches in the early stages of drug discovery can help determine feasibility of drugging a target, prioritize between targets, or define optimal drug properties for a target product profile (TPP). However, applying MID3 in early discovery can be challenging due to the lack of pharmacokinetic (PK) and pharmacodynamic (PD) data at this stage. Early Feasibility Assessment (EFA) is the application of mechanistic PKPD models, built from first principles, and parameterized by data that is readily available early in drug discovery to make effective dose predictions. This manuscript demonstrates the ability of EFA to make accurate predictions of clinical effective doses for nine approved biotherapeutics and outlines the potential of extending this approach to novel therapeutics to impact early drug discovery decisions.

Keywords: QSP, MID3, dose prediction, mAb, biotherapeutic, mechanistic PKPD

OPEN ACCESS

Edited by:
Rui Li,
Pfizer, United States

Reviewed by:
Shibin Mathew,
Pfizer, United States
Jeffrey D. Kearns,
Novartis Institutes for BioMedical Research, United States
Amy Meng,
Gilead, United States

****Correspondence:***
Joshua F. Apgar
apgar@appliedbiomath.com

†These authors have contributed equally to this work and share first authorship

Specialty section:
This article was submitted to Experimental Pharmacology and Drug Discovery, a section of the journal Frontiers in Pharmacology

Received: *28 January 2022*
Accepted: *16 May 2022*
Published: *08 June 2022*

Citation:
Marcantonio DH, Matteson A, Presler M, Burke JM, Hagen DR, Hua F and Apgar JF (2022) Early Feasibility Assessment: A Method for Accurately Predicting Biotherapeutic Dosing to Inform Early Drug Discovery Decisions. Front. Pharmacol. 13:864768. doi: 10.3389/fphar.2022.864768

INTRODUCTION

Dosage is fundamental to the success or failure of therapeutic agents (Paracelsus, 1538). The appropriate selection of dose is accordingly a critical component of decision making at all stages of drug development. An earlier understanding of dose, and how drug and target properties influence dose, can greatly improve the speed and quality of drug development. At later stages of development, model-informed drug discovery and development (MID3) approaches have been increasingly used to inform clinical trial dose selection with empirical and mechanistic-based models (Shen et al., 2019). These have been encouraged by the FDA through programs such as the model-informed drug development pilot program (U.S. Food and Drug Administration, 2021). Examples of clinical application include minimum anticipated biological effect (MABEL) dose calculations for first-in-human dose selection (Hu and Hansen 2013; Shen et al., 2019) and rational dose selection for pivotal trials; models are also used to justify simplified dosing for patients and providers, and to extrapolate to untested populations or dosing regimen to inform clinical decision making (Nayak et al., 2018).

Many decisions during discovery and early development can also be impacted by an understanding of the likely clinical dose and the impact of drug properties on the dose. Here, computational methods are essential because these decisions occur long before data from translational or clinical studies are available. For example, if the anticipated clinical dose could be determined to be infeasible to practically administer even assuming ideal drug properties, this could be used as a no-go criteria at the start of a new program and save significant research and development costs (Patel and Bueters 2020). Likewise, target prioritization, clinical candidate

selection, preclinical study design, prediction of the impact of formulations or the route of administration can all be informed by earlier understanding of the likely clinical dose (Hu and Hansen 2013; Patel and Bueters 2020). Even in the absence of drug-specific data, understanding the potential for target burden, target turnover, or decoy receptors to impact dose could help prioritize early experiments to fill key knowledge gaps (Hu and Hansen 2013; Glassman and Balthasar 2019; Patel and Bueters 2020). Moreover, progressing efficiently through the new target and lead generation (or biotherapeutics design) stages can impact return on investment, in terms of potentially being first-in-class or best-in-class (Shulze and Ringel 2013). Lalonde et al. (2007) emphasized the importance of starting modeling before compound selection to assist in these types of decisions and continually updating models throughout the development process to aid in decision making at each stage.

Despite the increasing use of such MID3 approaches in later stage programs, the application of these approaches to early stage drug discovery decisions has been more limited. In general, the methods applied in later stage development rely on pharmacokinetic (PK) data, pharmacodynamic (PD) data, or both (PKPD data) that was collected from studies where the drug candidate was administered. This data simply is not available at the early stages of drug discovery. The challenge has been how to develop these models in the absence of PKPD data, relying on what has been previously described in literature, and then validate the results (Hu and Hansen 2013).

The application of mechanistic PKPD models to describe the pharmacology of antibody-based biotherapeutics is an opportunity to overcome these challenges. Antibody-based therapeutics often have predictable linear PK properties (Deng et al., 2011; Dong et al., 2011; Betts et al., 2018), and the impact of binding to soluble and membrane receptor targets on the non-linear PK of antibodies has been well described (Mager and Jusko 2001; Peletier and Gabrielsson 2012; Dua et al., 2015). Mechanistic models can utilize these properties, biological data from the literature on the biophysical properties of the target, and physiological parameters such as compartment volumes, cell numbers, receptor expression levels, and soluble protein concentrations to describe the intended pharmacology of biotherapeutics. Kapitanov et al. provides an example of this application of mechanistic PKPD models, in a series of case studies for antagonist mAbs. In this work, the authors use typical PK and physiological parameters in a "site of action model" to provide insight to guide early discovery decisions (Kapitanov et al., 2021). A generalization of this framework, that is validated with benchmark data, could enable the expanded use of these approaches.

This manuscript presents Early Feasibility Assessment (EFA) as a workflow for the application of mechanistic PKPD models, without fitting to PK or PD data, to predict effective dose for biotherapeutics. The process of model selection, model parameterization, and criteria definition for dose prediction are described through specific case studies. EFA is used to predict the clinical efficacious doses of nine approved biotherapeutics across a range of targets and indications. These examples demonstrate the capabilities of EFA to make relevant predictions and establish a workflow that can be applied at an early stage, even before the generation of candidate or tool molecules (Applied BioMath 2021).

TABLE 1 | Biotherapeutics included in EFA analysis.

Drug	Indication[a]	Target
Remicade (infliximab)	RA	TNFa
Humira (adalimumab)	RA	TNFa
Stelara (ustekinumab)	Plaque psoriasis	IL-23/IL-12
Skyrizi (risankizumab)	Plaque psoriasis	IL-23
Benlysta (belimumab)	SLE	BLyS (BAFF)
Xolair (omalizumab)	Asthma	IgE
Herceptin (trastuzumab)	Breast Cancer	HER2
Vectibix (panitumumab)	Colon Cancer	EGFR
Rybrevant (amivantamab)	NSCLC (EGFR exon 2)	EGFR/c-Met

[a]*RA = rheumatoid arthritis, SLE = systemic lupus erythematosus.*

MATERIALS AND METHODS

Test Set of Drugs, Targets and Indication

A representative collection of 9 clinically approved biotherapeutics were modeled in this analysis. Drug targets include both soluble (TNFα, IL-23/IL-12, IL-23, BLyS, IgE) and membrane (HER2, EGFR, c-Met) targets. These biotherapeutics have been approved in a range of oncology and immune and inflammation (I&I) indications. The complete list of drugs, targets, and indications are provided in **Table 1**.

Model Strategy

Three different mechanistic PKPD models were used for the analyses in this manuscript. Full model descriptions are included later in the manuscript. All models are *in vivo* human models which describe drug administration, PK, target binding, and target dynamics in one or more compartments. The models were used to predict PK, target engagement, and target inhibition at different doses. Target engagement or inhibition criteria were used to define effective dose. Models were chosen according to each biotherapeutic's pharmacology.

For soluble targets, a 1-compartment monospecific anti-ligand model was chosen. Drug interactions with soluble targets are confined to the vascular and interstitial fluid spaces, and can be sufficiently described with a one-compartment model. While one-compartment models do not accurately describe the distribution phase of typical mAb PK, the analysis focuses on inhibition at trough concentrations, which can be captured by a one-compartment model.

For membrane targets, a 2-compartment monospecific anti-receptor model was chosen. Unlike soluble targets, membrane targets are often preferentially expressed in the peripheral tissues. Antibody distribution into peripheral tissues can

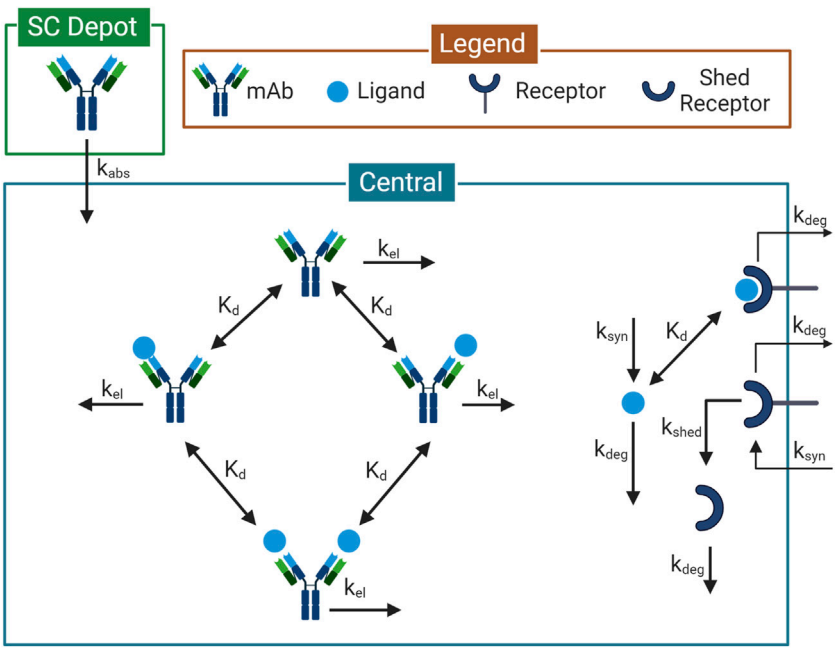

FIGURE 1 | Model Diagram for the 1-compartment monospecific anti-ligand model. Diagram illustrates the species and reactions comprising the pharmacological model describing the interaction between a monospecific anti-ligand antibody and its target. Model diagram was created with BioRender.com.

also be limited (Shah and Betts 2012). Physiologically-relevant representation of drug distribution into the lumped peripheral compartment, target expression in the peripheral compartment, and drug interactions with target were considered necessary to describe the drug pharmacology. While not used here, for targets with high or low tissue penetration, a three (or more) compartment model can be used with tissue specific antibody biodistribution coefficient to describe the transport (Shah and Betts 2013).

For the bispecific antibody case study, a 2-compartment bispecific anti-receptor x anti-receptor model was chosen. A 2-compartment model was chosen for more accurate representation of the membrane targets.

All models were parameterized using data obtained from literature (i.e. there is no parameter fitting). The only compound specific data was of the type typically available in early discovery (e.g. affinity, valency, etc.). Typical values, or expected ranges for these parameters can be used to apply this analysis even earlier. Detailed methods for model parameterization are described below. For each drug, a criterion for defining effective dose (e.g. 90% sustained target inhibition) was chosen. Models were then simulated to determine the dose required to achieve the criterion. This model predicted effective dose was compared to clinically approved doses for each drug. For model validation, it was assumed that dose predictions within 3-fold of the prescribed efficacious dose of drugs was sufficient for early decision making, especially for the prioritization of potential targets and to inform lead identification and optimization criteria.

Model Structure

The 1-compartment monospecific anti-ligand model is a single-compartment model describing drug administration, target-binding, and elimination (**Figure 1**). Drug administration can be described as an intravenous (IV) bolus, or subcutaneous (SC) administration with a 1st order absorption rate. Target ligand and its cognate receptor are synthesized in the compartment with a 0th order rate. Ligand binds reversibly to the receptor, specified by a monovalent equilibrium dissociation constant (Kd). Drug binds reversibly to the target ligand, specified by a separately parameterized Kd, and blocks ligand-receptor interactions. All species are eliminated through 1st order processes. This model is run using the Monospecific Anti-Ligand model in Applied BioMath Assess ™.

The 2-compartment monospecific anti-receptor model consists of a central and peripheral compartment. (**Supplementary Figure S1**) Drug is administered into the central compartment as an IV bolus. Target membrane receptor is synthesized through 0th order processes in both central and peripheral compartments. A soluble form of the receptor is generated through shedding from the membrane receptor by a 1st order process. Drug can reversibly bind either membrane or soluble forms of the receptor, specified by a binding Kd. Bivalent binding of drug to membrane or soluble

forms of the receptor are modeled as independent binding reactions with identical Kd values. All species are eliminated with 1st order rates in both compartments. All binding interactions occur in each compartment with identical Kd values. All soluble species can transport between compartments with 1st order rates. This model is run using the Monospecific Anti-Receptor (4 compartment) model in Applied BioMath Assess ™, with the tox and disease compartments disabled.

The 2-compartment bispecific anti-receptor x anti-receptor model consists of a central and peripheral compartment. (**Supplementary Figure S2**) Model reactions are constructed as in the monospecific anti-receptor model, except with 2 different target receptors. Free drug can bind with either receptor, specified by independent binding Kd's. Reversible binding of a second receptor is described as an independent binding process, parameterized by the same receptor-specific Kd. This model is run using the Bispecific Anti-Receptor x Anti-Receptor (4 compartment) model in Applied BioMath Assess ™, with the tox and disease compartments disabled.

Model Parameterization

Drug-specific parameters, defined as elimination half-life, target binding Kd, valency, and molecular weight, were identified from reported values. Target binding affinities were identified from *in vitro* measurements in biochemical or cell-based assays. Half-life was identified from reported PK data.

Target specific parameters, defined as target concentration and target turnover rate were calculated from literature measurements. Soluble target concentrations were parameterized by plasma measurements in indication-specific patients. Soluble target half-life may be measured from pharmacokinetic measurements of exogenously administered target. Membrane target concentrations were calculated using "bottom-up" methods. Target expression was calculated as the sum of the number of cells for each cell type expressing the target x % of each cell type expressing the target x receptors per cell. Target expression was divided by the interstitial volume of each relevant compartment to determine target concentrations. Examples of data supporting inputs include, but are not limited to, immunohistochemical staining of target across tissues, quantitative or semi-quantitative flow cytometry, Scatchard analysis of ligand binding sites, functional data on target activation or knock-down, RNA expression data. Membrane target turnover rates were identified from *in vitro* cell line measurements when available. When data is not available, assumptions based on other proteins of the same family, similar structure, molecular weight, or function were used.

Model Assumptions

For all models, compartments are assumed to be well-mixed. Non-specific elimination of the drug occurs in all compartments with equal 1st order rate constant. For the anti-ligand model, drug: target-ligand complex is assumed to eliminate at the same rate as the free drug. Ligand:receptor complex is assumed to eliminate at the same rate as free receptor. For the anti-receptor models, internalization and elimination of the membrane receptors are considered a single process. Drug:membrane receptor complexes eliminate at the same rate as free receptors. Drug:soluble-receptor complexes eliminate at the same rate as free drug. For multi-compartment models, all soluble species transport bi-directionally between compartments. Drug:soluble-receptor complexes are assumed to transport with the same rate constant as free drug. All multivalent binding interactions are assumed to be identical and independent.

Model Software

All simulations were performed using Applied BioMath Assess ™ version 2021.12.1 (https://www.appliedbiomath.com/assess). Run files in json format, Model files, and Assess Model Reports are included in **Supplementary Material**.

RESULTS

To assess the ability of the EFA methodology to accurately translate mechanistic parameters into likely clinical doses, we performed a set of simulation studies for nine approved biotherapeutics. Because these drugs have been approved there is data on the molecular properties (e.g. affinity Kd and half-life) as well as the approved clinical dose. Obviously this data is not typically available for an early stage program. Where EFA is used in practice these parameters would be set to a typical value for the modality, or scanned over a typical range to find the critical value where the pharmacology requirements are satisfied. However, here we are looking at the ability of the model to accurately translate the mechanistic parameters to predict a likely clinical dose. To assess this, we are looking at the degree of agreement (or disagreement) of the effective dose predicted by EFA compared to the approved clinical dose.

Case Study 1: Effective Dose Prediction for Adalimumab and Infliximab, Two Different Anti-TNFα Drugs

In case study 1, EFA was used to predict the effective dose of two well-studied anti-TNFα agents: adalimumab and infliximab for the treatment of rheumatoid arthritis (RA). Despite the shared target and indication, the two drugs have different binding and PK properties, and have different approved dose and regimen. The approved clinical dose for adalimumab in RA is 40 mg every other week administered through SC injection, although some patients not receiving methotrexate benefit from 40 mg every week. (Adalimumab, 2021) For RA patients treated with infliximab, the clinically approved dose begins at 3 mg/kg IV at 0, 2 and 6 weeks followed by a maintenance dose administered once every 8 weeks. There is a potential benefit of increasing dose to 10 mg/kg IV once a month. (Infliximab, 2013) For this analysis, model predictions are compared to the maintenance dose of infliximab. To predict these doses from first principles, drug-specific and target-specific parameters were defined for input into the model (**Table 2**).

TABLE 2 | Adalimumab and infliximab (TNFα) model parameters.

Parameter	Value	Unit	Reference
Drug Valency	1	-	Lim et al., 2018; Tran et al., 2017
Adalimumab Dosing Interval	2	weeks	Adalimumab, 2021
Infliximab Dosing Interval	8	weeks	Infliximab, 2013
Adalimumab Half-Life	20	days	Adalimumab, 2021; Weisman et al., 2003; Ternant et al., 2015
Infliximab Half-Life	14	days	Hemperly and Niels Vande, 2018
Adalimumab Molecular Weight	148,000	Daltons	Adalimumab, 2021
Infliximab Molecular Weight	149,100	Daltons	Infliximab, 2013
Adalimumab KD	8.6	pM	Kaymakcalan et al., 2009
Infliximab KD	4.2	pM	Kaymakcalan et al., 2009
TNF Concentration	5.73e-5	nM	Takeuchi et al., 2011
TNF Half-Life	30	min	Moritz et al., 1989
TNF:TNFR KD	19	pM	Grell et al., 1998
TNFR Concentration	0.23	nM	Bottom up calculation
TNFR receptor half-life	9	hr	Higuchi 1994
Volume	5	L	Typical volume of distribution for mAb
Body weight	70	kg	Typical body weight for man

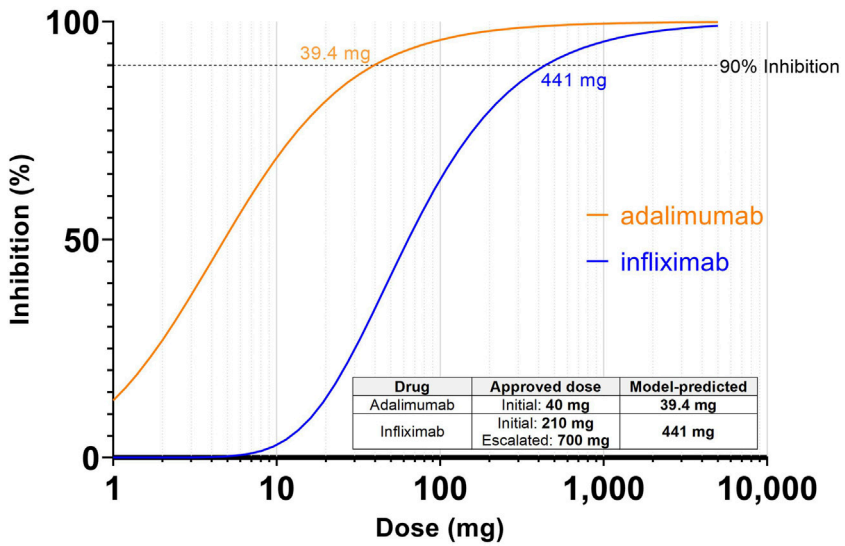

FIGURE 2 | Simulations predicting dose to achieve 90% inhibition of TNF:TNFR complex for adalimumab and infliximab. Inhibition is defined as reduction from the pretreatment target ligand:receptor binding at the steady state trough. Inset table shows the model-predicted dose based on inhibition vs. clinically approved dose for each drug. For infliximab, the milligram dosage assumes a 70 kg patient.

A 1-compartment monospecific anti-ligand model was chosen (**Figure 1**), focusing on the interaction of the soluble TNFα with drug within the vascular and interstitial fluid.

Target-specific parameters for TNFα included in the model include the representative TNFα concentration in plasma of RA patients (Tekeuchi et al., 2011), as well as its half-life as evaluated from PK studies of recombinant TNFα (Moritz et al., 1989). Membrane TNFR1 expression levels, its turnover half-life (Higuchi 1994) and the affinity of the TNFα:TNFR complex (Grell et al., 1998) were also included in the model. The TNFR1 expression level was calculated from the bottom-up approach described in the methods. (See **Supplementary Material** for detailed calculations.) TNFR1 is broadly expressed in all human tissues (Holbrook et al., 2019), so TNFR1 expressing cells were calculated assuming a high percentage of nucleated cells in the human body express the receptor (Sender et al., 2016). Absolute expression levels (receptors/cell) were determined from Scatchard analysis of TNFα binding sites (Imamura et al., 1987; Michishita et al., 1990).

Drug specific parameters included valency, target-binding affinity, and the drug half-life. The effective valency of adalimumab and infliximab was considered 1, based on observation of 1:1, 2:2 and 3:3 complexes of the bivalent antibodies to the TNFα homotrimer (Tran et al., 2017; Lim et al., 2018). The affinity of each drug to TNFα was taken from Kinexa measurements, with a Kd of 8.6 pM for adalimumab and 4.2 p.m. for infliximab (Kaymakcalan et al., 2009). Drug PK parameters (half-life of linear elimination) were

20 days for adalimumab (Weisman et al., 2003; Ternant et al., 2015) and 14 days for infliximab (Hemperly and Niels Vande, 2018). The absorption half-life for SC administration of adalimumab was assumed to be 2.5 days based on typical values for antibodies (Kagan, 2014).

Inhibition of pretreatment target ligand:receptor binding of >90% was selected as the target inhibition criteria for effective dose prediction in case study 1, where the complex of TNFα and TNFR is held at 90% lower than the pre-treatment levels for the entirety of the dosing interval, after 7 successive doses. Simulations were performed to assess the dose that achieves the target criteria. The model predicted that inhibition of pre-treatment TNFα:TNFR binding by adalimumab reaches 90% inhibition at 39.4 mg Q2W for a nominal patient at steady state (**Figure 2**). This corresponds closely to the clinically approved initial dosage of 40 mg every other week, and the estimated bioavailable dose of 25.6 mg based on 64% bioavailability. (Adalimumab, 2021) Likewise, infliximab reaches 90% inhibition at 6.3 mg/kg Q8W in the model (**Figure 2**), which also corresponds closely to the clinically approved dosage of 3 mg/kg to start, with a ramp up to 10 mg/kg if needed. The relationship between dose and trough target inhibition can also be observed in **Figure 2**. The model predicts ~2-fold lower dose would be required to sustain 85% inhibition, while ~2-fold higher dose would be required to sustain 95% inhibition.

Interestingly, these model predicted effective doses are significantly higher than the dose that might be predicted from a more straightforward exposure vs. potency comparison. At 39.4 mg, the trough concentration of adalimumab is predicted to be 93.0 nM which is over 10,000 times the Kd (8.6 pM). The model provides an explanation for this shift—when the drug binds to TNFα there is an increase of total TNFα levels from baseline. This has been shown to occur due to half-life extension effects where the short-lived soluble targets form longer-lived complexes with the administered antibodies (Finkelman et al., 1993; Charles et al., 1999; Berkhout et al., 2019). As a result a higher trough concentration than might be expected is required to achieve the desired inhibition level. This type of interaction between binding and total target levels demonstrated the advantage of applying a mechanistic PKPD model for dose predictions.

Sensitivity of Effective Dose Predictions for Adalimumab and Infliximab

To assess the sensitivity of model-predicted effective dose on the input parameters, a one-at-a-time parameter scan was performed. The model was simulated with each parameter individually varied 3-fold up and down, while all other parameters were held constant at their nominal value. The parameters were ranked based on the fold-difference between the maximum and minimum dose predicted to achieve 90% inhibition. Parameters that resulted in a greater than 3-fold range of predicted effective dose were further examined.

For both infliximab and adalimumab, target binding affinity (Kd), ligand half-life, drug molecular weight, and compartment volume were identified as sensitive parameters. (**Supplementary Tables S1, S2**) When varied over an order of magnitude, the resulting effective dose prediction ranged by greater than 3-fold. Drug molecular weight has a direct effect on molar drug concentrations, but is well-defined for antibody-based biotherapeutics. Systemic compartment volume is defined as the volume of distribution of the drug and has a direct effect on drug concentrations. For monoclonal antibodies, the volume of distribution is relatively well-defined (Pearson et al., 1995; Ovacik and Lin 2018). Target binding affinity was identified as an important drug-specific parameter. For both infliximab and adalimumab, binding Kd to TNFα was well-described in the literature and an unlikely source of uncertainty. Drug half-life was only identified as a sensitive parameter for infliximab. This is because infliximab is dosed less frequently (Q8W) than adalimumab (Q2W). This result highlights how the dosing regimen can affect drug parameter sensitivities.

The ligand half-life was the only sensitive target-specific parameter, while ligand concentration was not identified as sensitive. The model provides an explanation for this, as the ligand half-life will impact the degree of ligand accumulation over baseline due to half-life extension effects of drug binding. The fold-increase in ligand levels, rather than absolute baseline concentration, has a larger impact on predicted effective dose. For TNFα, the ligand half-life was identified from PK studies of recombinant TNFα. In the absence of such information, the model analysis suggests that measurements of ligand half-life may be a greater priority during drug development.

Case Study 2: Effective Dose Prediction for Amivantamab, an Anti-EGFR, Anti-c-Met Bispecific Antibody

In this case example, analysis was extended to a bispecific antibody (BsAb), amivantamab, which is approved for the treatment of patients with non-small cell lung cancer (NSCLC) with EGFR exon 20 insertion mutations. The approved clinical dose for patients under 80 kg body weight is 1050 mg administered weekly for the first 4 weeks, and every 2 weeks thereafter. (Rybrevant, 2021) Amivantamab targets epidermal growth factor receptor (EGFR) and hepatocyte growth factor receptor (c-Met) (Haura et al., 2019). A 2-compartment bispecific anti-receptor x anti-receptor model was chosen for this analysis.

Target-specific parameters included in the model were membrane receptor expression levels in the central and peripheral compartments, and membrane receptor turnover half-life. In addition, soluble c-Met is known to be elevated in patient plasma (Gao et al., 2016), so soluble receptor concentration and turnover were also included in the model. EGFR and c-Met expression levels were calculated from the bottom-up approach described in the methods. (See **Supplementary Material** for detailed calculations.) Briefly, EGFR expression on monocytes, macrophages, skin keratinocytes, tumor cells, and in various epithelial tissues were identified from functional and IHC staining data (Real et al., 1986; Yano et al., 2003; Chen et al., 2016). Absolute expression levels ranged from 50,000 to >400,000 receptors per

TABLE 3 | EGFR and c-met target parameters.

Parameter	Value	Unit	Reference
EGFR expression central	4.57E-02	nmoles	Bottom up calculation
EGFR expression peripheral	1.47E+01	nmoles	Bottom up calculation
EGFR receptor half-life	5	hours	Sigismund et al., 2008
Met expression central	3.20E-02	nmoles	Bottom up calculation
Met expression peripheral	5.86E+00	nmoles	Bottom up calculation
Met receptor half-life	4	hours	Li et al., 2008; Da Silva et al., 2020
soluble Met concentration	5.9	nM	Rosen et al., 2017; Gao et al., 2016
soluble Met half-life	48	hours	Estimate based on protein molecular weight; Li et al., 2017
Central compartment volume	3	L	Plasma volume; Shah and Betts, 2012
Peripheral Compartment volume	13	L	Interstitial volume of peripheral tissues; Shah and Betts, 2012
Body weight	70	kg	Typical body weight for man

TABLE 4 | Drug specific model parameters for panitumumab, emibetuzumab, amivantamab.

Parameter	Value	Unit	Reference
Panitumumab Valency	2	-	Yang et al., 2001; Ma et al., 2009
Panitumumab Dosing Interval	2	weeks	Ma et al., 2009
Panitumumab Half-Life	16	days	Yang et al., 2001; Ma et al., 2009
Panitumumab KD for EGFR	0.05	nM	Yang et al., 2001; Ma et al., 2009
Emibetuzumab Valency	-	2	Liu et al., 2014; Rosen et al., 2017
Emibetuzumab Dosing Interval	2	weeks	Rosen et al. (2017)
Emibetuzumab Half-Life	16	days	Liu et al., 2014; Rosen et al., 2017
Emibetuzumab KD for c-Met	0.1	nM	Liu et al., 2014; Rosen et al., 2017
Amivantamab Valency	-	1	Jarantow et al., 2015
Amivantamab Dosing Interval	2	weeks	Rybrevant, 2021
Amivantamab Half-Life	11	days	Rybrevant, 2021
Amivantamab KD for EGFR	1.4	nM	Jarantow et al. (2015)
Amivantamab KD for c-Met	0.04	nM	Jarantow et al. (2015)
Drug Molecular Weight	150,000	Daltons	Assumed typical mAb MW for all drugs
Pdist12	0.19	-	Partition coefficient between central and peripheral compartments assumed typical (Betts et al., 2018)
Tdist12	35	hours	Half-life of intercompartmental clearance between central and peripheral compartments assumed typical (Betts et al., 2018)

cell based on reported values from quantitative flow cytometry assays (Sandoval et al., 2012; Jarantow et al., 2015). Assumptions based on relative expression from semi-quantitative flow cytometry and IHC staining data were used to fill in any data gaps. c-Met expressing tissues and absolutely expression levels were similarly identified (Di Renzo et al., 1991; Bozkaya et al., 2012; Ma et al., 2008; Molnarfi et al., 2012; Panke et al., 2013; Jarantow et al., 2015; Kim et al., 2019). EGFR and c-Met receptor turnover half-lives were parameterized from *in vitro* cell line assays (Li et al., 2008; Sigismund et al., 2008; DaSilva et al., 2020). Target-specific parameters are listed in **Table 3**.

PK data from panitumumab, an anti-EGFR monoclonal antibody (mAb), and emibetuzumab (also known as LY2875358), an anti-c-Met mAb, were used to benchmark the target expression estimates since they both exhibit non-linear PK due to target mediated drug disposition (TMDD). For membrane targets such as EGFR and c-Met, the target mediated clearance can impact drug exposure, which then impacts target engagement (Stein and Peletier, 2018). A 2-compartment monospecific anti-receptor model was used to simulate pharmacokinetics (PK) and target engagement (TE) for each of the mAbs using their respective target parameters. Drug-specific parameters are listed in **Table 4**. Panitumumab target binding affinity (Kd = 0.05 nM) and drug half-life (half-life of linear elimination = 16 days) were taken from literature (Yang et al., 2001; Ma et al., 2009). Simulated PK agreed well with clinical PK measurements. Linear clearance was predicted at doses above 2.5 mg/kg for panitumumab. (**Figure 3A**). Model simulations of 6 mg/kg Q2W IV panitumumab (**Figure 3B**) projected peak and trough concentrations of 185 μg/ml and 54 μg/ml, respectively, after 3 doses, while reported values are 213 ± 59 and 39 ± 14 μg/ml (Ma et al., 2009). Since near complete inhibition of EGFR has been shown necessary to induce cell cycle arrest or cell death (Park and Lemmon 2012), a target engagement criteria of >98% in the peripheral compartment was chosen to predict effective dose. The dose projected to achieve >98% sustained target engagement for panitumumab was 162 mg Q2W, which is within 3-fold of the approved dose of 6 mg/kg every 14 days (*i.e.* 420 mg assuming 70 kg man). Emibetuzumab target affinity (Kd = 0.1 nM) and linear PK parameters (half-life of linear elimination = 16 days) were taken from literature (Liu et al., 2014; Rosen et al., 2017).

Model simulations of emibetuzumab predicted linear clearance at 700 mg and above, consistent with clinical measurements. (**Figure 3C**) (Rosen et al., 2017). Model also predicted >98% target engagement at doses 105 mg Q2W and higher, consistent with pharmacodynamic measurements demonstrating saturation of the increase of soluble c-Met at the 210 mg Q2W dose level (Rosen et al., 2017).

Next, dosing of amivantamab was simulated using the benchmarked target parameters. JNJ-61186372 binding to EGFR has a Kd ~1.4 nM; binding to c-Met has a Kd ~0.04 nM (Jarantow et al., 2015). The half-life of amivantamab was reported to be approximately 11 days (Rybrevant, 2021) Once again, a target engagement of >98% for both targets was set as criteria for the effective dose. The model predicted 326 mg Q1W or 740 mg Q2W is required to achieve sustained target engagement >98% for both targets (**Figure 4**). This dose prediction, generated with minimal data, is consistent with the 1050 mg Q2W dosing after the initial 4 weeks.

Case Study 3: Application of EFA to Predict Effective Dose of 6 Additional Biotherapeutic Drugs

The methodology described in case studies 1-2 was extended to predict effective dose of 6 additional biotherapeutic drugs targeting a range of soluble or membrane-bound targets. Simulations were run using the drug-specific and target-parameters for a total of 9 biotherapeutics. Targets include TNFα, IL-23/IL-2, BLyS (BAFF), IgE for soluble targets and HER2, EGFR, and EGFR/c-Met for membrane-bound targets.

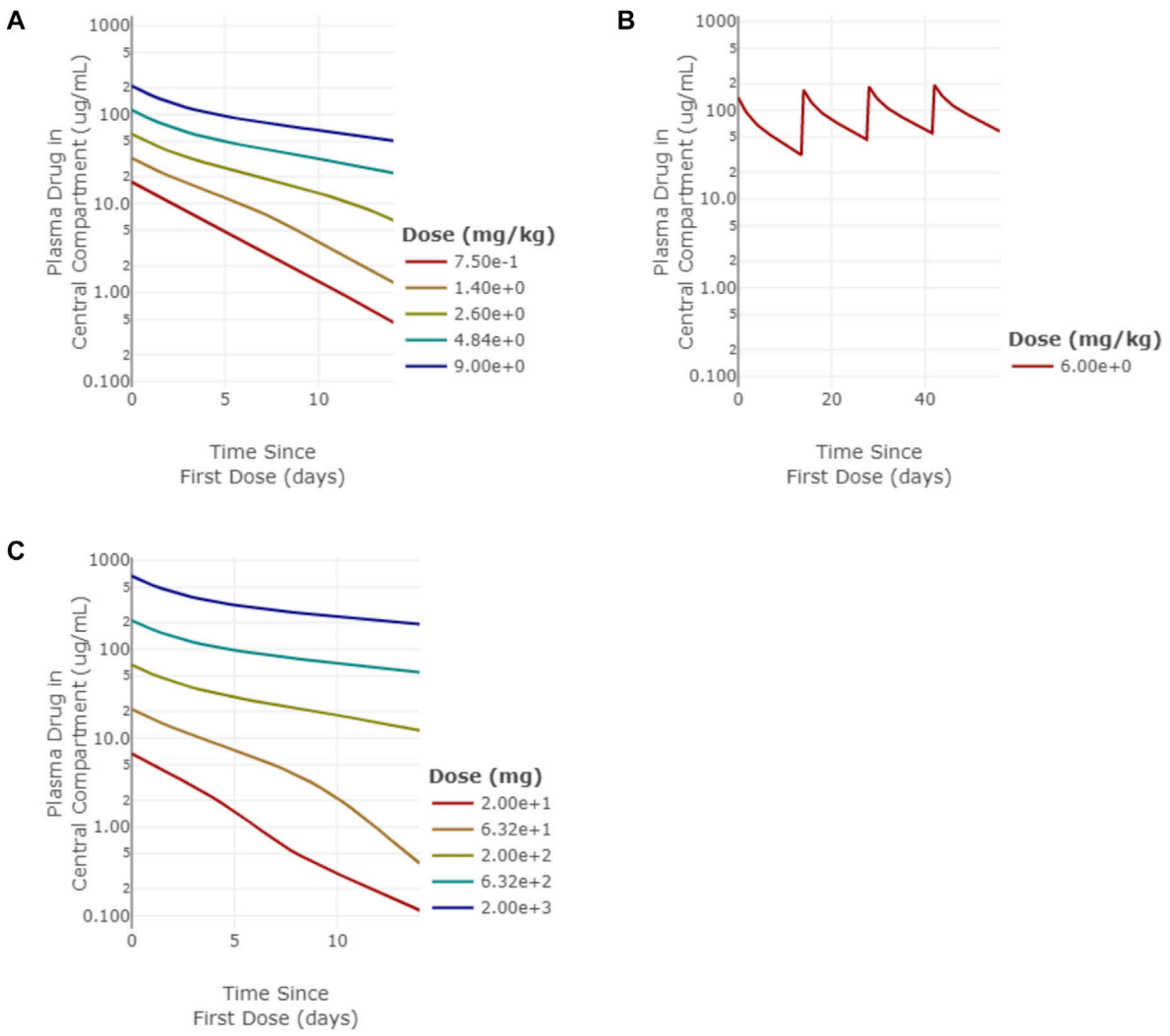

FIGURE 3 | Model simulations of panitumumb and emibetuzumab pharmacokinetics (PK). **(A)** single-dose PK for panitumumab from 0.75–9 mg/kg simulated out to 14 days, **(B)** multi-dose PK for 6 mg/kg Q2W panitumumab simulated out to 64 days, **(C)** single-dose PK for emibetuzumab for 20–2000 mg doses simulated out to 14 days.

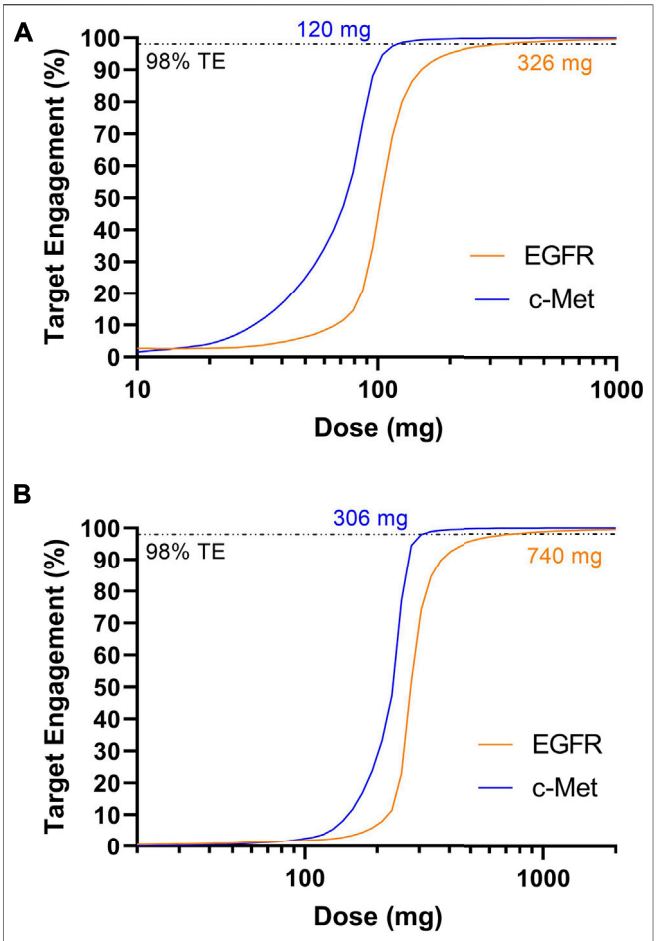

FIGURE 4 | Model predicted trough target engagement for amivantamab dosed Q1W **(A)** or Q2W **(B)**. 98% target engagement for EGFR was achieved at 326 mg Q1W or 740 mg Q2W. 98% target engagement for c-Met was achieved first at 120 mg Q1W and 306 mg Q2W.

Drug-specific and target-specific parameters were obtained from the literature as described in Methods and are listed in **Supplementary Tables S3–S7**. Approved doses and regimens for the respective indications in RA, plaque psoriasis, systemic lupus erythematosus (SLE), asthma, breast cancer, colon cancer, and non-small cell lung cancer (NSCLC) were collated for comparison to model predictions (**Table 5**).

Across the panel of drugs, the model-informed effective doses based either on 90% inhibition (soluble targets) or 98% target engagement (membrane targets) criteria were largely within 3-fold of the clinically approved doses (**Figure 5**; **Table 5**), for the diverse soluble targets (e.g., cytokines, IgE) as well as surface receptors (e.g., HER2). There appears to be a trend towards systematic overprediction of the doses for soluble targets and underprediction of the doses for membrane targets (**Figure 5**).

Overall, the analysis serves as a proof-of-principle that EFA with mechanistic PKPD modeling approaches can predict the effective doses with sufficient accuracy to inform drug design decisions and evaluation of the feasibility of drug targets and disease areas before PK and PD data are available for the drug.

DISCUSSION

At early stages of drug discovery and development, PKPD data required to inform clinical dosing is not yet available. To generate such data may involve the development of reagents, tool molecules, and assays, which is both costly and time consuming. Once that data is collected, it may suggest a different lead optimization strategy than was originally planned which can cause further delays. In this manuscript, Early Feasibility Assessment (EFA) is demonstrated, based upon integrating data that is available at an early stage, including in-house *in vitro* experiments and literature, into a

TABLE 5 | Effective dose predictions for a panel of biotherapeutics.

Drug	Model predicted dose		Clinically approved dose	
	Model in Applied BioMath Assess ™	ID90/TE98 (mg)[a]	Dose (mg)	Schedule[a]
Remicade (infliximab)	Monospecific anti-ligand	441	210	8 weeks IV
Humira (adalimumab)	Monospecific anti-ligand	39.4	40	2 weeks SC
Stelara (ustekinumab)	Monospecific anti-ligand	22.4	45	12 weeks SC
Skyrizi (risankizumab)	Monospecific anti-ligand	273	150	12 weeks SC
		37.1	150	4 weeks SC
Benlysta (belimumab)	Monospecific anti-ligand	252	200	1 week SC
		1700	700	4 weeks IV
Xolair (omalizumab)	Monospecific anti-ligand	330	225	2 weeks SC
Herceptin (trastuzumab)	Monospecific anti-receptor (4 compartment)	79.0	140	1 week IV
Vectibix (panitumumab)	Monospecific anti-receptor (4 compartment)	162	420	2 weeks IV
Rybrevant (amivantamab)	Bispecific anti-receptor x anti-receptor (4 compartment)	740	1050	2 weeks IV

[a]*ID90 = dose to achieve 90% inhibition, TE98 = dose to achieve 98% target engagement, SC = subcutaneous administration, IV = intravenous administration.*

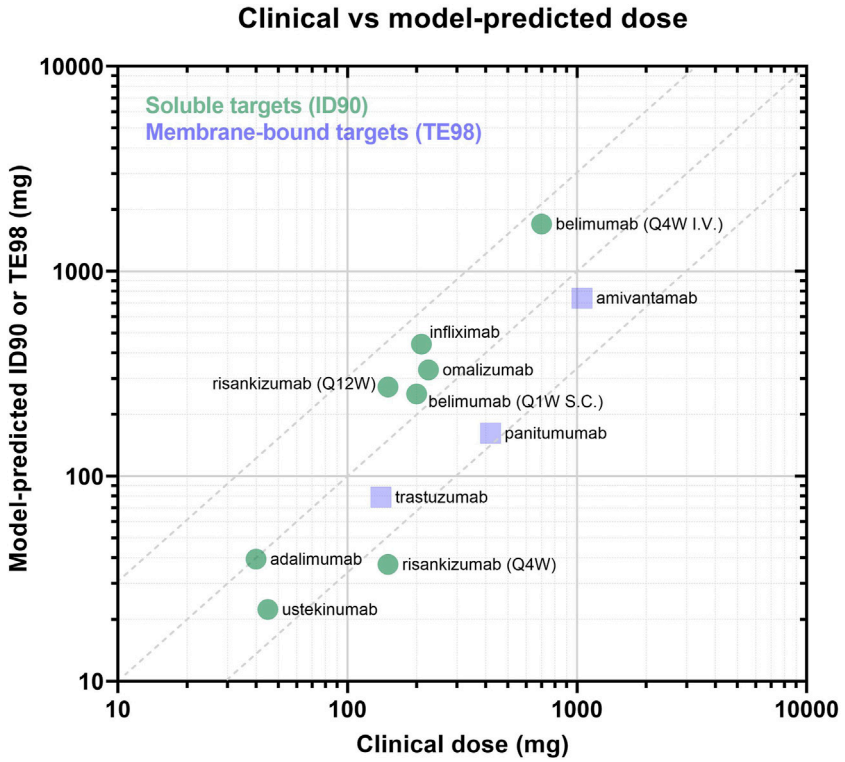

FIGURE 5 | Panel of model-predicted vs. clinically approved dose. Drugs with soluble targets are displayed as green circles and are evaluated based on ID90 (i.e., inhibition of baseline ligand:receptor complex). Drugs with membrane-bound targets are displayed in purple squares and are evaluated by TE98 (i.e., percent of target bound by drug). Dotted lines define the region where model-predicted effective doses fall within 3-fold of the clinically-approved doses.

mechanistic PKPD model of target binding to predict PK (including TMDD), target engagement, and effective dose. EFA centers on defining a notion of "dose feasibility," that a drug may be administered with a reasonable dosing regimen and conceivably achieve a therapeutic impact. Note that feasibility is distinct from efficacy which requires both a significant pharmacological impact and a meaningful biological response to the impact. However, there is still utility in using feasibility as a decision making criteria, to ensure that molecules are developed with the best chance to test the therapeutic hypothesis, and resources are not spent developing molecules unlikely to modulate the target to a sufficient degree to be drug candidates.

Two detailed case study examples, extended to a total of 9 biotherapeutics, were presented, demonstrating the ability of EFA to make clinically relevant predictions of effective dose. The predicted effective doses in this work were generally within ~3-fold of the clinically-approved dose. Factors not considered in these models, such as tolerability, can impact the final clinical dose; however, generating dose estimates within 3-fold during the early stages of a program can be useful for various decisions early in drug discovery, including target prioritization, optimal drug properties for a target product profile (TPP), prioritization of different drug concepts. Using validated mechanistic PKPD models parameterized from literature and *in vitro* measurements, questions about target druggability, ease of engineering a lead molecule with required drug properties, feasibility of novel drug concepts can be answered.

In all of the cases presented, the models were parameterized by data that should be available to an early program. It is significant that target-specific parameters can be identified from the "bottom-up" calculations leveraging literature data; however, there is uncertainty and biological variability in these values that should be considered. When extending this approach to novel targets, this uncertainty is higher. A sensitivity analysis by examining the impact of dose predictions over a range of target parameters can determine if they are important to the conclusions and help prioritize potential experiments that will minimize risk during drug development. For infliximab and adalimumab, a parameter scan identified TNFα half-life as a sensitive parameter that can impact the model-predicted effective dose, while varying TNFα concentration, TNF Receptor concentration, and TNF Receptor half-life had minimal impact. For a novel program, this result would suggest that measurement of TNFα half-life should be prioritized for accurate dose predictions during later stages of drug development.

When using EFA for early stage programs, drug-specific parameters (such as affinity and half-life) may be theoretical targets as part of a TPP. While drug-specific PK parameters were in this analysis, mAbs generally display similar linear pharmacokinetics, which enables predictions to be made using assumed standard values, or derived from measurements made in preclinical model species (Deng et al., 2011; Dong et al., 2011; Betts

et al., 2018). This approach is not limited to mAbs, but can be extended to other biotherapeutics with well-described PK and binding behavior. As demonstrated by the infliximab and adalimumab parameter scans, the sensitivity of effective dose predictions to drug design parameters can depend on the desired dosing interval. For a novel therapeutic, a sensitivity analysis on how much drug properties impact dose predictions can inform ease of the development and potential need for additional drug optimization through affinity maturation or half-life extension, for example.

Finally, there can be uncertainty in defining the criterion for efficacy, which is based on an understanding of the intended mechanism of action for each of these biotherapeutics. In the analyses presented here, the dose predicted to sustain >90% target inhibition was comparable to the clinically approved doses for all the biotherapeutics against soluble targets. For the membrane receptor targets discussed, sustained, near complete, target engagement is hypothesized to be necessary for therapeutic efficacy, and a criterion of >98% target engagement was used. When applying EFA to novel targets and drug concepts, an understanding of the intended mechanism of action is necessary, and an exploration of the impact of different metrics of efficacy may be warranted.

When performing EFA, model selection must be carefully considered. In each of the case studies presented in this manuscript, the selected models were built on first-principles that captured the key pharmacological mechanisms for each of the drugs. Drugs binding to a soluble target vs. a membrane receptor target require different models which are associated with different assumptions. For drugs targeting soluble factors, the binding and elimination of drug-bound target is an important factor to consider mechanistically. For drugs targeting membrane receptors, the elimination of drugs through target binding was captured mechanistically. For more complex biotherapeutic modalities where models of similar scale that capture the pharmacology exist, it would be reasonable to apply this type of analysis. For example, a model of T-cell engagers that describes crosslinking of target receptor and CD3 receptors on T-cells as a model endpoint is available in Applied BioMath Assess ™, and similar models have been reported in literature (Chen et al., 2021). This analysis could potentially be extended to questions of therapeutic index by comparing model endpoints in disease and toxicity compartments, for example. Striking a pragmatic balance between mechanistic detail and the cost or complexity of parameterizing a model is a defining feature of EFA.

The focus of this manuscript is on antibody therapeutics (mAbs, BsAbs) where typical PK properties such as half-life and biodistribution, and pharmacology parameters such as binding affinity are well known. mAbs are a large and growing category of new drugs approved each year—as of December 2019, there were 79 therapeutic mAbs approved, with 18 approved between 2018 and 2019 (Lu et al., 2020). In 2021, the 100th antibody was approved (Mullard 2021). There is the potential to expand this methodology to other pharmacologies (*e.g.* ADCs, LNPs, peptides, oncolytic viruses, etc.) if reasonable ranges for these parameters can be determined *a priori*, or in combination with methods that allow the prediction of PK properties such as *in vitro in vivo* correlation (IVIC).

Overall, the application of EFA at the early stages of a program, before the major clinical costs are incurred, has great potential to realize efficiencies and reduce attrition in drug development. By excluding targets that don't have a chance of "druggability" early, resources can be prioritized for those programs that may be more likely to succeed. By identifying parameters that strongly impact an eventual clinical dose, programs can also identify knowledge gaps that, once filled, could reduce program risk. As prioritized programs progress, preclinical data on the drug candidate(s) binding mechanisms and pharmacokinetics should be incorporated into these models. Additional complexity in terms of biological mechanisms, downstream pharmacology can also be incorporated. These updated models can then enable decisions at later stages of drug development, such as lead selection, first-in-human dose selection, and recommended phase 2 dosing.

DATA AVAILABILITY STATEMENT

The original contributions presented in the study are included in the article/**Supplementary Material**, further inquiries can be directed to the corresponding author.

AUTHOR CONTRIBUTIONS

DM, AM, JA contributed to the conception, design, implementation of this research. MP, DH contributed to the design and implementation of this research. JB, FH contributed to the conception and design of this research. DM, AM, MP wrote sections of the manuscript. All authors contributed to manuscript revision, read, and approved the submitted version.

FUNDING

Parts of this work were supported by the National Institutes of Health, through grants R44 GM116214, R44 AG058411, R44 GM134790 and R43 FD006606, and from the US Food and Drug Administration through grant 1R43FD006606-01A1. The funders were not involved in the study design, collection, analysis, interpretation of data, the writing of this article or the decision to submit it for publication.

ACKNOWLEDGMENTS

The authors would like to acknowledge Emily Pace, Jim Schaff, Vladimir Korolev, Amir Molavi, and Aurore Zyto for their contributions to the implementation of Applied BioMath Assess ™. The authors would like to thank Jim Schaff, Alison Betts, and Victor Chang for reviewing this manuscript.

SUPPLEMENTARY MATERIAL

The Supplementary Material for this article can be found online at: https://www.frontiersin.org/articles/10.3389/fphar.2022.864768/full#supplementary-material

REFERENCES

Adalimumab (2021). *Adalimumab - Humira*. North Chicago, IL: AbbVie Inc. [package Insert].

Berkhout, L. C., l'Ami, M. J., Ruwaard, J., Hart, M. H., Heer, P. O., Bloem, K., et al. (2019). Dynamics of Circulating TNF during Adalimumab Treatment Using a Drug-Tolerant TNF Assay. *Sci. Transl. Med.* 11 (477). eaat3356. doi:10.1126/scitranslmed.aat3356

Betts, A., Keunecke, A., van Steeg, T. J., van der Graaf, P. H., Avery, L. B., Jones, H., et al. (2018). Linear Pharmacokinetic Parameters for Monoclonal Antibodies Are Similar within a Species and across Different Pharmacological Targets: A Comparison between Human, Cynomolgus Monkey and hFcRn Tg32 Transgenic Mouse Using a Population-Modeling Approach. *mAbs* 10 (5), 751–764. doi:10.1080/19420862.2018.1462429

BioMath (2021). *De-Risking Drug Discovery with Applied BioMath Assess ™ , a New Early Feasibility Assessment Tool for Biotherapeutics*. White Paper. BioIT World. Available at: https://www.bio-itworld.com/applied-biomath-de-risking-drug-discovery-whitepaper.

Bozkaya, G., Korhan, P., Cokaklı, M., Erdal, E., Sağol, O., Karademir, S., et al. (2012). Cooperative Interaction of MUC1 with the HGF/c-Met Pathway during Hepatocarcinogenesis. *Mol. Cancer* 11 (1), 64. doi:10.1186/1476-4598-11-64

Charles, P., Elliott, M. J., Davis, D., Potter, A., Kalden, J. R., Antoni, C., et al. (1999). Regulation of Cytokines, Cytokine Inhibitors, and Acute-phase Proteins Following Anti-TNF-alpha Therapy in Rheumatoid Arthritis. *J. Immunol.* 163 (3), 1521–1528.

Chen, J., Zeng, F., Forrester, S. J., Eguchi, S., Zhang, M. Z., and Harris, R. C. (2016). Expression and Function of the Epidermal Growth Factor Receptor in Physiology and Disease. *Physiol. Rev.* 96 (3), 1025–1069. doi:10.1152/physrev.00030.2015

Chen, W., Yang, F., Wang, C., Narula, J., Pascua, E., Ni, I., et al. (2021). One Size Does Not Fit All: Navigating the Multi-Dimensional Space to Optimize T-Cell Engaging Protein Therapeutics. *mAbs* 13 (1), 1871171. doi:10.1080/19420862.2020.1871171

DaSilva, J. O., Yang, K., Perez Bay, A. E., Andreev, J., Ngoi, P., Pyles, E., et al. 2020. "A Biparatopic Antibody that Modulates MET Trafficking Exhibits Enhanced Efficacy Compared with Parental Antibodies in MET-Driven Tumor Models." *Clin. Cancer Res. An Official J. Am. Assoc. Cancer Res.* 26 (6): 1408–1419.doi:10.1158/1078-0432.ccr-19-2428

Deng, R., Iyer, S., Theil, F. P., Mortensen, D. L., Fielder, P. J., and Prabhu, S. (2011). Projecting Human Pharmacokinetics of Therapeutic Antibodies from Nonclinical Data: What Have We Learned? *mAbs* 3 (1), 61–66. doi:10.4161/mabs.3.1.13799

Di Renzo, M. F., Narsimhan, R. P., Olivero, M., Bretti, S., Giordano, S., et al. (1991). Expression of the Met/HGF Receptor in Normal and Neoplastic Human Tissues. *Oncogene* 6 (11), 1997–2003.

Dong, J. Q., Salinger, D. H., Endres, C. J., Gibbs, J. P., Hsu, C-P., Stouch, B. J., et al. (2011). Quantitative Prediction of Human Pharmacokinetics for Monoclonal Antibodies. *Clin. Pharmacokinet.* 50 (2), 131–142. doi:10.2165/11537430-000000000-00000

Dua, P., Hawkins, E., and van der Graaf, P. H. (2015). A Tutorial on Target-Mediated Drug Disposition (TMDD) Models. *CPT Pharmacometrics Syst. Pharmacol.* 4 (6), 324–337. doi:10.1002/psp4.41

Finkelman, F. D., Madden, K. B., Morris, S. C., Holmes, J. M., Boiani, N., Katona, I. M., et al. (1993). Anti-Cytokine Antibodies as Carrier Proteins. Prolongation of *In Vivo* Effects of Exogenous Cytokines by Injection of Cytokine-Anti-Cytokine Antibody Complexes. *J. Immunol.* 151 (3), 1235–1244.

Gao, H-F., Yang, J-J., Chen, Z-H., Zhang, X-C., Yan, H-H., Guo, W-B., et al. (2016). Plasma Dynamic Monitoring of Soluble C-Met Level for EGFR-TKI Treatment in Advanced Non-small Cell Lung Cancer. *Oncotarget* 7 (26), 39535–39543. doi:10.18632/oncotarget.9425

Glassman, P. M., and Balthasar, J. P. (2019). Physiologically-Based Modeling of Monoclonal Antibody Pharmacokinetics in Drug Discovery and Development. *Drug Metabolism Pharmacokinet.* 34 (1), 3–13. doi:10.1016/j.dmpk.2018.11.002

Grell, M., Wajant, H., Zimmermann, G., and Scheurich, P. (1998). The Type 1 Receptor (CD120a) Is the High-Affinity Receptor for Soluble Tumor Necrosis Factor. *Proc. Natl. Acad. Sci. U. S. A.* 95 (2), 570–575. doi:10.1073/pnas.95.2.570

Haura, E. B., Byoung, C. C., Jong, S. L., Ji-Youn, H., Ki Hyeong, L., Rachel E, S., et al. (2019). JNJ-61186372 (JNJ-372), an EGFR-cMet Bispecific Antibody, in EGFR-Driven Advanced Non-small Cell Lung Cancer (NSCLC). *J. Clin. Orthod. JCO* 37 (15_Suppl). 1. doi:10.1200/jco.2019.37.15_suppl.9009

Hemperly, A., and Niels Vande, C. (2018). Clinical Pharmacokinetics and Pharmacodynamics of Infliximab in the Treatment of Inflammatory Bowel Disease. *Clin. Pharmacokinet.* 57 (8), 929–942. doi:10.1007/s40262-017-0627-0

Higuchi, M., and Aggarwal, B. B. (1994). TNF Induces Internalization of the P60 Receptor and Shedding of the P80 Receptor. *J. Immunol.* 152 (7), 3550–3558.

Holbrook, J., Lara-Reyna, S., Jarosz-Griffiths, H., and McDermott, M. (2019). Tumour Necrosis Factor Signalling in Health and Disease. *F1000Research* 8 (January). F1000 Faculty Rev-111. doi:10.12688/f1000research.17023.1

Hu, L., and Hansen, R. J. (2013). Issues, Challenges, and Opportunities in Model-Based Drug Development for Monoclonal Antibodies. *J. Pharm. Sci.* 102 (9), 2898–2908. doi:10.1002/jps.23504

Imamura, K., Spriggs, D., and Kufe, D. (1987). Expression of Tumor Necrosis Factor Receptors on Human Monocytes and Internalization of Receptor Bound Ligand. *J. Immunol.* 139 (9), 2989–2992.

Infliximab (2013). *Remicade Infliximab*. Horsham, PA: Janssen Biotech, Inc. [package Insert].

Jarantow, S. W., Bushey, B. S., Pardinas, J. R., Boakye, K., Lacy, E. R., Renouard Sanders, M. A. S., et al. (2015). Impact of Cell-Surface Antigen Expression on Target Engagement and Function of an Epidermal Growth Factor Receptor × C-MET Bispecific Antibody. *J. Biol. Chem.* 290 (41), 24689–24704. doi:10.1074/jbc.M115.651653

Kagan, L. (2014). Pharmacokinetic Modeling of the Subcutaneous Absorption of Therapeutic Proteins. *Drug Metabolism Dispos. Biol. Fate Chem.* 42 (11), 1890–1905. doi:10.1124/dmd.114.059121

Kapitanov, G. I., Chabot, J. R., Narula, J., Roy, M., Neubert, H., Palandra, J., et al. (2021). A Mechanistic Site-Of-Action Model: A Tool for Informing Right Target, Right Compound, and Right Dose for Therapeutic Antagonistic Antibody Programs. *Front. Bioinforma.* 1. 1. doi:10.3389/fbinf.2021.731340

Kaymakcalan, Z., Paul, S., Bose, S., Scesney, S., Xiong, L., Karaoglu Hanzatian, D., et al. (2009). SassoComparisons of Affinities, Avidities, and Complement Activation of Adalimumab, Infliximab, and Etanercept in Binding to Soluble and Membrane Tumor Necrosis Factor. *Clin. Immunol.* 131 (2), 308–316. doi:10.1016/j.clim.2009.01.002

Kim, Y. C., Lee, J., Jung Nam, A., JinKim, H., Choi, Y-W., Li, L., et al. (2019). Renoprotective Effects of a Novel cMet Agonistic Antibody on Kidney Fibrosis. *Sci. Rep.* 9 (1), 13495. doi:10.1038/s41598-019-49756-z

Lalonde, R. L., Kowalski, K. G., Hutmacher, M. M., Ewy, W., Nichols, D. J., Milligan, P. A., et al. (2007). Model-Based Drug Development. *Clin. Pharmacol. Ther.* 82 (1), 21–32. doi:10.1038/sj.clpt.6100235

Li, N., Hill, K. S., and Elferink, L. A. (2008). Analysis of Receptor Tyrosine Kinase Internalization Using Flow Cytometry. *Methods Mol. Biol.* 457, 305–317. doi:10.1007/978-1-59745-261-8_23

Li, Z., Krippendorff, B-F., and Shah, D. K. (2017). Influence of Molecular Size on the Clearance of Antibody Fragments. *Pharm. Res.* 34 (10), 2131–2141. doi:10.1007/s11095-017-2219-y

Lim, H., Lee, S. H., Lee, H. T., Un Lee, J., Young Son, J., Shin, W., et al. (2018). Structural Biology of the TNFα Antagonists Used in the Treatment of Rheumatoid Arthritis. *Int. J. Mol. Sci.* 19 (3). doi:10.3390/ijms19030768

Liu, L., Zeng, W., Wortinger, M. A., Betty Yan, S., Paul, C., Peek, V. L., et al. (2014). LY2875358, a Neutralizing and Internalizing Anti-MET Bivalent Antibody, Inhibits HGF-dependent and HGF-independent MET Activation and Tumor Growth. *Clin. Cancer Res. An Official J. Am. Assoc. Cancer Res.* 20 (23), 6059–6070. doi:10.1158/1078-0432.CCR-14-0543

Lu, R-M., Hwang, Y-C., Liu, I-J., and Lee, C-C. (2020). Han-Zen Tsai, Hsin-Jung Li, and Han-Chung WuDevelopment of Therapeutic Antibodies for the Treatment of Diseases. *J. Biomed. Sci.* 27 (1), 1. doi:10.1186/s12929-019-0592-z

Ma, P. C., Tretiakova, M. S., MacKinnon, A. C., Ramnath, N., Johnson, C., Dietrich, S., et al. (2008). Expression and Mutational Analysis of MET in Human Solid Cancers. *Genes., Chromosomes Cancer* 47 (12), 1025–1037. doi:10.1002/gcc.20604

Ma, P., Yang, B-B., Wang, Y-M., Peterson, M., Narayanan, A., Sutjandra, L., et al. (2009). Population Pharmacokinetic Analysis of Panitumumab in Patients with Advanced Solid Tumors. *J. Clin. Pharmacol.* 49 (10), 1142–1156. doi:10.1177/0091270009344989

Mager, D. E., and Jusko, W. J. (2001). General Pharmacokinetic Model for Drugs Exhibiting Target-Mediated Drug Disposition. *J. Pharmacokinet. Pharmacodynamics* 28 (6), 507–532. doi:10.1023/a:1014414520282

Michishita, M., Yoshida, Y., Uchino, H., and Nagata, K. (1990). Induction of Tumor Necrosis Factor-Alpha and its Receptors during Differentiation in Myeloid Leukemic Cells along the Monocytic Pathway. A Possible Regulatory Mechanism for TNF-Alpha Production. *J. Biol. Chem.* 265 (15), 8751–8759. doi:10.1016/s0021-9258(19)38952-5

Molnarfi, N., Benkhoucha, M., Bjarnadóttir, K., Juillard, C., and Lalive, P. H. (2012). Interferon-β Induces Hepatocyte Growth Factor in Monocytes of Multiple Sclerosis Patients. *PloS One* 7 (11), e49882. doi:10.1371/journal.pone.0049882

Moritz, T., Niederle, N., Baumann, J., May, D., Kurschel, E., Osieka, R., et al. (1989). Phase I Study of Recombinant Human Tumor Necrosis Factor Alpha in Advanced Malignant Disease. *Cancer Immunol. Immunother. CII* 29 (2), 144–150. doi:10.1007/BF00199290

Mullard, A. (2021). FDA Approves 100th Monoclonal Antibody Product. *Nat. Rev. Drug Discov.* 20 (7), 491–495. doi:10.1038/d41573-021-00079-7

Nayak, S., Sander, O., Al-Huniti, N., de Alwis, D., Chain, A., Chenel, M., et al. (2018). Getting Innovative Therapies Faster to Patients at the Right Dose: Impact of Quantitative Pharmacology towards First Registration and Expanding Therapeutic Use. *Clin. Pharmacol. Ther.* 103 (3), 378–383. doi:10.1002/cpt.978

Ovacik, M., and Lin., K. (2018). Tutorial on Monoclonal Antibody Pharmacokinetics and its Considerations in Early Development. *Clin. Transl. Sci.* 11 (6), 540–552. doi:10.1111/cts.12567

Panke, C., Weininger, D., Haas, A., Schelter, F., Schlothauer, T., Bader, S., et al. (2013). Quantification of Cell Surface Proteins with Bispecific Antibodies. *Protein Eng. Des. Sel. PEDS* 26 (10), 645–654. doi:10.1093/protein/gzt035

Paracelsus (1538). Die dritte Defension wegen des Schreibens der neuen Rezepte. *Septem Defensiones* 1538. 1.

Park, J. H., and Lemmon, M. A. (2012). Occupy EGFR. *Cancer Discov.* 2 (5), 398–400. doi:10.1158/2159-8290.CD-12-0144

Patel, M., and Bueters, T. (2020). Can Quantitative Pharmacology Improve Productivity in Pharmaceutical Research and Development? *Expert Opin. Drug Discov.* 15 (10), 1111–1114. doi:10.1080/17460441.2020.1776257

Pearson, T. C., Guthrie, D. L., Simpson, J., Chinn, S., Barosi, G., Ferrant, A., et al. (1995). Interpretation of Measured Red Cell Mass and Plasma Volume in Adults: Expert Panel on Radionuclides of the International Council for Standardization in Haematology. *Br. J. Haematol.* 89 (4), 748–756. doi:10.1111/j.1365-2141.1995.tb08411.x

Peletier, L. A., and Gabrielsson, J. (2012). Dynamics of Target-Mediated Drug Disposition: Characteristic Profiles and Parameter Identification. *J. Pharmacokinet. Pharmacodynamics* 39 (5), 429–451. doi:10.1007/s10928-012-9260-6

Real, F. X., Rettig, W. J., Chesa, P. G., Melamed, M. R., Old, L. J., and Mendelsohn, J. (1986). Expression of Epidermal Growth Factor Receptor in Human Cultured Cells and Tissues: Relationship to Cell Lineage and Stage of Differentiation. *Cancer Res.* 46 (9), 4726–4731.

Rosen, L. S., Goldman, J. W., Algazi, A. P., Turner, P. K., Moser, B., Hu, T., et al. (2017). A First-In-Human Phase I Study of a Bivalent MET Antibody, Emibetuzumab (LY2875358), as Monotherapy and in Combination with Erlotinib in Advanced Cancer. *Clin. Cancer Res. An Official J. Am. Assoc. Cancer Res.* 23 (8), 1910–1919. doi:10.1158/1078-0432.CCR-16-1418

Rybrevant (2021). *Rybrevant (amivantamab-vmjw)*. Horsham, PA: Janssen Biotech, Inc. [package Insert].

Sandoval, M. A., Sloat, B. R., DharmikaLansakara, S. P.-P., Amit, K., Leticia Rodriguez, B., Kiguchi, K., et al. (2012). EGFR-targeted Stearoyl Gemcitabine Nanoparticles Show Enhanced Anti-tumor Activity. *J. Control. Release Official J. Control. Release Soc.* 157 (2), 287–296. doi:10.1016/j.jconrel.2011.08.015

Schulze, U., and Ringel, M. (2013). What Matters Most in Commercial Success: First-In-Class or Best-In-Class? *Nat. Rev. Drug Discov.* 12 (6), 419–420. doi:10.1038/nrd4035

Sender, R., Fuchs, S., and Milo, R. (2016). Revised Estimates for the Number of Human and Bacteria Cells in the Body. *PLoS Biol.* 14 (8), 1–14. doi:10.1371/journal.pbio.1002533

Shah, D. K., and Betts, A. M. (2013). Antibody Biodistribution Coefficients: Inferring Tissue Concentrations of Monoclonal Antibodies Based on the Plasma Concentrations in Several Preclinical Species and Human. *mAbs* 5 (2), 297–305. doi:10.4161/mabs.23684

Shah, D. K., and Betts, A. M. (2012). Towards a Platform PBPK Model to Characterize the Plasma and Tissue Disposition of Monoclonal Antibodies in Preclinical Species and Human. *J. Pharmacokinet. Pharmacodynamics* 39 (1), 67–86. doi:10.1007/s10928-011-9232-2

Shen, J., Swift, B., Mamelok, R., Pine, S., Sinclair, J., and Attar, M. (2019). Design and Conduct Considerations for First-In-Human Trials. *Clin. Transl. Sci.* 12 (1), 6–19. doi:10.1111/cts.12582

Sigismund, S., Argenzio, E., Tosoni, D., Cavallaro, E., Polo, S., and Pier Paolo Di Fiore (2008). Clathrin-Mediated Internalization Is Essential for Sustained EGFR Signaling but Dispensable for Degradation. *Dev. Cell.* 15 (2), 209–219. doi:10.1016/j.devcel.2008.06.012

Stein, A. M., and Peletier, L. A. (2018). Predicting the Onset of Nonlinear Pharmacokinetics. *CPT Pharmacometrics Syst. Pharmacol.* 7 (10), 670–677. doi:10.1002/psp4.12316

Takeuchi, T., Miyasaka, N., Tatsuki, Y., Yano, T., Yoshinari, T., Abe, T., et al. (2011). Baseline Tumour Necrosis Factor Alpha Levels Predict the Necessity for Dose Escalation of Infliximab Therapy in Patients with Rheumatoid Arthritis. *Ann. Rheumatic Dis.* 70 (7), 1208–1215. doi:10.1136/ard.2011.153023

Ternant, D., Ducourau, E., Fuzibet, P., Vignault, C., Watier, H., Lequerré, T., et al. (2015). Pharmacokinetics and Concentration-Effect Relationship of Adalimumab in Rheumatoid Arthritis. *Br. J. Clin. Pharmacol.* 79 (2), 286–297. doi:10.1111/bcp.12509

Tran, B. N., Chan, S. L., Ng, C., Shi, J., Correia, I., Radziejewski, C., et al. (2017). Higher Order Structures of Adalimumab, Infliximab and Their Complexes with TNFα Revealed by Electron Microscopy. *Protein Sci. A Publ. Protein Soc.* 26 (12), 2392–2398. doi:10.1002/pro.3306

U.S. Food and Drug Administration (2021). *Model-Informed Drug Development Pilot Program. November* 15, 2021. Available at: https://www.fda.gov/drugs/development-resources/model-informed-drug-development-pilot-program.

Weisman, M. H., Moreland, L. W., Furst, D. E., Weinblatt, M. E., Keystone, E. C., Paulus, H. E., et al. (2003). Efficacy, Pharmacokinetic, and Safety Assessment of Adalimumab, a Fully Human Anti-tumor Necrosis Factor-Alpha Monoclonal Antibody, in Adults with Rheumatoid Arthritis Receiving Concomitant Methotrexate: A Pilot Study. *Clin. Ther.* 25 (6), 1700–1721. doi:10.1016/s0149-2918(03)80164-9

Yang, X. D., Jia, X. C., Corvalan, J. R., Wang, P., and Davis, C. G. (2001). Development of ABX-EGF, a Fully Human Anti-EGF Receptor Monoclonal Antibody, for Cancer Therapy. *Crit. Rev. Oncology/hematology* 38 (1), 17–23. doi:10.1016/s1040-8428(00)00134-7

Yano, S., Kondo, K., Yamaguchi, M., Richmond, G., Hutchison, M., Wakeling, A., et al. (2003). Distribution and Function of EGFR in Human Tissue and the Effect of EGFR Tyrosine Kinase Inhibition. *Anticancer Res.* 23 (5A), 3639–3650.

Conflict of Interest: DM, AM, MP, JB, DH, FH, and JA were all employees of Applied BioMath, LLC during the course of this research.

Publisher's Note: All claims expressed in this article are solely those of the authors and do not necessarily represent those of their affiliated organizations, or those of the publisher, the editors and the reviewers. Any product that may be evaluated in this article, or claim that may be made by its manufacturer, is not guaranteed or endorsed by the publisher.

frontiers | Frontiers in Pharmacology

TYPE Original Research
PUBLISHED 02 September 2022
DOI 10.3389/fphar.2022.867457

OPEN ACCESS

EDITED BY
Alison Betts,
Applied BioMath, United States

REVIEWED BY
Erin Elizabeth Congdon,
Grossman School of Medicine, New York University, United States
Samuel Silvestre,
Universidade da Beira Interior, Portugal

*CORRESPONDENCE
Peter Bloomingdale,
PeterBloomingdale@Gmail.com

SPECIALTY SECTION
This article was submitted to Experimental Pharmacology and Drug Discovery,
a section of the journal Frontiers in Pharmacology

RECEIVED 01 February 2022
ACCEPTED 27 June 2022
PUBLISHED 02 September 2022

CITATION
Bloomingdale P, Bumbaca-Yadav D, Sugam J, Grauer S, Smith B, Antonenko S, Judo M, Azadi G and Yee KL (2022), PBPK-PD modeling for the preclinical development and clinical translation of tau antibodies for Alzheimer's disease.
Front. Pharmacol. 13:867457.
doi: 10.3389/fphar.2022.867457

PBPK-PD modeling for the preclinical development and clinical translation of tau antibodies for Alzheimer's disease

Peter Bloomingdale[1]*, Daniela Bumbaca-Yadav[2], Jonathan Sugam[3], Steve Grauer[3], Brad Smith[4], Svetlana Antonenko[5], Michael Judo[2], Glareh Azadi[2] and Ka Lai Yee[1]

[1]Quantitative Pharmacology and Pharmacometrics, Merck & Co., Inc., Boston, MA, United States, [2]ADME, Merck & Co., Inc., South San Francisco, CA, United States, [3]Discovery Neuroscience, Merck & Co., Inc., West Point, PA, United States, [4]Safety Assessment—Laboratory Animal Resources, Merck & Co., Inc., West Point, PA, United States, [5]Laboratory Animal Resources, Merck & Co., Inc., South San Francisco, CA, United States

Disrupted tau proteostasis and transneuronal spread is a pathological hallmark of Alzheimer's disease. Neurodegenerative diseases remain an unmet medical need and novel disease modifying therapeutics are paramount. Our objective was to develop a mechanistic mathematical model to enhance our understanding of tau antibody pharmacokinetics and pharmacodynamics in animals and humans. A physiologically-based pharmacokinetic-pharmacodynamic (PBPK-PD) modeling approach was employed to support the preclinical development and clinical translation of therapeutic antibodies targeting tau for the treatment of Alzheimer's disease. The pharmacokinetics of a tau antibody was evaluated in rat and non-human primate microdialysis studies. Model validation for humans was performed using publicly available clinical data for gosuranemab. In-silico analyses were performed to predict tau engagement in human brain for a range of tau antibody affinities and various dosing regimens. PBPK-PD modeling enabled a quantitative understanding for the relationship between dose, affinity, and target engagement, which supported lead candidate optimization and predictions of clinically efficacious dosing regimens.

KEYWORDS

PBPK, QSP, antibody, tau, Alzheimer's disease

Introduction

Alzheimer's disease is a central neurodegenerative disease and the leading cause of dementia. With an aging global population and the lack of effective disease modifying therapies, age-related neurodegenerative diseases are an increasing public health concern. In a collaborative effort, a systematic analysis was performed to assess the global burden of neurological disorders (Collaborators, 2019). Authors reported that the world-wide prevalence of Alzheimer's disease (AD) was 46 million and the number of individuals suffering from AD increased by over 100% between the years of 1990–2015. The number of individuals in the US with AD is projected to increase from the current 5.8 million to 13.8 million by 2050, which will increase associated annual US healthcare costs to exceed 1 trillion USD (Alzheimer's, 2016). Hence, there is a significant medical need for effective disease modifying therapeutics for the treatment of neurodegenerative diseases.

The complex nature of neurodegenerative disease makes it challenging to develop effective therapies. Over the last decade, there has been a considerable amount of investigation into passive immunotherapy strategies for the treatment of neurodegenerative disease. Therapeutic antibodies have been developed against proteins that aggregate under pathological conditions, such Aβ and tau, for the treatment of AD. However, the clinical success with these therapies has been limited (Panza et al., 2019). Aducanumab, an antibody against Aβ, was recently granted accelerated approval for the treatment of Alzheimer's disease. Although aducanumab significantly decreased brain Aβ burden in two phase three clinical trials, measured via amyloid PET, improvements on clinical endpoints of cognition were only observed in one of the two trials (Knopman et al., 2021). One argument for this discrepancy is that patients in the positive trial received greater exposures of aducanumab (Schneider, 2020). This exemplifies the importance for quantitatively understanding the relationship between drug potency, exposure, and response.

There has been a rising interest in the application of mechanism-based pharmacokinetics-pharmacodynamics (PK-PD) modeling approaches, such as physiologically-based pharmacokinetic (PBPK) (Gerlowski and Jain, 1983) and quantitative systems pharmacology (QSP) (Sorger et al., 2011) modeling. Several PBPK models of the brain have recently been developed for a variety of treatment modalities, including small molecules (Saleh et al., 2021), antibodies (Bloomingdale et al., 2021), and gene therapies (Monine et al., 2021). Mechanistic modeling, in comparison to either fit-for-purpose or empirical modeling, offers more realistic representations of physiological and pathophysiological systems. Parameter values are often within biological constraints and *a priori* predictions that deviate from observed data can shed light on additional phenomena in the system that has not been mechanistically described. Hence, mechanistic models can be a useful tool for integrating and transforming data into actionable knowledge to provide guidance for drug development programs.

The objective of our research was to develop a mechanistic mathematical model to enhance our quantitative understanding for pharmacokinetics and pharmacodynamics of tau antibodies in animals and humans. To demonstrate the application of PBPK modeling to support preclinical and early clinical development, we have expanded upon a previously published brain PBPK model for antibodies to include tau protein dynamics. Tau is a protein found predominately in neurons and is responsible for the stabilization of microtubules. Under pathological conditions, tau becomes hyperphosphorylated, dissociates from microtubules, aggregates, and spreads transneuronally throughout the brain, which thought to be a primary driver of dementia (Hardy and Higgins, 1992). There are at least nine tau-targeting antibody therapeutics in clinical development for the treatment of Alzheimer's disease, which makes this therapeutic strategy an interest across many pharmaceutical companies. Gosuranemab (BIIB092) is an N-terminal targeting tau-targeting antibody that displayed strong target engagement in the CSF of progressive supranuclear palsy (PSP) and AD patients, however it was subsequently discontinued due to a lack of efficacy (Boxer et al., 2019) (Shulman et al., 2021). The pharmacokinetics of an internally developed tau antibody was evaluated in rat and non-human primate microdialysis studies. Model validation for humans was performed using previously published clinical data for gosuranemab (Boxer et al., 2019). In-silico analyses were performed to predict tau engagement in human brain for a range of antibody affinities to tau and various dosing regimens. Using available preclinical and clinical data, our model was applied to evaluate several questions commonly faced in preclinical and early clinical development, including the design of preclinical experiments, quantitative evaluation of the benefits of affinity optimization and half-life extension, the potential impact of blood contamination in CSF samples, and clinical trial design.

Materials and methods

Physiologically-based pharmacokinetic-pharmacodynamic model development

A multi-species (mouse, rat, monkey, human) physiologically-based pharmacokinetic (PBPK) model for antibody therapeutics was originally developed by Shah and Betts in 2012 (Shah and Betts, 2012) and subsequently expanded by Chang et al., in 2019 (Chang et al., 2019) to include additional anatomical features and physiological processes of the brain. The Chang model consists of 100 differential equations, 15 tissues (lung, heart, kidney, muscle, skin, brain, adipose, thymus, small intestine, large intestine, spleen, pancreas, liver, bone, lymph), and a detailed

brain compartment. The brain component of the PBPK model consists of vasculature, endosomal spaces of the blood-brain-barrier (BBB) and blood-cerebral-spinal-fluid-barrier (BCSFB), interstitial fluid (ISF), and four cerebral spinal fluid (CSF) compartments. A slight modification to the model was made to update plasma volume. The volume of plasma in tissue vasculature was subtracted from the total plasma volume to obtain an updated plasma volume, which was not considered in the Shah-Betts and Chang models.

The Chang model was expanded to include tau dynamics. The half-life of tau in human CSF was reported to be 30.7 days based on a stable isotope labeling kinetics (SILK) experiment (Sato et al., 2018). The intracellular turnover rate of tau has been shown to be isoform and phosphorylation status dependent using iPSC-derived neurons *in vitro* (Sato et al., 2018). However, the impact of different isoforms and post-translational modifications on the tau turnover rate *in vivo* remains unclear. Therefore, for simplicity, we have assumed that there is no difference in the extracellular elimination rate of tau versus ptau. The baseline concentration of tau in human CSF has been shown to range from 78 to 3,652 pg/ml (Herukka et al., 2015). We used a value of 1,080 pg/ml for CSF tau, which was the average concentration between the CSF tau from Herukka et al. (2015) and Sato et al. (2018). Total tau CSF concentrations on average were comparable between both of the studies. Only 3 of the 11 patients in Herukka et al. (2015) were diagnosed with AD. The 24 patients in Sato et al. (2018) ranged between cognitively normal and very mild AD (CDR scores ranged between 0–0.5). Therefore, the initial concentration of total tau in the CSF best reflects a cognitively normal to early mild AD population. The percentage of phosphorylated tau (ptau) relative to total tau in CSF is 6.79% (Herukka et al., 2015). Note that the data used in this version of the model was specifically for phosphorylated threonine 181 (pT181). Depending on the tau protein target-site of interest, the model could be adjusted to account for differences in percent phosphorylated for different phospho-epitopes. The structure of our model can be generalizable to all tau antibodies; however, the parameterization should depend on the antibody and tau target-site of interest. Using a molecular weight of 40 kDa for tau and the percentage of ptau in CSF, the concentration of ptau in human CSF was calculated to be 1.83 pM. Human brain ISF concentrations of tau were reported from patients who had a cortical brain biopsy for idiopathic normal pressure hydrocephalus (Herukka et al., 2015). The concentration of brain ISF tau is 2745.7 pg/ml, 2.54 times greater than CSF tau concentrations. The percentages of ptau to total tau in brain ISF was 10.8% (Herukka et al., 2015). Using a molecular weight of 40 kDa for tau and the percentage of ptau in brain ISF, the concentration of ptau in human brain ISF was calculated to be 7.43 pM. The tau production rate in human CSF has been reported to be 25.7 fM/h (Sato et al., 2018). Therefore, the ptau production rate in human CSF was set to 1.75 fM/h considering 6.79% of CSF tau is phosphorylated. To account for the ptau concentration difference between CSF and ISF, the tau production rate in brain ISF was assumed to be 2.54 times greater. Therefore, the ptau production rate in human brain ISF was set to 7.06 fM/h considering 10.8% of brain ISF tau is phosphorylated. The antibody tau complex was assumed to be eliminated at the same rate as an anti-tau antibody with a half-life of 28 days.

The following target binding equations were introduced into the model to describe the interaction between antibody and phosphorylated-tau (ptau).

$$\frac{dC_{ptau_x}}{dt} = k_{in\_x} - k_{out\_x} \cdot C_{ptau_x} - k_{on} \cdot C_{ptau_x} \cdot C_{mAb_x} + k_{off} \cdot C_{mAb\_ptau_x} \quad (1)$$

$$\frac{dC_{mAb\_ptau_x}}{dt} = k_{on} \cdot C_{ptau_x} \cdot C_{mAb_x} - k_{off} \cdot C_{mAb\_ptau_x} - k_{deg} \cdot C_{mAb\_ptau_x} \quad (2)$$

Where, x represents the concentration of ptau (C_{ptau}) or antibody ptau complex (C_{mAb_ptau}) in one brain ISF and four CSF compartments: lateral ventricle (LV), third-fourth ventricle (TFV), cisterna magna (CM), subarachnoid space (SAS). We have assumed no distribution of target and antibody-target complex between compartments.

Rat microdialysis

Rat microdialysis studies were conducted by Charles River Laboratories, South San Francisco (SSF) in accordance with the Institutional Animal Care and Use Committee (IACUC) of Charles River laboratories SSF. Sixteen male Sprague Dawley rats (n = 5–6 per group) were group housed and provided access to food and water *ad libitum*. Animals were kept on a 12/12 h light/dark cycle with constant room temperature (22 + 2 °C) and humidity (~50%) and acclimated for at least 7 days prior to surgery. On the day of surgery, rats were anesthetized using isoflurane (2%, 800 ml/min O_2). Lidocaine was also used for local analgesia and carprofen for peri/post-operative analgesia. Animals were implanted with cannula into the cisterna magna and jugular vein for CSF and blood collection respectively. Animals were then implanted with a microdialysis probe (PEE membrane, CRL, the Netherlands) via stereotaxic surgery targeting the hippocampus at the following coordinates: antero-posterior = −5.3 mm to bregma, lateral = −4.8 mm to midline and ventral = −8.0 mm to dura, the tooth bar set at 0 mm. After surgery, animals were single-housed with *ad libitum* access to food and water. Approximately 24 h after surgery, brain ISF sampling was initiated for up to 28 h collection. On each ISF sampling day, microdialysis probes were connected with tubing (Peek inlet, FEP outlet) to a microperfusion pump (Harvard PHD 2000 Syringe pump, Holliston, MA or similar). Microdialysis probes were perfused with aCSF containing 147 mM NaCl, 3.0 mM KCl, 1.2 mM $CaCl_2$ and 1.2 mM

$MgCl_2$, and 0.15% BSA at a flow rate of 0.75 µL/min. After stabilization (2 h), microdialysis samples were collected for 60-minute periods by an automated fraction collector (820 Microsampler, Univentor, Malta) into polypropylene (300 µL) mini-vials. On day 1, ISF was collected at baseline for 2 h (i.e., 4 samples). Then, rats were administered with either 10, 50, or 100 mg/kg of antibody A at a dose volume of 2 ml/kg IV and ISF collections continued for 6 h. At the end of the first ISF collection day, rats were disconnected and remained undisturbed in their home cage until the next day. On day 2, ISF was collected at timepoints 24–28 h post dosing. Following collection, all ISF samples were stored at −80C. In addition to brain ISF, serum and CSF samples were collected at baseline (~2 h prior to treatment) (timepoints were −2, 0.5, 6, 24, and 28 h). For each serum sample, blood was collected *via* the jugular vein cannula into serum separator vials and kept at room temperature for 30 min before processing for serum (centrifugation at 4 °C, 10000 g for 5 min). Serum samples were then snap frozen on dry ice. For CSF, samples were collected via the cisterna magna cannula and snap frozen on dry ice. At the end of microdialysis experiment, rats were euthanized with CO_2. Terminal CSF and blood were collected and snap frozen. Brains were collected and verified for probe placement.

Monkey microdialysis

All procedures were performed in accordance with our institution's IACUC guidelines at the Merck & Co., Inc., Rahway, NJ, United States facility, which is AAALAC-accredited (AAALAC: The Association for Assessment and Accreditation of Laboratory Animal Care International). Rhesus microdialysis studies were conducted in-house on four monkeys. Monkeys were implanted with a silicone, 5 French Cisterna Magna Port (CMP) catheter (CMC-06-SAI Infusion Technologies-Lake Vila, IL) attached to a titanium port body (Solo Port MIN-C50-Access Technologies, Skokie, IL). The catheter tip (5 mm) was surgically implanted into the cisterna magna (Gilberto et al., 2021). Implantation of CMP allows for chronic CSF collection. Following, monkeys had microdialysis cannulation of commercially available head caps (Crist Instruments). The head cap that was used had a lower profile and the monkeys adapted well to it. The head cap/cannula placement targeting the cortex utilizing the following coordinates averaged for 4 monkeys: Ear bars set to 33.25 and head cap height set to 16 followed by +21.75 mm AP to bregma and +15.5 mm ML. The skull was drilled for placement of screws to hold the headcap in place followed by a placement of grid marked on the skull. Craniotomy performed on the area marked for placement of 4 cannulas/probes. Head cap was attached to the skull using bone screws and cement. Grid was placed in head cap and 16 mm microdialysis probes/cannulas were placed in 4 slots in the grid. Dental acrylic was applied to secure the cannulas/probes to the grid. A lid was screwed to the top of the head cap to cover the probes/cannulas. Monkeys recovered 14 days and then preliminary study work was performed (brain ISF and CSF collections).

The microdialysis flow rate was set to 0.5 µL/min utilizing a Harvard CMA 402 micro syringe pump and a 2.5 ml Hamilton syringe. Microdialysis probes (CRL-PP-PE-180-040—1000kDA-manufactured by CRL-Netherlands) were perfused with Hamilton syringes containing artificial CSF (CMA-Ref P000151) and 0.15% BSA (Invitrogen-Ref 15561-020, 50 mg/ml) solution. The solution was filtered using a 0.22 µm filter (Millex GP-Ref SLGP033RB). The probes were connected to the Hamilton syringe with PEEK tubing and the collection tube (Eicom/Richell low protein binding tubes -polypropylene) on wet ice was placed ~30 cm below the head cap. ISF collection was driven by gravity. For the study only one site was used for ISF collection. For three monkeys the same site was used for all the ISF collections days 0–21. For one monkey the same site was used for all ISF collections days 0–10 and then another site was used for days 15 and day 21 due to no patency in the original site. Collection tubes were then placed on dry ice following the 30 min collection. On study days monkeys were chaired and at 8:00 a.m. probes were inserted. A 2 h probe equilibration period was done. Dosing of antibody A at 40 mg/kg IV (cephalic vein-IV bolus over 2.25 min) was performed at 10:00 a.m. on day 0. Monkeys were in the lab on days 0 and 1 for a period of 8 h. For all study days after day 1 when serum, CSF, and brain ISF were collected, monkeys stayed in the lab for a period of 4 h. For all microdialysis sessions the first 2 h were used for probe equilibration and then the brain ISF samples were collected 2 h post-probe insert. For CSF collections the area over the CMP was prepped prior to the microdialysis probe insert utilizing 6 ml Duraprep applicator (Duraprep surgical solutions, #M Health Care). Area was allowed to dry 3 min and a single sterile Huber needle (Access Technologies) was placed and capped with a sterile injection cap. When a study time point was collected and the procedure was done under sterile conditions utilizing sterile gloves. The injection cap was removed and 0.9 ml of CSF was collected and discarded to allow for catheter volume (0.4 ml) plus an additional 0.5 ml waste. Following this a 500 µL study sample was collected and placed immediately on dry ice. The catheter was then locked using 0.4 ml sterile saline flush and the Huber needle was removed. For serum collection monkeys were bled using a butterfly and blood was taken from the saphenous veins. Blood was allowed to sit for 20 min then centrifuged at 10,000 rpm, 20°C for 5 min. A 200 and 300 µL serum sample was placed into a 1.4 ml alphanumeric tubes and immediately placed on dry ice. Feeding regimen for the study entailed on day 0, monkeys were fasted the night prior to dosing. Monkeys were given a Pedialyte 10% solution in study chairs at 2, 26, and 50 h timepoints. Monkeys were fed treats (grapes and bananas) after the 2 h, 26 h post time point in study chairs. Monkeys were fed

again upon return to cages at ~4:00 p.m. full ration on days 0 and 1. Upon return to their cages monkeys were fed a full ration. Enrichment (TV) was provided in the study room after the 4 and 28 h time points for ~1 h.

Bioanalysis

The concentration of Antibody A was measured by a bioanalytical method using an electrochemiluminescence based assay with a lower limit of quantitation (LLOQ) in rhesus monkey serum and CSF of 8.23 ng/ml. Briefly, 96-well flat-bottom Meso-Scale Discovery (MSD) Streptavidin Gold multi-array plates were blocked with 5% bovine serum albumin (BSA) in PBS followed by coating with biotinylated mouse anti-human Ig kappa light chain antibody in Modified ELISA Diluent buffer (MED) (0.5% BSA [wt/v], 0.05% Tween 20 [v/v], 0.25% CHAPS [wt/v], 5 mM EDTA in PBS at pH 7.4). For signal detection a sulfo-tagged mouse anti-human IgG CH2 domain antibody was used. Standards, controls, and sample dilutions followed by detection reagent were added in between sequential wash steps and incubations. Electrochemiluminescence signal proportional to captured Antibody A was captured on an MSD plate reader, Meso Sector S600. Concentrations of Antibody A were derived through comparison to a standard curve (0.41–300 ng/ml range) applying a 4 parameter non-linear regression fit. The method was qualified via assessment of accuracy, precision and dilutional linearity using spiked Antibody A samples serving as high, medium and low controls spanning the calibration curve. Assay run acceptance was determined by recovery of a minimum of 4 out 6 control samples (high, medium, low: tested in duplicates) within 20% of nominal value, as well as visual inspection of calibrator curve readings.

Tau physiologically-based pharmacokinetic-pharmacodynamic model validation in rats, monkey, and human

Three *in vivo* preclinical experimental studies investigating the PK of Antibody A were conducted. A rat microdialysis study was performed to investigate the PK of Antibody A at single IV doses of 10, 50, and 100 mg/kg. Concentrations of Antibody A were measured in serum, CSF, and brain ISF. The PK of Antibody A was then investigated in cynomolgus monkeys at single IV doses of 3, 10, 40, and 80 mg/kg. Only serum concentrations were measured. Lastly, a microdialysis study was conducted in rhesus monkeys at a single IV dose of 40 mg/kg. Concentrations of Antibody A were measured in serum, CSF, and brain ISF. For model validation, *a priori* predictions were performed for each of these experiments and compared to observed data.

Clinical PK-PD data for BIIB092, an N-terminal targeting anti-tau antibody, was obtained from the literature and digitized. PBPK-PD model predictions were generated and overlayed with the observed clinical data of serum PK, CSF PK, and CSF N-terminal tau for three dose levels (150, 700, 2100 mg IV Q4W) over a duration of 3 months. A binding affinity of 0.131 nM was used to predict the change in free N-terminal tau in CSF, which was previously determined using an *in vitro* tau binding assay (Bright et al., 2015).

Tau physiologically-based pharmacokinetic-pharmacodynamic model application to support antibody affinity and half-life optimization

The impact of affinity and half-life on the dynamics of tau concentrations in brain ISF was investigated using simulations from the model. Simulations were performed for four hypothetical antibodies (A1–A4) with varying levels of affinity (0.1, 0.3, 1, 3 nM). Simulations were also performed for four hypothetical antibodies (A1a–A1d) that have the same affinity (Kd = 0.1 nM) and different terminal half-lives (20, 40, 60, 80 days). For both simulation scenarios, each antibody was simulated across a range of doses from 0 to 100 mg/kg and tau occupancy at 8 weeks was calculated. Tau occupancy was calculated as follows:

$$\text{Tau Occupancy } (\%) = \frac{Bound\,Tau}{Total\,Tau} \times 100\% \quad (3)$$

Where bound tau is the amount of antibody tau complex, and total tau is the sum of free tau and antibody tau complex.

Tau physiologically-based pharmacokinetic-pharmacodynamic model application to predict the impact of blood contamination on cerebral spinal fluid samples

To assess the potential impact of blood contamination on Antibody A concentration and tau dynamics in human CSF, the percent error in antibody and tau concentrations were calculated as a function of different levels of blood contamination. Blood contamination was calculated as:

$$C_{CSF\_BC} = C_{CSF} \cdot (1 - F_{BC}) + C_{Serum} \cdot (1 - HCT) \cdot F_{BC} \quad (4)$$

Where, C_{CSF_BC} is the concentration of Antibody A in CSF when accounting for concentration difference due to blood contamination and F_{BC} is the fraction of blood contamination. HCT is the hematocrit, represented as a fraction. C_{CSF} and C_{Serum} are the concentration of antibody in the CSF and serum, respectively. CSF tau occupancy (TO_{CSF}) and CSF tau occupancy when accounting for blood contamination (TO_{CSF_BC}) were calculated as:

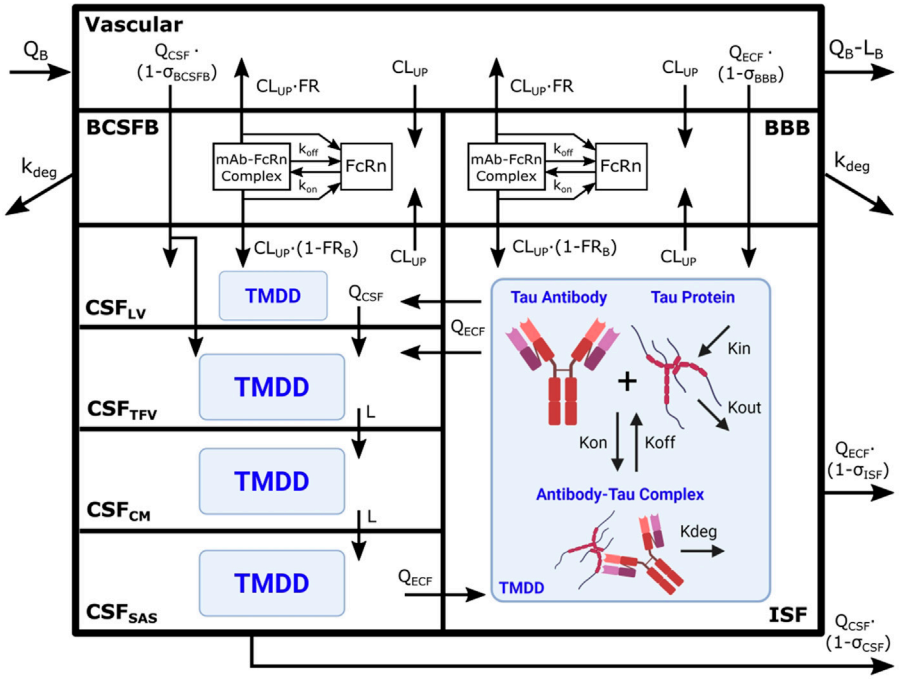

FIGURE 1
Brain PBPK model expanded to include tau dynamics. Tau antibody interactions with tau protein, or target-mediated drug disposition (TMDD), is incorporated in brain ISF and four CSF compartments. The model contains 111 differential equations and 15 tissues, but we are only depicting the brain components of the model for simplicity. Antibody enters the brain vasculature space from the plasma compartment at the brain blood flow rate (Q_B) and leaves at a flow rate of ($Q_B - L_B$). Antibody enters the brain ISF and CSF through paracellular transport across brain barriers, BBB and BCSFB. Paracellular transport across the BBB and BCSFB is governed by brain extracellular fluid (Q_{ECF}) and CSF (Q_{CSF}) flow and brain vasculature reflection coefficients (σ_{BBB} and σ_{BCSFB}). Antibody also enters the brain transcellularly, which is driven by non-specific pinocytosis represented in the model as an uptake clearance (CL_{UP}). Antibody in the endosomal space is able to bind FcRn, form an antibody-FcRn complex, and recycle to the vasculature space or the brain. FR_B is the fraction of antibody that is recycled to the brain vasculature. Unbound antibody in the endosome is subjected to endosomal degradation (k_{deg}). Antibody in the CSF traverses the four CSF compartments at a flow rate of Q_{CSF} or L. The four CSF compartments are lateral ventricle (LV), third-fourth ventricle (TFV), cisterna magna (CM), and subarachnoid space (SAS). Antibody is able to exchange between the brain ISF and CSF compartments via three unidirectional flows from brain ISF to CSF_{LV} and CSF_{TFV} as well as from CSF_{SAS} to brain ISF. Antibody is cleared from the brain via glymphatic clearance, which is governed by brain ISF and CSF flows (Q_{ECF} and Q_{CSF}) and reflection coefficients (σ_{ISF} and σ_{CSF}). Antibody in the brain ISF and CSF binds tau protein to form an antibody-tau complex, where K_{on} and K_{off} are association and dissociation rate constants. Antibody-tau complex degrades at a rate of K_{deg}. Tau protein turnover is governed by production (K_{in}) and elimination (K_{out}) rate constants. Model diagram was created using Inkscape and BioRender.

$$TO_{CSF} = \frac{C_{CSF}}{(C_{CSF} + K_D)} \quad (5)$$

$$TO_{CSF\_BC} = \frac{C_{CSF\_BC}}{(C_{CSF\_BC} + K_D)} \quad (6)$$

Where, K_D is the antibody affinity to tau. The percent error in antibody CSF concentration (PE_{C_CSF}) was calculated as:

$$PE_{C\_CSF} = \frac{|C_{CSF} - C_{CSF_{BC}}|}{C_{CSF}} \cdot 100\,\% \quad (7)$$

The precent error in CSF tau occupancy (PE_{TO_CSF}) was determined using the following equation:

$$PE_{TO\_CSF} = \frac{|TO_{CSF} - TO_{CSF_{BC}}|}{TO_{CSF}} \cdot 100\,\% \quad (8)$$

Figures were generated for PE_{C_CSF} and PE_{TO_CSF} verses a range of F_{BC} (0–10%) to visualize the impact of blood contamination on the error of antibody concentration and target occupancy. The PBPK model was utilized to predict the concentration of antibody in CSF and serum at 1-month post-administration, which were used in the percent error calculations.

Tau physiologically-based pharmacokinetic-pharmacodynamic model application to predict clinical exposure-response

Simulations were performed to predict the PK-PD of Antibody A in humans. Five dose levels (1, 3, 10, 30, 100 mg/kg) and three antibody affinities to tau (0.01, 0.1, 1 nM) were evaluated. The PK-PD profiles for Antibody A concentrations in serum, CSF, and brain ISF and the change in free CSF tau relative to baseline were simulated over 16 weeks.

TABLE 1 PBPK-PD model parameters for tau expression and turnover in humans.

Parameter description	Parameter	Units	Value	References
Baseline tau in CSF	Tau_{0_CSF}	pM	27.0	29566794, 25720406
Baseline tau in brain ISF	Tau_{0_ISF}	pM	68.6	25720406
Baseline ptau in CSF	$pTau_{0\_CSF}$	pM	1.83	29566794, 25720406
Baseline ptau in brain ISF	$pTau_{0\_ISF}$	pM	7.41	25720406
Percent ptau to total tau in CSF	—	%	6.79	25720406
Percent ptau to total tau in ISF	—	%	10.8	25720406
CSF ptau production rate	K_{in_CSF}	fM/h	1.75	29566794, 25720406
Brain ISF ptau production rate	K_{in_ISF}	fM/h	7.06	Assumption
ptau half-life	—	Days	30.7	29566794
ptau elimination rate	K_{out}	1/h	0.000941	29566794
Complex degradation rate	K_{deg}	1/h	0.001	Assumption

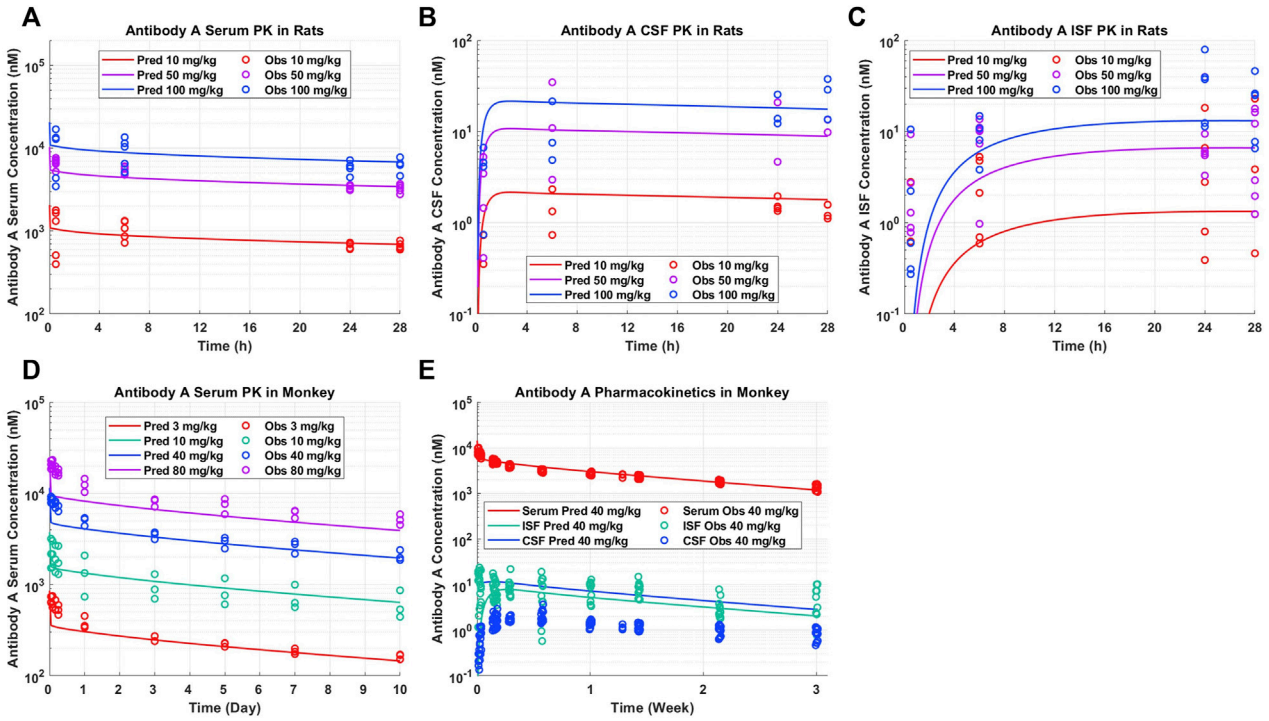

FIGURE 2
Antibody A pharmacokinetics in preclinical species. **(A)** Serum, **(B)** CSF, and **(C)** brain ISF concentrations in rats administered 10, 50, and 100 mg/kg IV. **(D)** Serum concentrations in cynomolgus monkeys administered 3, 10, 40, 80 mg/kg IV. **(E)** Serum, CSF, and brain ISF concentrations in rhesus monkeys administered 40 mg/kg IV. *A priori* model predictions are displayed as solid lines and observed data as circles.

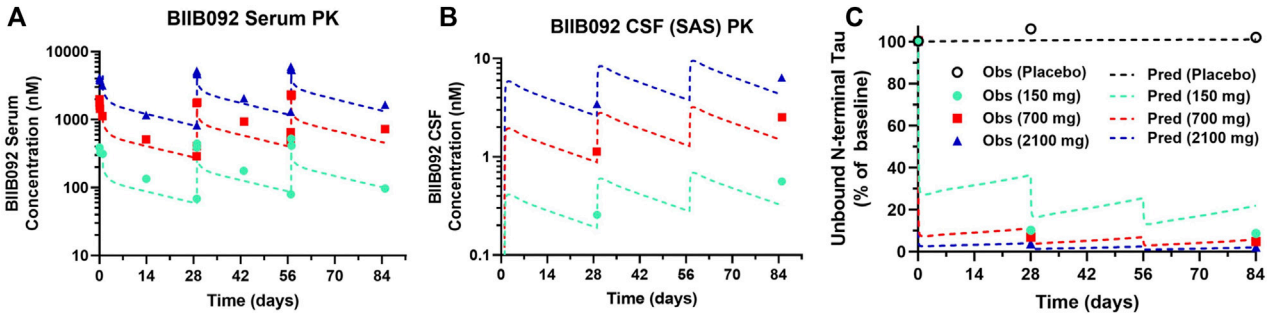

FIGURE 3
PBPK-PD model predictions overlayed with clinical BIIB092 pharmacokinetics and pharmacodynamics data. **(A)** Serum and **(B)** CSF concentrations of BIIB092 and **(C)** unbound N-terminal tau concentrations in CSF (relative to baseline). Three doses of BIIB092, 150, 700, and 2100 mg IV are depicted in cyan, red, and dark blue, respectively. Observed (Obs) data are represented as markers and model predictions (Pred) are represented by dashed lines.

Results

Tau physiologically-based pharmacokinetic-pharmacodynamic model development

The Chang brain PBPK model was expanded to include tau dynamics. The target-mediated effects of tau on the disposition of tau antibodies were incorporated in four CSF compartments and brain ISF (Figure 1). Model parameters for tau related dynamics are in Table 1.

Tau physiologically-based pharmacokinetic-pharmacodynamic model validation in rats, monkey, and human

A priori model simulations were able to adequately describe the pharmacokinetics of Antibody A in preclinical rat and NHP models in serum, CSF, and brain ISF across several dose levels (Figure 2). Antibody A is a humanized monoclonal antibody on an IgG4 backbone that specifically recognizes phosphorylated tau as assessed by ELISA, with a purity of 95% by SEC and SDS-PAGE. The serum concentrations of Antibody A in rats increased in a dose-dependent linear fashion, which was well captured by model predictions (Figure 2A). The CSF concentrations of Antibody A in rats increased in a dose-dependent linear fashion, paralleling serum concentrations, which was also well described by the model (Figure 2B). The brain ISF concentrations of Antibody A in rats increased in a dose-dependent linear fashion (Figure 2C). Model predictions were able to more accurately describe antibody concentrations at later time points and observations suggests that the distribution of the antibody in brain ISF occurs faster than what the model is currently predicting. However, there is a considerable amount of variability with this type of experiment.

The serum PK of Antibody A in cynomolgus monkeys increased in a dose-dependent linear fashion, which was well described by model predictions (Figure 2D). The serum and brain ISF concentrations of Antibody A in rhesus monkeys administered 40 mg/kg IV were well-predicted (Figure 2E). Unexpectedly, we observed a ~10-fold lower exposure in CSF compared to brain ISF. The concentration of antibody in CSF was <0.05% of serum concentrations, which is less than the typical reported average of ~0.1%–0.2% (Wang et al., 2018).

Clinical PK-PD data for BIIB092, an anti-tau antibody, from a phase 1b study in progressive supranuclear palsy (PSP) patients was digitized from the literature (Boxer et al., 2019). Model predictions well captured observed BIIB092 serum (Figure 3A) and CSF (Figure 3B) concentrations. Model predictions well described the decrease in unbound N-terminal tau for the medium (700 mg) and high (2100 mg) doses of BIIB092, but slightly underpredicted the level of target engagement for the lowest dose (150 mg) (Figure 3C).

Tau antibody affinity optimization and half-life extension simulations

The validated PBPK-PD model can be applied to understand the impact of anti-tau antibody affinity optimization and half-life extension on dose regimen. The tau occupancy in brain ISF at 8 weeks after a single IV dose for four theoretical antibodies (A1, A2, A3, A4) with different binding affinities to tau (0.1, 0.3, 1, 3 nM) was simulated across a range of doses (0–100 mg/kg) (Figure 4A). This enabled a quantitative understanding of the impact of antibody affinity on the dose required to effectively engage tau in human brain ISF. We observed that a dose of approximately 15 mg/kg and antibody affinity of 0.1 nM would

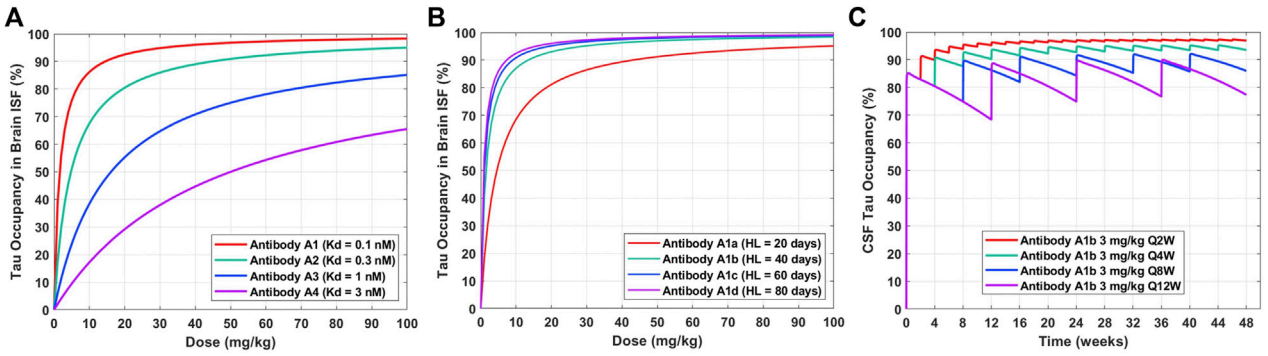

FIGURE 4
Model predictions for the impact of antibody affinity, half-life, and dosing frequency on tau dynamics in humans after a single IV dose. **(A)** Tau occupancy in brain ISF at 8 weeks as a function of dose for four theoretical antibodies (A1–A4) with varying affinities (0.1–3 nM). **(B)** Tau occupancy in brain ISF at 8 weeks as a function of dose for four theoretical antibodies (A1a–A1d) with the same affinity (Kd = 0.1 nM) and varying elimination half-lives (20–80 days). **(C)** CSF tau occupancy as a function of time for Antibody A1b (Kd = 0.1 nM, HL = 40 days) administered at a dose of 3 mg/kg IV for four different dosing frequencies (Q2W, Q4W, Q8W, Q12W).

be required to achieve 90% target occupancy at 2 months post administration (Figure 4A, Antibody A1). An antibody with an affinity of 0.3 nM would require a dose of 50 mg/kg to achieve the same level of occupancy (Figure 4A, Antibody A2). Antibodies with an affinity greater than 1 nM would likely not be clinically viable, due to very large required doses >100 mg/kg for a dosing frequency of every 8 weeks (Figure 4A, Antibody A3 and A4).

Tau occupancy in brain ISF at 8 weeks after a single IV dose for four antibodies (A1a, A1b, A1c, A1d) with the same binding affinity to tau (0.1 nM) and different elimination half-lives (20, 40, 60, 80 days) was simulated across a range of doses (0–100 mg/kg) (Figure 4B). This enabled a quantitative understanding for the impact of half-life on the dose required to effectively engage tau in human brain ISF. We observed that improvements in antibody half-life could significantly reduce the dose required to obtain high levels of tau occupancy in brain ISF (e.g. >90%). For example, a 3-fold increase in half-life (Antibody A1a vs. A1c; 20 vs. 60 days) resulted in a 4.5-fold reduction in the dose required to achieve 90% tau occupancy (45 mg/kg vs. 10 mg/kg). Additionally, our predictions suggest that there is not much of an added benefit between a half-life of 60 days compared to 80 days (Antibody A1c vs. A1d).

To understand how different clinical dosing regimens would impact tau engagement in the CSF, we performed simulations for an anti-tau antibody (Antibody A1b) with an affinity of 0.1 nM and half-life of 40 days (Figure 4C). We predicted the occupancy of tau over 48 weeks in human CSF for 3 mg/kg of Antibody A1b administered IV at four different dosing frequencies every 2 (Q2W), 4 (Q4W), 8 (Q8W), and 12 (Q12W) weeks. Model predictions suggest that a dosing regimen of 3 mg/kg Q4W will achieve >90% CSF tau occupancy after the 3rd dose (week 8) and at steady-state. However, less frequent administrations, Q8W and Q12W, were unable to achieve high levels of target engagement (>90%) in the brain. Simulations of this nature have been valuable for anticipating the level of tau engagement at the site of action for various clinical dosing regimens of interest.

Predictions for the impact of blood contamination on cerebral spinal fluid samples

For neuroscience therapeutics, CSF concentrations are often used as a surrogate for concentrations at the site of action (brain ISF). CSF is typically collected in the clinic via lumbar punctures. However, there is concern of potential blood contamination with this collection methodology. We utilized a quantitative approach to assess the impact of blood contamination on antibody concentrations and tau dynamics in CSF samples (Figure 5). CSF concentrations of Antibody A were calculated for a range of different levels of blood contamination using Eq. 4. Blood contamination in CSF of 0.1, 0.6, and 1.0% results in a percent error in antibody CSF concentrations of 20, 100, and 200%, respectively (Figure 5A). Blood contamination appears to start impacting CSF tau occupancy around 0.1% (Figure 5B). However, the impact on in CSF tau occupancy is dependent upon the dose administered. The percent error in CSF tau occupancy exemplifies this phenomenon, where low doses are more significantly impacted by blood contamination compared to higher doses (Figure 5C). Since CSF antibody concentrations for high doses are already close to saturating target binding, additional antibody exposure from blood does not meaningfully increase target occupancy.

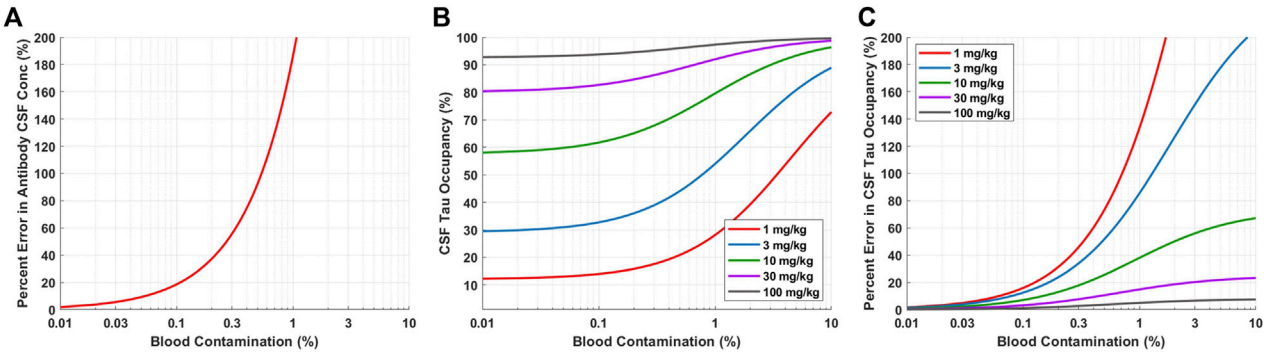

FIGURE 5
Model predictions for impact of blood contamination on antibody concentration and tau occupancy in CSF. **(A)** Predicted percent error in CSF concentration of Antibody A for various levels of blood contamination. **(B)** Predicted CSF tau occupancy for various doses and levels of blood contamination. **(B)** Predicted percent error in CSF tau occupancy for various doses and levels of blood contamination.

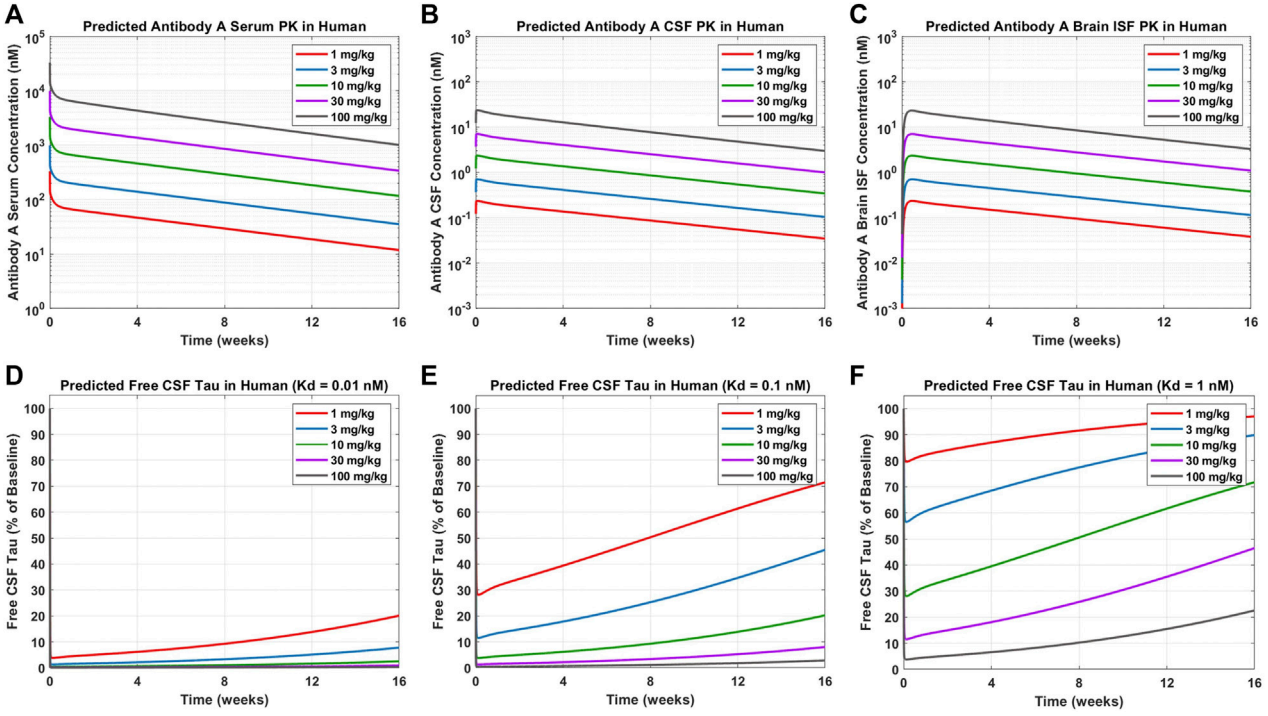

FIGURE 6
Model predictions for Antibody A PK and CSF ptau dynamics in humans. Antibody A concentrations in human **(A)** serum, **(B)** CSF, and **(C)** brain ISF at a single IV dose of 1, 3, 10, 30, 100 mg/kg. The change in free CSF tau is shown for three different scenarios of different antibody affinities to tau: **(D)** 0.01 nM, **(E)** 0.1 nM, and **(F)** 1 nM. Antibody and antibody-target complex elimination half-life was assumed to be approximately 40 days.

Clinical trial predictions for tau antibody pharmacokinetic-pharmacodynamic

Simulations were performed to predict Antibody A concentrations in serum, CSF, and brain ISF as well as tau dynamics in CSF in humans administered a single IV dose of 1, 3, 10, 30, and 100 mg/kg (Figure 6). Antibody A concentration in the brain is approximately three orders of magnitude less than antibody concentrations in serum (Figures 6A–C). The CSF-to-serum ratio for antibody concentration in the model is ~0.3%,

which is in agreement with previously reported clinical observations (Jankovic et al., 2018). Free CSF tau dynamics, depicted as percentage from baseline, were predicted for antibodies with three different affinities (0.01, 0.1, and 1 nM). The antibody with high affinity (0.01 nM), free CSF tau was reduced below 10% across all dose levels for at least 1 month (Figure 6D). The antibody with medium affinity (0.1 nM), free CSF tau was reduced below 10% for three of the dose groups (10, 30, and 100 mg/kg) for at least 1 month (Figure 6E). The antibody with low affinity (1 nM), free CSF tau was reduced below 10% only in the highest dose group (100 mg/kg) for at least 1 month (Figure 6F). These simulations help to inform what doses to select to achieve a desired response and to ensure the characterization of the full pharmacodynamic profile.

Discussion

We have demonstrated the application of PBPK-PD modeling to support various aspects of preclinical and early clinical development of antibody therapeutics for the treatment of Alzheimer's disease and tauopathies. The model was validated using preclinical and clinical data for antibody pharmacokinetics in serum, CSF, and brain ISF as well as clinical data for tau engagement in CSF. *A priori* predictions of antibody PK and tau dynamics in human serum and brain ISF/CSF were useful for understanding relationships between antibody affinity/half-life and target engagement, which may inform first-in-human dose selection and design of phase I clinical trials. We have only reported mean predictions as the level of variability around parameter values is unknown. Clinical population PK-PD data would help to inform inter-individual variability. The mechanistic PBPK approach offers an alternative to allometry for predicting serum exposures, but it's unclear whether a PBPK approach would be more or less predictive than traditional allometric scaling for preclinical-to-clinical translation of drug exposures. A head-to-head comparison between the two different approaches across multiple antibody therapeutics would be valuable.

Blood contamination may occur when collecting CSF via lumbar puncture. Blood contamination could change the concentration of drug and target in the CSF samples, which ultimately may alter the interpretation of target engagement. Therefore, it is crucial to quantitatively understand the level of blood contamination in each sample and perform an adjustment for the concentration of drug in CSF accordingly (Eq. 4). Simulations are able to help guide the selection of a threshold for an acceptable level of blood contamination where adjustments to the concentration of drug in CSF may not be required. For example, setting the acceptable level of blood contamination to <0.1% ensures that the percent error for the concentration of drug in CSF is <20% (Figure 5A). Blood contamination in CSF can determined by the concentration of hemoglobin in CSF relative to serum.

Simplifying assumptions were made throughout the model development process. We describe tau using a single compartment. However, pathological tau is present intra- and extra-cellularly, undergoes complex aggregation processes and post-translational modifications, and spreads throughout the brain in a transneuronal fashion. We have assumed one-to-one binding, where an antibody is able to only bind to a single target. In reality, a single antibody could bind to two targets as well as multiple antibodies could bind to one oligomeric protein aggregate. We used the molecular weight of monomeric protein for conversions to molar units. Although this approach accounts for multiple antibodies binding to oligomeric tau, it makes the assumption that antibodies are able to bind to all tau monomers within an oligomer. This may not be appropriate as tau proteins within an oligomer could create steric hinderance by shielding the antibody binding site of other tau proteins. However, from a modeling perspective, its not entirely clear on how the molecular weight for aggregated proteins with multiple binding sites should be best considered, especially when working with protein aggregates of variable sizes. We assumed static target-mediated drug disposition (TMDD), where TMDD processes occur independently in each brain compartment. In other words, there is no distribution of target or antibody-target complex between brain compartments. A dynamic TMDD model would include additional kinetic processes, such as endosomal uptake/escape, FcRn binding, and paracellular transport of the target and antibody-target complex.

The publicly available clinical data assessing the engagement of tau-antibodies in human CSF is currently only in PSP patients (Boxer et al., 2019). Considering the differences in tau biology between PSP and AD, data from AD patients is required for further model validation. The current parameterization of the model (tau abundance and turnover) represents a cognitively normal to early AD population. The change in free tau was not sensitive to changes in tau concentration and turnover within patho-physiologically reported ranges, which may be reflective of the very low concentrations of target (~ pM). However, different parameterizations of the model should be made depending upon the patient population and tau therapy of interest, which could improve the accuracy of predictions across different stages of Alzheimer's disease. Sato et al. (2018) is the only paper to our knowledge that has measured the turnover rate of tau in humans (~30 days). There are additional papers that have measured CSF tau concentrations in Alzheimer's disease. Andreasen et al. (1998) reported CSF tau concentrations in AD patients, which ranged from 5 to 33 p.m.. Riemenschneider et al. investigated CSF tau concentrations in AD and mild cognitive impairment (MCI) subjects, which ranged from ~2 p.m. in age-matched controls to ~10 p.m. in AD/MCI subjects (Riemenschneider et al., 2002). Overall, CSF tau concentrations across healthy

elderly and AD patients appear to range between single to double digit picomolar and are comparable to the CSF tau concentration used in Table 1 (27 p.m.). The concentration of tau in brain ISF is more challenging to obtain as this value is typically obtained through brain microdialysis studies. Relationships could be explored between predicted changes in free brain ISF tau and data from longitudinal tau PET imaging studies.

As more data begins to emerge from clinical trials investigating tau-targeted therapies in AD patients (Congdon and Sigurdsson, 2018; Ayalon et al., 2021), a QSP model platform could be developed for tau pathology in AD or an existing model could be expanded. For example, Madrasi et al. in 2020 developed an AD QSP model for amyloid-targeted therapies (Madrasi et al., 2021), which could be expanded to include tau biology. There are many complexities of tau biology that could be considered in future model development, such as detail on tau aggregation kinetics, tau isoforms and post-translational modifications, spatial localization, and various routes of tau spreading. Some of these features have been included in QSP models of tau pathology (Karelina et al., 2021). Systems models could include FcγR and clearance through microglial phagocytosis, depending on the effector function status of tau antibodies, as well as other neuroimmunological components. Data for tau peptide concentrations in clinical CSF samples from patients with neurodegenerative disease could be used to understand engagement toward different tau peptides and isoforms (Barthelemy et al., 2016). However, more detail on the exact concentration of tau fragments would be required. Tau seeding and spreading kinetics has been shown to be dependent upon differences in tau protein conformation and post-translational modifications, such as high molecular weight forms of soluble tau and the extent/site of phosphorylation (Dujardin et al., 2020). Differences in tau seeding propensity has been able to partially explain inter-individual differences in the rate of clinical neurodegenerative disease progression (Dujardin et al., 2020). Developing a mechanistic quantitative model that captures the complexities of tau pathology could help towards understanding clinical heterogeneity in disease progression and treatment response.

Conclusion

Our work exemplifies the utility of PBPK-PD modeling to address challenges faced in preclinical development and clinical translation of anti-tau antibody therapeutics for the treatment of Alzheimer's disease. This modeling approach provides a foundation that can be further expanded to incorporate additional complexities of tau biology. This tau PBPK-PD model can also be refined as clinical data emerges to inform late stages of clinical development. However, the size of this platform model may limit its applicability. Minimal PBPK models of the brain provide a framework that can be more easily adapted to incorporate targets of interest and integrated with quantitative systems pharmacology models of neurological diseases.

Data availability statement

The raw data supporting the conclusions of this article will be made available by the authors, without undue reservation.

Ethics statement

The animal study was reviewed and approved by Institutional Animal Care and Use Committee.

Author contributions

PB contributed to the conception, design, analysis, authoring, and revision of Ethe manuscript. DB-Y, JS, and KY contributed to the design and revision. SG, BS, SA, MJ, and GA contributed to the experimental design and conduction. All authors contributed to manuscript revision, read, and approved the submitted version.

Acknowledgments

We would like to acknowledge the University of Buffalo, the Center for Protein Therapeutics, and the lab of Dhaval Shah for their kindness in sharing model code from Chang et al., 2019.

Conflict of interest

Authors PB, DB-Y, JS, SG, BS, SA, MJ, GA, and KY were employed by Merck & Co., Inc.

Publisher's note

References

Alzheimer's, A. (2016). Alzheimer's disease facts and figures. *Alzheimers Dement.* 12, 459–509. doi:10.1016/j.jalz.2016.03.001

Andreasen, N., Vanmechelen, E., Van De Voorde, A., Davidsson, P., Hesse, C., Tarvonen, S., et al. (1998). Cerebrospinal fluid tau protein as a biochemical marker for Alzheimer's disease: a community based follow up study. *J. Neurol. Neurosurg. Psychiatry* 64, 298–305. doi:10.1136/jnnp.64.3.298

Ayalon, G., Lee, S. H., Adolfsson, O., Foo-Atkins, C., Atwal, J. K., Blendstrup, M., et al. (2021). Antibody semorinemab reduces tau pathology in a transgenic mouse model and engages tau in patients with Alzheimer's disease. *Sci. Transl. Med.* 13, eabb2639. doi:10.1126/scitranslmed.abb2639

Barthelemy, N. R., Gabelle, A., Hirtz, C., Fenaille, F., Sergeant, N., Schraen-Maschke, S., et al. (2016). Differential mass spectrometry profiles of tau protein in the cerebrospinal fluid of patients with alzheimer's disease, progressive supranuclear palsy, and dementia with lewy bodies. *J. Alzheimers Dis.* 51, 1033–1043. doi:10.3233/JAD-150962

Bloomingdale, P., Bakshi, S., Maass, C., Van Maanen, E., Pichardo-Almarza, C., Yadav, D. B., et al. (2021). Minimal brain PBPK model to support the preclinical and clinical development of antibody therapeutics for CNS diseases. *J. Pharmacokinet. Pharmacodyn.* 48, 861–871. doi:10.1007/s10928-021-09776-7

Boxer, A. L., Qureshi, I., Ahlijanian, M., Grundman, M., Golbe, L. I., Litvan, I., et al. (2019). Safety of the tau-directed monoclonal antibody BIIB092 in progressive supranuclear palsy: a randomised, placebo-controlled, multiple ascending dose phase 1b trial. *Lancet. Neurol.* 18, 549–558. doi:10.1016/S1474-4422(19)30139-5

Bright, J., Hussain, S., Dang, V., Wright, S., Cooper, B., Byun, T., et al. (2015). Human secreted tau increases amyloid-beta production. *Neurobiol. Aging* 36, 693–709. doi:10.1016/j.neurobiolaging.2014.09.007

Chang, H.-Y., Wu, S., Meno-Tetang, G., and Shah, D. K. (2019). A translational platform PBPK model for antibody disposition in the brain. *J. Pharmacokinet. Pharmacodyn.* 46, 319–338. doi:10.1007/s10928-019-09641-8

Collaborators, G. B. D. N. (2019). Global, regional, and national burden of neurological disorders, 1990-2016: a systematic analysis for the global burden of disease study 2016. *Lancet. Neurol.* 18, 459–480. doi:10.1016/S1474-4422(18)30499-X

Congdon, E. E., and Sigurdsson, E. M. (2018). Tau-targeting therapies for Alzheimer disease. *Nat. Rev. Neurol.* 14, 399–415. doi:10.1038/s41582-018-0013-z

Dujardin, S., Commins, C., Lathuiliere, A., Beerepoot, P., Fernandes, A. R., Kamath, T. V., et al. (2020). Tau molecular diversity contributes to clinical heterogeneity in Alzheimer's disease. *Nat. Med.* 26, 1256–1263. doi:10.1038/s41591-020-0938-9

Gerlowski, L. E., and Jain, R. K. (1983). Physiologically based pharmacokinetic modeling: Principles and applications. *J. Pharm. Sci.* 72, 1103–1127. doi:10.1002/jps.2600721003

Gilberto, D. B., Michener, M. S., Smith, B. E., Szczerba, P. J., Holahan, M. A., Gray, T. L., et al. (2021). Chronic collection of cerebrospinal fluid from rhesus macaques (*Macaca mulatta*) with cisterna magna ports: Update on refinements. *Comp. Med.* 72, 45–49. doi:10.30802/AALAS-CM-21-000060

Hardy, J. A., and Higgins, G. A. (1992). Alzheimer's disease: the amyloid cascade hypothesis. *Science* 256, 184–185. doi:10.1126/science.1566067

Herukka, S. K., Rummukainen, J., Ihalainen, J., Koivisto, A. M., Nerg, O., Puli, L. K., et al. (2015). Amyloid-beta and tau dynamics in human brain interstitial fluid in patients with suspected normal pressure hydrocephalus. *J. Alzheimers Dis.* 46, 261–269. doi:10.3233/JAD-142862(

Jankovic, J., Goodman, I., Safirstein, B., Marmon, T. K., Schenk, D. B., Koller, M., et al. (2018). Safety and tolerability of multiple ascending doses of PRX002/RG7935, an anti-alpha-synuclein monoclonal antibody, in patients with Parkinson disease: A randomized clinical trial. *JAMA Neurol.* 75, 1206–1214. doi:10.1001/jamaneurol.2018.1487

Karelina, T., Lerner, S., Stepanov, A., Meerson, M., and Demin, O. (2021). Monoclonal antibody therapy efficacy can be boosted by combinations with other treatments: Predictions using an integrated Alzheimer's Disease Platform. *CPT. Pharmacometrics Syst. Pharmacol.* 10, 543–550. doi:10.1002/psp4.12628

Knopman, D. S., Jones, D. T., and Greicius, M. D. (2021). Failure to demonstrate efficacy of aducanumab: An analysis of the EMERGE and ENGAGE trials as reported by Biogen, December 2019. *Alzheimers Dement.* 17, 696–701. doi:10.1002/alz.12213

Madrasi, K., Das, R., Mohmmadabdul, H., Lin, L., Hyman, B. T., Lauffenburger, D. A., et al. (2021). Systematic *in silico* analysis of clinically tested drugs for reducing amyloid-beta plaque accumulation in Alzheimer's disease. *Alzheimers Dement.* 17, 1487–1498. doi:10.1002/alz.12312

Monine, M., Norris, D., Wang, Y., and Nestorov, I. (2021). A physiologically-based pharmacokinetic model to describe antisense oligonucleotide distribution after intrathecal administration. *J. Pharmacokinet. Pharmacodyn.* 48, 639–654. doi:10.1007/s10928-021-09761-0

Panza, F., Lozupone, M., Logroscino, G., and Imbimbo, B. P. (2019). A critical appraisal of amyloid-β-targeting therapies for Alzheimer disease. *Nat. Rev. Neurol.* 15, 73–88. doi:10.1038/s41582-018-0116-6

Riemenschneider, M., Lautenschlager, N., Wagenpfeil, S., Diehl, J., Drzezga, A., and Kurz, A. (2002). Cerebrospinal fluid tau and β-amyloid 42 proteins identify Alzheimer disease in subjects with mild cognitive impairment. *Arch. Neurol.* 59, 1729–1734. doi:10.1001/archneur.59.11.1729

Saleh, M. A., Loo, C. F., Elassaiss-Schaap, J., and De Lange, E. C. (2021). Lumbar cerebrospinal fluid-to-Brain extracellular fluid surrogacy is context-specific: Insights from LeiCNS-PK3. 0 simulations. *J. Pharmacokinet. Pharmacodyn.* 48, 725–741. doi:10.1007/s10928-021-09768-7

Sato, C., Barthélemy, N. R., Mawuenyega, K. G., Patterson, B. W., Gordon, B. A., Jockel-Balsarotti, J., et al. (2018). Tau kinetics in neurons and the human central nervous system. *Neuron* 97, 1284–1298. doi:10.1016/j.neuron.2018.02.015

Schneider, L. (2020). A resurrection of aducanumab for Alzheimer's disease. *Lancet. Neurol.* 19, 111–112. doi:10.1016/S1474-4422(19)30480-6

Shah, D. K., and Betts, A. M. (2012). Towards a platform PBPK model to characterize the plasma and tissue disposition of monoclonal antibodies in preclinical species and human. *J. Pharmacokinet. Pharmacodyn.* 39, 67–86. doi:10.1007/s10928-011-9232-2

Shulman, M., Rajagovindan, R., Kong, J., O'gorman, J., Viollet, L., Huang, E., et al. (2021). Abstract (LBR05): Symposia, conferences, oral communications: 14th clinical trials on alzheimer's disease (CTAD) november 9-12, 2021. *J. Prev. Alzheimers Dis.* 8, S2–S72.doi:10.14283/jpad.2021.57

Sorger, P. K., Allerheiligen, S. R., Abernethy, D. R., Altman, R. B., Brouwer, K. L., Califano, A., et al. (2011). "Quantitative and systems pharmacology in the post-genomic era: new approaches to discovering drugs and understanding therapeutic mechanisms," in *An NIH white paper by the QSP workshop group* (Bethesda Bethesda, MD: NIH), 1–47.

Wang, Q., Delva, L., Weinreb, P. H., Pepinsky, R. B., Graham, D., Veizaj, E., et al. (2018). Monoclonal antibody exposure in rat and cynomolgus monkey cerebrospinal fluid following systemic administration. *Fluids Barriers CNS* 15, 10. doi:10.1186/s12987-018-0093-6

Frontiers in Pharmacology

Explores the interactions between chemicals and living beings

The most cited journal in its field, which advances access to pharmacological discoveries to prevent and treat human disease.

Discover the latest Research Topics

See more →

Frontiers

Avenue du Tribunal-Fédéral 34
1005 Lausanne, Switzerland
frontiersin.org

Contact us

+41 (0)21 510 17 00
frontiersin.org/about/contact